NEGATIVE THERMAL EXPANSION, BEHAVIOR ON COMPRESSION, AND OTHER ANOMALOUS PROPERTIES IN RHENIUM TRIOXIDE STRUCTURED MIXED METAL FLUORIDES

A Dissertation
Presented to
The Academic Faculty

By

Brett Robert Hester

In Partial Fulfillment
of the Requirements for the Degree
Doctor of Philosophy in Chemistry

Georgia Institute of Technology

May 2019

NEGATIVE THERMAL EXPANSION, BEHAVIOR ON COMPRESSION, AND OTHER ANOMALOUS PROPERTIES IN RHENIUM TRIOXIDE STRUCTURED MIXED METAL FLUORIDES

Approved by:

Dr. Angus P. Wilkinson, Advisor
School of Chemistry and Biochemistry
School of Materials Science and Engineering
Georgia Institute of Technology

Dr. Younan Xia
School of Chemistry and Biochemistry
School of Biomedical Engineering
Georgia Institute of Technology

Dr. Joseph Sadighi
School of Chemistry and Biochemistry
Georgia Institute of Technology

Dr. David Sholl
School of Chemical and Biomelcular Engineering
Georgia Institute of Technology

Dr. Z. John Zhang
School of Chemistry and Biochemistry
Georgia Institute of Technology

Date Approved: January 16, 2019

Dedicated to my wife, Ginni Reaves,

my parents, John and Patti,

and all my other family and friends

ACKNOWLEDGEMENTS

I could not have completed the work presented in this dissertation without my family. I would like to thank my parents, John and Patti Hester, for all their love and support. They taught me that kindness to others, love for your friends and family, strong faith, and a good sense of humor will take you a long way to a happy life. They always encouraged my interest in science, wanted me to dream big, afforded me every opportunity to pursue those dreams, and instilled in me the importance of an education as well as a respect for those who educate. I would also like to thank my twin sister Rachel and my brother Zack who always pushed me to be a better person and were there to share a laugh growing up. My siblings and my wonderful new sister-in-law Kylie have supported me through this graduate school process with love and interest in my work and wellbeing. I would like to thank my late grandparents (Frank and Myrtle Hester, G.W. and Jeanette Tuten) for all the cherished memories, their love, and all they did for my parents. I would also like to thank my aunts, uncles, and cousins who have always been there for me.

Furthermore, I could never have achieved this doctorate without my wife, Ginni Reaves McMillan Hester. My beautiful high school sweetheart has stood by me for 10 years, and I could never adequately articulate how much her love and support have meant to me. She was there to laugh and celebrate during the good times, and to empathize and encourage during the difficult times. She kept me on track and focused even while working on her own graduate degree. I can't thank her enough for the love she gives me and the joy she brings to my life. I would also like to thank my amazing in-laws George and Cindy McMillan. They have loved and supported me like a son. They have provided an example of the importance of faith and family. They have supported me even through their own

personal tragedy and loss. I am extremely grateful for all they have done and continue to do for me. I would also like thank my sister-in-law Brittney, her husband Bradley, and my nephew Wade. They have accepted me as part of their family and shown me lots of love and support through the years. I would also like to thank my wife's grandmothers (Mama Mac and Mema), aunts, uncles, and cousins who have all been so wonderful and supportive of me.

I have been blessed with many great friends. My high school was very small, but I had lots of great classmates. In particular my friends Austin Williams, Jamie Estes, Kevin Thomas, and Will Jones provided lots of laughs and shenanigans to help make high school enjoyable. I made lots of great friends while at Clemson, including Lauren Culler, Amanda Bethea, Player Aston, Lauren and Weston Ford, Ali James, Eric Drew, Robert Bonner, and many members of Lambda Chi Alpha fraternity, who have all continued to support me. I was lucky to make several great friends through my wife including Lauren Crapps, Tara Watters, Jackie Griffo, Allie Pedigo, Nicole Snoad, and Marcie Gettys. I was fortunate to meet lots of great people at Georgia Tech and in Atlanta such as Mark Cannatelli, Alyssa Blake, Gorman Stock (twitch.tv/mukfather), Brandon Bakr, Taylor Allen, Kevin Benham, Brian Schmatz, Brenny Olsen, Aman Mullee, and the members of the Atalanta Kookaburras Australian Rules Football team. I would like to thank my friends the BS Boys (Hunter Allen, John Epps, Kevin Thomas, Tim Levi, and Phil Bethea), the Midnight Ramblers (Ben Kaplan, Dipesh Kanal, Joe Richardson, Paul Balding, and Will Chamlee), and their wives/significant others (Kim Allen, Haley Freeman, Patricia Cantrell, Lindsey Raynor, Cassidy Bracewell, and Kristen Gee) for all their support. I would also like to thank Loid Atkinson who has been a great friend, has always looked out for me, and is like

family. It can be difficult to find good friends, and I am very blessed and thankful to have so many.

I would like to thank the teachers and staff at Pee Dee Academy who did an amazing job preparing me for college and graduate school. They do a wonderful and often thankless job of educating students like me in rural South Carolina and giving them opportunities to have successful and happy futures. Similarly, I would like to thank the professors and staff of Clemson University for my undergraduate education. My undergraduate research advisor Dr. Hwu and my Inorganic chemistry professor Dr. Kolis both played important roles in my decision to pursue a graduate degree in inorganic chemistry. Clemson has been and will always be an important part of my life.

In graduate school, I was very fortunate to have Dr. Angus Wilkinson, as my Ph. D. advisor. Dr. Wilkinson has far exceeded all my expectations as a mentor and advisor. He was able to push me to work hard, while still allowing me to have a work/life balance. Dr. Wilkinson taught me what it means to conduct quality scientific research, and how to present the results of that work. He has an amazing level of patience, organization, foresight, and knowledge, and he puts the wellbeing and happiness of his students above all else. We spent quite a lot of time together on trips to collect data, planning research goals, analyzing results, and writing manuscripts, and I am very proud of the work we have done together and present in this dissertation. I have nothing but respect and admiration for Dr. Wilkinson and coming to Georgia Tech and working for him was one the best decisions I have ever made.

I have also been fortunate to work with and befriend several other students at Georgia Tech. Dr. Cody Morelock and Dr. Leighanne Gallington were members of the Wilkinson Group when I first started who mentored and helped me immensely. Justin Hancock was an undergraduate my first year in the group who also helped teach me, and whose work served as a starting point for my research. My good friend Ben Kaplan also worked in the group, conducted experiments, and assisted on trips with me before completing his masters. I enjoyed helping mentor and working with two visiting undergraduate students, Daniel Stewart and Joshua Adkins. I am also very thankful that I got to train, mentor, and work closely with a few Georgia Tech undergraduates. I did a lot of great work with John Ticknor over the course of a few years, which I am very proud of. More recently I worked with Breaunna Wright, Eric Masterson, Katherina Loske, and Maria Furukawa. I am thankful for their enthusiasm, patience, and support of my work. I would also like to thank Anthony Lloyd and Samuel Baxter, two graduate students who joined the group in the years after me. They have been great coworkers and friends. They helped me immensely along the way and made being in the Wilkinson group a great experience. I'd also like to thank the most recent graduate student to join the group, Shangye Ma, for his support in the home stretch of my work. I am very grateful to all of these students for all their assistance, and I wish them nothing but the best going forward.

I would also like to acknowledge and thank my thesis committee members: Dr. Joseph Sadighi, Dr. David Sholl, Dr. Younan Xia, and Dr. Z. John Zhang. I am very grateful for all of their time and input through every step of this process. I would also like to thank John Bacsa, Vic Summey, Kenyetta Johnson, Monica Branch, Richard Bedell,

Chris Wright, and Brian Markowicz for their assistance and expertise they provided me at Georgia Tech.

Most of the data presented in this dissertation was collected at government laboratories. I was able to take many trips to Argonne National Laboratory in Chicago, IL to utilize the Advanced Photon Source. I would like to thank Dr. Greg Hlader, Dr. Andrey Yakovenko, and Dr. Wenqian Xu for their help at 17-BM, Dr. Karena Chapman, Dr. Olaf Borkiewicz, Dr. Kevin Beyer for their help at 11-ID-B, Dr. Saul Lapidus and Dr. Lynn Ribaud for their help at 11-BM, Dr. Vitali Prakapenka, Dr. Sergey Tkachev, and Dr. Eran Greenberg for their help at GSE CARS of sector 13, and Rick Spence for all of his help at sector 11. I also was fortunate to get to spend time doing experiments at Oak Ridge National Laboratory's Spallation Neutron Source. I would like to acknowledge Dr. Ashfia Huq and Dr. Pamela Whitfield for their assistance at POWGEN, Dr. Antonio dos Santos and Dr. Jamie Molaison for their assistance at SNAP, and Matt Rucker and Mark Loguillo and the entire SNS sample environment team for all their help. All of these great people along with the various staff at both the APS and SNS were wonderful to work with and invaluable to the results reported in this dissertation.

I would like to acknowledge the funding for this work was provided by the National Science Foundation grant DMR-1607316 and the Department of Education's Graduate Assistance in Areas of National Need (GAANN) fellowship. The Advanced Photon Source is a U. S. Department of Energy (DOE) Office of Science User Facility operated for the DOE Office of Science by Argonne National Laboratory under contract No. DE-AC02-06CH11357, and the Spallation Neutron Source is a DOE office of Science User Facility operated by the Oak Ridge National Laboratory.

Table of Contents

LIST OF TABLES

LIST OF FIGURES

LIST OF SYMBOLS AND ABBREVIATIONS

ADP	Atomic Displacement Parameter
BM	Birch-Murnaghan (Type of EoS)
BRIM	Background Reducing Internal Mask
CTE	Coefficient of Thermal Expansion (Plural CTEs)
DAC	Diamond Anvil Cell
EN	Electronegativity
EOS	Equation of State
EXPGUI	Graphical User Interface for GSAS
GSAS	General Structure Analysis System
GSAS-II	General Structure Analysis System II
GSECARS	GioSoilEnviro Center for Advanced Radiation Sources
IR	Infrared
MOF	Metal Organic Framework
NLC	Non-Linear Compressibility
NTE	Negative Thermal Expansion
PDF	Pair Distribution Function
PIA	Pressure-Induced Amorphization
PIS	Pressure-Induced Softening
PTE	Positive Thermal Expansion
RUM	Rigid Unit Mode
UV	Ultraviolet
ZTE	Zero Thermal Expansion

SUMMARY

Mixed metal fluorides can adopt a cubic ReO_3-type framework, which consists of a simple network of metal-centered octahedra corner-linked with fluorides. The transverse motion of the bridging fluorine atoms and the coupled rotation of the rigid octahedra can lead to negative thermal expansion (NTE). However, only a few mixed metal fluorides have been previously shown to exhibit NTE, and chemical composition and the application of pressure are believed to affect their thermal expansion properties. This thesis examines the thermal expansion and response to pressure of several mixed metal fluorides ($M^{2+}M^{4+}F_6$), through the use of variable-temperature/pressure x-ray and neutron diffraction. New NTE materials were identified and a greater understanding of the relationship between chemical composition, thermal expansion, and response to pressure was established. Other anomalous behaviors were seen such as pressure-induced softening and porosity to guest species. The effect of the introducing excess fluoride into the crystal structure was also examined.

The phase behavior, thermal expansion properties, and response to pressure of $CaNbF_6$, $MgZrF_6$, and $MgNbF_6$ were characterized and compared against the previously reported behavior of $CaZrF_6$ in Chapter 2. Similar to $CaZrF_6$, $CaNbF_6$ retains a cubic ReO_3-type structure down to 10 K and displays NTE up until at least 900 K. The NTE is very strong, reaching a minimum volumetric CTE of -65 ppm K^{-1} at 70 K. On compression at room temperature, $CaNbF_6$ undergoes a reconstructive phase transition at ~0.4 GPa and pressure-induced amorphization above ~4.0 GPa. The cubic phase was found to have a bulk modulus of 33.7(4) GPa with strong pressure-induced softening (K_0'= -23(2)).

$MgZrF_6$ adopts a cubic structure at 300 K and undergoes a symmetry-lowering phase transition involving octahedral tilts at ~100 K. Immediately above this transition, it shows modest NTE. Its thermal expansion increases on heating, crossing through zero at ~500 K. Below ~100 K, the rhombohedral phase shows strong anisotropic positive thermal expansion (PTE). Unlike $CaNbF_6$ and $CaZrF_6$, cubic $MgZrF_6$ undergoes an octahedral tilting transition consistent with the adoption of rhombohedral symmetry at ~0.37 GPa prior to a reconstructive transition at ~1.0 GPa. The cubic phase was found to be stiffer than $CaNbF_6$, but still relatively soft, K_0= 48.2(5) GPa, and showed stiffening on heating. Very large pressure-induced softening was also seen with K_0'= -53(2). On cooling, cubic $MgNbF_6$ undergoes a symmetry lowering octahedral tilting transition to a rhombohedral phase at ~280 K. It does not display NTE within the investigated temperature range (100-950 K), with a minimum CTE of α_v ~4 ppm K^{-1} at 495 K. Although the replacement of Zr(IV) by Nb(IV) leads to minor changes in phase behavior and properties, the replacement of calcium by the smaller and more polarizing magnesium leads to large changes in both phase behavior and thermal expansion.

The effects of a larger change in cation size and higher electronegativity of the M^{4+} species was seen in the analysis of the thermal expansion and response to pressure of $CaTiF_6$, Chapter 3. Similar to the results seen when substituting Mg for Ca, Ti^{4+} destabilizes the cubic structure on cooling, with $CaTiF_6$ undergoing a cubic to rhombohedral transition at ~120 K. However, the cubic material was still found to show strong NTE. It has a minimum volume CTE of ~-42 ppm K^{-1} at 180 K and a CTE of ~-32 ppm K^{-1} at room temperature. On compression at ambient temperature, the material remains cubic to ~0.25 GPa with K_0 = 29(1) GPa and K'_0 = −50(5). Cubic $CaTiF_6$ is

elastically softer and shows more pronounced pressure-induced softening than both $CaZrF_6$ and $CaNbF_6$. In sharp contrast to both $CaZrF_6$ and $CaNbF_6$, $CaTiF_6$ undergoes a first-order pressure-induced octahedral tilting transition to a rhombohedral phase on compression above 0.25 GPa. Just above the transition pressure, this phase is elastically very soft with a bulk modulus of only ~4 GPa as octahedral tilting associated with a reduction in the Ca–F–Ti angles provides a low energy pathway for volume reduction. This volume reduction mechanism leads to highly anisotropic elastic properties, with the rhombohedral phase displaying both a low bulk modulus and negative linear compressibility parallel to the crystallographic *c*-axis for pressures below ~2.5 GPa. At ~3 GPa, a further transition to a poorly ordered phase occurs.

While $MnNbF_6$ and $ZnNbF_6$ are not cubic at ambient conditions, analysis of their thermal expansion behavior and response to pressure, Chapter 4, helps to further the understanding of the effects chemical substitution has on these properties. On warming to just above room temperature, a phase transition from rhombohedral to cubic is seen for $MnNbF_6$ at ~315 K. The cubic phase displays PTE just above 315 K, zero thermal expansion (ZTE) around 380 K, and NTE at higher temperatures (α_v ~-8 ppm K^{-1} at 457 K). $ZnNbF_6$ is rhombohedral over the entire temperature range examined (~100-500 K). Both $ZnNbF_6$ and $MnNbF_6$ show strong anisotropic PTE when rhombohedral. When examining their response to pressure, $MnNbF_6$ became completely rhombohedral on initial compression and transformed to an unidentified phase at ~6 GPa. Rhombohedral $MnNbF_6$ is initially elastically very soft (K_0 ~5 GPa) but stiffens considerably on compression. Below ~3.5 GPa it displays negative linear compressibility. $ZnNbF_6$ remained rhombohedral over the entire pressure range examined (0 – 4 GPa) and displayed a similar

softness, stiffening on compression, and negative linear compressibility, which is consistent with the reported behavior on compression of other rhombohedral metal fluorides.

After exploring the effect of cation substitution on the thermal expansion and response to pressure in $M^{2+}M^{4+}F_6$, more complex composition changes were also explored. In particular, cubic ReO_3-related compositions $Ca[Zr^{(IV)}_{1-x}Nb^{(V)}_x]F_{6+x}$ with x = 0.25, 0.50 and 0.75 were prepared and examined to investigate the effect of incorporating excess fluoride, Chapter 5. Density measurements indicate that the excess fluoride is incorporated into the structure as interstitials. X-ray total scattering data show no major differences in local structure between the samples, which suggests that the interstitial fluoride is incorporated in a fashion distinct from that previously reported for other fluoride excess materials such as cubic $YbZrF_7$, $Ti^{2+}_xTi^{3+}_{1-x}ZrF_{7-x}$, and $Mg_{2-x}Zr_xF_{4+2x}$. In these later materials, the conversion of corner sharing to edge sharing polyhedra was proposed as the mechanism for interstitial fluoride incorporation. The thermal expansion of $Ca[Zr^{(IV)}_{1-x}Nb^{(V)}_x]F_{6+x}$ changes with composition, but it remains strongly negative and strongly dependent on thermal history indicating that the defects introduced by incorporating niobium (V) in place of zirconium (IV) are mobile at low temperatures. On compression, the x = 0.25, 0.50 and 0.75 samples all underwent crystalline to crystalline phase transitions at low pressure (< 0.8 GPa). The x= 0.25 sample showed a transition like that reported for $CaNbF_6$, whereas the x = 0.5 and 0.75 samples displayed transitions to a rhombohedral phase similar to that seen on compressing $MgZrF_6$. All the cubic $Ca[Zr^{(IV)}_{1-x}Nb^{(V)}_x]F_{6+x}$ samples had zero pressure bulk moduli close to ~40 GPa and displayed pronounced pressure-induced softening.

While exploring the response to pressure of these mixed metal fluorides, it was discovered that $CaZrF_6$ was porous to helium at 300 K, Chapter 6. These experiments showed that $CaZrF_6$ behaves as a molecular sieve with helium, but not nitrogen, able to penetrate the material. The insertion of helium at high pressures leads to the formation of a defect perovskite, $(He_{2-x}\square_x)(CaZr)F_6$. Due to the temperature dependence of the porosity, the defect perovskite can be recovered to ambient pressure and low temperatures. There are no prior examples of perovskites with noble gases on the A-sites. The insertion of helium gas into $CaZrF_6$ both elastically stiffens the material and reduces the magnitude of its negative thermal expansion. It also suppresses the onset of structural disorder, which is seen on compression in other media. Measurements of the gas released on warming to room temperature and Rietveld analyses of neutron diffraction data at low temperature indicate that exposure to helium gas at 500 MPa and 300 K leads to a stoichiometry close to $(He_1\square_1)(CaZr)F_6$.

The initial results on incorporating helium into $CaZrF_6$ represent a significant extension in perovskite chemistry, and a new set of physical properties to be explored for mixed metal fluorides. Therefore, further studies were done to explore the formation and properties of gas containing perovskites at higher pressures using helium and neon media in diamond anvil cells. In addition to $CaZrF_6$, the materials $CaNbF_6$ and $CaNb^{IV}_{0.5}Nb^{V}_{0.5}F_{6.5}$ were also examined to see if helium could insert into materials with smaller average pore size, Chapter 7. These experiments explored the behavior on compassion from ~0.2 GPa to > 4 GPa, which is much higher than the previous study (< 0.5 GPa). On compression in neon, $CaZrF_6$ showed no evidence for neon penetration. However, helium insertion was confirmed in $CaZrF_6$, with anomalous P-V behavior

indicative of helium incorporation into the structure until ~0.7 GPa. At higher pressures, the fully helium inserted material, $[He_2][CaZr]F_6$ remains cubic until amorphization at 3.5 GPa and has an estimated bulk modulus of ~47 GPa. $CaNbF_6$, which has a smaller unit cell volume than $CaZrF_6$, was also shown to incorporate helium until a pressure of ~0.9 GPa. The resulting perovskite, $[He_2][CaNb]F_6$, survived up to the highest measured pressure, ~3.7 GPa, and has a bulk modulus of ~47 GPa. Finally, $CaNb^{IV}_{0.5}Nb^{V}_{0.5}F_{6.5}$, which has the smallest unit cell volume of the materials examined and presumably contains interstitial fluoride, showed no evidence for neon penetration, but did display volume reduction on compression in helium consistent with helium insertion. The helium inserts below 0.9 GPa, and the newly formed $[He_2][CaNb^{IV}_{0.5}Nb^{V}_{0.5}]F_{6.5}$ amorphizes above 3.3 GPa and has a bulk modulus of ~50 GPa. Based on these results, it is anticipated that other hybrid perovskites with small neutral molecules on the A-site can also be prepared and that they will display rich chemistry. Changes in composition of the parent material will allow for tuning of the effective pore size of the ReO_3-type framework, which could affect the temperature at which gases are inserted, may allow other gases, including hydrogen, to be incorporated into perovskites and their uptake and release pressures to be controlled.

CHAPTER 1. INTRODUCTION

1.1 Thermal Expansion

1.1.1 Significance and Applications

The response of materials to heating and cooling, as well as the physics underpinning this response have been studied for over a century. It has been shown that generally materials expand on heating and contract on cooling. This behavior is referred to as positive thermal expansion (PTE). The understanding and characterization of PTE is important for materials scientist and engineers when using industrially significant materials for a variety of applications. There is however a class of materials that show the phenomenon of negative thermal expansion (NTE), meaning they contract on heating and expand on cooling. The thermal expansion of solids will be discussed in greater detail in the following sections, however understanding the thermal expansion properties of materials, PTE or NTE, and how they interact with each other has great significance for applications, creating an opening for industrial and scientifically impactful research. PTE presents issues with obtaining dimensional stability, which is important for precision components or the precisions positioning of components in optical applications. Another challenge presented by thermal expansion is that while the majority of materials exhibit PTE, the magnitude of the expansion can vary significantly. Commonly multiple materials are found in close contact with one another, and as they expand interfacial stress is generated. These stress concentrated regions can lead to cracking or even failure of one of the materials. These problems can be combatted by compensating strong PTE with the inclusion of a NTE material in a thermal expansion composite. The ratio of PTE to NTE material can be

manipulated in the composite to give the desired magnitude of thermal expansion, while maintaining other desired properties required for the application. These composites are discussed in greater detail in a later section (1.2.1).[1-3] Expansion mismatch between the PTE and NTE materials inside the composites can lead to stresses, consequently the response to stress of these materials is very important. This impact of hydrostatic stress, pressure, on thermal expansion will be discussed in section 1.3.

This work examines the synthesis, characterization, and design rules for a family of NTE materials. However, there is also considerable efforts made to understand the overall thermal expansion and behavior on compression of solids that can help grow knowledge of framework materials, see section 1.2.3, that sometimes exhibit NTE. As many of these materials transition to PTE, or always show PTE, understanding their thermal expansion and response to pressure is important for establishing the trends and design principles.

1.1.2 Theory of Thermal Expansion Behavior in Solids

As previously stated, the general trend for most solids is to expand upon heating, PTE. The opposite, NTE, is an unusual property seen only in a few classes of materials. One simple way to understand why PTE is the predominant behavior is to examine the expansion of just two bonded atoms.

1.1.2.1 Bond Anharmonicity

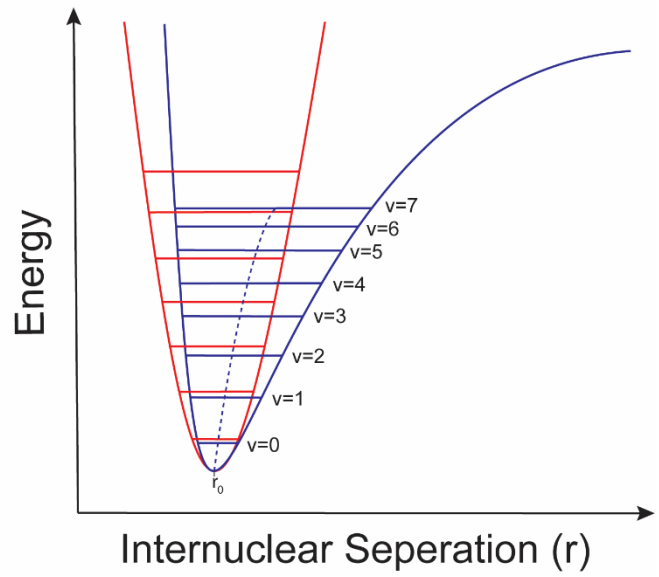

Figure 1.1 A comparison of a quantum harmonic oscillator (red) and Morse potential (blue) as an approximation for a molecular vibration.

A quantum harmonic oscillator can be used to approximate the potential energy curve of a molecular vibration and is represented in red in Figure 1.1. This approximation neglects the cubic (anharmonic) term of the potential energy curve expansion. The resulting curve is parabolic, and as higher energy vibrations are populated the average interatomic spacing stays the same. Therefore, this approximation gives no dimensional change with change in temperature. However, a better way to approximate molecular vibrations is with a Morse potential, shown in blue in Figure 1.1. Again, as thermal energy is supplied to the system discrete vibrations are populated, but due to the anharmonicity of the curve, the population of these vibrations results in an increase in the average interatomic separation (blue dotted line Figure 1.1). Therefore, as the temperature increases, higher energy vibrational modes become populated giving longer bond lengths. If it is axiomatic that all bond lengths expand upon heating, then this can explain why most solids are PTE since they are a large

network of bonded atoms. However, if this is the case then how do NTE materials exist at all? The actual thermal expansion properties of solids are more complicated than just the isolated interaction of atom pairs.

1.1.2.2 Phonons and the Grüneisen Theory of Thermal Expansion

To more accurately describe the effects of atomic vibrations on the thermal expansion of solids, more than the oscillation of two isolated atoms must be considered. A solid is made up of a large network of atoms, which interact strongly with each other. That means the atomic motions are also coupled. Vibrations propagate throughout the solid as a wave referred to as a phonon. This wave has a frequency and its energy is quantized. There are a finite number of independent phonons in a solid, and the total depends on the number of atoms. A specific lattice vibration can commonly be referred to as a phonon, or vibrational, mode. One way of relating the phonon modes of solids to their thermal expansion is through Grüneisen's work from the 1920's.[4-9]

$$\alpha_V = \gamma_T \frac{C_V}{K_T V} \qquad \textbf{(1.1)}$$

The thermal expansion of a material can be quantified by the coefficient of thermal expansion, CTE, which will be described in greater detail later. The volumetric CTE (α_V) is related to the isothermal bulk modulus (K_T see section 1.3.2), specific heat at constant volume (C_V), volume (V), and the thermodynamic Grüneisen parameter (γ_T) in Equation 1.1.

$$\gamma_T = \frac{\Sigma \gamma_i c_i}{\Sigma c_i} \quad \textbf{(1.2)}$$

The thermodynamic Grüneisen parameter considers the population of all vibrational modes at a given temperature, Equation 1.2. It is an average of the mode Grüneisen parameters (γ_i), which are characteristics of specific vibrational modes. The average is weighted (c_i) by the contribution of a mode to the specific heat.

$$\gamma_i = \frac{-d(ln\,\nu)}{d(ln\,V)} \quad \textbf{(1.3)}$$

The mode Grüneisen parameter can further be described by its relationship to the frequency (ν) of the vibration and the volume of the material, Equation 1.3. If a mode's frequency softens (decreases) on decrease in volume, the mode Grüneisen parameter is negative. However, more commonly the frequency of a vibration increases with decrease in volume, and γ_i is between 1 and 3. The weighted average, γ_T, is typically a positive value resulting in a positive α_v and PTE in the material.

1.1.3 Quantifying Thermal Expansion

To study the thermal expansion of a material, experimental measurements of its dimensions at known temperatures are needed. The dimensions of the solid and temperature can then be used to mathematically quantify the thermal expansion. One common method, which is used exclusively in this thesis, is diffraction. Other methods include mechanical, capacitance, and optical types of dilatometry.[10-16]

1.1.3.1 Diffraction Measurements

This work relies heavily on x-ray and neutron scattering to characterize structure of materials. Diffraction relies on Bragg's Law, Equation 1.4.

$$n\lambda = 2dsin\theta \tag{1.4}$$

In this equation n is an integer, λ is the wavelength of the incident radiation, d is the spacing between lattice planes, and θ is the angle between the lattice planes and the incident beam. A diffraction pattern is generally reported as intensity vs 2θ, where 2θ is the angle between the incident beam and scattered beam. The diffraction pattern of a crystalline powder can be analyzed using the Rietveld method to refine parameters in a structural model and achieve the best fit to the data.[17] Synchrotron x-ray or spallation neutron powder diffraction can result in accurate lattice constants for a material, which can be used to calculate reliable CTEs.

1.1.3.2 Coefficient of Thermal Expansion

The thermal expansion of a material can be quantified using a coefficient of thermal expansion, CTE. This coefficient was previously introduced in the context of phonons in a solid. A simple relation between the CTE and the dimensional change in one direction or all directions is given in Equation 1.5 and 1.6.

$$\alpha_L = \frac{d(lnL)}{dT} = \frac{1}{L}\frac{dL}{dT} \tag{1.5}$$

$$\alpha_V = \frac{d(\ln V)}{dT} = \frac{1}{V}\frac{dV}{dT} \quad \textbf{(1.6)}$$

The linear CTE (α_L) can be calculated by the change in length of one direction per change in temperature proportional to the original length of the material. The volumetric CTE (α_V) is calculated the same way except with the volume of the material, taking into account the changes in all three directions. In a cubic material where all three directions are equivalent then $\alpha_V = 3*\alpha_L$. However, if a material is not cubic the thermal expansion can be anisotropic, meaning the linear CTEs for the three directions are not equal. A representative linear and volumetric CTE can still be calculated for the material, but the crystal structure does not expand uniformly in a, b, and c. A material can be classified as displaying PTE, ZTE, or NTE based on the value of its CTE at a given temperature, Table 1.1.

Table 1.1 Classification of thermal expansion based on volumetric CTE.[18]

Positive Thermal Expansion (PTE)	High Expansion	α_V > 24 ppm K^{-1}
	Intermediate Expansion	6 < α_V < 24 ppm K^{-1}
Zero Thermal Expansion (ZTE) or close to zero	Very low Expansion	-6 < α_V < -6 ppm K^{-1}
Negative Thermal Expansion (NTE)	Intermediate Expansion	-6 > α_V > -24 ppm K^{-1}
	High Expansion	α_V < -24 ppm K^{-1}

The CTEs for different materials vary wildly. This impacts their interaction with one another and their potential for application. Table 1.2 shows the CTEs of several common materials. This table illustrates that materials have very different CTEs, and the CTE of a material can depend strongly on temperature.

Table 1.2: Linear CTE and experimental temperature establishing thermal expanison seen in various solids.[5,19-26]

Material	α_L [ppm K^{-1}]	Temperature [K]
Pyrex	56.2	50
Ice	37.6	200
Graphite (c-axis)	29	300
Aluminum	23.2	300
Copper	16.8	300
Ice	12.7	100
Quartz (cr)	7.6	300
Aluminum	3.8	50
Copper	3.8	50
Diamond	1.0	300
Invar	0.07	278-303
Diamond	0.004	50
Quartz (cr)	-0.33	50
Graphite (a-axis)	-1.0	300
Pyrex	-2.3	300
ZrV_2O_7	-7.1	400-500
ZrW_2O_8	-8.7	0.3-693
$AlPO_4$-17	-11.7	18-300
$Cu_3(btb)_2$	-13	400
ScF_3	-14	60-110
$CaZrF_6$	-18	100
$Zn(CN)_2$	-19.8	< 180

1.2 Negative Thermal Expansion

Negative thermal expansion (NTE) is an unusual phenomenon, but our knowledge of NTE and the number of materials classified as showing NTE has grown in recent years. Several excellent reviews cover the topic.[2,18,27-34] The understanding of NTE and study of NTE

materials is of fundamental interest, and an established area of consideration and importance for applications.

1.2.1 Significance and Applications

As previously stated, expansion mismatch can be a serious issue, see section 1.1.1. When multiple materials with different CTEs are in close contact, such as in devices, stresses can occur at their interface. This stress can lead to cracking and failure of the materials. This issue can be alleviated through the use of zero or controlled thermal expansion composites. These composites require the use of a NTE component to offset the PTE, while maintaining the physical properties (electrical conductivity, thermal conductivity, etc.) desired for their application. The magnitude of PTE in materials spans a very large range, and therefore the identification of new NTE materials with different CTEs and temperature ranges for their NTE is vital for advancing development of controlled thermal expansion composites.[3] There has already been work done on the fabrication and effectiveness on ceramic-ceramic, metal-matrix ceramic, and polymer ceramic composites containing NTE materials.[35-43] One such example is the use of the NTE material ZrW_2O_8 in combination with copper nanoparticles to form a metal-matrix composite with controllable thermal expansion that maintains its electrical and thermal conductivity.[44] Although materials showing NTE over a wide temperature range are desirable for many applications, it is important to note that materials with very large NTE over narrow ranges can be useful in composites. Materials such as $Bi_{0.95}La_{0.05}NiO_3$, which display extremely large NTE around room temperature can be utilized to offset the large PTE of plastics or in applications at close to room temperature.[45]

In order to make successful thermal expansion composites it is important to have a wide range of NTE materials with varying physical and chemical properties, and magnitudes of NTE. NTE is uncommon therefore synthesizing new compounds especially having very large NTE over a wide temperature range would have significant impact. The discovery of new NTE materials would also allow for the study of mechanisms underpinning their NTE. While the mechanisms leading to NTE have been studied, they can be complex. Studying materials with relatively simple NTE behavior allows for the perturbation of the chemistry, structure, and external stimuli to lead to methods for controlling thermal expansion. This expands the scientific knowledge about these rare materials and could facilitate the ability to design materials with specific NTE and physical properties for use in composites or standalone applications.

When considering this possibility, it becomes apparent that in many applications, outside of thermal expansion composites, zero thermal expansion (ZTE) would be ideal. If a material has ZTE it will not change size with changes in temperature. This can alleviate the thermal expansion mismatch issues previously discussed, as well as prevent other issues such as thermal shock failure. Thermal shock failure occurs when there is a localized rapid change in temperature, and due to high thermal expansion and low thermal conductivity local expansion or contraction leads to stress. This stress can exceed the strength of the material leading to cracking and possible failure. Therefore, having close to ZTE prevents failure due to thermal shock, this has been utilized in the fabrication of ZTE glassware such as Pyrex flasks, beakers, etc. The dimensional stability on temperature change in a ZTE material would be especially important in the use of precision components that may experience mild or even extreme temperature changes, like those associated with space

travel. The ability to design a material with optical transparency over a wide wavelength range and ZTE would allow for the fabrication of thermally stable optical components, such as lenses. The exploration of the rare NTE behavior seen in materials, for developing a greater understanding NTE, developing control over the thermal expansion in materials, and utilizing new NTE materials in composites or optical applications were the inspiration for the work presented in this dissertation.

1.2.2 Mechanisms Leading to NTE

In the growing field of NTE materials, several distinct mechanisms have been identified.[34,46] The most prevalent mechanisms will be discussed here, although there are others and sometimes multiple contributing factors in the NTE of a material.

1.2.2.1 Magnetic Transitions

Large volume changes can result from thermally induced transitions between magnetic states. This volume change is a magnetovolume effect (MVE). With changing temperature, a materials volume can gradually change as the amplitude of the magnetic moment changes. The reporting of unusually low thermal expansion in Invar alloys led to the investigation of how magnetic ordering effects thermal expansion.[47] MVE can counter a lattice expansion caused by increased vibrational motion. While magnetostriction leading to low or NTE is often referred to as the Invar effect, it has been identified as the NTE mechanism in several types of materials including Mn_3AN (A= transition metal), YMn_2, $MnCo_{0.98}Cr_{0.02}Ge$ and $La(Fe,Si,Co)_{13}$.[48-54] These types of materials can show extremely large NTE, but the large MVE leading to the NTE often occurs over a narrow temperature range. This can be seen in $(Mn_{0.96}Fe_{0.04})_3(Zn_{0.5}Ge_{0.5})N$ with a α_L= -25 ppm K^{-1} for ΔT:

316-386 K and $MnCo_{0.98}Cr_{0.02}Ge$ with a α_L= -116 ppm K^{-1} for ΔT: 250-305 K.[50,53] Away from the Currie temperature, and therefore the magnetic phase transition, these materials tend to show PTE due to the classical vibrational effects discussed previously.

1.2.2.2 Ferroelectric Transition

Ferroelectric materials show spontaneous electric polarization, which is reversible with applied external electric field. This transition has been shown to lead to NTE, and ferroelectrics, similar to ferromagnets, only show ferroelectricity below their Currie temperature. However, the physics leading to the NTE behavior are different than that for magnetic transitions. In ferroelectrics, the transition leads to polarization. This occurs due to the displacement of cations from the center of polyhedra generating a dipole moment. The displacement results in distorted larger polyhedra, which can lead to increased volume of the structure on cooling through the transition temperature. The NTE caused by this type of transition occurs over a narrow temperature range, but certain substitutions can increase the transition temperature range. This type of mechanism has been reported to generate NTE in materials like $0.4PbTiO_3$-$0.6BiFeO_3$ (α_L= -13 ppm K^{-1}, ΔT: 298-923 K) and $Pb(Ti,V)O_3$ (α_L= -12.5 ppm K^{-1}, ΔT: 298-823 K).[55,56]

1.2.2.3 Charge Transfer

Charge transfer between two atoms can result in NTE. When an atom loses valence electrons and its oxidation state increases, its ionic/atomic radius shrinks and vice a versa. The magnitude of the change in ionic/atomic radius depends on the element and several other factors. Additionally, the effect of ionic radius change on the lattice constant of the material depends on the crystal structure. This NTE mechanism relies on the effect of

contraction of atomic radii on heating outweighing the expansion, thus resulting in a net contraction on heating. This type of NTE or ZTE has been seen in several materials including $Sm_{1-x}Y_xS$, YbGaGe, $ACu_3Fe_4O_{12}$, and several variations of $BiNiO_3$.[45,57-62] Noticeably large NTE has been reported in $SrCu_3Fe_4O_{12}$ (α_L= -22.6 ppm K^{-1}, ΔT: 170-270 K) and $Bi_{0.95}La_{0.05}NiO_3$ (α_L= -82 ppm K^{-1}, ΔT: 320-380 K).[45,61] Again, the temperature range for NTE tends to be small, due to the charge transfer occurring over a small temperature range. When the materials are not undergoing the charge transfer transition, vibrational effects dominate the thermal expansion and lead to PTE. Interestingly, in $Bi_{0.95}La_{0.05}NiO_3$ the smooth change in volume on heating was attributed to a phase coexistence between low and high temperature phases, which proportionally changed on heating.[45]

1.2.2.4 Vibrational

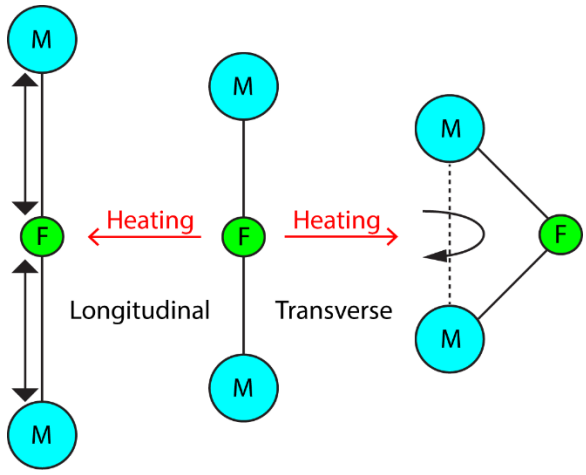

Figure 1.2: Example of longitudinal (bond lengthening) and transverse (shortening of M-M distance) vibrations that occur on heating.

As previously stated, bonds typically lengthen on heating, and generally vibrational motion in solids leads to PTE. However, NTE can result when the population of vibrational modes

that reduce volume dominate the low energy vibrational contributions to thermal expansion. As previously discussed, transverse vibrations of linking atoms can reduce volume, and outweigh contributions from longitudinal vibrations leading to NTE, Figure 1.2 .

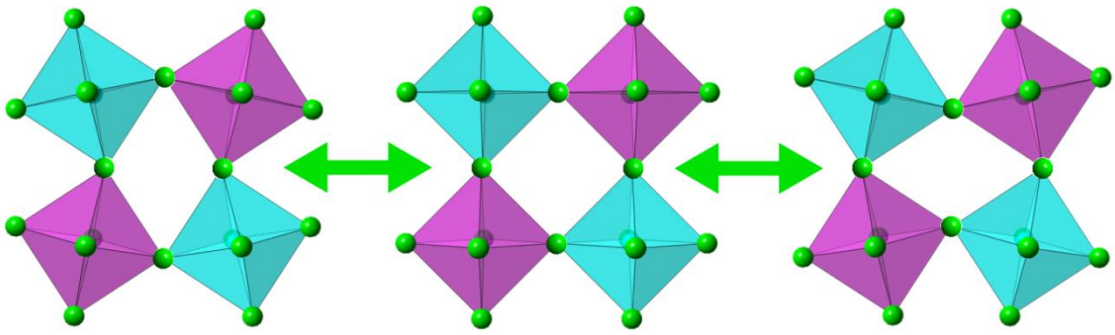

Figure 1.3: Transverse motion of linking atom between rigid octahedra or rigid unit modes (RUMs).

This type of mechanism has been seen in flexible open framework materials. These materials consist of linked polyhedra that contain strong bonds, which reduces the effects of longitudinal vibrations. Due to this the polyhedra can be considered as rigid units. Therefore, the transverse motion of the linking atoms results in coupled rotations of the polyhedra, which reduces the average distance between center atoms of polyhedra. This type of vibrational mode occurs with little distortion of the polyhedra and has been classified as a rigid unit mode (RUM). An example of a RUM in a simple corner linked octahedra system is shown in Figure 1.3. These RUMs and other similar modes contribute to NTE in several different classes of framework materials.[63-65] The rigidity of the polyhedra varies. Softer polyhedra can distort more easily, and these distortions lead to bond lengthening and contribute to expansion in the material. Therefore, the rigidity of the polyhedra is an important factor in weather NTE occurs in these types of systems.

1.2.3 Open Framework Materials

As this work focuses on materials whose NTE originates from vibrational motion, it is important to note what is already known about this class of materials. The materials known to display this type of NTE have open frameworks. They typically consist of ordered corner sharing polyhedra, although their structures, composition, density, and physical properties can vary. The thermal expansion and response to compression of framework materials will be discussed in the following sections.

1.2.3.1 Zeolites and Aluminophosphates

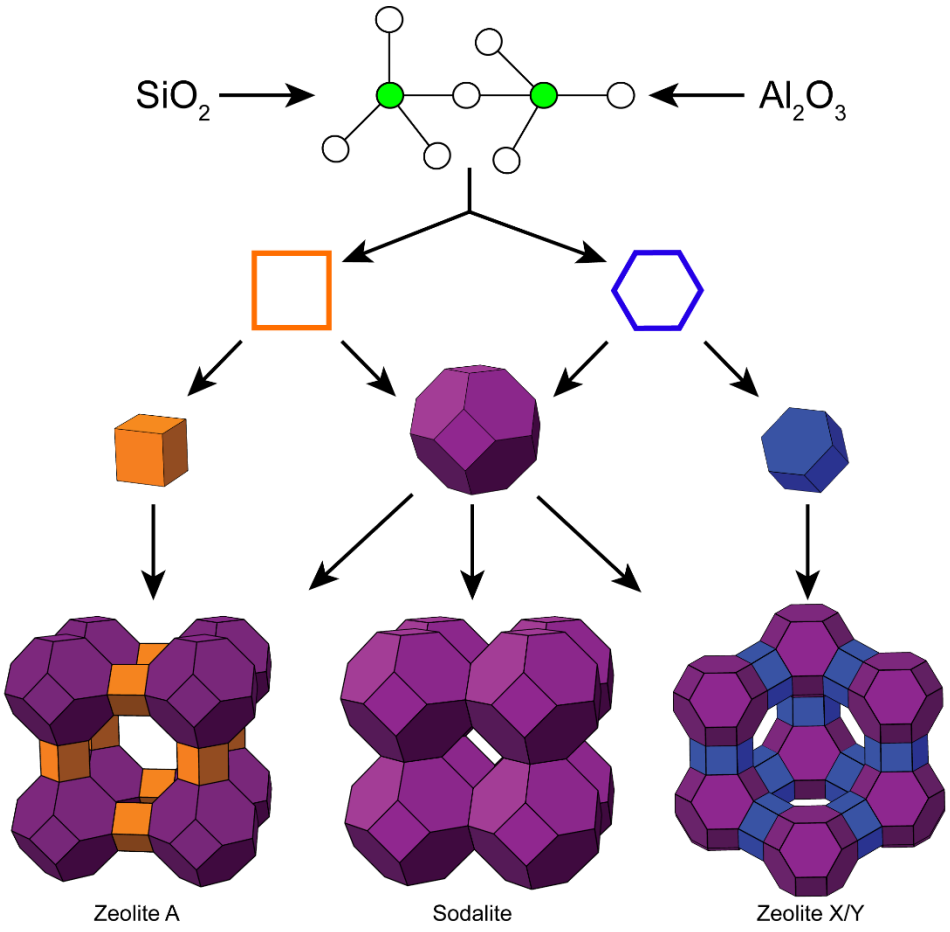

Figure 1.4: Structural unit and sub units that make up three well known zeolites.

Zeolites are microporous aluminosilicate materials that consists of three-dimensional framework of silica (SiO_4) and alumina (AlO_4) tetrahedra. These tetrahedra can arrange in different ways building up to the super cage structures that define different classes of zeolites, Figure 1.4. This class of microporous framework materials, which includes the structurally related aluminophosphates ($AlPO_4$s), have shown negative thermal expansion resulting from cooperative motions of these linked rigid tetrahedral units. Some of the earliest materials know to show NTE were aluminosilicates like β-eucryptite ($LiAlSiO_4$) and cordierite ($Mg_2Al_4Si_5O_8$).[66,67] Early lattice dynamic calculations by Tschaufeser and

Parker theoretically predicted NTE in many zeolites and $AlPO_4$s at elevated temperatures.[68] Soon thereafter a thorough study by Dove et al looked at RUMs and their effect on phase transitions in framework silicates.[69] Attfield and Sleight were among the first to experimentally identify NTE in zeolites and $AlPO_4$s, reporting NTE in siliceous faujasite α_L= -4.2 ppm K^{-1}, ΔT: 25-573 K and $AlPO_4$-17 α_L= -11.7 ppm K^{-1}, ΔT: 18-300 K.[20,70] They also note that the thermal expansion is anisotropic in $AlPO_4$-17, with greater contraction in the a/b plane than along the c-axis. Anisotropic thermal expansion can present issues in applications previously discussed. In the past few decades many zeolites have been predicted to and shown to display NTE.[71] Relatively large NTE has been seen in Chabazite with α_L= -16.7 ppm K^{-1} at temperatures approaching 873 K.[72] More recently, it has been reported that the thermal expansion can be affected by presence of guest molecules in pores, and this behavior can be utilized to control thermal expansion.[73]

1.2.3.2 Metal Cyanides

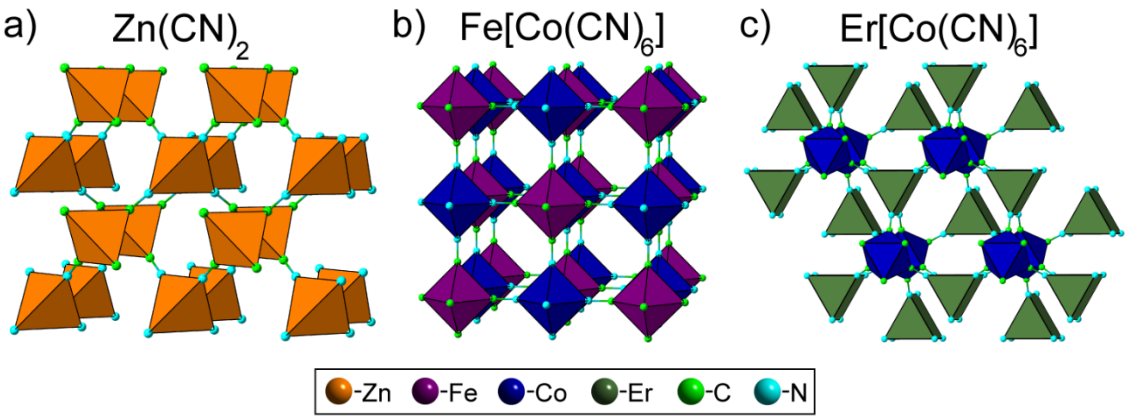

Figure 1.5: Comparison of a) tetrahedral, b) Prussian blue, and c) trigonal prismatic type metal cyanide frameworks.

Similar to zeolites, metal cyanides can adopt frameworks based on corner sharing tetrahedron, however instead of a corner linked by oxygen the tetrahedra are linked by a

diatomic cyanide, Figure 1.5a. The diatomic bridges give the framework greater flexibility resulting from an increase degree of freedom for the linker, leading to greater transverse motion and a greater number of low-energy RUMs. Two possible transverse displacements of a diatomic linker have been proposed, "skipping-rope" and "kinky" modes, where the two atoms displace to the same side or opposite sides, respectively.[21,74] The work of Williams et al. on $Zn(CN)_2$ showed the first experimental example of NTE in a metal cyanide framework.[75] This compound has been thoroughly investigated revealing a minimum CTE of α_L= -19.8 ppm K^{-1} below 180 K, and studies have confirmed the transverse motion of bridging CN atoms, counteracts the contributions from significant expansion of Zn-C/N bonds leading to NTE.[21,74,76] Although there is some debate on the exact nature of these modes.[21,74] The substitution of Cd into $Zn(CN)_2$ has been shown to lead to large NTE, with a α_L= -33.5 ppm K^{-1} for $Cd(CN)_2$ from 170 to 375 K.[77] Metal cyanides can also adopt an octahedral network similar to that of ReO_3 discussed in section 1.2.4. This structure is seen in Figure 1.5b for the material Prussian blue $Fe_7(CN)_{18}$. An early study of the Prussian blue analogue $Fe[Co(CN)_6]$, with Co and Fe centered octahedra connected by CN bridges, showed slight NTE with an average CTE of α_L= -1.47 ppm K^{-1}, ΔT: 4.2- 300 K.[78] These initial results led to the examination of $Ag_3[Co(CN)_6]$, which shows anisotropic thermal expansion with very large PTE in the a direction and "colossal" NTE in the c direction (α_L= -125 ppm K^{-1}).[79] A series of Prussian blue analogs $M^{2+}[Pt(CN)_6]$ with M= Mn, Fe, Co, Ni, Cu, Zn, and Cd) were studied and a compositional dependence of the NTE was observed. The NTE increased from α_L= -1.02 ppm K^{-1} for $NiPt(CN)_6$ to α_L= -10.02 ppm K^{-1} for $CdPt(CN)_6$ over the temperature range of 100-400 K.[80] The effects of guest inclusion, into the nanoporous structure, on thermal expansion

were studied in Zn and Cd $MPt(CN)_6$ x H_2O.[81] Guest molecules in the pores of the framework structure sterically dampen the transverse vibrational modes that lead to NTE. However, very large NTE has been seen in a few hydrated Prussian blue analogs such as $Mn_3[Co(CN)_6]_2 \cdot 12H_2O$ (α_L= -48 ppm K^{-1}, ΔT: 125-298 K).[82] This behavior is postulated to result from an increase in lattice flexibility due to water replacing cyanide linkers, but the thermal expansion in other hydrated Prussian blue analogs ranged from strong PTE to strong NTE. Recently NTE was observed in another type of framework metal cyanide, $ErCo(CN)_6$, consisting of linked trigonal prisms and octahedra, Figure 1.5c. The dehydrated material adopts a hexagonal structure and showed anisotropic CTE with α_a= -8 ppm K^{-1}, α_c= -9 ppm K^{-1}, and effective α_L=1/3 dV/VdT = -9 ppm K^{-1} from 100 to 375 K.[83] Shortly thereafter a series of $LnCo(CN)_6$ (Ln= La, Pr, Sm, Ho, Lu, and Y) materials with this structure were analyzed. The results indicate a general trend of increasing NTE with increasing ionic radius of the lanthanide. The CTE changes from an effective α_L= -9.56 ppm K^{-1} for Lu to α_L= -16.58 ppm K^{-1} for La in the 100-500 K range.[84]

1.2.3.3 Metal-Organic Frameworks (MOFs)

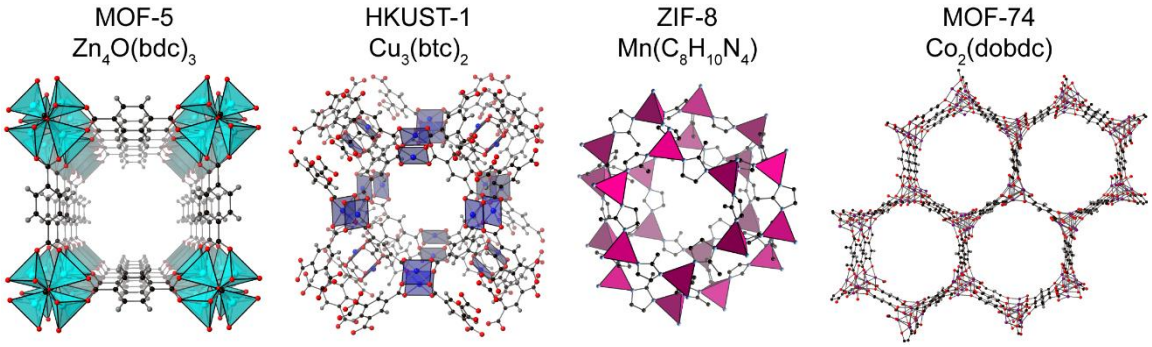

Figure 1.6: Changes in structure and pore size of several MOF types.

Metal-organic frameworks (MOFs) are materials where metal ions or clusters are linked by coordination to organic ligands. MOFs can adopt three-dimensional structures and are porous. The structure of the framework can vary greatly depending on choice of cluster and linker, Figure 1.6, allowing for the tuning of properties like pore size. Research on these materials garnered great interest in the mid-2000s due to their possible applications in the storage and separation of gases. It was first noted in gas absorption experiments by Yaghi et al that MOF-5 (Zn_4O_{13}-$(C_8H_4)_3$ showed an increase in unit cell volume of 1% on cooling from 293 to 30 K.[85] Shortly after, simulations showed that several isoreticular metal-organic frameworks (IRMOFs) and other MOF-5 related materials should show strong NTE.[86,87] While the NTE in MOF-5 has been attributed to low-energy RUMs involving the transverse motion of carboxyl linkers between rigid ZnO_4 clusters and benzene rings, work by Kepert et al simulating NTE in $[Cu_3(btc)_2]$, suggests the NTE mechanism can be more complex than in other framework systems.[88,89] The NTE in MOFs is attributed to the rigid or semi-rigid vibrations of large fragments, such as vibrations within the polynuclear metal center, transverse vibrations of rigid two-dimensional linkers,

and motion of whole cage structure. Experimentally MOFs have shown NTE behavior over wide temperature ranges including $Cu_3(btc)_2$ (α_L= -4.1 ppm K^{-1}, ΔT: 80-500 K), MOF-5 Zn_4O_{13}-$(C_8H_4)_3$ (α_L ~-16 ppm K^{-1}, ΔT: 4-600 K), and $Cu_3(btb)_2$ (α_L ~-4 ppm K^{-1} at 4 K decreasing linearly to α_L ~-13 ppm K^{-1} at 400 K).[22,88,89]

1.2.3.4 Metal Oxides

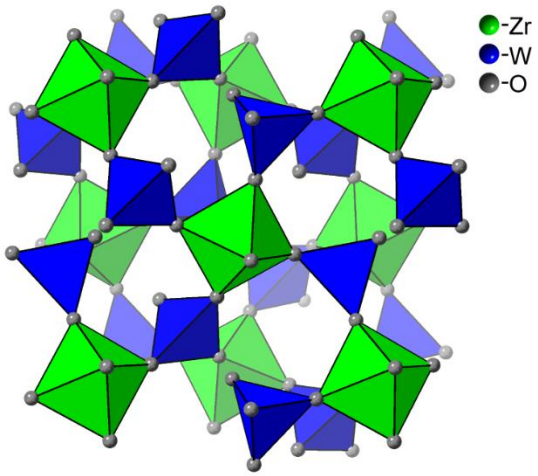

Figure 1.7: Structure of ZrW_2O_8 showing a combination of interlinked tetrahedra and polyhedra commonly seen in many NTE metal oxides.

Metal oxides are the most thoroughly studied compositions known to display NTE. Frameworks consisting of corner linked octahedra and tetrahedra, Figure 1.7, are commonly found in NTE metal oxides, with variations in distortions and connectivity. Early work on materials in the NZP family, $NaZr_2(PO_4)_3$, showed some of the first NTE in non-zeolitic metal oxides.[18] However, this area of research was invigorated by the discovery of NTE in ZrW_2O_8, which is now one of the most researched NTE materials. It was first reported in 1959, and first shown to display NTE by Hummel et al in 1968.[90,91] However the cause of its NTE wasn't elucidated until work done by Sleight and coworkers

a few decades later. They initially looked at NTE in $ZrV_{2-x}P_xO_7$ where low phosphorous compositions exhibited NTE.[23,92] Then in 1996, they reported strong NTE from 0.3 to 1050 K in ZrW_2O_8 (α_L= -8.7 ppm K^{-1}, ΔT: 0.3-693 K).[24] This was the first material to show large isotropic NTE over a wide temperature range, and the original work attributed the NTE to transverse thermal vibrations of bridging oxygen atoms leading to coupled rotations of rigid polyhedra. The mechanism leading to NTE in ZrW_2O_8 and many other metal oxide frameworks has been studied thoroughly since this initial work.[93-95] The consensus being that transverse vibration of oxygen in RUMs, discussed previously, generates NTE. The NTE of ZrW_2O_8 shows a discontinuity at 448 K due to an order-disorder phase transition.[24] This transition occurs between two cubic phases due to a disordering of oxygen in the high temperature phase. The Hf analog, HfW_2O_8, shows very similar behavior with strong NTE and an order-disorder phase transition at 463 K.[24,96] The analogous cubic $ZrMo_2O_8$ is metastable with an oxygen-disordered structure below 673 K, which transitions from dynamic to static disorder on cooling below 200 K.[97] The NTE was reported as α_L= -6.9 ppm K^{-1} from 2 to 200 K and α_L= -5.0 ppm K^{-1} from 250 to 502 K.[98]

After the initial studies of ZrV_2O_7, it was shown to display strong NTE at higher temperatures (α_L= -7-10 ppm K^{-1}, ΔT: > 375 K). However, it undergoes phase transitions on cooling.[23,99-101] The NTE seen in the highest temperature cubic phase is a result of transverse vibrations of the oxygens between corner-sharing polyhedra, but these modes also involve distortions of the polyhedra. Therefore, the modes contributing to the NTE are classified as quasi-RUMS or qRUMs.[65] This family of oxides, AM_2O_7, is quite large with M= V, P, or As and many tetravalent metals on the A site are known.[23,102-110] However, most of the phosphates, vanadates, and arsenates show PTE at all temperatures, and a few

of the larger tetravalent metal materials including CeP_2O_7, UP_2O_7, and ThP_2O_7 display NTE only in the high temperature phase.[23,102-108]

After NTE was identified in the AM_2O_8 and AM_2O_7 families, $A_2M_3O_{12}$ garnered interest. With M= W or Mo and A= small trivalent main group metals and rare earths, the structures of these materials are generally monoclinic or orthorhombic.[111-113] The materials with orthorhombic symmetry often undergo a phase transition to monoclinic on cooling.[65,114,115] This monoclinic phase shows PTE. The PTE is anisotropic with some NTE in the unique b direction.[115] The material $Sc_2W_3O_{12}$ adopts an orthorhombic structure, a study of its thermal expansion from 10-1300 K revealed NTE (α_L= -2.2 ppm K^{-1}, ΔT: 50-450 K).[113] The NTE in the orthorhombic phase is anisotropic with PTE in the b direction. The molybdenum analog, $Sc_2Mo_3O_{12}$, shows a transition from monoclinic to orthorhombic on warming above 180 K, and anisotropic NTE with a α_a of -8.41 ppm K^{-1}, α_b of 10.82 ppm K^{-1}, and α_c of -8.73 ppm K^{-1} from 200 to 300 K.[115] The thermal expansion of many of oxides in this family varies due to phase transitions leading to PTE.[116] However a few have shown notable NTE including $Lu_2W_3O_{12}$ (α_L= -6.8 ppm K^{-1}, ΔT: 400-900 K), $Y_2W_3O_{12}$ (α_L= -7.0 ppm K^{-1}, ΔT: 15-1373 K), and $Y_2Mo_3O_{12}$ (α_L= -12.6 ppm K^{-1}, ΔT: 403-1173 K).[117-119] The NTE in these materials cannot be classified as arising from RUMs as the polyhedra distort more readily than in other metal oxide structures, but the NTE is still a result of transverse vibrations of linking oxygens.[65] No NTE is seen in these materials when the A cation is smaller than Sc, and this is due to the greater flexibility of the larger polyhedra.[111,112,116]

Dozens of studies have been done on these families of oxides exploring NTE, phase transitions, and looking at the effect of chemical substitution and solid solution formation

on these properties. These results are summarized in several reviews.[27,28,30,31,33] A few less obvious substitutions have been studied. Sn^{4+} and Ti^{4+} both showed limited solubility of ~30% ($Zr_{0.7}Sn_{0.3}W_2O_8$) and 5% ($Zr_{0.95}Ti_{0.05}W_2O_8$), respectively. In both, the NTE showed little composition dependence, but increasing substitution lowered the order-disorder phase transition.[120,121] Several trivalent ions like Sc, In, and Y have been substituted with limited solubility, but showing significant effects to the phase transition temperature. The thermal expansion of the disordered phase remained the same, but the NTE weakened with increasing substitution.[122-126] A few aliovalent substitutions have been reported in the AM_2O_7 family including $Nb_{0.05}Y_{0.05}Zr_{0.9}P_{2-x}V_xO_7$, $ZrV_{2-x}Mo_xO_{7+x/2}$, and several different $A_{0.5}^{3+}A'_{0.5}^{5+}P_2O_7$ materials.[127-130] All of the phosphates showed PTE, which is consistent with the behavior of other AP_2O_7.[127,128] The substitution of Y^{3+} and Nb^{5+} reduced the PTE in the low temperature phase but showed little effect on the phase transition temperature or NTE of the high temperature phase.[129] The substitution of Mo resulted in very similar behavior to the parent ZrV_2O_7 material.[130] There have been reported aliovalent substitutions for the $A_2W_3O_{12}$ system as well, for example $MgZrW_3O_{12}$ and $MgHfW_3O_{12}$.[131-133] They adopt a PTE monoclinic phase below 400 K, and transition to an orthorhombic phase high temperature phase. The monoclinic phase is isostructural to that commonly seen in $A_2W_3O_{12}$, but the orthorhombic phase is slightly different than the structure of $Sc_2W_3O_{12}$.[132,133] The thermal expansion was reported as NTE in $MgHfW_3O_{12}$ (α_L= -1.2 ppm K^{-1}, ΔT: 400-800 K) and close to ZTE in $MgZrW_3O_{12}$ (α_L= ~0.4 ppm K^{-1}, ΔT: 423-873 K).[132,133] Molybdenum analogs of both materials have also been reported.[134,135] Only an orthorhombic phase was seen for $MgZrMo_3O_{12}$ from 303 to 873 K, and a CTE of α_L= 6.0 ppm K^{-1} was reported for this temperature range.[134] Similarly,

$MgHfMo_3O_{12}$ remains orthorhombic with a CTE of α_L= ~1.0 ppm K^{-1} from 298 to 973 K.[135] The material $Zr_2WP_2O_{12}$ was synthesized then characterized in several studies, which showed it adopted a orthorhombic phase.[136,137] This material was reported to show NTE of ~-3 ppm K^{-1} from 60 to 450 K and ~-5 ppm K^{-1} from 60 to 300 K.[138,139] The Hf and Mo analogs have been reported to have similar behavior.[138]

1.2.4 ReO_3-Type Metal Fluoride Materials

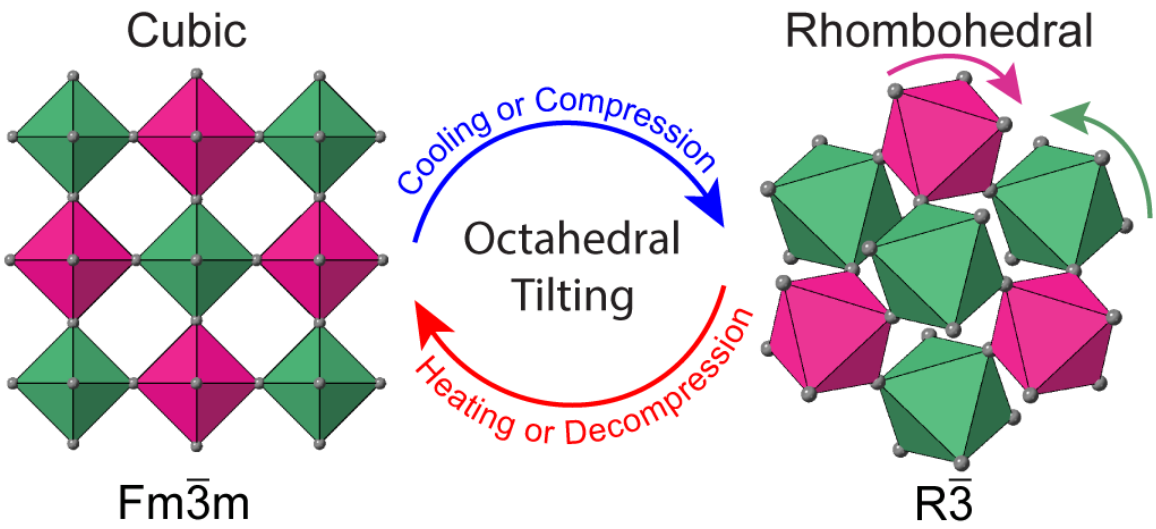

Figure 1.8: The structure of cubic and rhombohedral cation ordered ABF_6 with ReO_3-type connectivity.

The ReO_3-type structure is a simple three-dimensional framework of corner linked octahedra, named after ReO_3 which adopts this framework, Figure 1.8. This structure can be cubic with linear M-X-M bonds, or rhombohedral with M-X-M angle of < 180 degrees. The cubic structure could theoretically display NTE if contributions from transverse motion of linking atom outweighs bond lengthening in octahedra.

1.2.4.1 Rhenium Trioxide

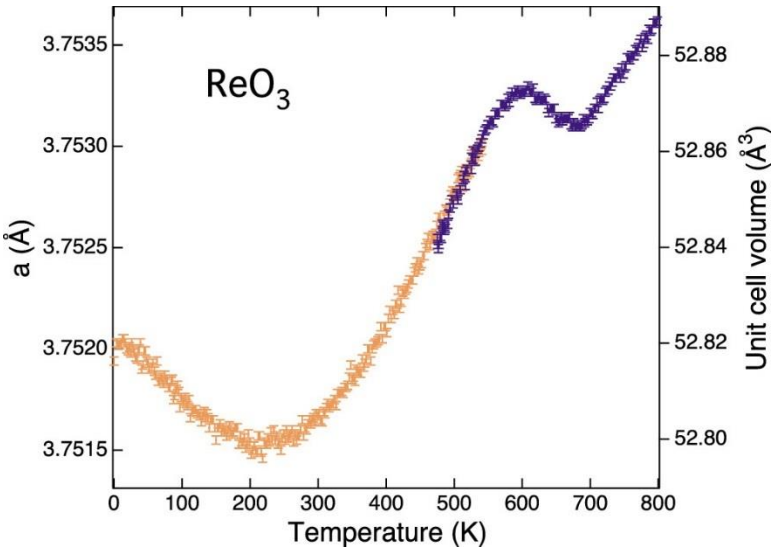

Figure 1.9: Change in lattice constant/unit cell volume of cubic ReO_3 with change in temperature from 2 to 800 K.[140] (Reprinted with permission from T. Chatterji et al. *Appl. Phys. Lett.* 2009, *94*, 241902-241903. Copyright 2009 AIP Publishing)

In 1979 ReO_3 was originally studied from 291 to 464 K, and found to display low PTE.[141] Several years later a clearer picture of its thermal expansion was established in several different studies.[140,142-145] In Figure 1.9 the work by Chatterji et al shows the thermal expansion of ReO_3 from 2-800 K.[140] Although this structure was thought to be able to generate NTE, this compound shows PTE above room temperature. ReO_3 does display NTE at temperatures below 200 K. The reason NTE does not occur at higher temperatures is attributed to the electrical conductivity and low resistivity of ReO_3, which has one unpaired electron.[146] The NTE at low temperatures is likely a consequence of RUMs generating rotation of neighboring ReO_6 octahedra due to transverse vibrations of oxygen.

1.2.4.2 Metal Trifluorides (MF_3)

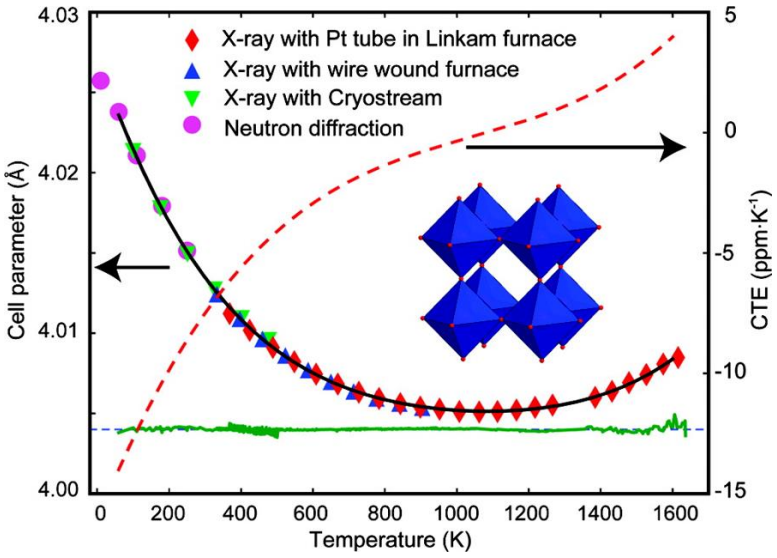

Figure 1.10: Change in unit cell constant and CTE for cubic ScF_3 from 10 to 1700 K.[25] (Reprinted with permission from B. K. Greeve et al. *J. Am. Chem. Soc.*, 2010, *132(44)*, 15496-15498. Copyright 2010 American Chemical Society)

While ReO_3 does not show large NTE over a wide temperature range, it did reinforce the ReO_3-type structure as a simple structure to study in the search to identify and understand NTE. Metal fluorides are also known to adopt this structure and soon drew interest as possible NTE materials. The crystal structures of many metal trifluorides, MF_3, have been studied, and found to be cubic at elevated temperatures. However, phase transitions to a "VF_3" rhombohedral phase are typically seen on cooling, with the transition temperature varying.[147-149] This rhombohedral phase is expected to show PTE contributions from transverse motion of bridging atoms, and therefore is undesirable for finding NTE in ReO_3-type systems. The first variable temperature measurements on MF_3 materials were for TiF_3 then AlF_3 in the early 2000s.[150,151] Both of these materials were shown to have a rhombohedral structure around room temperature with large PTE. TiF_3 and AlF_3 showed a phase transition to cubic on heating above 370 and 650 K, respectively. The cubic high

temperature phases show very slightly PTE. In 2010, Wilkinson et al identified ScF_3 as remaining cubic down to at least 10 K.[25] ScF_3 shows large isotropic NTE over a wide temperature range (α_L= -14 ppm K^{-1}, ΔT: 60-110 K), Figure 1.10. At the time this made ScF_3 one of the strongest vibrationally driven NTE materials known. The NTE in ScF_3 is comparable to that seen in other framework materials showing large NTE, but with the added benefit of being a powder formable into ceramics. This makes ScF_3 and other NTE metal fluorides reasonable candidates for application. The NTE mechanism for ScF_3 was attributed to transverse motion of linking fluoride generated by the correlated rocking of rigid ScF_6 octahedra (RUMs).[152,153] This NTE mechanism in ScF_3 was more recently described as a "guitar-string" effect.[154] Since NTE in ScF_3 was identified, changes in thermal expansion by chemical substitution have been explored.[155-161] While none of these materials showed stronger NTE, these results showed the effect of doping on the stability of the cubic material, as some substituted materials showed rhombohedral phase transitions on cooling, and on controlling thermal expansion or generating ZTE.

1.2.4.3 Mixed Metal Hexafluorides ($M^{2+}M^{4+}F_6$)

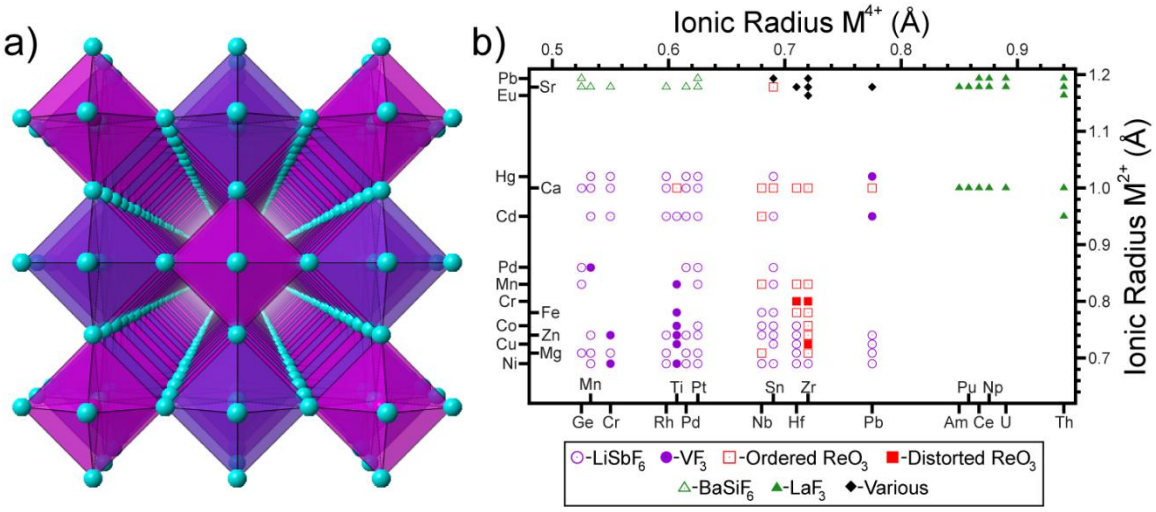

Figure 1.11: a) Cation ordered cubic ReO_3-type structure of ABF_6, and b) reported variation in structure with change in M^{2+} and/or M^{4+} cation.[162]

Once the search for cubic ReO_3-type MF_3 materials became exhausted, researchers turned to the aliovalent substitution of the M^{3+} cation for M^{2+} and M^{4+}. The metal hexafluorides, $M^{2+}M^{4+}F_6$, can adopt the desirable cubic ReO_3-type structure at room temperature, Figure 1.11a. Most of the original work on these materials studied synthesis, structure and magnetic properties.[163-171] The initial results revealed other phases including a rhombohedral distortion discussed previously, Figure 1.8. A compilation of the several different structures found in mixed metal hexafluorides at ambient conditions is given in Figure 1.11b, adapted from Hagenmuller.[162,170] The ReO_3, $LiSbF_6$, and VF_3 structure types are related and consist of corner linked octahedra. Materials with known room temperature cubic ReO_3-type structures, shown as squares in Figure 1.11b, were targeted for possible strong NTE. The first experimental results by Hancock et al showed that $CaZrF_6$, Figure 1.12, remains cubic over a wide temperature range, and displays very large isotropic

NTE.[26] With a linear CTE reaching as low as ~-18 ppm K^{-1} at 100 K, $CaZrF_6$ has stronger NTE than ScF_3 and many metal cyanides, MOFs, and oxides.

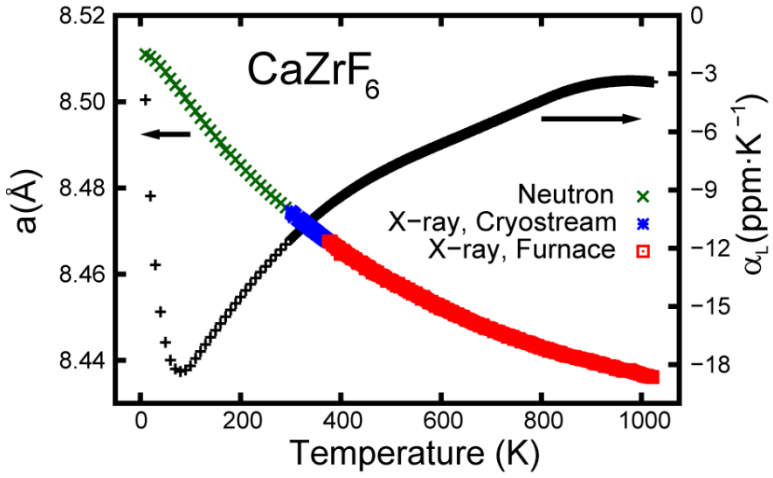

Figure 1.12: Contraction of lattice constant and change in linear CTE of $CaZrF_6$ with increasing temperature from 10 to 1100 K.[26] (Reprinted with permission from J. C. Hancock et al. *Chem. Mater.* 2015, *27(11)*, 3912-3918. Copyright 2015 American Chemical Society)

The $CaHfF_6$ analog showed very similar behavior and while the NTE of these two materials was strongly temperature dependent, their NTE was some of the strongest ever seen for framework materials. These initial results along with ScF_3 showed that cubic ReO_3-type metal fluorides have great potential for large isotropic NTE over a wide temperature range. One of the major focuses of the work presented in this thesis is take advantage of the great compositional flexibility of the $M^{2+}M^{4+}F_6$ family to explore the effects of chemical substitution on thermal expansion and phase behavior. The known room temperature structures reported in Figure 1.11b, and the reported behavior of $CaZrF_6$ were utilized to focus on materials with potential to display NTE.

1.2.4.4 Fluoride Excess ReO_3-type Materials

Early synthetic work showed that aliovalent substitutions could be made in the $M^{2+}M^{4+}F_6$ family of materials.[168,172-176] Substitutions of M^{3+} for M^{2+} and M^{4+} for M^{2+} were preformed and some resulted in cubic phase materials. These types of materials are intriguing as when a high valence metal is substituted the structure will develop either cation vacancies or incorporate excess fluoride to keep charge balanced. Poulain et al reported the synthesis of and structural examination of $YbZrF_7$, where the structure was determined to be a non-cation ordered cubic phase.[173,176] The authors stated that based off these results and earlier work on the oxyfluoride material, that $YbZrF_7$ kept charge balance through anion excess.[177] They believed the excess fluoride resulted in a displacement of normal anions from the middle of the cell edge, and a replacement of some of these anions by fluorine-fluorine pairs. These fluorine pairs caused a change in coordination of neighboring metal ions from octahedral to pentagonal bipyramidal. This transformation strictly corner sharing structures to ones containing edge shared polyhedra is diagrammatically shown in Figure 1.13.

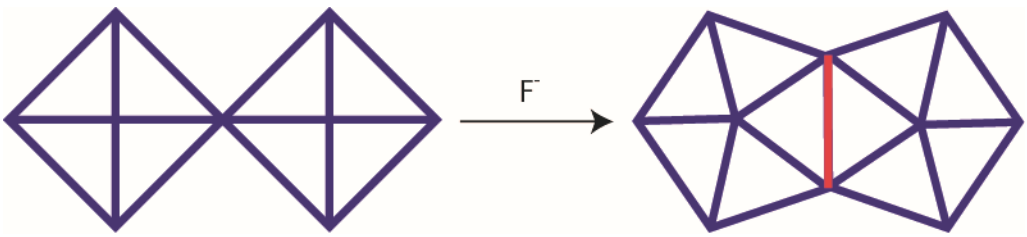

Figure 1.13: Schematic showing possible edge sharing defect arising from the incorporation of interstitial fluoride in a corner sharing framework.

These results along with others suggested that the substitution of high valent metals into metal fluorides would result in fluoride excess materials with interstitial fluorides and edge-sharing polyhedra. The introduction of this type of structural change should have a

large effect on vibrations responsible for thermal expansion, as the degrees of freedom associated with the linker fluorides decreases. Therefore, this type of local structural change could be a tool for controlling or tuning the thermal expansion seen in metal fluorides. One of the first thermal expansion studies on any fluoride excess framework material looked at $(Sc_{1-x}Zr_x)F_{3+\delta}$.[160] The results indicated a tuning of thermal expansion from NTE through zero to PTE on increasing Zr content. However, the author claims that the structure displays local rhombohedral-type octahedral tilting defects and not edge-sharing defects. Due to this, the introduction of excess fluoride to maintain charge balance is not accounted for, and the stoichiometry of the fluoride was represented as $F_{3+\delta}$.[160] Using aliovalent substitution as a strategy for generating defects to control NTE in metal fluorides was further explored for $YbZrF_7$.[178,179] This material as previously discussed was synthesized and characterized structurally, but its thermal expansion behavior was unknown. The new results did support the edge-sharing interstitial fluoride model; however, the thermal expansion behavior was complex. $YbZrF_7$ shows thermal history dependent expansion, while also displaying ZTE close to room temperature. While the insertion of excess fluoride didn't lead to simple weakening of NTE, work on $YbZrF_7$ did support the edge sharing interstitial model and showed some promise for utilizing excess fluorine to control thermal expansion. Another recent study reported the transition from partial edge-sharing to corner sharing octahedra to tune thermal expansion from PTE through zero to NTE in $Ti^{2+}_xTi^{3+}_{1-x}ZrF_{7-x}$ (x= 0,0.5, and 1).[180] The author indicated that the excess fluorine was incorporated interstitially, leading to a weakening of NTE through zero to PTE, and similar effects have seen in $Mg_{2-x}Zr_xF_{4+2x}$ and $Ti_{1-x}Zr_xF_{3+x}$.[181,182] The use of this method for designing materials with a certain magnitude of NTE or ZTE is still

relatively unexplored area of research. In CHAPTER 5 of this thesis the behavior of the fluoride excess material $CaZr_{1-x}Nb^{5+}{}_xF_{6+x}$ is explored.

1.3 Behavior of Negative Thermal Expansion Materials on Compression

Diffraction methods can also be utilized to probe the response of materials on compression. These measurements typically involve a diamond anvil cell (DAC) for high pressures (several GPa), or large metal gas pressure vessels for modest pressures (few kbar). These types of experiments can probe the change in lattice constant with pressure (and simultaneously temperature) and allow for the characterization of both a materials elastic properties and structure.

1.3.1 Significance and Applications

As discussed previously, NTE materials can be utilized to compensate for PTE materials to create composites with desired thermal expansion and physical properties. However, on a microlevel in these composites if one material is expanding while the other is contracting around it then the materials experience stresses. This type of stress from thermal expansion mismatch or stress from creating the composite can lead to changes in the material's structure and/or physical properties. This has been established as an issue, and one example is the Cu and ZrW_2O_8 metal matrix composites.[36,183] Research has shown that stress induced from making the composite resulted in partial conversion to high-pressure phase γ-ZrW_2O_8.[35] When thermally cycled, the composite shows reversible partial phase transitions between the high-pressure phase and cubic phases. This is attributed to stress induced by thermal expansion mismatch, and the presence of the orthorhombic γ-ZrW_2O_8, known to display PTE, complicates the thermal expansion of the bulk composite.[184-186]

Stress induced form thermal mismatch has also been seen for the large NTE material ScF_3. When ScF_3 powder was mixed and cooled with large PTE material GE-7031 varnish (utilized for its high thermal conductivity), the contraction of the varnish on the expanding ScF_3 resulted in a cubic to rhombohedral phase transition.[187] As previously discussed the large NTE in some framework materials, which makes them desirable to offset PTE, is directly tied to their structure. Therefore, phase transitions caused by stress from composite fabrication or thermal expansion mismatch can greatly affect the behavior of these composites. Making it very important to understand how NTE materials respond to stress. Which is why considerable work has been done and why this thesis includes variable pressure experiments.

1.3.2 Bulk Modulus

The isothermal bulk modulus (K_T sometimes abbreviated B_T) quantifies how resistant to compression a material is. The bulk modulus, which is inversely related to the compressibility, is defined in Equation 1.7.

$$K = V\left(\frac{\partial P}{\partial V}\right)_T \tag{1.7}$$

K_0, unless otherwise stated, refers to the room temperature isothermal bulk modulus at ambient pressure and quantifies how elastically soft/stiff a material is. A few examples of stiff materials with large bulk moduli are diamond 442 GPa and alumina 227 GPa.[188] Some solid materials can be quite soft with a small bulk modulus, for example NaCl with K_0=

23.9 GPa.[189] The bulk modulus can vary with pressure, and this dependence is quantified in the first derivative of the bulk modulus (K') with respect to pressure, see section 1.3.3.

1.3.3 Pressure-Induced Softening

As a material is compressed and its volume reduced, its resistance to further compression typically increases. Therefore, the bulk modulus typically gets larger with increase in pressure. This type of behavior is seen in most materials and referred to as pressure-induced stiffening. However, in some rare cases the phenomenon of pressure-induced softening (PIS) is seen. PIS is when a material becomes softer, lower bulk modulus, on compression. The first derivative of the bulk modulus (K') is negative for a material with PIS, and the more negative the larger the PIS. While PIS is an anomalous behavior for materials, it was actually predicted for framework NTE materials.[190,191] This theoretical study linked the PIS to the phonon modes that lead to NTE in framework materials.

1.3.4 Effect on CTE

Clearly phase transitions induced by stress on NTE materials will have a large impact on their thermal expansion, but there are also pressure effects on the ambient phase to consider. Extensive work has been done by Fang, Dove, and coworkers to examine the relationship between thermal expansion, temperature, and pressure in framework NTE materials. Molecular dynamic simulations and simple models were used to investigate ceramics like metal oxides, metal cyanides, zeolites, and metal fluorides as well as MOFs, all of which experimentally show "exotic" pressure-temperature behavior.[76,192]

$$\left(\frac{\partial \alpha}{\partial P}\right)_T = \left(\frac{1}{{K_T}^2}\right)\left(\frac{\partial K_T}{\partial T}\right)_P \quad \textbf{(1.8)}$$

$$K_T = K_{0K} - bTe^{-T_0/T} \quad \textbf{(1.9)}$$

The thermodynamic identity for change in thermal expansion with pressure is given in Equation 1.8.[193] Work based on this identity, observations, and theory developed the relationship shown in Equation 1.9.[194,195] In these equations α is the volume CTE, P is pressure, K_{0K} is bulk modulus at 0 K, T is temperature, and b and T_0 are constants. The temperature derivative of the bulk modulus at constant pressure can therefore be expressed as Equation 1.10.

$$\left(\frac{\partial K_T}{\partial T}\right)_P = -be^{-T_0/T}\left(1 + \frac{T_0}{T}\right) \quad \textbf{(1.10)}$$

It has been established that the T_0/T term is always positive, and that for most materials b is positive. Therefore, in equation 1.9 the temperature derivative of the bulk modulus at constant pressure is going to be negative for most materials. This makes physical sense as materials usually soften on heating. Now knowing that K_T is always positive and $\left(\frac{\partial K_T}{\partial T}\right)_P$ is generally negative, plugging into equation 1.7 shows that the pressure dependence of the

CTE, $\left(\frac{\partial \alpha}{\partial P}\right)_T$, will be negative. This shows that the CTE is expected to decrease for a material on compression meaning a weakening of PTE and strengthening of NTE.

This behavior can be explained more visually when considering the potential energy well for the octahedral rotations that can generates NTE in ReO_3-type materials. In a recent study exploring the relation between lattice parameter and phase transitions in several metal fluorides, the behavior under compression was also examined.[196] Calculations were performed to generate an energy scan for the F_{1g} vibrational mode in $CaZrF_6$, and Figure 1.14 was adapted from their work.[196]

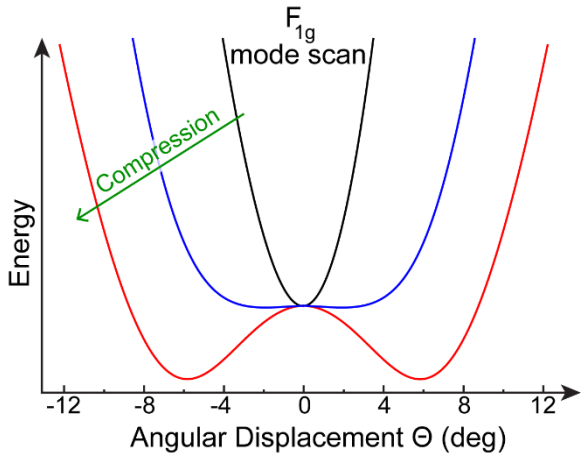

Figure 1.14: Energy scan for changing angular displacement in F_{1g} vibrational mode on compression.

The F_{1g} vibrational mode represents the rigid rotation of Zr and Ca octahedra. These calculations show that at ambient conditions in the cubic phase the energy scan generates a single-well potential, black line Figure 1.14. This potential well changes to a double-well potential as the material is forced through compression to a distorted phase such as rhombohedral, red line Figure 1.14. However, during this transition the vibrational energy scan behaves more like a quartic anharmonic potential, blue line Figure 1.14. In this type

of potential well the mode shows a larger angular range, and this larger rotation in the RUMs increases their contribution to NTE. This result shows that on compression the NTE should get stronger due to an increased contribution from RUMs. This pressure-induced increase in NTE magnitude is seen up until any pressure-induced phase transitions or amorphization. This vibrational analysis agrees with the thermodynamic analysis described earlier.

1.3.5 Pressure-Induced Amorphization

Another behavior seen in framework materials on compression is pressure-induced amorphization (PIA). This phenomenon is described as the transition from a crystalline material to an amorphous solid on compression. It is much more common to find materials that exhibit PIA than ones with PIS. The phonon modes that contribute to NTE in framework materials soften on compression. As a result, the frequency of these low energy modes will drop to zero on modest compression. When a phonon frequency becomes zero then the vibration turns into a static distortion, resulting in a structural phase transition. This phase transition can be to a disordered or amorphous structure. The presence of PIA at modest pressures in NTE materials would be of interest due to the large impacts on the materials thermal expansion. If the amorphization is not reversible then the NTE behavior would likely be lost.

1.3.6 Open Framework Materials

1.3.6.1 Zeolites and Aluminophosphates

The structure and NTE behavior of zeolites and AlPOs are discussed in section 1.2.3.1. These types of materials have a very rich behavior on compression that has been studied far less than their thermal expansion.[197-199] The insertion of guest molecules into the structure under pressure affects material's behavior.[200-202] The presence of sometimes reversible crystalline phase transitions and PIA have been seen in several zeolites.[203-205] The insertion of guest molecules, phase transitions, or amorphization would have a large effect on the thermal expansion of the material. Bulk moduli for zeolites have been determined in non-inserting pressure media for zeolite Na-A (K=22 GPa), Na-X (K=38 GPa), heulandite (K=27.5 GPa), yugawaralite (K=34 GPa), bikitaite (K=45 GPa), natrolite (K=53 GPa), scolecite (K=61 GPa), and sil-FAU (K=38 GPa) among others.[199,201,202,206] Zeolites typically have bulk moduli in the range of 20-60 GPa, which is not remarkably soft or stiff. While not much experimental work has been done to identify PIS in zeolites, the original work by Fang and Dove predicting PIS conducted simulations calculating bulk modulus and PIS for cubic siliceous zeolites. Some of the strongest PIS results were for the NTE zeolites MEP (K=58 GPa, K'= -30), AST (K=16 GPa, K'= -28), and LTA (K= 61.8 GPa, K'= -13).[190]

1.3.6.2 Metal Cyanides

The open framework structures of metal cyanides, section 1.2.3.2, were previously discussed. Similar to other framework materials, the open framework structure essential for NTE also makes them porous to guest molecules. Some Prussian blue type metal

cyanides have been shown to insert hydrogen under low pressures (< 1.18 atm).[207] Compression of the large NTE material $Zn(CN)_2$ led to no structural transformation in the examined pressure range (0-0.6 GPa), and a bulk modulus of K= 34.19(21) GPa.[208] The results also showed PIS not as large as the values projected for zeolites, but significant at K'= -6.0(7). This work also shows that the NTE is enhanced by increasing pressure, with the average CTE changing from α_v= -17.40(18) ppm K^{-1} at 0 GPa to α_v= -18.39(27) ppm K^{-1} at 0.2 GPa to α_v= -19.42(23) ppm K^{-1} at 0.4 GPa.[208] Further studies examined the temperature dependence of the elastic behavior of $Zn(CN)_2$. This study revealed that the bulk modulus gradually increased on cooling, and the PIS became slightly more negative down to 100 K before increasing through zero at the lowest temperatures.[209] On compression $Ag_3[Co(CN)_6]$ showed a structural phase transition at the modest pressure of 0.19 GPa, but still showed large anisotropic NTE. This material did not show PIS, but rather anisotropic compression with large compression in the a direction and expansion in the c direction.[210] Negative linear compressibility has also been seen in $KMn[Ag(CN)_2]_3$ and $Zn[Au(CN)_2]_2$ (also reported to have PIS with K'= -1.7) .[211,212] Metal cyanides are typically soft; $YFe(CN)_6$ (K=2.72 GPa), $LuFe(CN)_6$ (K=2.6 GPa), $Ag_3[Co(CN)_6]$ (K= 6.5 GPa).[210,213]

1.3.6.3 Metal-Organic Frameworks (MOFs)

The porous structure of metal-organic frameworks, section 1.2.3.3, can take up guests on compression, which can have an effect on their elastic properties and structure.[214,215] The open framework structure important for porosity and NTE can lead to phase transitions and PIA at low pressures. Phase transitions have been seen in several MOFs including $[Zn_2(C_3H_3N_2)_4]_n$ (ZIF-zni) at 0.8 GPa, and a reversible guest driven transition in both Zn(2-

MeIm)$_2$ (ZIF-8) at 1.47 GPa and Zn(Im)$_2$ (ZIF-4) at 0.56 GPa.[216-218] Amorphization occurs at just 0.0035 GPa in $Zn_4O(BDC)_3$ (MOF-5) with mechanical compression of solid pellet, at 0.34 GPa in Zn(2-MeIm)$_2$ (ZIF-8) in nonpenetrating medium, and reversible PIA at 0.35-0.98 GPa in nonpenetrating medium and at 2.02-6.48 GPa in penetrating medium for Zn(Im)$_2$ (ZIF-4).[218-220] The presence of a solvent in the pores of a MOF clearly effects the phase behavior for ZIF-4 and ZIF-8. It is interesting to note that amorphization can increase absorption of guest molecules, and irreversible PIA can be used to trap harmful substances.[221,222] The elastic properties of solvent free MOFs like ZIF-4 (K= 2.6 GPa), ZIF-8 (K= 6.52 GPa), ZIF-zni (K ~14 GPa), and Cu-btc (K= 29.5 GPa) indicate that these frameworks can be very soft.[216,218,220,223] The presence of different guest molecules in MOFs changes the behavior. Guest molecule inclusion resulted in a higher bulk modulus for ZIF-4 (K= 7.7 GPa) and a very hard (K= 117.6 GPa) region followed by softer (K= 25.9 GPa) regions for Cu-btc in isopropyl alcohol.[218,223] Pressure-induced softening has not reported for many MOFs. However ZIF-8 in nonpenetrating solvent, where K= 6.52 GPa, showed PIS with a K'= -4.6(14).[220]

1.3.6.4 Metal Oxides

Framework metal oxides have been more thoroughly studied than other NTE materials, possibly due to fewer instances of the pressure transmitting media inserting into the sample. The large NTE material, section 1.2.3.4, ZrW_2O_8 has been shown to undergo an reversible phase transition above 0.2 GPa, and a gradual PIA between 1.5 and 3.5 GPa.[224-226] Other AM_2O_8 materials have shown similar behavior, with HfW_2O_8 undergoing an irreversible phase transition to an orthorhombic phase at 0.62 GPa and PIA at ~2 to 3 GPa, and cubic $ZrMo_2O_8$ and $HfMo_2O_8$ both undergoing a reversible phase transition from 0.7-2.0 GPa

and PIA at 1.5-4.0 GPa and above 4.0 GPa, respectively.[226-232] The high-pressure behavior of a few NTE materials from the AM_2O_7 family all showed similar trends. Two reversible symmetry lowering phase transitions are seen in CeP_2O_7 one at 0.65 GPa and the other above 5.0 GPa.[104] A reversible crystalline phase transition at 1.6 GPa and 3.7 GPa for ZrV_2O_7 and HfV_2O_7, respectively. This is followed by irreversible PIA above 4 GPa for both, with the amorphization of the Hf analog being gradual.[233,234] The $A_2M_3O_{12}$ family, again, generally shows crystalline-to-crystalline phase transitions on compression at modest pressures, and PIA on further compression. An orthorhombic to monoclinic transition has been reported in $Sc_2W_3O_{12}$ (0.25-0.30 GPa), $Sc_2Mo_3O_{12}$ (0.25 GPa), $Al_2W_3O_{12}$ (0.1 GPa), and $Ga_2Mo_3O_{12}$ (3.2-4.1 GPa) .[235-239] A second crystalline phase transition was also seen for $Sc_2Mo_3O_{12}$ occurring between 2.5 and 3.0 GPa, while PIA is observed in $Sc_2W_3O_{12}$ (> 4 GPa), $Sc_2Mo_3O_{12}$ (~8 GPa), $Al_2W_3O_{12}$ (~7 GPa), $Y_2W_3O_{12}$ (~3 GPa), $Lu_2W_3O_{12}$ (5-8 GPa), and $Ga_2Mo_3O_{12}$ (~8 GPa).[236-241] These NTE metal oxides can range from being as soft as MOFs or metal cyanides to having higher bulk moduli. Some examples of bulk moduli include ZrW_2O_8 (K=72.5 GPa), HfW_2O_8 (K= 82.0 GPa), ZrV_2O_7 (17.0 GPa), HfV_2O_7 (K= 12.8 GPa), $Sc_2Mo_3O_{12}$ (K=32 GPa), and $Al_2W_3O_{12}$ (48 GPa).[227,233,234,237,242] A trend has also been seen that the bulk modulus of the high-pressure phases is softer, for example high-pressure monoclinic phase of $Sc_2Mo_3O_{12}$ (K=16 GPa) and $Al_2W_3O_{12}$ (K= 28 GPa) is softer than the low pressure phase.[237] While pressure-induced softening has been seen in ZrW_2O_8 (no reported K' value) no other NTE metal oxides have been reported to display PIS.[243]

1.3.6.5 ReO_3-type Metal Fluorides

As previously discussed, section 1.2.4, the cubic ReO_3-type structure can lead to large isotropic NTE, but metal fluorides often adopt a rhombohedral structure at ambient conditions or on cooling. There are only a few reports on metal fluorides at high pressures, and the only cubic ReO_3-type fluorides studied are ScF_3 and $CaZrF_6$.[25,26,244-246] Work by Aleksdrov et al on ScF_3 showed a crystalline phase transition from cubic to rhombohedral at ~0.7 GPa.[244,246] This transition is followed by another to an orthorhombic phase at ~3.0 GPa.[245] An examination of ScF_3's pressure-temperature behavior revealed that the phase transition to rhombohedral was pushed to lower pressures at lower temperature, with the transition occurring at ~0.15 GPa at 50 K.[25] The bulk modulus of ScF_3 was originally estimated to be ~70 GPa, but was later calculated at 57 GPa and ~60 GPa.[25,155,245] The high-pressure rhombohedral phase is much softer with a bulk modulus of ~9 GPa.[247] The effects of chemical substitution on the compressibility of ScF_3 has been studied in the systems $Sc_{1-x}Y_xF_3$ ($x \leq 0.25$) and $Sc_{1-x}Al_xF_3$ ($x \leq 0.5$). The yttrium doped materials showed a decrease in bulk modulus with increased substitution, with a K= ~34 GPa for x=0.25, and the bulk moduli of the substituted samples increased on heating.[157] The aluminum substituted materials showed very similar trends bulk moduli, however the $x > 0.2$ samples adopted a rhombohedral phase at room temperature, and showed lower bulk moduli, with K between 10 and 20 GPa.[159] Interestingly again no PIS was seen in any studies of ScF_3 or the substituted materials. Studies by Jorgensen et al explored the compressibility of CrF_3 and FeF_3 both of which are rhombohedral at ambient conditions. They both showed no phase transitions up to the highest measured pressures (8-9 GPa). However, their octahedra distorted on compression. This strain resulted in negative linear compressibility along the

unique c direction. The elastic behavior was characterized as K_0= 29.2 GPa and K_0'= 10.3 for CrF_3 and K_0= 14 GPa and K_0'= 12.[248,249] Prior to the current work, the only other known cubic NTE metal fluoride studied under pressure was $CaZrF_6$.[26] This material undergoes a phase transition at 0.4 GPa that irreversibly leads to a disordered, possibly amorphous, material. The cubic material is soft and displays PIS with K= 39.2 GPa and K'= -13. The magnitude of its NTE increased on compression with $\alpha_{L(298–514K)}$ changing from -9.2 ppm K^{-1} at 0.05 GPa to -9.9 ppm K^{-1} at 0.31 GPa.[26] The behavior of the fluoride excess ReO_3-type material $YbZrF_7$ on compression has also been reported. This material is believed to compensate for the aliovalent substitution of Yb^{3+} into the $M^{2+}M^{4+}F_6$ parent structure through interstitial fluoride, which generates edge-sharing polyhedra defects. This material shows a very abrupt amorphization at 0.95 GPa, and has K_0= 55.4 GPa, with large PIS, K_0'= -27.7.[178]

1.4 Porous Materials and Their Response to Pressure

The types of materials discussed in this work are open framework solids. The empty space or porosity of zeolites, metal cyanides, MOFs, metal oxides, and metal fluorides contributes to the presence of the low-energy transverse vibrations, which produce the previously discussed NTE, see section 1.2.2.4. The porous nature of these materials can and has been shown to lead to insertion of guest molecules into the framework cavities on compression, section 1.3. As the NTE materials discussed in this work can be considered porous, it is important to establish the significance and applications of porous materials, as well as what is already known about porous solids. A porous solid is defined as a material with accessible pores (cavities, voids, channels, or interstices) which can be permeable to liquids or gases. These solids can be classified based on pore size as either microporous (≤

2nm), mesoporous (2-50 nm), or macroporous (> 50 nm).[250] These types of materials are found naturally and have been man-made for industrial or scientific purposes.[251,252]

1.4.1 Significance and Applications

Porous solids uniquely show interaction with atoms, molecules, and ions in the bulk of the material, not just the external surface. This makes porous materials of scientific importance and useful in several types of application. The uptake of guest atoms, molecules, or ions can be used for catalysis, ion exchange, separations, and storage. There are many reviews that address these applications, and specific examples for separations, trapping, and storage will be discussed below.[250-254] Some specific applications of porous solids include: methane or hydrogen storage for use as alternatives to petroleum, olefin separation, pressure swing adsorption air separations, drying or CO_2 removal from natural gas, sulfur removal from petroleum gas, hydrocarbon conversion catalysis, removal of Cs^+ and Sr^{2+}, and removal of NH_4^+ from waste water.[252] The size, shape, and volume of pores in a solid can vary, and these properties along with their uniformity can impact the behavior and usefulness in certain applications. The chemical framework that creates the pores can also affect the properties and applications of these materials.

1.4.2 Industrial Materials

One of the major areas of research for porous materials since the mid-20th century has been as absorbents, which can store, trap, or separate gases or liquids. These materials are sometimes referred to as molecular sieves, which can be defined as a porous solid material which exhibits the property of acting as a sieves on a molecular scale.[255] Early technology relied on materials like activated carbons, clays, and alumina. These materials were not

ordered and therefore had nonuniform pore size that cause performance to suffer. Zeolites were explored as an emerging class of materials for use as molecular sieves, due to their uniform pore size that could be changed with change in crystal structure. There are many naturally occurring zeolite minerals which will be discussed in a later section, and work by Breck in 1974 thoroughly discusses the early work on zeolites as molecular sieves.[251] Notably the first industrial work can be seen in 1948 by Union Carbide Corporation in which they show the first controlled production of a synthetic zeolite molecular sieve in a series of patents.[256,257] This lead to the development and testing of many zeolites for adsorption. It was shown that silicalite selectively adsorbs organic molecules out of water.[258] After the work by Milton, zeolite types A, X, and Y have been the most used for industrial gas separations.[259] Breck and coworkers were able to characterize the properties including gas adsorption of some type A zeolites.[260] Another study also showed zeolites 3A, 4A, 5A, and 13X to adsorb several different gasses at modest pressures.[261] The previously mentioned work by Breck also showed that temperature could also be used to regulate access to pores, through variable temperature adsorption of argon and nitrogen gas in zeolite 4A.[260] This showed the accessibilities of the micropores can be regulated with stimuli like heat or light, not just pressure. This behavior can be manipulated to trap guest species in the solid for storage. Again, this was first put into practice by Union Carbide Corporation in a patent showing encapsulation of several gases in zeolite A.[262] This is of potential importance for applications like natural gas or hydrogen storage. Indeed, hydrogen was shown to be trapped in A type zeolites by Faenkel in the 1980's.[263] The smaller pores of many microporous materials like zeolites and AlPOs limited their use in practical applications. AlPO VPI-5 was reported as the first crystalline microporous

material with uniform pores larger than 1.0 nm.[264] However the relatively poor thermal stability of VPI-5, and AlPOs in general, limits their applications. This has led to the exploration of mesoporous materials, including many MOFs, for possible adsorbent applications. These materials don't always maintain permanent porosity and can undergo structural rearrangements or amorphization upon guest removal or exchange. MOFs like MOF-5 and MOF-15 have been prepared and shown to exhibit permanent porosity.[265,266] MOFs have been shown to be take up methane in large amounts at relatively low pressures.[265,267] Similar to other porous solids the porosity can be manipulated with temperature to trap gases, and recently the MOF MFU-4 was reported as having large storage capacity for xenon.[268] A comprehensive report of the gas absorption properties of MOFs and their selectivity for separations can be found in a review.[269] This area of research continues to grow, as more porous solids are characterized for testing in different applications.

1.4.3 Environmental Examples

As discussed previously, zeolites were very important to the early development of solids for molecular sieves and gas storage. While many synthetic materials were made for industrial applications, there are naturally occurring porous materials that have also been studied. There are many naturally occurring zeolite minerals that can be found in rocks or sedimentary deposits, and are sometimes found as single crystals a few millimeters in size.[251] The first experimental observations of gas absorption in zeolites were on naturally occurring zeolite minerals. One of the first being by Grandjean in 1909, which showed chabazite absorbs ammonia, air, hydrogen, carbon disulfide, hydrogen sulfide, iodine, and bromine.[270] The first definitive separation with zeolites was done with dehydrated zeolite

minerals like chabazite, gmelinite, mordenite etc. by Barrer beginning in the 1940's.[271,272] Natural zeolites began to be used for applications like drying natural gas, purifying waste water, soil amendment, and cement manufacturing.[252,273,274]

1.4.4 Helium Containing Compounds and Helium Gas Uptake

Of specific relevance to this thesis work are solids known to absorb or include helium. Helium and the other noble gases have a stable closed shell electron configuration, and therefore are very unreactive. Some noble gases like xenon and krypton were predicted to and eventually shown to react and form noble gas compounds.[275-278] Helium however is the most inert of the noble gases, and does not form compounds similar to those of Xe and Kr. There were early theoretical predictions for the existence of helium containing compounds, like HHeF.[279-281] However, this molecule, (HeO)(CsF), and the experimentally formed LiHe were metastable and very high in energy.[282,283] The real breakthrough in producing any stable helium compounds came from the use of high pressure. It has been known that high pressure can alter the chemical properties and reactivity of elements, and this was utilized to identify several theoretical and experimental noble gas compounds.[284-288] A few theoretical calculations showed helium can react with several ionic alkali oxide or sulfide compounds as well as form compounds with water at high pressures.[289,290] The first helium clathrate was formed from compression of helium in ice II at pressures just above 0.28 GPa.[291] It was recently shown that in water at 300 GPa helium forms $He@H_2O$, and that $Ne(He)_2$ forms in He-Ne gas mix above 13.7 GPa.[290,292] However, these are van der Waals compounds. Dong and co-workers were able to predict and experimentally verify a cubic phase Na_2He material.[293] This compound is stable from 113 GPa up to at least 1,000 GPa, and the compound Na_2HeO is also predicted to be thermodynamically

stable. Interestingly it is reported that in these compounds some of the electrons detach from the sodium and localize at the interstitial sites, where they behave like anions. This behavior makes these materials high-pressure electrides, however the origin of the stability in these and other helium compounds is not well understood.[294] More recently a computational study looked at the reaction of helium with ionic compounds containing unequal numbers of cations and anions. It showed that in the previous Na examples and in other systems predicted to form helium compounds at high pressures, the helium insertion lowers the strong repulsive Coulomb interactions allowing the formation of the compounds.[295] Even with the recent work in this field, helium containing compounds are quite rare. The ability to trap helium in porous materials to create helium insertion materials could be utilized to create new compounds. Helium has been purified at low temperatures through absorption in activated carbons and charcoal.[296,297] Helium has been shown to absorb in several zeolites.[261] Helium has also been shown to penetrate typically nonporous materials on compression, including C_{60}, arsenolite, cristobalite, silica glass, and melanophlogite.[298-304] However, absorbing helium into a structure then trapping the helium in the structure has not been well explored.

1.5 Perovskites

Perovskites have been studied for many decades. A material is considered to be a perovskite when it adopts the same crystal structure as $CaTiO_3$, which is the perovskite mineral. The basic structure for a cubic perovskite is shown in Figure 1.15 and consist of a repeating ABX_3 unit. The B cation has 6-fold coordination with the X anions, and these octahedra are corner linked. The empty cavity between the BX_3 units is occupied by the A cation with 12-fold coordination. The A cation is commonly a large cation from group I or

II like Na, Ba, or Cs, but small organic ions like methylammonium ($CH_3NH_4^+$) have also been utilized. The B site can be occupied by metals from almost any region of the periodic table, with even Xe containing perovskites forming.[305] The X site most commonly contains oxide or a halide. The large amount of compositional flexibly in this basic perovskite structure, has led to the formation of thousands of different perovskites. Perovskites have been identified with many different A,B, and X atoms or molecules, vacancies, stoichiometries, and crystal structures.[306]

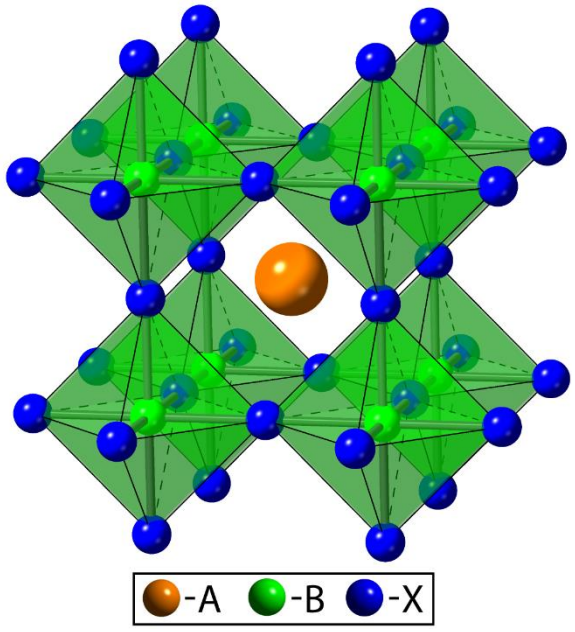

Figure 1.15: Cubic structure of $SrTiO_3$ a perovskite with ABX_3 formula.

1.5.1 Significance and Applications

The large compositional flexibility of perovskites has led to several interesting properties, and the exploration of perovskites for many types of applications. Early on Perovskites drew interest due to their stability and electrical properties.[307-310] Many oxide perovskites have been studied for use in catalysis due to their thermal stability and the ability to enhance

their surface area and properties.[309-312] Perovskites have been shown to display the piezoelectric effect, colossal magnetoresistance, superconductivity, and ferroelectricity.[309,310,313-317] These interesting properties have led to great strides in understanding perovskite materials. However, the behavior that has contributed the most to the study of perovskites in recent years has been their optoelectronic properties. Metal halide perovskites like $CsPbX_3$ (X= Cl, Br, and I) were originally reported and studied for use in pigments due to their vibrant colors.[318,319] These perovskites began to garner more attention for photovoltaic applications, when then first organic-inorganic halide perovskites (hybrid perovskites) that utilize a small organic cation like methylammonium (MA) were synthesized.[320] These types of materials were then shown to feature strong excitonic characteristics, and were explored for applications in thin film transistors and light-emitting diodes.[321] It became apparent that the extremely high optical absorption among other physical properties would lend itself to photovoltaics. In the beginning perovskites like $CH_3NH_3PbX_3$ were utilized in dye-sensitized solar cells with modest power conversion efficiencies from 2-7%.[322,323] Then with the use of a solid electrolyte and fine tuning of other solar cell components led to efficiencies above 10%.[324,325] Eventually it was shown that the band gap of these hybrid perovskites could also be adjusted to optimize their optoelectrical properties.[326] These early results led to a very large increase in the research done on perovskites as thin absorbers for solar cells, and the $CH_3NH_3PbX_3$ system was optimized up to an efficiency of 20.1% in just five years. This meteoric rise of efficiency in perovskite solar cells put these materials on the cutting-edge of optoelectronics research and has only attracted even more interest from scientist across multiple disciplines. These materials and devices have been heavily scrutinized from a

fundamental and applications standpoints in recent years, and much of this expansive work can be found in several reviews of the topic.[310,327-331] The wide array of interesting properties and applications, led by their photo absorption, continue to make perovskites of very high interest to the materials community. The development of new materials, deeper understanding of their properties, and development of design principles are important in continuing the large impact of perovskites.

1.6 Summary and Thesis Goals

Negative thermal expansion is a phenomenon where materials contract on heating and expand on cooling (section 1.2). NTE materials are important in a variety of applications, including in composites where they can be used to offset the PTE of another component (section 1.2.1). The mechanisms generating NTE in several different types of materials are well known (section 1.2.2). However, greater understanding of NTE will enhance our ability to control thermal expansion in materials. The ability to tailor thermal expansion would allow for the design of materials with an expansion match to avoid interface stresses. Generating close to zero thermal expansion in a material would provide dimensional stability and thermal shock resistance. The rarity of NTE materials and their potential for applications make identifying and characterizing the behavior of new NTE materials a goal of this thesis work.

While phase transitions can lead to NTE, the transition, and the resulting NTE, commonly occurs over a narrow temperature range (section 1.2.2). In contrast to this, NTE in open framework materials often extends over wide temperature range (section 1.2.3). Their NTE arises from the population of low energy vibrational modes on heating, which reduce the

volume of the material (section 1.2.2.4). In this thesis, the effects of chemical substitution, crystal structure, pressure, and temperature on NTE are explored. Materials with simple frameworks, amenable to generating the desired vibrational NTE, were chosen for study to simplify the interpretation of the relationships between composition, structure, sample environment and thermal expansion. Several metal fluorides adopt a cubic ReO_3-type structure, consisting of metal centered octahedra corner-linked by fluorides, and this framework structure can support vibrational NTE (section 1.2.4). The first and only metal trifluoride shown to display large isotropic NTE over a wide temperature range was ScF_3 (section 1.2.4.2). Many other metal trifluorides do not maintain the cubic ReO_3-type structure on cooling and show PTE. Replacing the M^{3+} metal by M^{2+} and M^{4+} can lead to mixed metal ReO_3-type fluorides (section 1.2.4.3). Immediately prior to the reported thesis work, cubic $CaZrF_6$ was shown to display large isotropic NTE over a wide temperature range. The $M^{2+}M^{4+}F_6$ family of materials was targeted for exploration due to both the properties of $CaZrF_6$ and the compositional flexibly available in this system. Several $M^{2+}M^{4+}F_6$ materials were known to adopt the cubic ReO_3-type structure at room temperature, but their thermal expansion behavior was unexplored. These materials combined, with other compositionally relevant materials, were targeted to explore the relationship between chemical composition and thermal expansion. To further investigate the control of thermal expansion in these materials, non-stoichiometric fluoride excess materials were examined. These materials must maintain charge balance while incorporating fluoride in excess of that required by a defect free ReO_3-type structure. Changes in local structure to accommodate the excess fluoride will influence thermal expansion (section 1.2.4.4). However, very little was known about the structure and

thermal expansion of these fluoride excess materials, and new insight could assist in developing design principles for controlling the thermal expansion of NTE framework materials.

The use of NTE materials in a variety of potential applications can be associated with thermal expansion mismatch issues. Even in controlled thermal expansion composites, where the composite may have low or close to ZTE, there can be considerable thermal expansion mismatch between the NTE and PTE components. Thermal expansion mismatch can lead to stresses at the interface between the materials (1.3.1). Therefore, it is important to understand a material's response to stress along with their expansion characteristics. A goal of this thesis work was to better understand the response to hydrostatic stress of the ReO_3-type metal fluorides discussed previously, through variable pressure experiments. While the high-pressure behavior of other NTE materials, including several metal trifluorides and $CaZrF_6$, has been reported, very little was known about the response to pressure of $M^{2+}M^{4+}F_6$ materials (section 1.3.6). To address this goal, identification of any crystalline to crystalline phase transitions or amorphization on compression and the characterization of elastic properties, such as bulk moduli (K), in these metal fluorides was necessary. This work will lead to a better understanding of how chemical composition relates to the properties of these metal fluorides and the problems that can be encountered in applications. While exotic behavior, such as pressure-induced softening, has been predicted to occur in framework NTE materials, very few materials have been experimentally examined (section 1.3.5 and 1.3.6). Therefore, determining the pressure derivative of the bulk modulus was undertaken to look for and characterize pressure-induced softening in mixed metal fluorides.

While many framework NTE materials such as zeolites and MOFs are known to be porous and have been studied for gas absorption on compression, metal fluoride NTE materials of the type studied in this thesis were generally considered as nonporous (section 1.4). However, their porosity had not been investigated. Additionally, the cubic ReO_3-type metal fluorides studied in this thesis have a pseudo-perovskite structure, with an empty "A-site" cavity between the corner-sharing octahedra. Insertion of a guest species into this pore generates a material with a perovskite structure. Perovskite materials often have interesting properties and are of great technological importance (section 1.5). In this thesis, the porosity of some mixed metal fluorides at high pressures is explored.

CHAPTER 2. COMPOSITION, RESPONSE TO PRESSURE, AND NEGATIVE THERMAL EXPANSION IN $M^{II}B^{IV}F_6$ (M = Ca, Mg; B = Zr, Nb)[1]

2.1 Introduction

While most materials expand on heating, a growing number are known to contract.[30-32,332] Such negative thermal expansion (NTE) can, in principle, be used to compensate for the response of positive thermal expansion (PTE) solids, either by preparing composites of the PTE and NTE materials or by assembling devices containing parts made from separate NTE and PTE components. There is a significant body of work examining the fabrication and performance of metal matrix-ceramic composites, polymer ceramic composites, and ceramic-ceramic composites containing NTE materials for various applications.[36,38,39,333-335] When NTE and PTE solids are used together in a composite, there can be considerable stresses within the composite due to differential thermal expansion. These stresses can lead to phase transitions and other unwanted phenomena,[187,336] as open framework NTE solids typically display quite rich behavior at low pressure.[26,225,226,236,337,338]

The mechanisms and compositions associated with NTE materials are varied. In open framework oxides, fluorides, cyanides, and MOFs, low frequency phonons can give

[1] Published in *Chem. Mater.*, **2017**, 29(2), pp 823-831

rise to NTE and other unusual phenomena, such as pressure-induced softening.[337] NTE can also be associated with structural phase transitions,[53] charge transfer,[45] ferroelectric instabilities,[339,340] and magnetic ordering effects.[48] It has also been reported in 2D materials such as graphene.[341]

While much of the earlier work on NTE solids focused on oxides, metal fluorides with ReO_3-type structures have recently attracted attention.[25,26,152,153,155,157,159,342-344] Materials such as ScF_3[25] and $CaZrF_6$[26] combine strong or very strong isotropic negative thermal expansion with optical transparency ranging from the mid-IR into the UV, suggesting optical applications. For some applications, less extreme NTE is desirable. There has been some success in tuning the characteristics of ScF_3 by solid solution formation[155-157,159,342] and nanosizing,[345] and very recently a suite of $MZrF_6$ compositions (M – Ca, Mn, Fe, Co, Ni and Zn)[344] have been examined in order to better understand the extent to which the very strong NTE found in $CaZrF_6$, and its close relative $CaHfF_6$, can be tailored. The remarkable NTE of both ScF_3 and $CaZrF_6$ is associated with the stability of the ideal cubic ReO_3 structure towards symmetry lowering phase transitions when cooled to very low temperatures. This has been attributed to the high ionicity of these compounds.[25,26] To the extent that information is available, MF_3 and $M^{II}B^{IV}F_6$ with ReO_3-type connectivity and symmetries lower than that of the ideal cubic structure ($Pm\bar{3}m$ and $Fm\bar{3}m$) at close to room temperature do not show strong NTE.

The literature on ReO_3-type $M^{II}B^{IV}F_6$ indicates that mid and late 3d metals on the M –site, such as Fe, Co, Ni and Zn destabilize the cubic structure and, hence, are likely to preclude strong NTE.[170,346] Phase transition temperatures have been reported to range from ~400 K for Ni to ~150 K for Mn in $MZrF_6$,[170] although contrary to this, and other literature

on $CoZrF_6$,[26,171] a very recent paper on thermal expansion in $MZrF_6$ reports no phase transitions for the Co and Ni materials above 125 K.[344] In this paper, we examine how the replacement of Ca^{2+} and Zr^{4+} by Mg^{2+} and Nb^{4+}, effects the thermal expansion and behavior under pressure of ReO_3-type $M^{II}B^{IV}F_6$. Variable-temperature neutron and/or synchrotron x-ray diffraction were employed to study the phase behavior and thermal expansion of $MgZrF_6$, $CaNbF_6$, and $MgNbF_6$, and high-pressure synchrotron x-ray powder diffraction was used to examine the behavior of $MgZrF_6$ and $CaNbF_6$.

2.2 Experimental

2.2.1 Synthesis

All syntheses were carried out in a dry, nitrogen-filled glove-box. NbF_5 (99.5%) was purchased from STREM Chemicals, ZrF_4 (99.9%) from Sigma Aldrich, and niobium metal powder (99.99% with < 500 ppm Ta), CaF_2 (99.5%) and MgF_2 (99.9% optical grade) from Alfa Aesar. As several different batches of material were used for the reported measurements on $CaNbF_6$ and $MgZrF_6$, we report representative syntheses for these materials.

NbF_4 was prepared via the solid state reaction of NbF_5 and niobium metal using a procedure similar to that reported by Chassaing et al.[347] The reactants were mixed in a 5:1 molar ratio and then placed into a copper tube, which was sealed by arc-welding under argon. The copper tube was then sealed in an evacuated fused quartz ampule. The ampule was heated to 300 °C (heating rate: 0.19 °C/min), held at 300 °C for 96 hrs, and then quenched. The excess NbF_5 was removed from the resulting mixture by vacuum sublimation. The resulting

NbF_4 was a black hygroscopic powder. Note that NbF_4 is reported to disproportionate at greater than 350 °C.[348]

$CaNbF_6$ and $MgNbF_6$ were prepared via the solid state reaction of NbF_4 and MF_2 (M= Ca, Mg), using a procedure based on that reported by Goubard et al.[349] The reactants were mixed in a 1:1 molar ratio and placed into a copper tube, which was then sealed via arc-welding under argon. The copper tube was then sealed in an evacuated fused quartz ampule. The ampule was heated to 520 °C (heating rate: 4.13 °/min), held at 520 °C for 5 days, and slowly cooled to room temperature. The final $CaNbF_6$ and $MgNbF_6$ products were grey and black powders respectively.

$MgZrF_6$ was prepared via the solid-state reaction of ZrF_4 and MgF_2. The reactants were mixed in a 1:1 molar ratio and placed into a copper tube, which was then sealed via arc-welding under an argon atmosphere. The copper tube was then sealed in an evacuated fused quartz ampule. The ampule was heated to 850 °C (heating rate: 4.13 °/min), held at 850 °C for 24 hrs, and then slowly cooled to room temperature. The final $MgZrF_6$ product was a white powder.

Sample syntheses for the x-ray measurements were performed typically on a ~500 mg scale. However, sample preparation for the $CaNbF_6$ neutron measurements was performed on a ~4 g scale.

The starting materials NbF_5 and ZrF_4 are moisture sensitive and the products $CaNbF_6$, $MgNbF_6$ and $MgZrF_6$ are expected to show some sensitivity to atmospheric exposure. After storage for several months, $CaNbF_6$ samples showed signs of decomposition, but exposure

to the laboratory atmosphere for several hours led to little change in the powder x-ray diffraction patterns for $MgNbF_6$ and $MgZrF_6$.

2.2.2 Variable Temperature X-ray Powder Diffraction Measurements

X-ray powder diffraction data were recorded using an Oxford Cryosystems Cryostream (100 – 500 K), for samples of $CaNbF_6$, $MgZrF_6$ and $MgNbF_6$. Data were also recorded using a resistively heated furnace (300 – ~1000 K). These measurements were performed at the 17-BM beamline of the Advanced Photon Source, Argonne National Laboratory, using precisely determined wavelengths close to 0.73 Å. The low temperature measurements were performed using samples that were sealed using epoxy in Kapton capillary tubes under an inert gas atmosphere. For the furnace measurements, the samples were contained in fused quartz capillaries with helium gas flowing very slowly though them.

Additionally, low temperature high resolution synchrotron powder diffraction data were recorded for a sample of $MgZrF_6$ at beam line 11-BM of the Advanced Photon Source,[350,351] using an Oxford Instruments closed-flow helium cryostat (OptistatCF). An average wavelength of 0.41421 Å was used for these measurements.

For each of the above measurements, < 100 mg of material was needed as small diameter (~1 mm or less) capillaries were used.

2.2.3 Neutron Powder Diffraction Measurements

Neutron diffraction measurements were made using the PAC (POWGEN Auto-Changer) sample environment on the POWGEN beam line at the Spallation Neutron Source, Oak

Ridge National Laboratory. A $CaNbF_6$ sample was loaded into a vanadium can under helium. The sample was cooled to 10 K and heated in steps to 300 K with 3-minute equilibration times at each temperature prior to recording a diffraction pattern.

2.2.4 High-Pressure X-ray Diffraction Measurements

High-pressure x-ray powder diffraction data (298 K and P < ~8.6 GPa) were recorded for samples of $CaNbF_6$ and $MgZrF_6$ at beam line 17-BM of the Advanced Photon Source using an EasyLab "Diacell Bragg-(G)" diaphragm diamond anvil cell (DAC) while the pressure was continuously increased. The sample was loaded under inert atmosphere with either NaCl or CaF_2 as an internal pressure calibrant and an Alfa silicone oil (molecular weight of 237 $g \cdot mol^{-1}$) as the pressure-transmitting fluid. Pressure was determined using the unit cell volumes of the NaCl or CaF_2, along with their known equations of state (Birch EoS for NaCl[189] and the EoS reported by Angel et al.[352] for CaF_2).

High-pressure x-ray diffraction data (P < 310 MPa, 298 K < T < 523 K) were also recorded for $MgZrF_6$ at the 11-ID-B beam-line of the Advanced Photon Source using a heated titanium pressure vessel and Background Reducing Internal Mask (BRIM)[353] as previously described.[155] This arrangement allows for precise control of both temperature and pressure.

2.2.5 Rietveld Analysis of the Powder Diffraction Data

Rietveld refinements were used to determine structural parameters and lattice constants. All the fits were done using the General Structure Analysis System (GSAS)[354] along with the EXPGUI[355] interface.

2.3 Results and Discussion

2.3.1 Phase Behavior and Expansion as a Function of Temperature

All the materials under study were examined using variable temperature synchrotron powder diffraction over the temperature interval 100 – 500 K. Additionally, $CaNbF_6$ was examined by powder neutron diffraction between 10 and 300 K and $MgZrF_6$ was studied by high resolution synchrotron x-ray diffraction at down to 10 K. High temperature synchrotron powder diffraction experiments were performed for all the materials, but in some cases the data are only qualitatively useful due to difficulties with temperature control.

2.3.1.1 Behavior of $CaNbF_6$ from 10 to 900 K

Powder x-ray and neutron diffraction show that $CaNbF_6$ remains cubic and displays negative thermal expansion over the entire temperature range studied. The 10 K neutron powder diffraction pattern is fully consistent with rock salt like cation ordering in a cubic ReO_3-type structure with $Fm\bar{3}m$ symmetry (Figure 2.1)

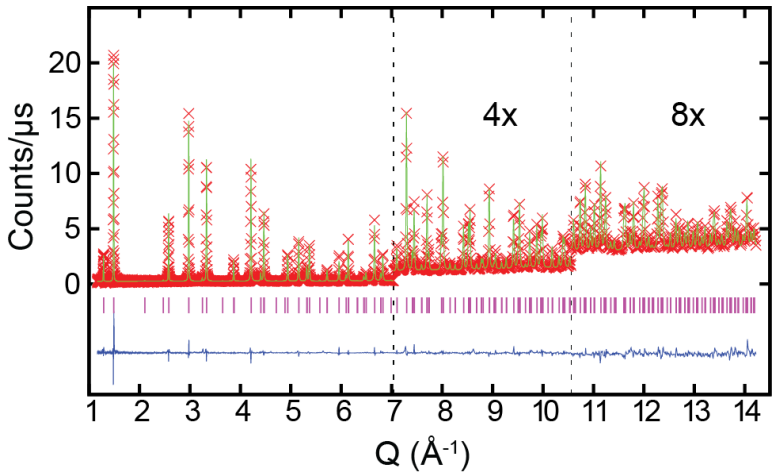

Figure 2.1: Rietveld fit to a 10 K time-of-flight powder neutron diffraction pattern for $CaNbF_6$ using a cation ordered cubic ReO_3-type model.

The lattice constants and derived thermal expansion coefficients from the neutron diffraction data (Figure 2.2) show strong NTE, very similar to that previously seen for $CaZrF_6$, but with greater magnitude; α_v ~-65 ppm K^{-1} at ~70 K for $CaNbF_6$ compared to α_v ~-56 ppm K^{-1} at ~75 K for $CaZrF_6$.

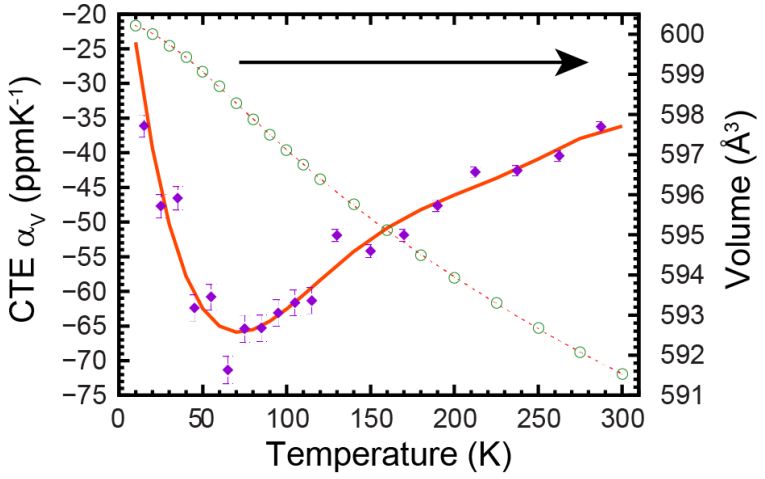

Figure 2.2: Unit cell volume and volume thermal expansion coefficient for $CaNbF_6$ determined from the powder neutron diffraction data. A six-term polynomial fit to the

volume (dashed line) was used to calculate the expansion coefficient (solid orange line). Additionally, the expansion coefficient was determined point by point (purple symbols).

The magnitude of the NTE generally decreases on heating (Figure A.1), but it persists to above the temperature used to synthesize the material (~800 K), even after the sample begins to decompose. The high temperature diffraction data for $CaNbF_6$ (Figure A.2 and Figure A.3) suggest that the initial decomposition products are CaF_2 and a ReO_3-type phase, which may be a niobium oxyfluoride. As NbF_4 is known to disproportionate at high temperatures,[347,348] and NbF_5 reacts with SiO_2,[356] the oxyfluoride could arise from reaction with the fused quartz capillary tube used to contain the sample.

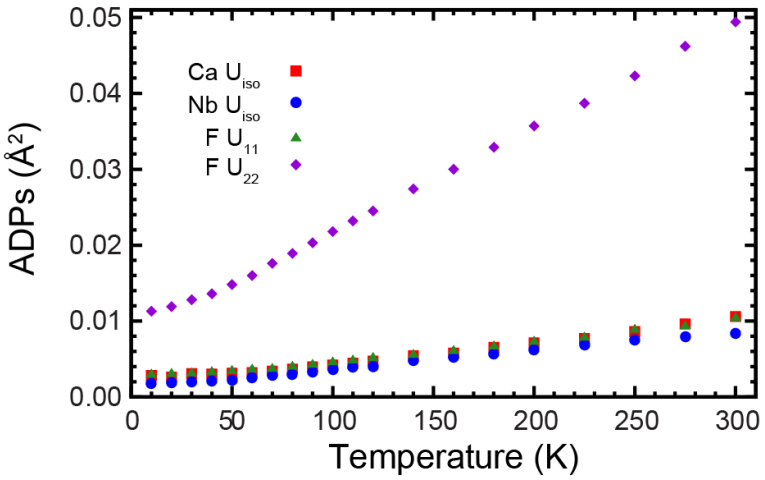

Figure 2.3: Atomic displacement parameters for $CaNbF_6$ determined from the Rietveld analyses of the neutron diffraction data.

The atomic displacement parameters (ADPs) obtained by Rietveld analysis of the neutron diffraction data (Figure 2.3) are consistent with the expected rigid unit mode (RUM) like mechanism for NTE in this material. The transverse component of the ADP for the fluoride is much bigger than the longitudinal one and it increases rapidly with temperature. The large value for U_{22}(F) at very low temperatures, similar to that found in $CaZrF_6$, is

indicative of large amplitude zero-point motion associated with a wide-bottomed potential for distortions involving the displacement of fluoride in this direction.

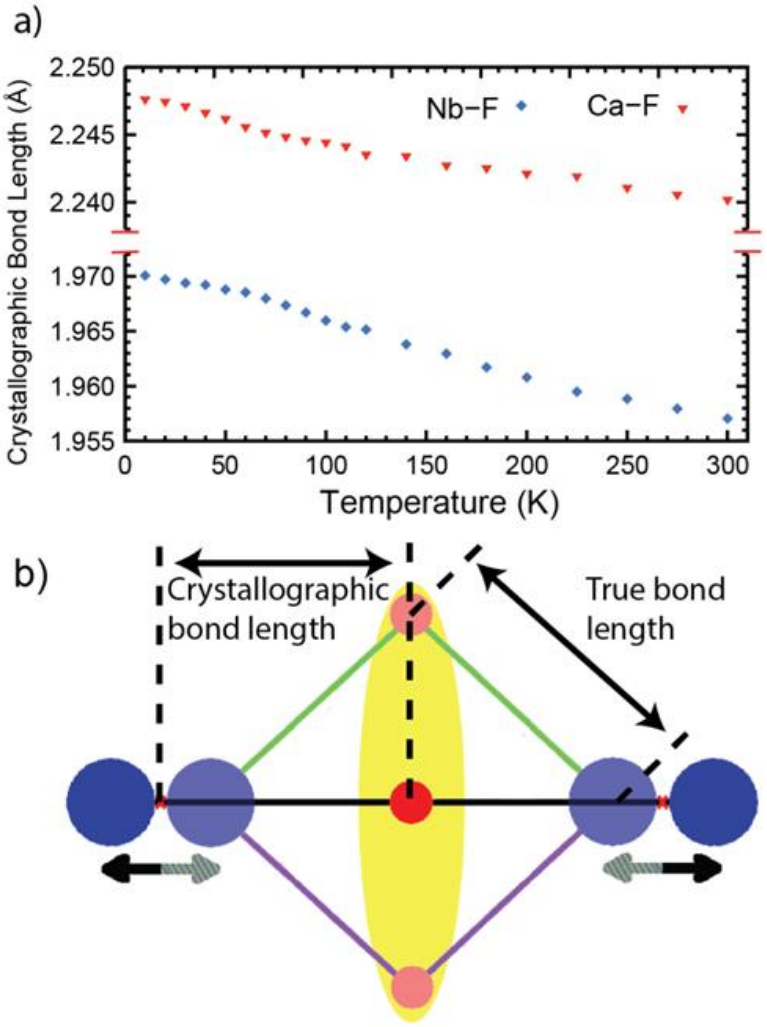

Figure 2.4: a) Apparent (crystallographic) Ca-F and Nb-F bond lengths, obtained from Rietveld analyses of the neutron diffraction data for $CaNbF_6$, as a function of temperature. b) Schematic showing how the transverse vibrational motion of fluoride (red/pink) couples to the motion the metals (blue) leading to an apparent decrease in crystallographic bond length when there is little, or no, increase in the true M-F distances.

Both the crystallographic (apparent) Ca-F and Nb-F bond lengths decrease as the sample is heated from 10 to 300 K (Figure 2.4a). These decreases, which are not constant with temperature or equal for the two different crystallographic bond lengths, arise from the

combination of an increase in the true bond lengths and an increase in the average displacement of the fluorine perpendicular to the Ca-Nb direction as the material is heated. The later contributes to a decrease in the crystallographic (apparent) bond lengths, as crystallography determines the distances between the average atomic positions, and the former partially counteracts this (Figure 2.4b). The inequivalent behavior of the Ca-F and Nb-F distances suggests a greater increase in the true Ca-F distance than the true Nb-F distance as the material is heated.

2.3.1.2 Behavior of $MgNbF_6$ from 100 to 900 K

Powder x-ray diffraction data for $MgNbF_6$ clearly show a structural phase transition from cubic ($Fm\bar{3}m$) to lower symmetry on cooling below ~280 K (Figure 2.5a). The diffraction data show evidence for phase coexistence over a narrow temperature range, suggesting that the transition is first order. The data for the low temperature phase could be fit using a cation ordered ReO_3-type model with $R\bar{3}$ symmetry similar to that previously reported for $CoZrF_6$,[171] although there was clear evidence of some scattering between the newly split Bragg peaks (Figure 2.5b). Scattering of this type is quite often seen below ferroelastic phase transitions and can be attributed to strains associated with domain boundaries in the twinned low temperature material.[357]

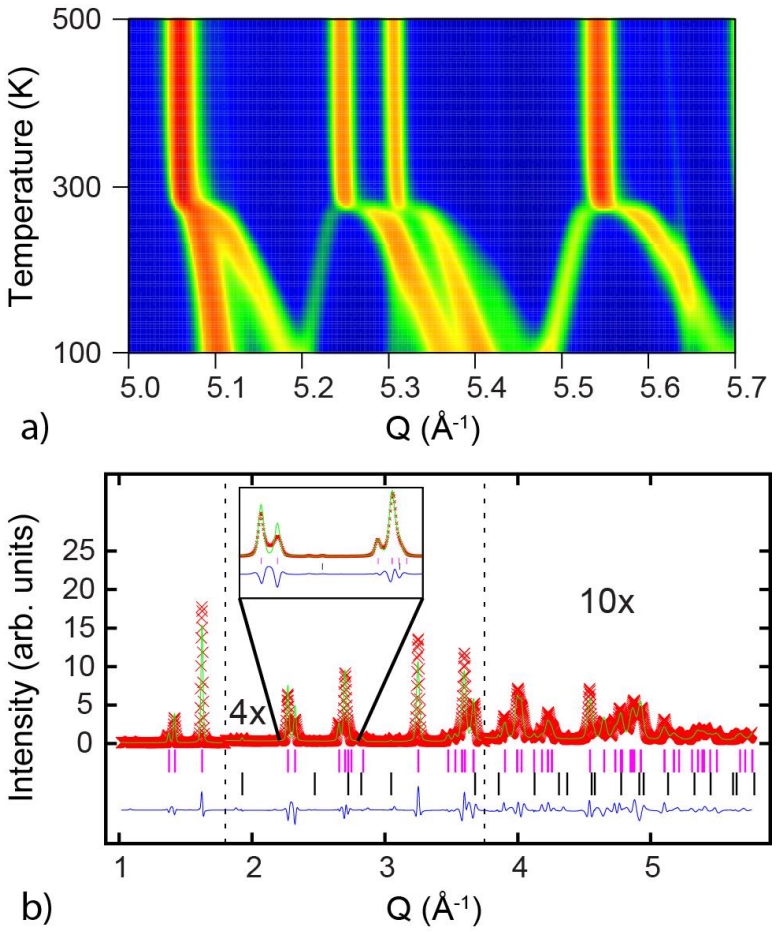

Figure 2.5: a) Synchrotron x-ray data for $MgNbF_6$ showing an apparently discontinuous phase transition at ~281 K. The individual diffraction patterns were recorded at 3 K intervals after equilibrating the sample. b) Data (100 K) for the low symmetry phase could be fit with a $R\bar{3}$ model. The fit quality suggests a significant contribution to the scattering from strained material in domain walls, which is not accounted for by the crystallographic model. The second phase (black tag marks) is unreacted MgF_2 (~2 wt %).

The phase transition is associated with a large increase in unit cell volume per formula unit (Figure 2.6a) on heating and a decrease in the magnitude of the volume CTE (Figure 2.6b) after the transition. However, the CTE remains positive, even in the cubic phase, until the decomposition of the sample ~950 K (Figure A.4), which probably arose from failure of the fused quartz sample tube during the measurement.

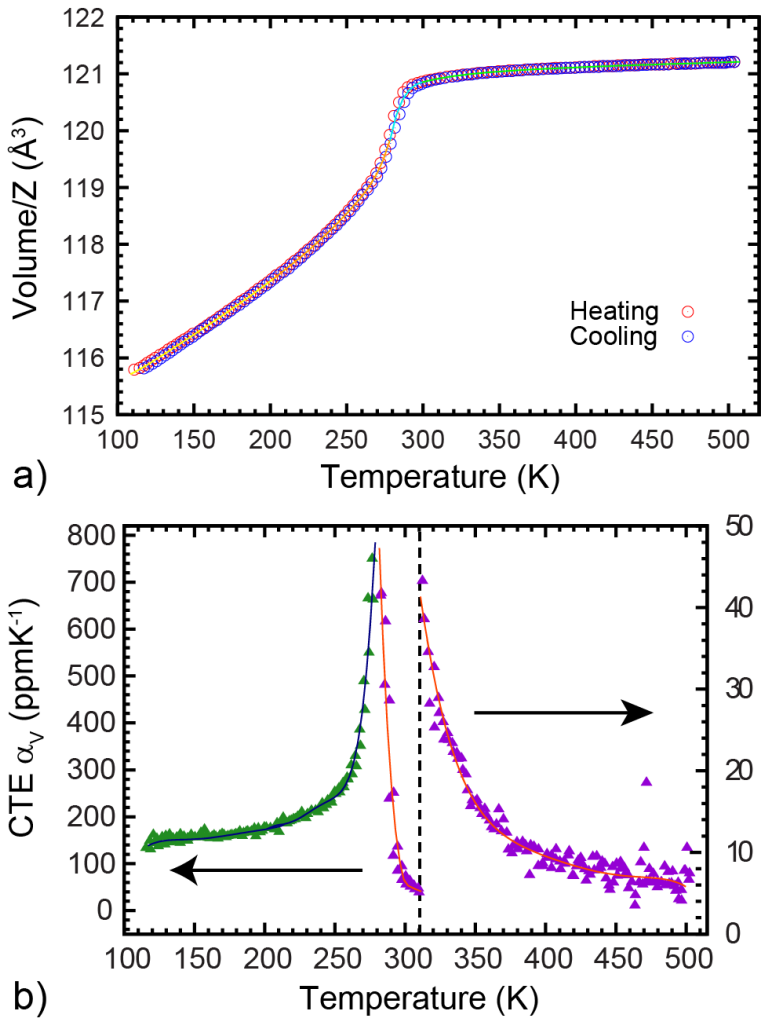

Figure 2.6: a) The volume per formula unit and b) volume thermal expansion coefficient for $MgNbF_6$ determined from powder x-ray diffraction data. The values were obtained from single phase Rietveld fits with a change from cubic to rhombohedral models at ~280 K.

The thermal expansion of $MgNbF_6$ in the $R\bar{3}$ phase is highly anisotropic (Figure A.5). The material displays very strong positive thermal expansion in the a – b plain ($\alpha_{a(200\text{-}250\ K)}$ ~120 ppm K^{-1}), which lies perpendicular to the 3-fold axis that the MF_6 octahedra are rotating around, and more modest negative thermal expansion parallel to the 3-fold axis ($\alpha_{c(200\text{-}250\ K)}$ ~-38 ppm K^{-1}).

2.3.1.3 Behavior of $MgZrF_6$ from 10 to 900 K

The response of $MgZrF_6$ to changes in temperature was examined by low temperature high resolution synchrotron powder diffraction (10 – 150 K and 300 K), and synchrotron powder diffraction over the range 100 – 500 K and 300 – 900 K. The low temperature experiments showed clear evidence of a symmetry lowering phase transition in the vicinity of 100 K (Figure 2.7). Unlike the case of $MgNbF_6$ shown in Figure 2.5, these data suggest a continuous, or almost continuous, phase transition. However, the precise transition temperature appeared to vary between experiments. While this may have a contribution from differences in thermometry between the measurements, it could also have a contribution from variations in stoichiometry between the different samples. $MgZrF_6$ can readily accommodate excess zirconium fluoride,[168] to form materials of the type $Mg_{1-x}Zr_{1+x}F_{6+2x}$, and although our syntheses targeted perfect stoichiometry, some unreacted MgF_2 (~3.5 wt % in the sample used for the high resolution measurements) are apparent in the diffraction data.

Rietveld analyses of the high-resolution x-ray data and the neutron data for the low temperature phase using an $R\bar{3}$ model produced less than ideal fit quality. Notably, scattering is seen between the Bragg peaks expected for this symmetry, which is probably related to the presence of strains at domain boundaries, as was suggested for $MgNbF_6$.

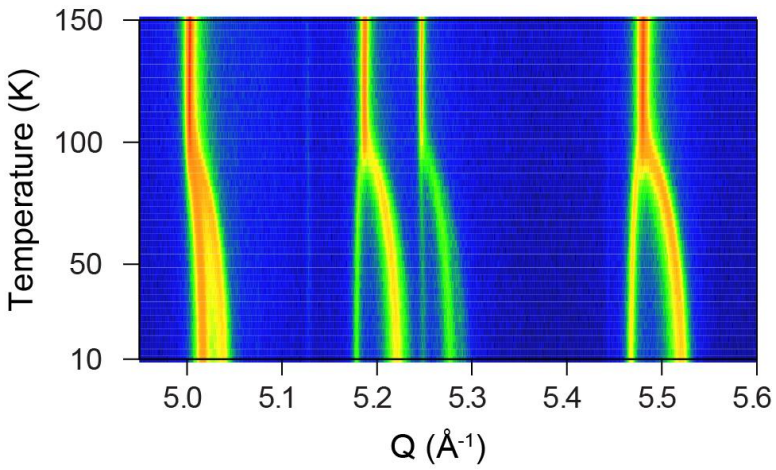

Figure 2.7: High resolution synchrotron powder x-ray diffraction data for $MgZrF_6$ showing a symmetry lowering phase transition at ~100 K, which appears to be continuous unlike that seen for $MgNbF_6$ (see Figure 2.5a).

Above the phase transition the data was fit with a cation ordered cubic ReO_3-type model ($Fm\bar{3}m$) (Figure A.6). The thermal expansion varied from modestly negative just above the transition, with a minimum α_v of ~-12 ppm K^{-1} at ~170 K, to modestly positive at high temperature, ~15 ppm K^{-1} at ~1000 K, crossing through zero at ~500 K (Figure 2.8). Below the phase transition at ~100 K, fits using a $R\bar{3}$ model were performed. The quality of these fits was less than ideal, presumably due to stresses as domain boundaries (Figure A.7). The low temperature phase displays strongly positive volume thermal expansion (Figure 2.8a), but the expansion is highly anisotropic with NTE ($\alpha_{c(30\text{-}80\ K)}$ ~-14 ppm K^{-1}), parallel to the 3-fold axis in the $R\bar{3}$ model and very strong positive thermal expansion ($\alpha_{a(30\text{-}80\ K)}$ ~70 ppm K^{-1}) in the a-b plain (Figure A.8).

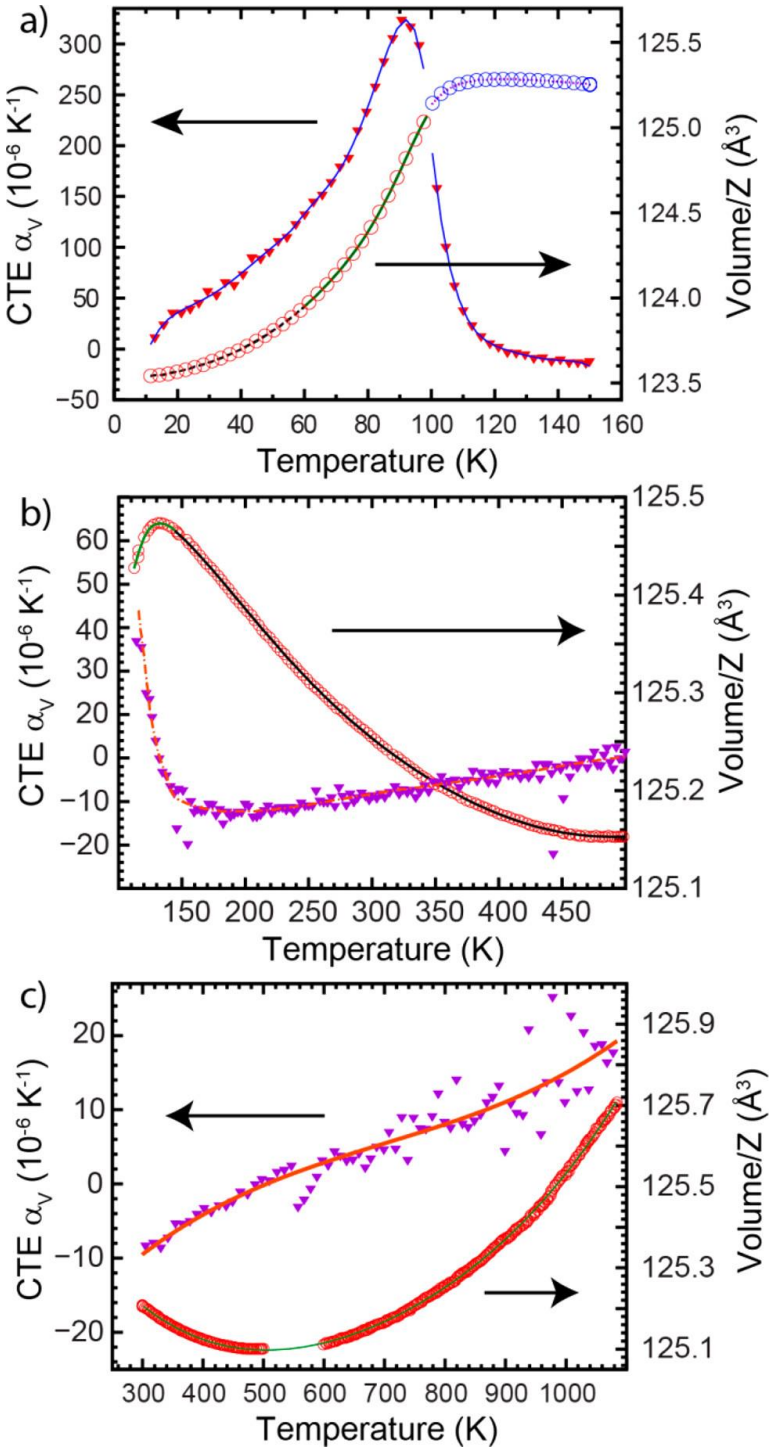

Figure 2.8: Volume per formula unit versus temperature and coefficient of thermal expansion for $MgZrF_6$ measured by synchrotron powder diffraction using a) a helium cryostat, b) a cryostream cooler and c) a wire wound furnace. The volumes were fit to a polynomial (solid line through the data) which was differentiated to estimate the CTE. The purple/red points are CTE estimates obtained by taking the difference between unit cell volumes. In a) separate polynomials were fit to the low-temperature ($R\bar{3}$) and high-temperature ($Fm\bar{3}m$) phases. The

volumes shown in these panels have not been scaled to take into account calibration differences between the different experimental arrangements.

2.3.2 Phase Behavior and Compressibility as a Function of Pressure

The behavior of $CaNbF_6$ on compression was examined using a DAC at pressures up to 8 GPa using a low molecular weight silicone oil as the pressure medium. $MgZrF_6$ was examined in the same way, however, additional measurements were performed for $MgZrF_6$ at pressures up to 300 MPa in the temperature range 300 – 525 K, using an oil-filled pressure cell.[353]

2.3.2.1 Behavior of $MgZrF_6$ on Compression

Diffraction data for $MgZrF_6$ as it is compressed in a DAC are shown in Figure 2.9a. These data indicate that at least two phase transitions occur below 8 GPa, with transitions at ~0.37 and 1.0 GPa.

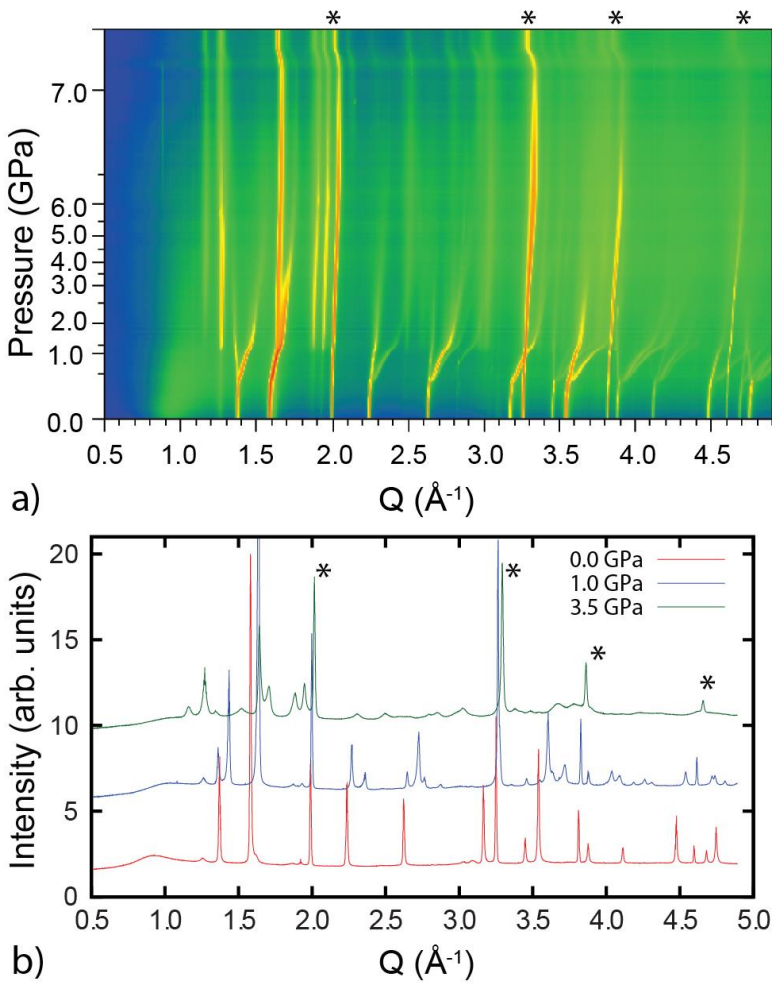

Figure 2.9: Diffraction data for $MgZrF_6$ on compression in a DAC (* indicate peaks from the CaF2 pressure marker). a) 2D contour plot providing an overview of the phase behavior and b) a comparison of the ambient, 1.0 and 3.5 GPa data.

The initial cubic ($Fm\bar{3}m$) phase persists until ~370 MPa. At this pressure, peak splitting consistent with a phase transition involving octahedral tilts while maintaining the connectivity and cation ordering of the original ReO_3-type structure is observed. The data for this phase are broadly consistent with $R\bar{3}$ symmetry. At ~1.0 GPa, the patterns change quite abruptly, consistent with a reconstructive phase transition. The data show evidence for this new phase up until the highest pressures explored and on decompression of the DAC. However, the diffraction patterns for this new phase (Figure 2.9b), which show

considerable broadening and peak overlap, could not be indexed. Interestingly, the strongest peaks from the new phase can be seen in the starting sample suggesting that the process of finely grinding the $MgZrF_6$ prior to loading it into the DAC irreversibly transformed some of the initial cubic material to this high-pressure phase.

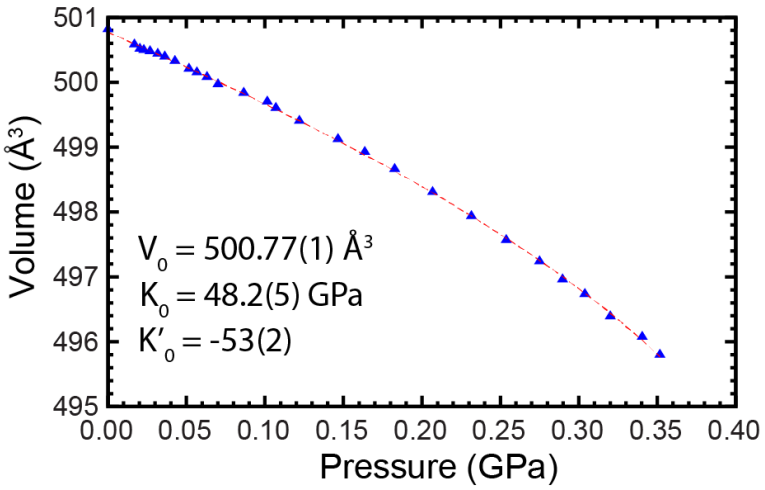

Figure 2.10: Volume versus pressure, determined from the Rietveld analysis of the DAC data for the ambient pressure form of $MgZrF_6$, along with a fit to a 3rd order Birch-Murnaghan equation of state (EoS). The best fit parameters for the EoS are given in the inset.

The variation of unit cell volume with pressure for cubic $MgZrF_6$ is shown in Figure 2.10, along with a best fit to a Birch-Murnaghan (BM) 3rd order equation of state (EoS), performed using EosFit7.[358,359] This phase, with K_0 48.2(5) GPa, is stiffer than $CaZrF_6$ ($K_{0(298\ K)}$ ~36 GPa)[26] but softer than ScF_3 ($K_{0(298\ K)}$ ~60 GPa).[155] Remarkably, it shows a dramatic softening on compression prior to the phase transition at ~350 MPa, with K_0', the pressure derivative of the bulk modulus, ~-53(2). Pressure-induced softening has been observed in other NTE materials, such as $Zn(CN)_2$,[208,209] and predicted by Dove and coworkers to be a general characteristic of frameworks solids that display NTE.[190,360,361]

However, softening on compression is also well known to be a precursor of structural phase transitions.

The behavior of cubic ReO_3-type $MgZrF_6$ was further investigated as a function of temperature and pressure using a heated oil-filled pressure cell that allows for the precise control of both temperature and pressure. A representative Rietveld fit and the lattice constants obtained from these data are available in Appendix A (Figure A.9 and Table S5). These lattice constants were analyzed using several different approaches. Bulk moduli as a function of temperature, derived from the lattice constants using straight lines fits of ln(V) versus P and the fit of a 2nd order BM EoS, are shown in Figure 2.11.

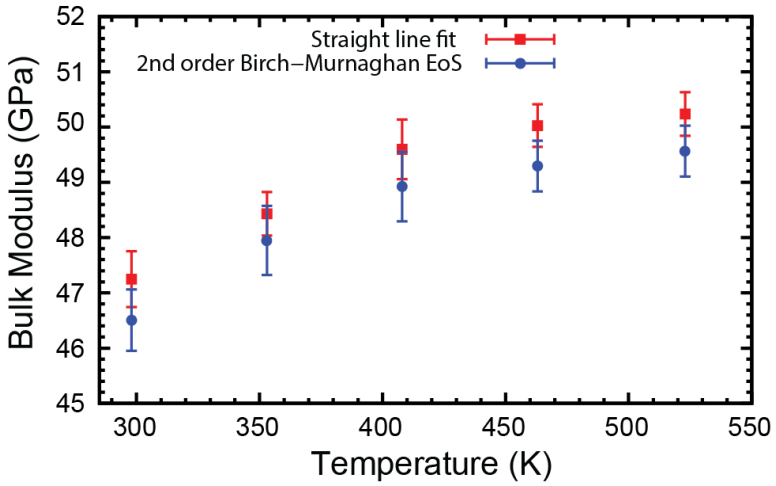

Figure 2.11: Bulk moduli as a function of temperature for cubic $MgZrF_6$, obtained by fitting a straight line to ln(V) versus P, and also a 2nd order Birch-Murnaghan equation of state.

Both of these analyses give room temperature zero pressure bulk moduli slightly lower than those obtained when using a 3rd order BM EoS to analyze the data acquired using a DAC (Figure 2.10) and indicate that the phase stiffens on heating, which is contrary to the behavior of most materials and that previously observed for $CaZrF_6$. We attribute the slight discrepancy between zero pressure bulk moduli to the different assumptions used for the

pressure derivative of the bulk modulus. In a simultaneous analysis of all the PVT data, obtained with a BRIM and heated pressure cell for cubic $MgZrF_6$, using a 3rd order BM EoS and the Berman model for temperature dependent thermal expansion in EOSFit7, the following parameters were obtained: $K_{0(298\ K)}$ = 50.4(7) GPa, K'_{298K} = -16(3), dK_0/dT = 0.015(2) $GPaK^{-1,}$ α_0 = -0.81(3) x 10^{-5} and α_L = 3.4(3).

2.3.2.2 Behavior of $CaNbF_6$ on Compression

Two independent DAC diffraction experiments, with different sample to detector distances, were performed. As the behavior seen in these experiments was the same, only the results from one are presented. Diffraction data for $CaNbF_6$ as it is compressed in a DAC are shown in Figure 2.12a. They indicate the onset of a reconstructive phase transition at ~400 MPa and a quite abrupt amorphization at ~4 GPa. This behavior contrasts with that seen for $MgZrF_6$, where the material was unstable with respect to an octahedral phase transition on compression but is similar to that previously reported for $CaZrF_6$. The diffraction data in Figure 2.12a and Figure 2.12b suggest that the initial sample contained traces of the high-pressure phase, presumably from grinding the sample prior to loading the DAC. A 3rd order BM EoS was used to fit the V versus P values obtained by Rietveld analysis of the data for cubic ReO_3-type $CaNbF_6$, Figure 2.12c. With $K_{0(298K)}$ = 33.7(4) GPa, $CaNbF_6$ is softer than $MgZrF_6$ ($K_{0(298K)}$ = 48.2(5) GPa) and comparable to, although apparently slightly softer than $CaZrF_6$ ($K_{0(298K)}$ ~36 GPa). $CaNbF_6$ displays quite large pressure-induced softening, with $K'_{0(298\ K)}$ ~-23(2).

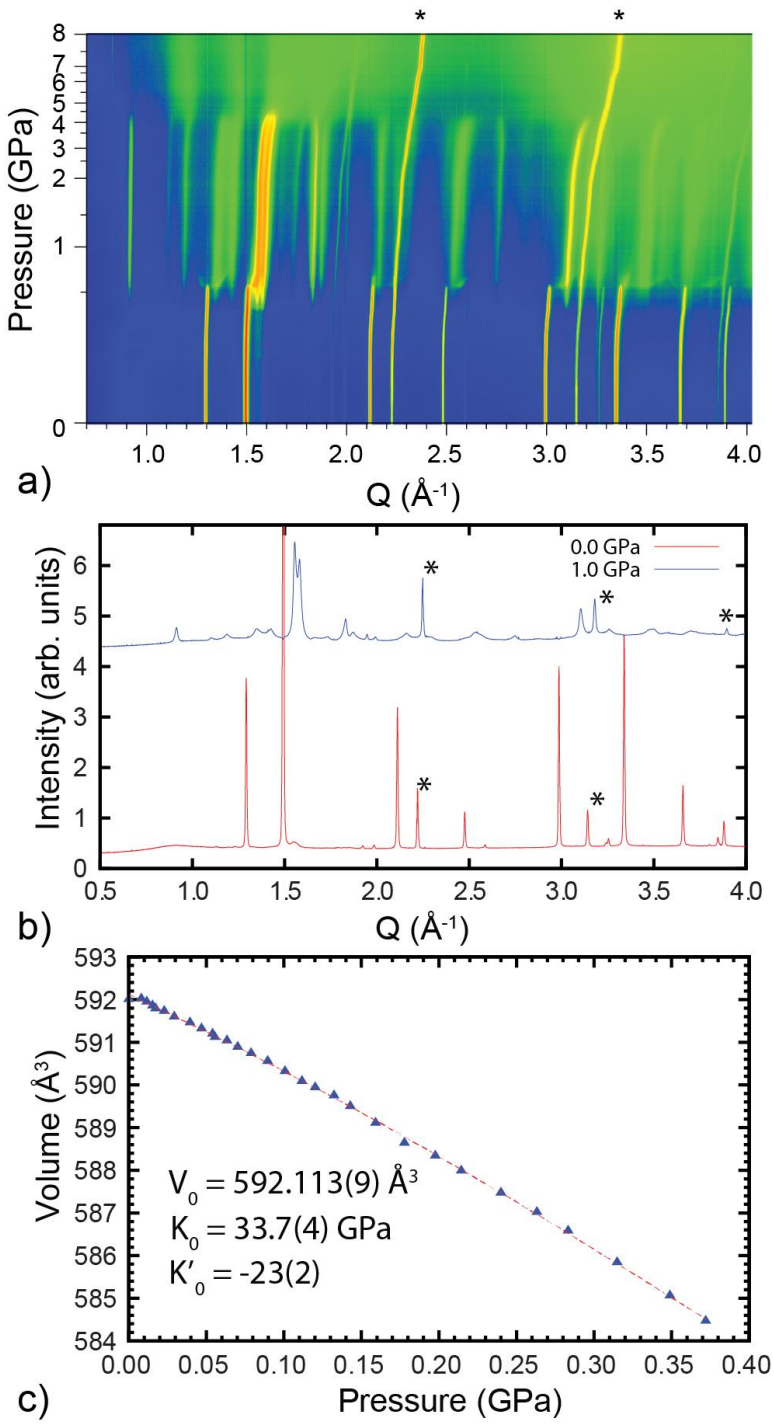

Figure 2.12: a) Diffraction data as a function of pressure for $CaNbF_6$ on compression in a DAC (* indicate peaks from the NaCl pressure marker). b) Selected diffraction patterns. c) Volume versus pressure for the ambient pressure phase along with a fit to a 3rd order Birch-Murnaghan equation of state.

2.4 Conclusions

The replacement of calcium in $CaZrF_6$ by magnesium has a far greater effect on the phase behavior, thermal expansion and elastic properties of ABF_6 than the substitution of zirconium by niobium (IV). Similar to $CaZrF_6$,[26] $CaNbF_6$ retains a cubic cation ordered ReO_3-type structure on cooling to at least 10 K. This phase displays very strong volume NTE with a maximum value of ~-65 ppm K^{-1} at 70 K, which is slightly larger in magnitude than that previously reported for $CaZrF_6$. High-pressure diffraction studies on $CaNbF_6$ indicate that on volume reduction a phase transition involving reconstruction of the framework becomes favorable (~400 MPa) before any of the vibration modes involving octahedral tilts fully soften and give rise to a lower symmetry ReO_3-type framework. Similar behavior was also reported for $CaZrF_6$,[26] but the details of the transition and the stability of the new phase upon further compression appear to be different. ReO_3-type $CaNbF_6$ is slightly softer than $CaZrF_6$ (K_0 ~34 versus ~36 GPa) and displays quite pronounced pressure-induced softening on compression. Such pressure-induced softening has been reported for other families of NTE solids[208,209] and has been predicted to be common among NTE materials.[190,360,361] Replacement of calcium by magnesium leads to major changes in phase behavior. On cooling, ReO_3-type $MgZrF_6$ undergoes a symmetry lowering phase transition at around 100 K. The transition appears to be either continuous or almost continuous. At temperatures immediately above the transition, $MgZrF_6$ displays modest NTE (greatest magnitude at ~175 K, α_v ~-15 ppm K^{-1}). On warming the thermal expansion becomes positive, crossing through zero at close to 500 K. Diffraction data for the low temperature phase are broadly consistent with an $R\bar{3}$ structure, as previously reported for the low temperature form of $CoZrF_6$.[26,171] However, the Rietveld fits were less

than optimal presumably due to the existence of strains in regions close to the domain boundaries below the ferroelastic transition. On compression at room temperature cubic $MgZrF_6$, unlike cubic $CaNbF_6$, undergoes a phase transition that is associated with octahedral tilts (370 MPa) prior to undergoing a reconstructive phase transition at ~1 GPa. This behavior is consistent with the transition seen on cooling the material. Cubic $MgZrF_6$ is considerably stiffer than $CaNbF_6$ (K_0 ~48 versus ~34 GPa) and shows a greater pressure-induced softening at room temperature [K'_0 -53(2) versus -23(2)]. The replacement of both calcium and zirconium to give $MgNbF_6$ leads to even greater destabilization of the cubic ReO_3-structure than the replacement of calcium alone. Cubic $MgNbF_6$ undergoes a symmetry lowering phase transition, to a material that probably has an $R\bar{3}$ structure, at just below room temperature (~280 K). The cubic phase does not show negative thermal expansion in the temperature range that was examined unlike $CoZrF_6$, which has a similar cubic to $R\bar{3}$ phase transition temperature (~270 K),[26] and displays modest NTE above the transition.

Metal fluorides such as $CaZrF_6$, $CaNbF_6$ and $MgZrF_6$ typically have good transparency into the infra-red, as was previously shown for $CaZrF_6$.[26] $CaZrF_6$ also has no transitions in the visible region due to the d^0 electron configurations of both Ca^{2+} and Zr^{4+} and the large electronegativity difference between fluorine and these metals. The replacement of zirconium in $CaZrF_6$ by niobium (IV) leads to absorptions in the visible region due to the d^1 electron configuration of Nb^{4+}. The replacement of calcium by magnesium does not introduce any transitions in the visible part of the spectrum and $MgZrF_6$ has a modest CTE at 300 K (α_V ~-8 ppm K^{-1}), which crosses through zero at ~500 K. This suggests possible

application in athermal multispectral optics for $MgZrF_6$ or appropriately substituted variants.

2.5 Acknowledgements

We are grateful for experimental assistance from the beamline staff of POWGEN at the SNS and beamlines 11-IDB and 17-BM at the APS. We are grateful to Dr. Abbie Mclaughlin for her comments regarding strains at domain boundaries. This work made use of the Advanced Photon Source, a U.S. Department of Energy (DOE) Office of Science User Facility operated for the DOE Office of Science by Argonne National Laboratory under contract DE-AC02-06CH11357. A portion of this research used resources at the Spallation Neutron Source, a DOE Office of Science User Facility operated by the Oak Ridge National Laboratory.

CHAPTER 3. NEGATIVE THERMAL EXPANSION, RESPONSE TO PRESSURE AND PHASE TRANSITIONS IN $CaTiF_6$[2]

3.1 Introduction

Control of thermal expansion is highly desirable for applications where dimensional stability or good thermal shock resistance are needed. The fabrication of composites from mixtures of positive and negative thermal expansion (NTE) materials[36,40-42,44,333,336,362] is a possible route for creating tailored thermal expansion materials.[3] However, in such composites the expansion mismatch between different components induces stresses on the materials, which can adversely affect their expansion characteristics.[36,183,186,187,336] Therefore, the response of NTE materials to stress, or less generally pressure, needs to be understood along with their expansion characteristics.

Several distinct mechanisms for NTE are well established.[30,332] In materials where phase transitions of various types are involved, strong NTE may occur over a somewhat limited temperature range, for example, $Bi_{0.95}La_{0.05}NiO_3$ (α_L= -82 ppm/K, ΔT: 320-380 K), $SrCu_3Fe_4O_{12}$ (α_L= -22.6 ppm/K, ΔT: 200-230 K), $(Mn_{0.96}Fe_{0.04})_3(Zn_{0.5}Ge_{0.5})N$ (α_L= -25 ppm/K, ΔT: 316-386 K), and $MnCo_{0.98}Cr_{0.02}Ge$ (α_L= -116 ppm/K, ΔT: 250-305 K).[45,50,53,363]

In open framework solids, with a phonon mechanism for negative thermal expansion, NTE can be present over a very wide temperature range, for example ZrW_2O_8 (α_L= -8.7 ppm/K, ΔT: 0.3-693 K), ScF_3 (α_L= -5 ppm/K, ΔT: 10 - 1000 K), $[Cu_3(btc)_2]$ (α_L= -4.1 ppm/K, ΔT:

[2] Published in *Inorg. Chem.*, **2018**, 57(17), pp 11275-11281

80-500 K), and $Zn(CN)_2$ (α_L= -16.9 ppm/K, ΔT: 25-375 K).[24,25,88,364] However, open framework NTE materials frequently undergo structural phase transition on modest compression, which can make their application in composites problematic.[220,224]

Amongst open framework NTE materials, there has been considerable recent interest in metal fluorides with ReO_3-related structures.[25,26,155-157,159-161,178,180,342,344,365-367] Using an appropriate choice of metal cations, low or negative thermal expansion can be combined with optical transparency ranging from the mid-IR into the UV, which is potentially valuable for multispectral optical applications.[26] Strong negative thermal expansion in ReO_3-type fluorides is typically found in compositions that maintain an ideal cubic structure to very low temperatures, for example, ScF_3,[25] $CaHfF_6$, $CaZrF_6$[26] and $CaNbF_6$.[365] However, only a small subset of ReO_3-type fluorides, where the cations are very electropositive, remain cubic on cooling rather than going through a symmetry lowering phase transition. $CaTiF_6$ was examined in an effort to expand the range of fluorides known to display strong isotropic NTE over a wide temperature range. The solid state synthesis and an initial characterization of $CaTiF_6$ was reported by Hagenmuller and co-workers in 1970,[368] with subsequent mention by Reinen and Steffen in their 1978 work on structure and bonding in $M^{(II)}M^{(IV)}F_6$.[170]

3.2 Experimental

3.2.1 Synthesis

CaF_2 and TiF_4, purchased from Sigma Aldrich and STREM respectively, were ground together in a 1:1 molar ratio under a dry nitrogen atmosphere. The mixture was pressed into a pellet and placed in a copper tube. The tube was sealed by arc welding in argon, and

then sealed inside an evacuated fused quartz ampoule. The ampoule was heated to 400 °C, held at 400 °C for 24 h, annealed at 350 °C for 24 h, and then cooled to room temperature. The reaction produced $CaTiF_6$, as an off-white powder, with ~2 wt % CaF_2 as an impurity (see Figure B.1).

3.2.2 High Resolution Variable Temperature X-ray Powder Diffraction Measurements

High resolution x-ray powder diffraction data were collected on the 11-BM beamline at the Advanced Photon Source, Argonne National Laboratory at a wavelength of 0.41272 Å using a sample sealed in a Kapton capillary tube. An Oxford Cryostream 700+ nitrogen gas blower was used for data collection between 300 and 500 K (denoted as "N_2" later in the paper). An Oxford Instruments closed-flow helium cryostat (OptistatCF), denoted "He", was used for data sets between 10 and 300 K.

3.2.3 High-Pressure X-ray Powder Diffraction Measurements

High-pressure powder x-ray diffraction data were collected on a Perkin-Elmer amorphous silicon 2D detector, using beamline 17-BM at the Advanced Photon Source, Argonne National Laboratory, at a precisely determined wavelength of 0.45240 Å. These measurements made use of an EasyLab "Diacell Bragg-(G)" diamond anvil cell, which was equipped with a diaphragm so that the pressure could be increased under computer control. A low molecular weight silicone oil (Alfa, MW = 237 $g \cdot mol^{-1}$) was used as the pressure transmitting medium. Pressure was determined from the lattice constant of CaF_2, which was added as pressure marker, using the equation of state reported by Angel.[352] Data were acquired while the pressure was continuously increased using a syringe pump to supply high-pressure methanol to the diaphragm.

3.2.4 Rietveld Analysis of the Powder Diffraction Data

All Rietveld refinements were performed using the General Structure Analysis System (GSAS) coupled with EXPGUI.[354,355] In the analyses of both the low temperature ambient pressure data and the high-pressure ambient temperature data, the fits to the rhombohedral model were less than ideal due to the presence of some scattering between Bragg peak maxima, which is attributed to strain associated with the domain structure that is present once the ferroelastic cubic to rhombohedral transition has occurred.[365] Representative profile fits for the cubic and rhombohedral phases are shown in Figs S1 –S4. As the high-pressure data had a high background and relatively low Q_{max} (5.5 $Å^{-1}$), a structural model consisting of isotropic atomic displacement parameters for each atom and fluorine coordinates was adopted. The accuracy of the structural information from these analyses, especially for pressures close to the phase transition at 3 GPa where there is significant peak broadening, is limited. Parameters for the refined structural models and the lattice constants are reported in the SI.

3.3 Results and Discussion

3.3.1 Response to Heating and Cooling

Above 120 K $CaTiF_6$ adopts a cubic cation ordered ReO_3-type structure. The peak splitting seen in the variable temperature x-ray powder diffraction data suggest a phase transition on cooling to ~120 K from cubic ($Fm\bar{3}m$) to rhombohedral ($R\bar{3}$), which involves correlated octahedral tilting (Glazer notation $a^-a^-a^-$).[369] Transitions of this type are commonly seen in ReO_3-type metal fluorides.[147,150,370,371]

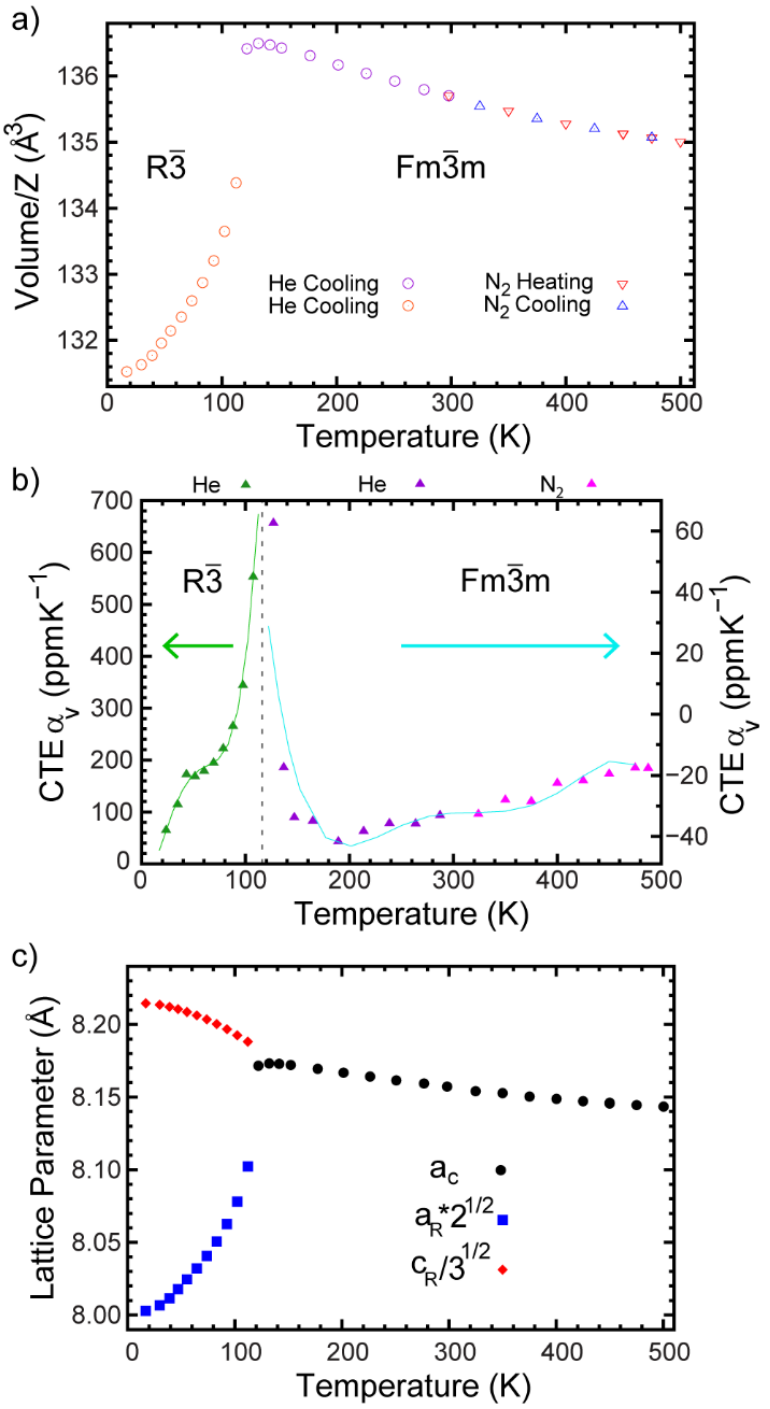

Figure 3.1: a) Unit cell volume per formula unit, b) volumetric coefficients of thermal expansion (CTE), and c) lattice constant versus temperature for $CaTiF_6$. The curves shown in (b) were obtained by differentiation of six and five-term polynomial fits to the unit cell volumes of the cubic and rhombohedral phases, respectively. Additionally, the CTE was

determined point by point (purple/magenta and green symbols). He and N_2 denote helium cryostat and nitrogen Cryostream sample environments respectively.

The volume per formula unit, volume thermal expansion coefficients and lattice constants versus temperature obtained from Rietveld analyses are shown in Figure 3.1. As is typical of ReO_3-type metal fluorides, the rhombohedral phase shows strong volumetric positive thermal expansion (PTE), which is highly anisotropic.[344,365] In the rhombohedral phase the octahedra are tilted so the Ti-F-Ca angle is < 180°. As this phase is heated the bond angle increases (~158.8° and ~165.5° at 16 and 112 K respectively), leading to very strong positive thermal expansion in the a-b plane of the hexagonal unit cell. Just above the phase transition temperature the cubic phase displays PTE, which is presumably due to the presence of local structural distortions away from the ideal cubic structure. This interpretation is supported by the atomic displacement parameters (ADPs) shown in Figure 3.2; the transverse component of the ADP (U_{22}) for fluorine increases on cooling from 130 to 120 K. Above 130 K the cubic phase of $CaTiF_6$ shows NTE up to the highest temperature studied (500 K). The NTE is strongest at 177 K with a α_v = -42 ppm K^{-1}. The expansion coefficient slowly increases up to -18 ppm K^{-1} at 488 K.

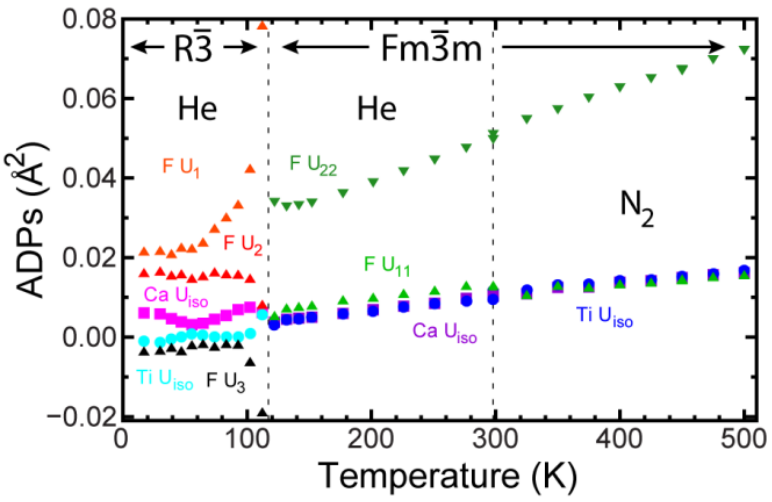

Figure 3.2: Atomic displacement parameters for $CaTiF_6$ determined by Rietveld analysis of data from variable temperature x-ray diffraction measurements using a helium cryostat (He) and nitrogen Cryostream (N_2). F U_i values are the principle components of the anisotropic atomic displacement ellipsoid for fluorine in the rhombohedral phase.

The thermal expansion of $CaM^{4+}F_6$ (M – Zr, Hf, Nb and Ti) are compared in Figure 3.3. At low temperatures, the behavior of $CaTiF_6$ is distinct from the other compositions, as it is the only one that undergoes a phase transition on cooling. The ideal cubic form of the ReO_3 structure is reported to be preferred on electrostatic grounds, with the commonly reported distortions away from cubic symmetry perhaps arising from polarization of fluoride or covalency.[372] Titanium has a higher electronegativity (1.32)[373] and smaller size (six coordinate Ti^{4+}, 0.605 Å)[374] than zirconium, hafnium and niobium (1.22, 1.23, 1.23;[373] 0.72 Å, 0.71 Å, 0.68 Å)[374] consistent with the occurrence of a distortion on cooling $CaTiF_6$, but not the other $CaM^{4+}F_6$.

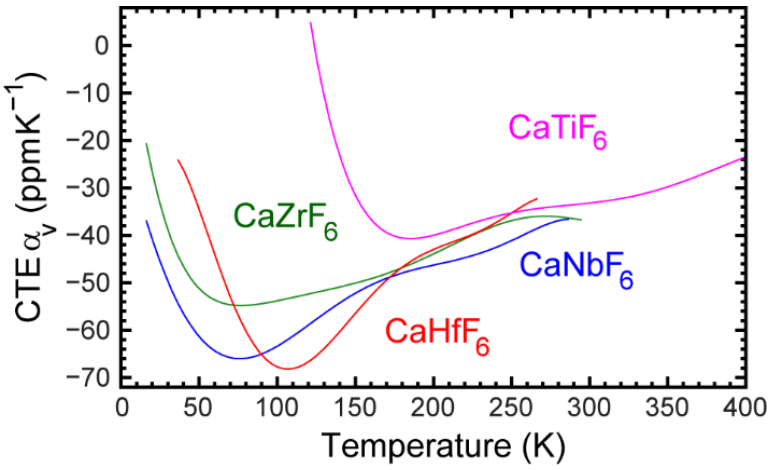

Figure 3.3: Temperature dependence of the volumetric coefficients of thermal expansion for $CaM^{4+}F_6$ (M – Zr, Hf, Nb, Ti).[26,365] The curves are six-term polynomials, which were fit to the point by point CTE data for each material to best represent the temperature dependence of their thermal expansion.

All four $CaM^{4+}F_6$ have similar CTEs at close to room temperature. However, $CaNbF_6$ and $CaHfF_6$ show the largest NTE at low temperatures, with the volumetric CTE of both dipping down to ~-70 ppm K^{-1}. The atomic displacement parameters (ADPs) obtained from Rietveld analyses of data for $CaTiF_6$ are shown in Figure 3.2. The overall pattern for the cubic phase is similar to that previously reported for $CaZrF_6$ and $CaNbF_6$. The transverse component of the ADP for F (U_{22}) is much larger than that of the component parallel to the M-F bonds, strongly dependent on temperature and extrapolates to a large value (~0.02 $Å^2$) at 0 K. This is consistent with a very soft potential for the transverse motion of the fluoride and the NTE in the material being driven by this transverse motion, as is typically the case of cubic ReO_3-type fluorides.[154] Below the phase transition to a rhombohedral structure, the values of the refined atomic displacement parameters are less well behaved. This is likely a consequence of parameter correlations for temperatures just below the transition, where the split peaks associated with the symmetry lowering are poorly resolved, and also less than ideal fits to the data for the rhombohedral material. As

mentioned earlier, the poor fits arise because there is scattering between the Bragg presumably due to strains in multiply twinned grains.[365] The refined ADPs for fluorine are consistent with a relatively soft potential for fluorine displacements even in the rhombohedral phase.

3.3.2 Response to Compression

The high-pressure x-ray diffraction data (Figure 3.4a) recorded at room temperature (~295 K) indicates the occurrence of at least two structural phase transitions in $CaTiF_6$ on compression to 6.5 GPa. Below ~0.25 GPa the material is cubic. On increasing pressure, the Bragg peaks split in a fashion consistent with an octahedral tilting transition to a rhombohedral ($R\bar{3}$) phase, as was seen on cooling $CaTiF_6$ to 120 K. Phase coexistence at ~0.25 GPa suggests that the transition is first order. Structural transitions of this type commonly occur at low pressures on compressing cubic MF_3 and $MM'F_6$ ReO_3-type phases[244,365] and they are a potential impediment to application in controlled thermal expansion composites, where the materials are likely to be subject to stresses from thermal expansion mismatch. However, $CaZrF_6$ and $CaNbF_6$ do not display an analogous octahedral tilting transition on compression. Cubic $CaZrF_6$ transforms to a disordered material on compression to ~0.4 GPa[26] at room temperature, and cubic $CaNbF_6$ transforms to a new crystalline phase at ~0.4 GPa.[365] These differences may arise in part because both Zr(IV) and Nb(IV) are much larger than Ti(IV), and can more readily accommodate an increase in coordination number.

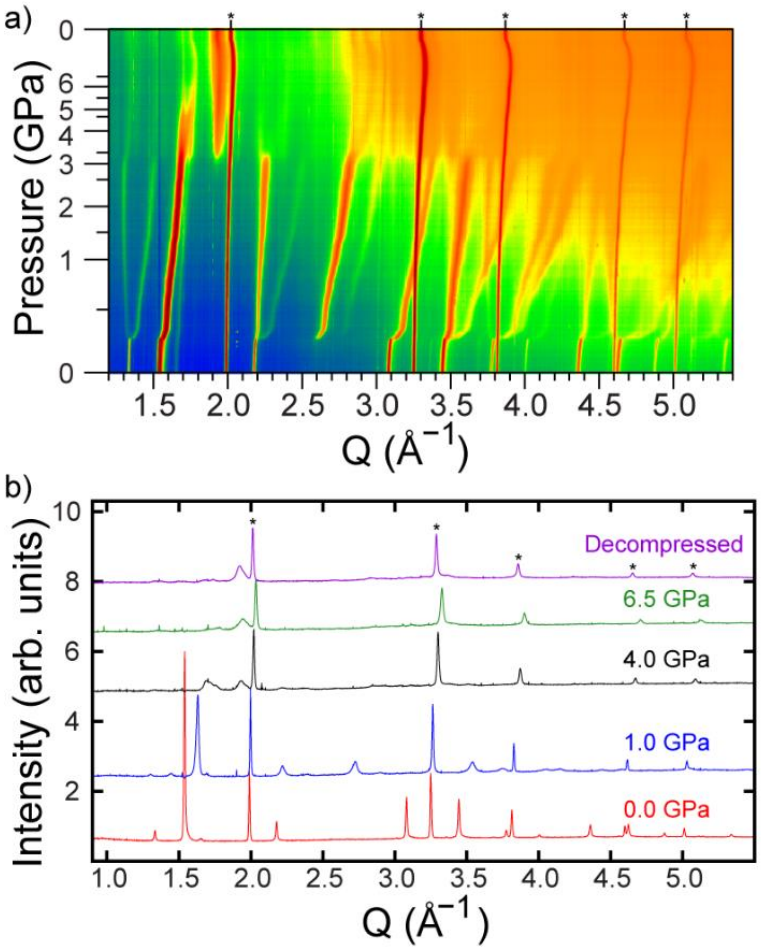

Figure 3.4: a) X-ray powder diffraction data for $CaTiF_6$ as it is compressed in a diamond anvil cell. b) Diffraction patterns for $CaTiF_6$ at selected pressures. Peaks from the CaF_2 pressure calibrant are marked *.

At ~3 GPa a further phase transformation occurs leading to the quite abrupt disappearance of the peak at ~2.2 Å^{-1} from the rhombohedral phase and the appearance of broad scattering maxima at ~1.75 and 1.9 Å^{-1}. Between 5 and 6 GPa the scattering pattern changes so that is dominated by a single broad maximum at 1.9 Å^{-1}. On decompression, the sample remained essentially amorphous. A comparison of the diffraction patterns in each pressure range of interest is given in Figure 3.4b.

In Figure 3.5, unit cell volume versus pressure (P < 0.25 GPa) is shown for cubic $CaTiF_6$ along with a fit to a 3rd order Birch-Murnaghan equation of state, which was performed using EoSFit7.[359] The zero pressure bulk modulus, K_0, was estimated to be ~29 GPa, indicating that $CaTiF_6$ is softer than both $CaZrF_6$ and $CaNbF_6$ (K_0 36 and 33.7, respectively). $CaTiF_6$, like several other cubic $MM'F_6$ phases and the anion excess ReO_3-type material $YbZrF_7$,[178] shows strong pressure-induced softening, K_0' ~-50(5), prior to undergoing a transformation to a rhombohedral phase. The magnitude of this softening is greater than that seen in both $CaZrF_6$ and $CaNbF_6$ (K_0' of -26 and -23, respectively). Most materials stiffen on compression as volume reduction brings atoms closer together and increases the repulsion between them. However, Dove et al. have argued that framework structures likely to display NTE are also likely to show pressure-induced softening.[191,375] Pressure-induced softening has previously been reported for the NTE materials ZrW_2O_8 and $Zn(CN)_2$.[209,243]

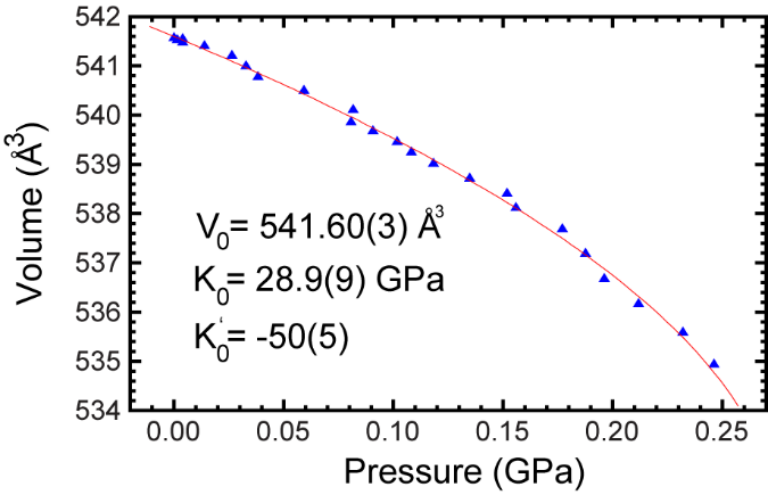

Figure 3.5: Volume versus pressure for cubic $CaTiF_6$ along with a best fit using a 3rd order Birch-Murnaghan equation of state.

The variation of unit cell volume and lattice constants with pressure (Figure 3.6) indicates that the elastic properties of rhombohedral ($R\bar{3}$) $CaTiF_6$ are very different from those of the cubic ($Fm\bar{3}m$) phase. In the rhombohedral phase further octahedral tilting ($a^-a^-a^-$), involving rotation around the 3-fold axes of the octahedra, is associated with a reduction in the Ca-F-Ti bond angles (see Figure 3.7a) and provides a relatively low energy pathway for volume reduction, at least for pressures where the Ca-F-Ti bond angle is significantly above that expected for close packing of the anions.

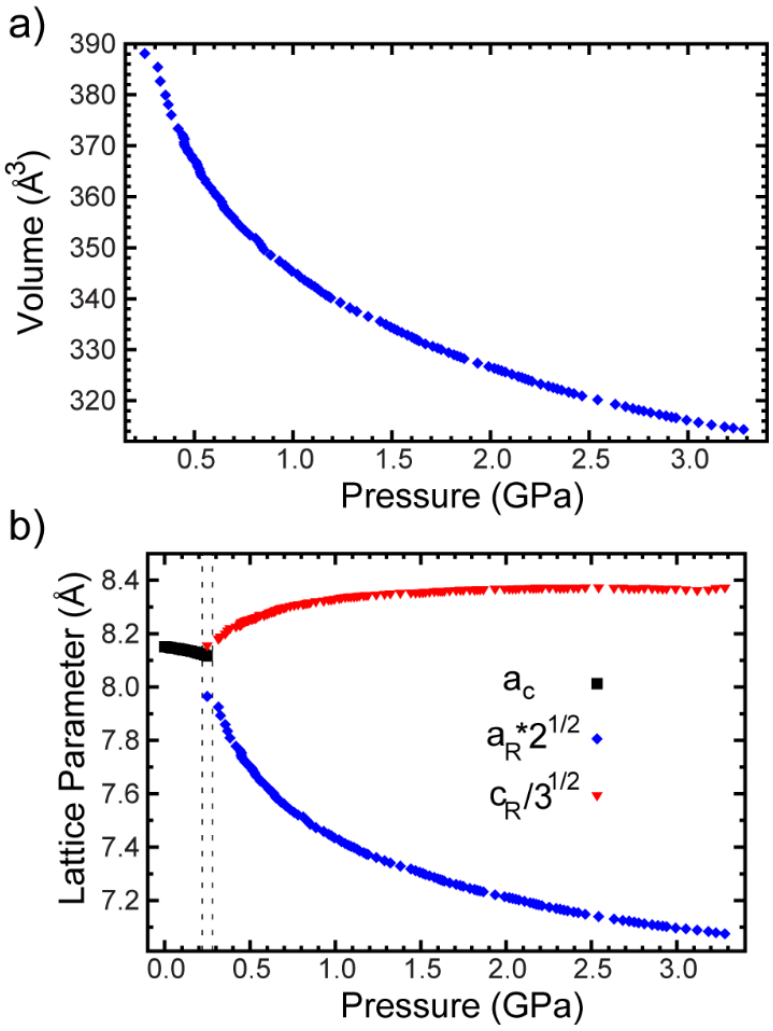

Figure 3.6: a) Pressure dependence of the unit cell volume, and b) lattice constants for the rhombohedral phase of $CaTiF_6$. The lattice constants for the rhombohedral phase have been scaled so that they can be compared to that of the cubic phase. There is phase coexistence in the region bounded by dashed lines.

The behavior of the rhombohedral phase on compression could not be adequately described using a Birch Murnaghan equation of state. A polynomial fit to ln(V) versus pressure was used to determine how the phase's bulk modulus varied with pressure (Figure B.5). At pressures just above the cubic to rhombohedral phase transition the material is very soft, with a bulk modulus of between 3 and 5 GPa for pressures below 0.5 GPa. However, its bulk modulus increases almost linearly on compression, becoming > 30 GPa for pressures

higher than 2.5 GPa. This stiffening is presumably due to the structure approaching that where the fluoride is closest packed. The compressibility of the rhombohedral phase is highly anisotropic. In the a-b plane, the material is soft as the volume reducing $a^-a^-a^-$ tilts involve rotation parallel to the c-axis. However, parallel to the crystallographic c-axis the material displays negative linear compressibility (NLC) up to ~2.5 GPa (see Figure 3.6b). Similar behavior has been reported in rhombohedral FeF_3 and other trifluorides.[248,249] The NLC was attributed to a distortion of the individual octahedra, where the F-F distances between fluorine on an octahedral face lying perpendicular to the c-axis (d_{1M}) decreased more readily on compression than the F-F distances between pairs of fluorine lying on opposite triangular faces of the same octahedron (d_{2M}). This distortion can be quantified as an octahedral strain using $\varepsilon_M = (d_{2M} - d_{1M})/(d_{2M} + {}_{d1M})$ (see Figure 3.7b)

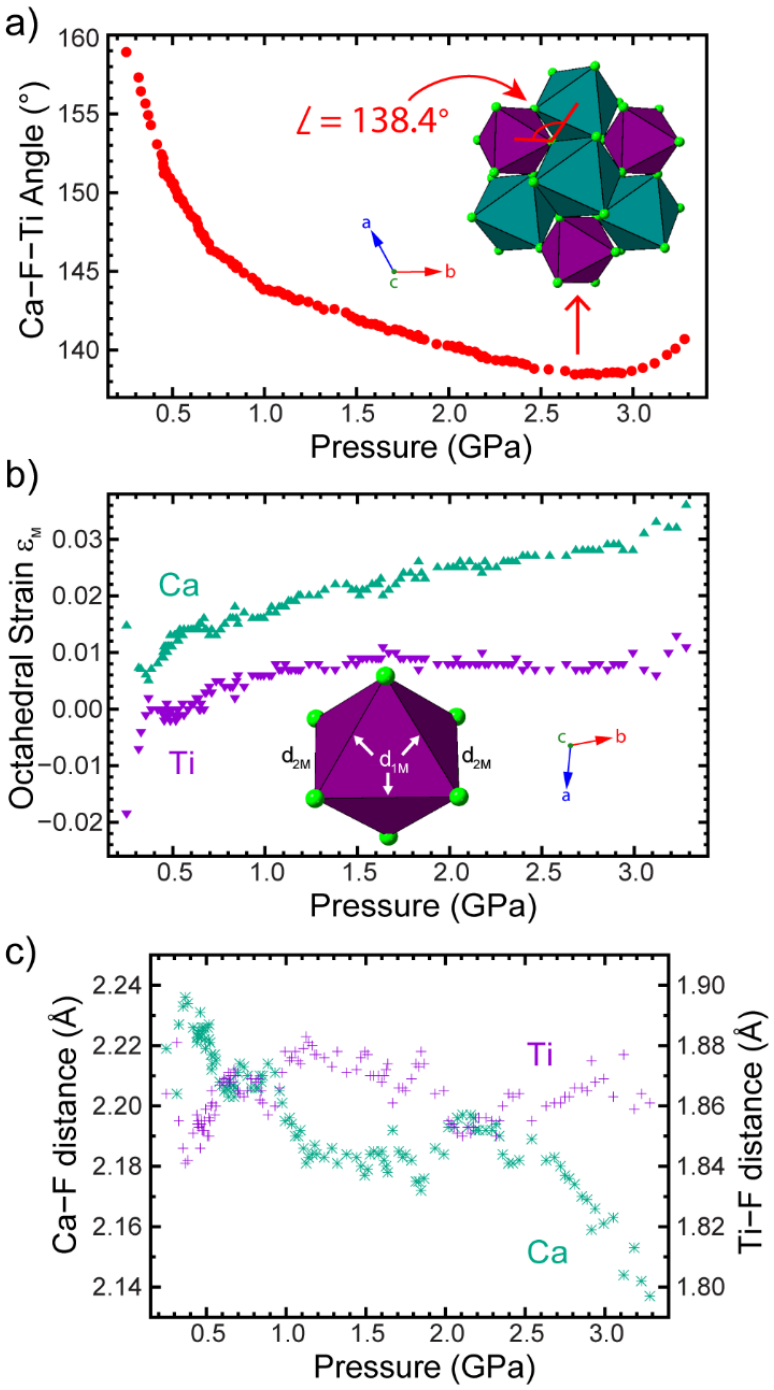

Figure 3.7: Pressure dependence of a) the Ca-F-Ti bond angle, b) the octahedral strain for the CaF_6 and TiF_6 units, as described in the text, and c) the Ti-F and Ca-F bond lengths.

The CaF_6 and TiF_6 octahedra that make up the rhombohedral structure respond differently to pressure. As might be expected, the longer Ca-F bond lengths are more compressible than the shorter Ti-F distances (Figure 3.7c), and on compression the CaF_6 units display

much greater octahedral strain than the TiF_6 units (Figure 3.7b). The maximum octahedral strain observed in the TiF_6 units is similar to that reported for FeF_3 on compression, but that seen in the CaF_6 is approximately three times greater.

At ~3 GPa, where rhombohedral $CaTiF_6$ transforms to a poorly ordered material, the Ca-Ti-F bond angle is approaching that expected for close packing (132°), consistent with a phase transition involving a new mechanism for volume reduction on compression.

3.4 Conclusions

The behavior of cooling and compressing $CaTiF_6$ is distinct from that of both $CaZrF_6$ and $CaNbF_6$, but similar to that of $MgZrF_6$.[26,365] $CaTiF_6$ undergoes an octahedral tilting transition on cooling below 120 K, which leads to anisotropic positive volume thermal expansion at low temperature, whereas $CaZrF_6$ and $CaNbF_6$ remain cubic to at least 10 K. This difference may be associated with the smaller size and higher electronegativity of Ti^{4+}, as highly ionic bonding is thought to favor the cubic structure over distorted variants. $CaTiF_6$ also undergoes an octahedral tilting transition on compression at ambient temperature. This is in contrast to $CaZrF_6$ and $CaNbF_6$, where other volume reduction mechanisms lead at ~0.4 GPa to disordering in the case of $CaZrF_6$ and what appears to be a reconstructive crystal to crystal transition in $CaNbF_6$. The pressure-induced cubic to rhombohedral transition in $CaTiF_6$ at 0.25 GPa is likely to limit its potential for application in controlled thermal expansion composites, as in such a composite it would experience stresses due to thermal expansion mismatch.

3.5 Acknowledgments

We are grateful to Anthony Lloyd, Sam Baxter, Ross Angel, and Saul Lapidus for assistance with various aspects of the experiments and data analysis. The activities at Georgia Tech were supported in part under NSF DMR-1607316. This work made use of the Advanced Photon Source, a U.S. Department of Energy (DOE) Office of Science User Facility operated for the DOE Office of Science by Argonne National Laboratory under contract DE-AC02-06CH11357.

CHAPTER 4. EFFECTS OF COMPOSITION ON CRYSTAL STRUCTURE, THERMAL EXPANSION, AND RESPONSE TO PRESSURE IN ReO_3-TYPE $MNbF_6$ (M= Mn AND Zn)[3]

4.1 Introduction

Since the 1996 report of negative thermal expansion (NTE) over a wide temperature range in ZrW_2O_8,[24,376] strong NTE has been observed in many different families of materials.[30,332,377] This interest in NTE has been partly motivated by a desire to control thermal expansion, using strategies such as the preparation of composites containing positive and negative thermal expansion phases.[3,378] When NTE materials are employed in composites they can experience significant stresses due to the thermal expansion mismatch between the NTE phase and the matrix. In the case of framework NTE materials, which often display structural phase transitions at low pressure, these stresses can degrade the performance of the composite. This motivates the study of such materials under pressure.

A wide variety of ReO_3-struture fluorides have received attention for their potential as negative and zero thermal expansion materials since the observation that cubic ScF_3 displays negative thermal expansion at all temperatures below ~1100 K.[25] With the correct choice of composition, fluorides displaying both negative thermal expansion and optical transparency from the mid-infrared through to the UV can be prepared.[26] A number of

[3] Published in *J. Solid State Chem.*, **2019**, 269, pp 428-433

strategies for controlling thermal expansion in this type of material have explored, including the formation of solid solutions based on ScF_3,[155-157,159] an exploration of cation ordered $M^{II}M^{IV}F_6$[26,180,365,379] notably including $CaZrF_6$[26] and $CaNbF_6$[365] which both display very strong NTE over a wide temperature range, the insertion of lithium,[161] and the introduction of excess fluoride to prepare ReO_3-related composition such as $Sc_{1-x}Zr_xF_{3+\delta}$,[160] $YbZrF_7$[178] and $TiZrF_{7-x}$.[180]

The current study builds up on prior examinations of $CaNbF_6$[365] and $MgNbF_6$,[365] to better understand how ReO_3-type $M^{(II)}NbF_6$ respond to compression and temperature changes as chemical composition is varied. $MnNbF_6$ and $ZnNbF_6$ were examined by synchrotron x-ray powder diffraction from 100- 500 K and upon compression to > 4 GPa. The synthesis, room temperature crystal structures and spectroscopic data for these two materials were reported by Chassaing and coworkers in 1982.[163] Magnetism and the magnetic structure of $MnNbF_6$ were reported in 1986,[380] and a synthesis and powder diffraction data for $ZnNbF_6$ were reported in 1998.[166]

4.2 Experimental

4.2.1 Synthesis

All syntheses were conducted in a dry nitrogen atmosphere, due to the moisture sensitivity of reagents. NbF_4 was prepared by solid state reaction of NbF_5 and niobium metal based on the procedures reported by Chassaing et al.[347] The reactants were ground together in a 5:1 molar ratio (NbF_5 to Nb), with excess Nb^{5+} needed to fully react with the Nb^0 according to Chassaing et al. The mixture was placed in a copper tube, which was sealed by arc-welding under argon. The copper tube was sealed in an evacuated fused silica ampule. The

reaction vessel was heated to 300 °C, held there for 99 h, and then quenched to room temperature. A vacuum sublimation, using a rotary pump and a temperature of ~100 °C, was used to separate product from excess reactant. The result was a black hygroscopic powder.

$MnNbF_6$ and $ZnNbF_6$ were prepared by solid state reaction of NbF_4 and MF_2 (M=Mn, Zn). These syntheses were based on the work of Goubard et al.[166] The reactants were ground together in a 1:1 ratio and loaded into a copper tube, which was sealed by arc-welding under argon. The copper tube was then sealed in an evacuated fused silica ampule. The ampule was quickly heated to 520 °C, held there for approximately one week, and slowly cooled to room temperature. The resulting $MnNbF_6$ and $ZnNbF_6$ products were grey powders.

4.2.2 Variable Temperature X-ray Powder Diffraction Measurements

X-ray powder diffraction data were recorded on a Perkin-Elmer amorphous silicon 2D detector using a wavelength of 0.72950 Å at beamline 17-BM of the Advanced Photon Source, Argonne National Laboratory. An Oxford Cryostream was used to control the sample temperature between 100 and 500 K. As the indicated temperature does not necessarily represent the true sample temperature, calibration data was collected using a thermocouple inserted into an empty Kapton capillary. The difference between the temperature recorded on the thermocouple and that indicated by the Cryostream controller was used as a correction to estimate the true sample temperature for the diffraction experiments.

4.2.3 High-Pressure X-ray Diffraction Measurements

High-pressure powder x-ray diffraction data were collected on the 17-BM beamline at the Advanced Photon Source, Argonne National Laboratory. Data were recorded on a Perkin-Elmer amorphous silicon 2D detector, using a wavelength of 0.72768 Å. An EasyLab "Diacell Bragg-(G)" diamond anvil cell (DAC), equipped with a diaphragm so that the pressure could be automatically increased, was used. Silicone oil (Alfa, MW = 237 $g \cdot mol^{-1}$) was used as the pressure medium. Pressure was determined from the lattice constant of NaCl, which was added as a pressure marker, using an equation of state reported by Birch.[189] Data were acquired while the pressure was continuously increased. Due to the pump program used and the non-linear relationship between pressure in the diaphragm and pressure in the sample chamber, the pressure increments associated with each frame of x-ray data are non-uniform.

4.2.4 Rietveld Analyses of the Powder Diffraction Data and the Calculation of Expansion Coefficients

All Rietveld refinements were performed using the General Structure Analysis System (GSAS)[354] and EXPGUI.[355] Examples of fit quality are given in Appendix C. The unit cell volumes and temperatures were used to calculate coefficients of thermal expansion (CTEs). The variation of the volume CTE with temperature was estimated in two ways, by differentiating a multi-term (six-term for $MnNbF_6$ and four-term for $ZnNbF_6$) polynomial fit to volume vs temperature and using a point by point approach.

4.3 Results and Discussion

4.3.1 Thermal Expansion and Phase Behavior of $MnNbF_6$

Synchrotron x-ray powder data, Figure 4.1a, recorded from 110 to 500 K show a first order phase transition from rhombohedral ($R\bar{3}$) to cubic ($Fm\bar{3}m$) at ~315 K in $MnNbF_6$ (see Figure 4.1b). This transition has previously been reported to occur at 323 K.[380] While some ReO_3-type metal fluorides remain cubic on cooling, many display similar cubic to rhombohedral phase transitions.[344,365,381] The observed transition involves correlated tilting of the MF_6 octahedra ($a^-a^-a^-$ type).[382]

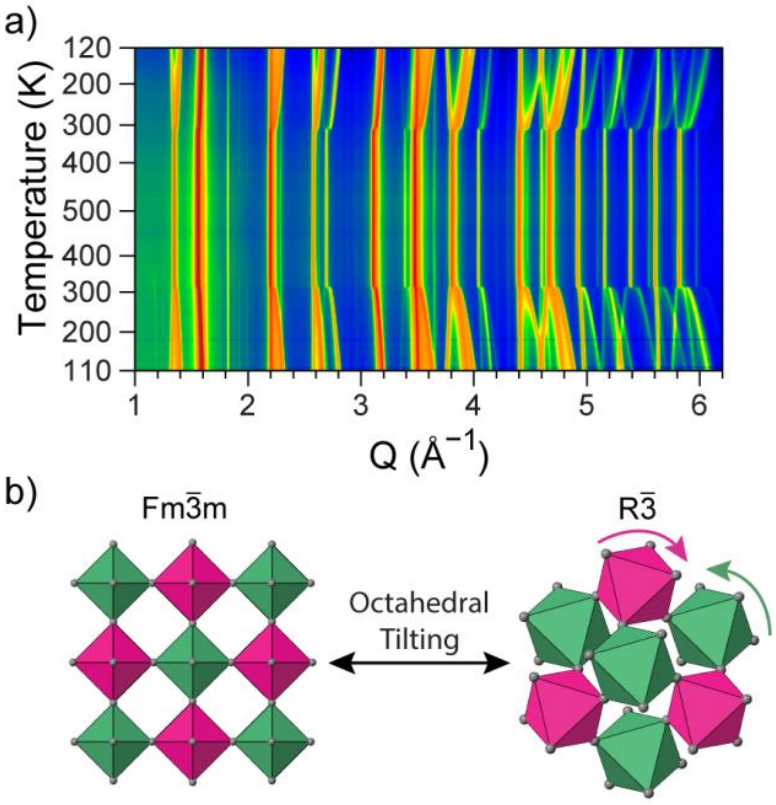

Figure 4.1: a) Synchrotron powder x-ray diffraction data as a function of temperature for $MnNbF_6$. There is a cubic to rhombohedral phase transition at ~315 K, b) which involves correlated octahedral tilts

The volume per formula unit and volumetric CTE are shown in Figure 4.2. The rhombohedral phase shows a large increase in volume on heating, with α_v ~200 ppmK^{-1} from 110 - 200 K. This is typical of ReO_3-type metal fluorides.[344,365] The increase in M-F-M bond angle on heating the rhombohedral phase more than compensates for any negative contribution to the CTE from transverse vibrations of the linking fluoride. The positive thermal expansion (PTE) increases on warming and becomes very large close to the phase transition as the octahedral tilt disappears and the material becomes cubic.

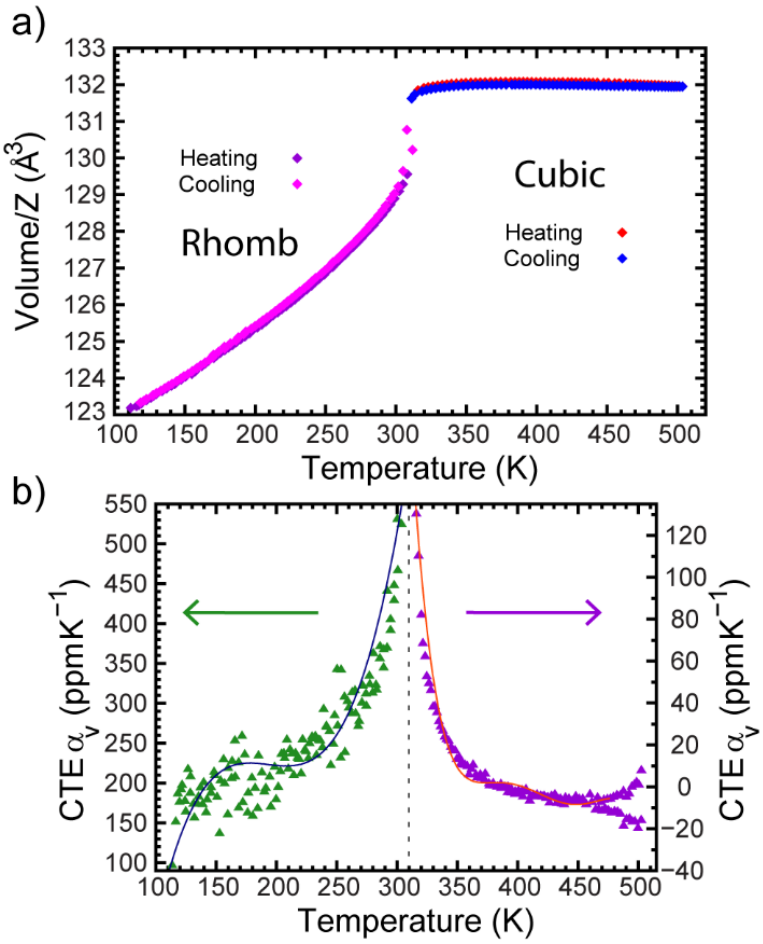

Figure 4.2: a) Volume per formula unit and b) volumetric coefficients of thermal expansion (CTE) determined from a six-term polynomial fit (solid lines) and using a point by point method for $MnNbF_6$. Single phase Rietveld fits were used to determine the volumes, with a change from a rhombohedral to a cubic model at ~315 K.

Immediately above the transition temperature the cubic phase shows PTE, which changes through zero to weak NTE at higher temperatures; α_v of 0.0 ppm K^{-1} at 382 K, and α_v of ~-6 ppm K^{-1} at 450 K. Above 450 K, the apparent CTEs on heating and cooling vary due to some hysteresis in the diffraction measurements. The origin of this behavior is unclear, but it may be an experimental artefact.

4.3.2 Thermal Expansion and Phase Behavior of $ZnNbF_6$

The response of $ZnNbF_6$ to changes in temperature was also probed by synchrotron x-ray powder diffraction. Unit cell volume and volumetric CTE versus temperature are shown in Figure 4.3. This sample adopted a rhombohedral ($R\bar{3}$) structure over the entire measured temperature range. Some apparent hysteresis is seen between the data recorded on heating and cooling, which is most likely an experimental artefact. As the experimentally determined unit cell volume varies smoothly on cooling, we believe that it most accurately represents the true sample behavior. The thermal expansion of $ZnNbF_6$, Figure 4.3b, is strongly positive, with a α_v of 107 ppm K^{-1} at 120 K. The CTE increases on further heating, with a $\alpha_v \sim 315$ ppm K^{-1} at 499 K.

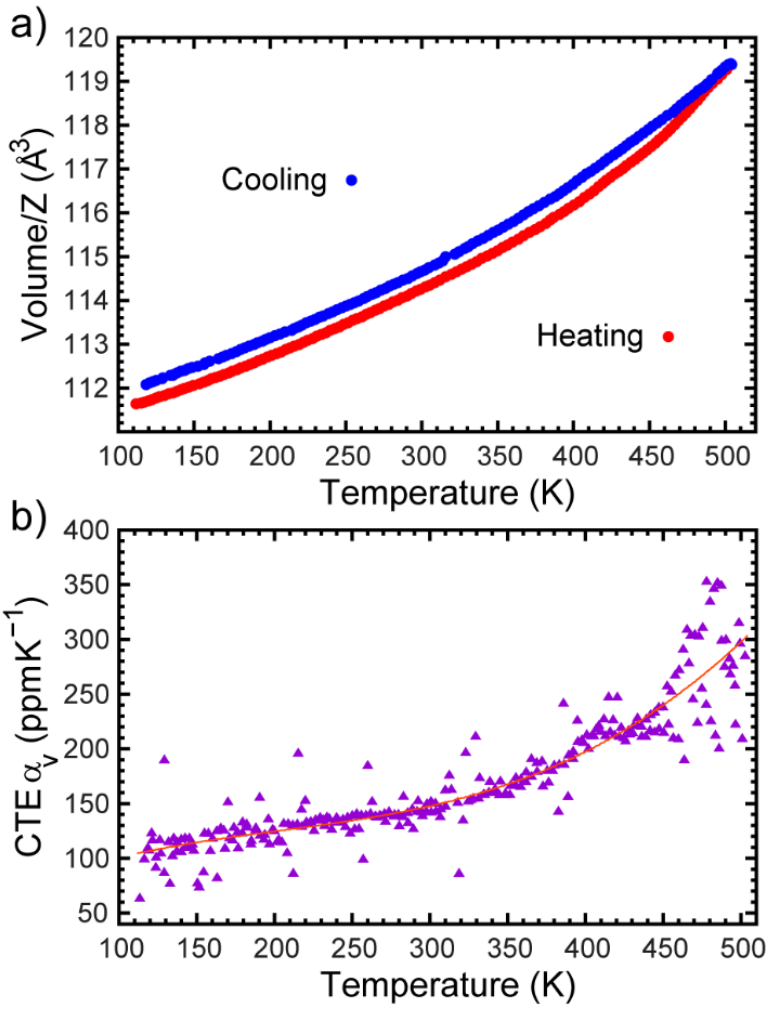

Figure 4.3: a) Volume per formula unit and b) volumetric coefficient of thermal expansion (CTE) determined from a four-term polynomial fit (solid line) and using a point by point approach for $ZnNbF_6$ as determined from Rietveld fits of a rhombohedral ($R\bar{3}$) model to the variable temperature x-ray powder diffraction data.

The thermal expansion of several rhombohedral ReO_3–connectivity metal fluorides[157,158,365,379,383] are compared in Figure 4.4. The expansion of $MnNbF_6$ is similar to that of $MgNbF_6$, with a large positive CTE that increases dramatically close to the rhombohedral to cubic phase transition. The successive replacement of Mg by Mn and then Zn stabilizes the rhombohedral structure to increasingly higher temperatures. This is not purely a consequence of changes in ionic radii, as the six coordinate ions have Shannon

effective radii of 72, 82 and 74 pm respectively.[384] It is likely related to an increase in the covalency of the bonding on moving from Mg to Zn, as highly ionic bonding stabilizes the maximum volume cubic structure[372] and Zn is significantly more electronegative than Mg (1.66 versus 1.23).[373] At the maximum temperature studied, $ZnNbF_6$ displays higher thermal expansion than InF_3 and AlF_3, which both remain rhombohedral to high temperatures (>650 K).[158,383]

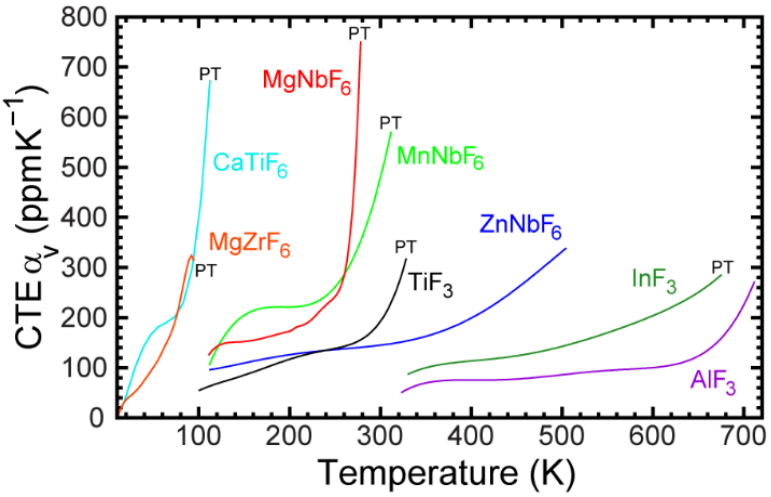

Figure 4.4: A comparison of the CTEs for rhombohedral ReO_3-type metal fluorides. The CTEs were estimated by differentiating six-term polynomial fits to volume vs temperature.

4.3.3 Compression of $MnNbF_6$

The response of $MnNbF_6$ to compression was studied by variable pressure powder x-ray diffraction in a DAC. The resulting data are shown as a 2D-contour plot in Figure 4.5a. This plot shows evidence of a phase transition at very low pressure, associated with peak splitting indicative of octahedral tilting on compression, and a transition to a poorly ordered phase at ~6 GPa. Close inspection of the data reveals that the initial diffraction patterns show phase coexistence of rhombohedral and cubic phases. This is not unreasonable given

the first order nature of the thermally induced transition and a transition temperature close to ambient. The phase coexistence persists during the first few frames of diffraction data, as there is a delay between the increase in methanol pressure supplied to the diaphragm on the DAC and any significant increase in the pressure experienced by the sample. An example Rietveld fit to data in this region is shown in Figure C.5.

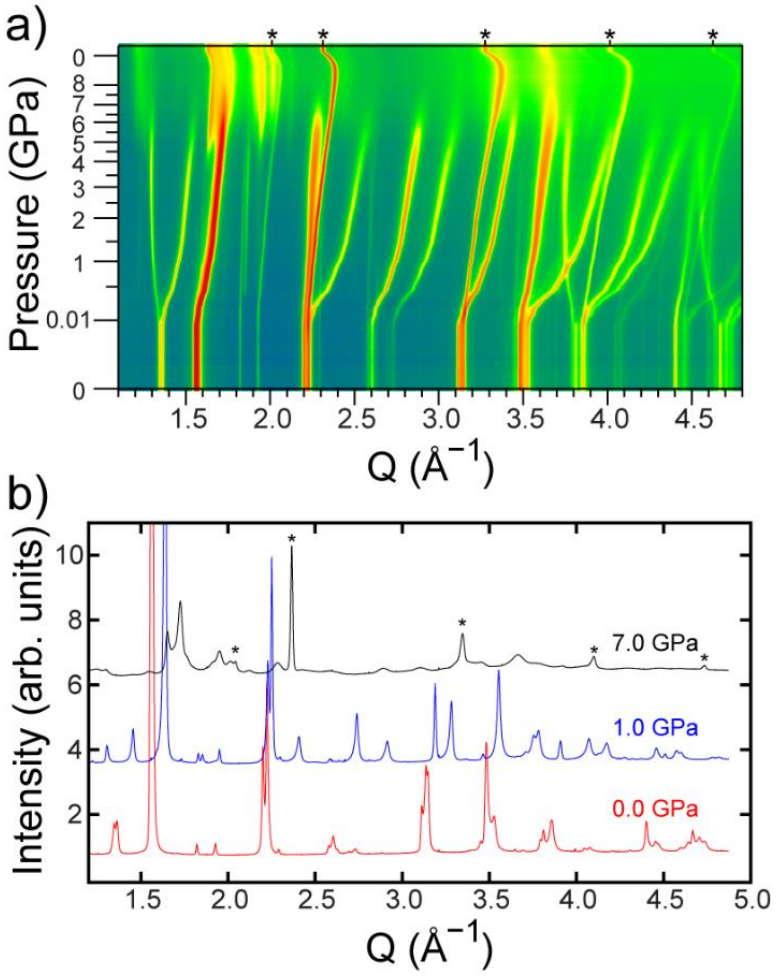

Figure 4.5: a) High-pressure powder x-ray diffraction data for $MnNbF_6$ and b) selected powder diffraction patterns. Diffraction peaks from the NaCl internal pressure standard are marked by *.

As the pressure increases, the $MnNbF_6$ sample completely transforms to rhombohedral material. On further compression, the evolution of the data is consistent with increasing

octahedral tilting in the $R\bar{3}$ phase. Above 6 GPa, the peaks from the rhombohedral phase disappear and broad peaks appear alongside those from NaCl indicating that $MnNbF_6$ transforms to a poorly ordered structure, Figure 4.5b. This behavior is distinct from that previously seen for $CaNbF_6$.[365] Unlike $MnNbF_6$, $CaNbF_6$ undergoes a transition from cubic $Fm\bar{3}m$ to a poorly ordered phase at ~0.4 GPa. The reason for the difference is unclear.

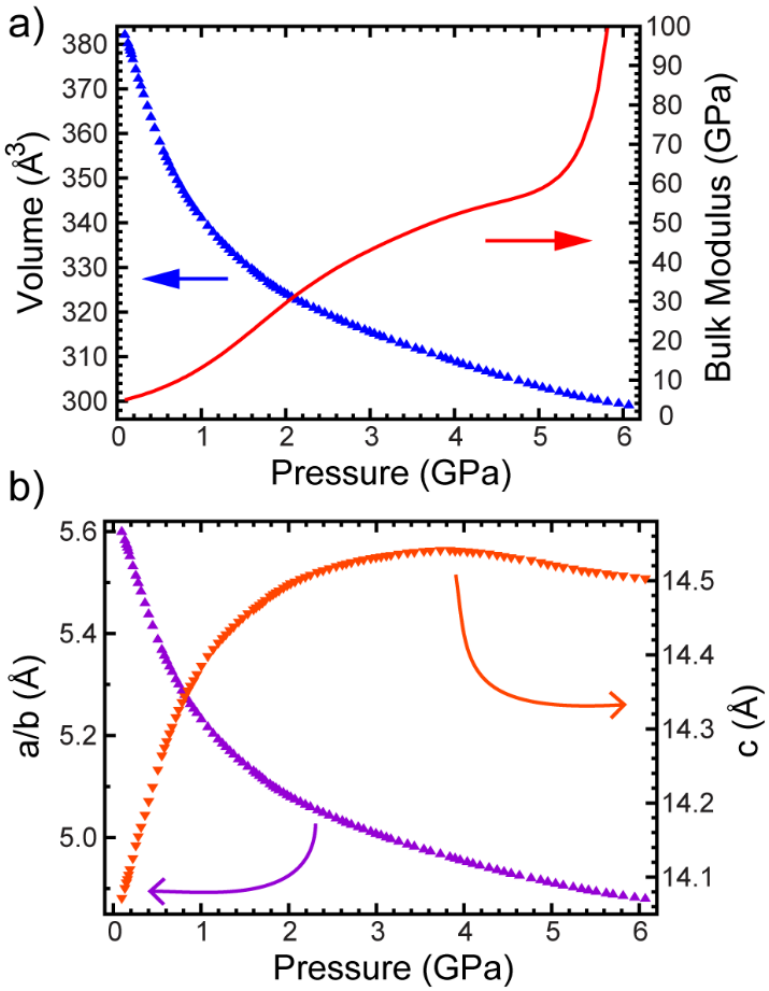

Figure 4.6: a) Unit cell volume, bulk modulus and b) lattice constants for $MnNbF_6$. Note the two y-axes are scaled differently.

Unit cell volume versus pressure for rhombohedral $MnNbF_6$ is shown in Figure 4.6a along with an estimate of how the bulk modulus evolves on compression. The later was calculated

by differentiating a six-term polynomial, which had been fit to ln(V) vs P. This approach was adopted as the V versus P data could not be fit satisfactorily using a conventional equation of state. At low pressures, the material is extremely soft. The bulk modulus increases from 5 to 12 GPa on compression to ~1 GPa. This contrasts with what is typically seen in cubic ReO_3-type metal fluorides, for example $CaNbF_6$ has $K_{0(298K)}$ = 33.7(4) GPa and displays pronounced softening on compression, $K'_{0(298\ K)}$ ~-23(2), rather than stiffening. However, behavior of this type is to be expected for rhombohedral ReO_3-connectivity phases, as tilting of the framework octahedra (bending Mn-F-Nb links) initially provides a low energy path for volume reduction on compression above 1 GPa, the structure continues to stiffen with the bulk modulus exceeding 60 GPa prior to the transition to a poorly ordered phase. This stiffening presumably occurs because the pressure-induced octahedral tilts bring the fluoride ions closer together. The compressibility of the rhombohedral phase is highly anisotropic (Figure 4.6b); it displays negative linear compressibility parallel to the c-axis up to ~3.8 GPa, and it is elastically very soft in the a-b plane. This occurs because the octahedral tilts involve rotation around crystallographic 3-fold axes leading to a reduction in metal – metal separation in the a-b plane, and in parallel with this there is an octahedral distortion that leads to negative linear compressibility parallel to the c-axis.[379] Similar behavior has been seen in other rhombohedral ReO_3-type fluorides.[248,249,379]

4.3.4 Compression of $ZnNbF_6$

The high-pressure powder x-ray diffraction data for $ZnNbF_6$ are presented in Figure 4.7.

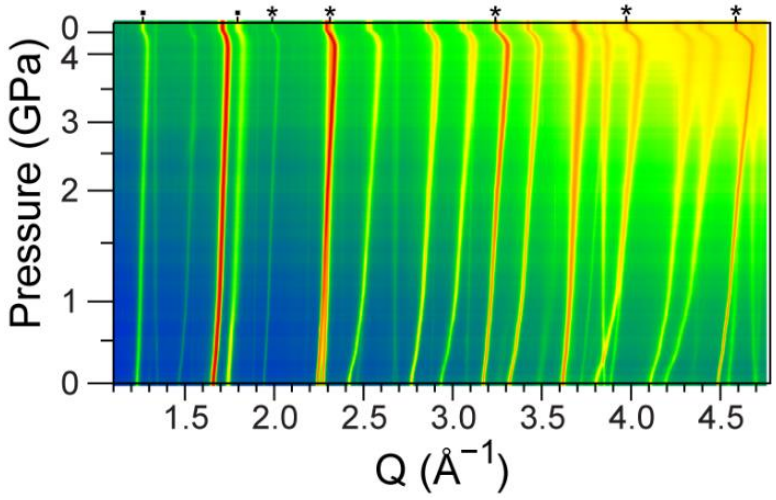

Figure 4.7: Diffraction data as a function of pressure for $ZnNbF_6$. Diffraction peaks from the internal pressure standard, NaCl, are marked with * and an impurity phase with ■. The sample was decompressed at the end of experiment.

The diffraction patterns evolve smoothly on increasing and decreasing pressure, without any additional peak splitting or new peaks indicating that $ZnNbF_6$ remains in the rhombohedral phase up to the highest pressures recorded, ~4 GPa. An additional minor phase, not seen in the variable temperature experiments for this sample, appears throughout these data. It seems likely that it formed while grinding the sample. Similar behavior has been seen in other ReO_3-type fluorides including $CaZrF_6$.[26]

An example Rietveld fit for rhombohedral $ZnNbF_6$ is given in Figure C.7. Unit cell volumes and bulk moduli, calculated from a six-term polynomial fit to ln(V) vs pressure, are shown in Figure 4.8. Similar to $MnNbF_6$, a conventional equation of state, such as Burch Murnaghan, did not give a satisfactory fit to the V versus P data. $ZnNbF_6$ is elastically soft at low pressures, with a bulk modulus of ~14 GPa at ambient. However, it stiffens rapidly on compression leading to a bulk modulus of > 50 GPa at pressures above 3.5 GPa. Similar to the Mn analog, the compressibility is highly anisotropic. The material

is very soft in the a-b plane, but parallel to the c-axis it displays negative linear compressibility below 2.0 GPa (Figure 4.8b). The greater ambient pressure bulk modulus for $ZnNbF_6$ versus $MnNbF_6$ (~14 and ~5 GPa respectively) and the much smaller fractional increase in the c-axis on compression prior to the onset of positive linear compressibility parallel to the c-axis presumably reflects the considerable octahedral tilting that is already present in the $ZnNbF_6$ at ambient pressure and temperature (Zn-F-Nb angle is ~148.8(5)° at ambient pressure).

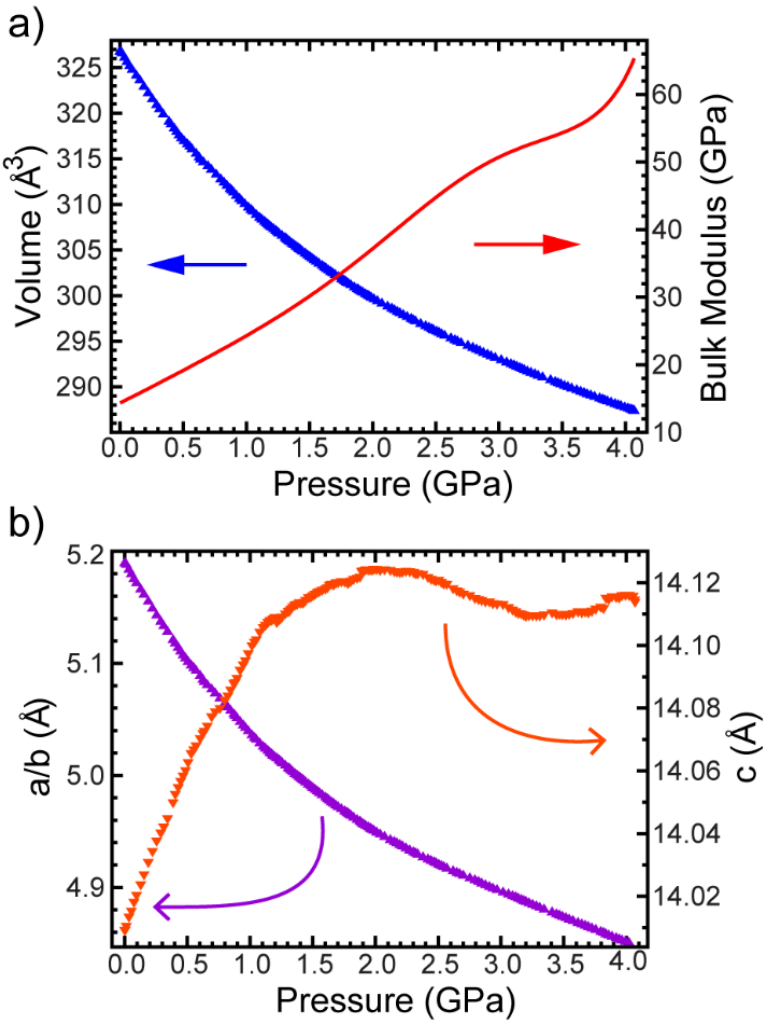

Figure 4.8: a) Unit cell volume, bulk modulus and b) lattice constants for $ZnNbF_6$. Note the two y-axes are scaled differently.

The compressibilities of $MnNbF_6$ and $ZnNbF_6$ are compared to those of some other ReO_3-related rhombohedral metal fluorides in Figure 4.9.[248,249,379] The general trend in elastic stiffness (slope of V versus P) at ambient, or close to ambient pressure, reflects the trend in M-F-M' bond angles at close to ambient pressure. CrF_3, which has the smallest M-F-M angle (~144.8° at ambient), is the stiffest phase and $CaTiF_6$ is the softest with a Ca-F-Ti angle of 158.9° at 0.25 GPa.

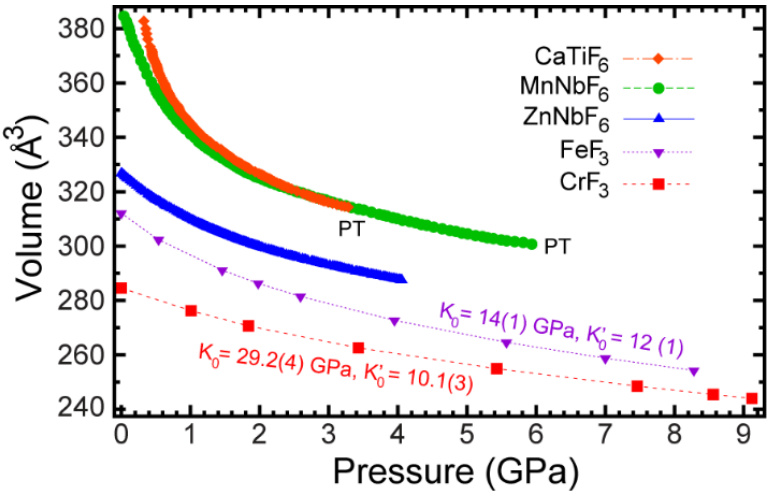

Figure 4.9: Unit cell volume versus pressure for several rhombohedral ReO_3-related fluorides.

4.4 Conclusions

The responses of ReO_3-type $ANbF_6$ (A = Ca, Mg, Mn and Zn) to changes in temperature and pressure are varied. $CaNbF_6$ has previously been reported to retain a cubic cation ordered structure over a wide temperature range (from less than 10 to at least 900 K).[365] However, $MgNbF_6$ and $MnNbF_6$ display rhombohedral to cubic transitions, involving the correlated titling or corner shared octahedral, on heating above ~280 and ~315 K respectively. Even though Zn^{2+} has a similar ionic radius to Mg^{2+}, $ZnNbF_6$ adopted a rhombohedral structure over the entire temperature rage investigated (~100 – 500 K). This is likely a consequence of zinc's greater electronegativity when compared to magnesium, as more ionic bonding is thought to favor the cubic phase.[372] The behavior of $CaNbF_6$ on compression is distinct from that of both $MnNbF_6$ and $ZnNbF_6$. $CaNbF_6$ transform from a cubic ReO_3 structure to a poorly ordered phase on compression to ~0.4 GPa.[365] However, both $MnNbF_6$ and $ZnNbF_6$ adopt rhombohedral ReO_3-type structures to quite high pressures (~6 GPa and > 4 GPa respectively). These rhombohedral phases are elastically

very soft at close to ambient pressure, as the reduction of the M-F-Nb bond angles associated with tilting of the octahedra provides a low energy pathway for volume reduction, but they rapidly stiffen as the M-F-Nb bond angles are reduced due increasing steric repulsion.

4.5 Acknowledgments

We are grateful for useful discussions with Ross Angel. The activities at Georgia Tech were supported in part under NSF DMR-1607316. This work made use of the Advanced Photon Source, a U.S. Department of Energy (DOE) Office of Science User Facility operated for the DOE Office of Science by Argonne National Laboratory under contract DE-AC02-06CH11357.

CHAPTER 5. THE EFFECTS OF EXCESS FLUORIDE ON THERMAL EXPANSION AND RESPONSE TO COMPRESSION IN CATION ORDERED ReO_3-TYPE FLUORIDES: $Ca[Zr^{(IV)}_{1-x}Nb^{(V)}_x]F_{6+x}$

5.1 Introduction

Negative thermal expansion (NTE) is unusual, but it has been observed in several families of material.[27,30-32,34,332] Its technological importance has been established for many applications, including the creation of controlled thermal expansion composites.[3,35-37,40-44,46] Control of thermal expansion is desired in order to achieve dimensional control or combat possible failure from thermal expansion mismatch or thermal shock. However, both the fabrication of composites and internal thermal expansion mismatch between components in a composite can lead to significant stresses.[35,36,183,186,187] Consequently, it is important to understand how NTE materials respond to stress in addition to changes in temperature.

Several different mechanisms for NTE are known, including changes in crystal structure, magnetic ordering, and electronic structure.[34,46,332] NTE can also arise from the transverse vibrational motion of bridging atoms. Open framework materials with low energy phonons corresponding to this type of transverse motion are known to display NTE.[65,154] The identification of strong NTE in ZrW_2O_8 led to the rapid growth of interest in framework NTE materials, with NTE being reported in zeolites, MOFs, and metal cyanides.[24,71,88,364,376]

A variety of fluorides are known to adopt ReO_3-type cubic structures, which consist of corner shared octahedra. This framework can support the vibrational modes needed for NTE. The search for NTE in metal fluorides is partly motivated by their potential for mid-IR to UV optical transparency, which could be utilized in multispectral optical applications. The first metal fluoride known to show large isotropic NTE was ScF_3. This material remains cubic with strong NTE over a wide temperature range.[25] Many mixed metal fluorides, including $CaZrF_6$ and $CaNbF_6$, have subsequently been studied with several showing strong isotropic NTE down to low temperatures.[26,344,365,379,385]

Many different strategies for controlling the thermal expansion of ReO_3-related fluorides are possible,[150,155-160,178,180,181,345] including the deliberate introduction defects. Cation ordered ReO_3-type fluorides, $M^{2+}M^{4+}F_6$, can accommodate the substitution of either metal by one in a higher oxidation state.[168,172,173,176] In order to maintain charge balance excess fluoride must be incorporated into the structure. This can be achieved by putting the fluoride on interstitial sites leading, in some cases, to the conversion of corner sharing polyhedra to edge-sharing units.[173,176,178-182] Defects of this type are expected to decrease the flexibility of the framework and interfere with the low-frequency transverse vibrations that are responsible for NTE. The formal replacement of Ca^{2+} by Yb^{3+} in $CaZrF_6$ leads to $YbZrF_7$. An x-ray total scattering study of this material suggests the presence of edge-sharing polyhedra. $YbZrF_7$, unlike $CaZrF_6$, shows ZTE at close to room temperature.[173,178,179] Changes in composition, driving a transition from partial edge-sharing to corner sharing, have been shown to tune thermal expansion from positive through zero to negative in $Ti^{2+}_xTi^{3+}_{1-x}ZrF_{7-x}$ (x= 0,0.5, and 1).[180] More recently, the system $Mg_{2-x}Zr_xF_{4+2x}$ was studied to probe the effect of replacing some Mg^{2+} in $MgZrF_6$ by Zr^{4+}.

This substitution was used to tune both the thermal expansion and response to pressure of these ReO_3-type solids.[181] In the current paper, we examine the controlled replacement of Zr^{4+} by Nb^{5+} in the NTE material $CaZrF_6$. Unlike $YbZrF_7$, $Mg_{2-x}Zr_xF_{4+2x}$ and $Ti^{2+}_xTi^{3+}_{1-x}ZrF_{7-x}$ a high level of cation ordering is maintained, even at high Nb^{5+} substitution levels, as the Nb^{5+} goes exclusively onto the Zr^{4+} site. Variable temperature and high-pressure synchrotron x-ray diffraction was utilized to study the thermal expansion and compression of $CaZr_{0.75}Nb_{0.25}F_{6.25}$, $CaZr_{0.5}Nb_{0.5}F_{6.5}$, and $CaZr_{0.25}Nb_{0.75}F_{6.75.}$ $CaNbF_7$ was not studied as well crystallized samples of this composition could not be prepared, although other workers have made this material.[172] The local structure of these materials was also examined by x-ray total scattering.

5.2 Experimental

5.2.1 Synthesis

CaF_2 (99.5%, Alfa Aesar) and NbF_5 (99.5%, STREM) and ZrF_4 (99.9%, STREM) were used to prepare $Ca[Zr^{(IV)}_{1-x}Nb^{(V)}_x]F_{6+x}$ via solid state reaction using a procedure adapted from Chassaing et al.[172] The appropriate molar ratios were thoroughly ground together under a dry nitrogen atmosphere and placed into a nickel tube, which was then sealed by arc-welding under argon. The nickel tube was then sealed in an evacuated fused silica ampoule. The samples were heated to 650 °C at a rate of 5.2 °C/min, held at 650 °C for 3 days, and cooled to 25 °C at a rate of 0.43 °C/min. This process was repeated to improve their crystallinity. The products were light grey powders, which were single phase by powder x-ray diffraction (see Figure 5.1 for example).

5.2.2 High Resolution Variable Temperature X-ray Powder Diffraction Measurements

Powder x-ray diffraction data were collected using the 17-BM beamline at the Advanced Photon Source, Argonne National Laboratory. Samples of $CaZr_{0.75}Nb_{0.25}F_{6.25}$, $CaZr_{0.5}Nb_{0.5}F_{6.5}$, and $CaZr_{0.25}Nb_{0.75}F_{6.75}$ were packed and sealed in 0.8 mm diameter Kapton tubes. Diffraction data were recorded on a Perkin-Elmer 2D detector using a wavelength of 0.72768 Å. A LaB_6 sample was used to determine the exact sample to detector distance and other parameters needed for accurate integration of the 2D diffraction data. The sample temperature was controlled using an Oxford Cryosystems Cryostream (100 – 500 K).

5.2.3 High-Pressure X-ray Diffraction Measurements

Variable pressure diffraction measurements were also performed at the 17-BM beamline, Advanced Photon Source, Argonne National Laboratory using a wavelength of 0.72768 Å. Samples of $CaZr_{0.75}Nb_{0.25}F_{6.25}$, $CaZr_{0.5}Nb_{0.5}F_{6.5}$, and $CaZr_{0.25}Nb_{0.75}F_{6.75}$ were compressed up to ~8 GPa in an easyLab Diacell Bragg-(G) diaphragm diamond anvil cell (DAC). Samples were loaded in a dry nitrogen filled glove-bag with NaCl as an internal pressure standard and Alfa silicone oil (molecular weight of 237 $g \cdot mol^{-1}$) as the pressure-transmitting fluid. The known equation of state and the measured unit cell volume for NaCl were used to calculate the pressure.[189]

5.2.4 Total Scattering Measurements

X-ray total scattering data were acquired using beam line 11-ID-B at the Advanced Photon Source, Argonne National Laboratory. Samples were sealed in Kapton capillary tubes

under dry nitrogen using an epoxy adhesive. Data were recorded using a Perkin Elmer 2D amorphous silicon detector, with a sample to detector distance of 22 cm and an x-ray energy of 86.7 keV. The resulting diffraction data had a usable Q_{max} of ~25 $Å^{-1}$. The software PDFgetX2 was used to obtain pair distribution functions from the x-ray scattering data.[386]

5.2.5 Density Measurements

Powder samples were lightly pressed into pellets, weighed and then loaded into a Micromeritics AccuPyc-2 1340 helium pycnometer for volume determination. The weight of each pellet was used along with its volume to determine the sample densities. All sample handling was performed in a glove box filled with dry nitrogen.

5.2.6 Rietveld Analyses

Rietveld refinements were performed using the General Structure Analysis System (GSAS)[354] coupled with EXPGUI[355] in order to determine unit cell constants as a function of temperature and pressure. A cation ordered cubic ($Fm\bar{3}m$) model was used in these analyses (see Appendix D), with niobium replacing some of the zirconium. Good fits could be achieved with this cation ordered model regardless of composition. No attempt was made to incorporate excess fluoride into these analyses due to the limited range of the data in Q-space (Q_{max} ~5.8 $Å^{-1}$ for Cryostream and ~4.6 $Å^{-1}$ for DAC). Examples of fit quality to both the variable temperature and high-pressure data are shown in Figure 5.1 and in Appendix D.

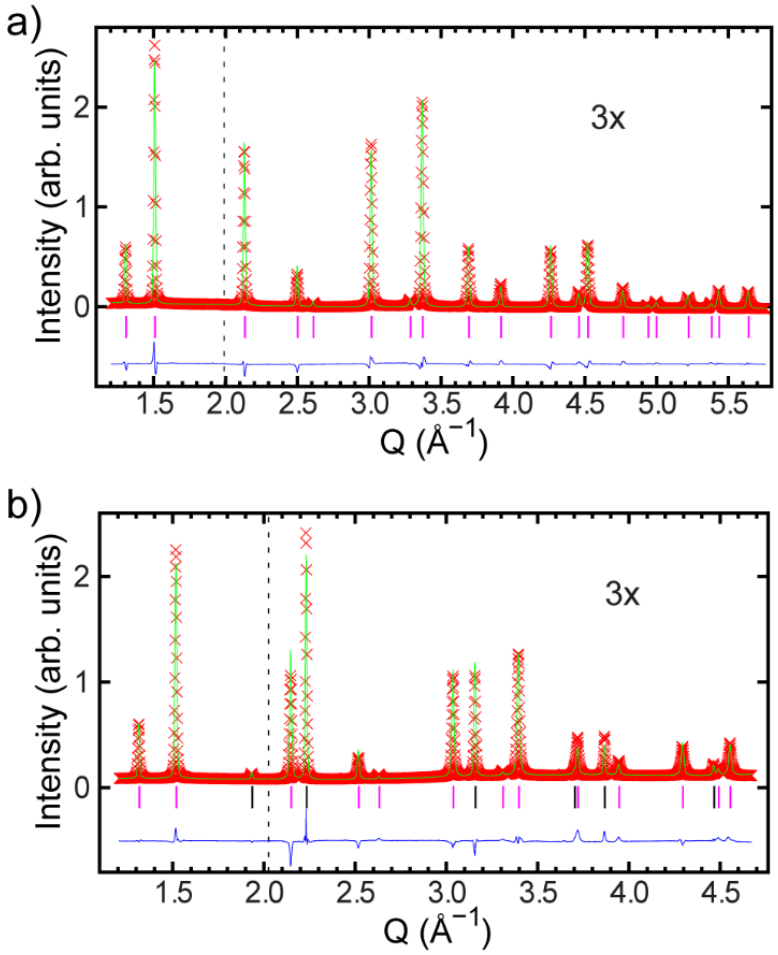

Figure 5.1: Rietveld fits, using a cubic Fm$\bar{3}$m model, to the a) 300 K cooling and b) 0.1 GPa powder diffraction data for $CaZr_{0.25}Nb_{0.75}F_{6.75}$. Tick marks for peaks from the sample (magenta) and NaCl pressure marker (black) are shown. The high Q data were scaled to show detail and shifted downwards so that the background levels appear to be the same.

5.3 Results and Discussion

5.3.1 Defect Mechanism and Local Structure

The $Ca[Zr^{(IV)}_{1-x}Nb^{(V)}_{x}]F_{6+x}$ samples were examined using x-ray total scattering. The resulting Pair Distribution Functions (PDFs), Figure 5.2, reveal very little difference between the local structures of each fluoride excess material and that of the parent phase

cubic $CaZrF_6$. This contrasts with reports for other fluoride excess ReO_3-type materials. The PDFs for $TiZrF_7$, $YbZrF_7$, and $Mg_{2-x}Zr_xF_{4+2x}$ show clear pair correlation peaks between 3 and 4 Å that are not expected for a defect free cubic ReO_3-structure.[178,180,181] In work on $TiZrF_7$,[355] this peak was attributed to a new M-F distance resulting from the presence of edge-sharing polyhedra. However, it was proposed in work on $YbZrF_7$[178] and for compositions in the $Mg_{2-x}Zr_xF_{4+2x}$ system[181] that this peak arises from short M-M distances generated when polyhedra share edges rather than corners. If the current niobium substituted materials accommodated excess fluoride as interstitials by creating edge shared polyhedra, as proposed for $TiZrF_7$, $YbZrF_7$, and $Mg_{2-x}Zr_xF_{4+2x}$, then the PDFs for $Ca[Zr^{(IV)}_{1-x}Nb^{(V)}_x]F_{6+x}$ should also show a correlation peak in the range 3 - 4 Å. However, the PDFs (Figure 5.2) do not show such a peak, suggesting that either the excess fluoride is not present as interstitials or that it is incorporated into $Ca[Zr^{(IV)}_{1-x}Nb^{(V)}_x]F_{6+x}$ by a different mechanism.

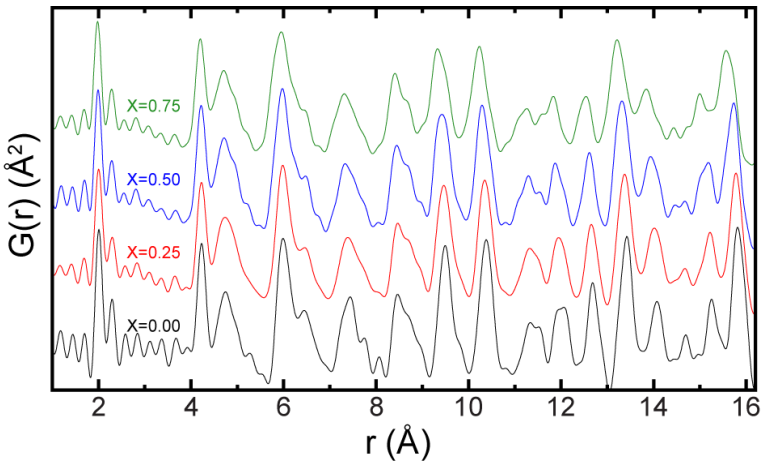

Figure 5.2: Pair distribution functions derived from the x-ray total scattering data for $Ca[Zr^{(IV)}_{1-x}Nb^{(V)}_{x}]F_{6+x}$.

To confirm that the aliovalent substitution of Nb^{5+} generates interstitial fluoride, and not cation vacancies, the density of each sample was measured. These values are compared to those calculated for both fluoride interstitial and cation vacancy defect models in Figure 5.3a. There is a close match between the measured values and those predicted for the interstitial model. Those calculated for the cation vacancy model are significantly lower than the measured ones. These results clearly indicate that niobium substitution leads to the creation of interstitial fluoride. However, given the absence of a peak in the PDFs in 3 -4 Å range, the interstitial fluoride is likely incorporated into the structure in a different way from that seen for $TiZrF_7$, $YbZrF_7$, and $Mg_{2-x}Zr_xF_{4+2x}$. It may be present as a terminal interstitial fluoride, rather than one bridging between two metal centers. Such a difference is not unreasonable, given that in $Ca[Zr^{(IV)}_{1-x}Nb^{(V)}_{x}]F_{6+x}$ the Zr/Nb always has six Ca nearest neighbor cations, but the cation disorder in $TiZrF_7$, $YbZrF_7$, and $Mg_{2-x}Zr_xF_{4+2x}$, allows for Zr-Zr nearest neighbor cation pairs.

The room temperature lattice constants for $Ca[Zr^{(IV)}_{1-x}Nb^{(V)}_{x}]F_{6+x}$ decrease with increasing $Nb^{(V)}$ content (Figure 5.3b). The values for $CaZrF_6$ and $CaNbF_7$ were taken from the literature.[26,172] The experimental values are compared to those expected if the reduction in lattice constant is solely due to the replacement of six coordinate Zr^{4+} (ionic radius 0.72 Å) by six coordinate Nb^{5+} (0.64 Å) (purple dotted line Figure 5.3b) and also the replacement of six coordinate Zr^{4+} (0.72 Å) by seven coordinate Nb^{5+} (0.69 Å) (solid cyan line Figure 5.3b) without any change in M-F-M link geometry. There is good agreement between experiment and the prediction based on the replacement of six coordinate Zr^{4+} by six coordinate Nb^{5+}. However, as the density data clearly indicate that there is interstitial fluoride present, the coordination numbers for some cations must be greater than six, suggesting that structural distortions such as bending of M-F-M links must be present. The presence of terminal fluoride interstitials would result in structural distortions.

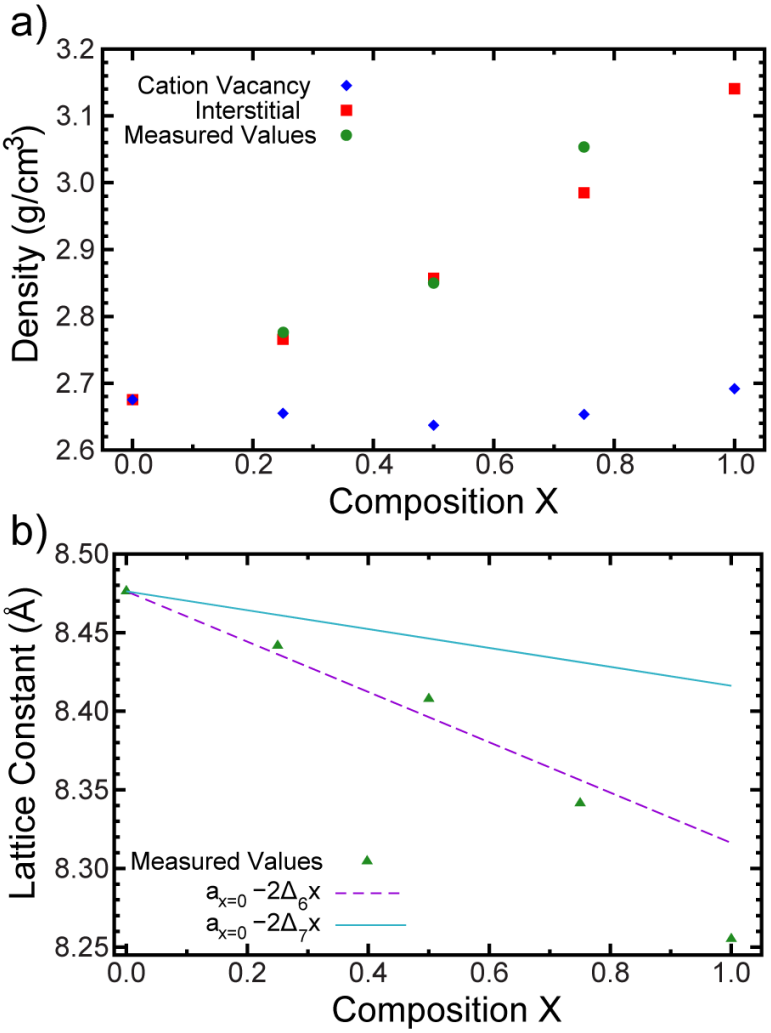

Figure 5.3: a) Densities and b) lattice constants versus composition for $Ca[Zr^{(IV)}_{1-x}Nb^{(V)}_{x}]F_{6+x}$. The lattice constants for x = 0 and 1 ($CaZrF_6$ and $CaNbF_7$) were obtained from the literature.[26,172] Δ_6 = (radius of 6 coordinate Zr^{4+} - radius of 6 coordinate Nb^{5+}) = 0.08, and Δ_7 = (radius of 6 coordinate Zr^{4+} - radius of 7 coordinate Nb^{5+}) = 0.03.

5.3.2 Thermal Expansion

The powder x-ray diffraction data were analyzed by the Rietveld method using a cubic $Fm\bar{3}m$ structure. The resulting unit cell volumes and coefficients of thermal expansion (CTEs) for $CaZr_{0.75}Nb_{0.25}F_{6.25}$ are shown in Figure 5.4a. On initial heating (red) from ~100 K the material shows a steady decrease in volume until ~300 K. At ~300 K, the volume levels out and then decreases again on heating above 400 K. On cooling (blue) a smooth

increase in volume is observed. This strong dependence of the unit cell volume on thermal history suggests that the defects in the material, introduced by niobium substitution, can rearrange at temperatures close to ambient. Thermal history dependent behavior has previously been observed in the fluoride excess material $YbZrF_7$.[178,179] On cooling from ambient to 100 K prior to recording the initial diffraction data, the defects are likely immobile on the time scale of the experiment and remain in their initial configuration, but on heating above 300 K they start to rearrange. On cooling back down from 500 K they do not revert to the original 300 K configuration as the cool down during the diffraction measurements is rapid when compared to the very long time period the sample had spent at 300 K prior to the start of the diffraction measurements. The CTE calculated from just the cooling data, Figure 5.4b, shows strong NTE across the entire temperature range, with maximum magnitude, α_v = -48 ppm K^{-1}, at 129 K.

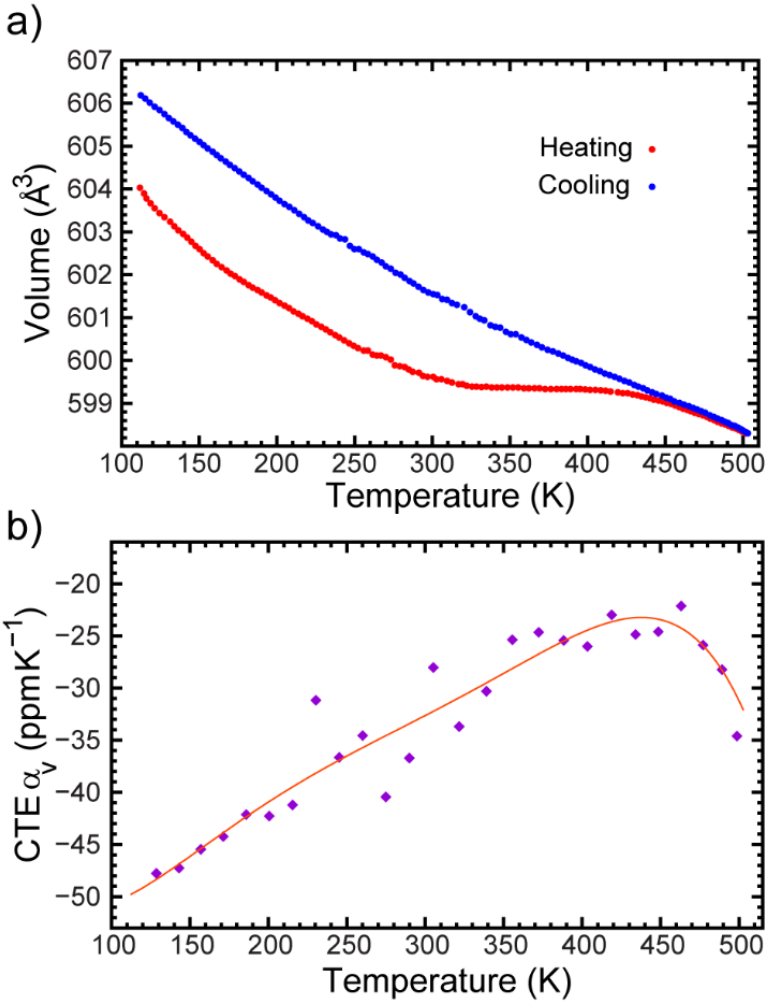

Figure 5.4: a) Unit cell volume on heating (red)/cooling (blue) and b) volumetric coefficient of thermal expansion (CTE) calculated between every fifth point (purple) and from a six-term polynomial (orange), which was fit to volume versus temperature for $CaZr_{0.75}Nb_{0.25}F_{6.25}$.

Similar to the x=0.25 sample, the response of $CaZr_{0.5}Nb_{0.5}F_{6.5}$ to changes in temperature was highly dependent on its thermal history and the material displayed strong NTE on cooling from 500 K (Figure 5.5). On initial heating from 100 K, there is an anomaly in the thermal expansion at just above 300 K, which is likely associated with defect rearrangement/relaxation. On cooling from 500 K, the evolution of the unit cell volume with temperature is very different from that seen on heating, as the defects can't relax back to their original 300 K arrangement on the time scale of the diffraction measurements. Very

strong NTE is seen at close to 500 K (α_v = -84 ppm K^{-1} at 499 K), but it weakens below 400 K (α_v = -31 ppm K^{-1} at 403.3 K) and then increases again on cooling to the lowest temperatures (α_v = -46 ppm K^{-1} at 129 K).

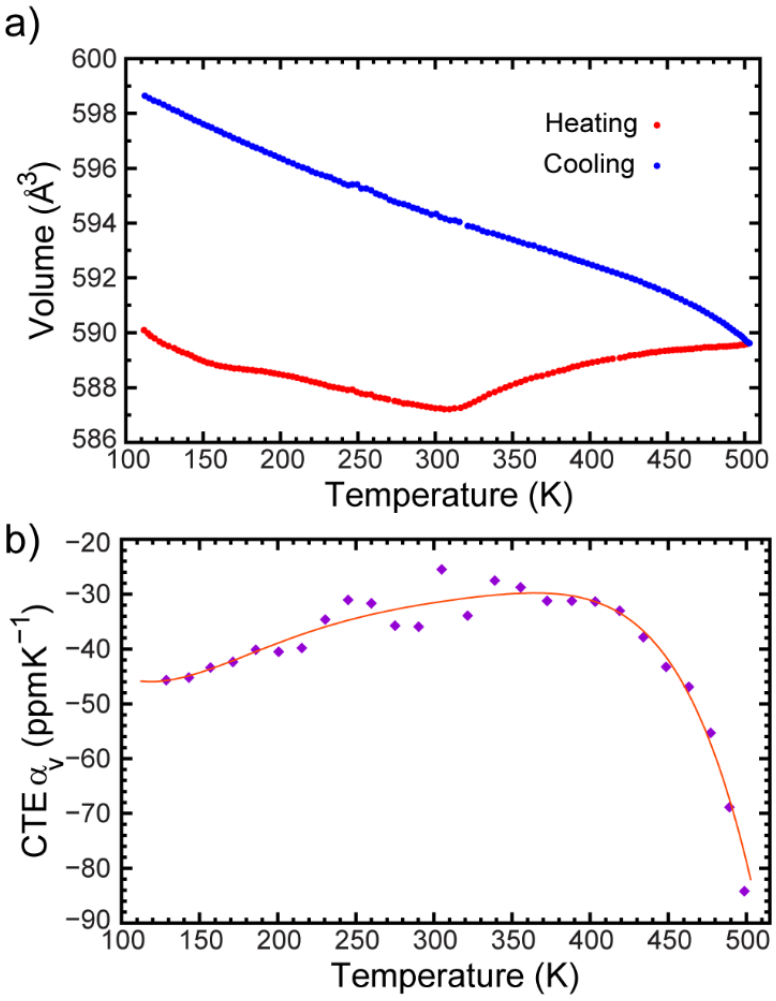

Figure 5.5: a) Unit cell volume on heating (red)/cooling (blue) and b) volumetric coefficient of thermal expansion (CTE) calculated between every fifth point (purple) and from six-term polynomial fit to volume curve (orange) versus temperature for $CaZr_{0.5}Nb_{0.5}F_{6.5}$.

The thermal expansion of the sample with most niobium substitution, $CaZr_{0.25}Nb_{0.75}F_{6.75,}$ showed the greatest dependence on thermal history (Figure 5.6), which is perhaps not surprising as it contains the greatest concentration of fluoride interstitials. Once again, there

is a major anomaly in the thermal expansion at just above 300 K on first heating the sample, and on cooling strong negative thermal expansion is observed.

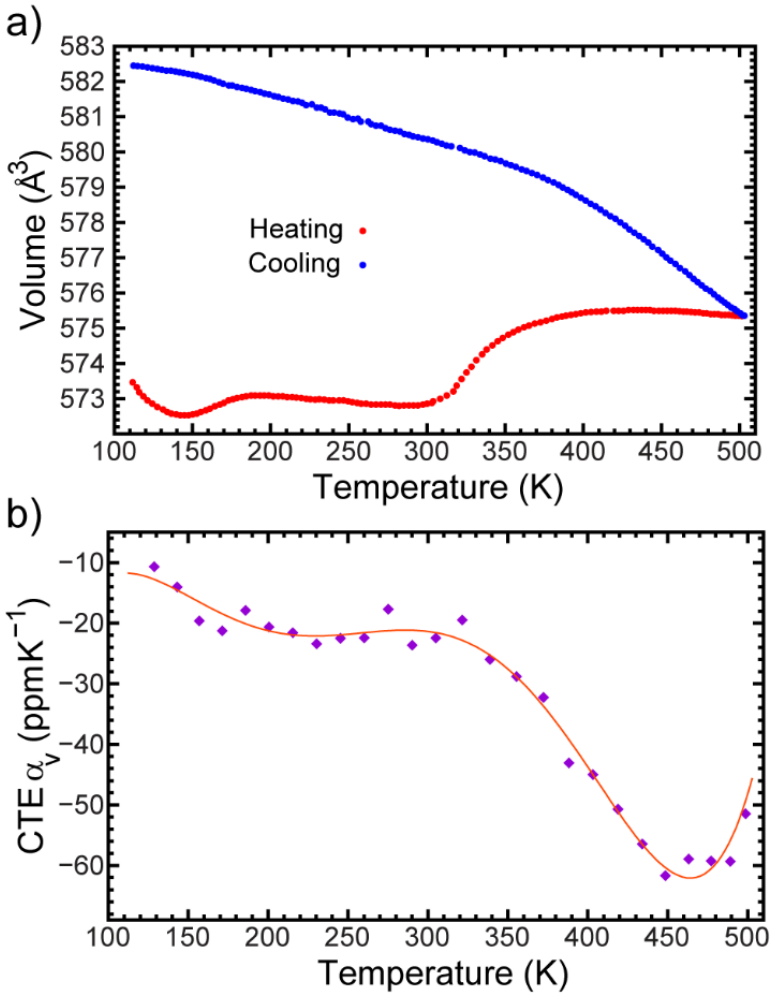

Figure 5.6: a) Unit cell volume on heating (red)/cooling (blue) and b) volumetric coefficient of thermal expansion (CTE) calculated between every fifth point (purple) and from six-term polynomial fit to volume curve (orange) versus temperature for $CaZr_{0.25}Nb_{0.75}F_{6.75}$.

A comparison of the negative thermal expansion seen for $Ca[Zr^{(IV)}_{1-x}Nb^{(V)}_{x}]F_{6+x,}$ on cooling from 300 K, with that reported for $CaZrF_6$ and $CaNbF_6$ is given in Table 5.1. The introduction of niobium (V), along with fluoride interstitials, into $CaZrF_6$ clearly affects the thermal expansion of the material. However, the very strong dependence of thermal

expansion on a samples thermal history indicates that this substitution is likely not a viable means of creating useful controlled thermal expansion materials.

Table 5.1 Comparison of CTEs at select temperatures for $Ca[Zr^{(IV)}_{1-x}Nb^{(V)}_{x}]F_{6+x}$ with those for $CaZrF_6$ and $CaNbF_6$.[26,365] The values were obtained from the data recorded while cooling from 500 K.

	$\alpha_{v(120K)}$	$\alpha_{v(300K)}$	$\alpha_{v(450K)}$
$CaNbF_6$	-67.3	-36.0	-24.7
$CaZrF_6$	-52.6	-34.6	-25.6
$CaZr_{0.75}Nb_{0.25}F_{6.25}$	-49.0	-32.6	-23.5
$CaZr_{0.5}Nb_{0.5}F_{6.5}$	-45.9	-31.5	-42.1
$CaZr_{0.25}Nb_{0.75}F_{6.75}$	-12.1	-21.4	-60.7

5.3.3 Response of $Ca[Zr^{(IV)}_{1-x}Nb^{(V)}_{x}]F_{6+x}$ to Compression

Both the high-pressure powder x-ray diffraction data and the variable temperature diffraction data were collected using material from the same syntheses. However, the material used in the high-pressure measurements was not subject to any temperature change prior to data collection.

$CaZr_{0.75}Nb_{0.25}F_{6.25}$ undergoes two phase transitions on compression up to 8 GPa (Figure 5.7a). At ~0.68 GPa the cubic ReO_3 structure transforms to phase that could not be indexed, but appear to be same as that previously seen on compressing $CaNbF_6$.[365] This phase persists up to ~2.5 GPa. Above this pressure, a gradual transition to a highly disordered material begins. On partial decompression to ~3 GPa, peaks indicative of the initially formed high-pressure phase reappear.

EoSFit7[359] was used to fit a 3rd order Birch Murnaghan equation of state to the unit cell volume versus pressure values obtained from Rietveld analyses of the diffraction data for

the cubic ReO_3-type phase (Figure 5.7b). This led to an estimated zero pressure bulk modulus of 40.5(8) GPa and $K_0' = -25(1)$, which is indicative of pronounced pressure-induced softening. These values are very close to those previously reported for $CaZrF_6$ [K_0 = 42.1(8) GPa and $K_0' = -26(1)$].[26]

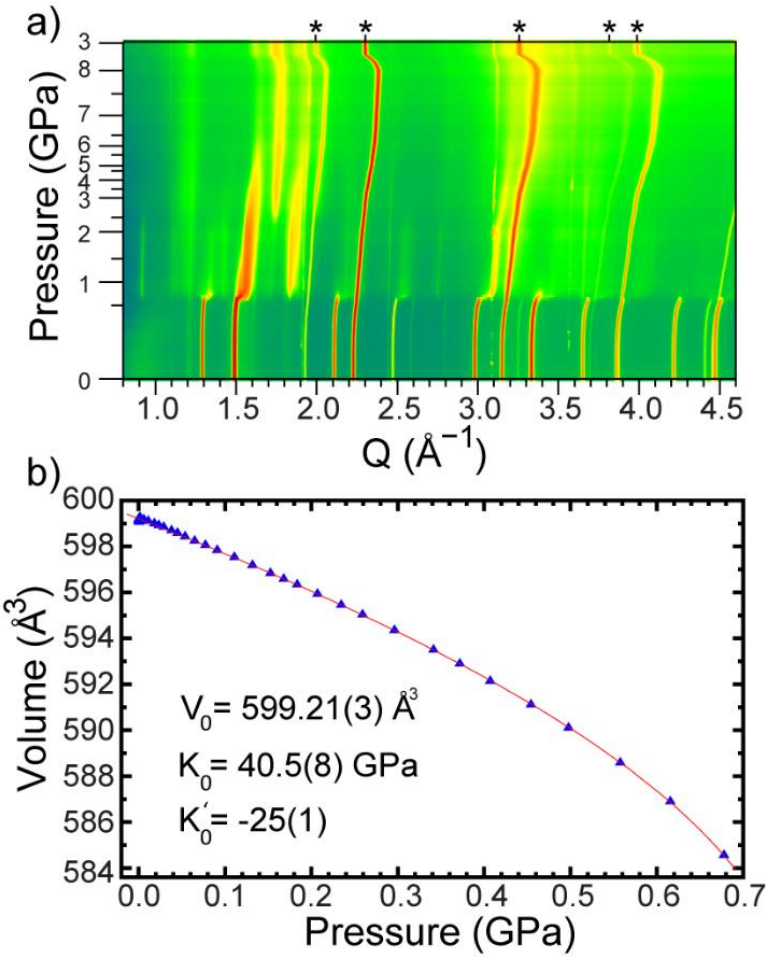

Figure 5.7: a) X-ray powder diffraction data versus pressure and b) unit cell volume versus pressure for cubic $CaZr_{0.75}Nb_{0.25}F_{6.25}$ along with the best fit using a 3rd order Birch-Murnaghan equation of state (red).

The behavior of $CaZr_{0.5}Nb_{0.5}F_{6.5}$ compression is very different from that of the x=0.25 sample, Figure 5.8a. Again, the material undergoes a symmetry lowering phase transition at modest pressures, 0.73 GPa. However, the diffraction data shows peak splitting

indicative of an octahedral tilting transition to a rhombohedral ($R\bar{3}$) structure. Transitions of this type are commonly seen on the compression or cooling of cubic ReO_3-type fluorides.[26,147,151,158,344,365,379,385] The diffraction data for this phase were fit to a rhombohedral model (Figure D.7) and lattice constants determined (Figure D.9). Like other ReO_3-connectivity rhombohedral fluorides, it display highly anisotropic elastic behavior with negative linear compressibility parallel to the crystallographic c-axis (Figure S9).[248,249,379,385] The rhombohedral phase is elastically very soft, with a bulk modulus of ~ 3- 7 GPa in the pressure range 0.7 – 1.1 GPa (Figure D.11). On further compression, the rhombohedral phase quite abruptly undergoes a further transition at ~1.1 GPa to a poorly ordered material with a single strong peak at Q ~1.6 $Å^{-1}$. This peak is no longer present at the highest pressure, leaving only the NaCl peaks and a fully amorphized sample (Figure D.8). On decompression to ~3.4 GPa, the amorphization does not reverse.

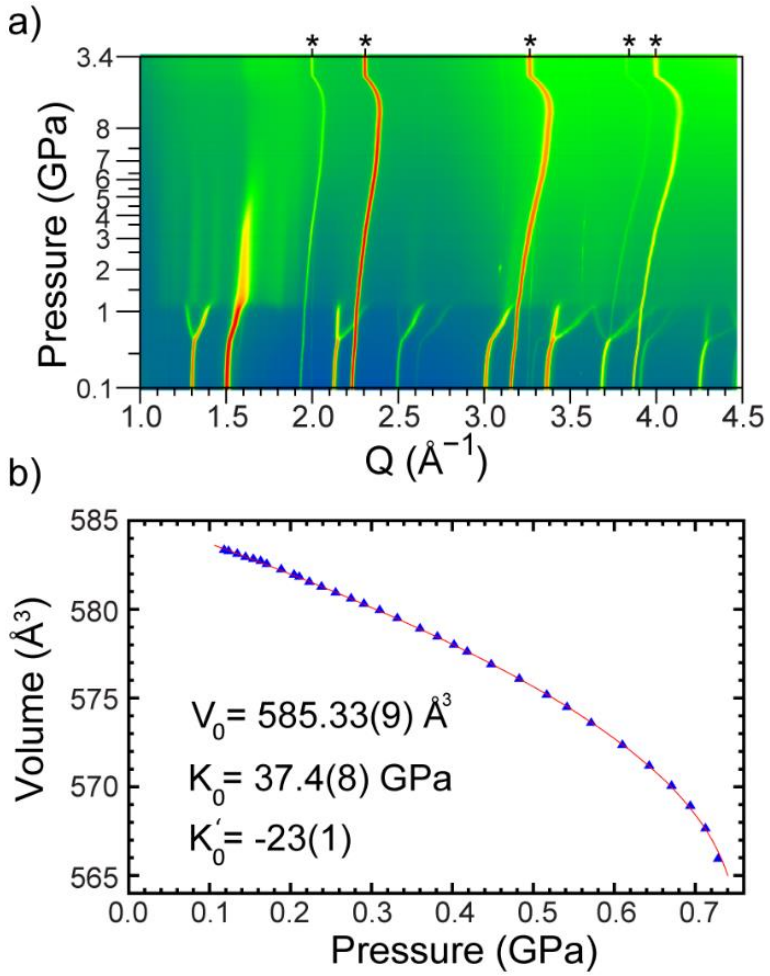

Figure 5.8: a) X-ray powder diffraction data versus pressure, and b) unit cell volume versus pressure for cubic $CaZr_{0.5}Nb_{0.5}F_{6.5}$ along with the best fit using a 3rd order Birch-Murnaghan equation of state (red). The starting pressure for the experiment was ~0.1 GPa.

While increasing the niobium (V) content of the sample from x = 0.25 to 0.5 altered the sequence of phases seen on compression, the elastic properties of the cubic phase changed little. A 3rd order Birch-Murnaghan equation of state, fit to volume versus pressure Figure 5.8b, indicates a zero-pressure bulk modulus of 37.4(8) GPa and significant pressure-induced softening, $K_0' = -23(1)$.

The highest niobium content sample, $CaZr_{0.25}Nb_{0.75}F_{6.75}$, shows similar behavior on compression to that seen for the x = 0.5 composition. The diffraction data (Figure 5.9a.)

indicate a cubic to rhombohedral transition at 0.77 GPa and a further transition at ~1.3 GPa. The peaks from this later phase exhibit broadening on compression.

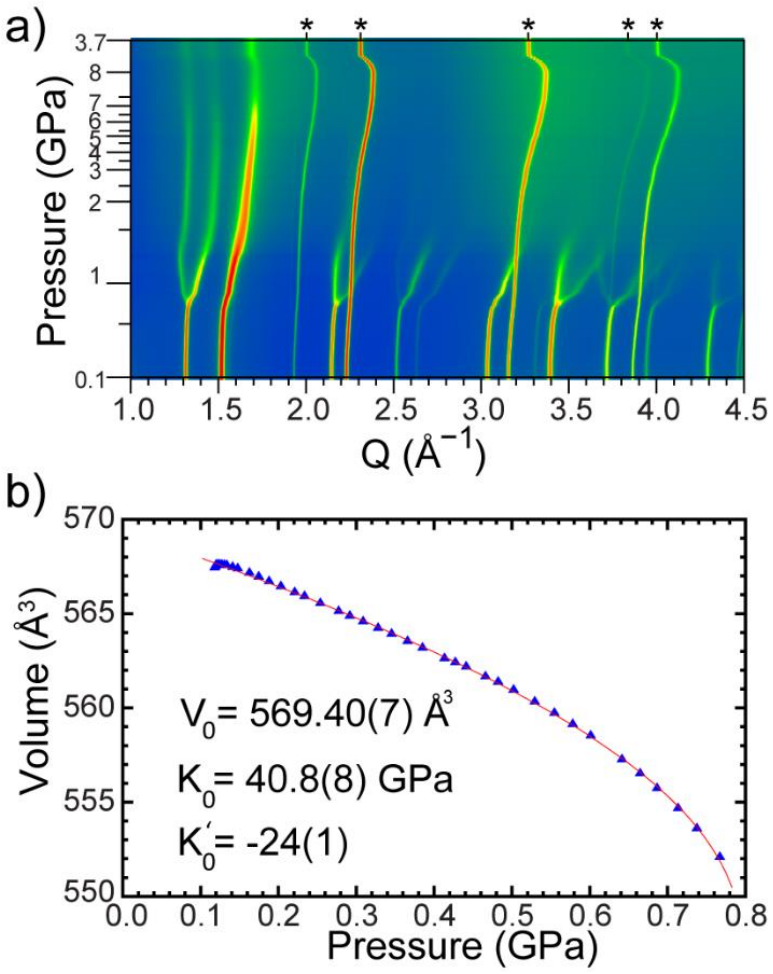

Figure 5.9: a) X-ray powder diffraction data versus pressure, and b) unit cell volume versus pressure for cubic $CaZr_{0.25}Nb_{0.75}F_{6.75}$ along with the best fit using a 3rd order Birch-Murnaghan equation of state (red). The starting pressure for the experiment was ~0.1 GPa.

A 3rd order Birch-Murnaghan equation of state fit to volume versus pressure, Figure 5.9b, indicates that $CaZr_{0.25}Nb_{0.75}F_{6.75}$ has very similar elastic properties to the lower niobium content samples and $CaZrF_6$. The zero-pressure bulk modulus was estimated to be 40.8(8) GPa with a pressure derivative, K_0', of -24(1).

Rietveld fits to the diffraction data for the rhombohedral phase were conducted, but the presence of scattering between the peaks for the rhombohedral phase made the refinements difficult (Figure D.12). The rhombohedral phase displayed highly anisotropic properties, with negative compressibility parallel to the c-axis (Figure D.14 and Figure D.15). The phase was very soft and did not stiffen dramatically on compression (Figure D.16). The response to pressure of the rhombohedral phases with x= 0.5 and x=0.75 are comparable to those reported for other rhombohedral ReO_3-connectivity fluorides.[248,249,379,385]

The behavior of $Ca[Zr^{(IV)}_{1-x}Nb^{(V)}_{x}]F_{6+x}$ on compression is summarized and compared with that previously reported for x = 0, in Table 5.2. While all three niobium substituted samples show a crystalline to crystalline phase transition at ~0.6 GPa, the phase formed above this pressure is not the same for the x = 0.25 sample as that for both the x = 0.5 and 0.75 samples. While all three niobium substituted materials became disordered at higher pressures than $CaZrF_6$, the extent of the disorder differs for all four materials. It is notable that niobium substitution has very little effect on the zero-pressure bulk modulus or pressure-induced softening of the cubic phase. The occurrence of low pressure phase transitions apparently involving octahedral tilting and the very similar bulk moduli for all $Ca[Zr^{(IV)}_{1-x}Nb^{(V)}_{x}]F_{6+x}$ stands in stark contrast to the behavior seen in the $Mg_{2-x}Zr_xF_{4+2x}$ system.[181] In $Mg_{2-x}Zr_xF_{4+2x}$ compositions, the aliovalent substitution of Zr^{4+} for Mg^{2+}, along with the incorporation of interstitial fluoride, suppressed the cubic to rhombohedral transition seen in $MgZrF_6$ and led to a significant increase in the zero pressure bulk modulus of the cubic phase. The suppression of the phase transition and elastic stiffening is consistent with the creation of edge-sharing polyhedra, which are expected to inhibit the correlated to tilting of framework polyhedra and generally stiffen the structure.

Table 5.2: Summary of the observed response to pressure for $Ca[Zr^{(IV)}_{1-x}Nb^{(V)}_{x}]F_{6+x}$. Values for x =0 are from a prior report,[26] where K_0' was only given for the analysis of unit cell volume versus both pressure and temperature.

	x=0	x=0.25	x=0.5	x=0.75
First crystalline to crystalline phase transition (GPa)	N/A	0.68(1)	0.73(1)	0.77(2)
Disordering pressure (GPa)	0.4	~2.5	~1.1	~1.3
K_0 for the cubic phase (GPa)	42.1(8)	40.5(8)	37.4(8)	40.8(8)
K_0'	-26(4)	-25(1)	-23(1)	-24(1)

5.4 Conclusions

Density measurements indicate that the replacement of Zr^{IV}, in $CaZrF_6$, by Nb^{V} to create fluoride excess compositions $Ca[Zr^{(IV)}_{1-x}Nb^{(V)}_{x}]F_{6+x}$ involves the creation of fluoride interstitials, not cation vacancies. However, x-ray total scattering data for $Ca[Zr^{(IV)}_{1-x}Nb^{(V)}_{x}]F_{6+x}$, show no evidence of a pair correlation peak in the range 3-4 Å, which has previously been attributed to the conversion of corner sharing polyhedra to edge shared units in related fluoride excess systems.[173,178-181] This suggests that the mechanism by which interstitial fluoride is incorporated into $Ca[Zr^{(IV)}_{1-x}Nb^{(V)}_{x}]F_{6+x}$ is different from that seen in $TiZrF_7$, $YbZrF_7$, and $Mg_{2-x}Zr_xF_{4+2x}$.[178,180,181] The substitution of Nb^{V}, along with excess fluoride, into $CaZrF_6$ modifies the thermal expansion of the material. However, the thermal expansion of $Ca[Zr^{(IV)}_{1-x}Nb^{(V)}_{x}]F_{6+x}$ depends strongly on the samples thermal history, indicating that the defects in these materials are mobile and can relax at quite low temperatures. On compression, $Ca[Zr^{(IV)}_{1-x}Nb^{(V)}_{x}]F_{6+x}$ with x= 0.25, 0.50, and 0.75 all

undergo crystalline to crystalline phase transitions at ~0.7 - 0.8 GPa and for the latter two samples this transition apparently involves the correlated tilting of framework polyhedra to generate a rhombohedral structure. This is not consistent with the presence of edge sharing polyhedra, as such units would inhibit the correlated tilting of framework polyhedra. However, it is unclear how the fluoride interstitials are incorporated into the structure so that this cooperative tilting can occur. The elastic properties of cubic $Ca[Zr^{(IV)}_{1-x}Nb^{(V)}_{x}]F_{6+x}$ are largely independent of composition, once again suggesting that the incorporation of interstitial fluoride does not lead to the formation of edge shared polyhedra, which would likely stiffen the structure.

5.5 Acknowledgments

I am grateful for the experimental assistance from the beamline staff at the 11-ID-B and 17-BM beamlines of APS. The activities at Georgia Tech were supported in part under NSF DMR-1607316. This work made use of the Advanced Photon Source, a U.S. Department of Energy (DOE) Office of Science User Facility operated for the DOE Office of Science by Argonne National Laboratory under contract DE-AC02-06CH11357.

CHAPTER 6. SYNTHESIS OF DEFECT PEROVSKITES ($He_{2-x}\square_x$)(CaZr)F_6 BY INSERTING HELIUM INTO THE NEGATIVE THERMAL EXPANSION MATERIAL $CaZrF_6$[4]

6.1 Introduction

Materials with a perovskite derived crystal structure are of great technological and mineralogical significance. This is in part because the parent cubic perovskite structure, with formula ABX_3, can accommodate a very wide range of substitutions and structural distortions. Common distortions include cooperative tilting of the corner sharing BX_6 octahedra[369,387,388] and off-center displacement of B and/or A-site cations.[389] Compositions where X is oxide, nitride and halide, or mixtures of them are common place. Metals from almost any region of the periodic table can be found on the B-sites for compositions with appropriately chosen species on the A and X site. Even perovskites with the noble gas Xe on the B-site have been reported.[305] The A-site is also amenable to many substitutions including the incorporation of small organic cations, which is attracting much attention due to their utility in preparing halide-based perovskites with good photovoltaic properties,[390] and also, intriguingly, diatomic nitrogen.[391-393] The inclusion of small neutral species, such as dinitrogen, onto the A-site of defect perovskites has been suggested as a means of controlling the band gap in semiconductors such as WO_3.[391] However, the reported syntheses for dinitrogen containing defect perovskites rely upon the adventitious trapping

[4] Published in *J. Am. Chem. Soc.*, **2017**, 139(38), pp 13284-13287

of dinitrogen on the A-site as a nitrogen rich precursor is thermally decomposed. In this paper we report the direct and well-controlled synthesis of defect perovskites $(He_{2-x}\square_x)(CaZr)F_6$ by inserting helium gas into the initially vacant A-sites of the negative thermal expansion (NTE) material $CaZrF_6$.[26] These materials can be recovered to ambient pressure at low temperature. There have been no prior experimental reports of perovskites containing significant amounts of helium, although there have been computational studies of noble gases included in WO_3.[394]

Metal fluorides with cubic ReO_3-type structures, such as ScF_3,[25] $CaZrF_6$[26] and other $BB'F_6$[344,365] are attracting attention due to their unusual thermal expansion characteristics. As NTE framework materials typically display rich behavior at modest pressures, and potential applications can expose them to significant stress from thermal expansion mismatch, it is important to understand their response to pressure.

6.2 Experimental

6.2.1 Synthesis

CaF_2 and ZrF_4 were purchased from Sigma Aldrich and STREM Chemicals respectively. Moisture sensitive compounds were handled in a glove box under nitrogen. A stoichiometric mixture of CaF_2 and ZrF_4 were mixed and ground together. The mixture was pressed into a pellet. The pellet was placed into a nickel tube, which was sealed by arc welding in an argon atmosphere. The nickel tube was sealed then in an evacuated fused quartz ampule. The ampule was heated to 750 °C (4.03 °C /min), held at 750 °C for 2 days, and cooled to 25 °C (1 °C /min). The resulting white powder was determined to be pure $CaZrF_6$ by power x-ray diffraction.

6.2.2 Neutron Powder Diffraction Measurements

Low-temperature high-pressure neutron powder diffraction measurements were performed at the SNAP beamline of the Spallation Neutron Source, Oak Ridge National Laboratory. The $CaZrF_6$ was contained in a thin walled aluminum can, which was placed inside an aluminum Harwood Engineering pressure cell. A custom engineered radial collimator with gadolinium foil blades, which was clamped to the pressure cell body, was used to block scattering from the aluminum pressure cell. A closed cycle refrigerator partially counteracted by two 50 Ω cartridge heaters was used to control the temperature of the sample. Powder diffraction data were recorded on two detectors banks, with one centered at 2θ ~84.8° and the other at 2θ ~48.1°. The helium pressure in the sample cell was raised in steps of 50 MPa from ambient to 450 MPa at 300 K. At each pressure a neutron powder diffraction pattern was recorded. The sample was then decompressed to ambient pressure in 50 MPa steps and then recompressed up to 500 MPa. Data were taken at each pressure. The pressure was maintained while cooling the sample to 70 K. Diffraction data were then collected every 50 MPa on decompression. The temperature was raised to 130 K and data were collected every 50 MPa on compression. The pressure was then released to ambient. This process of heating, compressing, and venting was repeated for temperatures of 190 and 250 K, and finally at 300 K an ambient pressure data set was collected. The pressure transmitting gas was then changed to nitrogen. Data were collected at 290, 240, 200 and 150 K on cooling at ~2MPa. The sample was warmed to 290 K and compressed to ~300 MPa in ~100 MPa steps. Data were recorded at each pressure. The sample was then cooled at pressure to 160 K, decompressed to ~2 MPa and then compressed to ~500 MPa in ~100 MPa steps. Data were collected at each pressure.

6.2.3 Direct Measurements of Helium Uptake by $CaZrF_6$

Helium uptake by $CaZrF_6$ was quantified by measurement of the gas released on warming a sample that had been loaded with helium at high pressure and then cooled under pressure to 100 K. These measurements were performed "off-line" at the Spallation Neutron Source using the same pressure cell design as employed in the earlier neutron diffraction studies along with a top loading closed cycle refrigerator. In order to quantify the helium inserted into the $CaZrF_6$, a known amount of sample was placed in a pressure cell. The dead space over the sample in the cell was determined by the expansion of low pressure helium into a calibrated volume. The sample was then exposed to high-pressure helium and cooled down to 100 K while maintaining the helium pressure. At 100 K, all the gas over the sample was pumped out of the system. The sample was then sealed off from the pumping system. The temperature was then raised to 150, 175, 200, 225, 250, 275, and 298 K holding for 30 minutes at each step. The pressure in the dead space over the sample was logged during the warming process. These pressure data along with the previously determined dead space volume were used to calculate the amount of helium released from the sample.

6.3 Results and Discussion

6.3.1 $CaZrF_6$ Response to Compression in Helium and Nitrogen Gas

ReO_3-type materials such as ScF_3 and $CaZrF_6$ are not typically viewed as porous, as the crystallographically determined F-F distances defining the "aperture" between the empty A-sites in this structure are only 4.01 and 4.23 Å respectively at room temperature. However, high-pressure neutron diffraction studies of $CaZrF_6$ using gas media reveal very different behavior on compression in nitrogen and helium (Figure 6.1A), indicating that

the material is porous to helium at room temperature. In nitrogen, at 300 K the unit cell volume decreases linearly on compression and the bulk modulus estimated from these data (K_0 = 36.7(2) GPa) is similar to that previously reported for compression in silicone oil using a Diamond Anvil Cell (K_0 = 36.5(5) GPa) or large volume cell equipped with a BRIM[353] (K_0 = 37.6(6) GPa).[26] In line with the disordering seen at > 400 MPa in silicone oil at room temperature, compression in nitrogen at 160 K led to amorphization at ~500 MPa (Figure E.1).

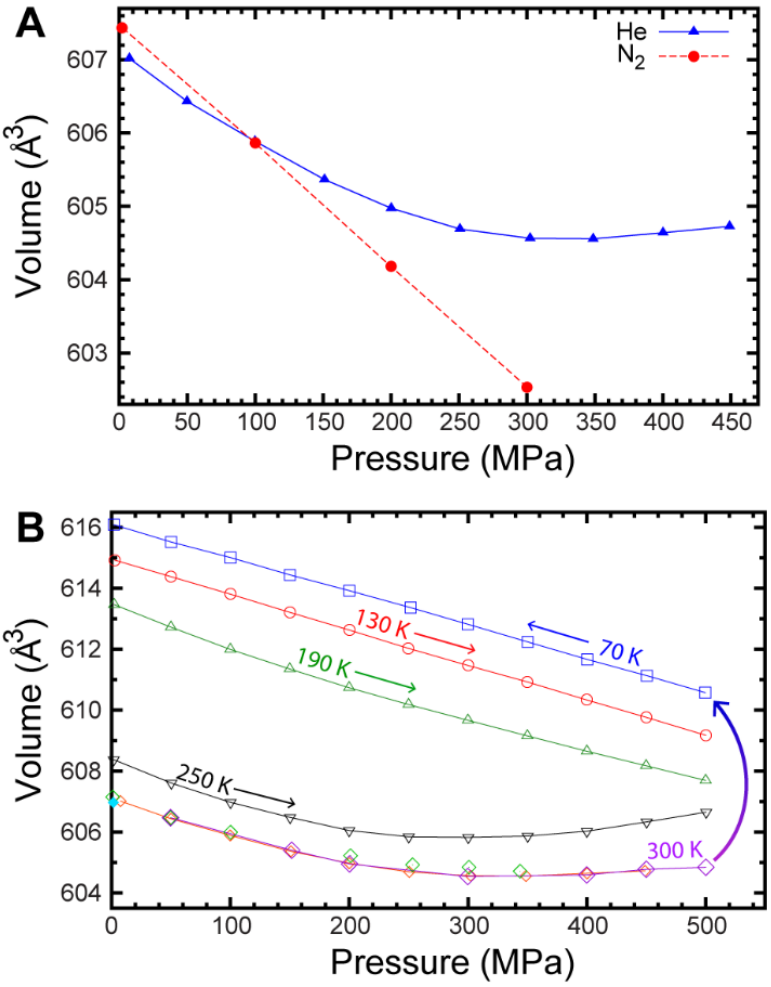

Figure 6.1 A) Unit cell volume of $CaZrF_6$ with increasing pressure in helium at 300 K (blue) and nitrogen at 290 K (red) gas. B) Change in unit cell volume for $CaZrF_6$ in helium at 300 K on compression (orange), decompression (green), and recompression (purple), cooled at

pressure to 70 K, decompressed at 70 K (blue), compressed at 130 K (red), compressed at 190 K (dark green), compressed at 250 K (black), and returned to ambient pressure at 300 K (cyan). Error bars are smaller than the symbols.

In contrast to the behavior in nitrogen, when compressed in helium at 300 K the unit cell volume for $CaZrF_6$ initially decreases, but above ~350 MPa it increases on further compression. This surprising result can be attributed to the insertion of helium into $CaZrF_6$. This behavior is reproducible on decompression and recompression at 300 K (Figure 6.1B). It is worth noting that expansion on compression in fluid media, due to the insertion of water, has also been seen in zeolites[201] and that an ammonium metal formate has recently been shown to take up neon at high pressure, but not argon.[395] In silicone oil at 300 K, and nitrogen at low temperature (Fig. S1), compression to ~500 MPa leads to a loss of order in the crystal structure,[26] which does not reverse on decompression. However, the insertion of helium stabilizes the structure against this process; a comparison of diffraction data at 0.075 MPa (Figure E.2) and 500 MPa (Figure E.3) at 300 K in helium reveal no loss of crystallinity, and the sample did not lose crystallinity, as judged by the absence of any significant change in peak to background ratio, throughout the reported neutron diffraction measurements in helium (Figure E.4). The stabilization of porous silicates against disordering, or amorphization, on compression by the insertion of guest species has previously been reported for a number of materials, for example, silicalite.[396]

After cooling from 300 to 70 K under a pressure of ~475 MPa, the decrease of the unit cell volume on decompression is linear and implies a bulk modulus of 55.5(2) GPa, which is much higher than that observed at 300 K in nitrogen. This behavior, and that revealed by diffraction measurements as the sample was compressed/decompressed at successively higher temperatures (Figure 6.1B and Figure E.5) is consistent with the helium being

trapped, on the time scale of the experiment (~40 minutes for data collection and a pressure increase of 50 MPa), in the $CaZrF_6$ framework at 130 K and below. The inclusion of helium not only stiffens the material (K_{70K} = 55.5(2) GPa, K_{130K} = 53.0(1) GPa), it modifies the thermal expansion. Prior ambient pressure neutron diffraction measurements indicate that $CaZrF_6$ has an expansion coefficient, α_v, of -52(2) ppm K^{-1} at 100 K. However, the current data show that a sample prepared by inserting helium into $CaZrF_6$ at ~475 MPa and then cooling under pressure, has an expansion coefficient, α_v, of -31(1) ppm K^{-1} at 100 K. The reduction in the magnitude of the expansion is not surprising, as the insertion of any species into the A-site cavities will impeded the transverse vibrational motion of the fluoride that is responsible for the NTE. It is notable that the deliberate insertion of lithium into redox active ReO_3-type fluorides has recently been demonstrated as a strategy for controlling the thermal expansion of such materials.[161]

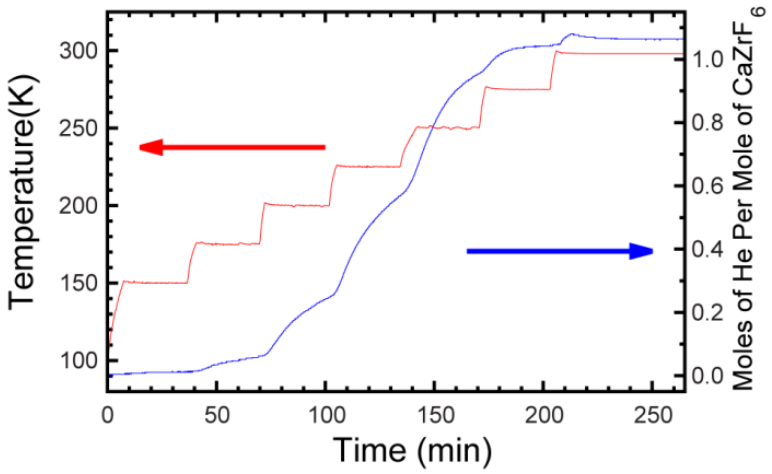

Figure 6.2 Helium release versus time and temperature for a sample of $(He_{2-x}\square_x)(CaZr)F_6$ that had been cooled down to 100K under a helium pressure of ~500 MPa.

The amount of helium inserted into $CaZrF_6$ was quantified by warming gas-loaded samples to room temperature and monitoring the pressure in the sample head space (Appendix E).

The major source of uncertainty in these measurements is likely to be the determination of the sample head space volume, which could be in error by up to 10%. Figure 6.2 shows the amount of helium released as a function of time and temperature for a sample loaded with helium at ~500 MPa. These data indicate that the $CaZrF_6$ had 54(5)% of its A-sites filled, corresponding to a defect perovskite with composition $(He_{1.08}\square_{0.92})(CaZr)F_6$. On the time scale of the measurements, there is no helium release at 150 K and the gas can be considered to be trapped. On warming, the rate of helium release increases quite dramatically, but even at close to room temperature the time scale for helium release is minutes not seconds.

Helium uptake measurements were also performed for loadings at 300 MPa and 150 MPa. As expected, at lower pressures a smaller fraction of the available A-sites were filled (21(2) % and 0.8(1) % respectively). However, when the same sample of $CaZrF_6$ was subsequently loaded with helium at 400 MPa, the gas uptake was much lower than anticipated (only 3.9(4) % of A-sites filled). As the data in Figure 6.2 indicate that the time scale for helium insertion at room temperature is of the order of minutes, and $CaZrF_6$ is known to disorder on compression to 400-500 MPa when there is nothing on the A-sites, the reduction in uptake during the final loading with helium at 400 MPa is almost certainly due to sample degradation. When the helium pressure is increased rapidly an irreversible disordering occurs before enough helium is inserted to stabilize the ReO_3-type structure. This interpretation suggests that the A-site occupancies shown in Figure E.6 for 500, 300, and 150 MPa represent a lower limit of what should be achievable with a pristine sample.

In order to both locate and confirm the quantity of helium in $(He_{2-x}\square_x)(CaZr)F_6$, Rietveld analyses of the neutron diffraction data were performed. Figure 6.3A shows a fit to 70 K,

500 MPa data with an $Fm\bar{3}m$ model for $CaZrF_6$ and no helium on the A-sites. The residual plot shows significant features well above the noise level of the data. Figure 6.3B shows a fit where helium was placed on the A-site of the perovskite with an occupancy of 0.54 and its isotropic thermal parameter refined (U_{iso} = 0.045(3) $Å^2$). The inclusion of helium in the model significantly improved the fit quality. Refinements were carried out for all of the neutron diffraction data acquired in helium. The A-site occupancies (Figure E.9) clearly show that at both 250 and 300 K helium goes into the structure as the pressure is increased, but at 70, 130 and 190 K there is little change in occupancy as the pressure varied.

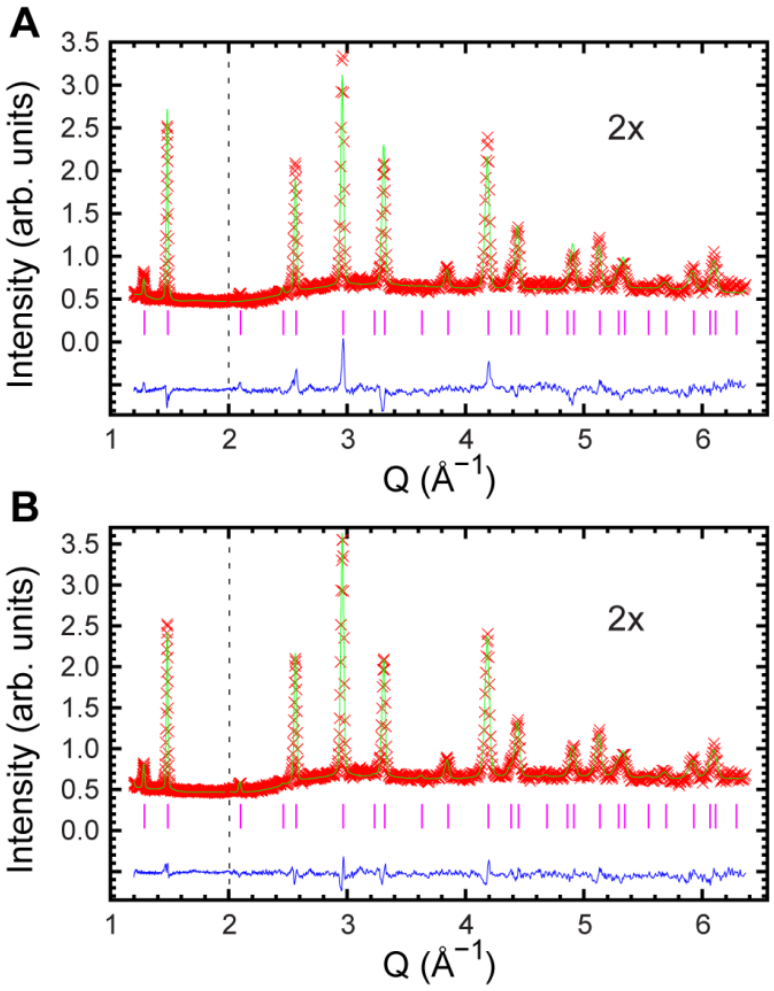

Figure 6.3 Rietveld fits to powder neutron diffraction data recorded on SNAP using a $Fm\bar{3}m$ model for $CaZrF_6$ A) containing no helium, detector bank 2 (2θ ~48°), R_F2= 27.4%, and B) using $(He_{2-x}\square_x)(CaZr)F_6$ with x = 1.08 detector bank 2, R_F2=18.0 %.

6.4 Conclusions

The penetration of helium into materials that are not typically viewed as porous is quite well known and can hinder the use of helium as a truly inert hydrostatic medium for high-pressure experiments. For example, molecular solids such as C_{60}[298] and arsenolite[299,300] take up significant amounts of helium. The silica clathrate melanophlogite,[304] which has a

type-I gas hydrate related structure, and both silica glass[302,303] and cristobalite,[301] which are denser than the clathrate framework, behave differently when compressed in helium versus media containing much larger molecules. In helium, they display higher bulk moduli, due to the insertion of helium, and it has been estimated that for silica glass the lower limit for helium solubility at 10 GPa is 1 mole of helium per mole of SiO_2.[302]The penetration of hydrogen at 250 ℃ and high pressures into silica glass[397] and cristobalite[398] has also been reported.

Helium is much more soluble in $CaZrF_6$ than silica glass at low (< 1 GPa) pressure, with approximately 1 mole of helium per mole of $CaZrF_6$ being taken up at ~500 MPa. This helium can be retained in the structure by cooling and then subsequently released on warming to room temperature, suggesting applications in gas storage. Temperature regulated uptake and release of gases in zeolitic materials is quiet well known,[251,399] particularly in materials showing a trapdoor like effect involving the thermally activated motion of extra-framework cations, and it has previously been proposed as a method for hydrogen storage.[399] It is notable that if a perovskite with one hydrogen per A-site could be prepared, $(H_2)_2(CaZr)F_6$, it would have a volumetric storage capacity of 0.044 kg H_2/L, which exceeds the US DOE 2025 technical target for hydrogen storage in fuel cell vehicles (0.04 kg H_2/L).[400]

The preparation of $(He_{2-x}\square_x)(CaZr)F_6$ is a significant extension of perovskite chemistry to include the controlled synthesis of materials with small gas molecules on the A-site. Modification of composition, to tune the effective pore size of the ReO_3-type framework, and the temperature at which gases are inserted into the parent material, should allow other gases to be incorporated into perovskites and their uptake and release pressures to be

controlled. We anticipate that this new family of hybrid perovskites will display a rich crystal chemistry as composition, temperature and pressure are varied.

6.5 Acknowledgment

We are grateful for experimental assistance from the sample environment team at the Spallation Neutron Source. We also appreciate the assistance of Craig Brown and Juscelino Leao during preliminary experiments on BT1 at the NIST NCNR. The work at Georgia Tech was partially supported under NSF DMR-1607316. A portion of this research used resources at the Spallation Neutron Source, a DOE Office of Science User Facility operated by the Oak Ridge National Laboratory.

CHAPTER 7. PREPARATION AND PROPERTIES OF THE PEROVSKITES $[He_2][CaZr]F_6$, $[He]_2[CaNb]F_6$, AND $[He_2][CaNb^{IV}_{0.5}Nb^{V}_{0.5}]F_{6.5}$

7.1 Introduction

Helium, as a member of the "noble gases", is notoriously unreactive due to its stable closed shell electron configuration and high ionization energy. While the other noble gases have a reasonably extensive chemistry, helium containing compounds remain rare.[275-278] Helium forms inclusion compounds such as clathrates, the first of which was formed with ice II at modest pressures.[291] Helium was subsequently predicted and shown to form other compounds including ones where van der Waals interactions dominate, such as $Ne(He)_2$.[279-283,289,290,292] Recently theoretical and experimental studies verified the creation of Na_2He at high pressures, which is believed to be a high-pressure electride.[293] New high-pressure helium compounds are expected to form between helium and other ionic compounds.[295] Helium has also been shown to penetrate some materials that are not generally viewed as porous, including silica glass, cristobalite, C_{60}, arsenolite, and the silica clathrate melanophlogite.[298-304]

Although several new helium compounds have recently been reported, such compounds are still rare. However, it has been recently shown that helium will insert into the ReO_3-type material $CaZrF_6$.[401] There are many fluorides of this type,[150,158,162,166,168,171,385] several of which show large isotropic negative thermal expansion (NTE).[25,26,344,365,379] The insertion of helium under pressure resulted in the formation of a defect perovskite with the

chemical formula of $[He_{2-x}\square_x][CaZr]F_6$. Perovskites with Xe on the B-site have been previously reported, and it has also been suggested that dinitrogen can be trapped in WO_3 form a defect perovskite.[305,394] However, $(He_{2-x}\square_x)(CaZr)F_6$ is the first example of a perovskite containing helium.

The current work builds on the previous study of helium insertion into $CaZrF_6$, which was limited to a maximum pressure of 0.5 GPa leading to x ~1.0 for $[He_{2-x}\square_x][CaZr]F_6$.[401] High-pressure synchrotron diffraction experiments, using diamond anvil cells along with helium and neon as pressure media, were performed to estimate the pressure required for formation of the stoichiometric perovskite $[He_2][CaZr]F_6$ and examine the high-pressure behavior of this material. The insertion of helium into $CaNbF_6$[365] and $CaNb^{IV}_{0.5}Nb^{V}_{0.5}F_{6.5}$ was also examined to determine if this gas could be inserted at room temperature into materials with smaller unit cells (pore apertures) than $CaZrF_6$. $CaNb^{IV}_{0.5}Nb^{V}_{0.5}F_{6.5}$ is an anion excess ReO_3-type material, which probably has a similar structure to that of the $Ca(Zr_{1-x}Nb_x)F_{6+x}$ materials discussed in Chapter 5 of this thesis.

7.2 Experimental

7.2.1 Synthesis

CaF_2 (99.5%, Sigma Aldrich) and ZrF_4 (99.9%, STREM) were used to prepare $CaZrF_6$ via solid state reaction using a procedure adapted from Hancock el al.[26] A 1:1 molar ratio of starting materials was thoroughly ground together under dry nitrogen. The reactant mixture was pressed into a pellet and loaded into a nickel tube. The tube was sealed by arc welding under argon and then sealed inside an evacuated fused silica ampoule. The reaction mixture

was heated to 750 °C, held at 750 °C for 48 h, and then cooled to room temperature. The product was a white powder, containing ~3 wt % CaF_2 impurity.

NbF_5 (99.5%, STREM), Nb (99.8%, Alfa Aesar) and CaF_2 (99.5%, Sigma Aldrich) were used to prepare $CaNbF_6$ and $CaNb^{IV}_{0.5}Nb^{V}_{0.5}F_{6.5}$ via solid state reaction using a procedure adapted from Chassaing et al.[163] 5:4:1 and 10:9:1 molar ratios of CaF_2:NbF_5:Nb were used to prepare $CaNbF_6$ and $CaNb^{IV}_{0.5}Nb^{V}_{0.5}F_{6.5}$ respectively. The reactants were ground together under dry nitrogen and then placed into a nickel tube, which was sealed by arc-welding under argon. The nickel tube was then sealed in an evacuated fused silica ampoule. The samples were heated from room temperature to 300 °C, held at 300 °C for 48 h, heated to 520 °C, held at 520 °C for 72 h, and cooled down from 520 °C to room temperature over 24 h. The products were grey powders.

7.2.2 High-Pressure Diffraction Measurements

High-pressure powder x-ray diffraction data were collected using GSE CARS beamline 13-BMD ($CaZrF_6$ and $CaNb^{IV}_{0.5}Nb^{V}_{0.5}F_{6.5}$) and the 17-BM ($CaNbF_6$) beamline of the Advanced Photon Source, Argonne National Laboratory. Diffraction data were recorded on Perkin-Elmer amorphous silicon 2D detectors using wavelengths of 0.3340 Å (13-BMD) and 0.45428 Å (17-BM). The measurements at 17BM used a ~100 μm diameter beam and those at 13BMD employed a defocused beam in order minimize difficulties with sampling statistics. In each experiment, the samples were compressed in BX-90 diamond anvil cells equipped with 800 μm cullet diamonds and stainless-steel gaskets (400 μm holes). Helium and neon, loaded using the high gas loading systems at GSE CARS, were

used as pressure transmitting media.[402] The known equation of state and the measured lattice constants of CaF_2 or NaCl were used to determine the pressure.[352,403]

7.2.3 Reduction, Le Bail, and Rietveld Analyses of the Powder Diffraction Data

The 2D powder diffraction data were integrated and the resulting 1D data background subtracted using DIOPTAS.[404] Le Bail and Rietveld refinements were performed using the General Structure Analysis System (GSAS), or GSAS II, coupled with EXPGUI to determine unit cell volume as a function of pressure.[354,355,405] A cation-ordered cubic ReO_3-type model ($Fm\bar{3}m$) was used in all the Le Bail and Rietveld analyses (see 0 details). In the Rietveld analyses of the data for the cubic and rhombohedral phase $CaNb^{IV}_{0.5}Nb^{V}_{0.5}F_{6.5}$ sample, no attempt was made to incorporate excess fluoride due to the limited quality and range of the data (Q_{max} ~7 $Å^{-1}$). The Nb^{IV} and Nb^{V} were assumed to be on the same crystallographic site and good fits were achieved.

7.3 Results and Discussion

7.3.1 Response of $CaZrF_6$ to Compression in Helium and Neon

Two independent high-pressure diffraction experiments using $CaZrF_6$ in a helium pressure medium were conducted. In one case CaF_2 was used as an internal pressure standard and in the other NaCl was used. Rietveld fits to the data recorded at the starting pressures (0.28 GPa and 0.21 GPa) for these measurements are shown in 0 (Figure F.1 and Figure F.2). The overall fit quality is quite good. However, in both cases there are two impurity peaks at ~1.2 and 1.7 $Å^{-1}$. These peaks were not present in the diffraction pattern of the sample prior to grinding the material for loading into the DACs, but we have previously observed

them for samples of $CaZrF_6$ and related materials that have been heavily ground[385] suggesting that this phase arises from the stresses generated during grinding and gas loading the sample. As the peaks from the impurity do not overlap significantly with those from cubic $CaZrF_6$, they should not adversely affect the lattice constants estimated for $CaZrF_6$.

High Q data from the set of measurements in helium with NaCl as the pressure standard are shown in Figure 7.1a. Interestingly, the peaks from cubic $CaZrF_6$ visibly shift to lower Q between ~0.3 and 0.7 GPa, indicating an increase in unit cell volume due to the insertion of helium into the empty "A site" of ReO_3-type structure. This is in agreement with our previously reported (0 - 0.5 GPa) neutron diffraction study, but shows that helium continues to be inserted up until at least ~0.7 GPa.[401] Peaks from the resulting helium containing perovskite $[He_2][CaZr]F_6$ persists up to ~3.5 GPa where amorphization occurs. No sample peaks remain above ~6 GPa. This behavior contrasts with that seen on compression in neon (Figure 7.1b). The $CaZrF_6$ begins to disorder at pressures above ~0.5 GPa, which is consistent with the previously reported behavior in silicone oil,[26] indicating that, unlike helium, neon can't be inserted into $CaZrF_6$ at room temperature.

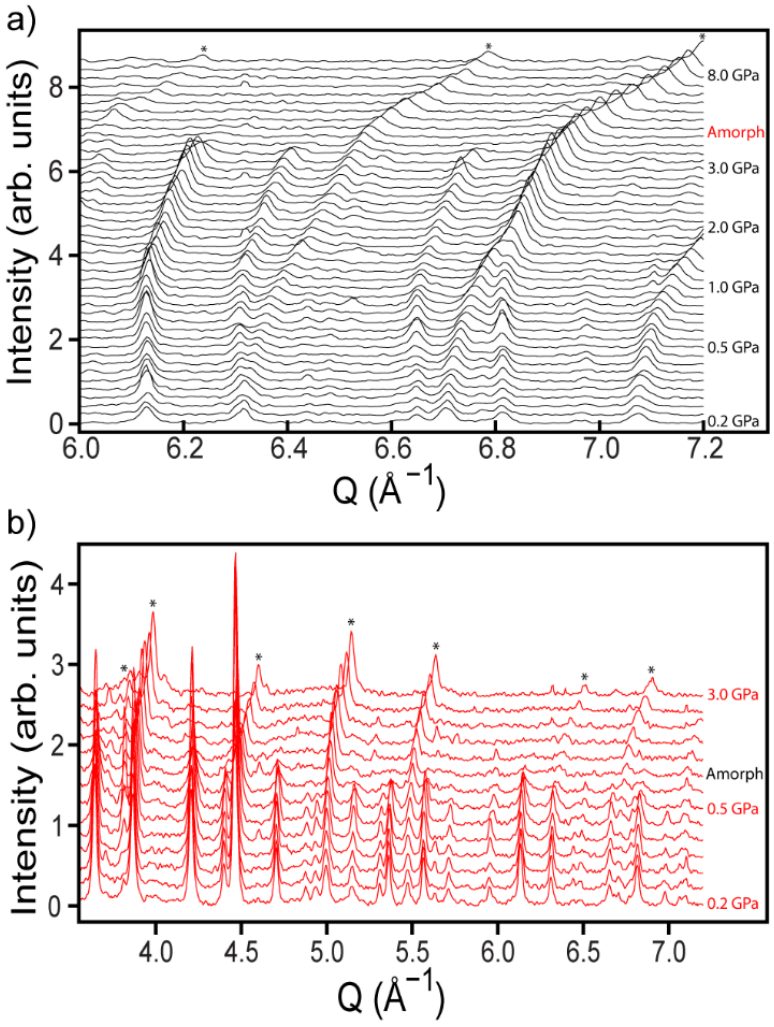

Figure 7.1: High-pressure x-ray diffraction data for $CaZrF_6$ in a) helium and b) neon. Peaks from the NaCl pressure standard are marked *.

Unit cell volume versus pressure in helium, obtained using Le Bail fits, are shown in Figure 7.2. The two sets of experiments with different internal pressure standards are in very good agreement. The unit cell volume increases until ~0.7 GPa due to the insertion of helium. The inserted helium stabilizes the cubic perovskite up to ~3.5 GPa. There is an almost linear variation of unit cell volume with pressure between ~1 and 3.5 GPa. A linear fit to lnV vs P over the range 1.5 - 3.6 GPa gave estimated bulk moduli of 48.83(3) and 45.66(2) GPa for the experiments using CaF_2 and NaCl, respectively.

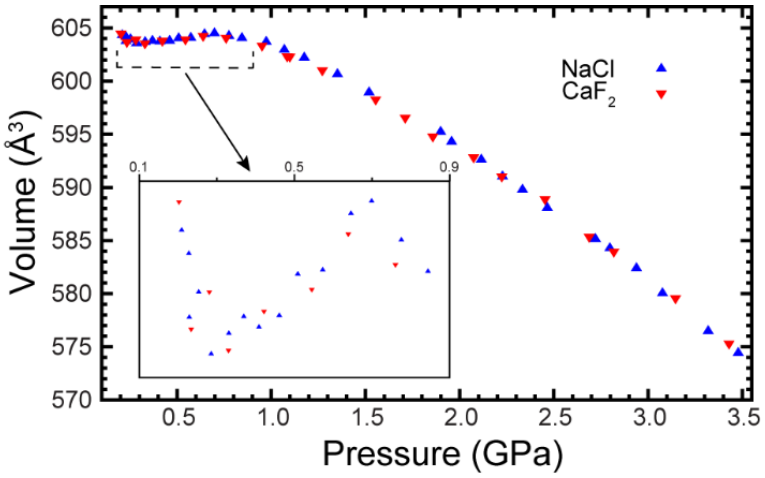

Figure 7.2: A comparison of unit cell volume for $CaZrF_6$ versus pressure in a helium for experiments with NaCl and CaF_2 as pressure calibrants. Inset shows details of low pressure behavior.

7.3.2 Response of $CaNbF_6$ to Compression in Helium

The high-pressure diffraction data for $CaNbF_6$ in helium (Figure 7.3a) indicate that the gas is inserted into the structure as the pressure is increased, in a similar fashion to $CaZrF_6$. At low pressure, the unit cell volume initially decreases and then increases before going through a maximum at ~0.9 GPa (Figure 7.3b). This unusual behavior is due to the insertion of helium into the ReO_3-type structure of $CaNbF_6$, which creates a new perovskite material with helium on the A-site. Presumably, above ~1.0 GPa the material is saturated with helium giving rise to $[He_2][CaNb]F_6$. Even though $CaNbF_6$ has a smaller lattice constant (a = 8.394 Å at 300 K and 1 bar) than $CaZrF_6$ (a = 8.476 Å at 300 K and 1 bar), penetration of helium into the structure is possible at room temperature on the time scale of the diffraction measurements (~10 minutes to increase pressure and take data). A linear fit to ln(V) versus P in the pressure range 1.4 to 3.7 GPa suggests that the perovskite has a bulk modulus of 51.47(2) GPa, which is slightly higher than that found for $[He_2][CaZr]F_6$ over a similar pressure range.

In non-penetrating media $CaNbF_6$ has been reported to undergo a crystalline to crystalline phase transition at ~0.4 GPa and amorphization at ~4 GPa.[365] In the current experiment, the perovskite generated by helium insertion is stable up to the highest pressures recorded ~3.7 GPa. However, there is some loss of peak intensity on compression, which might indicate an amorphization at pressures just above 3.7 GPa.

The diffraction data for $CaNbF_6$ show some quite broad peaks at low Q from an impurity phase (Figure F.3). They may arise from the creation of a new high-pressure phase when grinding or pressurizing the sample. This type of impurity has been previously reported for $ZnNbF_6$ and was also seen to a lesser extent in the previously discussed $CaZrF_6$ data.[385] Their presence did not impede the analysis of the data for the main phase.

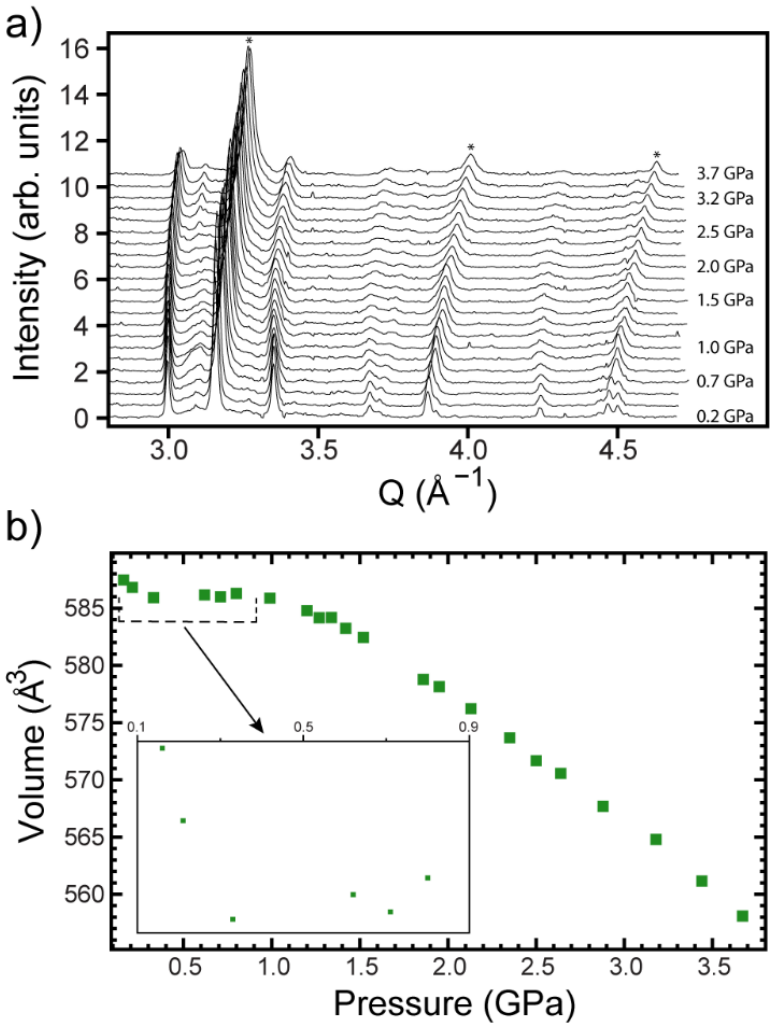

Figure 7.3: a) High-pressure x-ray diffraction data and b) unit cell volume versus pressure for $CaNbF_6$ compressed in helium. Peaks from the NaCl pressure standard are marked *.

7.3.3 Response of $CaNb^{IV}_{0.5}Nb^{V}_{0.5}F_{6.5}$ to Compression in Helium and Neon

High-pressure diffraction data for $CaNb^{IV}_{0.5}Nb^{V}_{0.5}F_{6.5}$ in helium and neon are shown in Figure 7.4a and b respectively. Two different runs were performed in helium. Unit cell volume versus pressure is shown for both in Figure 7.5. The response of this material to compression in helium indicates that, like $CaZrF_6$ and $CaNbF_6$, this gas inserts into the structure even though the lattice constant for $CaNb^{IV}_{0.5}Nb^{V}_{0.5}F_{6.5}$ is slightly smaller than that for $CaNbF_6$ and there is interstitial fluoride present which might be expected to impede

the motion of helium within the solid. At low pressure (< 0.9 GPa) the unit cell gets larger as the pressure increases due to the insertion of helium. The helium containing perovskite persists to ~4.5 GPa and amorphizes at higher pressures. Only peaks from the NaCl pressure marker remain at the highest pressure, 7.1 GPa. There is no evidence that neon can be inserted into $CaNb^{IV}_{0.5}Nb^{V}_{0.5}F_{6.5}$ on compression. The unit cell volume of the material decreases on initial compression in neon and a phase transition occurs at ~0.5 GPa. The peak splittings associated with this transition suggest that it involves a correlated tilting of polyhedra, leading to a rhombohedral phase closely related to that seen on compression or cooling many ReO_3-type metal fluorides, and also reported for $CaZr^{IV}_{0.5}Nb^{V}_{0.5}F_{6.5}$ above ~0.7 GPa (see CHAPTER 5). The data for the high-pressure phase could be satisfactorily fit to a $R\bar{3}$ model (see Figure F.6). Above 2 GPa the material amorphized, with only NaCl peaks remaining at 3.0 GPa.

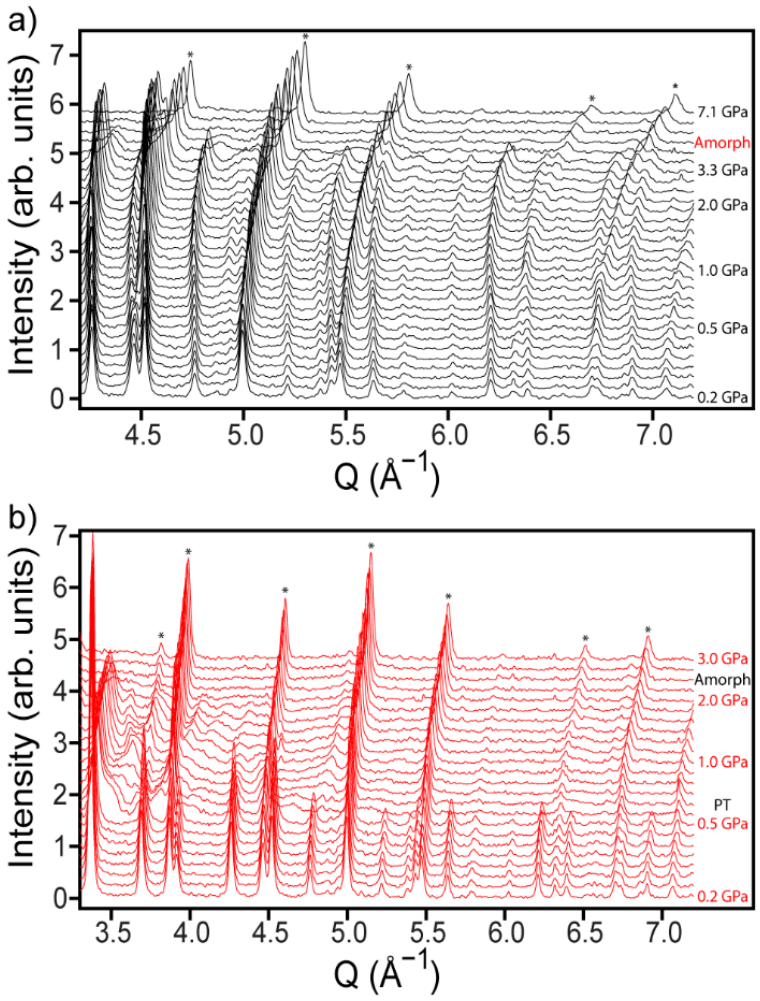

Figure 7.4: High-pressure x-ray diffraction data for $CaNb^{IV}_{0.5}Nb^{V}_{0.5}F_{6.5}$ in a) helium (run 2) and b) neon. Peaks from the NaCl pressure standard are marked *.

Linear fits to ln(V) versus P, over the range 1.35 – 3.56 GPa, indicate bulk moduli of 49.31(3) and 50.82(3) GPa based on values from runs 1 and 2 respectively. These values are similar to those seen for the other helium containing perovskites. Although a linear fit was employed, there is some evidence of softening on compression.

Both run 1 and 2 used the same synthetic batch of $CaNb^{IV}_{0.5}Nb^{V}_{0.5}F_{6.5}$. However, unlike the duplicate runs for $CaZrF_6$ in helium they do not fully reproduce, particularly at low pressure. While this could be a consequence of experimental variation not properly

accounted for in the single calibration used for both runs, it may also be indicative of the sample response to compression in helium. Helium does not instantly equilibrate on increasing the pressure and variations in the time allowed after raising the pressure before recording the diffraction data could be responsible for some of the differences between runs in Figure 7.5.

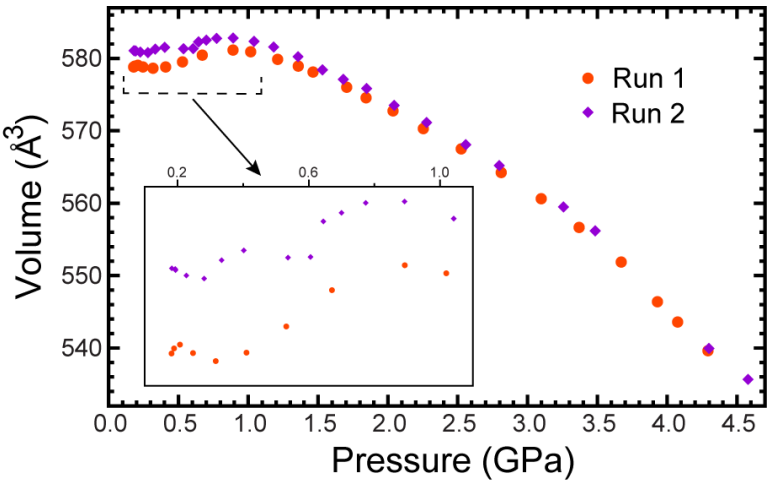

Figure 7.5: Unit cell volume versus pressure for $CaNb^{IV}_{0.5}Nb^{V}_{0.5}F_{6.5}$ in a helium pressure transmitting medium.

7.4 Conclusions

Helium can be inserted at 300 K into the cation ordered ReO_3-type fluorides $CaZrF_6$, $CaNbF_6$ and $CaNb^{IV}_{0.5}Nb^{V}_{0.5}F_{6.5}$ to form perovskites with helium on the A-site, even though the lattice constant of $CaNbF_6$ is significantly smaller than that of $CaZrF_6$ and $CaNb^{IV}_{0.5}Nb^{V}_{0.5}F_{6.5}$ presumably contains interstitial fluoride. In each case, the helium insertion process appears to be complete by ~1 GPa. The insertion of helium stabilizes the ReO_3-type frameworks against the low-pressure phase transitions that are known to occur in the parent phases. The resulting helium containing perovskites have similar bulk moduli.

7.5 Acknowledgments

I am grateful to Bree Wright for providing two of the materials analyzed in these experiments, and for her and Anthony Lloyd's assistance in data collection. I would also like to acknowledge the assistance of the GSE CARS beamline staff with these experiments. The activities at Georgia Tech were supported in part under NSF DMR-1607316. This work made use of the Advanced Photon Source, a U.S. Department of Energy (DOE) Office of Science User Facility operated for the DOE Office of Science by Argonne National Laboratory under contract DE-AC02-06CH11357.

CHAPTER 8. CONCLUSIONS

The behavior of several $M^{2+}M^{4+}F_6$ metal fluorides ($CaNbF_6$, $MgNbF_6$, $MnNbF_6$, $ZnNbF_6$, $MgZrF_6$, $CaZrF_6$, and $CaTiF_6$) has been examined using variable temperature neutron and synchrotron x-ray diffraction. These materials were chosen for study due to their ReO_3-type structures, which when cubic can display negative thermal expansion due to the rotation of rigid octahedra associated with the transverse thermal motion of bridging fluoride. The effects of chemical composition and temperature on the crystal structure and thermal expansion behavior of the mixed metal fluorides was explored. To better understand the effects of stress, which could be encountered during the possible application of these materials, their response to pressure was also examined to identify any structural changes and quantify their elastic properties. The examined $M^{2+}M^{4+}F_6$ materials were found to display thermal expansion ranging from strong NTE through ZTE to strong PTE. The thermal expansion and crystal structure varied with temperature and composition. These materials also displayed very rich behavior on compression, with a variety of different combinations of phase transitions and elastic properties, including several showing the phenomenon of pressure-induced softening. In investigating their response to pressure, it was found that under some conditions they are porous on compression. Further studies showed some of these materials to have temperature dependent porosity, behave as molecular sieves, and when guest molecules were inserted new perovskite materials were could be formed. These results, and others from this work, are summarize and commented on in this concluding chapter.

The thermal expansion of $CaNbF_6$, $MgNbF_6$, and $MgZrF_6$ were characterized and compared to previously reported results for $CaZrF_6$ in Chapter 2. On Cooling, $CaNbF_6$ was found to retain cubic ReO_3-type structure down to at least 10 K, similar to $CaZrF_6$. This resulted in very strong NTE, with its volumetric CTE reaching as low as -65 ppm K^{-1} at 70 K. The NTE in $CaNbF_6$ also persisted over a very wide temperature range, 10 K to almost 900 K. This magnitude of NTE is comparable to some of the largest seen in framework materials. When comparing the performance of NTE materials both the magnitude of the NTE and temperature range over which occurs should be considered. Recently Goodwin et al. proposed a new constant to quantify NTE referred to as the NTE capacity, which accounts for both magnitude and temperature range.[406] Their comparison of NTE materials, Figure 8.1, shows $CaNbF_6$ to have to highest NTE capacity of all the materials they considered, with χ_α = -3.37 %.

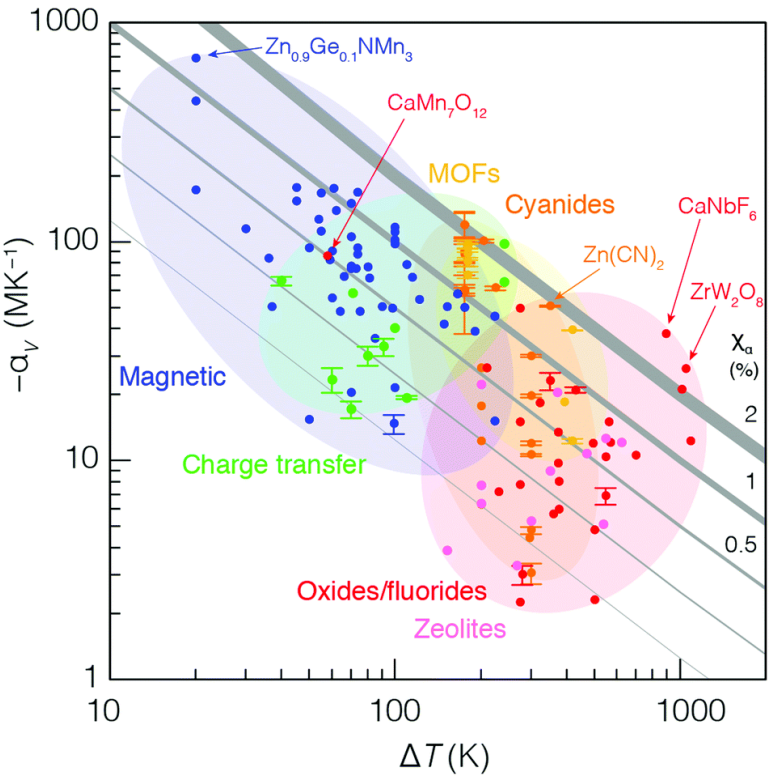

Figure 8.1: Plot of NTE magnitude against temperature range for experimentally-studied isotropic NTE materials color coded by NTE mechanism and chemical family. Diagonal lines represent constant NTE capacity $\chi_\alpha = -\Delta V/V = -\alpha_v \Delta T$. Reproduced from Coates, C. S.; Goodwin, A. L., How to quantify isotropic negative thermal expansion: magnitude, range, or both?, Mater. Horiz., 2019 with permission from The Royal Society of Chemistry.

These results for $CaNbF_6$ show that the substitution of Nb^{IV} for Zr, which have very similar ionic radii and electronegativities, has very little effect on the thermal expansion. However, the substitution of Mg for Ca led to greater changes in phase behavior and as a consequence thermal expansion. $MgZrF_6$ was found to undergo a symmetry lowering phase transition on cooling below 100 K. Above this phase transition temperature the material remains cubic and displays NTE. The NTE is the strongest at 175 K with α_v = -15 ppm K^{-1}. This thermal expansion is temperature dependent, and passes through zero near 500 K to PTE. The calculated NTE capacity was χ_α = -0.3 %, much lower than $CaNbF_6$ and $CaZrF_6$ (χ_α = -2.13%) due to the smaller magnitude and limited temperature range. Below 100 K $MgZrF_6$

transitions to the rhombohedral phase commonly seen on cooling in metal fluorides. This phase shows very strong anisotropic PTE consistent with what is expected for this structure, which consists of corner linked tilted octahedra. The substitution of both calcium and zirconium to give $MgNbF_6$ leads to an even greater destabilization of the cubic ReO_3-type structure. On cooling, cubic $MgNbF_6$ transitions to a rhombohedral phase just below room temperature (~280 K). The cubic material shows PTE all the way until decomposition at 950 K. Its' thermal expansion is low with a volumetric CTE below 10 ppm K^{-1} from 375 to 600 K. The low temperature rhombohedral phase showed the same strong anisotropic PTE seen in $MgZrF_6$ and other related rhombohedral materials.

To further investigate the effects of chemical substitution on thermal expansion in the $M^{2+}M^{4+}F_6$ family $CaTiF_6$ was characterized. The titanium analog completes the series of calcium with group four metals. As previously discussed, $CaZrF_6$ and $CaHfF_6$ have very similar behavior to $CaNbF_6$, and Nb, Zr, and Hf have similar ionic radii and electronegativities. However, Ti^{4+} has a smaller size and higher electronegativity and this produces a larger change in behavior. The results for $CaTiF_6$, Chapter 3, show a phase transition from cubic to rhombohedral on cooling below 120 K. The rhombohedral phase again shows anisotropic PTE. The cubic phase shows PTE close to the phase transition likely due to local structural distortions away from the ideal cubic structure. However, above 130 K $CaTiF_6$ shows strong NTE which persists up to the highest temperatures studied, ~500 K. The NTE reaches a value of α_v = -42 ppm K^{-1} at 177 K, and increases up to -18 ppm K^{-1} at 488 K. The thermal expansion of $CaTiF_6$ is different from that of the Nb, Zr, and Hf analogs, with the smaller size and larger electronegativity resulting in a phase transition and weaker NTE. The behavior of $CaTiF_6$ more closely mirrors that of $MgZrF_6$,

where substitution of Ca by Mg also leads to significant changes in cation size and electronegativity.

The final group of $M^{2+}M^{4+}F_6$ materials studied were $MnNbF_6$ and $ZnNbF_6$, Chapter 4. Although these metal fluorides were thought to adopt rhombohedral structures at room temperature, making them poor candidates for NTE, they were characterized to help further understand the effects of chemical composition and structure on thermal expansion in mixed metal fluorides. Classifying the behavior of these materials allows for comparison to the other known Nb and Zr analogs. A rhombohedral to cubic phase transition was seen for $MnNbF_6$ on warming to just above room temperature, 315 K. The rhombohedral phase showed large anisotropic PTE. Above 315 K cubic $MnNbF_6$ shows PTE due to the phase transition, which changes through zero to weak NTE at high temperatures. The volumetric CTE reaches -8 ppm K^{-1} at 457 K. The $ZnNbF_6$ results show the sample adopts a rhombohedral phase for all measured temperatures, 100 to 500 K. The thermal expansion is strongly positive and increases on heating. The substitution of Zn has a stronger effect than Mn on the stability of the cubic phase and thermal expansion.

To take a further look and draw more general conclusions about how size and electronegativity effect thermal expansion and phase behavior in $M^{2+}M^{4+}F_6$ materials, the thermal expansion results from this work are compared to one another, and relevant materials reported in literature, in Table 8.1. A comparison of their thermal expansion is also shown graphically in Figure 8.2.

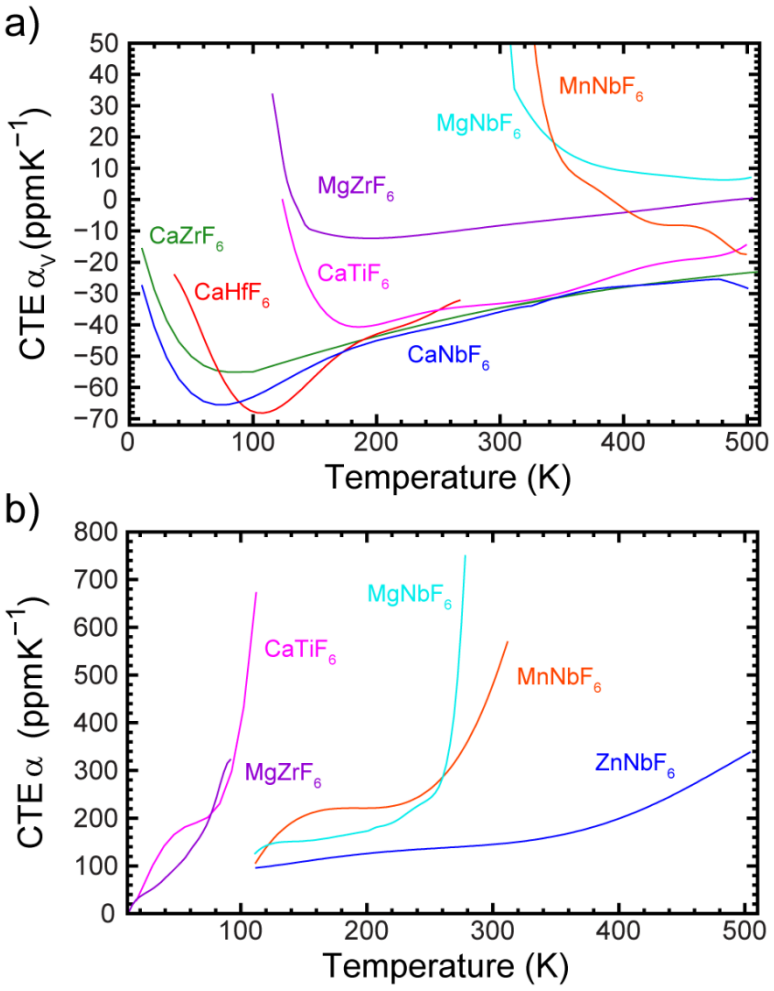

Figure 8.2: Temperature dependence of the volumetric coefficients of thermal expansion for a) cubic* and b) rhombohedral ReO_3-type metal fluorides. The CTEs were estimated by either differentiating polynomial fits to volume vs temperature or to point by point CTE data to best represent the temperature dependence of their thermal expansion. *CTEs for $CaZrF_6$ and $CaHfF_6$ calculated form published data.[26]

$CaNbF_6$ behaves so similarly to the previously reported $CaZrF_6$ and $CaHfF_6$ likely due to its very similar ionic radii and electronegativities.[26] However, as you decrease cation radius and/or increase cation electronegativity the cubic structure is destabilized, resulting in higher temperature transitions to a rhombohedral phase and weaker or no NTE while cubic. While ionic radius has been stated by others to be the key factor in the thermal expansion of these materials, and a decrease in radius and increase in electronegativity occur mostly

in tandem, there are examples where the change in thermal expansion can be attributed largely to a change in electronegativity.[344] Going from $MgNbF_6$ to $ZnNbF_6$ is only associated with a slight increase in ionic radius, but their thermal expansion behavior is quite different due to the increase in electronegativity. The reason for this is likely that lower electronegativity for the cation leads to a more ionic bonding nature for the metal fluoride octahedra, and this ionic bonding is believed to favor the cubic phase.[372] These results indicate that control of the ionic radii and electronegativity of the M^{2+} and M^{4+} cations allows for control of the stability of the cubic phase. Stabilizing the cubic phase down to low temperatures leads to strong NTE, and destabilizing the cubic phase leads to a transition to a PTE rhombohedral phase. The more the cubic phase is destabilized the higher the transition temperature to rhombohedral on cooling. In general, higher phase transition temperatures leads to weaker or no NTE in the cubic phase.

Table 8.1: Comparison of the stability of the cubic ReO_3-type phase, minimum volumetric CTE, and changes in ionic radii[374] and electronegativity[373] (EN) for different mixed metal fluorides.

$M^{2+}M^{4+}F_6$	Cubic to Rhombohedral Transition	Minimum α_V ($ppmK^{-1}$)	M^{2+} Ionic Radius (Å)	M^{4+} Ionic Radius (Å)	M^{2+} EN	M^{4+} EN	Average Change in IR & EN from $CaZrF_6$
$CaZrF_6$*	None	-55 at 85 K	1.00	0.720	1.04	1.22	0.000
$CaHfF_6$*	None	-68 at 105 K	1.00	0.710	1.04	1.23	0.006
$CaNbF_6$	None	-65 at 70 K	1.00	0.680	1.04	1.23	0.016
$CaTiF_6$	120 K	-42 at 177 K	1.00	0.605	1.04	1.32	0.060
$MgZrF_6$	100 K	-15 at 175 K	0.72	0.720	1.23	1.22	0.116
$MgNbF_6$	280 K	4 at 495 K	0.72	0.680	1.23	1.23	0.132
$MnNbF_6$	315 K	-8 at 457 K	0.67	0.680	1.60	1.23	0.233
$ZnNbF_6$	> 500 K	104 at 111 K	0.74	0.680	1.66	1.23	0.230

* Information obtained from literature[26]

The response to pressure of the same group of metal fluorides was also examined. A surprising variety of different structural responses was observed. High-pressure x-ray diffraction experiments in diamond anvil cells showed that $CaNbF_6$ and $MgZrF_6$ underwent different phase transitions on compression (Chapter 2), different even from that of $CaZrF_6$. The diffraction data for $CaNbF_6$ indicate that on compressions a phase transition likely involving reconstruction of the framework becomes favorable at 0.4 GPa. This occurs before any of the vibrational modes involving octahedral tilting fully soften and give rise to a lower symmetry ReO_3-type framework like the rhombohedral phase commonly seen on cooling. The high-pressure phase of $CaNbF_6$ persists until abrupt amorphization occurs at 4 GPa. In contrast to this behavior, $MgZrF_6$ undergoes a phase transition on compression to 0.37 GPa that is associated with octahedral tilts. The diffraction data for this high-pressure phase is consistent with the rhombohedral symmetry. It is followed by an abrupt phase transition at 1.0 GPa. No amorphization was observed for $MgZrF_6$, with the second high-pressure phase persisting up to the highest pressures measured, 7.0 GPa. Fits of a 3rd order Birch-Murnaghan equation of state to V versus P for the cubic phases of both $CaNbF_6$ and $MgZrF_6$ gave bulk moduli of K_0= 33.7(4) and 48.2(5) GPa, respectively. When compared to the bulk modulus reported for $CaZrF_6$ (K_0= 39.2 GPa), the Nb analog is softer and the Mg stiffer. These materials are rather soft when compared to most other solids, but their bulk moduli are comparable to those of other cubic ReO_3-type fluorides and framework solids. Both cubic $CaNbF_6$ and $MgZrF_6$ showed large pressure-induced softening with K_0'= -23(2) and -53(2), respectively. Pressure-induced softening is an anomalous property, which has been predicted to occur in these types of framework materials, but only been experimentally quantified in a few materials. The variable

temperature and pressure behavior of $MgZrF_6$ was also investigated and revealed a stiffening of the material on heating.

The response to pressure of $CaTiF_6$ was also characterized, Chapter 3. The material remains cubic only to the modest pressure of 0.25 GPa. The cubic phase was shown to be soft with very large pressure-induced softening, K_0= 28.9(9) GPa and K_0' = -50(5). On compression above 0.25 GPa cubic $CaTiF_6$ undergoes transition to a rhombohedral phase, which persists until disordering between 5 and 6 GPa. This rhombohedral phase showed very different behavior on compression than that of the cubic phase. Initially the material is very soft with a bulk modulus between 3 and 5 GPa at pressures < 0.5 GPa, but it linearly stiffens on compression. Rhombohedral $CaTiF_6$ displayed highly anisotropic compressibility, with a strong volume reduction in the a/b plane, but negative linear compressibility (NLC) parallel to the unique c-axis. The NLC was attributed to the distortion of individual octahedra on compression. The response of rhombohedral $CaTiF_6$ to compression is similar to what has been reported for other rhombohedral metal fluorides.[248,249] The results from high-pressure diffraction experiments on $MnNbF_6$ and $ZnNbF_6$, Chapter 4, indicate that both samples were already rhombohedral on initial compression. The rhombohedral phase persisted until 6 GPa for $MnNbF_6$ and up to the highest pressures recorded for $ZnNbF_6$, 4 GPa. Both materials were found to be elastically very soft with bulk moduli close to 10 GPa at low pressures, but both underwent rapid stiffening on compression. Anisotropic compressibility and NLC parallel to the c-axis were observed for both materials. This behavior was attributed to the same octahedral distortions discussed for $CaTiF_6$ and other materials.

When comparing the response to pressure of these mixed metal fluorides, Table 8.2, it is apparent that the structural response and elastic properties of these materials changes in a non-uniform way. It is clear that cubic phase metal fluorides tend to be very sensitive to pressure, undergoing phase transitions at modest pressures. This behavior makes them difficult to utilize for some applications, such as in controlled thermal expansion composites where they would likely experience stresses due to thermal expansion mismatch. The cubic phase materials are somewhat soft, and they show some of the largest pressure-induced softening seen experimentally in framework materials.[208,220,243] Materials with a rhombohedral structure do not undergo phase transitions at low pressure. However, they are elastically very soft and stiffen on compression.

Table 8.2: Comparison of the response to pressure for different $M^{2+}M^{4+}F_6$.

$M^{2+}M^{4+}F_6$	Crystalline Phase Transition	Other Phase Transitions	Bulk Modulus K_0 (GPa)	K_0'
$CaZrF_6$*	None	Disordering starting at 0.4 GPa	39.2	-13
$CaNbF_6$	Reconstructive at 0.4 GPa	Amorphization at 4 GPa	33.7	-23
$CaTiF_6$	Rhombohedral at 0.25 GPa	Amorphization at 5 GPa	29.9	-50
$MgZrF_6$	Rhombohedral at 0.37 GPa	Reconstructive at 1 GPa	48.2	-53
$MnNbF_6$	Initially Rhombohedral	Amorphization at 6 GPa	< 10	+
$ZnNbF_6$	Initially Rhombohedral	None to highest pressure ~4 GPa	< 10	+

* Information taken from literature[26]

The studies of $M^{2+}M^{4+}F_6$ indicate that changes in cation can have a large impact on thermal expansion. Therefore, other methods for obtaining finer control over the thermal expansion

in ReO_3-type fluorides were also investigated. Specifically, the fluoride excess system $Ca[Zr^{(IV)}_{1-x}Nb^{(V)}_{x}]F_{6+x}$ was examined, Chapter 5. The aliovalent substitution of Nb^{5+} for Zr^{4+} leads to the incorporation of excess fluoride to keep charge balance. These types of materials are thought to accommodate the excess fluoride interstitially, which can lead to conversion of some corner-linked octahedra to edge-sharing polyhedra, see for example work on $YbZrF_7$.[173,178,179] This type of local structure change limits the flexibility of the fluoride linkers, which weakens NTE, stiffens the structure, and may stabilize the cubic phase to higher pressures. Therefore, the thermal expansion and response to pressure of x= 0.25, 0.50, and 0.75 samples were examined to look at the effects of gradual introduction of excess fluoride. However, it became clear from the pair distribution function (PDF) and density measurements that while interstitial fluoride was present, edge-sharing polyhedra were not formed. The variable temperature diffraction analysis indicated the excess fluoride did impact the thermal expansion of these materials. However, it was not in a controlled way, and all three samples showed strong NTE indicating no systematic weakening on Nb^{5+} substitution. The thermal expansion of $Ca[Zr^{(IV)}_{1-x}Nb^{(V)}_{x}]F_{6+x}$ also depends strongly on the samples thermal history, indicating that the defects in these materials are mobile and can relax at quite low temperatures. On compression, all three samples undergo a crystalline to crystalline phase transition at close to 0.7 - 0.8 GPa. For $CaZr_{0.75}Nb_{0.25}F_{6.25}$ this transition is likely reconstructive to a phase apparently similar to the high-pressure phase of $CaNbF_6$, but both $CaZr_{0.5}Nb_{0.5}F_{6.5}$ and $CaZr_{0.25}Nb_{0.75}F_{6.75}$ transition to a rhombohedral structure. Analysis of the elastic properties of the cubic phase for each sample showed little change with composition, with K_0= 40.5, 37.4, and 40.8 GPa and K_0'= -25, -23, and -24 for x= 0.25, 0.50, and 0.75, respectively. The absence of

stiffening as excess fluoride is introduced, along with the observation of octahedral tilting transitions on compression, are consistent with the interstitial fluoride not leading to the formation of edge-shared polyhedra. While it is not entirely clear how the $Ca[Zr^{(IV)}_{1-x}Nb^{(V)}_{x}]F_{6+x}$ system incorporates excess fluoride, the results convincingly indicate that it does not involve the creation of edge-shared polyhedera, and that the excess fluoride is present as interstitials. The data suggest an alternative mechanism for the incorporation of interstitial fluoride, possibly through the formation of terminal fluoride protruding slightly into the empty cavity created by corner-linked polyhedra. This system is believed to behave differently from the other excess fluorides that have been studied in detail due to the retention of cation ordering as excess fluoride is introduced. In $Ca[Zr^{(IV)}_{1-x}Nb^{(V)}_{x}]F_{6+x}$ the Nb only substitutes onto the Zr site, so the Ca and Zr/Nb ordering is retained.[160,178-182] In materials where edge-sharing polyhedra are formed, such as $YbZrF_7$, $TiZrF_{7-x}$, $Ti_{1-x}Zr_xF_{3+x}$, and $Mg_{2-x}Zr_xF_{4+2x}$, the aliovalent substitution resulted in loss of cation ordering.[178-182] This loss of ordering allows for the cations which are more likely to adopt higher coordination to neighbor each other, which is not the case for $Ca[Zr^{(IV)}_{1-x}Nb^{(V)}_{x}]F_{6+x}$.

In the course of examining the response of $M^{2+}M^{4+}F_6$ to pressure, some experiments using high-pressure helium were conducted. This led to the discovery that $CaZrF_6$ was porous to helium at 300 K, Chapter 6. While helium penetration is commonly a consideration when using the gas as an inert hydrostatic pressure medium at very high pressure, the insertion of helium into $CaZrF_6$ was not anticipated due to the very small effective pore sizes in this material. Compression of $CaZrF_6$ in nitrogen gas showed close to linear reduction in volume, and the bulk modulus, K_0 = 36.7(2) GPa, was consistent with previously reported results for $CaZrF_6$ in a non-penetrating liquid. When compressed in nitrogen at 160 K them

material amorphized. These results clearly indicate nitrogen does not insert into $CaZrF_6$, which makes the material a molecular sieve that takes up helium, but not nitrogen at room temperature. Neutron diffraction experiments showed that on compression in helium between 300 and 500 MPa at 300 K the unit cell volume for $CaZrF_6$ increased. This response was attributed to insertion of helium into the material, which would lead to some volume expansion on compression. The helium containing $CaZrF_6$ was cooled down from 300 to 70 K while at pressure, and on decompression showed a linear increase volume. This suggested that the helium remained trapped in the structure on cooling. Subsequent warming and compression/decompression at 130, 190, and 250 K revealed that the temperature dependent porosity for $CaZrF_6$ with helium remaining trapped until temperatures above 190 K. Helium insertion was found to weaken the NTE, stiffen the structure to compression, and stabilize the structure against amorphization under pressure. Helium gas uptake measurements indicated that the insertion of helium was not instantaneous but occurred on a time scale of minutes at room temperature. These results, along with the Rietveld analysis of neutron diffraction data, indicated a helium loading of ~50%, or 1 mole of helium per mole of $CaZrF_6$, on compression to 500 MPa at 300 K. Rietveld refinements showed that the helium inserts into the cavities created by the corner-linked ReO_3-type structure of $CaZrF_6$. Therefore, the resulting helium inserted structure is denoted with the general formula $(He_{2-x}\square_x)(CaZr)F_6$. The insertion of helium leads to a double perovskite ($A_2BB'X_6$) with helium on the A-site. This is the first reported perovskite to contain helium, making the preparation of $(He_{2-x}\square_x)(CaZr)F_6$ materials a significant extension of perovskite chemistry to include the controlled synthesis of materials with small gas molecules on the A-site.

Finally, to further investigate the preparation and properties of these new helium containing perovskites, x-ray diffraction experiments using high-pressure helium and neon loaded diamond anvil cells were conducted for $CaZrF_6$, $CaNbF_6$, and $CaNb^{IV}_{0.5}Nb^{V}_{0.5}F_{6.5}$. These experiments were able to investigate the behavior from ~0.2 to > 4 GPa. The two samples studied in neon ($CaZrF_6$ and $CaNb^{IV}_{0.5}Nb^{V}_{0.5}F_{6.5}$) showed no evidence for neon penetration. They underwent phase transitions or disordering at low pressures when compressed in neon and showed no increase in volume on compression. For $CaZrF_6$ helium insertion was confirmed with an increase in unit cell volume seen on initial compression. Above ~0.7 GPa, the unit cell volume decreased on further compression. The now presumably fully helium loaded material, $[He_2][CaZr]F_6$, remained cubic until amorphization at 3.5 GPa, with an estimated bulk modulus of ~ 47 GPa. This shows the new helium perovskite to be stiffer and stable to higher pressures than the parent metal fluoride material. The smaller cubic $CaNbF_6$ was also shown to insert helium on initial compression. The volume increased up until a pressure of ~0.9 GPa. The $[He_2][CaNb]F_6$ perovskite had a bulk modulus of 51 GPa and survived until to the highest measured pressure of 3.7 GPa. Even the material with the smallest unit cell $CaNb^{IV}_{0.5}Nb^{V}_{0.5}F_{6.5}$, which also presumably contains interstitial fluoride, was shown to insert helium on compression. The helium inserts below 0.9 GPa, and the newly formed $[He_2][CaNb^{IV}_{0.5}Nb^{V}_{0.}5]F_{6.5}$ amorphizes above 3.3 GPa and has a bulk modulus of ~50 GPa. Based on these results modification of composition, to tune the effective pore size of the ReO_3-type framework, and the temperature at which gases are inserted into the parent material, may allow other gases, including hydrogen, to be incorporated into perovskites and their uptake and release pressures to be controlled.

APPENDIX A. SUPPLEMENTARY MATERIAL FOR CHAPTER 2

A.1 Experimental Details

A.1.1 Variable Temperature X-ray Diffraction Measurements on $CaNbF_6$

Low- and high-temperature x-ray powder diffraction data were recorded using an Oxford Cryosystems Cryostream (100 – 500 K) and a resistively heated furnace (300 – 900 K) at the 17-BM beamline of the Advanced Photon Source, Argonne National Laboratory. The data was collected at a wavelength of 0.7295 Å. When the Cryostream system was used, the sample was packed into a Kapton capillary under Argon and sealed with epoxy. The sample was cooled to 100 K, held there for 30 min, heated to 500 K, and cooled to 100 K. Data were collected every three Kelvin, after the target temperature had been reached and held for approximately two minutes. At the temperature points each measurement consisted of an exposure time of 0.5 seconds, 20 subframes, and a 10-degree rotation. A temperature calibration was done repeating the measurement with a thermocouple inside of an empty Kapton capillary. The furnace measurements consisted of a flow cell set up, which utilized a sample and thermocouple in a quartz capillary. Helium gas was flowed through, and the sample was heated at a constant rate. Each measurement had 1.0 second exposure times, 10 subframes, 10-degree rotation, and 60 second intervals between frames.

A.1.2 Variable Temperature Neutron Powder Diffraction Measurements on $CaNbF_6$

Neutron powder diffraction measurements were performed using the PAC sample environment on the POWGEN instrument at the Spallation Neutron Source, Oak Ridge National Laboratory. The sample was loaded into a vanadium can under helium. The sample was cooled down to 10 K and heated with 3-minute equilibration times. (Details:

mass= 3 grams, duration= 1545 s, proton charge= 1.8E12, frequency= 60, wavelength= 1.33, guide= -56.863, and total counts= 5800000.)

A.1.3 High-Pressure X-ray Powder Diffraction Measurements on $CaNbF_6$

High-pressure x-ray powder diffraction data (298 K and P < ~8.6 GPa) were recorded at 17-BM utilizing an EasyLab "Diacell Bragg-(G)" diaphragm diamond anvil cell (DAC) while the pressure was continuously increased. The sample was loaded under inert atmosphere with a NaCl internal pressure calibrant and an Alfa silicone oil, with a molecular weight of 237 $g \cdot mol^{-1}$, pressure-transmitting fluid. Pressure was determined using Bragg peaks from NaCl, and the Birch equation of state for NaCl.

A.2 Figures

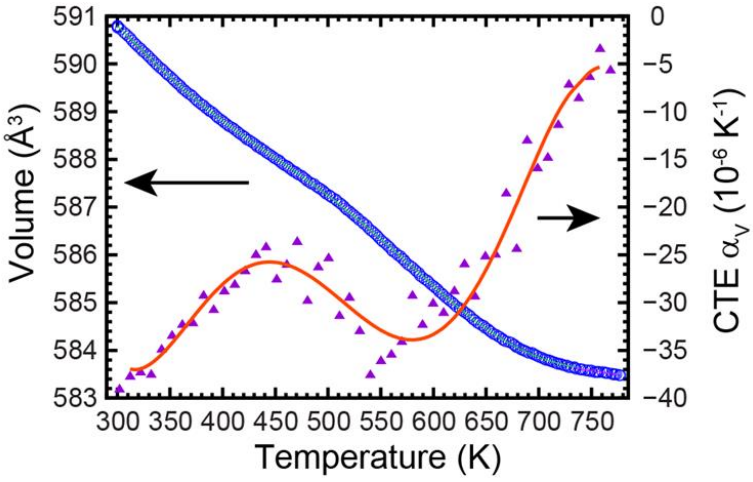

Figure A.1: Unit cell volume and thermal expansion coefficient for $CaNbF_6$ above room temperature, as determined by the Rietveld analyses of powder x-ray diffraction data

collected in a wire wound furnace. The red line was calculated by differentiating a polynomial fit to the unit cell volumes. The CTEs shown as purple points were calculated point by point.

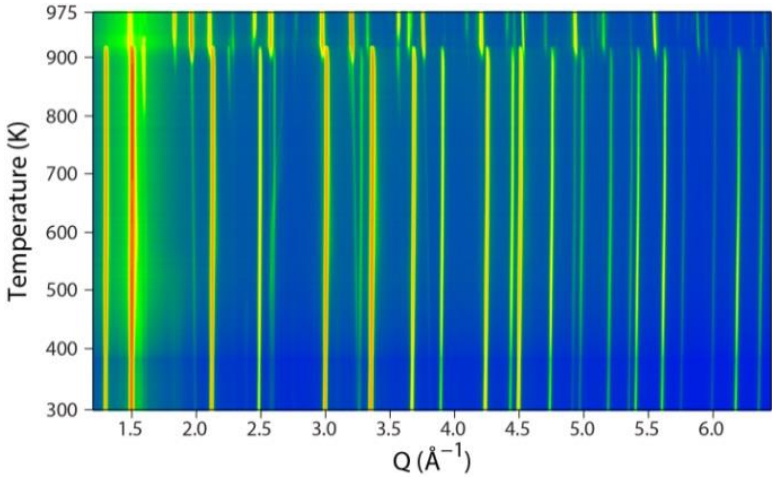

Figure A.2: Contour plot showing the high temperature diffraction data for $CaNbF_6$ and its decomposition. The dramatic change in the diffraction patterns at ~925K is probably associated with the failure of the sample tube.

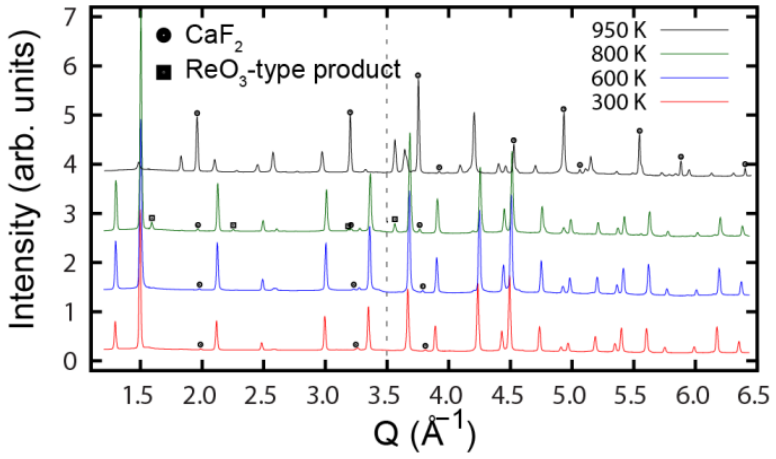

Figure A.3: Select high temperature diffractions patterns of $CaNbF_6$ with the decomposition products marked.

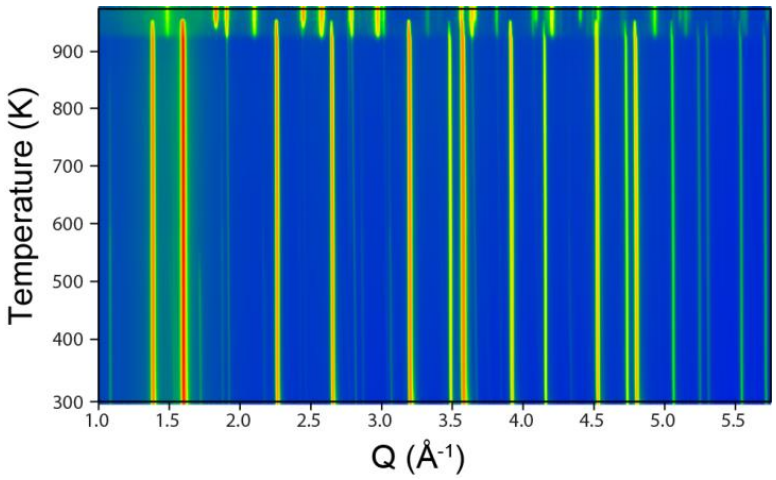

Figure A.4: Contour plot showing the high temperature diffraction data for $MgNbF_6$.

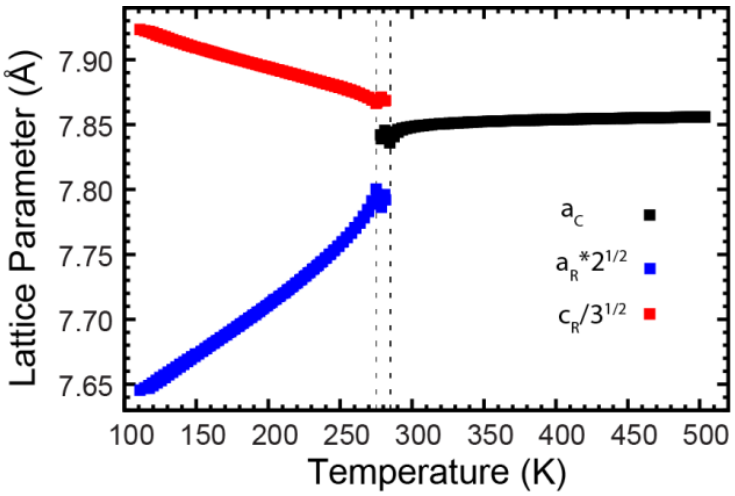

Figure A.5: Variation of the lattice constants for $MgNbF_6$ with temperature. At low temperature an $R\bar{3}$ model with a hexagonal cell was used and at high temperature a cubic $Fm\bar{3}m$ model was used. In the region between the two dashed lines two phase fits were employed.

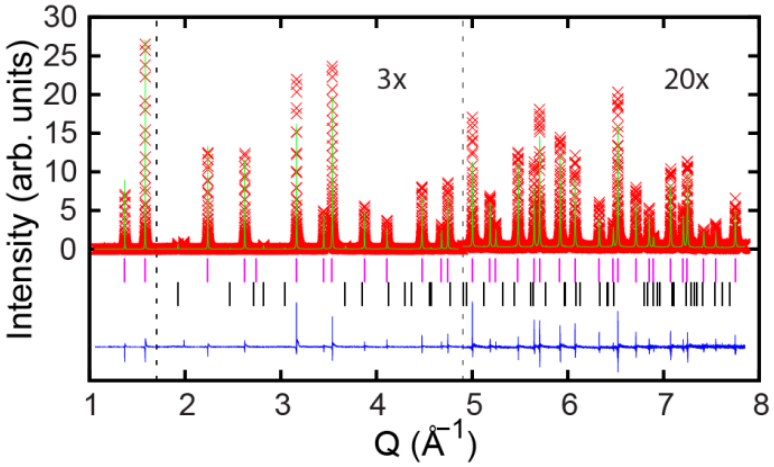

Figure A.6: Rietveld plot showing a fit of a cubic ReO_3-type model ($Fm\bar{3}m$) to the 150K high resolution synchrotron diffraction data for $MgZrF_6$.

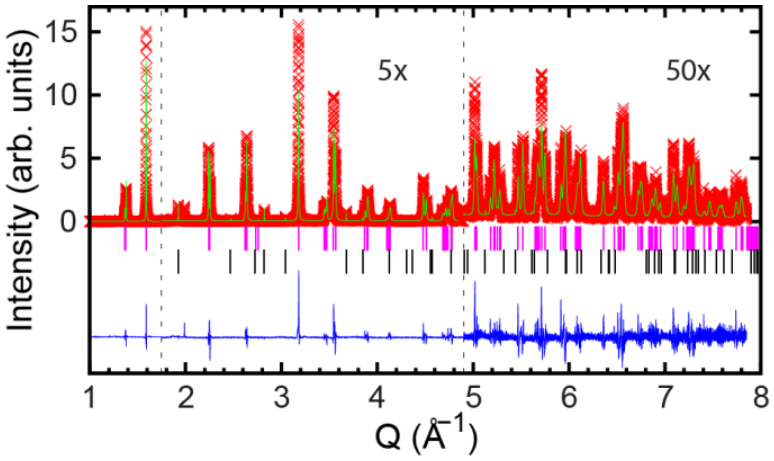

Figure A.7: Rietveld plot showing the fit of an $R\bar{3}$ model to low temperature (10K) high resolution synchrotron data for $MgZrF_6$.

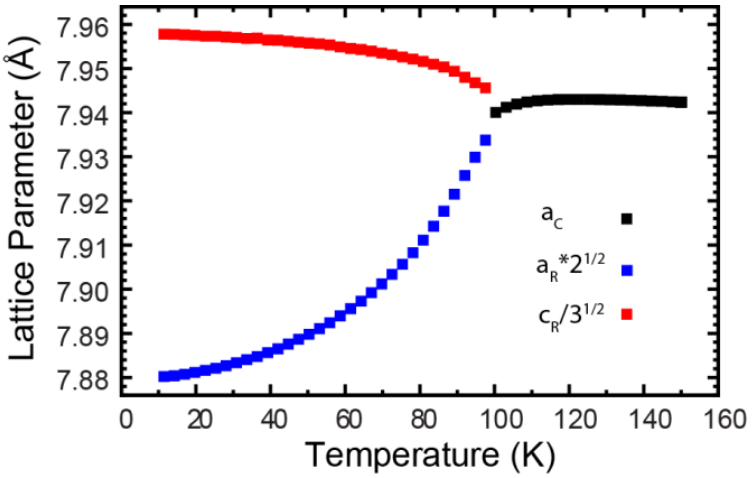

Figure A.8: Variation of the lattice constants for $MgZrF_6$ with temperature. At low temperature an $R\bar{3}$ model with a hexagonal cell was used and at high temperature a cubic $Fm\bar{3}m$ model was used.

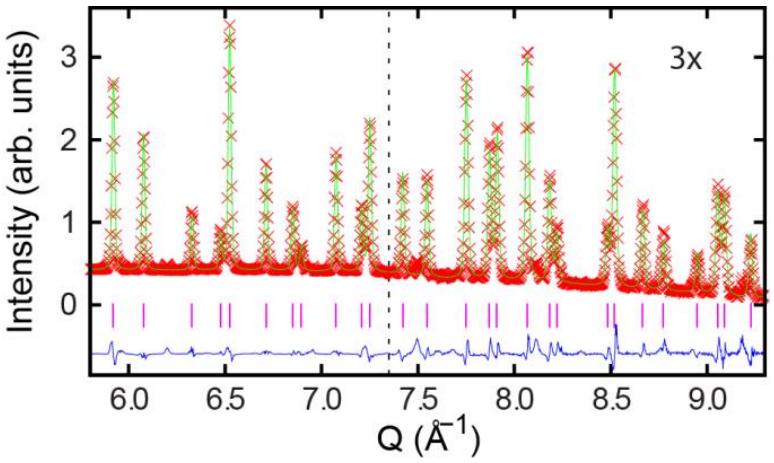

Figure A.9: Rietveld plot showing the fit of a cubic ReO_3-type model to data for $MgZrF_6$ obtained in an oil filled heatable pressure cell equipped with a Background Reducing Internal Mask (BRIM). These data were acquired at 298 K and ambient pressure. The high Q part has been scaled by a factor of 3X and shifted downwards so that the backgrounds for the two sections of the plot appear to be the same.

A.3 Tables

Table A.1: Lattice constant and unit cell volume for $CaNbF_6$ as determined from the Rietveld analysis of the neutron diffraction data.

Temperature (K)	Rwp	a (Å)	Volume (Å^3)
10.0	5.94E-02	8.43537(3)	600.222(6)
20.0	6.45E-02	8.43435(3)	600.005(6)
30.0	6.05E-02	8.43301(3)	599.719(6)
40.0	6.63E-02	8.43170(3)	599.440(6)
50.0	6.32E-02	8.42995(3)	599.066(6)
60.0	5.99E-02	8.42824(3)	598.702(6)
70.0	6.14E-02	8.42623(3)	598.275(6)
80.0	6.72E-02	8.42440(3)	597.884(6)
90.0	5.71E-02	8.42257(3)	597.494(6)
100.0	6.15E-02	8.42079(3)	597.117(6)
110.0	5.93E-02	8.41907(3)	596.749(6)
120.0	6.28E-02	8.41735(3)	596.383(6)
140.0	5.78E-02	8.41443(3)	595.764(6)
160.0	5.24E-02	8.41139(3)	595.119(6)
180.0	5.80E-02	8.40849(3)	594.502(6)
200.0	5.20E-02	8.40582(3)	593.936(6)
225.0	5.70E-02	8.40282(3)	593.301(6)
250.0	5.33E-02	8.39984(3)	592.670(6)
275.0	5.32E-02	8.39701(3)	592.071(6)
300.0	4.96E-02	8.39447(3)	591.535(6)

Table A.2: Lattice constant and unit cell volume for $CaNbF_6$ as determined from the Rietveld analysis of the x-ray diffraction data acquired while using a Cryostream.

Temperature (K)	Rwp	a (Å)	Volume (Å^3)
111	0.0872	8.41810(5)	596.54(1)
115	0.0872	8.41767(5)	596.45(1)
118	0.0870	8.41704(5)	596.32(1)
120	0.0869	8.41663(5)	596.23(1)
122	0.0895	8.41612(5)	596.12(1)
125	0.0867	8.41560(5)	596.01(1)
128	0.0866	8.41509(5)	595.90(1)

Table A.2 continued

Temperature (K)	Rwp	a (Å)	Volume (Å^3)
131	0.0865	8.41457(5)	595.79(1)
134	0.0865	8.41407(5)	595.69(1)
135	0.0863	8.41357(5)	595.58(1)
139	0.0862	8.41305(5)	595.47(1)
142	0.0862	8.41262(5)	595.38(1)
144	0.0860	8.41218(5)	595.29(1)
148	0.0859	8.41174(5)	595.19(1)
151	0.0859	8.41130(5)	595.10(1)
154	0.0859	8.41087(5)	595.01(1)
156	0.0858	8.41044(5)	594.92(1)
159	0.0858	8.41006(5)	594.84(1)
161	0.0857	8.40962(5)	594.74(1)
164	0.0856	8.40923(5)	594.66(1)
166	0.0856	8.40883(5)	594.58(1)
169	0.0856	8.40839(5)	594.48(1)
173	0.0856	8.40794(5)	594.39(1)
175	0.0856	8.40762(5)	594.32(1)
179	0.0855	8.40720(5)	594.23(1)
181	0.0855	8.40679(5)	594.14(1)
184	0.0854	8.40640(5)	594.06(1)
187	0.0854	8.40602(5)	593.98(1)
189	0.0855	8.40564(5)	593.90(1)
192	0.0855	8.40527(5)	593.82(1)
196	0.0854	8.40488(5)	593.74(1)
198	0.0854	8.40449(5)	593.66(1)
201	0.0855	8.40413(5)	593.58(1)
204	0.0856	8.40375(5)	593.50(1)
207	0.0856	8.40335(5)	593.41(1)
210	0.0856	8.40298(5)	593.33(1)
213	0.0856	8.40260(5)	593.25(1)
216	0.0856	8.40222(5)	593.18(1)
219	0.0857	8.40187(5)	593.10(1)
222	0.0857	8.40150(5)	593.02(1)
225	0.0857	8.40113(5)	592.94(1)
228	0.0858	8.40077(5)	592.87(1)
231	0.0858	8.40041(5)	592.79(1)

Table A.2 continued

Temperature (K)	Rwp	a (Å)	Volume (Å^3)
131	0.0865	8.41457(5)	595.79(1)
134	0.0865	8.41407(5)	595.69(1)
234	0.0859	8.40004(5)	592.71(1)
237	0.0859	8.39969(5)	592.64(1)
240	0.0860	8.39933(5)	592.56(1)
242	0.0861	8.39902(5)	592.50(1)
246	0.0861	8.39866(5)	592.42(1)
249	0.0862	8.39831(5)	592.35(1)
251	0.0862	8.39799(5)	592.28(1)
254	0.0862	8.39767(5)	592.21(1)
258	0.0863	8.39733(5)	592.14(1)
260	0.0864	8.39699(5)	592.07(1)
263	0.0864	8.39668(5)	592.00(1)
266	0.0864	8.39637(5)	591.94(1)
269	0.0865	8.39606(5)	591.87(1)
272	0.0865	8.39575(5)	591.81(1)
275	0.0866	8.39544(5)	591.74(1)
278	0.0866	8.39514(5)	591.68(1)
281	0.0867	8.39482(5)	591.61(1)
284	0.0867	8.39451(5)	591.54(1)
287	0.0869	8.39415(5)	591.47(1)
290	0.0870	8.39386(5)	591.41(1)
293	0.0870	8.39355(5)	591.34(1)
296	0.0871	8.39325(5)	591.28(1)
299	0.0871	8.39293(5)	591.21(1)
302	0.0872	8.39264(5)	591.15(1)
305	0.0872	8.39235(5)	591.09(1)
309	0.0873	8.39203(5)	591.02(1)
312	0.0873	8.39173(5)	590.96(1)
316	0.0874	8.39126(5)	590.86(1)
320	0.0875	8.39090(5)	590.78(1)
323	0.0876	8.39062(5)	590.72(1)
326	0.0877	8.39031(5)	590.66(1)
330	0.0877	8.39001(5)	590.59(1)
333	0.0878	8.38969(5)	590.53(1)
336	0.0880	8.38937(5)	590.46(1)
340	0.0880	8.38905(5)	590.39(1)
343	0.0881	8.38874(5)	590.32(1)
346	0.0881	8.38842(5)	590.26(1)

Table A.2 continued

Temperature (K)	Rwp	a (Å)	Volume (Å^3)
131	0.0865	8.41457(5)	595.79(1)
134	0.0865	8.41407(5)	595.69(1)
350	0.0882	8.38812(5)	590.19(1)
353	0.0883	8.38783(5)	590.13(1)
356	0.0884	8.38754(5)	590.07(1)
360	0.0884	8.38724(5)	590.01(1)
364	0.0876	8.38706(5)	589.97(1)
367	0.0874	8.38674(5)	589.90(1)
371	0.0873	8.38641(5)	589.83(1)
374	0.0873	8.38612(5)	589.77(1)
378	0.0874	8.38586(5)	589.72(1)
382	0.0875	8.38556(5)	589.65(1)
385	0.0875	8.38532(5)	589.60(1)
387	0.0875	8.38510(5)	589.56(1)
390	0.0877	8.38490(5)	589.51(1)
393	0.0876	8.38469(5)	589.47(1)
397	0.0875	8.38445(5)	589.42(1)
400	0.0876	8.38419(5)	589.36(1)
403	0.0877	8.38395(5)	589.31(1)
406	0.0877	8.38371(5)	589.26(1)
410	0.0877	8.38346(5)	589.21(1)
413	0.0877	8.38321(5)	589.16(1)
416	0.0877	8.38296(5)	589.11(1)
419	0.0880	8.38271(5)	589.05(1)
422	0.0881	8.38247(5)	589.00(1)
425	0.0881	8.38225(5)	588.95(1)
428	0.0880	8.38200(5)	588.90(1)
431	0.0878	8.38177(5)	588.85(1)
434	0.0876	8.38156(5)	588.81(1)
437	0.0874	8.38138(5)	588.77(1)
439	0.0873	8.38117(5)	588.73(1)
442	0.0870	8.38097(5)	588.68(1)
445	0.0867	8.38078(5)	588.64(1)
448	0.0865	8.38060(5)	588.61(1)
450	0.0863	8.38042(5)	588.57(1)
453	0.0860	8.38024(5)	588.53(1)
455	0.0855	8.38008(5)	588.50(1)
458	0.0853	8.37990(5)	588.46(1)
461	0.0850	8.37973(5)	588.42(1)

Table A.2 continued

Temperature (K)	Rwp	a (Å)	Volume (Å^3)
131	0.0865	8.41457(5)	595.79(1)
134	0.0865	8.41407(5)	595.69(1)
463	0.0849	8.37956(5)	588.39(1)
466	0.0847	8.37938(5)	588.35(1)
469	0.0847	8.37921(5)	588.31(1)
471	0.0846	8.37904(5)	588.28(1)
474	0.0845	8.37887(5)	588.24(1)
477	0.0845	8.37872(5)	588.21(1)
479	0.0844	8.37856(5)	588.18(1)
482	0.0844	8.37841(5)	588.15(1)
484	0.0846	8.37826(5)	588.11(1)
486	0.0847	8.37811(5)	588.08(1)
489	0.0849	8.37795(5)	588.05(1)
491	0.0849	8.37780(5)	588.02(1)
494	0.0850	8.37768(5)	587.99(1)
496	0.0851	8.37755(5)	587.96(1)
498	0.0851	8.37741(5)	587.94(1)
501	0.0852	8.37726(5)	587.90(1)
503	0.0853	8.37711(5)	587.87(1)
504	0.0851	8.37711(5)	587.87(1)
502	0.0851	8.37722(5)	587.90(1)
500	0.0851	8.37731(5)	587.91(1)
497	0.0849	8.37749(5)	587.95(1)
495	0.0848	8.37756(5)	587.97(1)
494	0.0846	8.37765(5)	587.99(1)
491	0.0845	8.37783(5)	588.02(1)
490	0.0845	8.37787(5)	588.03(1)
486	0.0843	8.37809(5)	588.08(1)
485	0.0843	8.37815(5)	588.09(1)
481	0.0842	8.37841(5)	588.15(1)
478	0.0840	8.37860(5)	588.19(1)
475	0.0839	8.37880(5)	588.23(1)
472	0.0838	8.37897(5)	588.26(1)
470	0.0837	8.37913(5)	588.30(1)
468	0.0836	8.37930(5)	588.33(1)
464	0.0835	8.37948(5)	588.37(1)
461	0.0834	8.37967(5)	588.41(1)
458	0.0832	8.37988(5)	588.45(1)
455	0.0832	8.38007(5)	588.50(1)

Table A.2 continued

Temperature (K)	Rwp	a (Å)	Volume (Å^3)
131	0.0865	8.41457(5)	595.79(1)
134	0.0865	8.41407(5)	595.69(1)
452	0.0831	8.38026(5)	588.54(1)
449	0.0832	8.38045(5)	588.58(1)
446	0.0831	8.38065(5)	588.62(1)
444	0.0830	8.38083(5)	588.66(1)
441	0.0828	8.38104(5)	588.70(1)
438	0.0827	8.38124(5)	588.74(1)
435	0.0826	8.38145(5)	588.79(1)
432	0.0824	8.38166(5)	588.83(1)
429	0.0824	8.38188(5)	588.88(1)
426	0.0823	8.38210(5)	588.92(1)
423	0.0822	8.38233(5)	588.97(1)
421	0.0822	8.38255(5)	589.02(1)
418	0.0821	8.38277(5)	589.06(1)
414	0.0819	8.38300(5)	589.11(1)
412	0.0818	8.38322(5)	589.16(1)
408	0.0817	8.38346(5)	589.21(1)
409	0.0816	8.38348(5)	589.21(1)
403	0.0815	8.38396(5)	589.32(1)
399	0.0813	8.38421(5)	589.37(1)
396	0.0811	8.38445(5)	589.42(1)
393	0.0809	8.38467(5)	589.46(1)
391	0.0809	8.38488(5)	589.51(1)
388	0.0807	8.38509(5)	589.55(1)
385	0.0805	8.38530(5)	589.60(1)
382	0.0804	8.38555(5)	589.65(1)
378	0.0801	8.38581(5)	589.71(1)
375	0.0800	8.38607(5)	589.76(1)
371	0.0799	8.38636(5)	589.82(1)
368	0.0798	8.38666(5)	589.88(1)
365	0.0797	8.38695(5)	589.95(1)
361	0.0797	8.38723(5)	590.01(1)
358	0.0797	8.38752(5)	590.07(1)
355	0.0795	8.38782(5)	590.13(1)
351	0.0794	8.38811(5)	590.19(1)
348	0.0794	8.38839(5)	590.25(1)
345	0.0792	8.38869(5)	590.31(1)
341	0.0792	8.38899(5)	590.38(1)

Table A.2 continued

Temperature (K)	Rwp	a (Å)	Volume (Å^3)
131	0.0865	8.41457(5)	595.79(1)
134	0.0865	8.41407(5)	595.69(1)
338	0.0791	8.38929(5)	590.44(1)
335	0.0790	8.38960(5)	590.51(1)
331	0.0790	8.38989(5)	590.57(1)
328	0.0789	8.39018(5)	590.63(1)
325	0.0789	8.39048(5)	590.69(1)
322	0.0789	8.39077(5)	590.75(1)
319	0.0788	8.39107(5)	590.82(1)
313	0.0787	8.39159(5)	590.93(1)
311	0.0786	8.39185(5)	590.98(1)
308	0.0785	8.39217(5)	591.05(1)
305	0.0783	8.39246(5)	591.11(1)
302	0.0784	8.39274(5)	591.17(1)
299	0.0783	8.39305(5)	591.24(1)
291	0.0776	8.39399(5)	591.43(1)
288	0.0776	8.39427(5)	591.49(1)
285	0.0775	8.39455(5)	591.55(1)
282	0.0775	8.39486(5)	591.62(1)
279	0.0774	8.39515(5)	591.68(1)
276	0.0773	8.39545(5)	591.74(1)
273	0.0773	8.39577(5)	591.81(1)
270	0.0771	8.39640(4)	591.94(1)
267	0.0772	8.39608(4)	591.87(1)
264	0.0770	8.39673(4)	592.01(1)
261	0.0769	8.39705(4)	592.08(1)
258	0.0769	8.39738(4)	592.15(1)
255	0.0768	8.39769(4)	592.22(1)
253	0.0768	8.39803(4)	592.29(1)
250	0.0768	8.39837(4)	592.36(1)
247	0.0768	8.39871(4)	592.43(1)
244	0.0788	8.39907(4)	592.51(1)
241	0.0787	8.39940(4)	592.58(1)
238	0.0766	8.39974(4)	592.65(1)
235	0.0766	8.40008(4)	592.72(1)
232	0.0765	8.40042(4)	592.79(1)
229	0.0765	8.40076(4)	592.87(1)
226	0.0764	8.40114(4)	592.95(1)
223	0.0764	8.40149(4)	593.02(1)

Table A.2 continued

Temperature (K)	Rwp	a (Å)	Volume (Å^3)
131	0.0865	8.41457(5)	595.79(1)
134	0.0865	8.41407(5)	595.69(1)
220	0.0764	8.40185(4)	593.10(1)
217	0.0764	8.40222(4)	593.17(1)
215	0.0764	8.40259(4)	593.25(1)
212	0.0763	8.40292(4)	593.32(1)
209	0.0764	8.40328(4)	593.40(1)
206	0.0763	8.40365(4)	593.48(1)
203	0.0764	8.40412(4)	593.58(1)
200	0.0763	8.40444(4)	593.64(1)
198	0.0763	8.40479(4)	593.72(1)
195	0.0765	8.40525(4)	593.82(1)
193	0.0766	8.40558(4)	593.89(1)
189	0.0767	8.40604(4)	593.98(1)
186	0.0768	8.40651(4)	594.08(1)
183	0.0768	8.40683(4)	594.15(1)
180	0.0769	8.40721(4)	594.23(1)
177	0.0769	8.40760(4)	594.31(1)
174	0.0770	8.40800(4)	594.40(1)
172	0.0771	8.40841(4)	594.49(1)
169	0.0771	8.40883(4)	594.58(1)
166	0.0773	8.40924(4)	594.66(1)
163	0.0774	8.40965(4)	594.75(1)
160	0.0775	8.41006(4)	594.84(1)
157	0.0777	8.41048(4)	594.93(1)
155	0.0778	8.41089(4)	595.01(1)
152	0.0779	8.41131(4)	595.10(1)
149	0.0780	8.41172(4)	595.19(1)
147	0.0781	8.41214(4)	595.28(1)
144	0.0781	8.41255(4)	595.36(1)
141	0.0783	8.41308(4)	595.48(1)
140	0.0784	8.41332(4)	595.53(1)
135	0.0788	8.41407(4)	595.69(1)
136	0.0787	8.41410(4)	595.69(1)
130	0.0792	8.41502(4)	595.89(1)
130	0.0793	8.41508(4)	595.90(1)
126	0.0798	8.41580(4)	596.06(1)
123	0.0799	8.41621(4)	596.14(1)
121	0.0801	8.41664(4)	596.23(1)

Table A.2 continued

Temperature (K)	Rwp	a (Å)	Volume (Å^3)
131	0.0865	8.41457(5)	595.79(1)
134	0.0865	8.41407(5)	595.69(1)
119	0.0804	8.41708(4)	596.33(1)

Table A.3: Unit cell volumes for both the $CaNbF_6$ and NaCl as determined from the Rietveld analysis of the high-pressure diffraction data acquired with a sample to detector distance of 300 mm. Pressures estimated from the unit cell volume of the NaCl using the Birch equation of state are also given, and have an average uncertainty of 0.012 GPa.

$CaNbF_6$ Volume (Å^3)	NaCl Volume (Å^3)	Pressure (GPa)
592.10(1)	179.841(6)	0.000
592.11(1)	179.822(6)	0.003
592.11(1)	179.785(7)	0.007
592.11(1)	179.785(7)	0.007
592.11(1)	179.800(6)	0.005
592.10(1)	179.804(6)	0.005
592.11(1)	179.804(6)	0.005
592.11(1)	179.801(6)	0.005
592.11(1)	179.808(6)	0.004
592.11(1)	179.811(6)	0.004
592.10(1)	179.813(6)	0.004
592.09(1)	179.816(7)	0.003
592.07(1)	179.812(6)	0.004
592.05(1)	179.813(6)	0.004
592.02(1)	179.807(6)	0.005
591.99(1)	179.782(7)	0.008
591.95(1)	179.765(6)	0.010
591.90(1)	179.757(6)	0.011
591.85(1)	179.740(6)	0.013
591.81(1)	179.722(7)	0.016
591.74(1)	179.700(6)	0.019

Table A.3 continued

$CaNbF_6$ Volume (Å^3)	NaCl Volume (Å^3)	Pressure (GPa)
591.69(1)	179.680(6)	0.021
591.64(1)	179.660(6)	0.024
591.60(1)	179.635(6)	0.027
591.54(1)	179.606(6)	0.031
591.50(1)	179.585(6)	0.034
591.45(1)	179.567(6)	0.037
591.41(1)	179.550(6)	0.039
591.36(1)	179.525(6)	0.042
591.31(1)	179.501(7)	0.045
591.26(1)	179.480(7)	0.048
591.19(1)	179.450(7)	0.052
591.12(1)	179.430(7)	0.055
591.03(1)	179.395(7)	0.060
590.94(1)	179.349(7)	0.066
590.84(1)	179.316(7)	0.070
590.73(1)	179.269(7)	0.077
590.56(1)	179.212(7)	0.084
590.39(1)	179.133(7)	0.095
590.17(1)	179.044(7)	0.107
589.95(1)	178.942(7)	0.121
589.77(1)	178.884(7)	0.129
589.55(1)	178.800(7)	0.141
589.23(1)	178.674(7)	0.158
588.75(1)	178.490(7)	0.184
588.35(1)	178.335(7)	0.205
587.97(1)	178.213(7)	0.222
587.57(1)	178.076(6)	0.242
586.84(1)	177.842(7)	0.275
586.04(1)	177.580(7)	0.312
585.23(1)	177.340(7)	0.347
584.41(1)	177.112(7)	0.380
583.54(1)	176.890(7)	0.412

Table A.4: Unit cell volumes for both the $CaNbF_6$ and NaCl as determined from the Rietveld analysis of the high-pressure diffraction data acquired with a sample to detector distance of 400 mm. Pressures estimated from the unit cell volume of the NaCl using the Birch equation of state are also given, and have an average uncertainty of 0.05 GPa.

CaNbF6 Volume (Å^3)	NaCl Volume (Å^3)	Pressure (GPa)
592.01(2)	179.80(3)	0.000
592.01(2)	179.80(3)	0.000
592.01(2)	179.80(3)	0.000
592.01(2)	179.79(3)	0.001
592.01(2)	179.79(3)	0.001
592.01(2)	179.79(3)	0.001
592.01(2)	179.79(3)	0.001
592.01(2)	179.78(3)	0.002
592.01(2)	179.78(3)	0.003
592.00(2)	179.78(3)	0.002
592.00(2)	179.79(3)	0.001
592.02(2)	179.79(3)	0.001
592.03(2)	179.79(3)	0.001
592.03(2)	179.79(3)	0.001
592.03(2)	179.79(3)	0.001
592.02(2)	179.79(3)	0.001
592.03(2)	179.79(3)	0.001
592.03(2)	179.79(3)	0.001
592.03(2)	179.79(3)	0.001
592.03(2)	179.78(3)	0.002
592.02(2)	179.78(3)	0.002
592.04(2)	179.78(4)	0.003
592.04(2)	179.77(4)	0.004
592.03(2)	179.77(4)	0.003
592.04(2)	179.77(4)	0.003
592.04(2)	179.77(4)	0.003
592.03(2)	179.76(4)	0.004
592.03(2)	179.77(4)	0.004
592.03(2)	179.77(4)	0.003
592.03(2)	179.76(4)	0.005

Table A.4 continued

CaNbF6 Volume (Å^3)	NaCl Volume (Å^3)	Pressure (GPa)
592.03(2)	179.76(4)	0.004
592.03(2)	179.75(4)	0.006
592.04(2)	179.75(4)	0.006
592.02(2)	179.75(4)	0.006
592.01(2)	179.77(4)	0.004
592.02(2)	179.74(4)	0.007
592.03(2)	179.76(3)	0.005
592.05(2)	179.75(3)	0.006
592.05(2)	179.74(3)	0.008
592.03(2)	179.71(3)	0.012
592.03(2)	179.70(3)	0.013
592.05(2)	179.68(3)	0.015
592.03(2)	179.70(4)	0.013
592.03(2)	179.72(4)	0.010
592.03(2)	179.72(4)	0.010
592.04(2)	179.72(4)	0.010
592.03(2)	179.72(4)	0.010
592.03(2)	179.73(4)	0.009
592.03(2)	179.74(4)	0.008
592.02(2)	179.74(4)	0.008
591.95(2)	179.71(4)	0.012
591.86(2)	179.68(4)	0.015
591.79(2)	179.67(4)	0.017
591.73(2)	179.63(4)	0.023
591.60(2)	179.58(4)	0.029
591.46(2)	179.50(4)	0.040
591.32(2)	179.45(4)	0.047
591.20(2)	179.39(4)	0.054
591.12(2)	179.38(4)	0.056
591.04(2)	179.32(4)	0.063
590.89(2)	179.27(4)	0.070
590.74(2)	179.21(4)	0.079
590.56(2)	179.13(4)	0.090
590.32(2)	179.05(3)	0.101
590.09(2)	178.97(3)	0.112
589.94(2)	178.91(3)	0.120
589.75(2)	178.82(3)	0.132
589.50(2)	178.74(3)	0.143
589.12(2)	178.62(3)	0.159

Table A.4 continued

CaNbF6 Volume (Å^3)	NaCl Volume (Å^3)	Pressure (GPa)
588.65(2)	178.49(3)	0.178
588.34(2)	178.35(3)	0.198
587.99(2)	178.23(3)	0.214
587.47(2)	178.04(3)	0.240
587.02(2)	177.88(3)	0.263
586.58(2)	177.74(3)	0.283
585.84(2)	177.52(3)	0.315
585.06(2)	177.28(3)	0.349
584.47(2)	177.12(3)	0.372

Table A.5: Lattice constants and unit cell volume for $MgNbF_6$ as determined from the Rietveld analysis of the x-ray diffraction data acquired while using a Cryostream.

Temperature (K)	Rwp	a (Å)	c (Å)	Volume (Å^3)
111	0.1702	5.4062(2)	13.724(1)	347.36(2)
114	0.1697	5.4073(2)	13.722(1)	347.47(2)
117	0.1691	5.4087(2)	13.720(1)	347.60(2)
120	0.1684	5.4101(2)	13.718(1)	347.73(2)
122	0.1677	5.4116(2)	13.716(1)	347.87(2)
125	0.1669	5.4131(2)	13.714(1)	348.01(2)
128	0.1661	5.4145(2)	13.713(1)	348.15(2)
130	0.1653	5.4159(2)	13.711(1)	348.29(2)
133	0.1645	5.4174(2)	13.709(1)	348.43(2)
136	0.1637	5.4188(2)	13.707(1)	348.57(2)
139	0.1629	5.4202(2)	13.706(1)	348.71(2)
141	0.1620	5.4216(2)	13.704(1)	348.85(2)
144	0.1611	5.4230(2)	13.703(1)	348.99(2)
147	0.1603	5.4244(2)	13.7009(9)	349.13(2)
149	0.1594	5.4258(2)	13.6994(9)	349.27(2)
153	0.1585	5.4272(2)	13.6979(9)	349.42(2)
156	0.1577	5.4287(2)	13.6963(9)	349.57(2)

Table A.5 continued

Temperature (K)	Rwp	a (Å)	c (Å)	Volume (Å^3)
158	0.1569	5.4302(2)	13.6948(9)	349.72(2)
161	0.1561	5.4316(2)	13.6933(9)	349.86(2)
164	0.1551	5.4331(2)	13.6918(9)	350.01(2)
167	0.1542	5.4346(2)	13.6902(9)	350.17(2)
170	0.1534	5.4361(2)	13.6887(9)	350.33(2)
172	0.1524	5.4377(2)	13.6872(9)	350.49(2)
175	0.1516	5.4392(2)	13.6857(9)	350.65(2)
178	0.1507	5.4407(2)	13.6842(9)	350.80(2)
181	0.1499	5.4423(2)	13.6828(9)	350.96(2)
184	0.1490	5.4438(2)	13.6813(9)	351.13(2)
186	0.1483	5.4454(2)	13.6799(9)	351.29(2)
189	0.1474	5.4470(2)	13.6784(9)	351.47(2)
192	0.1466	5.4486(2)	13.6769(9)	351.63(2)
195	0.1458	5.4503(2)	13.6754(9)	351.81(2)
198	0.1448	5.4519(2)	13.6740(9)	351.98(2)
201	0.1440	5.4536(2)	13.6725(9)	352.16(2)
204	0.1431	5.4553(2)	13.6710(9)	352.35(2)
207	0.1421	5.4571(2)	13.6695(9)	352.54(2)
210	0.1411	5.4589(2)	13.6679(9)	352.73(2)
213	0.1400	5.4607(2)	13.6665(9)	352.92(2)
216	0.1391	5.4625(2)	13.6649(9)	353.12(2)
219	0.1382	5.4643(2)	13.6635(9)	353.31(2)
222	0.1372	5.4662(2)	13.6620(9)	353.52(2)
225	0.1363	5.4681(2)	13.6605(9)	353.72(2)
228	0.1354	5.4700(2)	13.6590(9)	353.93(2)
231	0.1345	5.4719(2)	13.6575(9)	354.14(2)
234	0.1891	5.4737(2)	13.6558(9)	354.33(2)
237	0.1328	5.4760(2)	13.6544(9)	354.59(2)
240	0.1321	5.4780(2)	13.6529(9)	354.81(2)
242	0.1316	5.4801(2)	13.6514(9)	355.04(2)
245	0.1311	5.4822(2)	13.6499(9)	355.28(2)
248	0.1306	5.4845(2)	13.6483(9)	355.53(2)
251	0.1302	5.4869(2)	13.6466(9)	355.80(2)
254	0.1299	5.4893(2)	13.6448(9)	356.07(2)
257	0.1296	5.4919(2)	13.6430(9)	356.36(2)
260	0.1294	5.4946(2)	13.6409(9)	356.66(2)
263	0.1291	5.4976(2)	13.6386(9)	356.98(2)
266	0.1290	5.5008(2)	13.6360(9)	357.33(2)
269	0.1292	5.5046(2)	13.6329(9)	357.74(2)

Table A.5 continued

Temperature (K)	Rwp	a (Å)	c (Å)	Volume (Å^3)
272	0.1320	5.5093(2)	13.6296(9)	358.27(2)
275	0.1459	5.5158(2)	13.625(1)	358.98(2)
278	0.1679	5.5237(3)	13.616(1)	359.79(2)
281	0.1879	7.8354(2)	-	481.04(3)
284	0.1817	7.8407(2)	-	482.01(3)
287	0.1649	7.8444(1)	-	482.71(2)
290	0.1520	7.8463(1)	-	483.05(2)
293	0.1465	7.8472(1)	-	483.22(2)
296	0.1427	7.8479(1)	-	483.35(2)
299	0.1395	7.8484(1)	-	483.44(2)
302	0.1370	7.8489(1)	-	483.53(2)
305	0.1345	7.8493(1)	-	483.60(2)
308	0.1324	7.8496(1)	-	483.67(2)
311	0.1304	7.8500(1)	-	483.73(2)
316	0.1278	7.8504(1)	-	483.81(2)
319	0.1263	7.8506(1)	-	483.86(2)
323	0.1249	7.8509(1)	-	483.90(2)
326	0.1237	7.8511(1)	-	483.94(2)
329	0.1225	7.8513(1)	-	483.98(2)
333	0.1213	7.8515(1)	-	484.02(2)
336	0.1203	7.8517(1)	-	484.05(2)
339	0.1193	7.8519(1)	-	484.09(2)
343	0.1185	7.8521(1)	-	484.12(2)
346	0.1177	7.8522(1)	-	484.15(2)
349	0.1170	7.8524(1)	-	484.18(2)
353	0.1164	7.8525(1)	-	484.20(2)
356	0.1157	7.8527(1)	-	484.23(2)
360	0.1151	7.8528(1)	-	484.25(2)
363	0.1145	7.8529(1)	-	484.28(2)
367	0.1140	7.8530(1)	-	484.30(2)
370	0.1134	7.8532(1)	-	484.32(2)
374	0.1129	7.8533(1)	-	484.34(2)
378	0.1126	7.8534(1)	-	484.36(2)
381	0.1122	7.8535(1)	-	484.38(2)
384	0.1119	7.8536(1)	-	484.40(2)
387	0.1116	7.8536(1)	-	484.41(2)
390	0.1114	7.8537(1)	-	484.42(2)
393	0.1111	7.8538(1)	-	484.44(2)
396	0.1108	7.8539(1)	-	484.45(2)

Table A.5 continued

Temperature (K)	Rwp	a (Å)	c (Å)	Volume (Å^3)
399	0.1105	7.8539(1)	-	484.46(2)
403	0.1103	7.8540(1)	-	484.48(2)
406	0.1100	7.8541(1)	-	484.49(2)
409	0.1098	7.8542(1)	-	484.51(2)
412	0.1096	7.8542(1)	-	484.52(2)
415	0.1094	7.8543(1)	-	484.53(2)
418	0.1094	7.8544(1)	-	484.55(2)
422	0.1092	7.8545(1)	-	484.56(2)
425	0.1090	7.8545(1)	-	484.57(2)
427	0.1089	7.8546(1)	-	484.58(2)
430	0.1088	7.8546(1)	-	484.59(2)
433	0.1087	7.8547(1)	-	484.60(2)
436	0.1086	7.8547(1)	-	484.61(2)
439	0.1084	7.8548(1)	-	484.62(2)
442	0.1084	7.8549(1)	-	484.64(2)
444	0.1083	7.8549(1)	-	484.65(2)
447	0.1083	7.8550(1)	-	484.65(2)
450	0.1082	7.8550(1)	-	484.66(2)
452	0.1082	7.8550(1)	-	484.67(2)
455	0.1081	7.8551(1)	-	484.68(2)
457	0.1082	7.8552(1)	-	484.69(2)
460	0.1081	7.8552(1)	-	484.70(2)
463	0.1081	7.8552(1)	-	484.71(2)
465	0.1080	7.8553(1)	-	484.71(2)
468	0.1080	7.8553(1)	-	484.72(2)
471	0.1079	7.8554(1)	-	484.73(2)
473	0.1079	7.8554(1)	-	484.74(2)
476	0.1078	7.8555(1)	-	484.74(2)
478	0.1077	7.8555(1)	-	484.75(2)
481	0.1077	7.8555(1)	-	484.76(2)
483	0.1076	7.8556(1)	-	484.77(2)
486	0.1078	7.8556(1)	-	484.78(2)
488	0.1076	7.8557(1)	-	484.79(2)
491	0.1077	7.8557(1)	-	484.79(2)
493	0.1076	7.8558(1)	-	484.80(2)
495	0.1075	7.8558(1)	-	484.81(2)
498	0.1074	7.8558(1)	-	484.81(2)
501	0.1074	7.8559(1)	-	484.82(2)
503	0.1075	7.8559(1)	-	484.83(2)

Table A.5 continued

Temperature (K)	Rwp	a (Å)	c (Å)	Volume (Å^3)
503	0.1074	7.8559(1)	-	484.83(2)
502	0.1076	7.8559(1)	-	484.83(2)
500	0.1076	7.8559(1)	-	484.82(2)
498	0.1076	7.8558(1)	-	484.81(2)
496	0.1076	7.8558(1)	-	484.81(2)
494	0.1078	7.8558(1)	-	484.80(2)
491	0.1079	7.8557(1)	-	484.80(2)
489	0.1080	7.8557(1)	-	484.79(2)
487	0.1079	7.8556(1)	-	484.78(2)
484	0.1081	7.8556(1)	-	484.77(2)
481	0.1082	7.8555(1)	-	484.76(2)
478	0.1083	7.8555(1)	-	484.75(2)
475	0.1084	7.8555(1)	-	484.74(2)
472	0.1084	7.8554(1)	-	484.73(2)
471	0.1085	7.8553(1)	-	484.72(2)
469	0.1085	7.8553(1)	-	484.71(2)
467	0.1086	7.8552(1)	-	484.70(2)
461	0.1087	7.8552(1)	-	484.69(2)
458	0.1088	7.8551(1)	-	484.68(2)
455	0.1090	7.8551(1)	-	484.67(2)
452	0.1091	7.8550(1)	-	484.66(2)
449	0.1091	7.8549(1)	-	484.65(2)
446	0.1092	7.8549(1)	-	484.64(2)
444	0.1093	7.8548(1)	-	484.63(2)
441	0.1095	7.8548(1)	-	484.62(2)
438	0.1096	7.8547(1)	-	484.61(2)
435	0.1097	7.8546(1)	-	484.59(2)
432	0.1099	7.8546(1)	-	484.58(2)
429	0.1100	7.8545(1)	-	484.57(2)
426	0.1102	7.8544(1)	-	484.56(2)
424	0.1104	7.8544(1)	-	484.55(2)
421	0.1106	7.8543(1)	-	484.53(2)
418	0.1108	7.8543(1)	-	484.52(2)
415	0.1110	7.8542(1)	-	484.51(2)
412	0.1112	7.8541(1)	-	484.50(2)
409	0.1114	7.8540(1)	-	484.48(2)
406	0.1117	7.8540(1)	-	484.47(2)
403	0.1119	7.8539(1)	-	484.46(2)
400	0.1122	7.8538(1)	-	484.44(2)

Table A.5 continued

Temperature (K)	Rwp	a (Å)	c (Å)	Volume (Å^3)
396	0.1125	7.8538(1)	-	484.43(2)
394	0.1127	7.8537(1)	-	484.42(2)
391	0.1130	7.8536(1)	-	484.40(2)
388	0.1132	7.8535(1)	-	484.39(2)
385	0.1135	7.8535(1)	-	484.37(2)
382	0.1138	7.8534(1)	-	484.36(2)
379	0.1143	7.8533(1)	-	484.34(2)
375	0.1146	7.8532(1)	-	484.32(2)
372	0.1152	7.8531(1)	-	484.31(2)
368	0.1157	7.8530(1)	-	484.28(2)
365	0.1162	7.8528(1)	-	484.26(2)
362	0.1168	7.8527(1)	-	484.24(2)
358	0.1174	7.8526(1)	-	484.21(2)
355	0.1180	7.8525(1)	-	484.19(2)
352	0.1188	7.8523(1)	-	484.16(2)
348	0.1195	7.8522(1)	-	484.14(2)
345	0.1203	7.8520(1)	-	484.11(2)
342	0.1212	7.8519(1)	-	484.08(2)
338	0.1222	7.8517(1)	-	484.05(2)
335	0.1232	7.8515(1)	-	484.01(2)
332	0.1244	7.8513(1)	-	483.98(2)
329	0.1255	7.8511(1)	-	483.94(2)
325	0.1268	7.8509(1)	-	483.90(2)
322	0.1283	7.8506(1)	-	483.85(2)
319	0.1299	7.8504(1)	-	483.80(2)
314	0.1327	7.8499(1)	-	483.71(2)
311	0.1344	7.8495(1)	-	483.65(2)
308	0.1366	7.8492(1)	-	483.58(2)
305	0.1389	7.8488(1)	-	483.51(2)
302	0.1416	7.8483(1)	-	483.42(2)
299	0.1446	7.8477(1)	-	483.31(2)
296	0.1485	7.8470(1)	-	483.18(2)
293	0.1543	7.8460(1)	-	482.99(2)
290	0.1656	7.8441(1)	-	482.65(2)
287	0.1790	7.8407(2)	-	482.02(2)
285	0.1847	7.8360(2)	-	481.15(3)
282	0.1826	7.8308(2)	-	480.20(3)
279	0.1606	5.5188(3)	13.623(1)	359.33(2)
276	0.1446	5.5126(2)	13.627(1)	358.62(2)

Table A.5 continued

Temperature (K)	Rwp	a (Å)	c (Å)	Volume (Å^3)
273	0.1329	5.5075(2)	13.6300(9)	358.04(2)
270	0.1287	5.5034(2)	13.6326(9)	357.58(2)
267	0.1273	5.5001(2)	13.6350(9)	357.21(2)
264	0.1267	5.4971(2)	13.6371(9)	356.88(2)
261	0.1268	5.4944(2)	13.6391(9)	356.58(2)
258	0.1271	5.4917(2)	13.6409(9)	356.28(2)
255	0.1278	5.4893(2)	13.6427(9)	356.01(2)
252	0.1288	5.4869(2)	13.6445(9)	355.75(2)
249	0.1299	5.4846(2)	13.6461(9)	355.49(2)
246	0.1309	5.4825(2)	13.6476(9)	355.26(2)
243	0.1322	5.4803(2)	13.6493(9)	355.02(2)
241	0.1334	5.4783(2)	13.6509(9)	354.79(2)
238	0.1347	5.4762(2)	13.6524(9)	354.57(2)
235	0.1362	5.4742(2)	13.6540(9)	354.35(2)
232	0.1375	5.4723(2)	13.6556(9)	354.14(2)
229	0.1388	5.4703(2)	13.6571(9)	353.93(2)
226	0.1400	5.4684(2)	13.6587(9)	353.72(2)
223	0.1413	5.4665(2)	13.6602(9)	353.52(2)
220	0.1426	5.4647(2)	13.6618(9)	353.32(2)
217	0.1438	5.4628(2)	13.6634(9)	353.12(2)
215	0.1449	5.4611(2)	13.6648(9)	352.94(2)
212	0.1462	5.4593(2)	13.6664(9)	352.74(2)
209	0.1473	5.4575(2)	13.6680(9)	352.55(2)
206	0.1485	5.4557(2)	13.6696(9)	352.36(2)
203	0.1497	5.4540(2)	13.6711(9)	352.18(2)
200	0.1508	5.4523(2)	13.6727(9)	352.00(2)
197	0.1517	5.4507(2)	13.6742(9)	351.83(2)
194	0.1527	5.4490(2)	13.6757(9)	351.66(2)
191	0.1538	5.4474(2)	13.6772(9)	351.48(2)
188	0.1547	5.4458(2)	13.6787(9)	351.32(2)
186	0.1557	5.4442(2)	13.6802(9)	351.15(2)
183	0.1566	5.4427(2)	13.6817(9)	350.99(2)
180	0.1575	5.4411(2)	13.6832(9)	350.82(2)
177	0.1584	5.4395(2)	13.6847(9)	350.66(2)
174	0.1593	5.4380(2)	13.6862(9)	350.50(2)
171	0.1602	5.4364(2)	13.6877(9)	350.34(2)
168	0.1613	5.4348(2)	13.6894(9)	350.18(2)
165	0.1622	5.4333(2)	13.6909(9)	350.02(2)
163	0.1630	5.4318(2)	13.6924(9)	349.87(2)

Table A.5 continued

Temperature (K)	Rwp	a (Å)	c (Å)	Volume (Å^3)
160	0.1639	5.4304(2)	13.6939(9)	349.72(2)
157	0.1647	5.4289(2)	13.6955(9)	349.56(2)
154	0.1657	5.4274(2)	13.697(1)	349.41(2)
152	0.1665	5.4260(2)	13.699(1)	349.27(2)
149	0.1674	5.4245(2)	13.700(1)	349.12(2)
146	0.1682	5.4231(2)	13.702(1)	348.98(2)
144	0.1690	5.4217(2)	13.703(1)	348.84(2)
141	0.1698	5.4202(2)	13.705(1)	348.70(2)
139	0.1706	5.4188(2)	13.707(1)	348.55(2)
136	0.1713	5.4174(2)	13.708(1)	348.41(2)
134	0.1720	5.4160(2)	13.710(1)	348.27(2)
131	0.1727	5.4145(2)	13.712(1)	348.13(2)
128	0.1735	5.4130(2)	13.714(1)	347.98(2)
126	0.1742	5.4114(2)	13.716(1)	347.84(2)
123	0.1749	5.4100(3)	13.718(1)	347.70(2)
120	0.1755	5.4086(3)	13.719(1)	347.56(2)
117	0.1760	5.4072(3)	13.721(1)	347.44(2)

Table A.6: Lattice constants and unit cell volume for $MgZrF_6$ as determined from the Rietveld analysis of the x-ray diffraction data acquired while using a Cryostream.

Temperature (K)	Rwp	a (Å)	Volume (Å^3)
112	0.1414	7.94604(7)	501.71(2)
116	0.1407	7.94628(7)	501.76(1)
116	0.1396	7.94642(7)	501.78(1)
120	0.1375	7.94672(7)	501.84(1)
123	0.1367	7.94685(7)	501.86(1)
125	0.1353	7.94692(7)	501.88(1)
128	0.1334	7.94698(7)	501.89(1)
131	0.1319	7.94701(7)	501.89(1)
133	0.1307	7.94702(7)	501.89(1)
136	0.1305	7.94699(7)	501.89(1)
139	0.1285	7.94695(7)	501.88(1)

Table A.6 continued

Temperature (K)	Rwp	a (Å)	Volume (Å^3)
142	0.1275	7.94691(7)	501.87(1)
145	0.1271	7.94684(7)	501.86(1)
146	0.1254	7.94680(7)	501.85(1)
148	0.1244	7.94677(7)	501.85(1)
154	0.1240	7.94665(6)	501.83(1)
155	0.1244	7.94658(6)	501.81(1)
159	0.1226	7.94649(6)	501.80(1)
161	0.1215	7.94642(6)	501.78(1)
164	0.1204	7.94632(6)	501.76(1)
167	0.1201	7.94623(6)	501.75(1)
170	0.1196	7.94615(6)	501.73(1)
173	0.1192	7.94606(6)	501.71(1)
175	0.1186	7.94598(6)	501.70(1)
178	0.1182	7.94588(6)	501.68(1)
181	0.1174	7.94579(6)	501.66(1)
184	0.1164	7.94569(6)	501.64(1)
187	0.1163	7.94559(6)	501.63(1)
190	0.1156	7.94549(6)	501.61(1)
193	0.1152	7.94539(6)	501.59(1)
196	0.1149	7.94529(6)	501.57(1)
198	0.1147	7.94520(6)	501.55(1)
201	0.1142	7.94512(6)	501.54(1)
205	0.1139	7.94503(6)	501.52(1)
207	0.1140	7.94492(6)	501.50(1)
210	0.1136	7.94482(6)	501.48(1)
213	0.1133	7.94471(6)	501.46(1)
216	0.1129	7.94462(6)	501.44(1)
219	0.1125	7.94454(6)	501.43(1)
222	0.1122	7.94444(6)	501.41(1)
225	0.1118	7.94435(6)	501.39(1)
228	0.1115	7.94426(6)	501.37(1)
231	0.1112	7.94418(6)	501.36(1)
234	0.1109	7.94409(6)	501.34(1)
237	0.1110	7.94399(6)	501.32(1)
240	0.1106	7.94390(6)	501.30(1)
243	0.1101	7.94382(6)	501.29(1)
246	0.1098	7.94373(6)	501.27(1)
248	0.1098	7.94365(6)	501.26(1)
251	0.1097	7.94357(6)	501.24(1)

Table A.6 continued

Temperature (K)	Rwp	a (Å)	Volume (Å^3)
254	0.1095	7.94348(6)	501.23(1)
257	0.1092	7.94342(6)	501.21(1)
260	0.1090	7.94334(6)	501.20(1)
263	0.1087	7.94327(6)	501.18(1)
266	0.1090	7.94319(6)	501.17(1)
269	0.1087	7.94312(6)	501.16(1)
272	0.1087	7.94303(6)	501.14(1)
275	0.1083	7.94297(6)	501.13(1)
278	0.1077	7.94291(6)	501.12(1)
281	0.1077	7.94283(6)	501.10(1)
284	0.1076	7.94276(6)	501.09(1)
287	0.1074	7.94268(6)	501.07(1)
290	0.1074	7.94261(6)	501.06(1)
293	0.1071	7.94254(6)	501.05(1)
296	0.1068	7.94248(6)	501.04(1)
299	0.1065	7.94240(6)	501.02(1)
302	0.1062	7.94233(6)	501.01(1)
305	0.1062	7.94226(6)	500.99(1)
308	0.1063	7.94219(6)	500.98(1)
312	0.1063	7.94212(6)	500.97(1)
316	0.1063	7.94202(6)	500.95(1)
320	0.1060	7.94196(6)	500.94(1)
323	0.1062	7.94190(6)	500.93(1)
326	0.1056	7.94183(6)	500.91(1)
329	0.1053	7.94176(6)	500.90(1)
333	0.1046	7.94170(6)	500.89(1)
336	0.1044	7.94162(6)	500.87(1)
340	0.1044	7.94156(6)	500.86(1)
343	0.1040	7.94149(6)	500.85(1)
346	0.1040	7.94143(6)	500.84(1)
350	0.1038	7.94138(6)	500.83(1)
353	0.1037	7.94133(6)	500.82(1)
356	0.1036	7.94130(6)	500.81(1)
360	0.1033	7.94124(6)	500.80(1)
364	0.1035	7.94119(6)	500.79(1)
367	0.1036	7.94114(6)	500.78(1)
371	0.1040	7.94108(6)	500.77(1)
374	0.1042	7.94103(6)	500.76(1)
378	0.1038	7.94099(6)	500.75(1)

Table A.6 continued

Temperature (K)	Rwp	a (Å)	Volume (Å^3)
381	0.1037	7.94096(6)	500.75(1)
385	0.1038	7.94092(6)	500.74(1)
388	0.1036	7.94089(6)	500.74(1)
390	0.1034	7.94086(6)	500.73(1)
393	0.1033	7.94082(6)	500.72(1)
396	0.1040	7.94079(6)	500.72(1)
400	0.1033	7.94075(6)	500.71(1)
403	0.1033	7.94071(6)	500.70(1)
406	0.1032	7.94068(6)	500.70(1)
409	0.1029	7.94066(6)	500.69(1)
412	0.1028	7.94062(6)	500.68(1)
416	0.1028	7.94059(6)	500.68(1)
419	0.1027	7.94056(6)	500.67(1)
422	0.1025	7.94053(6)	500.67(1)
425	0.1025	7.94050(6)	500.66(1)
428	0.1023	7.94047(6)	500.66(1)
431	0.1022	7.94046(6)	500.65(1)
434	0.1020	7.94042(6)	500.65(1)
437	0.1020	7.94041(6)	500.64(1)
440	0.1019	7.94040(6)	500.64(1)
443	0.1017	7.94037(6)	500.64(1)
443	0.1017	7.94038(6)	500.64(1)
447	0.1016	7.94036(6)	500.63(1)
451	0.1014	7.94034(6)	500.63(1)
451	0.1012	7.94032(6)	500.63(1)
456	0.1010	7.94030(6)	500.62(1)
457	0.1008	7.94029(6)	500.62(1)
461	0.1007	7.94027(6)	500.62(1)
464	0.1006	7.94026(6)	500.62(1)
464	0.1004	7.94026(6)	500.62(1)
468	0.1003	7.94026(6)	500.62(1)
471	0.1002	7.94024(6)	500.61(1)
474	0.1001	7.94024(6)	500.61(1)
477	0.1002	7.94025(6)	500.61(1)
479	0.1001	7.94024(6)	500.61(1)
482	0.1000	7.94023(6)	500.61(1)
484	0.1001	7.94024(6)	500.61(1)
487	0.1001	7.94025(6)	500.61(1)
489	0.1002	7.94025(6)	500.61(1)

Table A.6 continued

Temperature (K)	Rwp	a (Å)	Volume (Å^3)
492	0.1001	7.94023(6)	500.61(1)
494	0.1001	7.94025(6)	500.61(1)
496	0.0999	7.94025(6)	500.61(1)
499	0.0998	7.94025(6)	500.61(1)
501	0.0999	7.94026(6)	500.62(1)
504	0.0998	7.94025(6)	500.61(1)
504	0.0997	7.94026(6)	500.62(1)
502	0.0994	7.94026(6)	500.61(1)
499	0.0995	7.94026(6)	500.62(1)
498	0.0995	7.94025(6)	500.61(1)
496	0.0995	7.94025(6)	500.61(1)
494	0.0995	7.94025(6)	500.61(1)
491	0.0996	7.94024(6)	500.61(1)
489	0.0994	7.94025(6)	500.61(1)
486	0.0994	7.94025(6)	500.61(1)
483	0.0995	7.94025(6)	500.61(1)
481	0.0994	7.94026(6)	500.62(1)
478	0.0994	7.94027(6)	500.62(1)
475	0.0997	7.94027(6)	500.62(1)
473	0.0995	7.94028(6)	500.62(1)
470	0.0994	7.94028(6)	500.62(1)
468	0.0992	7.94028(6)	500.62(1)
464	0.0994	7.94029(6)	500.62(1)
461	0.0991	7.94029(6)	500.62(1)
458	0.0993	7.94031(6)	500.63(1)
455	0.0993	7.94032(6)	500.63(1)
452	0.0992	7.94033(6)	500.63(1)
449	0.0993	7.94035(6)	500.63(1)
447	0.0994	7.94037(6)	500.64(1)
444	0.0995	7.94038(6)	500.64(1)
441	0.0995	7.94039(6)	500.64(1)
438	0.0998	7.94041(6)	500.65(1)
435	0.0999	7.94044(6)	500.65(1)
432	0.1001	7.94045(6)	500.65(1)
429	0.1000	7.94047(6)	500.66(1)
426	0.1002	7.94050(6)	500.66(1)
423	0.1002	7.94051(6)	500.66(1)
420	0.1000	7.94052(6)	500.67(1)
417	0.1002	7.94055(6)	500.67(1)

Table A.6 continued

Temperature (K)	Rwp	a (Å)	Volume (Å^3)
414	0.1003	7.94058(6)	500.68(1)
411	0.1002	7.94060(6)	500.68(1)
408	0.1002	7.94063(6)	500.68(1)
405	0.1001	7.94063(6)	500.68(1)
402	0.1000	7.94064(6)	500.69(1)
399	0.1000	7.94064(6)	500.69(1)
396	0.1005	7.94065(6)	500.69(1)
393	0.1010	7.94065(6)	500.69(1)
391	0.1012	7.94067(6)	500.69(1)
388	0.1015	7.94070(6)	500.70(1)
385	0.1014	7.94072(6)	500.70(1)
381	0.1014	7.94075(6)	500.71(1)
378	0.1014	7.94078(6)	500.71(1)
374	0.1016	7.94082(6)	500.72(1)
372	0.1015	7.94085(6)	500.73(1)
368	0.1017	7.94089(6)	500.73(1)
365	0.1015	7.94092(6)	500.74(1)
361	0.1016	7.94097(6)	500.75(1)
358	0.1016	7.94101(6)	500.76(1)
355	0.1015	7.94105(6)	500.76(1)
351	0.1015	7.94109(6)	500.77(1)
348	0.1017	7.94114(6)	500.78(1)
344	0.1019	7.94119(6)	500.79(1)
341	0.1020	7.94125(6)	500.80(1)
338	0.1020	7.94130(6)	500.81(1)
335	0.1022	7.94137(6)	500.83(1)
331	0.1021	7.94142(6)	500.84(1)
328	0.1023	7.94149(6)	500.85(1)
325	0.1025	7.94157(6)	500.86(1)
322	0.1024	7.94164(6)	500.88(1)
319	0.1022	7.94171(6)	500.89(1)
313	0.1021	7.94181(6)	500.91(1)
311	0.1023	7.94186(6)	500.92(1)
308	0.1023	7.94195(6)	500.93(1)
305	0.1024	7.94201(6)	500.95(1)
302	0.1025	7.94207(6)	500.96(1)
299	0.1026	7.94214(6)	500.97(1)
296	0.1028	7.94221(6)	500.98(1)
293	0.1030	7.94228(6)	501.00(1)

Table A.6 continued

Temperature (K)	Rwp	a (Å)	Volume (Å^3)
290	0.1033	7.94235(6)	501.01(1)
288	0.1033	7.94241(6)	501.02(1)
285	0.1036	7.94248(6)	501.04(1)
282	0.1035	7.94254(6)	501.05(1)
279	0.1038	7.94262(6)	501.06(1)
276	0.1044	7.94269(6)	501.08(1)
273	0.1046	7.94276(6)	501.09(1)
270	0.1048	7.94282(6)	501.10(1)
267	0.1047	7.94289(6)	501.11(1)
264	0.1053	7.94296(6)	501.13(1)
262	0.1056	7.94304(6)	501.14(1)
258	0.1058	7.94310(6)	501.15(1)
255	0.1060	7.94318(6)	501.17(1)
253	0.1059	7.94325(6)	501.18(1)
250	0.1063	7.94333(6)	501.20(1)
247	0.1065	7.94340(6)	501.21(1)
244	0.1073	7.94348(6)	501.22(1)
241	0.1081	7.94357(6)	501.24(1)
238	0.1086	7.94365(6)	501.26(1)
235	0.1086	7.94373(6)	501.27(1)
232	0.1093	7.94381(6)	501.29(1)
229	0.1096	7.94389(6)	501.30(1)
226	0.1096	7.94398(6)	501.32(1)
223	0.1100	7.94408(6)	501.34(1)
220	0.1103	7.94415(6)	501.35(1)
217	0.1111	7.94425(6)	501.37(1)
214	0.1116	7.94434(6)	501.39(1)
212	0.1119	7.94443(6)	501.40(1)
209	0.1120	7.94452(6)	501.42(1)
206	0.1126	7.94462(6)	501.44(1)
203	0.1130	7.94471(6)	501.46(1)
199	0.1136	7.94481(6)	501.48(1)
197	0.1134	7.94490(6)	501.49(1)
193	0.1142	7.94499(6)	501.51(1)
192	0.1140	7.94507(6)	501.53(1)
187	0.1142	7.94518(6)	501.55(1)
186	0.1152	7.94524(6)	501.56(1)
181	0.1162	7.94535(6)	501.58(1)
181	0.1166	7.94542(6)	501.59(1)

Table A.6 continued

Temperature (K)	Rwp	a (Å)	Volume (Å^3)
176	0.1171	7.94553(6)	501.61(1)
176	0.1176	7.94561(6)	501.63(1)
173	0.1188	7.94569(6)	501.64(1)
169	0.1196	7.94578(6)	501.66(1)
165	0.1194	7.94588(6)	501.68(1)
161	0.1204	7.94595(6)	501.69(1)
160	0.1216	7.94605(6)	501.71(1)
159	0.1229	7.94608(6)	501.72(1)
156	0.1232	7.94615(6)	501.73(1)
153	0.1244	7.94623(6)	501.75(1)
150	0.1251	7.94628(6)	501.75(1)
147	0.1273	7.94632(7)	501.76(1)
144	0.1273	7.94635(7)	501.77(1)
141	0.1282	7.94638(7)	501.77(1)
139	0.1299	7.94639(7)	501.78(1)
136	0.1307	7.94637(7)	501.77(1)
133	0.1324	7.94633(7)	501.76(1)
130	0.1339	7.94627(7)	501.75(1)
127	0.1360	7.94617(7)	501.74(1)
127	0.1366	7.94614(7)	501.73(1)
123	0.1369	7.94592(7)	501.69(1)
121	0.1392	7.94571(7)	501.65(1)
118	0.1397	7.94542(7)	501.59(1)

Table A.7: Lattice constants and unit cell volume for $MgZrF_6$ as determined from the Rietveld analysis of the high resolution x-ray diffraction data acquired using a helium cryostat.

Temperature (K)	Rwp	a (Å)	c (Å)	Volume (Å^3)
150.0	0.2463	7.94237(1)	-	501.014(2)
150.0	0.2481	7.94237(1)	-	501.014(2)
150.0	0.2472	7.94236(1)	-	501.012(2)
150.0	0.2472	7.94238(1)	-	501.016(2)
150.0	0.2474	7.94238(1)	-	501.016(2)
150.0	0.2477	7.94236(1)	-	501.013(2)
150.0	0.2469	7.94238(1)	-	501.017(2)
150.0	0.2462	7.94238(1)	-	501.016(2)

Table A.7 continued

Temperature (K)	Rwp	a (Å)	c (Å)	Volume (Å^3)
150.0	0.2466	7.94237(1)	-	501.014(2)
150.0	0.2471	7.94238(1)	-	501.016(2)
150.0	0.2468	7.94238(1)	-	501.016(2)
149.8	0.2472	7.94238(1)	-	501.017(2)
147.6	0.2505	7.94246(1)	-	501.032(2)
144.9	0.2536	7.94256(1)	-	501.050(2)
142.1	0.2568	7.94265(1)	-	501.068(2)
139.3	0.2602	7.94273(1)	-	501.082(2)
136.5	0.2641	7.94281(1)	-	501.098(2)
133.7	0.2685	7.94287(1)	-	501.109(2)
131.0	0.2737	7.94293(1)	-	501.121(2)
128.2	0.2789	7.94297(1)	-	501.128(2)
125.4	0.2836	7.94300(1)	-	501.133(2)
122.6	0.2899	7.94301(1)	-	501.137(2)
119.8	0.2967	7.94300(1)	-	501.134(2)
117.1	0.3033	7.94296(1)	-	501.126(2)
114.3	0.3089	7.94286(1)	-	501.108(3)
111.5	0.3166	7.94269(2)	-	501.075(3)
108.7	0.3206	7.94241(2)	-	501.022(3)
105.9	0.3280	7.94195(2)	-	500.935(3)
103.1	0.3348	7.94121(2)	-	500.795(4)
100.4	0.3425	7.94004(2)	-	500.574(5)
97.6	0.3310	5.61003(6)	13.7622(3)	375.102(4)
94.8	0.3110	5.60729(5)	13.7642(2)	374.790(4)
92.0	0.2920	5.60438(4)	13.7664(2)	374.460(4)
89.2	0.2702	5.60138(3)	13.7687(2)	374.123(4)
86.5	0.2528	5.59866(3)	13.7704(1)	373.805(3)
83.7	0.2421	5.59622(3)	13.7715(1)	373.511(3)
80.9	0.2356	5.59400(3)	13.7726(1)	373.243(3)
78.1	0.2325	5.59200(3)	13.7735(1)	373.001(3)
75.3	0.2301	5.59016(3)	13.7743(1)	372.778(3)
72.6	0.2310	5.58852(3)	13.7752(1)	372.583(3)
69.8	0.2283	5.58699(3)	13.7759(1)	372.397(3)
67.0	0.2301	5.58558(3)	13.7766(1)	372.227(3)
64.2	0.2293	5.58425(3)	13.7773(1)	372.070(3)
61.4	0.2296	5.58304(3)	13.7777(1)	371.919(3)

Table A.7 continued

Temperature (K)	Rwp	a (Å)	c (Å)	Volume (Å^3)
58.6	0.2322	5.58187(3)	13.7783(1)	371.781(3)
55.9	0.2334	5.58078(3)	13.7790(1)	371.654(3)
53.1	0.2310	5.57983(3)	13.7795(1)	371.540(3)
50.3	0.2327	5.57894(3)	13.7798(1)	371.430(3)
47.5	0.2337	5.57813(3)	13.7801(1)	371.331(3)
44.7	0.2338	5.57736(3)	13.7805(1)	371.239(3)
42.0	0.2340	5.57659(3)	13.7809(1)	371.146(3)
39.2	0.2344	5.57598(3)	13.7810(1)	371.070(3)
36.4	0.2346	5.57537(3)	13.7817(1)	371.005(3)
33.6	0.2354	5.57487(3)	13.7816(1)	370.937(3)
30.9	0.2365	5.57438(3)	13.7820(1)	370.882(3)
28.1	0.2353	5.57389(3)	13.7822(1)	370.823(3)
25.3	0.2360	5.57348(3)	13.7825(1)	370.776(3)
22.5	0.2370	5.57316(3)	13.7825(1)	370.735(3)
19.7	0.2375	5.57284(3)	13.7828(1)	370.698(3)
17.0	0.2368	5.57252(3)	13.7830(1)	370.661(3)
14.2	0.2377	5.57228(3)	13.7832(1)	370.636(3)
11.3	0.2390	5.57217(3)	13.7833(1)	370.624(3)

Table A.8: Lattice constants and unit cell volume for the $MgZrF_6$ as determined from the Rietveld analysis of the x-ray diffraction data acquired while using a furnace.

Temperature (K)	Rwp	a (Å)	Volume (Å^3)
299	0.1112	7.94134(7)	500.82(1)
299	0.1111	7.94137(7)	500.83(1)
299	0.1112	7.94139(7)	500.83(1)
299	0.1112	7.94140(7)	500.83(1)
300	0.1112	7.94139(7)	500.83(1)
301	0.1112	7.94136(7)	500.82(1)
304	0.1112	7.94128(7)	500.81(1)
307	0.1112	7.94123(7)	500.80(1)

Table A.8 continued

Temperature (K)	Rwp	a (Å)	Volume (Å^3)
309	0.1112	7.94118(7)	500.79(1)
311	0.1113	7.94114(7)	500.78(1)
313	0.1111	7.94108(7)	500.77(1)
315	0.1112	7.94104(7)	500.76(1)
317	0.1111	7.94099(7)	500.75(1)
319	0.1111	7.94093(7)	500.74(1)
320	0.1111	7.94092(7)	500.74(1)
323	0.1111	7.94087(7)	500.73(1)
325	0.1110	7.94083(7)	500.72(1)
327	0.1109	7.94077(7)	500.71(1)
329	0.1109	7.94073(7)	500.71(1)
331	0.1108	7.94069(7)	500.70(1)
333	0.1107	7.94064(7)	500.69(1)
336	0.1107	7.94059(7)	500.68(1)
336	0.1108	7.94059(7)	500.68(1)
340	0.1107	7.94052(7)	500.67(1)
341	0.1106	7.94049(7)	500.66(1)
343	0.1107	7.94045(7)	500.65(1)
345	0.1107	7.94044(7)	500.65(1)
347	0.1106	7.94039(7)	500.64(1)
349	0.1105	7.94033(7)	500.63(1)
351	0.1104	7.94031(7)	500.63(1)
354	0.1103	7.94026(7)	500.61(1)
355	0.1102	7.94025(7)	500.61(1)
357	0.1102	7.94022(7)	500.61(1)
360	0.1102	7.94018(7)	500.60(1)
361	0.1100	7.94015(7)	500.59(1)
362	0.1100	7.94013(7)	500.59(1)
363	0.1099	7.94010(7)	500.59(1)
367	0.1098	7.94005(7)	500.58(1)
369	0.1097	7.94003(7)	500.57(1)
372	0.1096	7.93999(7)	500.56(1)
374	0.1097	7.93994(7)	500.56(1)
374	0.1096	7.93994(7)	500.55(1)
377	0.1095	7.93990(7)	500.55(1)
379	0.1096	7.93987(7)	500.54(1)
381	0.1096	7.93984(7)	500.54(1)
383	0.1095	7.93982(7)	500.53(1)
384	0.1095	7.93981(7)	500.53(1)

Table A.8 continued

Temperature (K)	Rwp	a (Å)	Volume (Å^3)
387	0.1095	7.93978(7)	500.53(1)
389	0.1095	7.93974(7)	500.52(1)
391	0.1095	7.93972(7)	500.51(1)
394	0.1094	7.93969(7)	500.51(1)
395	0.1094	7.93970(7)	500.51(1)
397	0.1093	7.93965(7)	500.50(1)
399	0.1094	7.93965(7)	500.50(1)
401	0.1094	7.93963(7)	500.50(1)
401	0.1094	7.93959(7)	500.49(1)
405	0.1093	7.93957(7)	500.49(1)
407	0.1094	7.93956(7)	500.48(1)
406	0.1094	7.93956(7)	500.48(1)
411	0.1093	7.93951(7)	500.47(1)
412	0.1092	7.93950(7)	500.47(1)
415	0.1092	7.93947(7)	500.47(1)
419	0.1092	7.93943(7)	500.46(1)
419	0.1091	7.93944(7)	500.46(1)
423	0.1090	7.93940(7)	500.45(1)
424	0.1092	7.93940(7)	500.45(1)
423	0.1091	7.93938(7)	500.45(1)
428	0.1091	7.93937(7)	500.45(1)
429	0.1089	7.93934(7)	500.44(1)
431	0.1090	7.93933(7)	500.44(1)
434	0.1089	7.93933(7)	500.44(1)
435	0.1089	7.93932(7)	500.44(1)
436	0.1088	7.93931(7)	500.44(1)
439	0.1088	7.93929(7)	500.43(1)
441	0.1088	7.93929(7)	500.43(1)
444	0.1089	7.93926(7)	500.43(1)
445	0.1088	7.93926(7)	500.43(1)
445	0.1087	7.93926(7)	500.43(1)
449	0.1087	7.93925(7)	500.42(1)
449	0.1087	7.93923(7)	500.42(1)
451	0.1086	7.93923(7)	500.42(1)
454	0.1084	7.93921(7)	500.42(1)
455	0.1085	7.93920(7)	500.42(1)
460	0.1084	7.93918(7)	500.41(1)
458	0.1083	7.93918(7)	500.41(1)
463	0.1082	7.93917(7)	500.41(1)

Table A.8 continued

Temperature (K)	Rwp	a (Å)	Volume (Å^3)
465	0.1082	7.93916(7)	500.41(1)
467	0.1082	7.93917(7)	500.41(1)
468	0.1080	7.93916(7)	500.41(1)
471	0.1080	7.93915(7)	500.41(1)
473	0.1079	7.93914(7)	500.40(1)
475	0.1079	7.93913(7)	500.40(1)
477	0.1079	7.93913(7)	500.40(1)
479	0.1078	7.93912(7)	500.40(1)
481	0.1078	7.93911(7)	500.40(1)
483	0.1078	7.93912(7)	500.40(1)
484	0.1078	7.93912(7)	500.40(1)
488	0.1078	7.93913(7)	500.40(1)
488	0.1076	7.93912(7)	500.40(1)
492	0.1076	7.93912(7)	500.40(1)
492	0.1075	7.93912(7)	500.40(1)
496	0.1075	7.93912(7)	500.40(1)
495	0.1075	7.93912(7)	500.40(1)
497	0.1073	7.93913(7)	500.40(1)
600	0.1056	7.94049(7)	500.44(1)
600	0.1048	7.94051(7)	500.45(1)
603	0.1043	7.94057(7)	500.46(1)
604	0.1038	7.94054(7)	500.45(1)
609	0.1032	7.94057(7)	500.46(1)
608	0.1028	7.94058(7)	500.46(1)
610	0.1025	7.94062(7)	500.47(1)
613	0.1021	7.94062(7)	500.47(1)
616	0.1020	7.94066(7)	500.48(1)
616	0.1016	7.94066(7)	500.48(1)
619	0.1014	7.94067(7)	500.48(1)
623	0.1012	7.94073(7)	500.49(1)
623	0.1010	7.94074(7)	500.49(1)
623	0.1010	7.94077(7)	500.50(1)
628	0.1009	7.94079(7)	500.50(1)
629	0.1011	7.94083(7)	500.51(1)
632	0.1009	7.94082(7)	500.51(1)
634	0.1010	7.94085(7)	500.51(1)
635	0.1009	7.94085(7)	500.51(1)
638	0.1007	7.94088(7)	500.52(1)
639	0.1008	7.94091(7)	500.52(1)

Table A.8 continued

Temperature (K)	Rwp	a (Å)	Volume (Å^3)
640	0.1009	7.94090(7)	500.52(1)
644	0.1010	7.94094(7)	500.53(1)
645	0.1011	7.94099(7)	500.54(1)
648	0.1010	7.94101(7)	500.54(1)
649	0.1011	7.94101(7)	500.54(1)
651	0.1010	7.94101(7)	500.54(1)
654	0.1012	7.94107(7)	500.55(1)
656	0.1012	7.94108(7)	500.55(1)
658	0.1013	7.94112(7)	500.56(1)
659	0.1013	7.94115(7)	500.57(1)
663	0.1015	7.94117(7)	500.57(1)
664	0.1017	7.94123(7)	500.58(1)
666	0.1018	7.94125(7)	500.59(1)
669	0.1019	7.94124(7)	500.59(1)
670	0.1021	7.94127(7)	500.59(1)
672	0.1021	7.94128(7)	500.59(1)
675	0.1023	7.94136(7)	500.61(1)
674	0.1023	7.94138(7)	500.61(1)
678	0.1024	7.94136(7)	500.61(1)
679	0.1025	7.94138(7)	500.61(1)
681	0.1026	7.94142(7)	500.62(1)
683	0.1026	7.94148(7)	500.63(1)
686	0.1027	7.94151(7)	500.64(1)
686	0.1028	7.94152(7)	500.64(1)
690	0.1029	7.94155(7)	500.64(1)
690	0.1029	7.94158(7)	500.65(1)
694	0.1029	7.94160(7)	500.65(1)
697	0.1031	7.94160(7)	500.65(1)
698	0.1031	7.94163(7)	500.66(1)
701	0.1032	7.94169(7)	500.67(1)
703	0.1031	7.94170(7)	500.67(1)
704	0.1032	7.94172(7)	500.68(1)
704	0.1033	7.94176(7)	500.68(1)
708	0.1033	7.94179(7)	500.69(1)
711	0.1034	7.94187(7)	500.70(1)
711	0.1035	7.94186(7)	500.70(1)
715	0.1034	7.94191(7)	500.71(1)
714	0.1036	7.94192(7)	500.71(1)
719	0.1036	7.94195(7)	500.72(1)

Table A.8 continued

Temperature (K)	Rwp	a (Å)	Volume (Å^3)
721	0.1036	7.94195(7)	500.72(1)
722	0.1037	7.94200(7)	500.73(1)
725	0.1037	7.94203(7)	500.73(1)
727	0.1037	7.94210(7)	500.75(1)
728	0.1038	7.94211(7)	500.75(1)
731	0.1039	7.94216(7)	500.76(1)
732	0.1039	7.94219(7)	500.77(1)
735	0.1040	7.94222(7)	500.77(1)
736	0.1042	7.94225(7)	500.78(1)
739	0.1043	7.94232(7)	500.79(1)
740	0.1043	7.94231(7)	500.79(1)
743	0.1045	7.94230(7)	500.79(1)
744	0.1045	7.94238(7)	500.80(1)
743	0.1046	7.94242(7)	500.81(1)
748	0.1051	7.94252(7)	500.83(1)
751	0.1051	7.94256(7)	500.84(1)
753	0.1052	7.94260(7)	500.84(1)
755	0.1052	7.94263(7)	500.85(1)
756	0.1053	7.94267(7)	500.86(1)
760	0.1054	7.94271(7)	500.86(1)
762	0.1055	7.94273(7)	500.87(1)
763	0.1056	7.94279(7)	500.88(1)
764	0.1057	7.94283(7)	500.89(1)
768	0.1059	7.94292(7)	500.90(1)
768	0.1060	7.94292(7)	500.90(1)
771	0.1061	7.94296(7)	500.91(1)
772	0.1062	7.94298(7)	500.91(1)
775	0.1063	7.94300(7)	500.92(1)
777	0.1063	7.94306(7)	500.93(1)
780	0.1065	7.94309(7)	500.94(1)
781	0.1065	7.94314(7)	500.94(1)
783	0.1067	7.94318(7)	500.95(1)
785	0.1069	7.94320(7)	500.96(1)
786	0.1070	7.94326(7)	500.97(1)
789	0.1072	7.94329(7)	500.97(1)
791	0.1072	7.94330(7)	500.97(1)
793	0.1074	7.94344(7)	501.00(1)
796	0.1075	7.94344(7)	501.00(1)
798	0.1075	7.94346(7)	501.00(1)

Table A.8 continued

Temperature (K)	Rwp	a (Å)	Volume (Å^3)
799	0.1076	7.94347(7)	501.01(1)
799	0.1080	7.94355(7)	501.02(1)
804	0.1086	7.94361(7)	501.03(1)
806	0.1092	7.94360(7)	501.03(1)
807	0.1092	7.94366(7)	501.04(1)
808	0.1092	7.94372(7)	501.05(1)
811	0.1093	7.94373(7)	501.06(1)
813	0.1093	7.94375(7)	501.06(1)
816	0.1094	7.94382(7)	501.07(1)
817	0.1094	7.94384(7)	501.08(1)
819	0.1089	7.94395(7)	501.10(1)
821	0.1090	7.94401(7)	501.11(1)
823	0.1092	7.94407(7)	501.12(1)
825	0.1094	7.94407(7)	501.12(1)
827	0.1096	7.94412(7)	501.13(1)
828	0.1096	7.94420(7)	501.14(1)
831	0.1097	7.94426(7)	501.16(1)
833	0.1099	7.94426(7)	501.16(1)
833	0.1100	7.94427(7)	501.16(1)
837	0.1100	7.94429(7)	501.16(1)
838	0.1101	7.94439(7)	501.18(1)
840	0.1102	7.94441(7)	501.18(1)
842	0.1105	7.94445(7)	501.19(1)
845	0.1109	7.94454(7)	501.21(1)
846	0.1115	7.94457(7)	501.22(1)
848	0.1118	7.94465(7)	501.23(1)
851	0.1119	7.94470(7)	501.24(1)
852	0.1120	7.94472(7)	501.24(1)
856	0.1121	7.94478(7)	501.25(1)
857	0.1122	7.94482(7)	501.26(1)
859	0.1123	7.94485(7)	501.27(1)
861	0.1124	7.94488(7)	501.27(1)
863	0.1126	7.94495(7)	501.29(1)
865	0.1125	7.94502(7)	501.30(1)
867	0.1127	7.94510(7)	501.32(1)
868	0.1131	7.94513(7)	501.32(1)
871	0.1134	7.94523(7)	501.34(1)
874	0.1134	7.94528(7)	501.35(1)
875	0.1137	7.94532(7)	501.36(1)

Table A.8 continued

Temperature (K)	Rwp	a (Å)	Volume (Å^3)
877	0.1134	7.94539(7)	501.37(1)
879	0.1136	7.94546(7)	501.38(1)
881	0.1137	7.94553(7)	501.40(1)
883	0.1140	7.94557(7)	501.41(1)
885	0.1144	7.94560(7)	501.41(1)
887	0.1146	7.94568(7)	501.43(1)
890	0.1153	7.94572(7)	501.43(1)
892	0.1151	7.94581(7)	501.45(1)
893	0.1153	7.94588(7)	501.46(1)
895	0.1154	7.94592(7)	501.47(1)
896	0.1157	7.94596(7)	501.48(1)
899	0.1158	7.94603(7)	501.49(1)
902	0.1161	7.94600(7)	501.49(1)
903	0.1161	7.94602(7)	501.49(1)
905	0.1166	7.94612(8)	501.51(1)
907	0.1172	7.94613(8)	501.51(1)
909	0.1175	7.94618(8)	501.52(1)
910	0.1173	7.94623(8)	501.53(1)
912	0.1177	7.94632(8)	501.55(1)
916	0.1185	7.94640(8)	501.56(1)
917	0.1185	7.94643(8)	501.57(1)
917	0.1183	7.94653(8)	501.59(1)
919	0.1185	7.94652(8)	501.58(1)
923	0.1189	7.94659(8)	501.60(1)
923	0.1193	7.94661(8)	501.60(1)
927	0.1196	7.94668(8)	501.62(1)
929	0.1200	7.94670(8)	501.62(2)
930	0.1203	7.94682(8)	501.64(2)
934	0.1204	7.94686(8)	501.65(2)
935	0.1207	7.94686(8)	501.65(2)
936	0.1214	7.94695(8)	501.67(2)
938	0.1218	7.94699(8)	501.67(2)
941	0.1219	7.94711(8)	501.70(2)
942	0.1215	7.94722(8)	501.72(2)
947	0.1215	7.94725(8)	501.72(2)
947	0.1218	7.94731(8)	501.74(2)
949	0.1223	7.94739(8)	501.75(2)
950	0.1223	7.94739(8)	501.75(2)
954	0.1227	7.94749(8)	501.77(2)

Table A.8 continued

Temperature (K)	Rwp	a (Å)	Volume (Å^3)
955	0.1229	7.94763(8)	501.80(2)
958	0.1229	7.94768(8)	501.80(2)
957	0.1231	7.94772(8)	501.81(2)
961	0.1233	7.94775(8)	501.82(2)
963	0.1237	7.94776(8)	501.82(2)
964	0.1237	7.94792(8)	501.85(2)
965	0.1240	7.94791(8)	501.85(2)
969	0.1240	7.94805(8)	501.88(2)
970	0.1238	7.94803(8)	501.87(2)
972	0.1241	7.94821(8)	501.91(2)
975	0.1244	7.94824(8)	501.91(2)
976	0.1248	7.94840(8)	501.94(2)
976	0.1252	7.94848(8)	501.96(2)
980	0.1255	7.94863(8)	501.98(2)
982	0.1252	7.94874(8)	502.01(2)
982	0.1253	7.94881(8)	502.02(2)
987	0.1257	7.94894(8)	502.04(2)
989	0.1261	7.94905(8)	502.06(2)
989	0.1270	7.94905(8)	502.06(2)
992	0.1278	7.94915(8)	502.08(2)
993	0.1284	7.94928(8)	502.11(2)
996	0.1291	7.94932(8)	502.12(2)
1000	0.1298	7.94932(8)	502.11(2)
1000	0.1305	7.94943(8)	502.14(2)
1002	0.1305	7.94954(8)	502.16(2)
1005	0.1310	7.94952(8)	502.15(2)
1005	0.1318	7.94974(9)	502.19(2)
1008	0.1322	7.94982(9)	502.21(2)
1010	0.1326	7.94988(9)	502.22(2)
1013	0.1330	7.95001(9)	502.25(2)
1014	0.1332	7.95009(9)	502.26(2)
1015	0.1335	7.95010(9)	502.26(2)
1017	0.1339	7.95025(9)	502.29(2)
1022	0.1340	7.95039(9)	502.32(2)
1022	0.1345	7.95035(9)	502.31(2)
1025	0.1348	7.95057(9)	502.35(2)
1027	0.1357	7.95063(9)	502.36(2)
1030	0.1361	7.95071(9)	502.38(2)
1032	0.1369	7.95086(9)	502.41(2)

Table A.8 continued

Temperature (K)	Rwp	a (Å)	Volume (Å^3)
1032	0.1368	7.95093(9)	502.42(2)
1035	0.1367	7.95100(9)	502.43(2)
1036	0.1378	7.95109(9)	502.45(2)
1037	0.1383	7.95106(9)	502.45(2)
1039	0.1374	7.95119(9)	502.47(2)
1042	0.1382	7.95123(9)	502.48(2)
1044	0.1384	7.95132(9)	502.50(2)
1045	0.1385	7.95142(9)	502.51(2)
1049	0.1383	7.95152(9)	502.53(2)
1050	0.1385	7.95173(9)	502.57(2)
1052	0.1384	7.95173(9)	502.57(2)
1056	0.1385	7.95181(9)	502.59(2)
1058	0.1385	7.95189(9)	502.60(2)
1060	0.1388	7.95208(9)	502.64(2)
1060	0.1390	7.95213(9)	502.65(2)
1063	0.1394	7.95219(9)	502.66(2)
1065	0.1392	7.95218(9)	502.66(2)
1064	0.1391	7.95224(9)	502.67(2)
1068	0.1393	7.95236(9)	502.69(2)
1070	0.1397	7.95237(9)	502.69(2)
1073	0.1400	7.95252(9)	502.72(2)
1074	0.1397	7.95265(9)	502.75(2)
1075	0.1404	7.95267(9)	502.75(2)
1079	0.1407	7.95283(9)	502.78(2)
1080	0.1409	7.95278(9)	502.77(2)
1081	0.1409	7.95298(9)	502.81(2)
1084	0.1410	7.95296(9)	502.81(2)
1084	0.1413	7.95309(9)	502.83(2)
1049	0.1428	7.95244(9)	502.92(2)

Table A.9: Unit cell volumes for both the $MgZrF_6$ and a CaF_2 pressure marker as determined from the Rietveld analysis of the high-pressure diffraction data acquired using a DAC. Pressures estimated from the unit cell volume of the CaF_2 are also given.

$MgZrF_6$ Volume (Å^3)	CaF_2 Volume (Å^3)	Pressure (GPa)
500.82(2)	163.429(7)	0.000(5)
500.58(2)	163.395(7)	0.017(5)
500.52(2)	163.388(7)	0.020(5)
500.50(2)	163.383(6)	0.023(5)

Table A.9 continued

$MgZrF_6$ Volume (Å^3)	CaF_2 Volume (Å^3)	Pressure (GPa)
500.48(2)	163.375(6)	0.027(5)
500.44(2)	163.365(6)	0.032(5)
500.40(2)	163.356(6)	0.036(5)
500.33(2)	163.343(6)	0.043(5)
500.21(2)	163.325(6)	0.052(5)
500.15(2)	163.315(6)	0.057(5)
500.08(2)	163.302(6)	0.063(5)
499.97(2)	163.288(6)	0.070(5)
499.84(2)	163.255(6)	0.087(6)
499.70(2)	163.225(7)	0.102(6)
499.60(2)	163.214(6)	0.107(6)
499.40(2)	163.184(7)	0.122(7)
499.12(2)	163.135(7)	0.147(8)
498.92(2)	163.101(7)	0.164(8)
498.66(2)	163.063(7)	0.183(9)
498.31(2)	163.015(6)	0.21(1)
497.94(2)	162.966(7)	0.23(1)
497.57(2)	162.922(7)	0.25(1)
497.24(2)	162.880(7)	0.27(1)
496.96(2)	162.851(7)	0.29(1)
496.74(2)	162.823(7)	0.30(1)
496.39(2)	162.791(7)	0.32(1)
496.07(2)	162.751(7)	0.34(1)
495.80(2)	162.729(7)	0.35(1)

Table A.10: Unit cell volume for $MgZrF_6$ as a function of temperature and pressure. These values were derived from Rietveld analysis of data collected using an oil filled pressure cell incorporating a Background Reducing Internal Mask (BRIM).

Temperature (K)	Volume (Å^3)	Pressure (GPa)
298.0(5)	500.920(6)	0.000(1)
298.0(5)	499.899(6)	0.103(1)
298.0(5)	498.803(6)	0.207(1)

Table A.10 continued

Temperature (K)	Volume (Å^3)	Pressure (GPa)
298.0(5)	497.630(6)	0.310(1)
298.0(5)	498.228(7)	0.259(1)
298.0(5)	499.358(6)	0.155(1)
298.0(5)	497.163(6)	0.362(1)
298.0(5)	500.431(6)	0.052(1)
353.0(5)	499.707(6)	0.103(1)
353.0(5)	498.657(8)	0.207(1)
353.0(5)	497.544(7)	0.310(1)
353.0(5)	498.120(6)	0.259(1)
353.0(5)	499.178(7)	0.155(1)
353.0(5)	500.205(6)	0.052(1)
407.0(5)	499.562(9)	0.103(1)
407.0(5)	498.541(7)	0.207(1)
407.0(5)	497.459(9)	0.310(1)
407.0(5)	498.015(8)	0.259(1)
407.0(5)	499.070(7)	0.155(1)
407.0(5)	500.065(8)	0.052(1)
459.0(5)	499.505(8)	0.103(1)
459.0(5)	498.478(7)	0.207(1)
459.0(5)	497.420(8)	0.310(1)
459.0(5)	497.971(7)	0.259(1)
459.0(5)	498.997(6)	0.155(1)
459.0(5)	500.004(8)	0.052(1)
513.0(5)	499.474(7)	0.103(1)
513.0(5)	498.456(7)	0.207(1)
513.0(5)	497.405(9)	0.310(1)
513.0(5)	497.950(7)	0.259(1)
513.0(5)	498.982(7)	0.155(1)
513.0(5)	499.978(7)	0.052(1)

Table A.11: Parameters from fitting a third order Birch Murnaghan equation of state to volume versus pressure, obtained in two independent DAC experiments, for cubic $CaNbF_6$.

	Run 1*	Run 2*
V_0 (Å^3)	592.128(9)	592.113(9)
K_0(GPa)	34.0(3)	33.7(4)
K_0'	-22(1)	-23(2)

* The two runs were for the same sample, but with different sample to detector distances.

Table A.12: Crystallographic parameters for $CaNbF_6$ at 300 K derived from the Rietveld analysis of the neutron diffraction data.

Chemical Formula	$CaNbF_6$
Space group	$Fm\bar{3}m$
a (Å)	8.39447(3)
μ (central λ = 1.33Å)	~0.006 cm^{-1}
Temperature (K)	300
R_{wp}	0.049
R_F^2	0.108

	x	y	z	U_{iso}/U_{eq} (Å^2)	U_{11} (Å^2)	U_{22}/U_{33} (Å^2)
Ca	0	0	0	0.0106(4)	-	-
Nb	$\frac{1}{2}$	$\frac{1}{2}$	$\frac{1}{2}$	0.0083(2)	-	-
F	0.26686(8)	0	0	0.0363	0.0103(3)	0.0494(3)

Table A.13: Crystallographic parameters for $MgNbF_6$ at 300 K derived from the Rietveld analysis of the x-ray diffraction data acquired while using a Cryostream.

Chemical Formula	$MgNbF_6$
Space group	$Fm\bar{3}m$
a (Å)	7.84886(9)
λ (Å)	0.72768
μ (cm^{-1})	19.
Temperature (K)	302
R_{wp}	0.137
R_F^2	0.097

	x	y	z	U_{iso}/U_{eq} (Å^2)	U_{11} (Å^2)	U_{22}/U_{33} (Å^2)
Mg	0	0	0	0.006(1)	-	-
Nb	$\frac{1}{2}$	$\frac{1}{2}$	$\frac{1}{2}$	0.0213(6)	-	-
F	0.2481(4)	0	0	0.0337	0.017(2)	0.042(2)

APPENDIX B. SUPPLEMENTARY MATERIAL FOR CHAPTER 3

B.1 Figures

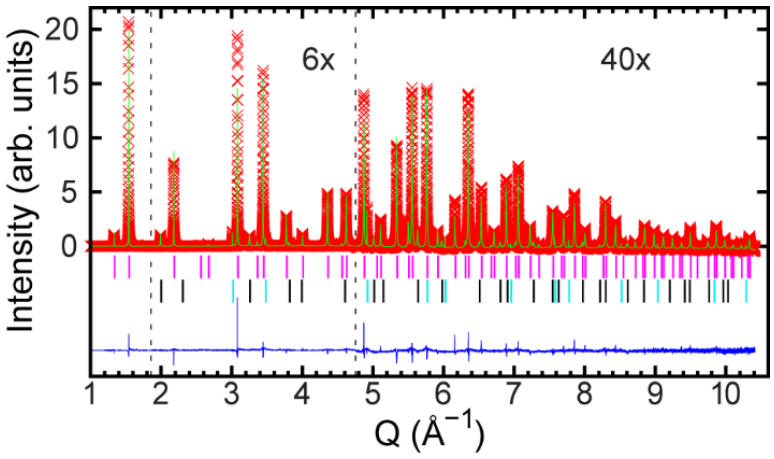

Figure B.1: Rietveld plot showing a fit for a cubic ReO_3-type model ($Fm\bar{3}m$) to the 300 K high resolution synchrotron diffraction data collected with a nitrogen gas blower. The high Q data have been scaled to show detail, but shifted downwards so that the backgrounds for the sections of the plot are similar. The phase flags denote $CaTiF_6$ (magenta), CaF_2 (black), and Cu metal (cyan). The Cu metal is presumably from a chip introduced into the sample when the copper reaction vessel was cut open.

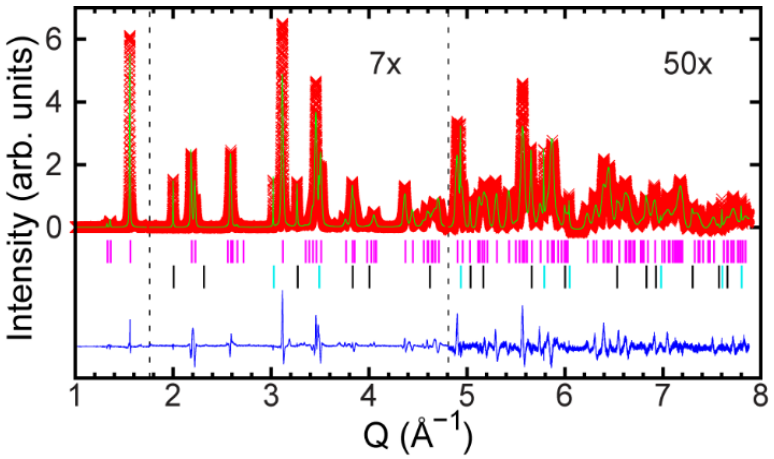

Figure B.2: Rietveld plot showing the fit for an $R\bar{3}$ model to low temperature (16 K) high resolution synchrotron data collected with a helium cryostat. The high Q data have been

scaled to show detail, but shifted downwards so that the backgrounds for the sections of the plot are similar. The phase flags denote $CaTiF_6$ (magenta), CaF_2 (black), and Cu metal (cyan).

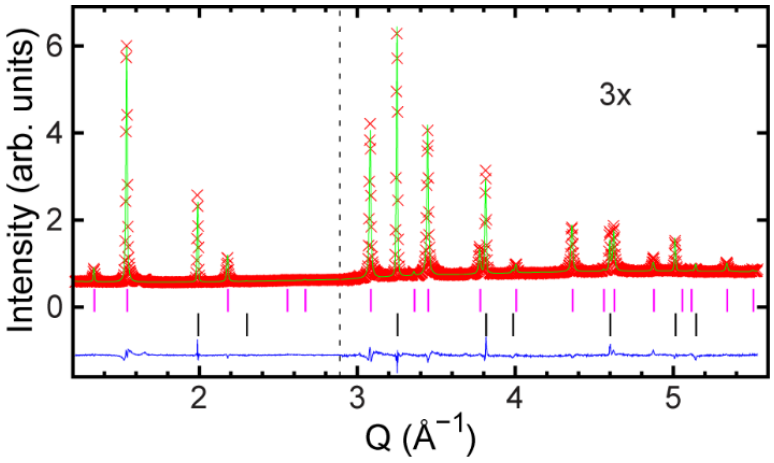

Figure B.3: Rietveld plot showing a fit for a cubic ReO_3-type model ($Fm\bar{3}m$) to the nominally 0 GPa powder x-ray diffraction data obtained in a diamond anvil cell. The high Q data have been scaled to show detail, but shifted downwards so that the backgrounds for the sections of the plot are similar. The phase flags denote $CaTiF_6$ (magenta) and CaF_2 (black).

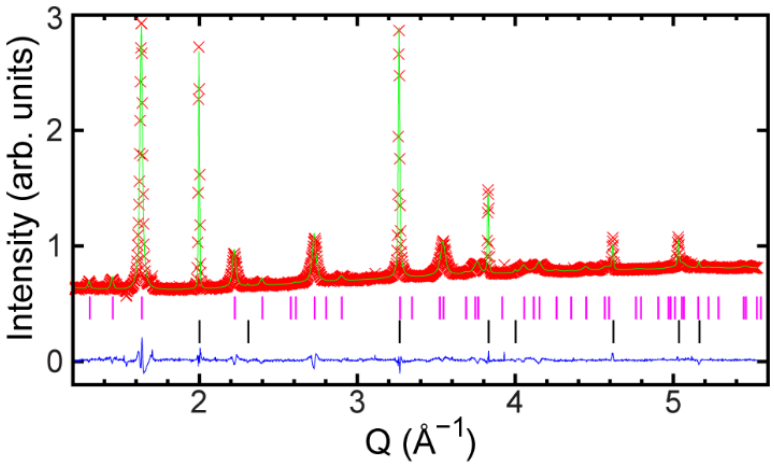

Figure B.4: Rietveld plot showing a fit for an R$\bar{3}$ model to the 1 GPa powder x-ray diffraction data obtained in a diamond anvil cell. The phase flags denote $CaTiF_6$ (magenta) and CaF_2 (black).

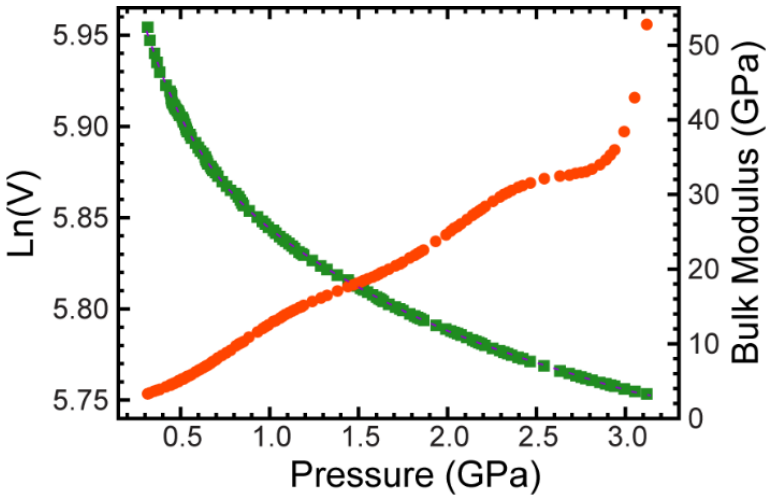

Figure B.5: Pressure dependence of ln(V) and the bulk modulus for $CaTiF_6$. A six-term polynomial (Purple dotted line) was fit to the ln(V) data, and used to calculate bulk moduli.

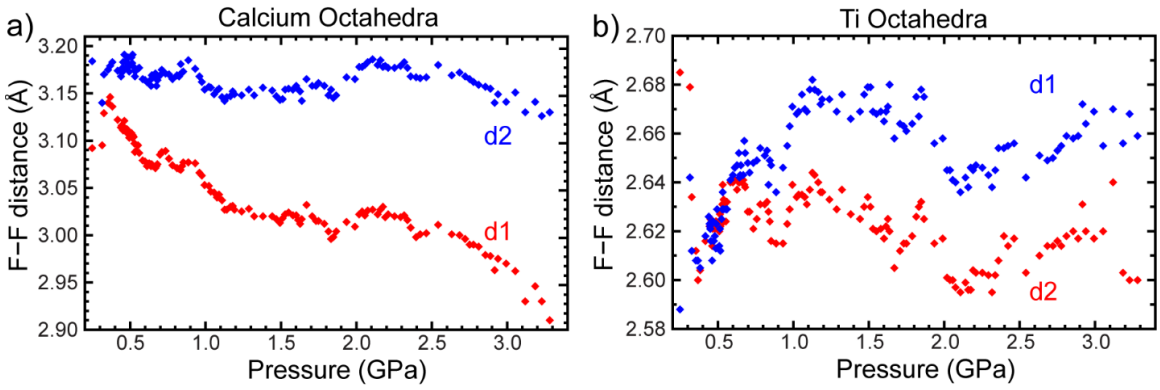

Figure B.6: Fluorine-Fluorine distances within the a) CaF_6 and b) TiF_6 octahedra. d1 is the distance between pairs of fluorines lying on a triangular face that is perpendicular to the crystallographic three fold axis and d2 is the distance between pairs of fluorines lying on opposite triangular faces of the octahedral - see Figure 3.7b for a drawing showing these relationships.

B.2 Tables

Table B.1: Lattice constants and unit cell volumes, as a function of temperature, for cubic and rhombohedral $CaTiF_6$ as determined from the Rietveld analyses of the high resolution low temperature x-ray diffraction data acquired while using a helium cryostat.

Temperature (K)	R_{wp}	a (Å)	c (Å)	Volume (Å^3)
298.00	0.1495	8.15728(1)	-	542.795(2)
276.30	0.149	8.15925(1)	-	543.189(2)
250.90	0.1516	8.16172(1)	-	543.683(2)
226.00	0.1553	8.16414(1)	-	544.166(2)
201.40	0.1622	8.16670(1)	-	544.679(2)
177.14	0.1727	8.16945(1)	-	545.229(3)
152.10	0.1932	8.17184(2)	-	545.707(3)
141.64	0.2128	8.17280(2)	-	545.900(3)
131.78	0.2388	8.17327(2)	-	545.994(4)
121.97	0.3068	8.17168(3)	-	545.674(7)
112.22	0.1574	5.72917(5)	14.1821(2)	403.141(6)
102.36	0.1566	5.71205(5)	14.1898(2)	400.950(6)
92.71	0.16	5.70112(5)	14.1970(2)	399.621(6)
83.19	0.164	5.69269(6)	14.2032(2)	398.614(6)
73.82	0.1666	5.68565(6)	14.2088(2)	397.785(6)
64.54	0.1693	5.67958(6)	14.2135(2)	397.067(6)
55.49	0.1699	5.67420(6)	14.2175(2)	396.426(6)

Table B.1 continued

Temperature (K)	R_{wp}	a (Å)	c (Å)	Volume (Å^3)
47.04	0.1692	5.66944(6)	14.2211(3)	395.863(6)
39.06	0.1693	5.66503(6)	14.2237(3)	395.319(6)
30.00	0.1698	5.66161(6)	14.2261(3)	394.909(6)
16.92	0.1696	5.65885(6)	14.2279(3)	394.575(7)

Table B.2: Lattice constant and unit cell volumes, as a function of temperature, for cubic $CaTiF_6$ as determined from the Rietveld analyses of the high resolution low temperature x-ray diffraction data acquired while using a nitrogen blower. Given in order of collection.

Temperature (K)	Rwp	a (Å)	Volume (Å^3)
298	0.1379	8.15738(1)	542.815(2)
350	0.1311	8.15275(1)	541.891(2)
400	0.1287	8.14887(1)	541.118(2)
450	0.126	8.14592(1)	540.530(2)
450	0.1275	8.14580(1)	540.506(2)
450	0.1275	8.14580(1)	540.506(2)
500	0.1269	8.14341(1)	540.030(2)
475	0.1275	8.14461(1)	540.269(2)
425	0.1281	8.14726(1)	540.797(2)
375	0.1296	8.15032(1)	541.407(2)
325	0.1315	8.15413(1)	542.167(2)

Table B.3: Atomic displacement parameters for cubic $CaTiF_6$ as determined from the Rietveld analyses of the high resolution x-ray diffraction data acquired using both a nitrogen gas blower and a helium cryostat.

Temperature (K)	Ca U_{iso} (Å^2)	Ti U_{iso} (Å^2)	F U_{11} (Å^2)	F $U_{22/33}$ (Å^2)
500	0.0162(2)	0.0167(2)	0.0153(5)	0.0725(4)
475	0.0157(2)	0.0160(2)	0.0148(4)	0.0702(4)
450	0.0149(2)	0.0153(2)	0.0142(4)	0.0674(4)
450	0.0149(2)	0.0151(2)	0.0140(4)	0.0677(4)
450	0.0150(2)	0.0152(2)	0.0142(4)	0.0676(4)
425	0.0142(2)	0.0145(2)	0.0134(4)	0.0654(4)
400	0.0138(2)	0.0142(2)	0.0130(4)	0.0631(4)

Table B.3 continued

Temperature (K)	Ca U_{iso} (Å^2)	Ti U_{iso} (Å^2)	F U_{11} (Å^2)	F $U_{22/33}$ (Å^2)
375	0.0126(2)	0.0134(2)	0.0122(4)	0.0605(4)
350	0.0125(2)	0.0131(2)	0.0126(4)	0.0576(4)
325	0.0109(2)	0.0118(2)	0.0103(4)	0.0551(4)
298	0.0108(2)	0.0117(2)	0.0116(4)	0.0514(4)
298	0.0103(2)	0.0095(2)	0.0126(5)	0.0501(4)
276.3	0.0097(2)	0.0091(2)	0.0126(5)	0.0479(4)
250.9	0.0085(2)	0.0084(2)	0.0114(5)	0.0449(4)
226	0.0078(2)	0.0075(2)	0.0106(5)	0.0420(4)
201.4	0.0069(2)	0.0066(2)	0.0096(5)	0.0392(4)
177.14	0.0060(2)	0.0059(2)	0.0090(5)	0.0365(4)
152.1	0.0050(2)	0.0050(2)	0.0077(6)	0.0341(4)
141.64	0.0048(3)	0.0046(2)	0.0073(6)	0.0335(4)
131.78	0.0045(3)	0.0044(3)	0.0069(7)	0.0332(5)
121.97	0.0038(3)	0.0030(4)	0.0050(9)	0.0343(7)

Table B.4: Unit cell volumes for cubic $CaTiF_6$ and CaF_2 as determined from the Rietveld analysis of the high-pressure diffraction data. Pressures estimated from the unit cell volume of the CaF_2 using an equation of state are also given.

$CaTiF_6$ a (Å)	$CaTiF_6$ Volume (Å^3)	CaF_2 Volume (Å^3)	Pressure (GPa)
8.15108(8)	541.56(2)	163.070(5)	0.000(4)
8.15096(8)	541.54(2)	163.062(4)	0.004(3)
8.15089(8)	541.52(2)	163.067(4)	0.001(3)
8.15064(8)	541.47(2)	163.062(4)	0.004(3)
8.15026(8)	541.40(2)	163.042(4)	0.014(3)
8.14929(8)	541.20(2)	163.017(4)	0.026(3)
8.14825(8)	540.99(2)	163.004(4)	0.033(3)
8.14711(8)	540.77(2)	162.993(4)	0.038(4)
8.14572(8)	540.49(2)	162.951(4)	0.059(4)
8.14376(8)	540.10(2)	162.906(4)	0.081(5)
8.14250(9)	539.85(2)	162.908(5)	0.081(5)
8.14159(9)	539.67(2)	162.888(5)	0.091(5)
8.14048(8)	539.45(2)	162.866(5)	0.102(5)
8.13946(9)	539.25(2)	162.853(5)	0.108(6)

Table B.4 continued

$CaTiF_6$ a (Å)	$CaTiF_6$ Volume (Å^3)	CaF_2 Volume (Å^3)	Pressure (GPa)
8.13826(9)	539.01(2)	162.833(5)	0.118(6)
8.13677(9)	538.71(2)	162.800(5)	0.135(7)
8.13520(9)	538.40(2)	162.766(5)	0.152(7)
8.1337(1)	538.11(2)	162.758(5)	0.156(7)
8.1316(1)	537.68(2)	162.716(5)	0.177(8)
8.1291(1)	537.18(2)	162.695(6)	0.188(9)
8.1265(1)	536.67(2)	162.678(6)	0.196(9)
8.1239(1)	536.16(2)	162.647(6)	0.211(9)
8.1210(1)	535.58(3)	162.607(8)	0.232(10)
8.1177(1)	534.93(3)	162.579(8)	0.246(10)
8.1171(1)	534.82(2)	162.575(3)	0.248(10)

Table B.5: Unit cell volumes for rhombohedral $CaTiF_6$ and CaF_2 as determined from the Rietveld analyses of the high-pressure diffraction data. Pressures estimated from the unit cell volume of the CaF_2 using an equation of state are also given.

$CaTiF_6$ a (Å)	$CaTiF_6$ c (Å)	$CaTiF_6$ Volume (Å^3)	CaF_2 Volume (Å^3)	Pressure (GPa)
5.6321(7)	14.128(4)	388.11(5)	162.575(3)	0.25(1)
5.6040(6)	14.171(3)	385.41(6)	162.444(9)	0.32(2)
5.5812(5)	14.185(2)	382.67(3)	162.420(5)	0.33(1)
5.5576(5)	14.204(3)	379.94(3)	162.367(5)	0.35(1)
5.5400(5)	14.224(3)	378.07(3)	162.340(5)	0.37(2)
5.5222(7)	14.239(4)	376.03(3)	162.311(6)	0.38(2)
5.5002(6)	14.251(3)	373.35(3)	162.243(5)	0.42(2)
5.4897(5)	14.259(3)	372.15(3)	162.199(5)	0.44(2)
5.4852(5)	14.264(3)	371.67(3)	162.190(5)	0.44(2)
5.4819(6)	14.267(3)	371.28(3)	162.181(5)	0.45(2)
5.4762(5)	14.273(3)	370.67(3)	162.184(5)	0.45(2)
5.4721(5)	14.276(3)	370.21(3)	162.180(5)	0.45(2)
5.4682(5)	14.280(3)	369.79(3)	162.173(5)	0.45(2)
5.4654(5)	14.279(3)	369.38(3)	162.157(5)	0.46(2)
5.4619(5)	14.285(3)	369.07(3)	162.148(5)	0.47(2)
5.4597(5)	14.286(3)	368.79(3)	162.143(5)	0.47(2)

Table B.5 continued

$CaTiF_6$ a (Å)	$CaTiF_6$ c (Å)	$CaTiF_6$ Volume (Å^3)	CaF_2 Volume (Å^3)	Pressure (GPa)
5.4575(5)	14.289(3)	368.56(3)	162.135(5)	0.47(2)
5.4549(5)	14.291(3)	368.27(3)	162.122(5)	0.48(2)
5.4529(5)	14.293(3)	368.05(3)	162.109(5)	0.49(2)
5.4502(5)	14.294(3)	367.70(3)	162.104(5)	0.49(2)
5.4469(5)	14.296(3)	367.32(3)	162.094(5)	0.49(2)
5.4430(5)	14.299(3)	366.85(3)	162.065(5)	0.51(2)
5.4387(5)	14.302(3)	366.36(3)	162.055(5)	0.51(2)
5.4350(5)	14.305(3)	365.95(3)	162.051(5)	0.52(2)
5.4311(5)	14.306(3)	365.45(3)	162.036(5)	0.52(2)
5.4270(5)	14.304(3)	364.84(3)	162.025(5)	0.53(2)
5.4227(5)	14.309(3)	364.40(3)	162.020(5)	0.53(2)
5.4194(6)	14.310(3)	363.99(3)	162.009(5)	0.54(2)
5.4129(5)	14.321(3)	363.39(3)	161.981(5)	0.55(2)
5.4073(5)	14.327(3)	362.77(3)	161.966(5)	0.56(2)
5.4001(6)	14.324(3)	361.75(3)	161.922(5)	0.58(2)
5.3917(6)	14.333(3)	360.86(3)	161.890(5)	0.60(2)
5.3848(5)	14.341(3)	360.14(3)	161.867(5)	0.61(2)
5.3807(5)	14.345(3)	359.68(3)	161.837(5)	0.63(3)
5.3747(5)	14.350(3)	359.00(3)	161.815(5)	0.64(3)
5.3704(5)	14.351(3)	358.44(3)	161.807(5)	0.64(3)
5.3668(5)	14.356(3)	358.08(3)	161.798(5)	0.65(3)
5.3628(5)	14.360(3)	357.65(3)	161.789(5)	0.65(3)
5.3581(5)	14.363(3)	357.12(3)	161.758(5)	0.67(3)
5.3545(5)	14.367(3)	356.72(3)	161.746(5)	0.67(3)
5.3514(5)	14.370(3)	356.39(3)	161.734(5)	0.68(3)
5.3475(6)	14.373(3)	355.93(3)	161.702(5)	0.70(3)
5.3412(6)	14.377(3)	355.20(3)	161.679(5)	0.71(3)
5.3323(5)	14.383(3)	354.17(3)	161.632(5)	0.73(3)
5.3245(5)	14.390(3)	353.30(3)	161.587(4)	0.76(3)
5.3176(5)	14.394(3)	352.47(3)	161.544(5)	0.78(3)
5.3123(5)	14.397(3)	351.85(3)	161.487(5)	0.81(3)
5.3070(5)	14.401(3)	351.24(3)	161.460(4)	0.82(3)
5.3015(5)	14.405(3)	350.61(3)	161.439(5)	0.84(3)
5.2967(6)	14.407(3)	350.04(3)	161.423(6)	0.84(3)
5.2930(6)	14.408(3)	349.57(3)	161.408(6)	0.85(3)
5.2841(5)	14.413(3)	348.53(3)	161.345(4)	0.89(4)

Table B.5 continued

$CaTiF_6$ a (Å)	$CaTiF_6$ c (Å)	$CaTiF_6$ Volume (Å^3)	CaF_2 Volume (Å^3)	Pressure (GPa)
5.2743(5)	14.418(3)	347.36(3)	161.259(4)	0.93(4)
5.2669(5)	14.424(3)	346.53(3)	161.206(4)	0.96(4)
5.2627(5)	14.426(3)	346.01(3)	161.176(4)	0.98(4)
5.2573(5)	14.430(3)	345.41(3)	161.143(5)	0.99(4)
5.2519(5)	14.436(3)	344.82(3)	161.090(5)	1.02(4)
5.2473(5)	14.439(3)	344.29(3)	161.066(5)	1.03(4)
5.2418(4)	14.442(3)	343.65(3)	161.024(4)	1.06(4)
5.2375(4)	14.444(3)	343.15(3)	160.989(4)	1.08(4)
5.2348(4)	14.445(3)	342.80(3)	160.963(4)	1.09(4)
5.2313(4)	14.446(3)	342.37(3)	160.928(4)	1.11(4)
5.2273(4)	14.448(3)	341.89(3)	160.896(4)	1.13(4)
5.2228(4)	14.452(3)	341.39(3)	160.869(4)	1.14(5)
5.2178(4)	14.452(3)	340.76(3)	160.824(4)	1.17(5)
5.2149(4)	14.455(3)	340.44(3)	160.796(4)	1.18(5)
5.2127(5)	14.456(3)	340.17(3)	160.776(4)	1.19(5)
5.2050(5)	14.458(3)	339.22(3)	160.688(4)	1.24(5)
5.1964(5)	14.462(3)	338.20(3)	160.599(4)	1.29(5)
5.1906(5)	14.465(3)	337.51(3)	160.536(4)	1.32(5)
5.1820(5)	14.469(3)	336.50(3)	160.430(4)	1.38(5)
5.1745(5)	14.471(3)	335.56(3)	160.318(4)	1.44(6)
5.1699(4)	14.471(3)	334.96(3)	160.268(4)	1.47(6)
5.1657(4)	14.472(3)	334.44(3)	160.224(4)	1.49(6)
5.1629(4)	14.472(3)	334.08(3)	160.192(4)	1.51(6)
5.1600(4)	14.475(3)	333.78(3)	160.163(4)	1.53(6)
5.1566(4)	14.477(3)	333.37(3)	160.121(4)	1.55(6)
5.1522(4)	14.479(3)	332.86(3)	160.070(4)	1.58(6)
5.1487(4)	14.482(3)	332.46(3)	160.031(4)	1.60(6)
5.1462(4)	14.483(3)	332.17(3)	160.007(4)	1.61(6)
5.1446(4)	14.483(3)	331.97(3)	159.985(4)	1.63(6)
5.1426(4)	14.483(3)	331.71(3)	159.965(4)	1.64(6)
5.1378(4)	14.486(3)	331.14(3)	159.909(4)	1.67(7)
5.1338(4)	14.487(3)	330.65(3)	159.842(4)	1.71(7)
5.1309(4)	14.488(3)	330.31(3)	159.798(4)	1.73(7)
5.1287(5)	14.488(3)	330.03(3)	159.767(4)	1.75(7)
5.1232(5)	14.491(3)	329.40(3)	159.699(4)	1.79(7)
5.1203(5)	14.490(3)	329.00(3)	159.651(4)	1.81(7)
5.1181(5)	14.492(3)	328.74(3)	159.621(4)	1.83(7)
5.1166(5)	14.491(3)	328.54(3)	159.594(4)	1.85(7)

Table B.5 continued

$CaTiF_6$ a (Å)	$CaTiF_6$ c (Å)	$CaTiF_6$ Volume (Å^3)	CaF_2 Volume (Å^3)	Pressure (GPa)
5.1140(5)	14.493(3)	328.25(3)	159.561(4)	1.87(7)
5.1064(5)	14.495(3)	327.33(3)	159.440(4)	1.93(8)
5.1011(5)	14.496(3)	326.68(3)	159.343(4)	1.99(8)
5.0983(5)	14.497(3)	326.33(3)	159.294(4)	2.02(8)
5.0965(5)	14.498(3)	326.11(3)	159.260(4)	2.04(8)
5.0947(5)	14.497(3)	325.87(3)	159.228(4)	2.06(8)
5.0924(5)	14.498(3)	325.61(3)	159.196(5)	2.08(8)
5.0889(5)	14.498(3)	325.15(3)	159.139(5)	2.11(8)
5.0852(5)	14.500(3)	324.73(3)	159.082(5)	2.14(8)
5.0834(5)	14.500(3)	324.50(3)	159.050(5)	2.16(8)
5.0812(5)	14.503(3)	324.28(3)	159.022(5)	2.18(8)
5.0797(5)	14.502(3)	324.06(3)	158.995(5)	2.19(9)
5.0776(5)	14.501(3)	323.78(3)	158.963(5)	2.21(9)
5.0732(5)	14.502(3)	323.25(3)	158.889(5)	2.25(9)
5.0700(5)	14.502(3)	322.84(3)	158.821(5)	2.29(9)
5.0680(5)	14.501(3)	322.55(3)	158.780(5)	2.32(9)
5.0658(5)	14.502(3)	322.30(3)	158.744(5)	2.34(9)
5.0638(5)	14.503(3)	322.06(4)	158.707(5)	2.36(9)
5.0606(5)	14.503(3)	321.65(4)	158.646(5)	2.40(9)
5.0586(5)	14.503(3)	321.39(4)	158.600(5)	2.42(9)
5.0547(5)	14.505(3)	320.94(4)	158.531(5)	2.46(10)
5.0487(5)	14.505(3)	320.18(4)	158.399(5)	2.54(10)
5.0422(5)	14.501(3)	319.28(4)	158.248(5)	2.63(10)
5.0385(5)	14.502(3)	318.83(4)	158.162(5)	2.68(10)
5.0362(5)	14.498(3)	318.46(4)	158.100(5)	2.72(10)
5.0340(5)	14.498(3)	318.19(4)	158.051(5)	2.75(11)
5.0320(5)	14.499(3)	317.95(4)	158.008(5)	2.78(11)
5.0294(5)	14.501(3)	317.66(4)	157.952(5)	2.81(11)
5.0266(5)	14.499(3)	317.27(4)	157.878(5)	2.86(11)
5.0248(5)	14.498(3)	317.01(4)	157.823(5)	2.89(11)
5.0232(5)	14.496(3)	316.77(4)	157.777(5)	2.92(11)
5.0218(5)	14.497(3)	316.61(4)	157.740(5)	2.94(11)
5.0182(5)	14.497(4)	316.16(4)	157.653(5)	2.99(11)
5.0158(6)	14.490(4)	315.71(4)	157.554(5)	3.05(12)
5.0128(7)	14.487(5)	315.25(5)	157.447(6)	3.12(12)
5.0091(8)	14.490(6)	314.85(6)	157.340(6)	3.19(12)
5.006(1)	14.500(7)	314.63(7)	157.270(7)	3.23(12)
5.003(1)	14.503(9)	314.36(9)	157.185(7)	3.28(12)

Table B.6: Pressure dependence of the Ca-F-Ti bond angle and bond lengths in rhombohedral $CaTiF_6$.

Pressure (GPa)	Ca-F-Ti Bond Angle (°)	Ca-F Bond Length (Å)	Ti-F Bond Length (Å)
0.25(1)	158.9(4)	2.219(12)	1.864(13)
0.32(2)	157.3(3)	2.204(10)	1.881(10)
0.33(1)	156.4(3)	2.227(8)	1.855(8)
0.35(1)	155.7(3)	2.233(7)	1.846(8)
0.37(2)	154.9(3)	2.236(7)	1.841(8)
0.38(2)	154.3(4)	2.234(10)	1.842(11)
0.42(2)	153.1(3)	2.226(8)	1.851(9)
0.44(2)	152.4(3)	2.221(9)	1.857(9)
0.44(2)	152.3(3)	2.223(8)	1.854(9)
0.45(2)	152.2(3)	2.224(9)	1.854(9)
0.45(2)	151.8(3)	2.224(8)	1.854(9)
0.45(2)	151.7(3)	2.223(8)	1.855(9)
0.45(2)	151.2(3)	2.225(8)	1.853(9)
0.46(2)	151.4(3)	2.231(8)	1.846(8)
0.47(2)	151.3(3)	2.223(8)	1.854(9)
0.47(2)	151.1(3)	2.223(8)	1.855(9)
0.47(2)	151.0(3)	2.226(8)	1.852(9)
0.48(2)	151.0(3)	2.225(8)	1.852(9)
0.49(2)	150.9(3)	2.226(8)	1.852(9)
0.49(2)	150.8(3)	2.222(8)	1.855(9)
0.49(2)	150.6(3)	2.219(9)	1.859(10)
0.51(2)	150.6(3)	2.226(8)	1.850(9)
0.51(2)	150.3(3)	2.222(8)	1.856(9)
0.52(2)	150.2(3)	2.227(8)	1.850(9)
0.52(2)	150.0(3)	2.221(8)	1.855(9)
0.53(2)	149.8(3)	2.217(9)	1.86(10)
0.53(2)	149.6(3)	2.212(9)	1.865(10)
0.54(2)	149.7(3)	2.214(10)	1.861(11)
0.55(2)	149.5(3)	2.217(9)	1.857(10)
0.56(2)	149.3(3)	2.215(9)	1.86(10)
0.58(2)	148.9(3)	2.208(11)	1.867(12)
0.60(2)	148.6(3)	2.207(11)	1.868(12)
0.61(2)	148.4(3)	2.205(11)	1.869(12)
0.63(3)	148.3(3)	2.206(11)	1.868(11)

Table B.6 continued

Pressure (GPa)	Ca-F-Ti Bond Angle (°)	Ca-F Bond Length (Å)	Ti-F Bond Length (Å)
0.64(3)	148.0(3)	2.203(11)	1.871(11)
0.64(3)	147.7(3)	2.208(10)	1.868(11)
0.65(3)	147.6(3)	2.208(10)	1.868(11)
0.65(3)	147.4(3)	2.206(11)	1.870(12)
0.67(3)	147.3(3)	2.207(11)	1.868(12)
0.67(3)	147.1(3)	2.203(12)	1.872(12)
0.68(3)	147.0(3)	2.206(11)	1.870(12)
0.70(3)	146.8(3)	2.211(11)	1.865(12)
0.71(3)	146.4(3)	2.214(11)	1.864(12)
0.73(3)	146.2(3)	2.213(10)	1.863(11)
0.76(3)	146.1(3)	2.210(10)	1.865(11)
0.78(3)	145.8(3)	2.206(11)	1.869(11)
0.81(3)	145.7(3)	2.206(11)	1.868(12)
0.82(3)	145.5(3)	2.206(11)	1.869(11)
0.84(3)	145.5(3)	2.210(11)	1.862(11)
0.84(3)	145.2(4)	2.208(14)	1.865(14)
0.85(3)	145.3(4)	2.210(13)	1.861(13)
0.89(4)	144.9(3)	2.214(10)	1.857(10)
0.93(4)	144.6(3)	2.211(10)	1.860(10)
0.96(4)	144.3(3)	2.205(12)	1.866(12)
0.98(4)	144.1(3)	2.201(12)	1.871(12)
0.99(4)	143.8(3)	2.195(13)	1.878(14)
1.02(4)	143.9(3)	2.196(12)	1.875(12)
1.03(4)	143.7(3)	2.194(12)	1.876(12)
1.06(4)	143.7(3)	2.190(11)	1.878(11)
1.08(4)	143.8(3)	2.190(11)	1.875(12)
1.09(4)	143.6(3)	2.192(11)	1.874(12)
1.11(4)	143.5(3)	2.186(11)	1.879(12)
1.13(4)	143.5(3)	2.181(11)	1.883(12)
1.14(5)	143.4(3)	2.183(11)	1.881(12)
1.17(5)	143.2(3)	2.184(11)	1.880(12)
1.18(5)	143.1(3)	2.187(12)	1.877(13)
1.19(5)	143.2(3)	2.184(12)	1.877(13)
1.24(5)	143.1(3)	2.183(12)	1.876(12)
1.29(5)	142.8(3)	2.186(13)	1.873(14)
1.32(5)	142.6(3)	2.181(12)	1.878(12)

Table B.6 continued

Pressure (GPa)	Ca-F-Ti Bond Angle (°)	Ca-F Bond Length (Å)	Ti-F Bond Length (Å)
1.38(5)	142.6(3)	2.184(12)	1.871(13)
1.44(6)	142.4(3)	2.183(13)	1.872(13)
1.47(6)	142.1(3)	2.180(11)	1.876(12)
1.49(6)	142.0(3)	2.177(12)	1.878(13)
1.51(6)	141.8(3)	2.179(12)	1.877(13)
1.53(6)	141.9(2)	2.184(12)	1.870(13)
1.55(6)	141.7(2)	2.185(12)	1.870(13)
1.58(6)	141.7(2)	2.184(12)	1.870(12)
1.60(6)	141.6(2)	2.185(12)	1.868(13)
1.61(6)	141.6(2)	2.182(12)	1.870(13)
1.63(6)	141.5(2)	2.180(12)	1.872(12)
1.64(6)	141.5(2)	2.178(11)	1.874(12)
1.67(7)	141.2(2)	2.192(12)	1.861(13)
1.71(7)	141.3(2)	2.185(12)	1.866(13)
1.73(7)	141.3(2)	2.183(12)	1.866(13)
1.75(7)	141.2(3)	2.184(13)	1.865(14)
1.79(7)	141.0(3)	2.182(13)	1.869(14)
1.81(7)	140.9(3)	2.175(12)	1.874(13)
1.83(7)	140.9(3)	2.175(12)	1.873(13)
1.85(7)	140.7(3)	2.172(12)	1.878(13)
1.87(7)	140.7(3)	2.176(13)	1.874(14)
1.93(8)	140.4(2)	2.186(14)	1.864(15)
1.99(8)	140.3(2)	2.184(13)	1.865(14)
2.02(8)	140.3(2)	2.193(14)	1.855(14)
2.04(8)	140.1(2)	2.194(14)	1.854(15)
2.06(8)	140.3(2)	2.193(14)	1.853(15)
2.08(8)	140.1(2)	2.196(14)	1.851(14)
2.11(8)	139.9(2)	2.197(14)	1.850(15)
2.14(8)	139.9(2)	2.193(14)	1.853(15)
2.16(8)	139.7(2)	2.197(14)	1.851(15)
2.18(8)	139.6(2)	2.196(14)	1.853(15)
2.19(9)	139.6(2)	2.192(15)	1.856(16)
2.21(9)	139.5(2)	2.192(15)	1.856(16)
2.25(9)	139.4(2)	2.192(15)	1.856(16)
2.29(9)	139.3(2)	2.192(15)	1.855(16)
2.32(9)	139.4(3)	2.194(15)	1.850(16)
2.34(9)	139.3(3)	2.190(15)	1.855(16)
2.36(9)	139.3(3)	2.184(16)	1.860(17)

Table B.6 continued

Pressure (GPa)	Ca-F-Ti Bond Angle (°)	Ca-F Bond Length (Å)	Ti-F Bond Length (Å)
2.40(9)	139.2(3)	2.181(15)	1.864(17)
2.42(9)	139.1(3)	2.181(15)	1.863(16)
2.46(10)	138.8(3)	2.182(16)	1.864(17)
2.54(10)	138.8(2)	2.189(16)	1.855(17)
2.63(10)	138.7(3)	2.182(16)	1.860(17)
2.68(10)	138.5(3)	2.183(16)	1.861(17)
2.72(10)	138.5(2)	2.180(16)	1.861(17)
2.75(11)	138.5(3)	2.177(16)	1.863(17)
2.78(11)	138.5(3)	2.176(16)	1.863(17)
2.81(11)	138.4(3)	2.174(16)	1.866(18)
2.86(11)	138.6(3)	2.170(17)	1.866(18)
2.89(11)	138.6(3)	2.169(17)	1.865(18)
2.92(11)	138.6(3)	2.159(17)	1.875(18)
2.94(11)	138.5(3)	2.166(19)	1.868(20)
2.99(11)	138.7(3)	2.161(20)	1.869(21)
3.05(12)	138.9(3)	2.163(22)	1.863(23)
3.12(12)	139.2(3)	2.144(27)	1.877(29)
3.19(12)	139.7(4)	2.153(19)	1.859(19)
3.23(12)	140.1(4)	2.142(23)	1.864(23)
3.28(12)	140.7(5)	2.137(23)	1.861(23)

Table B.7: Pressure dependence of the F-F bond distances and strain in Ca and Ti octahedra in rhombohedral $CaTiF_6$.

Pressure (GPa)	Ca Octahedra F-F d1 (Å)	Ca Octahedra F-F d2 (Å)	Ti Octahedra F-F d1 (Å)	Ti Octahedra F-F d2 (Å)	Ca Octahedral Strain	Ti Octahedral Strain
0.25(1)	3.092(19)	3.184(23)	2.685(20)	2.588(23)	0.0147	-0.0184
0.32(2)	3.095(15)	3.140(17)	2.679(16)	2.642(17)	0.0072	-0.0070
0.33(1)	3.129(12)	3.170(15)	2.634(13)	2.612(15)	0.0065	-0.0042
0.35(1)	3.140(11)	3.175(14)	2.612(15)	2.608(15)	0.0055	-0.0008
0.37(2)	3.146(11)	3.179(15)	2.600(12)	2.608(15)	0.0052	0.0015
0.38(2)	3.136(16)	3.183(20)	2.604(17)	2.605(21)	0.0074	0.0002
0.42(2)	3.122(13)	3.174(16)	2.616(14)	2.618(17)	0.0083	0.0004
0.44(2)	3.114(13)	3.168(16)	2.626(14)	2.626(17)	0.0086	0.0000
0.44(2)	3.116(13)	3.172(16)	2.622(13)	2.623(16)	0.0089	0.0002
0.45(2)	3.115(13)	3.174(16)	2.622(14)	2.621(17)	0.0094	-0.0002
0.45(2)	3.115(12)	3.176(15)	2.623(13)	2.622(16)	0.0097	-0.0002

Table B.7 continued

Pressure (GPa)	Ca Octahedra F-F d1 (Å)	Ca Octahedra F-F d2 (Å)	Ti Octahedra F-F d1 (Å)	Ti Octahedra F-F d2 (Å)	Ca Octahedral Strain	Ti Octahedral Strain
0.45(2)	3.112(13)	3.177(15)	2.625(13)	2.621(16)	0.0103	-0.0008
0.45(2)	3.111(13)	3.183(16)	2.625(14)	2.616(16)	0.0114	-0.0017
0.46(2)	3.121(12)	3.191(15)	2.614(13)	2.608(15)	0.0111	-0.0011
0.47(2)	3.113(12)	3.176(15)	2.621(13)	2.624(15)	0.0100	0.0006
0.47(2)	3.110(13)	3.176(15)	2.624(13)	2.624(15)	0.0105	0.0000
0.47(2)	3.112(12)	3.184(15)	2.622(13)	2.616(15)	0.0114	-0.0011
0.48(2)	3.112(12)	3.182(15)	2.621(13)	2.618(15)	0.0111	-0.0006
0.49(2)	3.107(13)	3.188(15)	2.624(14)	2.613(16)	0.0129	-0.0021
0.49(2)	3.107(13)	3.178(16)	2.624(14)	2.623(16)	0.0113	-0.0002
0.49(2)	3.103(14)	3.173(17)	2.629(15)	2.629(17)	0.0112	0.0000
0.51(2)	3.108(12)	3.188(15)	2.620(13)	2.614(15)	0.0127	-0.0011
0.51(2)	3.103(13)	3.182(15)	2.627(13)	2.621(15)	0.0126	-0.0011
0.52(2)	3.106(13)	3.191(18)	2.622(14)	2.612(16)	0.0135	-0.0019
0.52(2)	3.104(13)	3.178(15)	2.623(14)	2.625(16)	0.0118	0.0004
0.53(2)	3.097(14)	3.174(16)	2.631(14)	2.629(16)	0.0123	-0.0004
0.53(2)	3.088(14)	3.168(16)	2.639(15)	2.636(17)	0.0128	-0.0006
0.54(2)	3.089(15)	3.174(17)	2.633(16)	2.629(18)	0.0136	-0.0008
0.55(2)	3.095(14)	3.176(16)	2.624(14)	2.629(16)	0.0129	0.0010
0.56(2)	3.087(14)	3.177(16)	2.632(15)	2.629(17)	0.0144	-0.0006
0.58(2)	3.079(17)	3.165(19)	2.640(18)	2.641(19)	0.0138	0.0002
0.60(2)	3.078(17)	3.164(18)	2.640(18)	2.643(19)	0.0138	0.0006
0.61(2)	3.073(17)	3.162(18)	2.641(18)	2.646(19)	0.0143	0.0009
0.63(3)	3.076(16)	3.163(18)	2.637(17)	2.647(18)	0.0139	0.0019
0.64(3)	3.073(16)	3.158(18)	2.640(17)	2.652(18)	0.0136	0.0023
0.64(3)	3.075(16)	3.169(17)	2.640(17)	2.642(18)	0.0151	0.0004
0.65(3)	3.074(16)	3.169(17)	2.641(17)	2.643(17)	0.0152	0.0004
0.65(3)	3.073(17)	3.167(18)	2.641(18)	2.647(18)	0.0151	0.0011
0.67(3)	3.071(17)	3.171(18)	2.641(18)	2.643(19)	0.0160	0.0004
0.67(3)	3.073(18)	3.158(19)	2.639(18)	2.657(19)	0.0136	0.0034
0.68(3)	3.075(17)	3.164(18)	2.638(18)	2.652(19)	0.0143	0.0026
0.70(3)	3.085(17)	3.169(19)	2.628(18)	2.648(19)	0.0134	0.0038
0.71(3)	3.088(17)	3.175(18)	2.628(18)	2.644(19)	0.0139	0.0030
0.73(3)	3.089(16)	3.171(17)	2.621(16)	2.648(18)	0.0131	0.0051
0.76(3)	3.081(16)	3.170(17)	2.625(16)	2.649(17)	0.0142	0.0046
0.78(3)	3.074(17)	3.165(17)	2.631(17)	2.654(18)	0.0146	0.0044

Table B.7 continued

Pressure (GPa)	Ca Octahedra F-F d1 (Å)	Ca Octahedra F-F d2 (Å)	Ti Octahedra F-F d1 (Å)	Ti Octahedra F-F d2 (Å)	Ca Octahedral Strain	Ti Octahedral Strain
0.81(3)	3.071(17)	3.169(18)	2.631(17)	2.651(18)	0.0157	0.0038
0.82(3)	3.070(17)	3.168(17)	2.632(17)	2.653(18)	0.0157	0.0040
0.84(3)	3.069(17)	3.181(17)	2.628(17)	2.639(17)	0.0179	0.0021
0.84(3)	3.073(22)	3.172(22)	2.624(22)	2.649(23)	0.0159	0.0047
0.85(3)	3.077(20)	3.173(21)	2.616(20)	2.647(21)	0.0154	0.0059
0.89(4)	3.077(15)	3.185(16)	2.615(15)	2.636(16)	0.0172	0.0040
0.93(4)	3.076(15)	3.176(16)	2.615(15)	2.646(16)	0.0160	0.0059
0.96(4)	3.066(18)	3.168(18)	2.623(18)	2.655(18)	0.0164	0.0061
0.98(4)	3.063(19)	3.162(19)	2.629(19)	2.663(19)	0.0159	0.0064
0.99(4)	3.053(20)	3.154(20)	2.639(21)	2.671(20)	0.0163	0.0060
1.02(4)	3.052(19)	3.157(18)	2.634(19)	2.668(19)	0.0169	0.0064
1.03(4)	3.046(18)	3.156(18)	2.635(18)	2.669(18)	0.0177	0.0064
1.06(4)	3.045(17)	3.149(17)	2.635(17)	2.676(17)	0.0168	0.0077
1.08(4)	3.040(17)	3.153(17)	2.634(18)	2.670(18)	0.0182	0.0068
1.09(4)	3.043(17)	3.155(17)	2.631(18)	2.669(17)	0.0181	0.0072
1.11(4)	3.037(17)	3.146(17)	2.637(18)	2.678(17)	0.0176	0.0077
1.13(4)	3.027(17)	3.142(17)	2.644(18)	2.682(17)	0.0186	0.0071
1.14(5)	3.027(17)	3.146(17)	2.643(18)	2.678(17)	0.0193	0.0066
1.17(5)	3.030(17)	3.147(17)	2.640(18)	2.677(17)	0.0189	0.0070
1.18(5)	3.031(18)	3.152(18)	2.636(19)	2.672(18)	0.0196	0.0068
1.19(5)	3.027(18)	3.149(18)	2.636(19)	2.674(19)	0.0198	0.0072
1.24(5)	3.025(18)	3.148(18)	2.633(19)	2.674(18)	0.0199	0.0077
1.29(5)	3.028(20)	3.154(19)	2.629(21)	2.669(20)	0.0204	0.0076
1.32(5)	3.020(18)	3.148(18)	2.637(19)	2.676(18)	0.0208	0.0073
1.38(5)	3.020(19)	3.156(18)	2.627(20)	2.666(19)	0.0220	0.0074
1.44(6)	3.020(19)	3.153(19)	2.625(20)	2.669(19)	0.0215	0.0083
1.47(6)	3.017(17)	3.147(17)	2.630(18)	2.676(18)	0.0211	0.0087
1.49(6)	3.013(18)	3.143(18)	2.634(20)	2.679(19)	0.0211	0.0085
1.51(6)	3.018(19)	3.144(19)	2.630(20)	2.679(19)	0.0204	0.0092
1.53(6)	3.022(18)	3.154(18)	2.621(20)	2.669(18)	0.0214	0.0091
1.55(6)	3.024(19)	3.155(18)	2.620(20)	2.668(19)	0.0212	0.0091
1.58(6)	3.021(18)	3.154(17)	2.621(19)	2.669(18)	0.0215	0.0091
1.60(6)	3.021(19)	3.158(18)	2.617(20)	2.665(19)	0.0222	0.0091
1.61(6)	3.016(18)	3.154(17)	2.622(19)	2.669(18)	0.0224	0.0089
1.63(6)	3.012(18)	3.152(17)	2.625(19)	2.671(18)	0.0227	0.0087
1.64(6)	3.017(17)	3.142(17)	2.620(19)	2.680(18)	0.0203	0.0113
1.67(7)	3.032(19)	3.165(18)	2.605(20)	2.658(19)	0.0215	0.0101
1.71(7)	3.020(19)	3.158(18)	2.612(20)	2.664(19)	0.0223	0.0099

Table B.7 continued

Pressure (GPa)	Ca Octahedra F-F d1 (Å)	Ca Octahedra F-F d2 (Å)	Ti Octahedra F-F d1 (Å)	Ti Octahedra F-F d2 (Å)	Ca Octahedral Strain	Ti Octahedral Strain
1.73(7)	3.015(19)	3.158(18)	2.615(20)	2.663(19)	0.0232	0.0091
1.75(7)	3.015(20)	3.161(19)	2.615(21)	2.661(19)	0.0236	0.0087
1.79(7)	3.012(19)	3.158(19)	2.618(21)	2.664(19)	0.0237	0.0087
1.81(7)	3.004(18)	3.148(18)	2.626(20)	2.675(19)	0.0234	0.0092
1.83(7)	2.996(19)	3.154(18)	2.630(21)	2.667(19)	0.0257	0.0070
1.85(7)	2.998(18)	3.145(18)	2.632(20)	2.678(18)	0.0239	0.0087
1.87(7)	3.004(20)	3.148(19)	2.625(22)	2.675(20)	0.0234	0.0094
1.93(8)	3.014(21)	3.167(20)	2.615(23)	2.656(20)	0.0248	0.0078
1.99(8)	3.009(21)	3.165(19)	2.617(23)	2.658(20)	0.0253	0.0078
2.02(8)	3.022(21)	3.178(20)	2.601(22)	2.645(20)	0.0252	0.0084
2.04(8)	3.025(22)	3.178(20)	2.600(23)	2.645(20)	0.0247	0.0086
2.06(8)	3.021(22)	3.180(20)	2.600(23)	2.641(21)	0.0256	0.0078
2.08(8)	3.026(22)	3.183(20)	2.597(22)	2.640(20)	0.0253	0.0082
2.11(8)	3.027(22)	3.186(20)	2.595(23)	2.636(21)	0.0256	0.0078
2.14(8)	3.022(22)	3.180(20)	2.599(23)	2.642(21)	0.0255	0.0082
2.16(8)	3.027(22)	3.185(20)	2.596(23)	2.638(20)	0.0254	0.0080
2.18(8)	3.030(22)	3.178(21)	2.596(23)	2.646(21)	0.0238	0.0095
2.19(9)	3.019(23)	3.179(21)	2.604(24)	2.645(22)	0.0258	0.0078
2.21(9)	3.022(23)	3.177(21)	2.603(24)	2.647(21)	0.0250	0.0084
2.25(9)	3.020(23)	3.177(21)	2.603(25)	2.646(22)	0.0253	0.0082
2.29(9)	3.019(23)	3.179(21)	2.602(24)	2.643(21)	0.0258	0.0078
2.32(9)	3.021(23)	3.183(21)	2.595(25)	2.638(22)	0.0261	0.0082
2.34(9)	3.016(24)	3.177(22)	2.602(26)	2.645(23)	0.0260	0.0082
2.36(9)	3.008(24)	3.168(22)	2.608(26)	2.654(23)	0.0259	0.0087
2.40(9)	2.998(24)	3.167(22)	2.618(26)	2.654(23)	0.0274	0.0068
2.42(9)	3.001(23)	3.166(21)	2.614(26)	2.655(22)	0.0268	0.0078
2.46(10)	3.002(24)	3.167(22)	2.617(26)	2.656(23)	0.0267	0.0074
2.54(10)	3.011(24)	3.180(22)	2.603(26)	2.642(23)	0.0273	0.0074
2.63(10)	3.001(25)	3.169(23)	2.610(27)	2.651(23)	0.0272	0.0078
2.68(10)	3.000(25)	3.172(23)	2.614(27)	2.649(23)	0.0279	0.0067
2.72(10)	2.996(25)	3.168(22)	2.614(27)	2.650(23)	0.0279	0.0068
2.75(11)	2.990(25)	3.165(22)	2.616(27)	2.653(23)	0.0284	0.0070
2.78(11)	2.990(25)	3.162(23)	2.614(27)	2.655(24)	0.0280	0.0078
2.81(11)	2.988(25)	3.159(23)	2.618(27)	2.659(24)	0.0278	0.0078
2.86(11)	2.979(26)	3.157(23)	2.62(28)	2.658(24)	0.0290	0.0072
2.89(11)	2.978(26)	3.155(24)	2.617(29)	2.659(25)	0.0289	0.0080
2.92(11)	2.963(26)	3.140(24)	2.631(29)	2.672(25)	0.0290	0.0077
2.94(11)	2.975(29)	3.149(26)	2.620(31)	2.664(26)	0.0284	0.0083

Table B.7 continued

Pressure (GPa)	Ca Octahedra F-F d1 (Å)	Ca Octahedra F-F d2 (Å)	Ti Octahedra F-F d1 (Å)	Ti Octahedra F-F d2 (Å)	Ca Octahedral Strain	Ti Octahedral Strain
2.99(11)	2.970(31)	3.141(27)	2.617(33)	2.669(28)	0.0280	0.0098
3.05(12)	2.962(35)	3.151(30)	2.620(40)	2.655(31)	0.0309	0.0066
3.12(12)	2.930(40)	3.130(40)	2.640(50)	2.670(40)	0.0330	0.0056
3.19(12)	2.946(31)	3.141(28)	2.603(30)	2.656(28)	0.0320	0.0101
3.23(12)	2.930(40)	3.126(33)	2.600(40)	2.668(33)	0.0324	0.0129
3.28(12)	2.910(40)	3.130(35)	2.600(40)	2.659(35)	0.0364	0.0112

Table B.8: Crystallographic parameters for $CaTiF_6$ at 298 K derived from the Rietveld analysis of the high resolution synchrotron diffraction data collected using a helium cryostat (see Figure B.1).

Chemical Formula	$CaTiF_6$
Space group	$Fm\bar{3}m$
a (Å)	8.15728(1)
λ (Å)	0.41272
μ (cm^{-1})	4.05
Temperature (K)	298
R_{wp}	0.1495
R_F^2	0.1092

	x	y	z	U_{iso}/U_{eq} (Å^2)	U_{11} (Å^2)	U_{22}/U_{33} (Å^2)
Ca	0	0	0	0.0103(2)	-	-
Ti	$\frac{1}{2}$	$\frac{1}{2}$	$\frac{1}{2}$	0.0095(2)	-	-
F	0.26686(8)	0	0	0.0376	0.0126(5)	0.0501(4)

Table B.9: Crystallographic parameters for $CaTiF_6$ at 16 K derived from the Rietveld analysis of the high resolution synchrotron diffraction data collected using a helium cryostat (see Figure B.2).

Chemical Formula	$CaTiF_6$
Space group	$R\bar{3}$
a (Å)	5.65886(6)
c (Å)	14.2279(3)
λ (Å)	0.41272
μ (cm^{-1})	4.05
Temperature (K)	16.92
R_{wp}	0.1696
R_F^2	0.0515

	x	**y**	**z**	**U_{iso} ($Å^2$)**	**U_{11} ($Å^2$)**	**U_{22} ($Å^2$)**	**U_{33} ($Å^2$)**
Ca	0	0	0	0.0061(6)	-	-	-
Ti	0	0	$\frac{1}{2}$	-0.0010(9)	-	-	-
F	0.1153(2)	0.3628(3)	0.0905(1)	-	0.017(1)	0.0192(9)	0.0025(7)

Table B.10: Crystallographic parameters for $CaTiF_6$ at room temperature and nominally zero pressure derived from the Rietveld analysis of the high-pressure synchrotron diffraction data collected in a DAC (see Figure B.3).

Chemical Formula	$CaTiF_6$
Space group	$Fm\bar{3}m$
a (Å)	8.15110(8)
λ (Å)	0.45240
Pressure (GPa)	~ 0
R_{wp}	0.0215
R_F^2	0.0862

	x	**y**	**z**	**U_{iso}/U_{eq} ($Å^2$)**	**U_{11} ($Å^2$)**	**U_{22}/U_{33} ($Å^2$)**
Ca	0	0	0	0.032(3)	-	-
Ti	$\frac{1}{2}$	$\frac{1}{2}$	$\frac{1}{2}$	0.033(3)	-	-
F	0.2724(5)	0	0	0.0529	0.032(3)	0.063(3)

Table B.11: Crystallographic parameters for $CaTiF_6$ at room temperature and ~1 GPa derived from the Rietveld analysis of the high-pressure synchrotron diffraction data collected using a DAC (see Figure B.4).

Chemical Formula	$CaTiF_6$
Space group	$R\bar{3}$
a (Å)	5.2418(4)
c (Å)	14.442(3)
λ (Å)	0.45240
Pressure (GPa)	1.06(4)
R_{wp}	0.0182
R_F^2	0.0645

	x	**y**	**z**	**U_{iso} (Å^2)**
Ca	0	0	0	0.055(11)
Ti	0	0	$\frac{1}{2}$	0.0318)
F	0.061(2)	0.362(2)	0.0904(6)	0.042(3)

APPENDIX C. SUPPLEMENTARY MATERIAL FOR CHAPTER 4

C.1 Figures

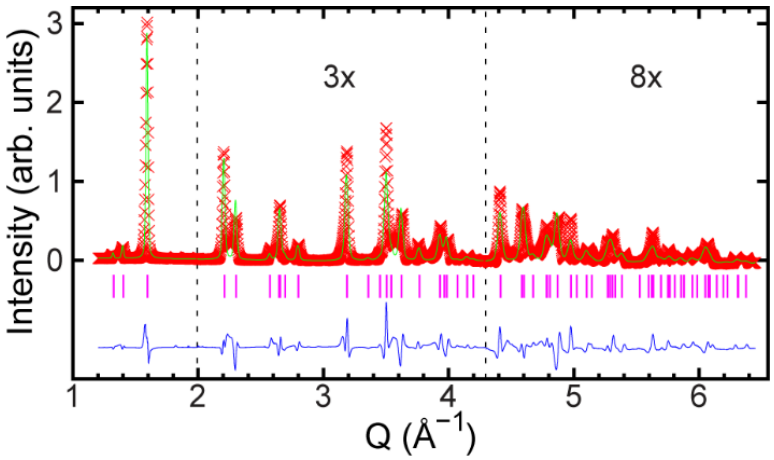

Figure C.1: Rietveld plot showing a fit of a $MnNbF_6$ $R\bar{3}$ model to the 111 K synchrotron diffraction data. The two sections of Q have been scaled to show detail, but shifted downwards so that the backgrounds for the sections of the plot appear to be the same.

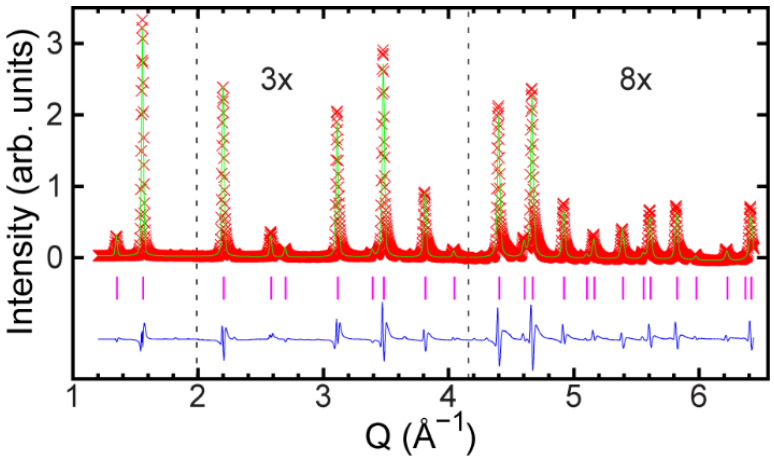

Figure C.2: Rietveld plot showing a fit of a $MnNbF_6$ cubic ReO_3-type model ($Fm\bar{3}m$) to the 315 K synchrotron diffraction data. The two sections of Q have been scaled to show detail, but shifted downwards so that the backgrounds for the sections of the plot appear to be the same.

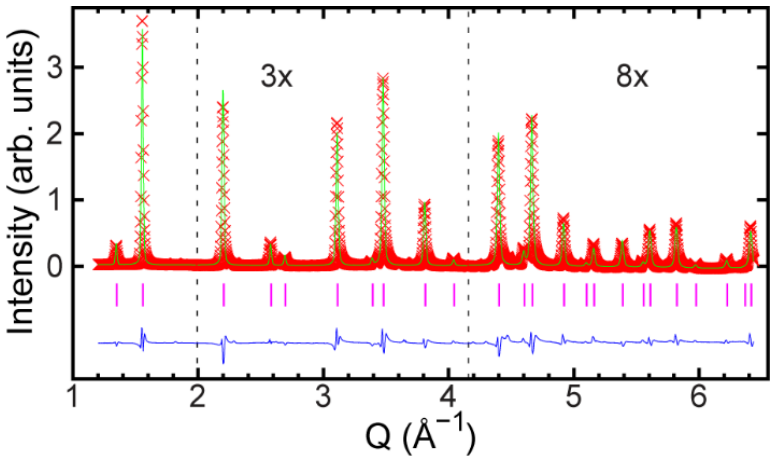

Figure C.3: Rietveld plot showing a fit of a $MnNbF_6$ cubic ReO_3-type model ($Fm\bar{3}m$) to the 500 K synchrotron diffraction data. The two sections of Q have been scaled to show detail, but shifted downwards so that the backgrounds for the sections of the plot appear to be the same.

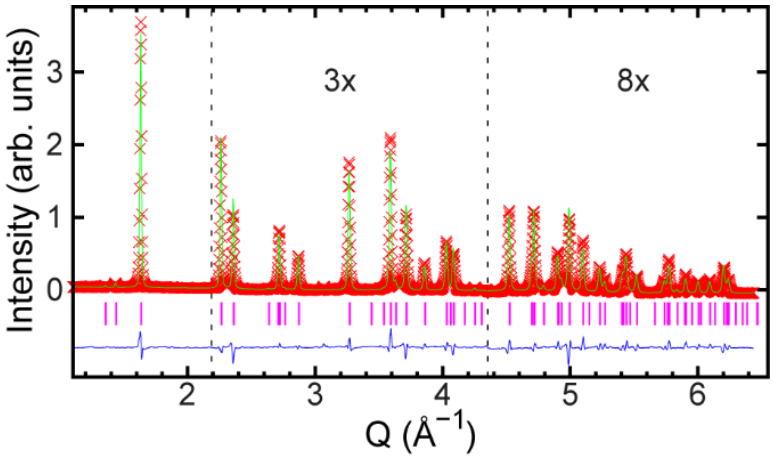

Figure C.4: Rietveld plot showing a fit of a $ZnNbF_6$ $R\bar{3}$ model to the 300 K synchrotron diffraction data. The two sections of Q have been scaled to show detail, but shifted downwards so that the backgrounds for the sections of the plot appear to be the same.

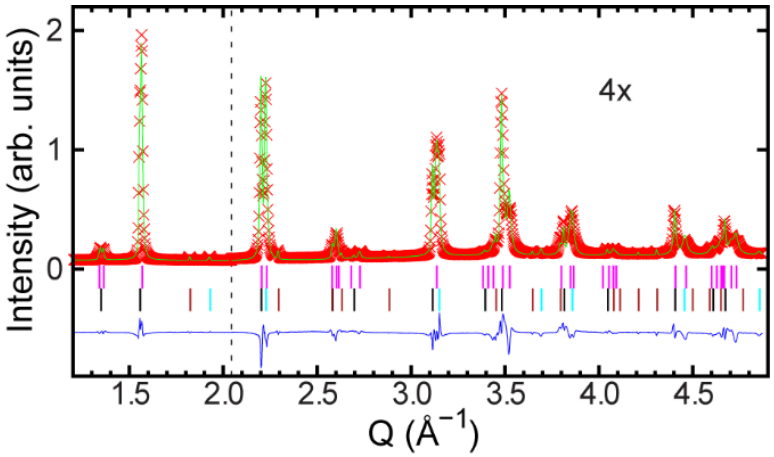

Figure C.5: Rietveld plot showing a fit of $MnNbF_6$ $Fm\bar{3}m$ and $R\bar{3}$ models to the nominally 0 GPa powder x-ray diffraction data obtained in a diamond anvil cell. The high Q section has been scaled to show detail, but shifted downwards so that the backgrounds for the sections of the plot appear to be the same. The phase flags denote $MnNbF_6$ $R\bar{3}$ (magenta), $MnNbF_6$ $Fm\bar{3}m$ (black), NaCl (cyan), MnF_2 (brown).

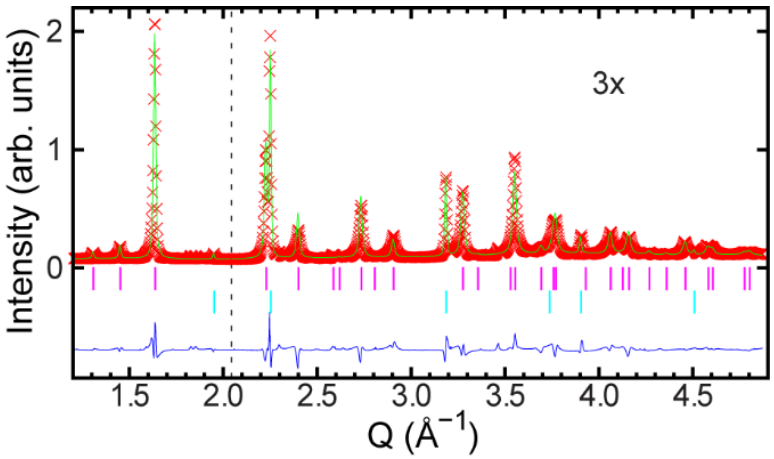

Figure C.6: Rietveld plot showing a fit of $MnNbF_6$ $R\bar{3}$ model to the 1.0 GPa powder x-ray diffraction data obtained in a diamond anvil cell. The high Q section has been scaled to show detail, but shifted downwards so that the backgrounds for the sections of the plot appear to be the same. The phase flags denote $MnNbF_6$ (magenta) and NaCl (cyan).

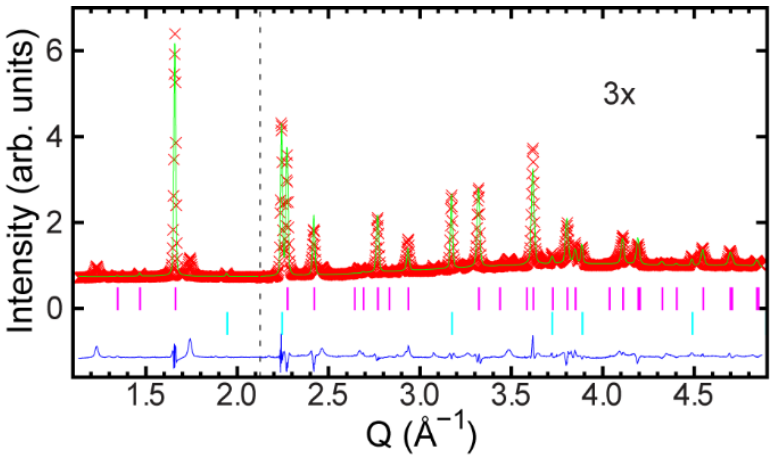

Figure C.7: Rietveld plot showing a fit of $ZnNbF_6$ $R\bar{3}$ model to the nominally 0 GPa powder x-ray diffraction data obtained in a diamond anvil cell. The high Q section has been scaled to show detail, but shifted downwards so that the backgrounds for the sections of the plot appear to be the same. The phase flags denote $ZnNbF_6$ (magenta) and NaCl (cyan).

C.2 Tables

Table C.1: Lattice constant(s) and unit cell volume for cubic or rhombohedral $MnNbF_6$ as determined from Rietveld analyses of the variable temperature x-ray diffraction data.

Temperature (K)	Rwp	a (Å)	c (Å)	Volume (Å^3)
111.50	0.2280	5.4675(4)	14.275(2)	369.56(4)
115.57	0.2274	5.4691(4)	14.273(2)	369.71(4)
117.30	0.2267	5.4701(4)	14.271(2)	369.80(4)
119.08	0.2420	5.4714(4)	14.269(2)	369.93(4)
122.64	0.2247	5.4739(4)	14.265(2)	370.18(4)
125.71	0.2238	5.4760(4)	14.263(2)	370.38(4)
127.65	0.2231	5.4775(4)	14.260(2)	370.54(3)
129.79	0.2226	5.4791(4)	14.258(2)	370.70(3)
133.86	0.2215	5.4815(4)	14.255(2)	370.94(3)
136.96	0.2208	5.4835(4)	14.253(2)	371.15(3)
140.48	0.2201	5.4857(4)	14.250(2)	371.37(3)
142.82	0.2196	5.4871(4)	14.248(2)	371.52(3)
144.09	0.2192	5.4884(4)	14.247(2)	371.65(3)
147.40	0.2186	5.4906(3)	14.244(2)	371.88(3)
150.55	0.2178	5.4930(3)	14.241(2)	372.12(3)
154.97	0.2172	5.4952(3)	14.238(2)	372.35(3)

Table C.1 continued

Temperature (K)	Rwp	a (Å)	c (Å)	Volume (Å^3)
157.42	0.2164	5.4972(3)	14.236(2)	372.56(3)
157.17	0.2159	5.4985(3)	14.234(2)	372.69(3)
162.07	0.2149	5.5013(3)	14.231(2)	372.98(3)
164.45	0.2140	5.5033(3)	14.228(2)	373.19(3)
166.70	0.2135	5.5053(3)	14.226(2)	373.40(3)
170.49	0.2124	5.5077(3)	14.223(2)	373.64(3)
172.48	0.2116	5.5095(3)	14.220(1)	373.83(3)
175.04	0.2108	5.5118(3)	14.218(1)	374.05(3)
178.23	0.2099	5.5140(3)	14.215(1)	374.28(3)
180.94	0.2088	5.5160(3)	14.212(1)	374.49(3)
183.74	0.2232	5.5180(3)	14.209(1)	374.69(3)
186.47	0.2065	5.5204(3)	14.206(1)	374.93(3)
189.45	0.2052	5.5228(3)	14.203(1)	375.17(3)
192.70	0.2040	5.5252(3)	14.200(1)	375.40(3)
195.91	0.2027	5.5276(3)	14.197(1)	375.65(3)
197.81	0.2015	5.5298(3)	14.194(1)	375.88(3)
201.53	0.2003	5.5323(3)	14.191(1)	376.13(3)
204.73	0.1990	5.5348(3)	14.187(1)	376.39(3)
207.56	0.1978	5.5373(3)	14.184(1)	376.64(3)
209.80	0.1969	5.5393(3)	14.182(1)	376.86(3)
212.74	0.1957	5.5418(3)	14.179(1)	377.12(3)
215.96	0.1948	5.5442(3)	14.176(1)	377.38(3)
218.90	0.1940	5.5466(3)	14.174(1)	377.64(3)
222.02	0.1931	5.5490(3)	14.171(1)	377.89(3)
225.05	0.1922	5.5516(3)	14.168(1)	378.16(3)
228.07	0.1913	5.5540(3)	14.166(1)	378.43(3)
230.90	0.1904	5.5566(3)	14.163(1)	378.70(3)
233.73	0.1891	5.5593(3)	14.160(1)	378.98(3)
236.56	0.1880	5.5618(3)	14.157(1)	379.25(3)
239.88	0.1864	5.5647(3)	14.154(1)	379.56(3)
242.81	0.1845	5.5675(3)	14.150(1)	379.86(3)
245.36	0.1828	5.5699(3)	14.148(1)	380.12(3)
248.98	0.1804	5.5731(3)	14.144(1)	380.46(3)
251.34	0.1784	5.5760(3)	14.141(1)	380.77(3)
254.88	0.1761	5.5789(3)	14.138(1)	381.08(3)
257.83	0.1737	5.5820(3)	14.135(1)	381.43(3)
260.10	0.1719	5.5844(3)	14.133(1)	381.69(3)

Table C.1 continued

Temperature (K)	Rwp	a (Å)	c (Å)	Volume (Å^3)
263.76	0.1688	5.5881(3)	14.129(1)	382.09(3)
266.44	0.1664	5.5910(2)	14.126(1)	382.41(3)
269.12	0.1645	5.5935(2)	14.124(1)	382.69(3)
272.70	0.1614	5.5972(2)	14.120(1)	383.10(2)
275.69	0.1588	5.6004(2)	14.117(1)	383.46(2)
278.48	0.1567	5.6035(2)	14.115(1)	383.82(2)
280.87	0.1548	5.6061(2)	14.112(1)	384.10(2)
284.17	0.1525	5.6097(2)	14.109(1)	384.51(2)
287.27	0.1502	5.6134(2)	14.106(1)	384.94(2)
290.28	0.1480	5.6170(2)	14.103(1)	385.34(2)
293.20	0.1459	5.6206(2)	14.100(1)	385.75(2)
296.02	0.1439	5.6246(2)	14.096(1)	386.19(2)
298.95	0.1415	5.6288(2)	14.092(1)	386.68(2)
302.30	0.1388	5.6342(2)	14.088(1)	387.28(2)
305.06	0.1373	5.6391(2)	14.083(1)	387.85(2)
308.05	0.1419	5.6462(2)	14.078(1)	388.68(2)
311.80	0.1884	5.6629(2)	14.067(2)	390.66(2)
315.66	0.1899	8.0794(2)	-	527.39(3)
319.79	0.1799	8.0806(2)	-	527.63(3)
322.95	0.1751	8.0812(1)	-	527.74(3)
326.30	0.1710	8.0817(1)	-	527.84(3)
329.59	0.1674	8.0821(1)	-	527.92(3)
332.90	0.1642	8.0824(1)	-	527.98(3)
336.24	0.1615	8.0827(1)	-	528.04(3)
339.50	0.1588	8.0829(1)	-	528.09(3)
343.01	0.1565	8.0831(1)	-	528.13(3)
346.41	0.1547	8.0833(1)	-	528.16(3)
349.70	0.1528	8.0835(1)	-	528.19(2)
353.21	0.1512	8.0836(1)	-	528.22(2)
356.61	0.1497	8.0837(1)	-	528.24(2)
359.93	0.1484	8.0838(1)	-	528.25(2)
363.52	0.1472	8.0839(1)	-	528.27(2)
367.18	0.1464	8.0839(1)	-	528.28(2)
370.79	0.1449	8.0840(1)	-	528.29(2)
374.33	0.1442	8.0840(1)	-	528.30(2)
377.96	0.1430	8.0840(1)	-	528.30(2)
381.44	0.1420	8.0840(1)	-	528.30(2)
384.55	0.1411	8.0840(1)	-	528.30(2)
387.59	0.1405	8.0840(1)	-	528.31(2)

Table C.1 continued

Temperature (K)	Rwp	a (Å)	c (Å)	Volume (Å^3)
390.45	0.1397	8.0840(1)	-	528.30(2)
393.35	0.1395	8.0840(1)	-	528.30(2)
396.37	0.1386	8.0840(1)	-	528.30(2)
399.56	0.1377	8.0840(1)	-	528.29(2)
402.73	0.1372	8.0840(1)	-	528.29(2)
405.95	0.1363	8.0839(1)	-	528.28(2)
409.13	0.1357	8.0839(1)	-	528.28(2)
412.35	0.1352	8.0839(1)	-	528.27(2)
415.56	0.135	8.0838(1)	-	528.26(2)
418.60	0.1342	8.0840(1)	-	528.29(2)
422.15	0.1337	8.0839(1)	-	528.28(2)
424.93	0.1333	8.0839(1)	-	528.27(2)
427.92	0.1327	8.0838(1)	-	528.26(2)
430.96	0.1324	8.0838(1)	-	528.25(2)
434.09	0.1320	8.0837(1)	-	528.24(2)
437.07	0.1316	8.0836(1)	-	528.23(2)
440.00	0.1313	8.0836(1)	-	528.22(2)
442.94	0.1311	8.0835(1)	-	528.20(2)
443.31	0.1311	8.0835(1)	-	528.20(2)
447.68	0.1306	8.0834(1)	-	528.18(2)
450.73	0.1304	8.0834(1)	-	528.17(2)
451.33	0.1304	8.0833(1)	-	528.16(2)
455.45	0.1299	8.0832(1)	-	528.14(2)
458.37	0.1297	8.0831(1)	-	528.13(2)
459.40	0.1296	8.0831(1)	-	528.12(2)
463.27	0.1295	8.0830(1)	-	528.10(2)
466.05	0.1294	8.0829(1)	-	528.09(2)
468.67	0.1292	8.0829(1)	-	528.07(2)
471.29	0.1291	8.0828(1)	-	528.06(2)
473.83	0.1291	8.0827(1)	-	528.04(2)
476.36	0.1288	8.0826(1)	-	528.03(2)
478.96	0.1287	8.0825(1)	-	528.01(2)
481.53	0.1285	8.0825(1)	-	528.00(2)
484.06	0.1285	8.0824(1)	-	527.98(2)
486.54	0.1284	8.0823(1)	-	527.96(2)
488.97	0.1285	8.0822(1)	-	527.94(2)
491.53	0.1284	8.0821(1)	-	527.92(2)
493.90	0.1285	8.0820(1)	-	527.90(2)
496.05	0.1286	8.0819(1)	-	527.88(2)

Table C.1 continued

Temperature (K)	Rwp	a (Å)	c (Å)	Volume (Å^3)
498.34	0.1285	8.0818(1)	-	527.86(2)
501.02	0.1286	8.0816(1)	-	527.83(2)
503.75	0.1287	8.0815(1)	-	527.81(2)
503.54	0.1290	8.0814(1)	-	527.80(2)
501.59	0.1295	8.0814(1)	-	527.79(2)
499.44	0.1299	8.0814(1)	-	527.79(2)
497.64	0.1301	8.0814(1)	-	527.78(2)
495.60	0.1304	8.0814(1)	-	527.78(2)
493.59	0.1307	8.0814(1)	-	527.78(2)
491.31	0.1311	8.0814(1)	-	527.79(2)
488.99	0.1314	8.0814(1)	-	527.79(2)
486.37	0.1318	8.0814(1)	-	527.80(2)
483.69	0.1321	8.0815(1)	-	527.80(2)
480.85	0.1324	8.0815(1)	-	527.81(2)
478.15	0.1329	8.0815(1)	-	527.82(2)
475.53	0.1332	8.0816(1)	-	527.82(2)
472.98	0.1336	8.0816(1)	-	527.83(2)
469.99	0.1340	8.0817(1)	-	527.84(2)
467.93	0.1342	8.0817(1)	-	527.85(2)
464.63	0.1346	8.0818(1)	-	527.86(2)
461.41	0.1342	8.0817(1)	-	527.84(2)
458.34	0.1345	8.0817(1)	-	527.85(2)
455.37	0.1349	8.0818(1)	-	527.86(2)
452.46	0.1352	8.0818(1)	-	527.87(2)
449.58	0.1355	8.0819(1)	-	527.88(2)
446.71	0.1359	8.0819(1)	-	527.88(2)
443.94	0.1361	8.0819(1)	-	527.89(2)
440.97	0.1365	8.0820(1)	-	527.90(2)
438.07	0.1368	8.0820(1)	-	527.91(2)
435.26	0.1372	8.0821(1)	-	527.92(2)
432.42	0.1376	8.0821(1)	-	527.93(2)
429.38	0.1382	8.0822(1)	-	527.94(2)
426.41	0.1386	8.0822(1)	-	527.94(2)
423.44	0.1392	8.0822(1)	-	527.95(2)
420.46	0.1397	8.0823(1)	-	527.96(2)
417.47	0.1398	8.0823(1)	-	527.97(2)
414.47	0.1405	8.0823(1)	-	527.97(2)
411.56	0.1411	8.0824(1)	-	527.98(2)
408.44	0.1415	8.0824(1)	-	527.99(2)

Table C.1 continued

Temperature (K)	Rwp	a (Å)	c (Å)	Volume (Å^3)
405.40	0.1421	8.0824(1)	-	527.99(2)
402.23	0.1428	8.0825(1)	-	527.99(2)
399.24	0.1435	8.0825(1)	-	528.00(2)
395.97	0.1441	8.0825(1)	-	528.00(2)
393.26	0.1448	8.0825(1)	-	528.01(2)
390.50	0.1453	8.0825(1)	-	528.01(2)
387.66	0.1463	8.0825(1)	-	528.01(2)
384.80	0.1468	8.0825(1)	-	528.01(2)
382.41	0.1476	8.0825(1)	-	528.01(2)
378.25	0.1485	8.0825(1)	-	528.01(2)
374.81	0.1494	8.0825(1)	-	528.01(2)
371.41	0.1506	8.0825(1)	-	528.00(2)
368.15	0.1517	8.0824(1)	-	527.99(2)
364.65	0.1528	8.0824(1)	-	527.98(3)
361.38	0.1542	8.0823(1)	-	527.96(3)
358.11	0.1554	8.0822(1)	-	527.95(3)
354.63	0.1569	8.0821(1)	-	527.93(3)
351.17	0.1584	8.0820(1)	-	527.91(3)
347.86	0.1601	8.0819(1)	-	527.89(3)
344.45	0.1619	8.0818(1)	-	527.86(3)
341.07	0.1640	8.0816(1)	-	527.82(3)
337.81	0.1661	8.0814(1)	-	527.78(3)
334.43	0.1686	8.0811(1)	-	527.73(3)
331.49	0.1710	8.0808(1)	-	527.67(3)
328.11	0.1739	8.0805(1)	-	527.61(3)
324.85	0.1772	8.0800(2)	-	527.52(3)
321.64	0.1806	8.0795(2)	-	527.42(3)
318.48	0.1853	8.0788(2)	-	527.28(3)
313.25	0.1965	8.0770(2)	-	526.92(4)
311.06	0.2113	8.0747(2)	-	526.48(4)
311.80	0.2303	5.4736(4)	14.260(2)	392.31(4)
307.72	0.2296	5.4751(4)	14.258(2)	388.94(4)
305.10	0.2289	5.4765(4)	14.256(2)	387.67(4)
301.68	0.2278	5.4791(4)	14.252(2)	387.08(4)
298.79	0.2277	5.4798(4)	14.251(2)	386.65(4)
296.30	0.2270	5.4815(4)	14.249(2)	386.13(4)
292.85	0.2264	5.4834(4)	14.247(2)	385.73(4)
290.55	0.2258	5.4852(4)	14.244(2)	385.28(4)
287.36	0.2253	5.4871(4)	14.242(2)	384.87(4)

Table C.1 continued

Temperature (K)	Rwp	a (Å)	c (Å)	Volume (Å^3)
284.45	0.2247	5.4889(4)	14.240(2)	384.53(4)
281.71	0.2243	5.4911(4)	14.237(2)	384.16(4)
279.05	0.2236	5.4932(4)	14.234(2)	383.77(4)
275.89	0.2232	5.4949(4)	14.232(2)	383.44(4)
273.01	0.2227	5.4968(4)	14.229(2)	383.07(4)
270.03	0.2222	5.4990(4)	14.227(2)	382.76(4)
267.06	0.2213	5.5016(4)	14.223(2)	382.44(4)
264.19	0.2207	5.5037(4)	14.220(2)	382.11(4)
261.43	0.2199	5.5060(4)	14.217(2)	381.78(4)
258.48	0.2190	5.5085(4)	14.214(2)	381.48(4)
255.16	0.2183	5.5106(4)	14.211(2)	381.07(4)
252.05	0.2175	5.5125(4)	14.208(2)	380.80(4)
249.44	0.2164	5.5150(4)	14.205(2)	380.53(4)
246.94	0.2154	5.5176(4)	14.201(2)	380.20(4)
243.01	0.2145	5.5192(4)	14.199(2)	379.93(3)
240.33	0.2133	5.5218(4)	14.195(2)	379.65(3)
237.85	0.2120	5.5244(4)	14.192(2)	379.36(3)
234.79	0.2105	5.5268(4)	14.188(2)	379.08(4)
231.72	0.2091	5.5296(4)	14.184(2)	378.80(4)
228.84	0.2079	5.5316(4)	14.182(2)	378.53(3)
225.95	0.2067	5.5340(4)	14.178(2)	378.27(3)
223.05	0.2056	5.5362(4)	14.176(2)	377.99(3)
220.16	0.2048	5.5383(4)	14.173(2)	377.74(3)
217.29	0.2036	5.5405(4)	14.170(2)	377.48(3)
214.35	0.2027	5.5429(4)	14.168(2)	377.22(3)
211.48	0.2017	5.5454(3)	14.165(2)	376.96(3)
208.28	0.2007	5.5478(3)	14.162(2)	376.71(3)
205.44	0.1997	5.5503(3)	14.159(2)	376.49(3)
202.89	0.1991	5.5527(3)	14.156(2)	376.27(3)
199.92	0.1979	5.5553(3)	14.153(2)	376.04(3)
197.17	0.1969	5.5578(3)	14.150(1)	375.80(3)
193.40	0.1957	5.5604(3)	14.147(1)	375.60(3)
191.80	0.1943	5.5630(3)	14.144(1)	375.32(3)
187.92	0.1928	5.5656(3)	14.142(1)	375.08(3)
186.40	0.1910	5.5683(3)	14.139(1)	374.83(3)
182.39	0.1892	5.5709(3)	14.136(1)	374.57(3)
178.06	0.1871	5.5735(3)	14.133(1)	374.41(3)
178.15	0.1846	5.5765(3)	14.130(1)	374.16(3)
174.01	0.1826	5.5790(3)	14.127(1)	373.91(3)

Table C.1 continued

Temperature (K)	Rwp	a (Å)	c (Å)	Volume (Å^3)
170.27	0.1804	5.5815(3)	14.125(1)	373.72(3)
169.89	0.1772	5.5851(3)	14.121(1)	373.51(3)
167.41	0.1748	5.5879(3)	14.119(1)	373.27(3)
164.29	0.1722	5.5908(3)	14.116(1)	373.03(3)
161.20	0.1696	5.5938(3)	14.113(1)	372.83(3)
158.71	0.1672	5.5966(3)	14.111(1)	372.56(3)
155.07	0.1648	5.5994(3)	14.108(1)	372.34(3)
152.21	0.1621	5.6026(3)	14.105(1)	372.15(3)
149.31	0.1597	5.6055(3)	14.103(1)	371.97(3)
147.13	0.1571	5.6090(2)	14.100(1)	371.76(3)
144.20	0.1547	5.6122(2)	14.097(1)	371.54(2)
140.86	0.1529	5.6152(2)	14.095(1)	371.35(2)
138.39	0.1503	5.6188(2)	14.092(1)	371.16(2)
135.66	0.1478	5.6228(2)	14.088(1)	370.97(2)
132.73	0.1459	5.6263(2)	14.085(1)	370.78(2)
129.77	0.1433	5.6309(2)	14.081(1)	370.61(2)
127.37	0.1413	5.6347(2)	14.078(1)	370.55(2)
127.02	0.1391	5.6398(2)	14.073(1)	370.28(2)
122.65	0.1520	5.6502(3)	14.068(1)	370.14(3)
120.79	0.2154	5.6822(7)	14.030(3)	369.99(4)

Table C.2: Lattice constants and unit cell volume for rhombohedral $ZnNbF_6$ as determined by Rietveld analyses of the variable temperature x-ray diffraction data.

Temperature (K)	Rwp	a (Å)	c (Å)	Volume (Å^3)
111.61	0.1108	5.2531(1)	14.0132(4)	334.88(1)
115.12	0.1109	5.2538(1)	14.0120(4)	334.95(1)
117.47	0.1108	5.2547(1)	14.0109(4)	335.03(1)
119.77	0.1107	5.2556(1)	14.0096(4)	335.12(1)
122.19	0.1105	5.2566(1)	14.0082(4)	335.22(1)
125.07	0.1104	5.2575(1)	14.0070(4)	335.30(1)
127.37	0.1102	5.2585(1)	14.0057(4)	335.39(1)
130.72	0.1101	5.2595(1)	14.0044(4)	335.49(1)
133.03	0.1100	5.2604(1)	14.0032(4)	335.58(1)
135.87	0.1098	5.2614(1)	14.0019(4)	335.68(1)
138.67	0.1095	5.2624(1)	14.0006(4)	335.78(1)
141.38	0.1093	5.2634(1)	13.9993(4)	335.87(1)

Table C.2 continued

Temperature (K)	Rwp	a (Å)	c (Å)	Volume (Å^3)
143.91	0.1156	5.2644(1)	13.9979(4)	335.97(1)
146.61	0.1088	5.2655(1)	13.9967(4)	336.07(1)
149.53	0.1085	5.2666(1)	13.9954(4)	336.18(1)
153.71	0.1083	5.2676(1)	13.9941(4)	336.28(1)
156.24	0.1080	5.2687(1)	13.9928(4)	336.39(1)
158.88	0.1077	5.2698(1)	13.9915(4)	336.49(1)
161.53	0.1074	5.2708(1)	13.9901(4)	336.60(1)
164.17	0.1071	5.2720(1)	13.9888(4)	336.71(1)
166.70	0.1069	5.2731(1)	13.9875(4)	336.82(1)
169.54	0.1130	5.2741(1)	13.9861(4)	336.92(1)
172.67	0.1064	5.2754(1)	13.9848(4)	337.05(1)
175.13	0.1061	5.2764(1)	13.9836(4)	337.15(1)
178.23	0.1058	5.2776(1)	13.9823(4)	337.27(1)
180.85	0.1056	5.2787(1)	13.9810(4)	337.38(1)
183.74	0.1054	5.2800(1)	13.9796(4)	337.51(1)
186.47	0.1053	5.2810(1)	13.9784(4)	337.62(1)
189.35	0.1050	5.2822(1)	13.9771(4)	337.74(1)
192.30	0.1047	5.2834(1)	13.9757(4)	337.86(1)
195.21	0.1045	5.2846(1)	13.9745(4)	337.98(1)
198.30	0.1043	5.2857(1)	13.9732(4)	338.10(1)
201.17	0.1040	5.2869(1)	13.9719(4)	338.22(1)
204.44	0.1038	5.2882(1)	13.9706(4)	338.35(1)
207.36	0.1034	5.2895(1)	13.9693(4)	338.48(1)
210.29	0.1031	5.2907(1)	13.9680(4)	338.61(1)
213.22	0.1028	5.2920(1)	13.9667(4)	338.73(1)
216.16	0.1026	5.2932(1)	13.9654(4)	338.86(1)
219.09	0.1023	5.2945(1)	13.9642(4)	338.99(1)
222.02	0.1018	5.2957(1)	13.9629(4)	339.12(1)
224.95	0.1016	5.2970(1)	13.9616(4)	339.26(1)
227.88	0.1013	5.2983(1)	13.9604(4)	339.39(1)
230.81	0.1009	5.2996(1)	13.9592(4)	339.53(1)
233.83	0.1006	5.3009(1)	13.9579(4)	339.66(1)
236.76	0.1002	5.3022(1)	13.9567(4)	339.79(1)
239.69	0.0999	5.3034(1)	13.9554(4)	339.93(1)
242.62	0.0995	5.3047(1)	13.9542(4)	340.06(1)
245.55	0.0992	5.3060(1)	13.9530(4)	340.20(1)
248.49	0.0988	5.3073(1)	13.9518(4)	340.33(1)

Table C.2 continued

Temperature (K)	Rwp	a (Å)	c (Å)	Volume (Å^3)
251.43	0.0985	5.3086(1)	13.9506(4)	340.47(1)
254.38	0.0981	5.3099(1)	13.9493(4)	340.61(1)
257.34	0.0978	5.3113(1)	13.9481(4)	340.75(1)
260.30	0.0975	5.3126(1)	13.9469(4)	340.89(1)
263.27	0.0971	5.3139(1)	13.9457(4)	341.03(1)
266.24	0.0969	5.3152(1)	13.9445(4)	341.17(1)
269.22	0.0966	5.3166(1)	13.9432(4)	341.32(1)
272.20	0.0962	5.3179(1)	13.9420(4)	341.46(1)
275.19	0.0960	5.3193(1)	13.9407(4)	341.60(1)
278.18	0.0957	5.3206(1)	13.9395(4)	341.74(1)
281.17	0.0955	5.3220(1)	13.9382(4)	341.89(1)
284.17	0.0953	5.3233(1)	13.9370(4)	342.03(1)
287.17	0.0952	5.3247(1)	13.9358(4)	342.17(1)
290.18	0.0948	5.3261(1)	13.9345(4)	342.32(1)
293.20	0.0947	5.3275(1)	13.9332(4)	342.47(1)
296.22	0.0945	5.3288(1)	13.9319(4)	342.62(1)
299.25	0.0944	5.3302(1)	13.9307(4)	342.76(1)
302.30	0.0943	5.3316(1)	13.9294(4)	342.91(1)
305.37	0.0942	5.3330(1)	13.9282(4)	343.06(1)
308.56	0.0940	5.3345(1)	13.9268(4)	343.22(1)
311.70	0.0940	5.3360(1)	13.9255(4)	343.38(1)
315.94	0.0938	5.3382(1)	13.9235(4)	343.62(1)
319.67	0.0937	5.3400(1)	13.9219(4)	343.81(1)
323.06	0.0936	5.3415(1)	13.9207(4)	343.97(1)
326.30	0.0935	5.3431(1)	13.9193(4)	344.14(1)
329.59	0.0935	5.3447(1)	13.9179(4)	344.31(1)
332.90	0.0932	5.3463(1)	13.9166(4)	344.49(1)
336.24	0.0931	5.3480(1)	13.9151(4)	344.67(1)
339.61	0.0928	5.3497(1)	13.9137(4)	344.85(1)
343.01	0.0929	5.3515(1)	13.9122(4)	345.04(1)
346.41	0.0929	5.3532(1)	13.9108(4)	345.23(1)
349.81	0.0929	5.3549(1)	13.9094(4)	345.41(1)
353.21	0.0928	5.3566(1)	13.9080(4)	345.60(1)
356.61	0.0930	5.3584(1)	13.9065(4)	345.79(1)
360.04	0.0933	5.3602(1)	13.9051(4)	345.99(1)
363.52	0.0939	5.3620(1)	13.9036(4)	346.19(1)
367.18	0.0942	5.3641(1)	13.9019(4)	346.41(1)
370.79	0.0943	5.3661(1)	13.9003(4)	346.64(1)
374.57	0.0942	5.3681(1)	13.8987(4)	346.85(1)

Table C.2 continued

Temperature (K)	Rwp	a (Å)	c (Å)	Volume (Å^3)
378.20	0.0940	5.3701(1)	13.8971(4)	347.07(1)
381.66	0.0937	5.3721(1)	13.8954(4)	347.29(1)
384.83	0.0934	5.3740(1)	13.8939(4)	347.49(1)
387.02	0.0932	5.3757(1)	13.8925(4)	347.68(1)
390.64	0.0930	5.3775(1)	13.8910(4)	347.87(1)
393.64	0.0929	5.3793(1)	13.8895(4)	348.07(1)
396.78	0.0927	5.3814(1)	13.8879(4)	348.30(1)
400.28	0.0927	5.3837(1)	13.8860(4)	348.55(1)
403.71	0.0926	5.3859(1)	13.8842(4)	348.79(1)
407.07	0.0927	5.3881(1)	13.8823(4)	349.04(1)
410.29	0.0928	5.3904(1)	13.8804(4)	349.28(1)
413.49	0.0928	5.3927(1)	13.8785(4)	349.54(1)
416.37	0.0929	5.3950(1)	13.8766(4)	349.79(1)
419.33	0.0932	5.3972(1)	13.8748(4)	350.02(1)
421.71	0.0934	5.3991(1)	13.8731(4)	350.23(1)
424.33	0.0939	5.4010(1)	13.8715(4)	350.43(1)
427.16	0.0943	5.4029(1)	13.8698(4)	350.63(1)
429.73	0.0948	5.4047(1)	13.8682(4)	350.82(1)
432.34	0.0954	5.4065(1)	13.8666(4)	351.03(1)
434.69	0.0962	5.4083(1)	13.8651(4)	351.21(1)
437.79	0.0971	5.4104(1)	13.8632(4)	351.44(1)
440.57	0.0979	5.4125(1)	13.8615(4)	351.67(1)
443.25	0.0988	5.4145(1)	13.8598(4)	351.88(1)
445.92	0.0997	5.4165(1)	13.8580(5)	352.10(1)
448.61	0.1008	5.4186(1)	13.8563(5)	352.33(1)
451.28	0.1020	5.4206(1)	13.8546(5)	352.55(1)
453.80	0.1033	5.4227(1)	13.8528(5)	352.78(1)
456.44	0.1046	5.4249(1)	13.8510(5)	353.01(1)
458.97	0.1060	5.4271(1)	13.8491(5)	353.25(1)
461.69	0.1074	5.4295(1)	13.8471(5)	353.51(1)
464.22	0.1089	5.4319(1)	13.8450(5)	353.77(1)
466.60	0.1109	5.4343(1)	13.8429(5)	354.03(1)
469.19	0.1131	5.4369(1)	13.8406(5)	354.31(1)
471.72	0.1151	5.4394(1)	13.8383(5)	354.59(1)
474.21	0.1170	5.4419(1)	13.8360(6)	354.85(1)
476.77	0.1192	5.4446(1)	13.8336(6)	355.13(1)
479.03	0.1215	5.4472(1)	13.8312(6)	355.42(1)
481.43	0.1240	5.4499(1)	13.8287(6)	355.70(1)
483.81	0.1265	5.4527(1)	13.8261(6)	356.00(1)

Table C.2 continued

Temperature (K)	Rwp	a (Å)	c (Å)	Volume (Å^3)
486.18	0.1295	5.4554(2)	13.8234(7)	356.29(2)
488.99	0.1325	5.4583(2)	13.8207(7)	356.59(2)
491.66	0.1358	5.4610(2)	13.8180(7)	356.88(2)
494.66	0.1393	5.4637(2)	13.8153(8)	357.16(2)
497.84	0.1432	5.4665(2)	13.8125(8)	357.46(2)
501.02	0.1473	5.4698(2)	13.8091(8)	357.79(2)
504.43	0.1524	5.4731(2)	13.8058(9)	358.14(2)
503.50	0.1565	5.4740(2)	13.8046(9)	358.24(2)
501.90	0.1592	5.4734(2)	13.8049(9)	358.16(2)
499.91	0.1604	5.4720(2)	13.8059(9)	358.01(2)
497.78	0.1611	5.4698(2)	13.8077(9)	357.77(2)
495.27	0.1612	5.4680(2)	13.8092(9)	357.57(2)
494.67	0.1615	5.4675(2)	13.8095(9)	357.51(2)
490.87	0.1615	5.4640(2)	13.8125(9)	357.13(2)
488.08	0.1613	5.4615(2)	13.8147(9)	356.85(2)
486.89	0.1613	5.4601(2)	13.8158(9)	356.70(2)
485.04	0.1610	5.4589(2)	13.8168(9)	356.57(2)
482.22	0.1605	5.4569(2)	13.8184(9)	356.36(2)
479.22	0.1602	5.4547(2)	13.8203(9)	356.12(2)
476.31	0.1597	5.4524(2)	13.8223(9)	355.87(2)
473.60	0.1592	5.4502(2)	13.8241(9)	355.62(2)
470.54	0.1588	5.4480(2)	13.8260(9)	355.38(2)
467.87	0.1581	5.4458(2)	13.8279(9)	355.15(2)
465.42	0.1576	5.4436(2)	13.8297(9)	354.91(2)
461.66	0.1572	5.4413(2)	13.8317(9)	354.65(2)
458.21	0.1568	5.4389(2)	13.8336(9)	354.40(2)
454.94	0.1563	5.4367(2)	13.8354(8)	354.16(2)
451.98	0.1558	5.4346(2)	13.8371(8)	353.92(2)
448.97	0.1553	5.4325(2)	13.8388(8)	353.69(2)
446.00	0.1549	5.4304(2)	13.8405(8)	353.47(2)
443.04	0.1546	5.4284(2)	13.8421(8)	353.24(2)
440.18	0.1540	5.4264(2)	13.8436(8)	353.02(2)
437.39	0.1535	5.4245(2)	13.8451(8)	352.81(2)
434.69	0.1529	5.4226(2)	13.8466(8)	352.60(2)
431.97	0.1523	5.4207(2)	13.8481(8)	352.39(2)
429.13	0.1517	5.4187(2)	13.8496(8)	352.18(2)
426.28	0.1509	5.4168(2)	13.8512(8)	351.96(2)
423.22	0.1501	5.4147(2)	13.8528(8)	351.74(2)
420.34	0.1494	5.4127(2)	13.8544(8)	351.52(2)

Table C.2 continued

Temperature (K)	Rwp	a (Å)	c (Å)	Volume (Å^3)
417.46	0.1485	5.4108(2)	13.8561(8)	351.31(2)
414.47	0.1475	5.4087(2)	13.8578(8)	351.08(2)
411.37	0.1464	5.4066(2)	13.8597(8)	350.85(2)
408.46	0.1454	5.4045(2)	13.8615(8)	350.63(2)
405.54	0.1445	5.4024(2)	13.8634(7)	350.41(2)
402.40	0.1435	5.4002(2)	13.8653(7)	350.18(2)
399.34	0.1425	5.3981(2)	13.8673(7)	349.95(2)
396.15	0.1415	5.3959(2)	13.8692(7)	349.72(2)
393.60	0.1405	5.3941(2)	13.8708(7)	349.52(2)
390.66	0.1398	5.3922(1)	13.8725(7)	349.31(2)
387.80	0.1392	5.3904(1)	13.8741(7)	349.12(2)
384.85	0.1385	5.3886(1)	13.8756(7)	348.93(2)
380.53	0.1381	5.3866(1)	13.8773(7)	348.71(2)
377.15	0.1375	5.3847(1)	13.8789(7)	348.50(2)
373.76	0.1373	5.3827(1)	13.8806(7)	348.29(2)
370.38	0.1371	5.3807(1)	13.8823(7)	348.07(2)
367.00	0.1370	5.3786(1)	13.8839(7)	347.85(2)
363.63	0.1369	5.3766(1)	13.8856(7)	347.62(1)
360.27	0.1371	5.3747(1)	13.8872(7)	347.42(1)
356.95	0.1370	5.3729(1)	13.8886(7)	347.22(1)
353.65	0.1371	5.3710(1)	13.8901(7)	347.02(1)
350.27	0.1373	5.3693(1)	13.8916(7)	346.82(1)
346.90	0.1375	5.3675(1)	13.8930(7)	346.64(1)
343.62	0.1377	5.3658(1)	13.8944(7)	346.45(1)
340.26	0.1380	5.3640(1)	13.8958(7)	346.26(1)
336.98	0.1383	5.3623(1)	13.8972(7)	346.06(1)
333.51	0.1388	5.3605(1)	13.8986(7)	345.87(1)
330.42	0.1393	5.3588(1)	13.9000(7)	345.69(1)
328.38	0.1395	5.3574(1)	13.9012(7)	345.54(1)
324.32	0.1401	5.3555(1)	13.9028(7)	345.32(1)
321.73	0.1406	5.3539(1)	13.9041(7)	345.15(2)
315.81	0.1409	5.3522(1)	13.9054(7)	344.97(2)
313.68	0.1418	5.3498(1)	13.9075(7)	344.71(2)
311.28	0.1423	5.3484(1)	13.9087(7)	344.56(2)
308.40	0.1427	5.3469(1)	13.9099(7)	344.40(2)
304.93	0.1431	5.3454(2)	13.9113(7)	344.24(2)
302.05	0.1435	5.3440(2)	13.9125(7)	344.09(2)
299.36	0.1440	5.3427(2)	13.9136(7)	343.95(2)
296.75	0.1444	5.3415(2)	13.9147(7)	343.82(2)

Table C.2 continued

Temperature (K)	Rwp	a (Å)	c (Å)	Volume (Å^3)
293.71	0.1446	5.3401(2)	13.9159(7)	343.67(2)
290.95	0.1450	5.3388(2)	13.9171(7)	343.53(2)
287.69	0.1454	5.3374(2)	13.9183(7)	343.39(2)
284.31	0.1459	5.3360(2)	13.9196(7)	343.23(2)
281.74	0.1461	5.3347(2)	13.9208(7)	343.09(2)
278.76	0.1466	5.3334(2)	13.9220(7)	342.96(2)
275.79	0.1470	5.3321(2)	13.9233(7)	342.82(2)
272.93	0.1474	5.3308(2)	13.9246(7)	342.68(2)
269.89	0.1476	5.3294(2)	13.9259(7)	342.54(2)
267.05	0.1482	5.3282(2)	13.9272(7)	342.41(2)
264.14	0.1486	5.3268(2)	13.9285(7)	342.27(2)
261.44	0.1491	5.3255(2)	13.9299(7)	342.13(2)
258.45	0.1516	5.3235(2)	13.9325(7)	341.95(2)
255.79	0.1517	5.3227(2)	13.9334(7)	341.86(2)
253.01	0.1522	5.3215(2)	13.9345(7)	341.74(2)
250.14	0.1525	5.3203(2)	13.9357(7)	341.61(2)
247.20	0.1529	5.3191(2)	13.9369(7)	341.49(2)
244.10	0.1535	5.3178(2)	13.9382(7)	341.35(2)
241.31	0.1538	5.3166(2)	13.9394(7)	341.23(2)
238.52	0.1543	5.3154(2)	13.9406(7)	341.10(2)
234.94	0.1548	5.3139(2)	13.9421(7)	340.94(2)
232.66	0.1553	5.3129(2)	13.9431(7)	340.84(2)
229.87	0.1556	5.3116(2)	13.9443(7)	340.71(2)
227.03	0.1560	5.3104(2)	13.9455(7)	340.58(2)
223.90	0.1567	5.3091(2)	13.9468(8)	340.44(2)
221.07	0.1570	5.3079(2)	13.9480(8)	340.32(2)
218.66	0.1575	5.3067(2)	13.9492(8)	340.19(2)
216.11	0.1580	5.3055(2)	13.9504(8)	340.07(2)
214.29	0.1583	5.3043(2)	13.9515(8)	339.95(2)
209.87	0.1587	5.3031(2)	13.9528(8)	339.82(2)
206.46	0.1593	5.3019(2)	13.9539(8)	339.70(2)
203.22	0.1597	5.3007(2)	13.9552(8)	339.57(2)
200.14	0.1600	5.2995(2)	13.9564(8)	339.45(2)
197.38	0.1604	5.2984(2)	13.9576(8)	339.33(2)
194.80	0.1608	5.2972(2)	13.9588(8)	339.21(2)
191.44	0.1612	5.2959(2)	13.9601(8)	339.08(2)
189.60	0.1616	5.2950(2)	13.9611(8)	338.98(2)
186.40	0.1619	5.2936(2)	13.9626(8)	338.85(2)
183.31	0.1625	5.2925(2)	13.9639(8)	338.73(2)

Table C.2 continued

Temperature (K)	Rwp	a (Å)	c (Å)	Volume (Å^3)
180.79	0.1627	5.2914(2)	13.9651(8)	338.62(2)
177.73	0.1631	5.2901(2)	13.9665(8)	338.49(2)
174.74	0.1634	5.2889(2)	13.9678(8)	338.36(2)
171.26	0.1638	5.2875(2)	13.9694(8)	338.23(2)
168.78	0.1640	5.2862(2)	13.9709(8)	338.10(2)
166.01	0.1643	5.2851(2)	13.9722(8)	337.98(2)
160.23	0.1647	5.2834(2)	13.9741(8)	337.82(2)
157.17	0.1650	5.2823(2)	13.9755(8)	337.71(2)
156.34	0.1652	5.2814(2)	13.9766(8)	337.62(2)
152.39	0.1655	5.2802(2)	13.9780(8)	337.51(2)
148.50	0.1656	5.2792(2)	13.9793(8)	337.40(2)
145.93	0.1658	5.2782(2)	13.9806(8)	337.31(2)
143.59	0.1662	5.2773(2)	13.9817(8)	337.22(2)
141.28	0.1663	5.2763(2)	13.9829(8)	337.13(2)
138.67	0.1665	5.2753(2)	13.9843(8)	337.02(2)
136.26	0.1668	5.2743(2)	13.9856(8)	336.93(2)
134.20	0.1669	5.2735(2)	13.9867(8)	336.85(2)
136.01	0.1670	5.2734(2)	13.9867(8)	336.85(2)
129.57	0.1674	5.2717(2)	13.9890(8)	336.68(2)
128.77	0.1674	5.2712(2)	13.9897(8)	336.63(2)
125.09	0.1677	5.2698(2)	13.9916(8)	336.50(2)
122.67	0.1680	5.2689(2)	13.9928(8)	336.42(2)
120.47	0.1681	5.2680(2)	13.9941(8)	336.33(2)
118.19	0.1682	5.2672(2)	13.9953(8)	336.25(2)

Table C.3: Unit cell volumes and lattice constants for cubic and rhombohedral $MnNbF_6$ and NaCl as determined from Rietveld analyses of the high-pressure diffraction data. Pressures estimated using an equation of state and the unit cell volume of NaCl are also given.

$MnNbF_6$ cubic a (Å)	$MnNbF_6$ cubic Volume (Å^3)	$MnNbF_6$ $R\bar{3}$ a (Å)	$MnNbF_6$ $R\bar{3}$ c (Å)	$MnNbF_6$ $R\bar{3}$ Vol (Å^3)	NaCl Vol (Å^3)	Pressure (GPa)
8.0696(2)	525.48(5)	5.6319(3)	14.065(1)	386.34(3)	179.65(3)	0.03(5)
8.0695(2)	525.47(5)	5.6318(3)	14.065(1)	386.33(3)	179.65(3)	0.03(6)
8.0695(2)	525.47(5)	5.6317(3)	14.065(1)	386.32(3)	179.65(3)	0.03(6)
8.0695(2)	525.47(5)	5.6317(3)	14.065(1)	386.32(3)	179.64(3)	0.03(5)
8.0695(2)	525.45(5)	5.6316(3)	14.065(1)	386.31(3)	179.65(3)	0.03(6)
8.0694(2)	525.45(5)	5.6316(3)	14.065(1)	386.31(3)	179.65(3)	0.03(6)

Table C.3 continued

$MnNbF_6$ cubic a (Å)	$MnNbF_6$ cubic Volume (Å^3)	$MnNbF_6$ $R\bar{3}$ a (Å)	$MnNbF_6$ $R\bar{3}$ c (Å)	$MnNbF_6$ $R\bar{3}$ Vol (Å^3)	NaCl Vol (Å^3)	Pressure (GPa)
8.0694(2)	525.44(5)	5.6315(3)	14.065(1)	386.30(3)	179.65(3)	0.03(6)
8.0693(2)	525.43(5)	5.6315(3)	14.065(1)	386.30(3)	179.65(3)	0.03(5)
8.0693(2)	525.43(5)	5.6314(3)	14.066(1)	386.29(3)	179.65(3)	0.03(6)
8.0694(2)	525.44(5)	5.6314(3)	14.065(1)	386.28(3)	179.65(3)	0.03(5)
8.0694(2)	525.44(5)	5.6313(3)	14.065(1)	386.27(3)	179.65(3)	0.03(5)
8.0695(2)	525.46(5)	5.6317(3)	14.065(1)	386.31(3)	179.64(3)	0.03(5)
8.0696(2)	525.48(4)	5.6314(3)	14.063(1)	386.23(3)	179.64(3)	0.03(5)
8.0695(2)	525.45(4)	5.6313(3)	14.064(1)	386.22(3)	179.65(3)	0.03(5)
8.0694(2)	525.44(4)	5.6316(3)	14.063(1)	386.24(3)	179.67(3)	0.03(5)
8.0696(2)	525.48(4)	5.6318(3)	14.061(1)	386.23(3)	179.68(3)	0.03(5)
8.0693(2)	525.43(4)	5.6316(3)	14.063(1)	386.26(3)	179.70(3)	0.03(5)
8.0693(2)	525.41(4)	5.6312(3)	14.064(1)	386.23(3)	179.71(3)	0.02(5)
8.0690(2)	525.36(4)	5.6308(3)	14.065(1)	386.20(3)	179.72(3)	0.02(5)
8.0691(2)	525.38(5)	5.6309(3)	14.065(1)	386.22(3)	179.69(3)	0.03(5)
8.0690(2)	525.36(5)	5.6308(3)	14.066(1)	386.22(3)	179.70(3)	0.03(5)
8.0691(2)	525.39(5)	5.6308(3)	14.065(1)	386.19(3)	179.70(3)	0.02(5)
8.0690(2)	525.37(5)	5.6306(3)	14.065(1)	386.17(3)	179.72(3)	0.02(5)
8.0690(2)	525.35(5)	5.6305(3)	14.066(1)	386.17(3)	179.74(3)	0.02(5)
8.0690(2)	525.36(5)	5.6306(3)	14.065(1)	386.17(3)	179.76(3)	0.02(5)
8.0691(3)	525.38(5)	5.6308(3)	14.064(1)	386.17(3)	179.75(3)	0.02(5)
8.0692(3)	525.40(5)	5.6307(3)	14.064(1)	386.16(3)	179.77(3)	0.02(5)
8.0686(3)	525.29(5)	5.6305(3)	14.065(1)	386.16(3)	179.77(2)	0.02(5)
8.0688(3)	525.31(5)	5.6305(3)	14.066(1)	386.18(3)	179.81(2)	0.01(5)
8.0684(3)	525.24(5)	5.6298(3)	14.068(1)	386.16(3)	179.84(2)	0.01(5)
8.0687(3)	525.30(5)	5.6302(3)	14.065(1)	386.12(3)	179.85(2)	0.01(5)
8.0685(3)	525.26(5)	5.6303(3)	14.065(1)	386.13(3)	179.86(2)	0.00(5)
8.0686(3)	525.28(5)	5.6303(3)	14.065(1)	386.12(3)	179.88(2)	0.00(5)
8.0657(4)	524.72(9)	5.6267(3)	14.069(1)	385.73(3)	179.89(2)	0.00(5)
8.0250(7)	516.81(14)	5.6164(3)	14.084(1)	384.76(3)	179.73(2)	0.02(5)
8.0127(6)	514.45(11)	5.6086(3)	14.088(1)	383.78(3)	179.62(2)	0.04(5)
-	-	5.5991(3)	14.072(1)	382.06(2)	179.20(2)	0.09(5)
-	-	5.5827(3)	14.086(1)	380.18(2)	178.93(2)	0.13(5)
-	-	5.5741(3)	14.093(1)	379.21(2)	178.80(2)	0.15(5)
-	-	5.5684(3)	14.098(1)	378.56(2)	178.71(2)	0.16(5)
-	-	5.5615(3)	14.103(1)	377.78(2)	178.63(2)	0.17(5)

Table C.3 continued

$MnNbF_6$ cubic a (Å)	$MnNbF_6$ cubic Volume (Å^3)	$MnNbF_6$ $R\bar{3}$ a (Å)	$MnNbF_6$ $R\bar{3}$ c (Å)	$MnNbF_6$ $R\bar{3}$ Vol (Å^3)	NaCl Vol (Å^3)	Pressure (GPa)
-	-	5.5512(3)	14.111(1)	376.58(2)	178.51(2)	0.19(5)
-	-	5.5315(3)	14.126(1)	374.31(2)	178.27(2)	0.22(5)
-	-	5.5131(3)	14.143(1)	372.27(2)	178.04(2)	0.25(5)
-	-	5.4987(3)	14.156(1)	370.67(2)	177.84(2)	0.28(5)
-	-	5.4821(3)	14.168(1)	368.76(2)	177.62(2)	0.31(5)
-	-	5.4591(3)	14.184(1)	366.08(2)	177.30(2)	0.36(5)
-	-	5.4373(3)	14.203(2)	363.64(2)	177.02(2)	0.40(5)
-	-	5.4148(3)	14.222(2)	361.12(3)	176.71(2)	0.45(5)
-	-	5.3877(4)	14.245(2)	358.11(3)	176.30(2)	0.51(6)
-	-	5.3678(3)	14.264(2)	355.94(3)	176.00(2)	0.55(5)
-	-	5.3562(3)	14.275(2)	354.67(3)	175.81(2)	0.58(5)
-	-	5.3466(3)	14.284(2)	353.60(3)	175.65(2)	0.61(5)
-	-	5.3348(3)	14.294(2)	352.31(3)	175.44(2)	0.64(5)
-	-	5.3247(3)	14.303(2)	351.20(3)	175.25(2)	0.67(5)
-	-	5.3101(3)	14.316(2)	349.60(3)	174.97(2)	0.71(5)
-	-	5.2997(3)	14.326(2)	348.46(2)	174.76(2)	0.74(5)
-	-	5.2881(3)	14.336(2)	347.19(2)	174.52(2)	0.78(5)
-	-	5.2792(3)	14.344(2)	346.21(2)	174.32(2)	0.81(5)
-	-	5.2700(3)	14.352(2)	345.19(2)	174.12(2)	0.85(5)
-	-	5.2619(3)	14.358(2)	344.28(2)	173.93(2)	0.88(6)
-	-	5.2526(3)	14.366(2)	343.25(2)	173.70(2)	0.92(6)
-	-	5.2439(3)	14.374(2)	342.31(2)	173.48(2)	0.95(6)
-	-	5.2319(3)	14.385(2)	341.01(2)	173.17(2)	1.00(6)
-	-	5.2161(3)	14.398(2)	339.27(2)	172.74(2)	1.08(6)
-	-	5.2036(3)	14.408(2)	337.87(2)	172.37(2)	1.14(6)
-	-	5.1924(3)	14.417(1)	336.61(2)	172.04(2)	1.20(6)
-	-	5.1841(3)	14.423(1)	335.67(2)	171.77(2)	1.24(6)
-	-	5.1770(3)	14.428(1)	334.88(2)	171.54(2)	1.28(6)
-	-	5.1691(3)	14.433(1)	333.99(2)	171.28(2)	1.33(6)
-	-	5.1622(3)	14.438(1)	333.21(2)	171.04(2)	1.37(6)
-	-	5.1535(3)	14.445(1)	332.24(2)	170.73(2)	1.43(6)
-	-	5.1467(3)	14.450(1)	331.48(2)	170.48(2)	1.47(6)
-	-	5.1384(3)	14.456(1)	330.54(2)	170.15(2)	1.53(6)
-	-	5.1299(2)	14.462(1)	329.59(2)	169.81(2)	1.60(6)
-	-	5.1258(2)	14.464(1)	329.11(2)	169.65(2)	1.63(6)
-	-	5.1207(2)	14.467(1)	328.54(2)	169.46(2)	1.66(6)
-	-	5.1158(2)	14.471(1)	327.98(2)	169.26(2)	1.70(6)
-	-	5.1111(2)	14.474(1)	327.45(2)	169.09(1)	1.73(6)

Table C.3 continued

$MnNbF_6$ cubic a (Å)	$MnNbF_6$ cubic Volume (Å^3)	$MnNbF_6$ $R\bar{3}$ a (Å)	$MnNbF_6$ $R\bar{3}$ c (Å)	$MnNbF_6$ $R\bar{3}$ Vol (Å^3)	NaCl Vol (Å^3)	Pressure (GPa)
-	-	5.1041(2)	14.479(1)	326.66(2)	168.82(1)	1.79(6)
-	-	5.0999(2)	14.482(1)	326.20(2)	168.63(1)	1.82(6)
-	-	5.0962(2)	14.484(1)	325.78(2)	168.46(1)	1.85(6)
-	-	5.0926(2)	14.487(1)	325.37(2)	168.29(1)	1.89(6)
-	-	5.0874(2)	14.491(1)	324.80(2)	168.04(1)	1.94(6)
-	-	5.0828(2)	14.494(1)	324.27(2)	167.82(1)	1.98(6)
-	-	5.0789(2)	14.496(1)	323.83(2)	167.62(1)	2.02(6)
-	-	5.0745(2)	14.499(1)	323.33(2)	167.38(1)	2.07(6)
-	-	5.0690(2)	14.502(1)	322.72(2)	167.07(1)	2.13(6)
-	-	5.0642(2)	14.505(1)	322.17(2)	166.80(1)	2.19(6)
-	-	5.0595(3)	14.508(1)	321.63(2)	166.52(1)	2.25(6)
-	-	5.0533(3)	14.512(2)	320.92(2)	166.13(1)	2.33(6)
-	-	5.0484(3)	14.514(2)	320.35(2)	165.83(2)	2.39(7)
-	-	5.0432(3)	14.517(2)	319.75(2)	165.51(2)	2.46(7)
-	-	5.0375(3)	14.520(2)	319.09(2)	165.14(2)	2.54(7)
-	-	5.0324(3)	14.522(2)	318.50(2)	164.82(2)	2.61(7)
-	-	5.0289(3)	14.523(2)	318.09(2)	164.62(2)	2.66(7)
-	-	5.0249(3)	14.525(2)	317.62(3)	164.36(2)	2.71(7)
-	-	5.0200(3)	14.527(2)	317.04(3)	164.01(2)	2.79(7)
-	-	5.0159(3)	14.529(2)	316.56(3)	163.74(2)	2.86(7)
-	-	5.0110(3)	14.531(2)	315.98(3)	163.39(2)	2.94(7)
-	-	5.0072(3)	14.532(2)	315.52(3)	163.13(2)	3.00(8)
-	-	5.0037(3)	14.533(2)	315.11(3)	162.89(2)	3.05(8)
-	-	5.0000(3)	14.534(2)	314.66(3)	162.63(2)	3.11(8)
-	-	4.9967(4)	14.535(2)	314.28(3)	162.42(2)	3.17(8)
-	-	4.9918(4)	14.537(2)	313.70(3)	162.05(2)	3.25(8)
-	-	4.9863(4)	14.538(2)	313.03(3)	161.63(2)	3.36(8)
-	-	4.9820(4)	14.539(2)	312.51(3)	161.32(2)	3.43(8)
-	-	4.9765(4)	14.540(2)	311.85(3)	160.88(2)	3.54(8)
-	-	4.9724(4)	14.541(2)	311.35(3)	160.58(2)	3.62(8)
-	-	4.9669(4)	14.542(2)	310.68(3)	160.14(2)	3.73(8)
-	-	4.9617(4)	14.541(2)	310.02(3)	159.72(2)	3.84(9)
-	-	4.9585(4)	14.541(2)	309.60(3)	159.50(2)	3.90(9)
-	-	4.9554(4)	14.541(2)	309.22(3)	159.28(2)	3.96(9)
-	-	4.9516(4)	14.540(2)	308.73(3)	158.98(2)	4.04(9)
-	-	4.9483(4)	14.539(2)	308.31(3)	158.73(2)	4.10(9)
-	-	4.9446(4)	14.538(2)	307.83(3)	158.44(2)	4.18(9)
-	-	4.9401(4)	14.537(3)	307.23(3)	158.06(2)	4.29(9)

Table C.3 continued

$MnNbF_6$ cubic a (Å)	$MnNbF_6$ cubic Volume (Å^3)	$MnNbF_6$ $R\bar{3}$ a (Å)	$MnNbF_6$ $R\bar{3}$ c (Å)	$MnNbF_6$ $R\bar{3}$ Vol (Å^3)	NaCl Vol (Å^3)	Pressure (GPa)
-	-	4.9361(4)	14.535(3)	306.70(3)	157.73(2)	4.38(9)
-	-	4.9325(4)	14.534(3)	306.22(4)	157.45(2)	4.46(9)
-	-	4.9290(4)	14.532(3)	305.75(4)	157.16(2)	4.54(9)
-	-	4.9252(4)	14.530(3)	305.24(4)	156.83(2)	4.63(9)
-	-	4.9202(5)	14.528(3)	304.58(4)	156.37(2)	4.77(10)
-	-	4.9158(5)	14.525(3)	303.98(4)	156.00(2)	4.88(10)
-	-	4.9125(5)	14.523(3)	303.51(4)	155.72(2)	4.96(10)
-	-	4.9091(5)	14.521(3)	303.05(4)	155.43(2)	5.05(10)
-	-	4.9059(5)	14.519(3)	302.61(4)	155.14(2)	5.13(10)
-	-	4.9022(6)	14.517(3)	302.12(4)	154.77(2)	5.25(10)
-	-	4.8990(6)	14.514(4)	301.67(5)	154.46(2)	5.34(11)
-	-	4.8963(6)	14.513(4)	301.31(5)	154.20(2)	5.42(11)
-	-	4.8936(7)	14.512(4)	300.95(5)	153.93(2)	5.51(11)
-	-	4.8904(7)	14.510(4)	300.54(6)	153.57(2)	5.62(11)
-	-	4.8882(8)	14.508(5)	300.22(6)	153.33(2)	5.70(11)
-	-	4.8853(8)	14.507(5)	299.84(7)	152.97(2)	5.82(11)
-	-	4.8824(9)	14.505(6)	299.44(7)	152.57(3)	5.95(12)
-	-	4.8796(9)	14.503(6)	299.06(8)	152.21(3)	6.07(12)

Table C.4: Unit cell volumes for rhombohedral $ZnNbF_6$ and NaCl as determined from Rietveld analyses of the high-pressure diffraction data. Pressures estimated from the unit cell volume of the NaCl using an equation of state are also given.

$ZnNbF_6$ a (Å)	$ZnNbF_6$ c (Å)	$ZnNbF_6$ Volume (Å^3)	NaCl Volume (Å^3)	Pressure (GPa)
5.1896(3)	14.009(1)	326.74(2)	175.35(2)	0.00(5)
5.1894(3)	14.009(1)	326.72(2)	175.34(2)	0.00(5)
5.1892(3)	14.009(1)	326.70(2)	175.32	0.00(5)
5.1878(3)	14.011(1)	326.56(2)	175.25	0.01(5)
5.1835(3)	14.014(1)	326.08(2)	175.10	0.04(5)
5.1794(3)	14.016(1)	325.61(2)	174.96	0.05(5)
5.1751(3)	14.018(1)	325.14(2)	174.80	0.08(5)
5.1715(3)	14.021(1)	324.73(2)	174.66(2)	0.10(5)
5.1658(3)	14.024(1)	324.10(2)	174.42(2)	0.13(5)
5.1612(3)	14.027(1)	323.59(2)	174.23(2)	0.16(5)
5.1549(3)	14.031(1)	322.90(2)	174.00(2)	0.19(5)

Table C.4 continued

$ZnNbF_6$ a (Å)	$ZnNbF_6$ c (Å)	$ZnNbF_6$ Volume (Å^3)	NaCl Volume (Å^3)	Pressure (GPa)
5.1487(3)	14.035(1)	322.19(2)	173.76(2)	0.22(5)
5.1426(3)	14.038(1)	321.51(2)	173.53(2)	0.26(5)
5.1371(3)	14.040(2)	320.88(2)	173.31(2)	0.29(5)
5.1331(3)	14.042(1)	320.42(2)	173.15(2)	0.31(5)
5.1280(3)	14.045(2)	319.86(2)	172.95(2)	0.34(5)
5.1207(3)	14.050(2)	319.05(2)	172.65(2)	0.39(5)
5.1178(3)	14.053(2)	318.75(2)	172.53(2)	0.40(5)
5.1138(3)	14.055(1)	318.31(2)	172.37(2)	0.43(5)
5.1104(3)	14.057(1)	317.93(2)	172.25(2)	0.45(5)
5.1070(3)	14.059(1)	317.54(2)	172.11(2)	0.47(5)
5.1042(3)	14.060(1)	317.24(2)	171.99(2)	0.49(5)
5.1012(3)	14.063(1)	316.92(2)	171.86(2)	0.51(5)
5.0980(3)	14.066(1)	316.59(2)	171.69(2)	0.53(5)
5.0956(3)	14.067(1)	316.32(2)	171.57	0.55(5)
5.0931(3)	14.068(1)	316.04(2)	171.45(2)	0.57(5)
5.0886(3)	14.071(1)	315.53(2)	171.24(2)	0.60(5)
5.0852(3)	14.072(1)	315.14(2)	171.10(2)	0.63(5)
5.0832(3)	14.073(2)	314.91(2)	171.03(2)	0.64(5)
5.0804(3)	14.075(2)	314.60(2)	170.88(2)	0.66(5)
5.0765(3)	14.077(2)	314.18(2)	170.66(2)	0.69(5)
5.0731(3)	14.079(2)	313.80(2)	170.49(2)	0.72(5)
5.0686(3)	14.080(2)	313.26(2)	170.26(2)	0.76(5)
5.0638(3)	14.083(2)	312.73(2)	170.03(2)	0.80(5)
5.0605(3)	14.084(2)	312.35(2)	169.87(2)	0.82(6)
5.0576(3)	14.086(2)	312.04(2)	169.73(2)	0.85(5)
5.0543(3)	14.088(2)	311.67(2)	169.58(2)	0.87(5)
5.0529(3)	14.088(2)	311.51(2)	169.52(2)	0.88(5)
5.0509(3)	14.090(2)	311.29(2)	169.43(2)	0.90(5)
5.0475(3)	14.092(2)	310.93(2)	169.28(2)	0.92(5)
5.0445(3)	14.094(2)	310.59(2)	169.14(2)	0.95(5)
5.0423(3)	14.095(2)	310.36(2)	169.04(2)	0.96(5)
5.0392(3)	14.098(2)	310.03(2)	168.90(2)	0.99(5)
5.0357(3)	14.100(2)	309.65(2)	168.73(2)	1.02(6)
5.0334(3)	14.101(2)	309.39(2)	168.61(2)	1.04(6)
5.0317(3)	14.102(2)	309.21(2)	168.53(2)	1.05(6)
5.0284(3)	14.104(2)	308.85(2)	168.37(2)	1.08(6)

Table C.4 continued

$ZnNbF_6$ a (Å)	$ZnNbF_6$ c (Å)	$ZnNbF_6$ Volume (Å^3)	NaCl Volume (Å^3)	Pressure (GPa)
5.0254(3)	14.106(2)	308.52(2)	168.21(2)	1.10(6)
5.0236(3)	14.107(2)	308.31(2)	168.11(2)	1.12(6)
5.0216(3)	14.108(2)	308.08(2)	168.00(2)	1.14(6)
5.0200(3)	14.108(2)	307.90(2)	167.91(2)	1.16(6)
5.0188(3)	14.108(2)	307.76(2)	167.84(2)	1.17(6)
5.0176(3)	14.109(2)	307.61(2)	167.77(2)	1.18(6)
5.0162(3)	14.109(2)	307.46(2)	167.70(2)	1.20(6)
5.0151(3)	14.108(2)	307.28(2)	167.60(2)	1.21(6)
5.0133(3)	14.108(2)	307.08(2)	167.50(2)	1.23(6)
5.0122(3)	14.109(2)	306.95(2)	167.43(2)	1.24(6)
5.0108(3)	14.109(2)	306.80(2)	167.36(2)	1.26(6)
5.0085(3)	14.110(2)	306.54(2)	167.22(2)	1.28(6)
5.0064(3)	14.111(2)	306.29(2)	167.09(2)	1.31(6)
5.0054(3)	14.111(2)	306.18(2)	167.03(2)	1.32(6)
5.0042(3)	14.112(2)	306.04(2)	166.97(2)	1.33(6)
5.0028(3)	14.113(2)	305.88(2)	166.89(2)	1.34(6)
5.0011(3)	14.113(2)	305.69(2)	166.79(2)	1.36(6)
4.9998(3)	14.113(2)	305.53(2)	166.71(2)	1.37(6)
4.9983(3)	14.114(2)	305.36(2)	166.62(2)	1.39(6)
4.9971(3)	14.114(2)	305.22(2)	166.54(2)	1.41(6)
4.9960(3)	14.114(2)	305.08(2)	166.47(2)	1.42(6)
4.9949(3)	14.114(2)	304.96(2)	166.41(2)	1.43(6)
4.9936(3)	14.115(2)	304.81(2)	166.33(2)	1.44(6)
4.9917(3)	14.115(2)	304.59(2)	166.22(2)	1.47(6)
4.9901(3)	14.116(2)	304.40(2)	166.12(2)	1.48(6)
4.9886(3)	14.116(2)	304.23(2)	166.03(2)	1.50(6)
4.9871(3)	14.117(2)	304.05(2)	165.94(2)	1.52(6)
4.9855(3)	14.117(2)	303.88(2)	165.85(2)	1.54(6)
4.9841(3)	14.117(2)	303.70(2)	165.76(2)	1.55(6)
4.9823(3)	14.118(2)	303.49(2)	165.64(2)	1.57(6)
4.9801(3)	14.118(2)	303.25(2)	165.51(2)	1.60(6)
4.9787(3)	14.119(2)	303.07(2)	165.42(2)	1.62(6)
4.9773(3)	14.119(2)	302.92(2)	165.35(2)	1.63(6)
4.9758(3)	14.120(2)	302.75(2)	165.25(2)	1.65(6)
4.9744(3)	14.120(2)	302.58(2)	165.17(2)	1.67(6)
4.9730(3)	14.120(2)	302.42(2)	165.08(2)	1.68(6)
4.9716(3)	14.120(2)	302.25(2)	164.98(2)	1.70(6)
4.9697(3)	14.121(2)	302.02(2)	164.85(2)	1.73(6)

Table C.4 continued

$ZnNbF_6$ a (Å)	$ZnNbF_6$ c (Å)	$ZnNbF_6$ Volume (Å^3)	NaCl Volume (Å^3)	Pressure (GPa)
4.9678(3)	14.121(2)	301.79(2)	164.72(2)	1.75(6)
4.9666(3)	14.120(2)	301.65(2)	164.64(2)	1.77(7)
4.9659(3)	14.120(2)	301.55(2)	164.58(2)	1.78(7)
4.9649(3)	14.120(2)	301.44(2)	164.53(2)	1.79(7)
4.9638(3)	14.121(2)	301.31(2)	164.46(2)	1.81(7)
4.9622(3)	14.121(2)	301.13(2)	164.36(2)	1.83(7)
4.9602(3)	14.122(2)	300.89(2)	164.22(2)	1.85(7)
4.9585(3)	14.122(2)	300.70(2)	164.10(3)	1.88(7)
4.9573(3)	14.124(2)	300.58(2)	164.04(2)	1.89(7)
4.9561(3)	14.124(2)	300.45(2)	163.97(2)	1.90(7)
4.9549(3)	14.124(2)	300.31(2)	163.89(2)	1.92(7)
4.9536(3)	14.124(2)	300.15(2)	163.79(2)	1.94(7)
4.9524(3)	14.124(2)	300.01(2)	163.70(2)	1.96(7)
4.9515(3)	14.124(2)	299.90(2)	163.63(3)	1.97(7)
4.9504(3)	14.125(2)	299.77(2)	163.56(3)	1.99(7)
4.9489(3)	14.124(2)	299.58(2)	163.45(3)	2.01(7)
4.9472(3)	14.124(2)	299.37(2)	163.32(3)	2.04(7)
4.9450(3)	14.124(2)	299.11(2)	163.15(3)	2.07(7)
4.9422(3)	14.124(2)	298.77(2)	162.93(3)	2.12(7)
4.9404(3)	14.124(2)	298.54(2)	162.77(3)	2.15(7)
4.9392(3)	14.124(2)	298.40(2)	162.68(3)	2.17(7)
4.9377(3)	14.124(2)	298.21(2)	162.57(3)	2.19(7)
4.9364(3)	14.124(2)	298.06(2)	162.47(3)	2.21(7)
4.9347(3)	14.124(2)	297.85(2)	162.34(3)	2.24(7)
4.9329(3)	14.124(2)	297.63(2)	162.20(3)	2.27(8)
4.9312(3)	14.124(2)	297.43(2)	162.06(3)	2.30(8)
4.9302(3)	14.123(2)	297.30(2)	161.98(3)	2.32(8)
4.9291(3)	14.123(2)	297.17(2)	161.90(3)	2.34(8)
4.9268(3)	14.123(2)	296.88(2)	161.71(3)	2.38(8)
4.9248(3)	14.122(2)	296.62(2)	161.53(3)	2.42(8)
4.9235(3)	14.121(2)	296.45(2)	161.41(3)	2.44(8)
4.9223(3)	14.121(2)	296.30(2)	161.31(3)	2.47(8)
4.9215(3)	14.121(2)	296.20(2)	161.24(3)	2.48(8)
4.9201(3)	14.121(2)	296.04(2)	161.14(3)	2.50(8)
4.9191(3)	14.120(2)	295.90(2)	161.05(3)	2.52(8)
4.9180(3)	14.120(2)	295.76(2)	160.96(3)	2.54(8)
4.9166(3)	14.120(2)	295.59(2)	160.85(3)	2.57(8)
4.9144(3)	14.118(2)	295.29(2)	160.64(3)	2.62(8)

Table C.4 continued

$ZnNbF_6$ a (Å)	$ZnNbF_6$ c (Å)	$ZnNbF_6$ Volume (Å^3)	NaCl Volume (Å^3)	Pressure (GPa)
4.9129(3)	14.118(2)	295.10(2)	160.50(3)	2.65(9)
4.9118(3)	14.117(2)	294.96(2)	160.41(3)	2.67(9)
4.9103(4)	14.117(2)	294.77(2)	160.28(3)	2.70(9)
4.9080(4)	14.116(2)	294.47(3)	160.05(3)	2.75(9)
4.9062(4)	14.115(2)	294.25(3)	159.88(3)	2.79(9)
4.9047(4)	14.115(3)	294.06(3)	159.75(3)	2.82(9)
4.9033(4)	14.115(2)	293.89(3)	159.65(3)	2.85(9)
4.9018(4)	14.114(3)	293.70(3)	159.52(3)	2.88(9)
4.9003(4)	14.114(3)	293.51(3)	159.38(3)	2.91(9)
4.8990(4)	14.114(3)	293.34(3)	159.27(3)	2.94(9)
4.8974(4)	14.113(3)	293.15(3)	159.13(3)	2.97(9)
4.8954(4)	14.113(3)	292.91(3)	158.93(3)	3.02(9)
4.8935(4)	14.112(3)	292.67(3)	158.75(3)	3.06(9)
4.8921(4)	14.112(3)	292.47(3)	158.61(3)	3.09(9)
4.8909(4)	14.111(3)	292.33(3)	158.51(3)	3.12(9)
4.8900(4)	14.110(3)	292.20(3)	158.43(3)	3.14(9)
4.8888(4)	14.110(3)	292.06(3)	158.33(3)	3.16(9)
4.8878(4)	14.110(3)	291.93(3)	158.25(3)	3.18(9)
4.8870(4)	14.110(3)	291.82(3)	158.18(3)	3.20(9)
4.8857(4)	14.110(3)	291.67(3)	158.08(3)	3.22(9)
4.8843(4)	14.110(3)	291.51(3)	157.97(3)	3.25(9)
4.8831(4)	14.110(3)	291.36(3)	157.85(3)	3.28(9)
4.8817(4)	14.110(3)	291.20(3)	157.74(3)	3.31(9)
4.8802(4)	14.110(3)	291.02(3)	157.60(3)	3.34(9)
4.8775(4)	14.111(3)	290.72(3)	157.35(3)	3.41(9)
4.8759(4)	14.110(3)	290.51(3)	157.21(3)	3.44(10)
4.8748(4)	14.110(3)	290.38(3)	157.11(3)	3.47(9)
4.8737(4)	14.110(3)	290.26(3)	157.03(3)	3.49(9)
4.8724(4)	14.110(3)	290.10(3)	156.92(3)	3.52(9)
4.8712(4)	14.110(3)	289.96(3)	156.81(3)	3.54(9)
4.8699(4)	14.110(3)	289.81(3)	156.70(3)	3.57(9)
4.8681(4)	14.111(3)	289.61(3)	156.55(3)	3.61(9)
4.8668(4)	14.111(3)	289.45(3)	156.43(2)	3.65(8)
4.8656(5)	14.111(3)	289.31(3)	156.32(3)	3.67(9)
4.8645(5)	14.111(3)	289.17(3)	156.23(3)	3.70(9)
4.8633(5)	14.111(3)	289.04(3)	156.12(3)	3.72(9)
4.8619(5)	14.112(3)	288.89(3)	156.01(3)	3.76(9)
4.8603(5)	14.112(4)	288.70(3)	155.85(3)	3.80(9)

Table C.4 continued

$ZnNbF_6$ a (Å)	$ZnNbF_6$ c (Å)	$ZnNbF_6$ Volume ($Å^3$)	NaCl Volume ($Å^3$)	Pressure (GPa)
4.8593(5)	14.112(4)	288.58(3)	155.77(3)	3.82(9)
4.8580(5)	14.115(4)	288.49(3)	155.70(2)	3.84(9)
4.8571(5)	14.115(4)	288.37(3)	155.62(3)	3.86(9)
4.8558(5)	14.116(4)	288.24(3)	155.52(2)	3.89(9)
4.8546(5)	14.116(4)	288.09(3)	155.40(2)	3.92(9)
4.8536(5)	14.115(4)	287.97(3)	155.31(2)	3.94(9)
4.8525(5)	14.116(4)	287.86(3)	155.23(2)	3.96(9)
4.8514(5)	14.116(4)	287.72(3)	155.12(2)	3.99(9)
4.8503(5)	14.116(4)	287.60(3)	155.02(2)	4.02(9)
4.8495(5)	14.116(4)	287.50(3)	154.96(2)	4.04(9)
4.8489(5)	14.116(4)	287.43(3)	154.90(2)	4.05(9)
4.8485(5)	14.115(4)	287.36(3)	154.86(2)	4.07(8)
4.8484(5)	14.114(3)	287.33(3)	154.85(2)	4.07(8)

Table C.5: Crystallographic parameters for $MnNbF_6$ at 111 K derived from the Rietveld analysis of the synchrotron diffraction data (see Figure C.1).

Chemical Formula	$MnNbF_6$
Space group	$R\bar{3}$
a (Å)	5.4675(4)
c (Å)	14.274(2)
λ (Å)	0.72950
μ (cm^{-1})	1.53
Temperature (K)	111
R_{wp}	0.2280
R_F^2	0.1036

	x	**y**	**z**	**U_{iso} ($Å^2$)**
Mn	0	0	0	0.023(3)
Nb	0	0	$\frac{1}{2}$	0.029(2)
F	0.079(1)	0.329(2)	0.0831(6)	0.018(2)

Table C.6: Crystallographic parameters for $MnNbF_6$ at 500 K derived from the Rietveld analysis of the synchrotron diffraction data (see Figure C.3).

Chemical Formula	$MnNbF_6$
Space group	$Fm\bar{3}m$
a (Å)	8.0816(1)
λ (Å)	0.72950
μ (cm^{-1})	1.53
Temperature (K)	501
R_{wp}	0.1286
R_F^2	0.0545

	x	**y**	**z**	**U_{iso}/U_{eqv} (Å²)**	**U_{11} (Å²)**	**U_{22} (Å²)**	**U_{33} (Å²)**
Mn	0	0	0	0.0226(8)	-	-	-
Nb	$\frac{1}{2}$	$\frac{1}{2}$	$\frac{1}{2}$	0.0333(6)	-	-	-
F	0.2542(4)	0	0	0.0585	0.025(3)	0.075(2)	0.075(2)

Table C.7: Crystallographic parameters for $ZnNbF_6$ at 300 K derived from the Rietveld analysis of the synchrotron diffraction data (see Figure C.4).

Chemical Formula	$ZnNbF_6$
Space group	$R\bar{3}$
a (Å)	5.33023(8)
c (Å)	13.9307(4)
λ (Å)	0.72950
μ (cm^{-1})	2.28
Temperature (K)	299.3
R_{wp}	0.0944
R_F^2	0.0723

	x	**y**	**z**	**U_{iso}/U_{eqv} (Å²)**	**U_{11} (Å²)**	**U_{22} (Å²)**	**U_{33} (Å²)**
Zn	0	0	0	0.010(1)	-	-	-
Nb	0	0	$\frac{1}{2}$	0.034(2)	-	-	-
F	0.0729(7)	0.333(1)	0.0827(4)	0.0242	0.013(6)	0.019(2)	0.026(3)

Table C.8: Crystallographic parameters for $MnNbF_6$ at room temperature and 1.0 GPa derived from the Rietveld analysis of the high-pressure synchrotron diffraction data collected in a DAC (see Figure C.6).

Chemical Formula	$MnNbF_6$
Space group	$R\bar{3}$
a (Å)	5.2319(3)
c (Å)	14.385(2)
λ (Å)	0.72768
Pressure (GPa)	1.00
R_{wp}	0.0723
R_F^2	0.1076

	x	**y**	**z**	**U_{iso} (Å^2)**
Mn	0	0	0	-0.014(4)
Nb	0	0	$\frac{1}{2}$	0.121(6)
F	0.067(1)	0.348(2)	0.0856(6)	0.024(3)

Table C.9: Crystallographic parameters for $ZnNbF_6$ at room temperature and nominally zero pressure derived from the Rietveld analysis of the high-pressure synchrotron diffraction data collected in a DAC (see Figure C.7).

Chemical Formula	$ZnNbF_6$
Space group	$R\bar{3}$
a (Å)	5.1895(3)
c (Å)	14.009(1)
λ (Å)	0.72768
Pressure (GPa)	~0.0
R_{wp}	0.0387
R_F^2	0.1400

	x	**y**	**z**	**U_{iso} (Å^2)**
Zn	0	0	0	0.006(6)
Nb	0	0	$\frac{1}{2}$	0.099(9)
F	0.067(3)	0.338(5)	0.081(3)	0.016(4)

APPENDIX D. SUPPLEMENTARY MATERIAL FOR CHAPTER 5

D.1 Figures

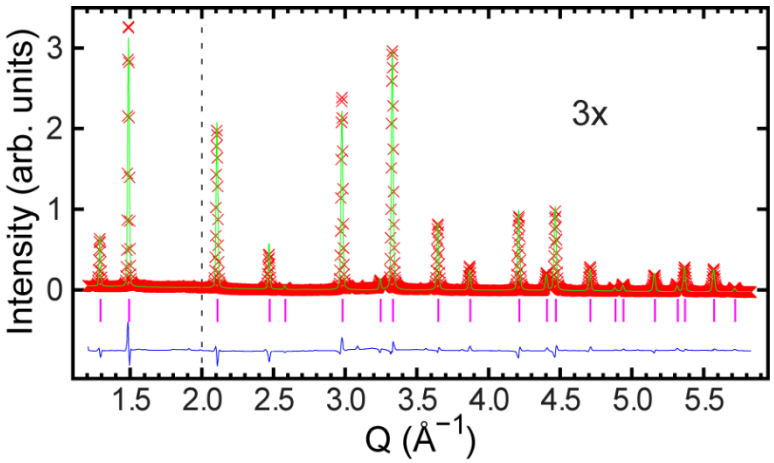

Figure D.1: Rietveld plot showing a fit of a $CaZr_{0.75}Nb_{0.25}F_{6.25}$ cubic $Fm\bar{3}m$ model to the 300 K cooling synchrotron diffraction data. The section of Q has been scaled to show detail but shifted downwards so that the backgrounds for the sections of the plot appear to be the same.

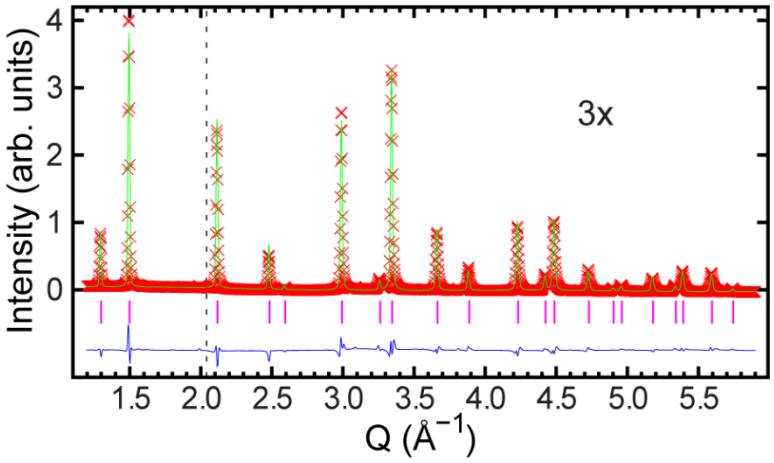

Figure D.2: Rietveld plot showing a fit of a $CaZr_{0.5}Nb_{0.5}F_{6.5}$ cubic $Fm\bar{3}m$ model to the 300 K cooling synchrotron diffraction data. The section of Q has been scaled to show detail but shifted downwards so that the backgrounds for the sections of the plot appear to be the same.

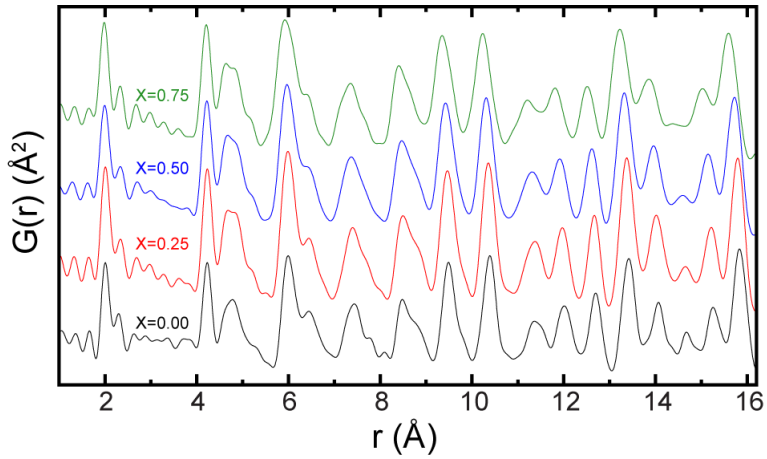

Figure D.3: Pair distribution functions derived from the x-ray total scattering data for $Ca[Zr^{(IV)}_{1-x}Nb^{(V)}_{x}]F_{6+x}$ with a Q_{max} of 20 $Å^{-1}$.

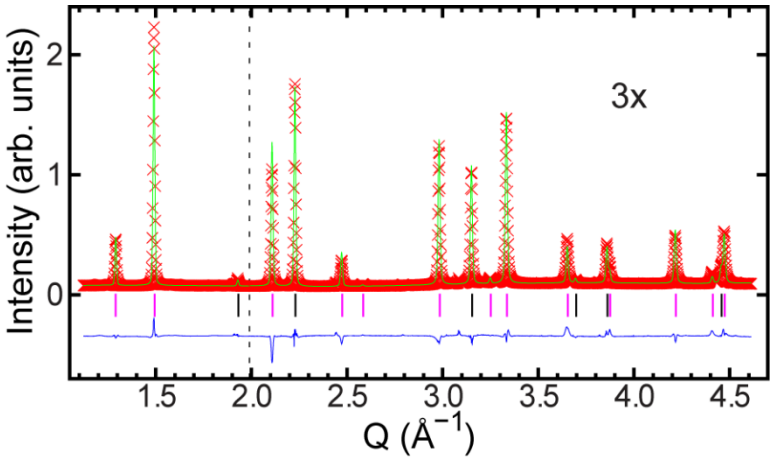

Figure D.4: Rietveld plot showing a fit of a $CaZr_{0.75}Nb_{0.25}F_{6.25}$ cubic $Fm\bar{3}m$ model to the 0 GPa powder x-ray diffraction data obtained in a diamond anvil cell. The section of Q has been scaled to show detail but shifted downwards so that the backgrounds for the sections of the plot appear to be the same.

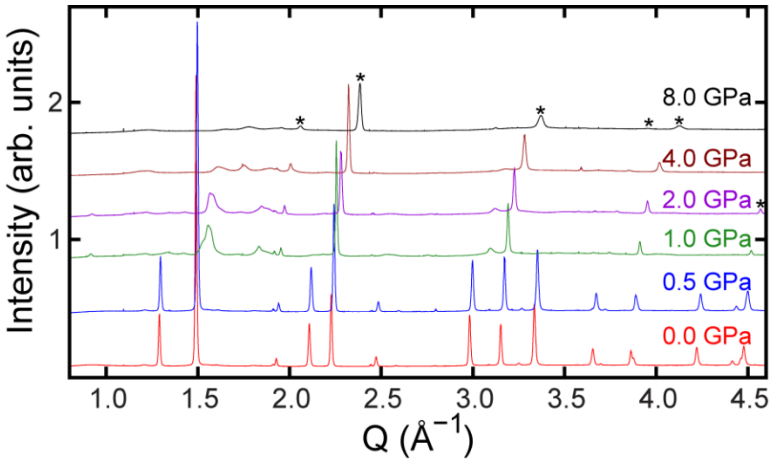

Figure D.5: Select high-pressure diffraction patterns of $CaZr_{0.75}Nb_{0.25}F_{6.25}$ showing phase transition and amorphization, with peaks from NaCl internal pressure standard marked with *.

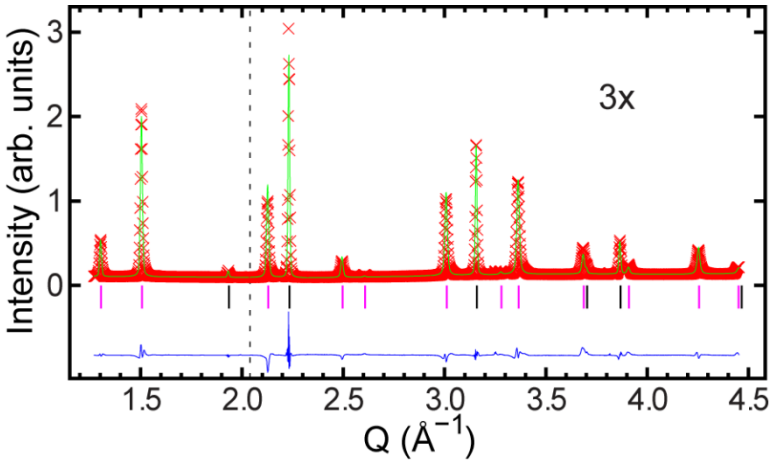

Figure D.6: Rietveld plot showing a fit of a $CaZr_{0.5}Nb_{0.5}F_{6.5}$ cubic $Fm\bar{3}m$ model to the 0.1 GPa powder x-ray diffraction data obtained in a diamond anvil cell. The section of Q has been scaled to show detail but shifted downwards so that the backgrounds for the sections of the plot appear to be the same.

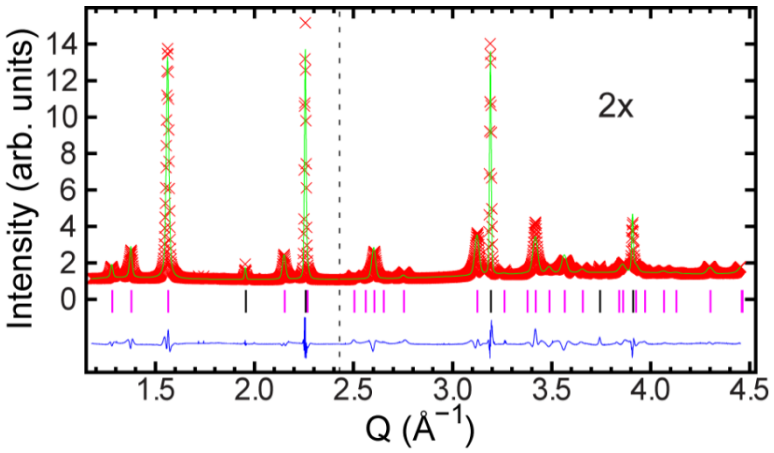

Figure D.7: Rietveld plot showing a fit of a $CaZr_{0.5}Nb_{0.5}F_{6.5}$ cubic $R\bar{3}$ model to the 1.0 GPa powder x-ray diffraction data obtained in a diamond anvil cell. The section of Q has been scaled to show detail but shifted downwards so that the backgrounds for the sections of the plot appear to be the same.

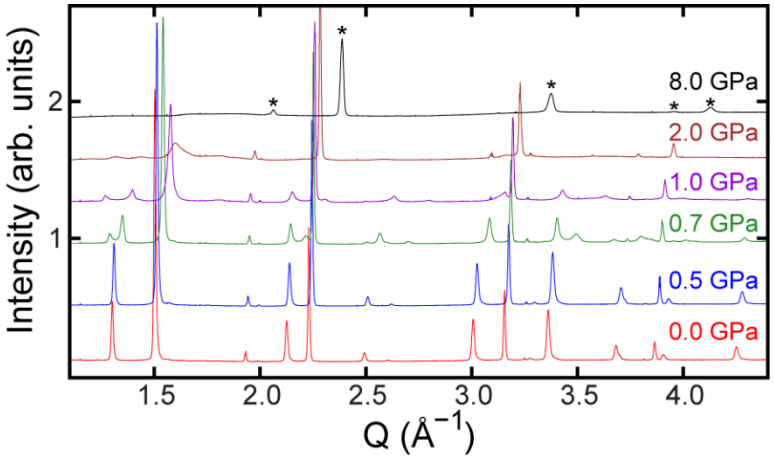

Figure D.8: Select high-pressure diffraction patterns of $CaZr_{0.5}Nb_{0.5}F_{6.5}$ showing phase transition and amorphization, with peaks from NaCl internal pressure standard marked with *.

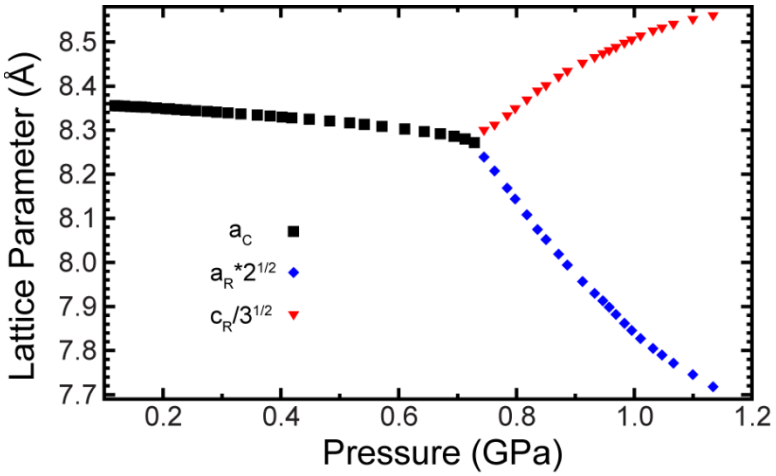

Figure D.9: Pressure dependence of the lattice constants for both the cubic and rhombohedral phase of $CaZr_{0.5}Nb_{0.5}F_{6.5}$. The lattice constants of the rhombohedral phase have been scaled so that they can be compared to the that of the cubic phase.

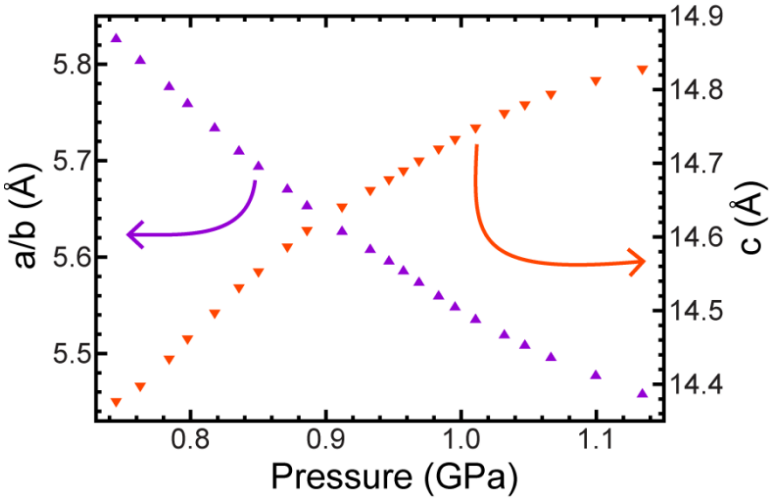

Figure D.10: Lattice constants for high-pressure rhombohedral phase of $CaZr_{0.5}Nb_{0.5}F_{6.5}$ showing anisotropic compressibility between a/b and c-axes and negative linear compressibility parallel to c-axis. Note slight differences in scaling of the two y-axes.

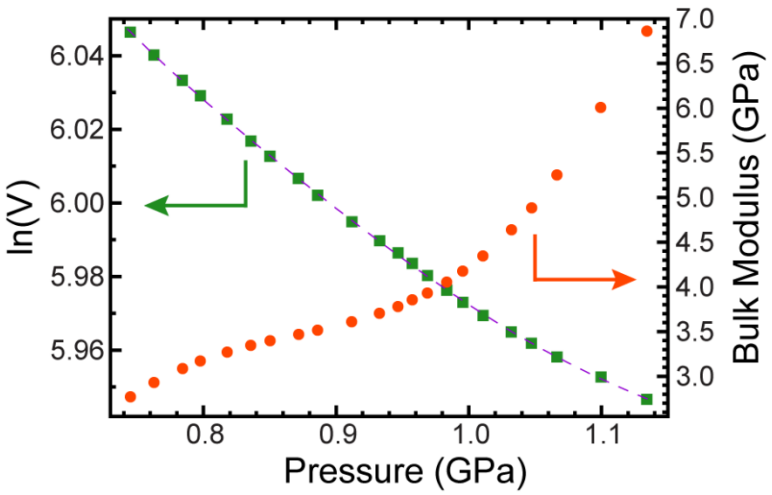

Figure D.11: Pressure dependence of ln(V) and the bulk modulus for rhombohedral $CaZr_{0.5}Nb_{0.5}F_{6.5}$. A five-term polynomial (purple dotted line) was fit to the ln(V) data and used to calculate bulk moduli.

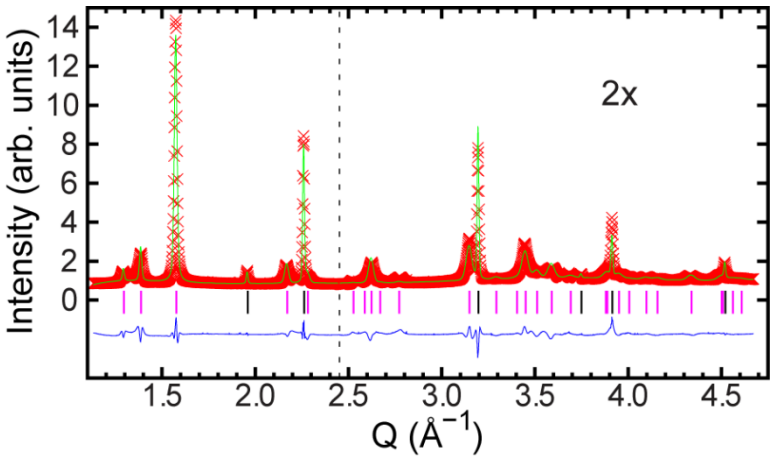

Figure D.12: Rietveld plot showing a fit of a $CaZr_{0.25}Nb_{0.75}F_{6.75}$ cubic $R\bar{3}$ model to the 1.1 GPa powder x-ray diffraction data obtained in a diamond anvil cell. The section of Q has been scaled to show detail but shifted downwards so that the backgrounds for the sections of the plot appear to be the same.

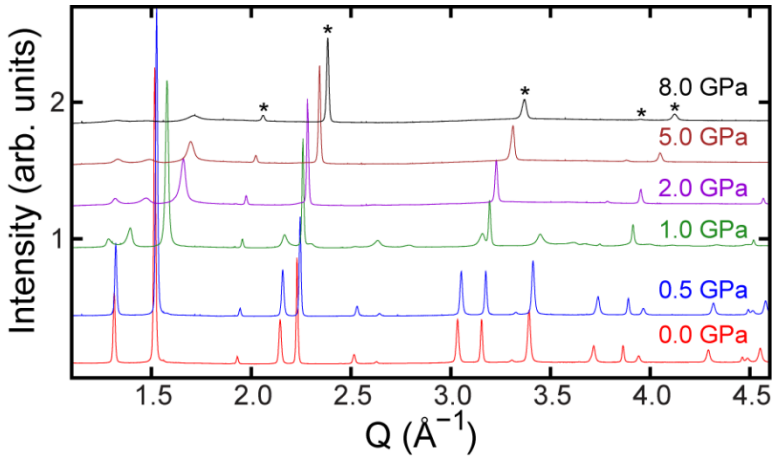

Figure D.13: Select high-pressure diffraction patterns of $CaZr_{0.25}Nb_{0.75}F_{6.75}$ showing phase transition, with peaks from NaCl internal pressure standard marked with *.

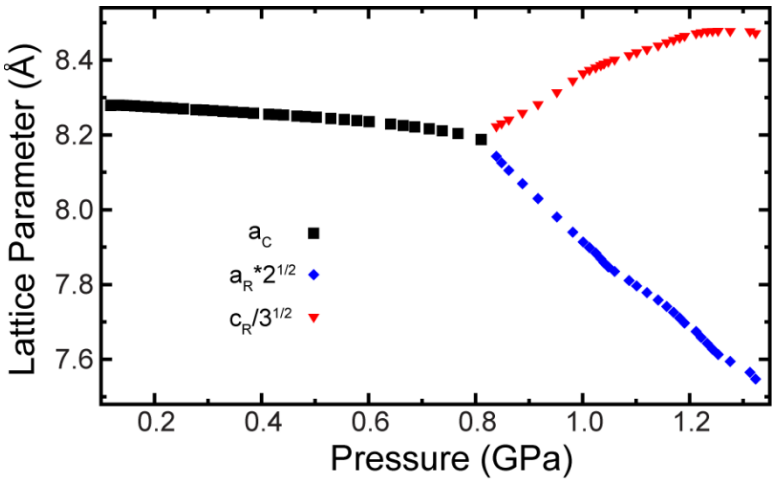

Figure D.14: Pressure dependence of the lattice constants for both the cubic and rhombohedral phase of $CaZr_{0.25}Nb_{0.75}F_{6.75}$. The lattice constants of the rhombohedral phase have been scaled so that they can be compared to the that of the cubic phase.

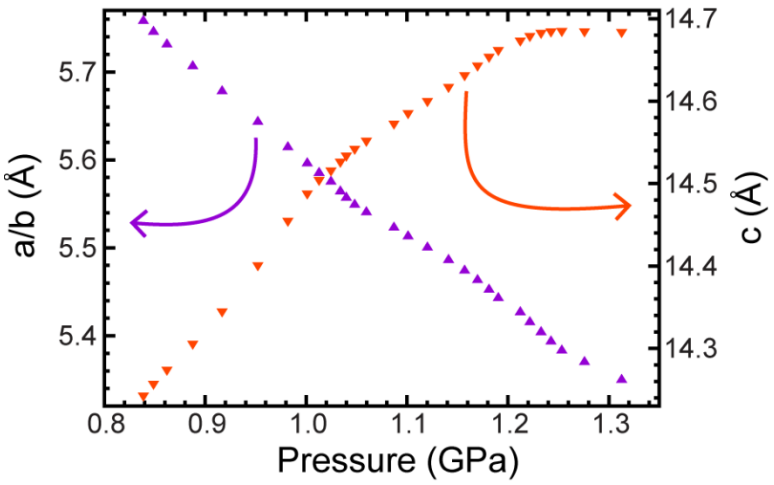

Figure D.15: Lattice constants for high-pressure rhombohedral phase of $CaZr_{0.25}Nb_{0.75}F_{6.75}$ showing anisotropic compressibility between a/b and c-axes and negative linear compressibility parallel to c-axis. Note slight differences in scaling of the two y-axes.

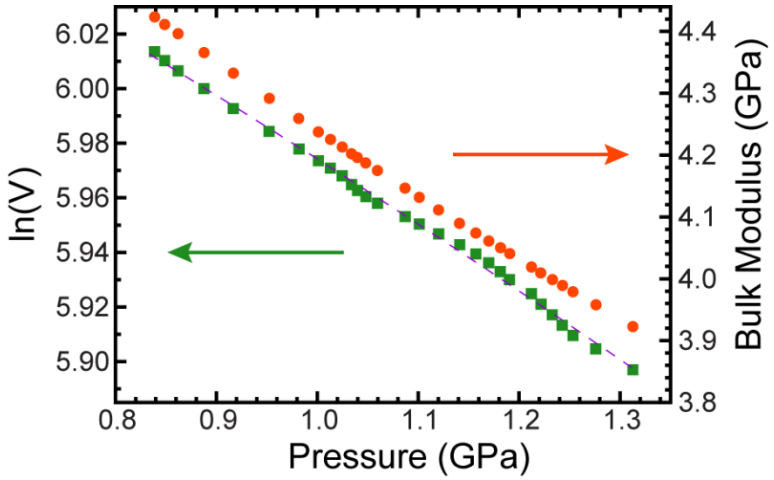

Figure D.16: Pressure dependence of ln(V) and the bulk modulus for rhombohedral $CaZr_{0.25}Nb_{0.75}F_{6.75}$. A two-term polynomial (purple dotted line) was fit to the ln(V) data and used to calculate bulk moduli.

D.2 Tables

Table D.1: Lattice constant and unit cell volume for cubic $CaZr_{0.75}Nb_{0.25}F_{6.25}$ as determined from Rietveld analyses of the variable temperature x-ray diffraction data.

Temperature (K)	Rwp	a (Å)	Volume (Å^3)
111.46	0.1086	8.45316(8)	604.03(2)
114.12	0.1086	8.45257(8)	603.90(2)
116.07	0.1086	8.45203(8)	603.79(2)
118.65	0.1086	8.45150(8)	603.67(2)
121.37	0.1086	8.45097(8)	603.56(2)
124.19	0.1086	8.45044(8)	603.45(2)
127.46	0.1087	8.44995(8)	603.34(2)
131.11	0.1087	8.44947(8)	603.24(2)
133.81	0.1087	8.44901(8)	603.14(2)
136.62	0.1087	8.44856(8)	603.04(2)
139.47	0.1088	8.44813(8)	602.95(2)
142.26	0.1087	8.44770(8)	602.86(2)
144.97	0.1087	8.44728(8)	602.77(2)
147.61	0.1086	8.44686(8)	602.68(2)
150.20	0.1086	8.44645(8)	602.59(2)
152.81	0.1086	8.44604(8)	602.50(2)
155.51	0.1086	8.44565(8)	602.42(2)
158.33	0.1085	8.44527(8)	602.34(2)
161.25	0.1085	8.44490(8)	602.26(2)
164.16	0.1086	8.44455(8)	602.19(2)
167.27	0.1087	8.44419(8)	602.11(2)
170.10	0.1087	8.44384(8)	602.03(2)
172.94	0.1087	8.44350(8)	601.96(2)
175.79	0.1087	8.44318(8)	601.89(2)
178.66	0.1087	8.44288(8)	601.83(2)
181.54	0.1087	8.44258(8)	601.76(2)
184.42	0.1088	8.44228(8)	601.70(2)
187.29	0.1088	8.44199(8)	601.64(2)
190.16	0.1089	8.44172(8)	601.58(2)
193.02	0.1088	8.44144(8)	601.52(2)
195.89	0.1088	8.44117(8)	601.46(2)
198.78	0.1088	8.44090(8)	601.40(2)
201.71	0.1089	8.44062(8)	601.34(2)
204.68	0.1089	8.44032(8)	601.28(2)
207.68	0.1089	8.44002(8)	601.22(2)
210.69	0.1089	8.43973(8)	601.15(2)

Table D.1 continued

Temperature (K)	Rwp	a (Å)	Volume (Å^3)
213.63	0.1089	8.43944(8)	601.09(2)
216.41	0.1089	8.43917(8)	601.03(2)
219.55	0.1089	8.43888(8)	600.97(2)
222.45	0.1089	8.43859(8)	600.91(2)
225.35	0.1089	8.43830(8)	600.85(2)
228.45	0.1088	8.43800(8)	600.78(2)
231.45	0.1088	8.43770(8)	600.72(2)
234.35	0.1088	8.43741(8)	600.66(2)
237.25	0.1088	8.43712(8)	600.6(2)
240.25	0.1088	8.43680(8)	600.53(2)
243.35	0.1088	8.43652(8)	600.47(2)
246.35	0.1087	8.43624(8)	600.41(2)
249.25	0.1087	8.43596(8)	600.35(2)
252.25	0.1087	8.43569(8)	600.29(2)
256.05	0.1087	8.43544(8)	600.24(2)
258.45	0.1087	8.43539(8)	600.23(2)
261.65	0.1087	8.43496(8)	600.14(2)
264.35	0.1087	8.43486(8)	600.11(2)
266.95	0.1087	8.43485(8)	600.11(2)
270.05	0.1087	8.43467(8)	600.07(2)
273.35	0.1087	8.43441(8)	600.02(2)
275.87	0.1086	8.43379(8)	599.89(2)
278.87	0.1086	8.43369(8)	599.87(2)
282.35	0.1087	8.43364(8)	599.85(2)
284.86	0.1087	8.43337(8)	599.80(2)
287.63	0.1087	8.43312(8)	599.74(2)
291.35	0.1087	8.43301(8)	599.72(2)
293.93	0.1086	8.43268(8)	599.65(2)
296.73	0.1085	8.43253(8)	599.62(2)
300.45	0.1086	8.43257(8)	599.63(2)
302.86	0.1085	8.43228(8)	599.56(2)
306.04	0.1085	8.43225(8)	599.56(2)
309.67	0.1085	8.43211(8)	599.53(2)
312.65	0.1085	8.43194(8)	599.49(2)
316.76	0.1085	8.43171(8)	599.44(2)
319.25	0.1086	8.43177(8)	599.45(2)
322.07	0.1086	8.43157(8)	599.41(2)

Table D.1 continued

Temperature (K)	Rwp	a (Å)	Volume (Å^3)
325.59	0.1087	8.43144(8)	599.39(2)
328.41	0.1087	8.43150(8)	599.40(2)
331.44	0.1088	8.43143(8)	599.38(2)
334.87	0.1092	8.43149(8)	599.39(2)
338.13	0.1093	8.43137(8)	599.37(2)
341.74	0.1095	8.43136(8)	599.37(2)
344.89	0.1095	8.43138(8)	599.37(2)
348.59	0.1096	8.43136(8)	599.37(2)
351.82	0.1097	8.43140(8)	599.38(2)
355.17	0.1097	8.43138(8)	599.37(2)
358.88	0.1098	8.43133(8)	599.36(2)
362.08	0.1099	8.43132(8)	599.36(2)
365.71	0.1100	8.43128(8)	599.35(2)
369.18	0.1101	8.43127(8)	599.35(2)
372.72	0.1101	8.43124(8)	599.34(2)
376.52	0.1102	8.43121(8)	599.33(2)
380.09	0.1102	8.43119(8)	599.33(2)
383.25	0.1102	8.43120(8)	599.33(2)
386.01	0.1104	8.43121(8)	599.34(2)
389.13	0.1104	8.43123(8)	599.34(2)
392.39	0.1103	8.43119(8)	599.33(2)
395.10	0.1103	8.43121(8)	599.34(2)
398.24	0.1103	8.43117(8)	599.33(2)
401.56	0.1103	8.43112(8)	599.32(2)
404.97	0.1103	8.43110(8)	599.31(2)
408.32	0.1104	8.43106(8)	599.30(2)
411.63	0.1104	8.43100(8)	599.29(2)
414.72	0.1104	8.43093(8)	599.28(2)
419.40	0.1104	8.43087(8)	599.26(2)
422.55	0.1104	8.43079(8)	599.25(2)
425.65	0.1104	8.43073(8)	599.23(2)
429.05	0.1105	8.43062(8)	599.21(2)
431.85	0.1104	8.43053(8)	599.19(2)
434.85	0.1104	8.43044(8)	599.17(2)
437.26	0.1105	8.43033(8)	599.15(2)
439.99	0.1105	8.43020(8)	599.12(2)
442.66	0.1105	8.43007(8)	599.09(2)
445.52	0.1105	8.42994(8)	599.07(2)
448.27	0.1106	8.42984(8)	599.04(2)

Table D.1 continued

Temperature (K)	Rwp	a (Å)	Volume (Å^3)
450.98	0.1106	8.42970(8)	599.01(2)
453.65	0.1106	8.42957(8)	598.99(2)
456.29	0.1106	8.42939(9)	598.95(2)
458.80	0.1107	8.42926(9)	598.92(2)
461.37	0.1107	8.42908(9)	598.88(2)
464.01	0.1107	8.42893(9)	598.85(2)
466.46	0.1107	8.42876(9)	598.81(2)
469.06	0.1107	8.42861(9)	598.78(2)
471.49	0.1108	8.42847(9)	598.75(2)
473.99	0.1109	8.42830(9)	598.71(2)
476.55	0.1108	8.42812(9)	598.68(2)
479.09	0.1108	8.42796(9)	598.64(2)
481.44	0.1109	8.42778(9)	598.61(2)
483.75	0.1108	8.42763(9)	598.57(2)
486.10	0.1167	8.42744(9)	598.53(2)
488.48	0.1110	8.42732(9)	598.51(2)
490.72	0.1110	8.42714(9)	598.47(2)
492.85	0.1110	8.42699(9)	598.44(2)
495.09	0.1109	8.42688(9)	598.41(2)
497.18	0.1109	8.42675(9)	598.38(2)
499.37	0.1109	8.42657(9)	598.35(2)
501.73	0.1109	8.42637(9)	598.30(2)
502.87	0.1109	8.42634(9)	598.30(2)
501.76	0.1110	8.42649(9)	598.33(2)
500.16	0.1110	8.42668(9)	598.37(2)
498.56	0.1110	8.42682(9)	598.40(2)
496.65	0.1110	8.42698(9)	598.43(2)
494.66	0.1110	8.42714(9)	598.47(2)
492.72	0.1111	8.42730(9)	598.50(2)
490.64	0.1110	8.42749(9)	598.54(2)
488.47	0.1109	8.42763(9)	598.57(2)
486.18	0.1109	8.42781(9)	598.61(2)
483.77	0.1109	8.42801(9)	598.65(2)
481.25	0.1109	8.42818(9)	598.69(2)
478.63	0.1108	8.42837(9)	598.73(2)
475.96	0.1108	8.42856(9)	598.77(2)
473.25	0.1108	8.42875(9)	598.81(2)
470.54	0.1109	8.42897(9)	598.86(2)
467.92	0.1109	8.42914(9)	598.89(2)

Table D.1 continued

Temperature (K)	Rwp	a (Å)	Volume (Å^3)
465.20	0.1108	8.42932(9)	598.93(2)
461.85	0.1108	8.42951(9)	598.97(2)
459.11	0.1109	8.42971(9)	599.02(2)
455.75	0.1108	8.42989(8)	599.05(2)
452.93	0.1108	8.43009(8)	599.10(2)
450.25	0.1108	8.43027(8)	599.14(2)
447.73	0.1108	8.43048(8)	599.18(2)
444.38	0.1107	8.43068(8)	599.22(2)
441.44	0.1107	8.43088(8)	599.26(2)
438.59	0.1107	8.43107(8)	599.31(2)
435.78	0.1107	8.43127(8)	599.35(2)
432.70	0.1107	8.43146(8)	599.39(2)
429.76	0.1107	8.43168(8)	599.44(2)
426.67	0.1107	8.43191(8)	599.48(2)
423.56	0.1108	8.43210(8)	599.53(2)
420.45	0.1108	8.43232(8)	599.57(2)
417.25	0.1108	8.43252(8)	599.61(2)
414.26	0.1107	8.43273(8)	599.66(2)
411.07	0.1107	8.43291(8)	599.70(2)
408.07	0.1107	8.43314(8)	599.75(2)
404.94	0.1108	8.43337(8)	599.80(2)
401.56	0.1107	8.43358(8)	599.84(2)
398.60	0.1108	8.43382(8)	599.89(2)
395.56	0.1110	8.43405(8)	599.94(2)
392.60	0.1108	8.43423(8)	599.98(2)
389.99	0.1106	8.43438(8)	600.01(2)
387.10	0.1105	8.43457(8)	600.05(2)
384.21	0.1106	8.43482(8)	600.11(2)
381.08	0.1106	8.43509(8)	600.16(2)
377.56	0.1106	8.43536(8)	600.22(2)
374.29	0.1106	8.43551(8)	600.25(2)
370.67	0.1107	8.43577(8)	600.31(2)
367.21	0.1107	8.43604(8)	600.37(2)
363.58	0.1107	8.43630(8)	600.42(2)
360.67	0.1106	8.43658(8)	600.48(2)
357.24	0.1106	8.43683(8)	600.53(2)
353.59	0.1106	8.43721(8)	600.62(2)
350.61	0.1106	8.43721(8)	600.62(2)
347.50	0.1106	8.43745(8)	600.67(2)

Table D.1 continued

Temperature (K)	Rwp	a (Å)	Volume (Å^3)
343.59	0.1106	8.43794(8)	600.77(2)
340.57	0.1107	8.43798(8)	600.78(2)
337.34	0.1107	8.43820(8)	600.83(2)
333.49	0.1107	8.43874(8)	600.94(2)
330.47	0.1107	8.43890(8)	600.98(2)
327.70	0.1108	8.43916(8)	601.03(2)
324.24	0.1109	8.43964(8)	601.13(2)
320.74	0.1110	8.44012(8)	601.24(2)
315.72	0.1110	8.44038(8)	601.29(2)
312.79	0.1111	8.44057(8)	601.33(2)
309.35	0.1111	8.44098(8)	601.42(2)
306.34	0.1111	8.44108(8)	601.44(2)
303.28	0.1110	8.44151(8)	601.53(2)
300.40	0.1109	8.44156(8)	601.55(2)
297.49	0.1107	8.44178(8)	601.59(2)
294.47	0.1105	8.44201(8)	601.64(2)
291.16	0.1108	8.44236(8)	601.72(2)
287.94	0.1108	8.44270(8)	601.79(2)
285.15	0.1109	8.44302(8)	601.86(2)
282.15	0.1111	8.44337(8)	601.93(2)
279.35	0.1111	8.44376(8)	602.01(2)
276.35	0.1111	8.44386(8)	602.04(2)
273.05	0.1112	8.44433(8)	602.14(2)
270.15	0.1114	8.44458(8)	602.19(2)
267.61	0.1114	8.44502(8)	602.29(2)
264.09	0.1115	8.44533(8)	602.35(2)
261.39	0.1119	8.44566(8)	602.42(2)
258.59	0.1120	8.44595(8)	602.48(2)
255.70	0.1121	8.44608(8)	602.51(2)
252.67	0.1119	8.44647(8)	602.60(2)
249.83	0.1119	8.44647(8)	602.60(2)
246.75	0.1119	8.44686(8)	602.68(2)
243.77	0.1119	8.44755(8)	602.83(2)
240.47	0.1119	8.44765(8)	602.85(2)
237.73	0.1120	8.44801(8)	602.93(2)
234.92	0.1121	8.44808(8)	602.94(2)
232.17	0.1120	8.44832(8)	602.99(2)
229.27	0.1121	8.44864(8)	603.06(2)
226.35	0.1121	8.44898(8)	603.13(2)

Table D.1 continued

Temperature (K)	Rwp	a (Å)	Volume (Å^3)
222.94	0.1121	8.44931(8)	603.20(2)
220.04	0.1122	8.44963(8)	603.27(2)
217.25	0.1122	8.44995(8)	603.34(2)
214.25	0.1123	8.45032(8)	603.42(2)
211.25	0.1125	8.45071(8)	603.50(2)
207.86	0.1124	8.45106(8)	603.58(2)
204.81	0.1123	8.45140(8)	603.65(2)
201.86	0.1122	8.45172(8)	603.72(2)
198.96	0.1122	8.45206(8)	603.79(2)
196.09	0.1123	8.45245(8)	603.88(2)
193.21	0.1125	8.45281(8)	603.95(2)
190.31	0.1125	8.45317(8)	604.03(2)
187.40	0.1125	8.45352(8)	604.10(2)
184.46	0.1125	8.45387(8)	604.18(2)
181.51	0.1124	8.45421(8)	604.25(2)
178.55	0.1124	8.45455(8)	604.33(2)
175.59	0.1125	8.45493(8)	604.41(2)
172.64	0.1125	8.45529(8)	604.48(2)
169.71	0.1124	8.45564(8)	604.56(2)
166.80	0.1124	8.45601(8)	604.64(2)
163.93	0.1125	8.45637(8)	604.72(2)
161.09	0.1125	8.45675(8)	604.80(2)
158.28	0.1124	8.45710(8)	604.87(2)
155.50	0.1124	8.45746(8)	604.95(2)
152.74	0.1123	8.45782(8)	605.03(2)
150.00	0.1122	8.45816(8)	605.10(2)
147.27	0.1122	8.45853(8)	605.18(2)
144.53	0.1122	8.45889(8)	605.26(2)
141.78	0.1122	8.45925(8)	605.33(2)
138.99	0.1122	8.45963(8)	605.42(2)
136.16	0.1122	8.46000(8)	605.50(2)
133.28	0.1122	8.46039(8)	605.58(2)
130.35	0.1122	8.46075(8)	605.66(2)
127.35	0.1121	8.46116(8)	605.75(2)
124.31	0.1121	8.46159(8)	605.84(2)
121.23	0.1121	8.46201(8)	605.93(2)
118.15	0.1121	8.46242(8)	606.02(2)
115.10	0.1120	8.46284(8)	606.11(2)
112.14	0.1121	8.46324(8)	606.19(2)

Table D.2: Lattice constant and unit cell volume for cubic $CaZr_{0.5}Nb_{0.5}F_{6.5}$ as determined from Rietveld analyses of the variable temperature x-ray diffraction data.

Temperature (K)	Rwp	a (Å)	Volume (Å^3)
111.53	0.1087	8.3876(1)	590.08(2)
114.12	0.1086	8.3871(1)	589.98(2)
116.07	0.1087	8.3867(1)	589.89(2)
118.65	0.1086	8.3862(1)	589.79(2)
121.51	0.1085	8.3857(1)	589.69(2)
124.19	0.1085	8.3853(1)	589.60(2)
127.46	0.1085	8.3849(1)	589.51(2)
131.11	0.1085	8.3845(1)	589.44(2)
133.81	0.1085	8.3842(1)	589.36(2)
136.62	0.1085	8.3838(1)	589.29(2)
139.47	0.1086	8.3835(1)	589.22(2)
142.26	0.1085	8.3832(1)	589.16(2)
144.97	0.1085	8.3829(1)	589.09(2)
147.61	0.1084	8.3826(1)	589.02(2)
150.20	0.1084	8.3823(1)	588.97(2)
152.81	0.1084	8.3820(1)	588.91(2)
155.51	0.1083	8.3818(1)	588.87(2)
158.33	0.1083	8.3816(1)	588.83(2)
161.25	0.1083	8.3815(1)	588.79(2)
164.16	0.1084	8.3813(1)	588.76(2)
167.27	0.1084	8.3812(1)	588.73(2)
170.06	0.1084	8.3811(1)	588.70(2)
172.94	0.1085	8.3810(1)	588.69(2)
175.79	0.1085	8.3809(1)	588.68(2)
178.66	0.1085	8.3808(1)	588.65(2)
181.54	0.1085	8.3807(1)	588.63(2)
184.42	0.1086	8.3806(1)	588.61(2)
187.29	0.1087	8.3806(1)	588.60(2)
190.16	0.1087	8.3805(1)	588.58(2)
193.02	0.1087	8.3804(1)	588.56(2)
195.89	0.1087	8.3802(1)	588.53(2)
198.78	0.1086	8.3801(1)	588.49(2)
201.71	0.1086	8.3799(1)	588.46(2)
204.68	0.1085	8.3797(1)	588.42(2)
207.68	0.1085	8.3796(1)	588.39(2)

Table D.2 continued

Temperature (K)	Rwp	a (Å)	Volume (Å^3)
210.64	0.1085	8.3794(1)	588.35(2)
213.63	0.1086	8.3792(1)	588.32(2)
216.40	0.1086	8.3791(1)	588.28(2)
219.50	0.1085	8.3788(1)	588.23(2)
222.45	0.1085	8.3786(1)	588.19(2)
225.31	0.1084	8.3784(1)	588.15(2)
228.45	0.1083	8.3782(1)	588.10(2)
231.40	0.1082	8.3780(1)	588.05(2)
234.45	0.1083	8.3778(1)	588.01(2)
237.45	0.1083	8.3776(1)	587.98(2)
240.00	0.1082	8.3775(1)	587.95(2)
243.20	0.1081	8.3773(1)	587.91(2)
246.35	0.1081	8.3773(1)	587.92(2)
249.30	0.1081	8.3769(1)	587.82(2)
252.20	0.1081	8.3767(1)	587.79(2)
255.25	0.1080	8.3765(1)	587.74(2)
258.40	0.1080	8.3765(1)	587.74(2)
261.35	0.1079	8.3761(1)	587.66(2)
264.20	0.1078	8.3759(1)	587.62(2)
267.35	0.1078	8.3758(1)	587.60(2)
269.55	0.1077	8.3757(1)	587.58(2)
273.55	0.1077	8.3755(1)	587.52(2)
276.55	0.1076	8.3752(1)	587.48(2)
279.45	0.1075	8.3750(1)	587.43(2)
282.30	0.1075	8.3750(1)	587.43(2)
285.30	0.1074	8.3748(1)	587.39(2)
288.30	0.1074	8.3747(1)	587.37(2)
291.30	0.1073	8.3746(1)	587.33(2)
294.40	0.1072	8.3744(1)	587.30(2)
297.20	0.1072	8.3743(1)	587.27(2)
300.25	0.1071	8.3741(1)	587.23(2)
303.11	0.1071	8.3741(1)	587.25(2)
305.69	0.1070	8.3740(1)	587.23(2)
309.23	0.1069	8.3740(1)	587.22(2)
312.45	0.1069	8.3741(1)	587.23(2)
316.23	0.1067	8.3742(1)	587.25(2)
319.25	0.1066	8.3746(1)	587.34(2)

Table D.2 continued

Temperature (K)	Rwp	a (Å)	Volume (Å^3)
322.21	0.1066	8.3748(1)	587.39(2)
325.33	0.1066	8.3753(1)	587.48(2)
328.36	0.1064	8.3756(1)	587.56(2)
331.82	0.1063	8.3761(1)	587.65(2)
334.98	0.1063	8.3766(1)	587.77(2)
338.29	0.1062	8.3769(1)	587.83(2)
341.85	0.1060	8.3774(1)	587.92(2)
345.00	0.1060	8.3777(1)	588.00(2)
348.48	0.1059	8.3781(1)	588.08(2)
352.10	0.1058	8.3784(1)	588.15(2)
355.23	0.1057	8.3787(1)	588.21(2)
358.54	0.1060	8.3791(1)	588.29(2)
361.97	0.1063	8.3793(1)	588.33(2)
365.53	0.1063	8.3796(1)	588.40(2)
369.06	0.1062	8.3798(1)	588.44(2)
372.91	0.1061	8.3801(1)	588.49(2)
376.34	0.1060	8.3803(1)	588.55(2)
379.97	0.1059	8.3806(1)	588.60(2)
383.35	0.1062	8.3808(1)	588.65(2)
386.11	0.1061	8.3811(1)	588.70(2)
389.13	0.1060	8.3813(1)	588.75(2)
392.19	0.1060	8.3815(1)	588.80(2)
395.15	0.1060	8.3817(1)	588.84(2)
398.35	0.1059	8.3819(1)	588.88(2)
401.61	0.1059	8.3821(1)	588.92(2)
405.02	0.1058	8.3822(1)	588.95(2)
408.37	0.1057	8.3824(1)	588.99(2)
411.52	0.1056	8.3826(1)	589.03(2)
414.77	0.1056	8.3827(1)	589.06(2)
419.29	0.1054	8.3829(1)	589.09(2)
422.60	0.1054	8.3831(1)	589.12(2)
425.70	0.1053	8.3832(1)	589.16(2)
429.05	0.1053	8.3833(1)	589.18(2)
431.90	0.1052	8.3835(1)	589.21(2)
434.85	0.1051	8.3836(1)	589.23(2)
437.21	0.1051	8.3837(1)	589.26(2)
439.94	0.1050	8.3838(1)	589.28(2)
442.71	0.1050	8.3839(1)	589.30(2)
445.43	0.1049	8.3840(1)	589.32(2)

Table D.2 continued

Temperature (K)	Rwp	a (Å)	Volume (Å^3)
448.32	0.1048	8.3841(1)	589.33(2)
450.94	0.1047	8.3841(1)	589.35(2)
453.56	0.1046	8.3842(1)	589.37(2)
456.29	0.1045	8.3843(1)	589.38(2)
458.84	0.1044	8.3843(1)	589.39(2)
461.50	0.1043	8.3844(1)	589.40(2)
463.97	0.1042	8.3844(1)	589.41(2)
466.54	0.1042	8.3845(1)	589.42(2)
469.02	0.1041	8.3845(1)	589.44(2)
471.57	0.1040	8.3846(1)	589.44(2)
474.07	0.1040	8.3846(1)	589.46(2)
476.59	0.1039	8.3846(1)	589.46(2)
479.05	0.1038	8.3847(1)	589.47(2)
481.44	0.1038	8.3847(1)	589.47(2)
483.83	0.1037	8.3848(1)	589.49(2)
486.18	0.1036	8.3848(1)	589.49(2)
488.44	0.1035	8.3849(1)	589.51(2)
490.69	0.1034	8.3849(1)	589.51(2)
492.92	0.1033	8.3850(1)	589.52(2)
495.06	0.1032	8.3850(1)	589.54(2)
497.18	0.1031	8.3851(1)	589.56(2)
499.41	0.1030	8.3852(1)	589.57(2)
501.65	0.1029	8.3852(1)	589.58(2)
502.87	0.1029	8.3853(1)	589.61(2)
501.69	0.1029	8.3857(1)	589.69(2)
500.19	0.1029	8.3861(1)	589.76(2)
498.50	0.1030	8.3865(1)	589.85(2)
496.65	0.1029	8.3869(1)	589.93(2)
494.69	0.1030	8.3873(1)	590.01(2)
492.66	0.1031	8.3877(1)	590.10(2)
490.64	0.1031	8.3881(1)	590.19(2)
488.47	0.1032	8.3885(1)	590.28(2)
486.18	0.1033	8.3889(1)	590.37(2)
483.77	0.1035	8.3894(1)	590.46(2)
481.20	0.1036	8.3898(1)	590.55(2)
478.68	0.1037	8.3902(1)	590.63(2)
475.96	0.1038	8.3906(1)	590.72(2)
473.29	0.1038	8.3910(1)	590.81(2)
470.54	0.1040	8.3914(1)	590.89(2)

Table D.2 continued

Temperature (K)	Rwp	a (Å)	Volume (Å^3)
467.88	0.1041	8.3918(1)	590.97(2)
465.16	0.1044	8.3922(1)	591.05(2)
461.75	0.1043	8.3926(1)	591.14(2)
459.05	0.1045	8.3930(1)	591.22(2)
455.75	0.1046	8.3934(1)	591.30(2)
452.93	0.1047	8.3937(1)	591.37(2)
450.25	0.1049	8.3941(1)	591.45(2)
447.73	0.1050	8.3944(1)	591.52(2)
444.28	0.1051	8.3948(1)	591.59(2)
441.48	0.1052	8.3951(1)	591.66(2)
438.59	0.1053	8.3954(1)	591.73(2)
435.73	0.1054	8.3957(1)	591.80(2)
432.75	0.1055	8.3960(1)	591.87(2)
429.71	0.1056	8.3964(1)	591.93(2)
426.62	0.1057	8.3967(1)	592.00(2)
423.51	0.1057	8.3970(1)	592.06(2)
420.35	0.1059	8.3973(1)	592.12(2)
417.25	0.1059	8.3975(1)	592.18(2)
414.21	0.1061	8.3978(1)	592.24(2)
411.07	0.1061	8.3981(1)	592.30(2)
407.96	0.1062	8.3984(1)	592.36(2)
404.88	0.1062	8.3986(1)	592.42(2)
401.72	0.1064	8.3989(1)	592.48(2)
398.49	0.1064	8.3992(1)	592.54(2)
395.51	0.1065	8.3995(1)	592.59(2)
392.46	0.1064	8.3997(1)	592.63(2)
389.81	0.1065	8.3999(1)	592.69(2)
387.10	0.1067	8.4002(1)	592.74(2)
384.21	0.1067	8.4004(1)	592.80(2)
381.08	0.1067	8.4007(1)	592.86(2)
377.62	0.1068	8.4010(1)	592.92(2)
374.11	0.1068	8.4013(1)	592.98(2)
370.49	0.1069	8.4016(1)	593.05(2)
367.26	0.1069	8.4018(1)	593.09(2)
363.75	0.1070	8.4022(1)	593.18(2)
360.34	0.1070	8.4024(1)	593.21(2)
357.02	0.1070	8.4027(1)	593.27(2)
353.70	0.1071	8.4030(1)	593.33(2)
350.61	0.1071	8.4032(1)	593.39(2)

Table D.2 continued

Temperature (K)	Rwp	a (Å)	Volume (Å^3)
347.22	0.1071	8.4036(1)	593.46(2)
343.87	0.1071	8.4037(1)	593.50(2)
340.40	0.1072	8.4040(1)	593.56(2)
337.12	0.1072	8.4043(1)	593.62(2)
333.71	0.1072	8.4046(1)	593.67(2)
330.63	0.1073	8.4048(1)	593.73(2)
327.33	0.1073	8.4052(1)	593.80(2)
324.13	0.1073	8.4055(1)	593.87(2)
320.90	0.1073	8.4057(1)	593.90(2)
315.53	0.1074	8.4063(1)	594.04(2)
312.46	0.1074	8.4066(1)	594.10(2)
309.35	0.1074	8.4066(1)	594.10(2)
306.19	0.1075	8.4069(1)	594.16(2)
303.43	0.1076	8.4072(1)	594.22(2)
300.55	0.1076	8.4077(1)	594.33(2)
297.54	0.1076	8.4076(1)	594.32(2)
294.37	0.1077	8.4080(1)	594.41(2)
291.36	0.1077	8.4082(1)	594.45(2)
288.36	0.1077	8.4086(1)	594.52(2)
285.57	0.1077	8.4088(1)	594.56(2)
282.75	0.1078	8.4091(1)	594.64(2)
279.75	0.1077	8.4094(1)	594.69(2)
276.44	0.1077	8.4096(1)	594.73(2)
273.50	0.1078	8.4098(1)	594.78(2)
270.50	0.1078	8.4101(1)	594.84(2)
267.56	0.1079	8.4107(1)	594.96(2)
264.02	0.1080	8.4109(1)	595.01(2)
261.44	0.1080	8.4112(1)	595.08(2)
258.54	0.1081	8.4118(1)	595.19(2)
255.45	0.1081	8.4120(1)	595.26(2)
252.33	0.1081	8.4120(1)	595.25(2)
249.44	0.1082	8.4127(1)	595.40(2)
246.51	0.1082	8.4127(1)	595.40(2)
243.77	0.1081	8.4126(1)	595.38(2)
240.81	0.1082	8.4129(1)	595.44(2)
237.88	0.1084	8.4133(1)	595.51(2)
234.92	0.1084	8.4135(1)	595.57(2)
232.12	0.1085	8.4140(1)	595.67(2)
229.27	0.1086	8.4142(1)	595.71(2)

Table D.2 continued

Temperature (K)	Rwp	a (Å)	Volume (Å^3)
226.40	0.1086	8.4144(1)	595.76(2)
222.94	0.1087	8.4147(1)	595.82(2)
220.04	0.1088	8.4150(1)	595.89(2)
217.25	0.1089	8.4154(1)	595.96(2)
214.30	0.1089	8.4157(1)	596.04(2)
211.30	0.1090	8.4160(1)	596.11(2)
207.86	0.1091	8.4164(1)	596.18(2)
204.81	0.1092	8.4167(1)	596.25(2)
201.86	0.1093	8.4171(1)	596.32(2)
198.96	0.1094	8.4174(1)	596.39(2)
196.09	0.1095	8.4177(1)	596.46(2)
193.21	0.1095	8.4181(1)	596.53(2)
190.36	0.1096	8.4184(1)	596.61(2)
187.40	0.1098	8.4187(1)	596.68(2)
184.46	0.1099	8.4191(1)	596.75(2)
181.51	0.1100	8.4194(1)	596.82(2)
178.55	0.1101	8.4197(1)	596.89(2)
175.59	0.1102	8.4201(1)	596.96(2)
172.64	0.1104	8.4204(1)	597.03(2)
169.71	0.1105	8.4207(1)	597.10(2)
166.80	0.1106	8.4211(1)	597.18(2)
163.93	0.1107	8.4214(1)	597.26(2)
161.09	0.1108	8.4218(1)	597.33(2)
158.28	0.1110	8.4221(1)	597.40(2)
155.50	0.1111	8.4225(1)	597.47(2)
152.70	0.1112	8.4228(1)	597.55(2)
150.00	0.1113	8.4231(1)	597.62(2)
147.22	0.1114	8.4235(1)	597.69(2)
144.53	0.1116	8.4239(1)	597.77(2)
141.78	0.1116	8.4242(1)	597.84(2)
138.99	0.1117	8.4245(1)	597.91(2)
136.16	0.1119	8.4249(1)	597.99(2)
133.28	0.1120	8.4253(1)	598.07(2)
130.35	0.1122	8.4256(1)	598.14(2)
127.35	0.1123	8.4260(1)	598.23(2)
124.31	0.1124	8.4264(1)	598.31(2)
121.23	0.1126	8.4268(1)	598.40(2)
118.15	0.1128	8.4272(1)	598.48(2)
115.10	0.1128	8.4276(1)	598.56(2)

Table D.2 continued

Temperature (K)	Rwp	a (Å)	Volume (Å^3)
112.05	0.1129	8.4280(1)	598.64(2)

Table D.3: Lattice constant and unit cell volume for cubic $CaZr_{0.25}Nb_{0.75}F_{6.75}$ as determined from Rietveld analyses of the variable temperature x-ray diffraction data.

Temperature (K)	Rwp	a (Å)	Volume (Å^3)
111.53	0.0833	8.30812(8)	573.47(2)
114.12	0.0832	8.30742(8)	573.32(2)
116.07	0.0831	8.30678(8)	573.19(2)
118.65	0.0830	8.30619(8)	573.07(2)
121.37	0.0829	8.30566(8)	572.96(2)
124.19	0.0829	8.30517(8)	572.86(2)
127.46	0.0829	8.30474(8)	572.77(2)
131.11	0.0829	8.30437(8)	572.69(2)
133.81	0.0829	8.30407(8)	572.63(2)
136.62	0.0830	8.30382(8)	572.58(2)
139.47	0.0830	8.30368(8)	572.55(2)
142.26	0.0831	8.30358(8)	572.53(2)
144.97	0.0831	8.30356(8)	572.52(2)
147.61	0.0832	8.30362(8)	572.54(2)
150.11	0.0832	8.30371(8)	572.55(2)
152.81	0.0831	8.30384(8)	572.58(2)
155.51	0.0832	8.30403(8)	572.62(2)
158.33	0.0833	8.30427(8)	572.67(2)
161.25	0.0835	8.30457(8)	572.73(2)
164.16	0.0836	8.30482(8)	572.78(2)
167.25	0.0836	8.30508(8)	572.84(2)
170.10	0.0837	8.30533(8)	572.89(2)
172.94	0.0838	8.30559(8)	572.94(2)
175.75	0.0837	8.30579(8)	572.99(2)
178.66	0.0838	8.30596(8)	573.02(2)
181.54	0.0839	8.30612(8)	573.05(2)
184.42	0.0840	8.30624(8)	573.08(2)
187.29	0.0840	8.30631(8)	573.09(2)
190.16	0.0840	8.30632(8)	573.10(2)
193.02	0.0840	8.30632(8)	573.10(2)
195.89	0.0840	8.30631(8)	573.09(2)

Table D.3 continued

Temperature (K)	Rwp	a (Å)	Volume (Å^3)
198.78	0.0839	8.30629(8)	573.09(2)
201.71	0.0839	8.30623(8)	573.08(2)
204.68	0.0838	8.30618(8)	573.06(2)
207.68	0.0839	8.30615(8)	573.06(2)
210.69	0.0839	8.30611(8)	573.05(2)
213.63	0.0839	8.30607(8)	573.04(2)
216.35	0.0839	8.30602(8)	573.03(2)
219.36	0.0839	8.30598(8)	573.02(2)
222.89	0.0838	8.30587(8)	573.00(2)
225.35	0.0837	8.30581(8)	572.99(2)
228.50	0.0837	8.30577(8)	572.98(2)
231.25	0.0840	8.3058(8)	572.99(2)
234.40	0.0840	8.30576(8)	572.98(2)
237.40	0.0839	8.30567(8)	572.96(2)
240.20	0.0841	8.30564(8)	572.95(2)
243.60	0.0843	8.30564(8)	572.95(2)
246.65	0.0844	8.30562(8)	572.95(2)
249.40	0.0843	8.30557(8)	572.94(2)
252.25	0.0840	8.30540(8)	572.90(2)
255.15	0.0838	8.30532(8)	572.89(2)
258.10	0.0835	8.30517(8)	572.86(2)
261.35	0.0837	8.30516(8)	572.85(2)
264.15	0.0838	8.30512(8)	572.85(2)
267.35	0.0839	8.30507(8)	572.84(2)
270.40	0.0839	8.30512(8)	572.85(2)
273.50	0.0840	8.30506(8)	572.83(2)
276.60	0.0842	8.30505(8)	572.83(2)
279.45	0.0842	8.30500(8)	572.82(2)
282.20	0.0841	8.30491(8)	572.80(2)
285.25	0.0840	8.30495(8)	572.81(2)
288.25	0.0839	8.30494(8)	572.81(2)
291.35	0.0838	8.30493(8)	572.81(2)
294.45	0.0837	8.30494(8)	572.81(2)
297.30	0.0837	8.30501(8)	572.82(2)
300.20	0.0836	8.30514(8)	572.85(2)
303.20	0.0835	8.30530(8)	572.88(2)
303.99	0.0834	8.30552(8)	572.93(2)

Table D.3 continued

Temperature (K)	Rwp	a (Å)	Volume (Å^3)
308.63	0.0834	8.30586(8)	573.00(2)
312.55	0.0833	8.30632(8)	573.09(2)
316.86	0.0832	8.30690(8)	573.21(2)
318.87	0.0833	8.30764(8)	573.37(2)
321.92	0.0833	8.30852(8)	573.55(2)
325.12	0.0834	8.30945(8)	573.74(2)
328.57	0.0833	8.31029(8)	573.92(2)
331.66	0.0833	8.31117(8)	574.10(2)
335.20	0.0833	8.31190(8)	574.25(2)
338.18	0.0833	8.31261(8)	574.40(2)
341.85	0.0833	8.31315(8)	574.51(2)
345.12	0.0833	8.31370(8)	574.62(2)
348.37	0.0833	8.31415(8)	574.72(2)
352.05	0.0833	8.3146(8)	574.81(2)
355.11	0.0832	8.31496(8)	574.88(2)
358.60	0.0832	8.31531(8)	574.96(2)
361.97	0.0832	8.31564(8)	575.03(2)
365.47	0.0831	8.31589(8)	575.08(2)
369.12	0.0830	8.31616(8)	575.13(2)
372.66	0.0829	8.31636(8)	575.18(2)
376.40	0.0829	8.31659(8)	575.22(2)
379.97	0.0830	8.31680(8)	575.27(2)
383.25	0.0831	8.31697(8)	575.30(2)
386.21	0.0830	8.31713(8)	575.33(2)
389.13	0.0831	8.31728(8)	575.37(2)
392.14	0.0830	8.31740(8)	575.39(2)
395.10	0.0831	8.31750(8)	575.41(2)
398.29	0.0831	8.31759(8)	575.43(2)
401.61	0.0830	8.31767(8)	575.45(2)
404.97	0.0830	8.31773(8)	575.46(2)
408.37	0.0830	8.31778(8)	575.47(2)
411.63	0.0829	8.31783(8)	575.48(2)
414.77	0.0830	8.31787(8)	575.49(2)
419.40	0.0831	8.31792(8)	575.50(2)
422.60	0.0830	8.31794(8)	575.50(2)
425.75	0.0831	8.31796(8)	575.51(2)
429.05	0.0832	8.31799(8)	575.51(2)
431.90	0.0832	8.31801(8)	575.52(2)
434.90	0.0836	8.31801(8)	575.52(2)

Table D.3 continued

Temperature (K)	Rwp	a (Å)	Volume (Å^3)
437.26	0.0835	8.31799(8)	575.51(2)
439.99	0.0835	8.31797(8)	575.51(2)
442.76	0.0834	8.31797(8)	575.51(2)
445.48	0.0834	8.31795(8)	575.51(2)
448.22	0.0834	8.31795(8)	575.50(2)
450.94	0.0834	8.31793(8)	575.50(2)
453.61	0.0834	8.31793(8)	575.50(2)
456.24	0.0834	8.31793(8)	575.50(2)
458.89	0.0834	8.31790(8)	575.50(2)
461.46	0.0833	8.31785(8)	575.48(2)
463.97	0.0832	8.31784(8)	575.48(2)
466.46	0.0832	8.31778(8)	575.47(2)
469.06	0.0831	8.31775(8)	575.46(2)
471.57	0.0830	8.31771(8)	575.46(2)
474.07	0.0829	8.31766(8)	575.45(2)
476.55	0.0828	8.3176(8)	575.43(2)
479.01	0.0826	8.31757(8)	575.43(2)
481.44	0.0825	8.31751(7)	575.41(2)
483.87	0.0824	8.31747(7)	575.41(2)
486.22	0.0823	8.31742(7)	575.39(2)
488.48	0.0821	8.31738(7)	575.39(2)
490.72	0.0820	8.31734(7)	575.38(2)
492.92	0.0819	8.31732(7)	575.38(2)
495.09	0.0818	8.31729(7)	575.37(2)
497.25	0.0814	8.31723(7)	575.36(2)
499.45	0.0811	8.31719(7)	575.35(2)
501.69	0.0809	8.31718(7)	575.35(2)
502.89	0.0807	8.31720(7)	575.35(2)
501.71	0.0805	8.31738(7)	575.39(2)
500.22	0.0805	8.31759(7)	575.43(2)
498.50	0.0805	8.31785(7)	575.48(2)
496.62	0.0805	8.31812(7)	575.54(2)
494.69	0.0804	8.31837(7)	575.59(2)
492.69	0.0803	8.31868(7)	575.66(2)
490.64	0.0802	8.31900(7)	575.72(2)
488.47	0.0802	8.31936(7)	575.8(2)
486.14	0.0802	8.31976(7)	575.88(2)
483.77	0.0802	8.32017(7)	575.97(2)
481.25	0.0801	8.32056(7)	576.05(2)

Table D.3 continued

Temperature (K)	Rwp	a (Å)	Volume (Å^3)
478.59	0.0800	8.32097(7)	576.13(2)
475.96	0.0799	8.32142(7)	576.23(2)
473.25	0.0800	8.32188(7)	576.32(2)
470.58	0.0800	8.32233(7)	576.42(2)
467.83	0.0799	8.32281(7)	576.51(2)
465.11	0.0799	8.32330(7)	576.62(2)
461.75	0.0800	8.32379(7)	576.72(2)
458.93	0.0799	8.32428(7)	576.82(2)
455.75	0.0798	8.32476(7)	576.92(2)
452.93	0.0798	8.32523(7)	577.02(2)
450.25	0.0797	8.32572(7)	577.12(2)
447.69	0.0798	8.32622(7)	577.22(2)
444.28	0.0797	8.32670(7)	577.32(2)
441.48	0.0797	8.32720(7)	577.43(2)
438.64	0.0797	8.32766(7)	577.52(2)
435.68	0.0797	8.32814(7)	577.62(2)
432.70	0.0797	8.32860(7)	577.72(1)
429.66	0.0797	8.32907(7)	577.82(1)
426.67	0.0797	8.32952(7)	577.91(1)
423.51	0.0796	8.32997(7)	578.00(1)
420.35	0.0797	8.33043(7)	578.10(1)
417.30	0.0797	8.33086(7)	578.19(1)
414.21	0.0797	8.33129(7)	578.28(1)
411.12	0.0797	8.33171(7)	578.37(1)
408.02	0.0797	8.33213(7)	578.45(1)
404.88	0.0797	8.33254(7)	578.54(1)
401.72	0.0798	8.33293(7)	578.62(1)
398.54	0.0798	8.33333(7)	578.70(1)
395.40	0.0799	8.33368(7)	578.78(1)
392.51	0.0799	8.33404(7)	578.85(1)
389.77	0.0798	8.33436(7)	578.92(1)
387.06	0.0799	8.33472(7)	578.99(1)
384.16	0.0800	8.33506(7)	579.06(1)
380.97	0.0800	8.33540(7)	579.14(1)
377.50	0.0800	8.33571(7)	579.20(1)
374.06	0.0800	8.33605(7)	579.27(1)
370.67	0.0800	8.33638(7)	579.34(1)
367.09	0.0801	8.33668(7)	579.40(1)
363.63	0.0801	8.33696(7)	579.46(1)

Table D.3 continued

Temperature (K)	Rwp	a (Å)	Volume (Å^3)
360.45	0.0801	8.33723(7)	579.52(1)
356.96	0.0801	8.33751(7)	579.57(1)
353.87	0.0801	8.33778(7)	579.63(1)
350.61	0.0801	8.33801(7)	579.68(1)
347.16	0.0801	8.33828(7)	579.73(1)
343.81	0.0801	8.33852(7)	579.79(1)
340.35	0.0801	8.33870(7)	579.82(1)
336.96	0.0802	8.33899(7)	579.88(1)
333.99	0.0802	8.33921(7)	579.93(1)
330.58	0.0801	8.33947(7)	579.98(1)
327.28	0.0802	8.33955(7)	580.00(1)
324.34	0.0802	8.33978(7)	580.05(1)
321.07	0.0802	8.34007(7)	580.11(1)
315.53	0.0803	8.34033(7)	580.16(1)
312.35	0.0803	8.34046(7)	580.19(1)
309.30	0.0803	8.34068(7)	580.24(1)
306.39	0.0803	8.34085(7)	580.27(1)
303.47	0.0803	8.34106(7)	580.32(1)
300.64	0.0804	8.34129(7)	580.36(1)
297.54	0.0803	8.34138(7)	580.38(1)
294.37	0.0803	8.34159(7)	580.43(1)
291.26	0.0803	8.34171(7)	580.45(1)
288.36	0.0803	8.34192(7)	580.50(1)
285.57	0.0802	8.34205(7)	580.52(1)
282.75	0.0802	8.34236(7)	580.59(1)
279.75	0.0803	8.34247(7)	580.61(1)
276.35	0.0803	8.34260(7)	580.64(1)
273.50	0.0803	8.34274(7)	580.67(1)
270.50	0.0803	8.34315(7)	580.75(1)
267.47	0.0803	8.34311(7)	580.74(1)
264.22	0.0802	8.34336(7)	580.80(1)
262.37	0.0803	8.34368(7)	580.86(1)
257.76	0.0802	8.34371(7)	580.87(1)
256.01	0.0802	8.34408(7)	580.95(1)
252.72	0.0802	8.34403(7)	580.94(1)
249.25	0.0802	8.34422(7)	580.97(1)
246.42	0.0802	8.34464(7)	581.06(1)
244.06	0.0801	8.34482(7)	581.10(1)
240.37	0.0801	8.34486(7)	581.11(1)

Table D.3 continued

Temperature (K)	Rwp	a (Å)	Volume (Å^3)
237.73	0.0802	8.34497(7)	581.13(1)
234.88	0.0801	8.34532(7)	581.21(1)
232.17	0.0801	8.34562(7)	581.27(1)
229.41	0.0801	8.34559(7)	581.26(1)
226.35	0.0800	8.34607(7)	581.36(1)
222.90	0.0801	8.34594(7)	581.33(1)
220.13	0.0800	8.34628(7)	581.41(1)
217.40	0.0800	8.34643(7)	581.44(1)
214.35	0.0800	8.34650(7)	581.45(1)
211.25	0.0800	8.34669(7)	581.49(1)
207.91	0.0800	8.34684(7)	581.52(1)
204.81	0.0800	8.34700(7)	581.56(1)
202.05	0.0799	8.34720(7)	581.60(1)
199.01	0.0799	8.34736(7)	581.63(1)
196.14	0.0798	8.34752(7)	581.66(1)
193.26	0.0797	8.34767(7)	581.70(1)
190.31	0.0798	8.34783(7)	581.73(1)
187.40	0.0797	8.34798(7)	581.76(1)
184.46	0.0797	8.34812(7)	581.79(1)
181.51	0.0796	8.34827(7)	581.82(1)
178.55	0.0796	8.34841(7)	581.85(1)
175.54	0.0796	8.34856(7)	581.88(1)
173.28	0.0796	8.34864(7)	581.90(1)
169.61	0.0794	8.34880(7)	581.93(1)
166.80	0.0794	8.34904(7)	581.98(1)
163.93	0.0793	8.34927(7)	582.03(1)
161.09	0.0792	8.34950(7)	582.08(1)
158.28	0.0792	8.34964(7)	582.11(1)
155.50	0.0790	8.34977(7)	582.14(1)
152.74	0.0789	8.34989(7)	582.16(1)
150.00	0.0788	8.35003(7)	582.19(1)
147.27	0.0788	8.35016(7)	582.22(1)
144.53	0.0787	8.35026(7)	582.24(1)
141.78	0.0786	8.35035(7)	582.26(1)
138.99	0.0785	8.35046(7)	582.28(1)
136.16	0.0784	8.35057(7)	582.30(1)
133.28	0.0783	8.35063(7)	582.31(1)
130.35	0.0782	8.35071(7)	582.33(1)
127.35	0.0781	8.35079(7)	582.35(1)

Table D.3 continued

Temperature (K)	Rwp	a (Å)	Volume (Å^3)
124.31	0.0780	8.35091(7)	582.37(1)
121.23	0.0779	8.35102(7)	582.40(1)
118.15	0.0777	8.35111(7)	582.42(1)
115.05	0.0777	8.35120(7)	582.43(1)
112.09	0.0776	8.35128(7)	582.45(1)

Table D.4: Unit cell volumes for cubic $CaZr_{0.75}Nb_{0.25}F_{6.25}$ and NaCl as determined from the Rietveld analysis of the high-pressure diffraction data. Pressures estimated from the unit cell volume of the NaCl using an equation of state are also given.

a (Å)	$CaZr_{0.75}Nb_{0.25}F_{6.25}$ Volume (Å^3)	NaCl Volume (Å^3)	Pressure (GPa)
8.42993(6)	599.06(1)	179.506(6)	0.000(11)
8.43003(6)	599.08(1)	179.506(6)	0.000(11)
8.43011(6)	599.10(1)	179.506(7)	0.000(12)
8.43018(6)	599.12(1)	179.505(7)	0.001(12)
8.43024(6)	599.13(1)	179.505(6)	0.001(11)
8.43031(6)	599.14(1)	179.507(6)	0.000(11)
8.43037(6)	599.16(1)	179.506(6)	0.000(11)
8.43042(6)	599.17(1)	179.507(6)	0.000(11)
8.43047(6)	599.18(1)	179.509(6)	0.000(11)
8.43052(8)	599.19(2)	179.505(8)	0.001(13)
8.43060(8)	599.20(2)	179.504(8)	0.001(13)
8.43066(6)	599.22(1)	179.505(6)	0.001(11)
8.43072(6)	599.23(1)	179.503(6)	0.001(11)
8.43070(6)	599.23(1)	179.498(6)	0.001(11)
8.43068(6)	599.22(1)	179.498(6)	0.001(11)
8.43075(6)	599.24(1)	179.498(7)	0.001(12)
8.43070(6)	599.23(1)	179.492(6)	0.002(11)
8.43042(6)	599.17(1)	179.462(6)	0.006(11)
8.43008(6)	599.10(1)	179.425(7)	0.011(12)
8.42961(7)	598.99(2)	179.372(8)	0.018(13)
8.42928(6)	598.92(1)	179.333(7)	0.023(12)
8.42887(6)	598.84(1)	179.291(7)	0.029(12)
8.42820(6)	598.69(1)	179.223(7)	0.038(12)
8.42765(6)	598.58(1)	179.172(6)	0.045(11)
8.42698(6)	598.43(1)	179.107(6)	0.054(11)

Table D.4 continued

a (Å)	$CaZr_{0.75}Nb_{0.25}F_{6.25}$ Volume (Å^3)	NaCl Volume (Å^3)	Pressure (GPa)
8.42610(6)	598.25(1)	179.025(6)	0.065(11)
8.42516(6)	598.05(1)	178.933(6)	0.077(11)
8.42415(7)	597.83(2)	178.832(7)	0.091(13)
8.42274(6)	597.53(1)	178.688(6)	0.111(12)
8.42109(6)	597.18(1)	178.535(6)	0.132(12)
8.41944(6)	596.83(1)	178.384(6)	0.153(12)
8.41826(6)	596.58(1)	178.272(5)	0.168(11)
8.41707(6)	596.33(1)	178.160(5)	0.184(11)
8.41520(6)	595.93(1)	177.992(5)	0.207(11)
8.41296(6)	595.45(1)	177.797(5)	0.235(11)
8.41097(6)	595.03(1)	177.623(5)	0.259(11)
8.40777(6)	594.35(1)	177.364(5)	0.296(11)
8.40372(6)	593.49(1)	177.050(5)	0.341(11)
8.40087(6)	592.89(1)	176.840(5)	0.372(11)
8.39736(6)	592.15(1)	176.599(5)	0.407(11)
8.39248(6)	591.11(1)	176.281(6)	0.454(12)
8.38771(6)	590.11(1)	175.990(5)	0.498(12)
8.38046(6)	588.58(1)	175.593(6)	0.558(13)
8.37244(7)	586.89(1)	175.215(6)	0.616(13)
8.36136(8)	584.56(2)	174.814(6)	0.678(13)

Table D.5: Unit cell volumes for cubic $CaZr_{0.5}Nb_{0.5}F_{6.5}$ and NaCl as determined from the Rietveld analysis of the high-pressure diffraction data. Pressures estimated from the unit cell volume of the NaCl using an equation of state are also given.

a (Å)	c (Å)	$CaZr_{0.5}Nb_{0.5}F_{6.5}$ Volume (Å^3)	NaCl Volume (Å^3)	Pressure (GPa)
8.35553(8)	-	583.341(17)	178.552(5)	0.118(10)
8.35518(8)	-	583.268(17)	178.512(5)	0.123(10)
8.35448(8)	-	583.120(17)	178.433(5)	0.134(10)
8.35362(8)	-	582.941(17)	178.360(5)	0.144(10)
8.35310(8)	-	582.831(17)	178.291(5)	0.154(10)
8.35253(8)	-	582.712(17)	178.224(5)	0.163(10)
8.35170(8)	-	582.538(17)	178.171(5)	0.171(10)

Table D.5 continued

a (Å)	c (Å)	$CaZr_{0.5}Nb_{0.5}F_{6.5}$ Volume (Å^3)	NaCl Volume (Å^3)	Pressure (GPa)
8.35025(8)	-	582.235(17)	178.042(5)	0.189(10)
8.34887(8)	-	581.946(17)	177.929(5)	0.204(10)
8.34824(8)	-	581.815(17)	177.882(5)	0.211(10)
8.34695(8)	-	581.545(17)	177.795(5)	0.223(10)
8.34562(9)	-	581.268(18)	177.688(5)	0.238(10)
8.34404(8)	-	580.938(17)	177.565(5)	0.256(10)
8.34245(8)	-	580.605(17)	177.430(5)	0.275(10)
8.34100(8)	-	580.302(17)	177.319(5)	0.291(10)
8.33924(8)	-	579.935(17)	177.183(5)	0.310(10)
8.33709(8)	-	579.486(18)	177.032(5)	0.332(10)
8.33428(9)	-	578.900(18)	176.839(5)	0.360(10)
8.33211(9)	-	578.448(18)	176.691(5)	0.382(10)
8.32989(9)	-	577.987(18)	176.552(5)	0.402(10)
8.32804(9)	-	577.601(18)	176.441(5)	0.418(10)
8.32463(9)	-	576.893(18)	176.240(5)	0.448(10)
8.32067(9)	-	576.069(19)	176.007(5)	0.483(11)
8.31633(9)	-	575.168(19)	175.782(5)	0.517(11)
8.31302(9)	-	574.482(19)	175.617(5)	0.542(11)
8.30871(9)	-	573.589(19)	175.420(5)	0.572(11)
8.30267(9)	-	572.339(19)	175.168(5)	0.610(11)
8.29703(9)	-	571.173(19)	174.954(5)	0.643(11)
8.29154(10)	-	570.041(20)	174.777(5)	0.671(11)
8.28603(10)	-	568.905(20)	174.629(5)	0.694(11)
8.27989(10)	-	567.640(20)	174.510(5)	0.713(11)
8.27153(11)	-	565.923(23)	174.411(6)	0.728(12)
5.8258(2)	14.3771(9)	422.584(15)	174.306(5)	0.745(11)
5.8035(2)	14.3982(11)	419.968(18)	174.194(5)	0.763(11)
5.7761(3)	14.4351(12)	417.078(19)	174.060(6)	0.784(12)
5.7587(3)	14.4622(13)	415.346(20)	173.975(6)	0.798(12)
5.7334(3)	14.4974(14)	412.704(21)	173.850(6)	0.818(13)
5.7096(3)	14.5319(14)	410.258(19)	173.739(5)	0.836(11)
5.6936(3)	14.5534(14)	408.569(19)	173.650(5)	0.850(11)
5.6700(3)	14.5871(14)	406.130(19)	173.518(5)	0.872(11)
5.6526(3)	14.6096(13)	404.271(20)	173.429(5)	0.886(11)
5.6262(3)	14.6414(13)	401.362(20)	173.271(5)	0.912(12)
5.6074(3)	14.6640(13)	399.307(19)	173.145(5)	0.933(12)

Table D.5 continued

a (Å)	c (Å)	$CaZr_{0.5}Nb_{0.5}F_{6.5}$ Volume (Å^3)	NaCl Volume (Å^3)	Pressure (GPa)
5.5954(3)	14.6785(13)	397.994(19)	173.061(5)	0.947(12)
5.5851(3)	14.6906(13)	396.852(19)	172.996(4)	0.957(10)
5.5734(3)	14.7039(13)	395.549(19)	172.927(4)	0.969(10)
5.5592(3)	14.7201(15)	393.977(21)	172.840(5)	0.983(12)
5.5477(3)	14.7332(15)	392.695(22)	172.767(4)	0.996(11)
5.5348(3)	14.7489(16)	391.291(23)	172.676(4)	1.011(11)
5.5187(3)	14.7685(18)	389.532(25)	172.550(4)	1.032(11)
5.5082(4)	14.7801(20)	388.351(27)	172.460(4)	1.047(11)
5.4953(4)	14.7945(21)	386.910(29)	172.346(4)	1.066(11)
5.4768(4)	14.8133(25)	384.804(32)	172.151(4)	1.100(11)
5.4575(6)	14.8285(34)	382.483(41)	171.950(4)	1.134(11)

Table D.6: Unit cell volumes for cubic $CaZr_{0.25}Nb_{0.75}F_{6.75}$ and NaCl as determined from the Rietveld analysis of the high-pressure diffraction data. Pressures estimated from the unit cell volume of the NaCl using an equation of state are also given.

a (Å)	c (Å)	$CaZr_{0.25}Nb_{0.75}F_{6.75}$ Volume (Å^3)	NaCl Volume (Å^3)	Pressure (GPa)
8.27884(7)	-	567.425(14)	178.551(6)	0.118(12)
8.27911(7)	-	567.480(14)	178.547(6)	0.119(12)
8.27936(7)	-	567.532(14)	178.542(6)	0.119(12)
8.27957(7)	-	567.575(14)	178.537(6)	0.120(12)
8.27968(7)	-	567.598(14)	178.524(6)	0.122(12)
8.27968(7)	-	567.598(14)	178.505(6)	0.124(12)
8.27966(7)	-	567.594(14)	178.485(6)	0.127(12)
8.27955(7)	-	567.572(14)	178.461(6)	0.130(12)
8.27948(7)	-	567.556(14)	178.438(6)	0.134(12)
8.27900(7)	-	567.457(14)	178.384(6)	0.141(12)
8.27860(7)	-	567.376(14)	178.335(6)	0.148(12)
8.27749(7)	-	567.148(14)	178.227(6)	0.163(12)
8.27651(7)	-	566.945(14)	178.142(6)	0.175(12)
8.27531(7)	-	566.700(14)	178.046(6)	0.188(12)
8.27404(7)	-	566.438(14)	177.938(6)	0.203(12)
8.27251(7)	-	566.125(14)	177.811(6)	0.221(12)
8.27151(7)	-	565.918(14)	177.721(6)	0.234(12)
8.26972(7)	-	565.552(14)	177.578(6)	0.254(12)
8.26760(7)	-	565.116(14)	177.413(6)	0.277(12)

Table D.6 continued

a (Å)	c (Å)	$CaZr_{0.25}Nb_{0.75}F_{6.75}$ Volume (Å^3)	NaCl Volume (Å^3)	Pressure (GPa)
8.26639(7)	-	564.870(14)	177.313(6)	0.292(12)
8.26492(7)	-	564.568(14)	177.193(6)	0.309(12)
8.26325(7)	-	564.226(14)	177.059(6)	0.328(12)
8.26175(7)	-	563.919(14)	176.940(6)	0.345(12)
8.25987(7)	-	563.533(14)	176.798(6)	0.366(12)
8.25813(7)	-	563.176(14)	176.667(6)	0.385(12)
8.25541(7)	-	562.621(14)	176.474(6)	0.413(12)
8.25439(7)	-	562.413(14)	176.381(6)	0.427(13)
8.25326(7)	-	562.182(14)	176.287(6)	0.441(13)
8.25069(7)	-	561.656(14)	176.119(6)	0.466(13)
8.24928(7)	-	561.370(14)	176.011(6)	0.482(13)
8.24724(7)	-	560.951(14)	175.878(6)	0.502(13)
8.24413(7)	-	560.318(14)	175.698(6)	0.529(13)
8.24120(7)	-	559.720(14)	175.532(6)	0.554(13)
8.23832(7)	-	559.134(14)	175.378(6)	0.578(13)
8.23532(7)	-	558.524(14)	175.227(6)	0.601(13)
8.22908(7)	-	557.255(14)	174.967(6)	0.641(13)
8.22539(7)	-	556.506(15)	174.816(7)	0.665(14)
8.22158(8)	-	555.733(15)	174.677(7)	0.686(14)
8.21632(8)	-	554.667(16)	174.506(7)	0.713(14)
8.21103(8)	-	553.595(17)	174.353(7)	0.737(15)
8.20353(9)	-	552.080(19)	174.167(8)	0.767(16)
8.18764(12)	-	548.878(25)	173.895(9)	0.811(17)
5.7578(2)	14.2429(9)	408.930(16)	173.720(7)	0.839(15)
5.7456(2)	14.2573(10)	407.603(18)	173.659(8)	0.849(16)
5.7312(2)	14.2743(11)	406.043(20)	173.577(8)	0.862(16)
5.7063(3)	14.3059(14)	403.422(22)	173.420(9)	0.888(18)
5.6779(3)	14.3452(17)	400.508(25)	173.242(9)	0.917(18)
5.6431(4)	14.4012(20)	397.160(36)	173.028(9)	0.952(18)
5.6143(4)	14.4551(21)	394.580(36)	172.849(9)	0.982(18)
5.5959(4)	14.4881(20)	392.905(25)	172.734(8)	1.001(17)
5.5851(4)	14.5046(19)	391.833(24)	172.664(8)	1.013(17)
5.5751(3)	14.5161(18)	390.735(24)	172.594(8)	1.025(17)
5.5641(3)	14.5267(18)	389.477(24)	172.538(8)	1.034(17)
5.5568(3)	14.5341(18)	388.651(24)	172.503(8)	1.040(17)
5.5489(3)	14.5424(19)	387.776(24)	172.454(8)	1.048(17)

Table D.6 continued

a (Å)	c (Å)	$CaZr_{0.25}Nb_{0.75}F_{6.75}$ Volume (Å^3)	NaCl Volume (Å^3)	Pressure (GPa)
5.5402(4)	14.5521(19)	386.821(25)	172.385(8)	1.060(17)
5.5228(4)	14.5729(21)	384.947(27)	172.225(8)	1.087(17)
5.5128(4)	14.5858(21)	383.893(27)	172.142(7)	1.101(16)
5.5002(4)	14.6004(22)	382.515(28)	172.030(7)	1.120(16)
5.4861(4)	14.6175(22)	381.008(29)	171.908(7)	1.141(16)
5.4740(4)	14.6318(23)	379.696(29)	171.816(7)	1.157(16)
5.4632(4)	14.6433(23)	378.500(29)	171.742(7)	1.170(16)
5.4522(4)	14.6540(23)	377.256(29)	171.676(7)	1.181(16)
5.4427(4)	14.6622(23)	376.144(30)	171.623(7)	1.190(16)
5.4266(4)	14.6737(23)	374.224(30)	171.498(6)	1.212(15)
5.4152(4)	14.6792(23)	372.790(30)	171.444(6)	1.222(15)
5.4040(4)	14.6831(24)	371.345(31)	171.380(6)	1.233(15)
5.3933(4)	14.6848(25)	369.918(32)	171.324(6)	1.243(15)
5.3831(4)	14.6854(26)	368.540(33)	171.263(6)	1.253(15)
5.3699(5)	14.6849(27)	366.716(35)	171.136(5)	1.276(14)
5.3496(5)	14.6842(28)	363.929(36)	170.928(5)	1.313(14)

Table D.7: Crystallographic parameters for $CaZr_{0.75}Nb_{0.25}F_{6.25}$ at 300 K on cooling derived from the Rietveld analysis of the x-ray diffraction data acquired while using a Cryostream, see Figure D.1.

Chemical Formula	$CaZr_{0.75}Nb_{0.25}F_{6.25}$
Space group	$Fm\bar{3}m$
a (Å)	8.44156(8)
λ (Å)	0.72768
μ (cm^{-1})	24
Temperature (K)	300
R_{wp}	0.1109
R_F^2	0.1156

	x	y	z	Occupancy	U_{iso}/U_{eq} (Å^2)	U_{11} (Å^2)	U_{22}/U_{33} (Å^2)
Ca	0	0	0	1.0	0.0107(9)	-	-
Zr	$\frac{1}{2}$	$\frac{1}{2}$	$\frac{1}{2}$	0.75	0.0274(6)	-	-
Nb	$\frac{1}{2}$	$\frac{1}{2}$	$\frac{1}{2}$	0.25	0.0274(6)		
F	0.2617(4)	0	0	1.0	0.0362	0.013(2)	0.048(2)

Table D.8: Crystallographic parameters for $CaZr_{0.5}Nb_{0.5}F_{6.5}$ at 300 K derived on cooling from the Rietveld analysis of the x-ray diffraction data acquired while using a Cryostream, see Figure D.2.

Chemical Formula	$CaZr_{0.5}Nb_{0.5}F_{6.5}$
Space group	$Fm\bar{3}m$
a (Å)	8.40767(9)
λ (Å)	0.72768
μ (cm^{-1})	24
Temperature (K)	300
R_{wp}	0.1076
R_F^2	0.1493

	x	**y**	**z**	**Occupancy**	**U_{iso}/U_{eq} ($Å^2$)**	**U_{11} ($Å^2$)**	**U_{22}/U_{33} ($Å^2$)**
Ca	0	0	0	1.0	0.0139(9)	-	-
Zr	$\frac{1}{2}$	$\frac{1}{2}$	$\frac{1}{2}$	0.5	0.0305(6)	-	-
Nb	$\frac{1}{2}$	$\frac{1}{2}$	$\frac{1}{2}$	0.5	0.0305(6)		
F	0.2637(4)	0	0	1.0	0.0393	0.018(2)	0.050(2)

Table D.9: Crystallographic parameters for $CaZr_{0.25}Nb_{0.75}F_{6.75}$ at 300 K on cooling derived from the Rietveld analysis of the x-ray diffraction data acquired while using a Cryostream, see Figure 5.1a.

Chemical Formula	$CaZr_{0.25}Nb_{0.75}F_{6.75}$
Space group	$Fm\bar{3}m$
a (Å)	8.34129(7)
λ (Å)	0.72768
μ (cm^{-1})	24
Temperature (K)	300
R_{wp}	0.0804
R_F^2	0.0943

	x	**y**	**z**	**Occupancy**	**U_{iso}/U_{eq} ($Å^2$)**	**U_{11} ($Å^2$)**	**U_{22}/U_{33} ($Å^2$)**
Ca	0	0	0	1.0	0.0150(8)	-	-
Zr	$\frac{1}{2}$	$\frac{1}{2}$	$\frac{1}{2}$	0.25	0.0345(5)	-	-
Nb	$\frac{1}{2}$	$\frac{1}{2}$	$\frac{1}{2}$	0.75	0.0345(5)		
F	0.2666(3)	0	0	1.0	0.0454	0.012(2)	0.062(2)

Table D.10: Crystallographic parameters for $CaZr_{0.75}Nb_{0.25}F_{6.25}$ at room temperature and ~0.0 GPa derived from the Rietveld analysis of the high-pressure synchrotron diffraction data collected using a DAC, see Figure D.4.

Chemical Formula	$CaZr_{0.75}Nb_{0.25}F_{6.25}$
Space group	$Fm\bar{3}m$
a (Å)	8.43047(6)
λ (Å)	0.72768
Pressure (GPa)	0.0
R_{wp}	0.0410
R_F^2	0.0760

	x	**y**	**z**	**Occupancy**	**U_{iso} ($Å^2$)**
Ca	0	0	0	1.0	0.029(1)
Zr	$\frac{1}{2}$	$\frac{1}{2}$	$\frac{1}{2}$	0.75	0.0576(9)
Nb	$\frac{1}{2}$	$\frac{1}{2}$	$\frac{1}{2}$	0.25	0.0576(9)
F	0.2619(3)	0	0	1.0	0.041(1)

Table D.11: Crystallographic parameters for $CaZr_{0.5}Nb_{0.5}F_{6.5}$ at room temperature and ~0.1 GPa derived from the Rietveld analysis of the high-pressure synchrotron diffraction data collected using a DAC, see Figure D.6.

Chemical Formula	$CaZr_{0.5}Nb_{0.5}F_{6.5}$
Space group	$Fm\bar{3}m$
a (Å)	8.35554(8)
λ (Å)	0.72768
Pressure (GPa)	0.12
R_{wp}	0.0407
R_F^2	0.0823

	x	**y**	**z**	**Occupancy**	**U_{iso} (Å^2)**
Ca	0	0	0	1.0	0.037(2)
Zr	$\frac{1}{2}$	$\frac{1}{2}$	$\frac{1}{2}$	0.5	0.065(1)
Nb	$\frac{1}{2}$	$\frac{1}{2}$	$\frac{1}{2}$	0.5	0.065(1)
F	0.2656(4)	0	0	1.0	0.049(2)

Table D.12: Crystallographic parameters for $CaZr_{0.5}Nb_{0.5}F_{6.5}$ at room temperature and ~1.0 GPa derived from the Rietveld analysis of the high-pressure synchrotron diffraction data collected using a DAC, see Figure D.7.

Chemical Formula	$CaZr_{0.5}Nb_{0.5}F_{6.5}$
Space group	$R\bar{3}$
a (Å)	5.5477(3)
ac(Å)	14.733(2)
λ (Å)	0.72768
Pressure (GPa)	1.0
R_{wp}	0.0402
R_F^2	0.0769

	x	**y**	**z**	**Occupancy**	**U_{iso} (Å^2)**
Ca	0	0	0	1.0	-0.013(4)
Zr	0	0	$\frac{1}{2}$	0.5	0.197(6)
Nb	0	0	$\frac{1}{2}$	0.5	0.197(6)
F	0.093(1)	0.358(1)	0.0882(4)	1.0	0.057(3)

Table D.13: Crystallographic parameters for $CaZr_{0.25}Nb_{0.75}F_{6.75}$ at room temperature and ~0.1 GPa derived from the Rietveld analysis of the high-pressure synchrotron diffraction data collected using a DAC, see Figure 5.1b

Chemical Formula	$CaZr_{0.25}Nb_{0.75}F_{6.75}$
Space group	$Fm\bar{3}m$
a (Å)	8.27884(7)
λ (Å)	0.72768
Pressure (GPa)	0.12
R_{wp}	0.0388
R_F^2	0.0766

	x	**y**	**z**	**Occupancy**	**U_{iso} (Å^2)**
Ca	0	0	0	1.0	0.040(1)
Zr	$\frac{1}{2}$	$\frac{1}{2}$	$\frac{1}{2}$	0.25	0.062(9)
Nb	$\frac{1}{2}$	$\frac{1}{2}$	$\frac{1}{2}$	0.75	0.062(9)
F	0.2686(3)	0	0	1.0	0.054(1)

Table D.14: Crystallographic parameters for $CaZr_{0.25}Nb_{0.75}F_{6.75}$ at room temperature and ~1.1 GPa derived from the Rietveld analysis of the high-pressure synchrotron diffraction data collected using a DAC, see Figure D.12.

Chemical Formula	$CaZr_{0.25}Nb_{0.75}F_{6.75}$
Space group	$R\bar{3}$
a (Å)	5.5128(4)
ac(Å)	14.586(2)
λ (Å)	0.72768
Pressure (GPa)	1.1
R_{wp}	0.0525
R_F^2	0.1054

	x	**y**	**z**	**Occupancy**	**U_{iso} (Å^2)**
Ca	0	0	0	1.0	-0.019(6)
Zr	0	0	$\frac{1}{2}$	0.25	0.259(7)
Nb	0	0	$\frac{1}{2}$	0.75	0.259(7)
F	0.103(1)	0.361(1)	0.0869(5)	1.0	0.064(4)

APPENDIX E. SUPPLEMENTARY MATERIAL FOR CHAPTER 6

E.1 Figures

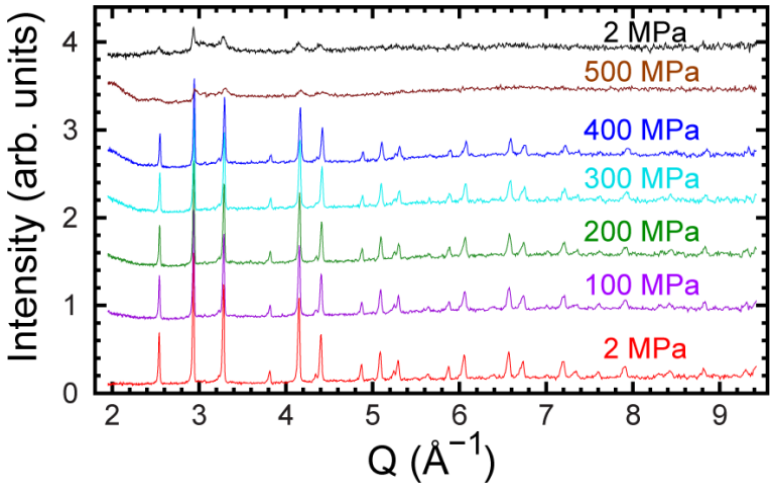

Figure E.1: Neutron diffraction data for $CaZrF_6$ on compression in N_2 gas at 160 K from 2 to 500 MPa, followed by decompression back to 2 MPa (black line).

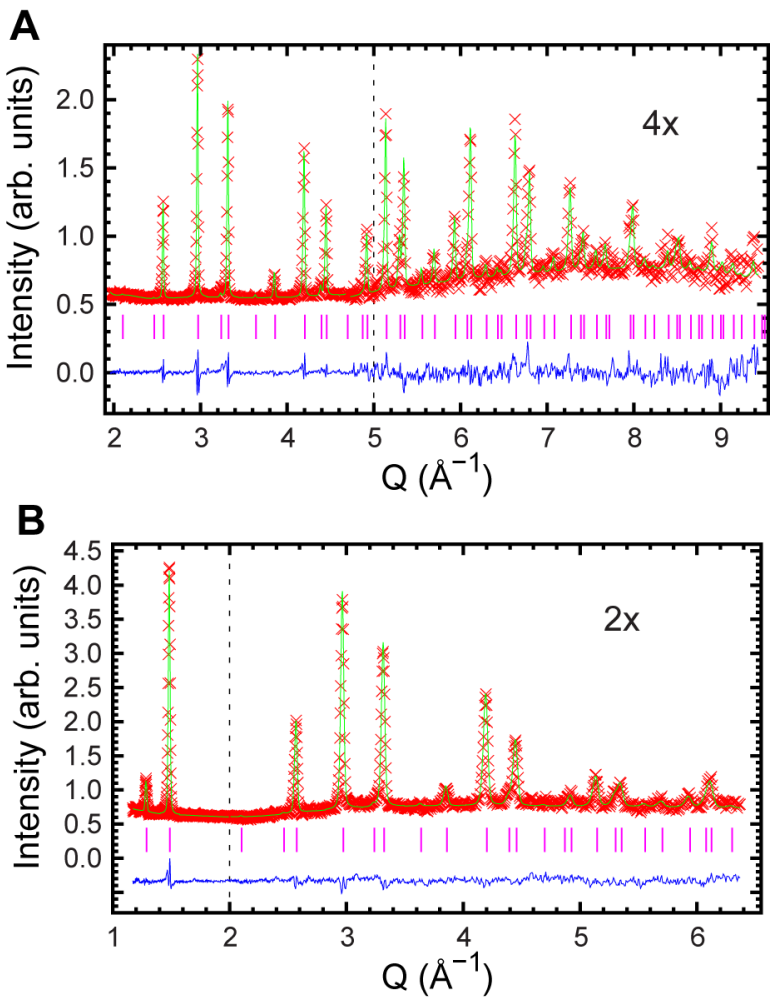

Figure E.2: Rietveld fits to 300 K, 0.075 MPa powder neutron diffraction data recorded on SNAP using an Fm$\bar{3}$m model for $CaZrF_6$ with no helium included: A) detector bank 1 (2θ ~84.777°), R_{F2}=17.34%, and B) detector bank 2 (2θ ~48.097°), R_{F2}=22.55%.

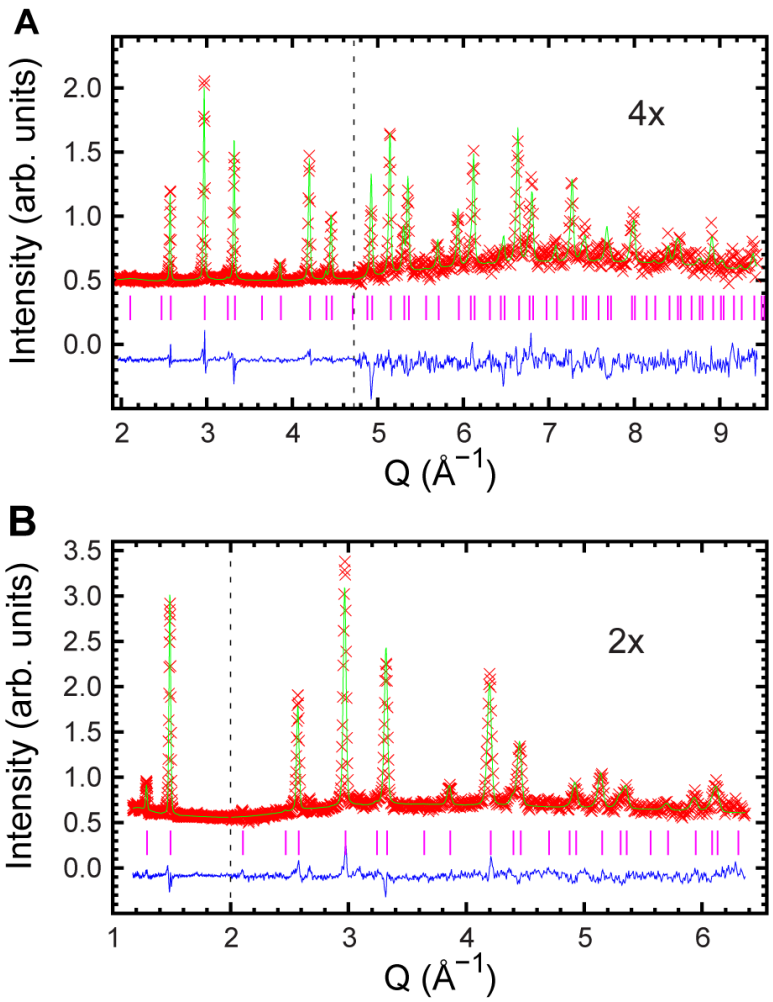

Figure E.3: Rietveld fits to 300 K, 500 MPa powder neutron diffraction data recorded on SNAP using $Fm\bar{3}m$ model for $CaZrF_6$ with no helium included: A) detector bank 1 (2θ ~84.777°), R_{F2}=14.59%, and B) detector bank 2 (2θ ~48.097°), R_{F2}=34.24%.

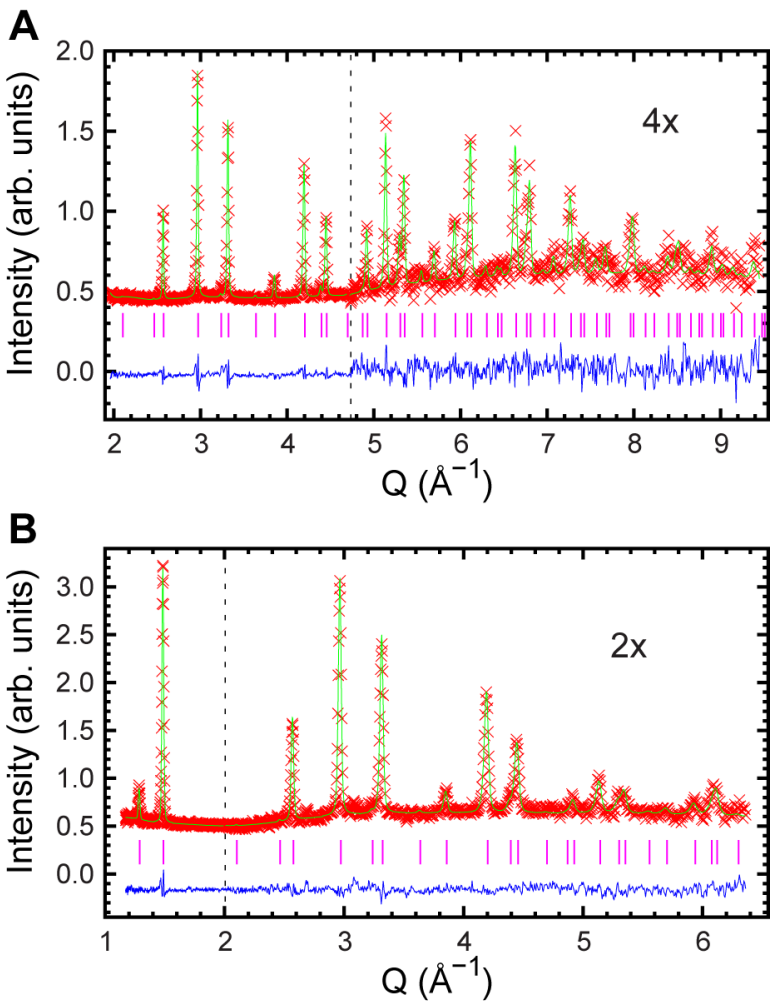

Figure E.4: Rietveld fits to 300 K 0.015 MPa powder neutron diffraction data recorded on SNAP using $Fm\bar{3}m$ model for $CaZrF_6$ with no helium included, at end of helium gas experiment: A) detector bank 1 (2θ ~84.777°), R_{F^2}=12.02%, and B) detector bank 2 (2θ ~48.097°), R_{F^2}=26.63%.

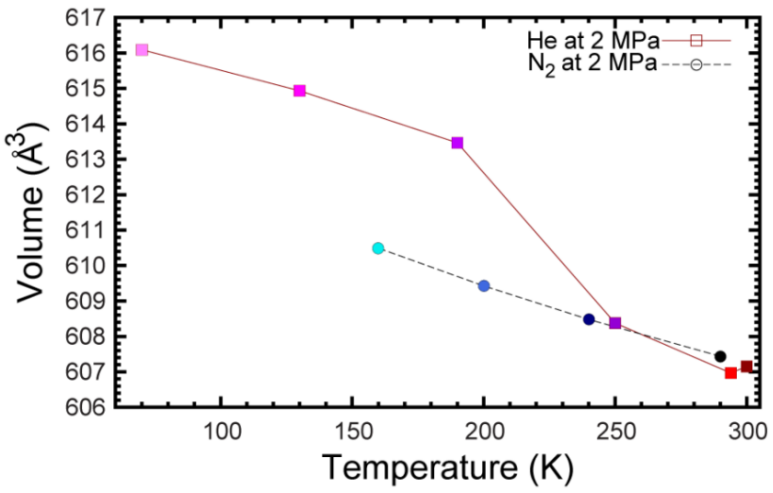

Figure E.5: A comparison of the unit cell volumes for $CaZrF_6$ cooled under high-pressure helium and then warmed up in stages from 70 K ("He at 2 MPa") with those for $CaZrF_6$ cooled in low pressure nitrogen.

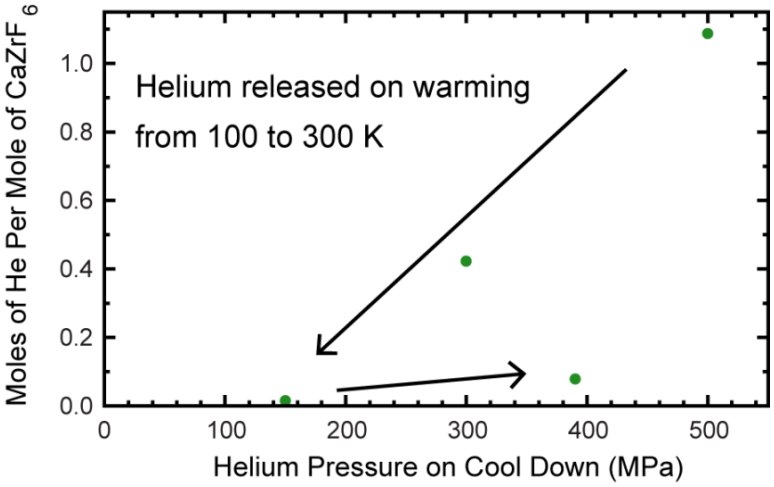

Figure E.6: Amount of helium trapped in $CaZrF_6$ by loading at high pressure and then cooling at pressure as a function of the loading pressure.

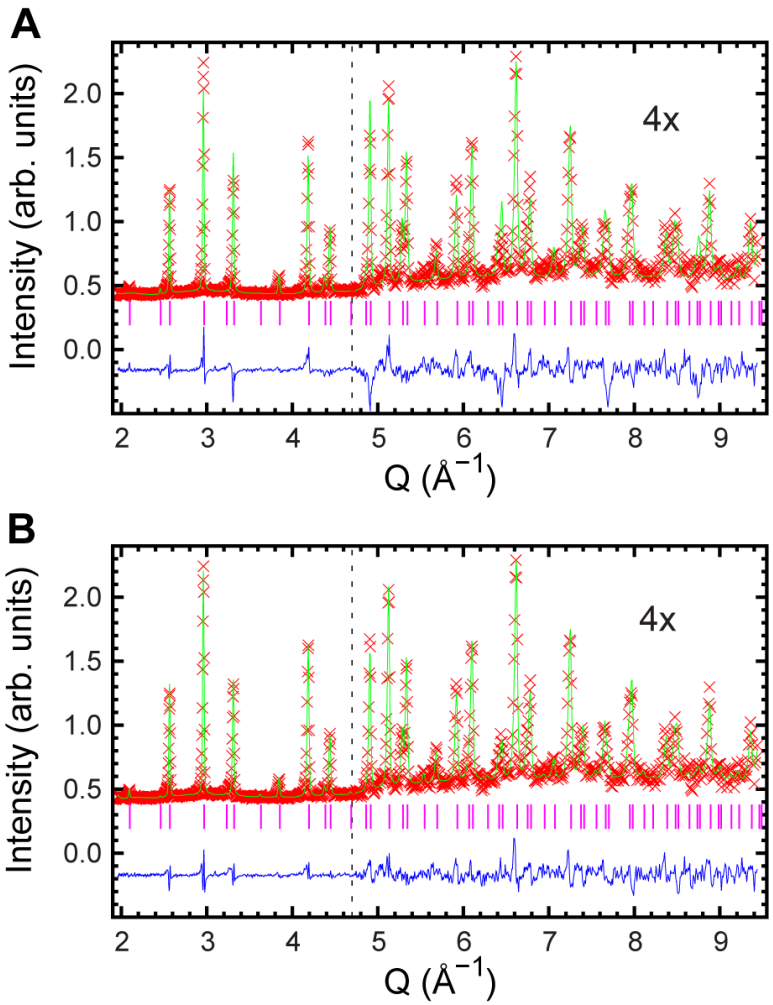

Figure E.7: Rietveld fits to 70 K 500 MPa powder neutron diffraction data recorded on SNAP using A) $Fm\bar{3}m$ model for $CaZrF_6$ containing no helium: A) detector bank 1 (2θ ~84.777°), R_{F^2}=12.39%, and refinements B) using $(He_{2-x}\square_x)(CaZr)F_6$ with x=1.08: detector bank 1 (2θ ~84.777°), R_{F^2}=7.26%.

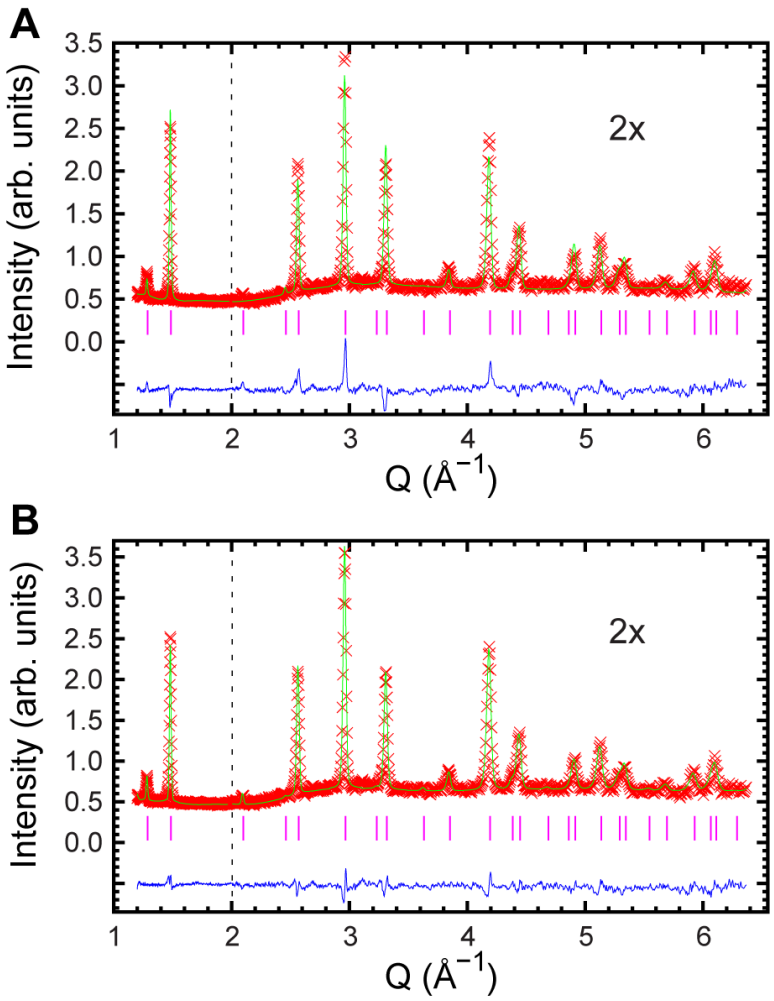

Figure E.8: Rietveld fits to 70 K 500 MPa powder neutron diffraction data recorded on SNAP using A) $Fm\bar{3}m$ model for $CaZrF_6$ containing no helium: A)) detector bank 2 (2θ ~48.097°), R_{F^2}=27.43%, and refinements B) using $(He_{2-x}\square_x)(CaZr)F_6$ with x=1.08: detector bank 2 (2θ ~48.097°), R_{F^2}=17.99%.

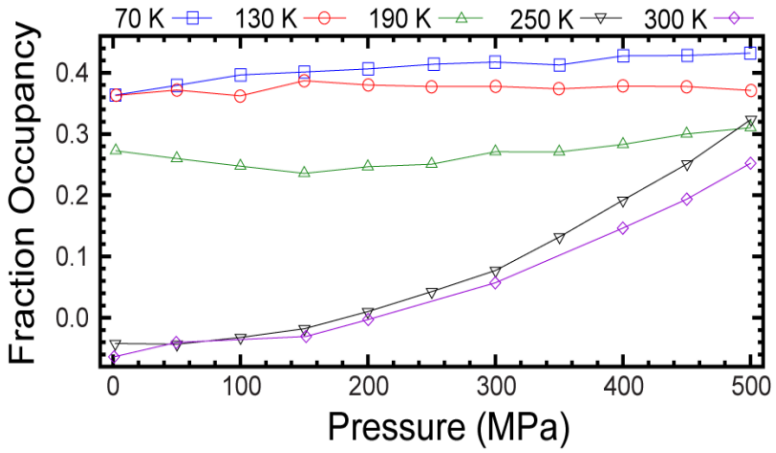

Figure E.9: Pressure dependence of the He refined fractional occupancy on the "A-site" of $(He_{2-x}\square_x)(CaZr)F_6$ from Rietveld analyses of data collected at 70, 130, 190, 250, and 300 K. The analyses were conducted using fixed isotropic atomic displacement parameters of 0.015, 0.019, 0.023, 0.027, and 0.03 Å^2 respectively.

E.2 Tables

Table E.1: Crystallographic parameters for $CaZrF_6$ at 70 K under 500 MPa of helium, derived from the Rietveld analysis of the neutron diffraction data acquired on SNAP with no helium in the model.

Chemical Formula	$CaZrF_6$
Space group	$Fm\bar{3}m$
a (Å)	8.4836(2)
Pressure (MPa)	500
Temperature (K)	70
Bank 1 R_{wp}	0.0424
Bank 1 R_F^2	0.1239
Bank 2 R_{wp}	0.0391
Bank 2 R_F^2	0.2743

	x	y	z	Occupancy	U_{iso}/U_{eq} (Å^2)	U_{11} (Å^2)	U_{22}/U_{33} (Å^2)
Ca	0	0	0	1.00	0.085(5)	-	-
Zr	$\frac{1}{2}$	$\frac{1}{2}$	$\frac{1}{2}$	1.00	0.001(1)	-	-
F	0.2600(4)	0	0	1.00	0.0072	0.012(2)	0.0049(9)

Table E.2: Crystallographic parameters for $CaZrF_6$ at 70 K under 500 MPa of helium, derived from the Rietveld analysis of the neutron diffraction data acquired on SNAP with helium in the model at a fixed occupancy, which was derived from gas uptake and release measurements.

Chemical Formula	$CaZrF_6$
Space group	$Fm\bar{3}m$
a (Å)	8.4835(1)
Pressure (MPa)	500
Temperature (K)	70
Bank 1 R_{wp}	0.0331
Bank 1 R_F^2	0.0726
Bank 2 R_{wp}	0.0310
Bank 2 R_F^2	0.1799

	x	**y**	**z**	**Occupancy**	**U_{iso}/U_{eq} (Å^2)**	**U_{11} (Å^2)**	**U_{22}/U_{33} (Å^2)**
Ca	0	0	0	1.00	0.005(2)	-	-
Zr	$\frac{1}{2}$	$\frac{1}{2}$	$\frac{1}{2}$	1.00	0.000(1)	-	-
F	0.2644(2)	0	0	1.00	0.0097	0.004(1)	0.0121(8)
He	$\frac{1}{4}$	$\frac{1}{4}$	$\frac{1}{4}$	0.54	0.045(3)	-	-

Table E.3: Crystallographic parameters for $CaZrF_6$ at 70 K and under 500 MPa of helium, derived from the Rietveld analysis of the neutron diffraction data acquired on SNAP with the helium isotropic displacement parameter and occupancy refined.

Chemical Formula	$CaZrF_6$
Space group	$Fm\bar{3}m$
a (Å)	8.4835 (1)
Pressure (MPa)	500
Temperature (K)	70
Bank 1 R_{wp}	0.0328
Bank 1 R_F^2	0.0568
Bank 2 R_{wp}	0.0303
Bank 2 R_F^2	0.1451

	x	**y**	**z**	**Occupancy**	**U_{iso}/U_{eq} (Å^2)**	**U_{11} (Å^2)**	**U_{22}/U_{33} (Å^2)**
Ca	0	0	0	1.00	0.005(2)	-	-
Zr	$\frac{1}{2}$	$\frac{1}{2}$	$\frac{1}{2}$	1.00	-0.001(1)	-	-
F	0.2645(2)	0	0	1.00	0.0099	0.004(1)	0.0124(8)
He	$\frac{1}{4}$	$\frac{1}{4}$	$\frac{1}{4}$	0.43(1)	0.015(3)	-	-

APPENDIX F. SUPPLEMENTARY MATERIAL FOR CHAPTER 7

F.1 Figures

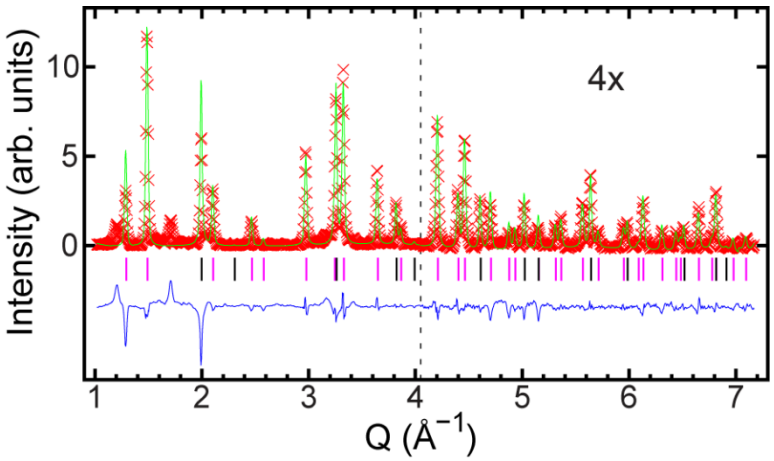

Figure F.1: Le Bail plot showing a fit of $CaZrF_6$ $Fm\bar{3}m$ model to the initial helium gas loading pressure of 0.28 GPa powder x-ray diffraction data obtained in a diamond anvil cell. The high Q section has been scaled to show detail but shifted downwards so that the backgrounds for the sections of the plot appear to be the same. The phase flags denote $CaZrF_6$ (magenta) and CaF_2 (black).

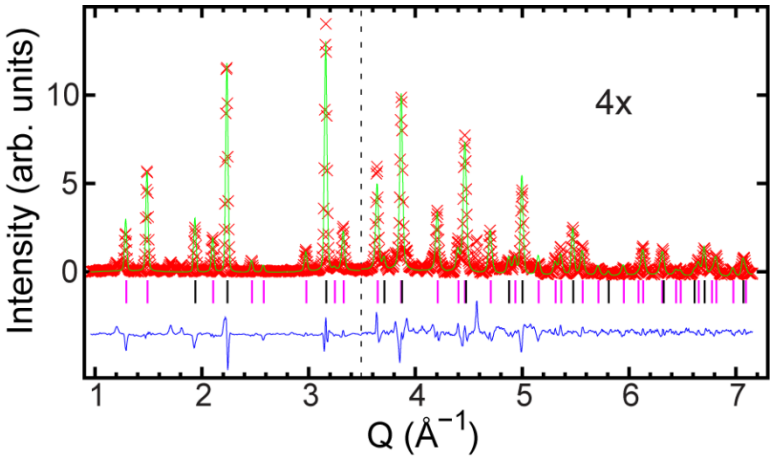

Figure F.2: Le Bail plot showing a fit of $CaZrF_6$ $Fm\bar{3}m$ model to the initial helium gas loading pressure of 0.21 GPa powder x-ray diffraction data obtained in a diamond anvil cell. The high Q section has been scaled to show detail but shifted downwards so that the backgrounds for the sections of the plot appear to be the same. The phase flags denote $CaZrF_6$ (magenta) and NaCl (black).

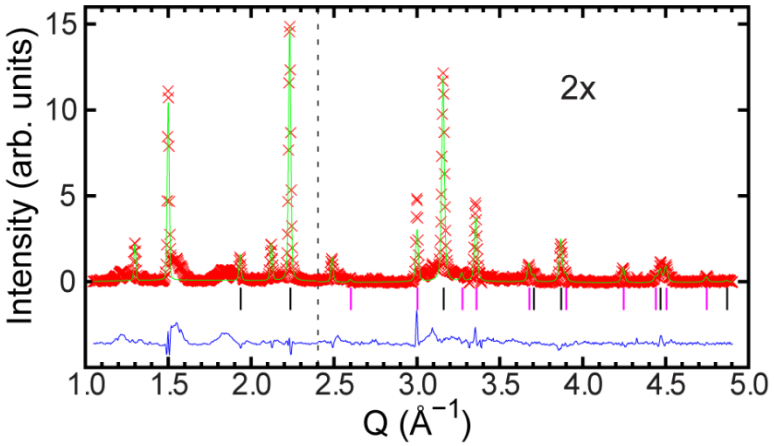

Figure F.3: Rietveld plot showing a fit of $CaNbF_6$ $Fm\bar{3}m$ model to the initial helium gas loading pressure of 0.16 GPa powder x-ray diffraction data obtained in a diamond anvil cell. The high Q section has been scaled to show detail but shifted downwards so that the backgrounds for the sections of the plot appear to be the same. The phase flags denote $CaNbF_6$ (magenta) and NaCl (black).

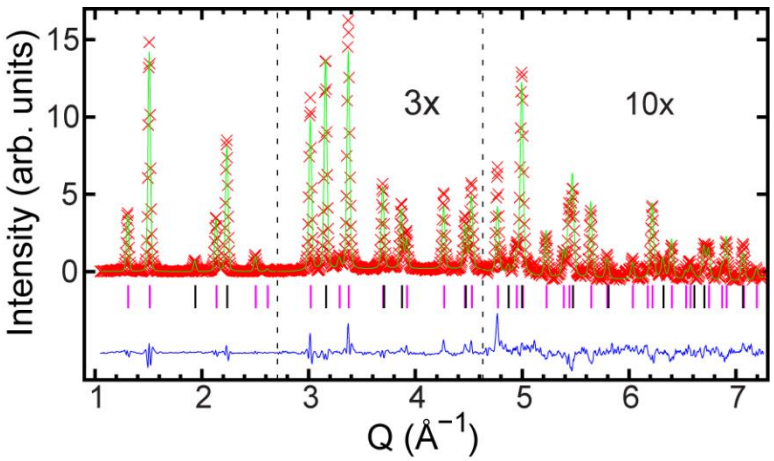

Figure F.4: Rietveld plot showing a fit of $CaNb^{IV}_{0.5}Nb^{V}_{0.5}F_{6.5}$ $Fm\bar{3}m$ model to the initial helium gas loading pressure of 0.18 GPa powder x-ray diffraction data of the first run obtained in a diamond anvil cell. The high Q section has been scaled to show detail but shifted downwards so that the backgrounds for the sections of the plot appear to be the same. The phase flags denote $CaNb^{IV}_{0.5}Nb^{V}_{0.5}F_{6.5}$ (magenta) and NaCl (black).

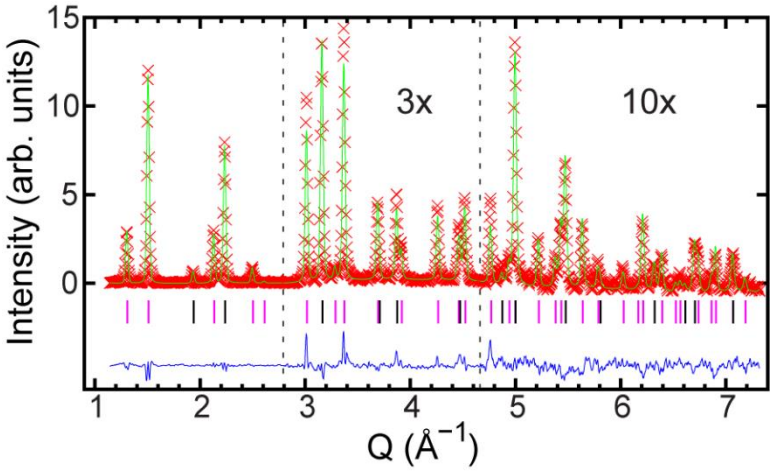

Figure F.5: Rietveld plot showing a fit of $CaNb^{IV}_{0.5}Nb^{V}_{0.5}F_{6.5}$ $Fm\bar{3}m$ model to the initial helium gas loading pressure of 0.19 GPa powder x-ray diffraction data of the second run obtained in a diamond anvil cell. The high Q section has been scaled to show detail but shifted downwards so that the backgrounds for the sections of the plot appear to be the same. The phase flags denote $CaNb^{IV}_{0.5}Nb^{V}_{0.5}F_{6.5}$ (magenta) and NaCl (black).

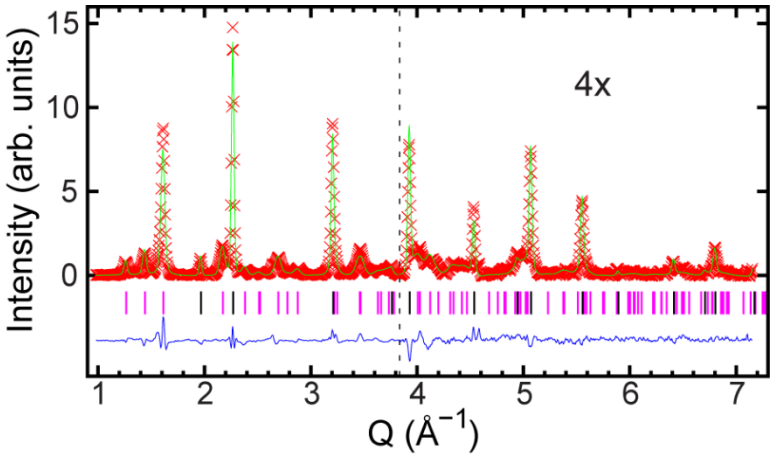

Figure F.6: Rietveld plot showing a fit of $CaNb^{IV}_{0.5}Nb^{V}_{0.5}F_{6.5}$ $R\bar{3}$ model to the neon gas loading pressure of 1.6 GPa powder x-ray diffraction data obtained in a diamond anvil cell. The high Q section has been scaled to show detail but shifted downwards so that the backgrounds for the sections of the plot appear to be the same. The phase flags denote $CaNb^{IV}_{0.5}Nb^{V}_{0.5}F_{6.5}$ (magenta) and NaCl (black).

F.2 Tables

Table F.1: Unit cell volumes for cubic $CaZrF_6$ and CaF_2 in a helium load diamond anvil cell as determined from Rietveld analyses of the high-pressure diffraction data. Pressures estimated from the unit cell volume of the CaF_2 using an equation of state are also given.

$CaZrF_6$ a (Å)	$CaZrF_6$ Volume (Å^3)	CaF_2 Volume (Å^3)	Pressure (GPa)
8.4527(5)	603.92(11)	162.57(4)	0.28(6)
8.4552(5)	604.47(11)	162.63(5)	0.20(3)
8.4516(5)	603.70(11)	162.56(4)	0.23(3)
8.4510(5)	603.57(12)	162.37(4)	0.33(3)
8.4521(5)	603.81(11)	162.20(4)	0.42(3)
8.4527(6)	603.94(12)	161.96(5)	0.54(4)
8.4543(6)	604.28(12)	161.78(5)	0.64(4)
8.4534(5)	604.09(10)	161.54(4)	0.76(4)
8.4500(6)	603.36(12)	161.18(4)	0.95(5)
8.4452(6)	602.33(12)	160.91(4)	1.10(5)
8.4392(5)	601.04(12)	160.59(4)	1.27(6)
8.4263(5)	598.28(10)	160.08(4)	1.55(7)
8.4182(5)	596.56(11)	159.80(4)	1.71(8)
8.4099(6)	594.80(13)	159.54(5)	1.86(8)

Table F.1 continued

$CaZrF_6$ a (Å)	$CaZrF_6$ Volume ($Å^3$)	CaF_2 Volume ($Å^3$)	Pressure (GPa)
8.4006(5)	592.84(11)	159.16(5)	2.07(9)
8.3922(6)	591.05(12)	158.90(5)	2.22(9)
8.3820(6)	588.90(12)	158.51(5)	2.45(10)
8.3652(6)	585.37(13)	158.12(4)	2.69(11)
8.3585(6)	583.97(13)	157.90(5)	2.82(11)
8.3376(6)	579.59(13)	157.37(5)	3.15(13)
8.3170(7)	575.31(14)	156.91(5)	3.43(14)

Table F.2: Unit cell volumes for cubic $CaZrF_6$ and NaCl in a helium load diamond anvil cell as determined from Le Bail analyses of the high-pressure diffraction data. Pressures estimated from the unit cell volume of the NaCl using an equation of state are also given.

$CaZrF_6$ a (Å)	$CaZrF_6$ Volume ($Å^3$)	NaCl Volume ($Å^3$)	Pressure (GPa)
8.4544(6)	604.3(14)	177.89(3)	0.21(6)
8.4538(6)	604.16(14)	177.76(3)	0.23(6)
8.4518(5)	603.77(11)	177.75(3)	0.23(6)
8.4528(5)	603.92(11)	177.58(3)	0.25(6)
8.4509(4)	603.54(9)	177.36(3)	0.29(6)
8.4518(5)	603.67(10)	177.04(5)	0.33(8)
8.4520(5)	603.77(10)	176.78(3)	0.37(7)
8.4517(5)	603.71(12)	176.51(4)	0.41(7)
8.4520(8)	603.78(16)	176.15(5)	0.46(8)
8.4532(5)	604.03(10)	175.84(3)	0.51(7)
8.4533(5)	604.06(10)	175.41(4)	0.57(7)
8.4549(4)	604.40(9)	174.94(3)	0.65(7)
8.4553(4)	604.48(10)	174.60(4)	0.70(7)
8.4541(5)	604.24(11)	174.11(4)	0.78(8)
8.4533(5)	604.05(11)	173.69(4)	0.84(8)
8.4515(5)	603.68(10)	172.90(4)	0.97(8)
8.4480(5)	602.93(11)	172.33(3)	1.07(7)
8.4446(5)	602.19(10)	171.71(3)	1.18(8)
8.4373(5)	600.64(10)	170.71(3)	1.35(8)
8.4293(5)	598.92(10)	169.79(3)	1.52(8)
8.4119(6)	595.22(13)	167.80(4)	1.90(9)
8.4074(5)	594.28(11)	167.51(3)	1.96(9)

Table F.2 continued

$CaZrF_6$ a (Å)	$CaZrF_6$ Volume ($Å^3$)	NaCl Volume ($Å^3$)	Pressure (GPa)
8.3995(4)	592.59(10)	166.73(3)	2.12(8)
8.3920(5)	591.00(10)	166.18(4)	2.23(9)
8.3861(4)	589.76(9)	165.68(4)	2.33(10)
8.3780(5)	588.05(11)	165.06(4)	2.47(10)
8.3640(5)	585.12(10)	163.91(3)	2.72(10)
8.3599(5)	584.26(10)	163.57(3)	2.80(10)
8.3509(5)	582.38(11)	162.96(3)	2.94(10)
8.3397(7)	580.03(14)	162.37(4)	3.08(12)
8.3225(6)	576.46(12)	161.36(3)	3.32(11)
8.3126(8)	574.40(16)	160.72(4)	3.48(11)
8.3028(11)	572.37(22)	160.08(4)	3.64(12)

Table F.3: Unit cell volumes for cubic $CaNbF_6$ and NaCl in first run with a helium load diamond anvil cell as determined from Rietveld analyses of the high-pressure diffraction data. Pressures estimated from the unit cell volume of the NaCl using an equation of state are also given.

$CaNbF_6$ a (Å)	$CaNbF_6$ Volume ($Å^3$)	NaCl Volume ($Å^3$)	Pressure (GPa)
8.3751(8)	587.44(17)	178.23(4)	0.16(8)
8.3720(8)	586.80(17)	177.86(4)	0.21(8)
8.3678(9)	585.92(19)	177.05(4)	0.33(8)
8.3689(11)	586.14(22)	175.09(5)	0.62(10)
8.3681(12)	585.99(24)	174.51(5)	0.71(10)
8.3696(12)	586.29(24)	173.95(5)	0.80(10)
8.3676(12)	585.87(25)	172.81(5)	0.99(11)
8.3623(12)	584.77(25)	171.58(5)	1.20(11)
8.3594(12)	584.15(26)	171.19(5)	1.27(11)
8.3595(12)	584.17(25)	170.78(5)	1.34(11)
8.3551(12)	583.25(26)	170.35(5)	1.42(11)
8.3512(12)	582.43(26)	169.79(5)	1.52(12)
8.3336(14)	578.76(28)	167.98(5)	1.86(13)
8.3306(14)	578.14(28)	167.53(5)	1.95(13)
8.3214(13)	576.22(28)	166.68(5)	2.13(13)
8.3091(14)	573.67(30)	165.60(5)	2.35(14)
8.2994(14)	571.67(28)	164.91(5)	2.50(13)

Table F.3 continued

$CaNbF_6$ a (Å)	$CaNbF_6$ Volume (Å^3)	NaCl Volume (Å^3)	Pressure (GPa)
8.2941(14)	570.57(29)	164.28(5)	2.64(14)
8.2801(13)	567.68(27)	163.19(5)	2.88(14)
8.2660(14)	564.79(29)	161.94(5)	3.18(15)
8.2483(15)	561.16(31)	160.89(5)	3.44(15)
8.2333(18)	558.10(36)	159.97(5)	3.67(16)

Table F.4: Unit cell volumes for cubic $CaNb^{IV}_{0.5}Nb^{V}_{0.5}F_{6.5}$ and NaCl in first run with a helium load diamond anvil cell as determined from Rietveld analyses of the high-pressure diffraction data. Pressures estimated from the unit cell volume of the NaCl using an equation of state are also given.

$CaNb^{IV}_{0.5}Nb^{V}_{0.5}F_{6.5}$ a (Å)	$CaNb^{IV}_{0.5}Nb^{V}_{0.5}F_{6.5}$ Volume (Å^3)	NaCl Volume (Å^3)	Pressure (GPa)
8.3340(3)	578.84(7)	178.09(3)	0.18(6)
8.3347(3)	578.98(7)	178.04(3)	0.19(6)
8.3351(3)	579.07(7)	177.91(3)	0.21(6)
8.3341(3)	578.85(7)	177.63(3)	0.25(6)
8.3330(4)	578.64(7)	177.14(3)	0.32(6)
8.3341(3)	578.86(7)	176.49(3)	0.41(6)
8.3374(3)	579.54(7)	175.68(3)	0.53(6)
8.3419(3)	580.50(7)	174.78(3)	0.67(6)
8.3451(4)	581.15(8)	173.39(3)	0.89(7)
8.3440(4)	580.93(7)	172.63(3)	1.02(7)
8.3390(3)	579.89(6)	171.50(2)	1.21(7)
8.3344(4)	578.93(8)	170.67(3)	1.36(7)
8.3304(4)	578.10(8)	170.08(3)	1.47(7)
8.3205(4)	576.04(7)	168.81(3)	1.70(7)
8.3134(4)	574.57(8)	168.07(3)	1.85(8)
8.3046(4)	572.73(7)	167.10(3)	2.04(8)
8.2931(4)	570.36(8)	166.06(3)	2.25(9)
8.2791(4)	567.48(8)	164.79(3)	2.53(9)
8.2631(4)	564.20(8)	163.51(3)	2.81(9)
8.2455(4)	560.59(8)	162.29(3)	3.10(9)
8.2263(4)	556.68(8)	161.14(3)	3.37(9)
8.2023(4)	551.83(8)	159.95(3)	3.67(10)
8.1755(4)	546.44(9)	158.97(3)	3.93(10)
8.1612(6)	543.57(11)	158.42(3)	4.08(10)
8.1415(9)	539.66(18)	157.63(3)	4.29(11)

Table F.5: Unit cell volumes for cubic $CaNb^{IV}_{0.5}Nb^{V}_{0.5}F_{6.5}$ and NaCl in second run with a helium load diamond anvil cell as determined from Rietveld analyses of the high-pressure diffraction data. Pressures estimated from the unit cell volume of the NaCl using an equation of state are also given.

$CaNb^{IV}_{0.5}Nb^{V}_{0.5}F_{6.5}$ a (Å)	$CaNb^{IV}_{0.5}Nb^{V}_{0.5}F_{6.5}$ Volume (Å^3)	NaCl Volume (Å^3)	Pressure (GPa)
8.3444(4)	581.02(8)	178.00(3)	0.19(6)
8.3447(4)	581.07(8)	178.09(3)	0.18(6)
8.3446(4)	581.05(9)	178.01(3)	0.19(6)
8.3438(4)	580.88(9)	177.77(3)	0.23(7)
8.3434(3)	580.80(7)	177.39(3)	0.28(6)
8.3457(4)	581.28(7)	177.02(3)	0.33(6)
8.3469(4)	581.54(8)	176.55(3)	0.40(6)
8.3460(4)	581.35(9)	175.65(3)	0.54(7)
8.3461(4)	581.36(8)	175.20(3)	0.61(7)
8.3505(4)	582.29(8)	174.95(3)	0.64(7)
8.3516(4)	582.52(9)	174.59(3)	0.70(7)
8.3528(4)	582.77(8)	174.13(3)	0.77(7)
8.3530(4)	582.81(7)	173.39(3)	0.89(7)
8.3509(4)	582.37(8)	172.49(3)	1.04(7)
8.3471(4)	581.57(8)	171.67(3)	1.18(7)
8.3407(4)	580.25(7)	170.68(3)	1.36(7)
8.3319(3)	578.41(7)	169.72(3)	1.53(7)
8.3256(4)	577.10(8)	168.93(3)	1.68(8)
8.3196(4)	575.85(9)	168.06(3)	1.85(8)
8.3084(4)	573.52(8)	167.07(3)	2.05(8)
8.2970(4)	571.16(8)	165.95(3)	2.28(9)
8.2821(4)	568.10(8)	164.64(3)	2.56(9)
8.2680(5)	565.19(10)	163.57(3)	2.80(14)
8.2401(6)	559.50(12)	161.61(4)	3.26(12)
8.2238(6)	556.18(12)	160.69(4)	3.48(12)
8.143(11)	539.95(22)	157.60(3)	4.30(11)
8.1215(14)	535.68(27)	156.61(3)	4.58(11)

Table F.6: Crystallographic parameters for cubic $CaNbF_6$ at room temperature and initial gas loading pressure derived from the Rietveld analysis of the high-pressure synchrotron diffraction data collected using a DAC (see Figure F.3). *GSAS-II outputs R_F^2 of each phase

Chemical Formula	$CaNbF_6$
Space group	$Fm\bar{3}m$
a (Å)	8.3751(8)
Pressure (GPa)	0.16
Temperature (K)	300
R_{wp}	0.4499
R_F^2 $CaNbF_6$*	0.3171
R_F^2 NaCl*	0.1434

	x	y	z	Occupancy	U_{iso} (Å^2)
Ca	0	0	0	1.00	0.06(1)
Nb	$\frac{1}{2}$	$\frac{1}{2}$	$\frac{1}{2}$	1.00	0.040(6)
F	0.256(3)	0	0	1.00	0.08(1)

Table F.7: Crystallographic parameters for cubic $CaNb^{IV}_{0.5}Nb^{V}_{0.5}F_{6.5}$ at room temperature and initial gas loading in helium pressure derived from the Rietveld analysis of the first run high-pressure synchrotron diffraction data collected using a DAC (see Figure F.4).

Chemical Formula	$CaNb^{IV}_{0.5}Nb^{V}_{0.5}F_{6.5}$
Space group	$Fm\bar{3}m$
a (Å)	8.3340(3)
Pressure (GPa)	0.18
Temperature (K)	300
R_{wp}	0.2041
R_F^2	0.1159

	x	y	z	Occupancy	U_{iso} (Å^2)
Ca	0	0	0	1.00	0.019(2)
Nb	$\frac{1}{2}$	$\frac{1}{2}$	$\frac{1}{2}$	1.00	0.0223(9)
F	0.2671(9)	0	0	1.00	0.051(3)

Table F.8: Crystallographic parameters for rhombohedral $CaNb^{IV}_{0.5}Nb^{V}_{0.5}F_{6.5}$ at room temperature and 1.6 GPa loading in neon pressure derived from the Rietveld analysis of the first run high-pressure synchrotron diffraction data collected using a DAC (Figure F.6).

Chemical Formula	$CaNb^{IV}_{0.5}Nb^{V}_{0.5}F_{6.5}$
Space group	$R\bar{3}$
a (Å)	5.286(1)
c (Å)	14.974(7)
Pressure (GPa)	1.6
Temperature (K)	300
R_{wp}	0.2267
R_F^2	0.1295

	x	y	z	Occupancy	U_{iso} (Å^2)
Ca	0	0	0	1.00	0.059(6)
Nb	0	0	$\frac{1}{2}$	1.00	0.045(4)
F	0.041(2)	0.343(2)	0.0871(7)	1.00	0.042(3)

APPENDIX G. COPYRIGHT AGREEMENT LETTERS

Permission for Figure 1.9 in Chapter 1

AIP PUBLISHING LICENSE
TERMS AND CONDITIONS

Nov 01, 2018

This Agreement between Georgia Institute of Technology -- Brett Hester ("You") and AIP Publishing ("AIP Publishing") consists of your license details and the terms and conditions provided by AIP Publishing and Copyright Clearance Center.

License Number	4460360543453
License date	Nov 01, 2018
Licensed Content Publisher	AIP Publishing
Licensed Content Publication	Applied Physics Letters
Licensed Content Title	Negative thermal expansion of ReO3 in the extended temperature range
Licensed Content Author	Tapan Chatterji, Thomas C. Hansen, Michela Brunelli, et al
Licensed Content Date	Jun 15, 2009
Licensed Content Volume	94
Licensed Content Issue	24
Type of Use	Thesis/Dissertation
Requestor type	Student
Format	Print and electronic
Portion	Figure/Table
Number of figures/tables	1

Permission for Figure 1.10 in Chapter 1

Title:	Pronounced Negative Thermal Expansion from a Simple Structure: Cubic ScF3
Author:	Benjamin K. Greve, Kenneth L. Martin, Peter L. Lee, et al
Publication:	Journal of the American Chemical Society
Publisher:	American Chemical Society
Date:	Nov 1, 2010

PERMISSION/LICENSE IS GRANTED FOR YOUR ORDER AT NO CHARGE

This type of permission/license, instead of the standard Terms & Conditions, is sent to you because no fee is being charged for your order. Please note the following:

- Permission is granted for your request in both print and electronic formats, and translations.
- If figures and/or tables were requested, they may be adapted or used in part.
- Please print this page for your records and send a copy of it to your publisher/graduate school.
- Appropriate credit for the requested material should be given as follows: "Reprinted (adapted) with permission from (COMPLETE REFERENCE CITATION). Copyright (YEAR) American Chemical Society." Insert appropriate information in place of the capitalized words.
- One-time permission is granted only for the use specified in your request. No additional uses are granted (such as derivative works or other editions). For any other uses, please submit a new request.

If credit is given to another source for the material you requested, permission must be obtained from that source.

Permission for Figure 1.12 in Chapter 1

Title:	Large Negative Thermal Expansion and Anomalous Behavior on Compression in Cubic ReO3-Type AIIBIVF6: CaZrF6 and CaHfF6
Author:	Justin C. Hancock, Karena W. Chapman, Gregory J. Halder, et al
Publication:	Chemistry of Materials
Publisher:	American Chemical Society
Date:	Jun 1, 2015

PERMISSION/LICENSE IS GRANTED FOR YOUR ORDER AT NO CHARGE

This type of permission/license, instead of the standard Terms & Conditions, is sent to you because no fee is being charged for your order. Please note the following:

- Permission is granted for your request in both print and electronic formats, and translations.
- If figures and/or tables were requested, they may be adapted or used in part.
- Please print this page for your records and send a copy of it to your publisher/graduate school.
- Appropriate credit for the requested material should be given as follows: "Reprinted (adapted) with permission from (COMPLETE REFERENCE CITATION). Copyright (YEAR) American Chemical Society." Insert appropriate information in place of the capitalized words.
- One-time permission is granted only for the use specified in your request. No additional uses are granted (such as derivative works or other editions). For any other uses, please submit a new request.

If credit is given to another source for the material you requested, permission must be obtained from that source.

Permission for Figure 8.1 in Chapter 8

Materials Horizons

Order detail ID:	71744150
Order License Id:	4499391003052
ISSN:	2051-6355
Publication Type:	e-Journal
Volume:	
Issue:	
Start page:	
Publisher:	Royal Society of Chemistry
Author/Editor:	Royal Society of Chemistry (Great Britain)

Permission Status: **Granted**

Permission type: Republish or display content
Type of use: Thesis/Dissertation

⊞ View details

REFERENCES

(1) Sleight, A. W. Negative thermal expansion materials. *Curr. Opin. Solid State Mater. Sci.* **1998**, *3*, 128-131.

(2) Chu, C. N.; Saka, N.; Suh, N. P. Negative Thermal Expansion Ceramics: A Review. *Mater. Sci. Eng.* **1987**, *95*, 303-308.

(3) Takenaka, K. Negative thermal expansion materials: technological key for control of thermal expansion. *Sci. Technol. Adv. Mater.* **2012**, *13*.

(4) Grüneisen, E. Zustand des festen Korpers. *Handb. Phys.* **1926**, *10*, 1-59.

(5) Evans, J. S. O. Negative Thermal Expansion Materials. *J. Chem. Soc. Dalton Trans.* **1999**, 3317-3326.

(6) Kasap, S. O.: *Principles of Electronic Materials and Devices*; 3 ed., 2006.

(7) R. J. Borg, G. J. D.: *The Physical Chemistry of Solids*, 1992.

(8) Ziman, J. M.: *Principles of the Theory of Solids*; 2 ed., 1972.

(9) White, G. K. Solids: thermal expansion and contraction. *Contemporary Physics* **1993**, *34*, 193-204.

(10) Bekkedahl, N. Volume Dilatometry. *J. Res. Natl. Bur. Stand.* **1949**, *42*, 145.

(11) White, G. K. Measurement of thermal expansion at low temperatures. *Cryogenics* **1961**, *1*, 135.

(12) Bijl, D.; Pullan, H. A new method for measuring the thermal expansion of solids at low temperatures; the thermal expansion of copper and aluminium and the Grüneisen rule. *Physica* **1954**, *21*, 285-298.

(13) Thompson, A. M. The Precise Measurement of Small Capacitances. *IRE Transactions on Instrumentation* **1958**, *I-7*, 245-253.

(14) James, J. D.; Spittle, J. A.; Brown, S. G. R.; Evans, R. W. A review of measurement techniques for the thermal expansion coefficient of metals and alloys at elevated temperatures. *Meas. Sci. Technol.* **2001**, *12*, R1.

(15) Valentich, J. A vitreous silica tube dilatometer for the measurement of thermal expansion of solids from-195 to 1000° C. *J. Mater. Sci.* **1979**, *14*, 371-378.

(16) Rothrock, B. D., Kirby R. K. . *J. Res. Natl. Bur. Stand. C* **1967**, *71*, 85-91.

(17) Young, R. A.: *The Rietveld Method*; Oxford University Press and International Union of Crystallography, 1995.

(18) Roy, R.; Agrawal, D. K.; McKinstry, H. A. Very Low Thermal Expansion Coefficient Materials. *Annu. Rev. Mater. Sci.* **1989**, *19*, 59-81.

(19) White, M. A.: *Physical Properties of Materials*; 2 ed.; CRC Press, 2012. pp. 172-181.

(20) Attfield, M. P.; Sleight, A. W. Exceptional Negative Thermal Expansion in $AlPO_4$-17. *Chem. Mater.* **1998**, *10*, 2013-2019.

(21) Chapman, K. W.; Chupas, P. J.; Kepert, C. J. Direct observation of a transverse vibrational mechanism for negative thermal expansion in $Zn(CN)_2$: An atomic pair distribution function analysis. *J. Am. Chem. Soc.* **2005**, *127*, 15630-15636.

(22) Wu, Y.; Peterson, V. K.; Luks, E.; Darwish, T. A.; Kepert, C. J. Interpenetration as a Mechanism for Negative Thermal Expansion in the Metal–Organic Framework $Cu_3(btb)_2$ (MOF-14). *Angew. Chem.* **2014**.

(23) Korthuis, V.; Khosrovani, N.; Sleight, A. W.; Roberts, N.; Dupree, R.; Warren, W. W. Negative Thermal Expansion and Phase Transitions in the $ZrV_{2-x}P_xO_7$ Series. *Chem. Mater.* **1995**, *7*, 412-417.

(24) Evans, J. S. O.; Mary, T. A.; Vogt, T.; Subramanian, M. A.; Sleight, A. W. Negative Thermal Expansion in ZrW_2O_8 and HfW_2O_8. *Chem. Mater.* **1996**, *8*, 2809-2823.

(25) Greve, B. K.; Martin, K. L.; Lee, P. L.; Chupas, P. J.; Chapman, K. W.; Wilkinson, A. P. Pronounced Negative Thermal Expansion from a Simple Structure: Cubic ScF_3. *J. Am. Chem. Soc.* **2010**, *132*, 15496-15498.

(26) Hancock, J. C.; Chapman, K. W.; Halder, G. J.; Morelock, C. R.; Kaplan, B. S.; Gallington, L. C.; Bongiorno, A.; Han, C.; Zhou, S.; Wilkinson, A. P. Large negative thermal expansion and anomalous behavior on compression in cubic ReO_3-type $A^{II}B^{IV}F_6$: $CaZrF_6$ and $CaHfF_6$. *Chem. Mater.* **2015**.

(27) Barrera, G. D.; Bruno, J. A. O.; Barron, T. H. K.; Allan, N. L. Negative Thermal Expansion. *J. Phys. Condens. Matter* **2005**, *17*, R217-R252.

(28) Evans, J. S. O.; Mary, T. A.; Sleight, A. W. Negative thermal expansion materials. *Physica B* **1998**, *241-243*, 311-316.

(29) Jakubinek, M. B.; Whitman, C. A.; White, M. A. Negative thermal expansion materials. *J. Therm. Anal. Calorim.* **2010**, *99*, 165-172.

(30) Lind, C. Two Decades of Negative Thermal Expansion Research: Where Do We Stand? *Materials* **2012**, *5*, 1125-1154.

(31) Miller, W.; Smith, C. W.; Mackenzie, D. S.; Evans, K. E. Negative thermal expansion: a review. *J. Mater. Sci.* **2009**, *44*, 5441-5451.

(32) Romao, C. P.; Miller, K. J.; Whitman, C. A.; White, M. A.; Marinkovic, B. A.: Negative Thermal Expansion (Thermomiotic) Materials. In *Comprehensive Inorganic Chemistry II*; Reedijk, J., Poeppelmeier, K. R., Eds.; Elsevier: Oxford, 2013; Vol. 4; pp 128-151.

(33) Sleight, A. W.; Thundathil, M. A.; Evans, J. S. O. Materials with Low or Negative Thermal Expansion. United States Patent US 5,919,720.

(34) Attfield, J. P. Mechanisms and Materials for NTE. *Front. Chem.* **2018**, *6*.

(35) Balch, D. K.; Dunand, D. C. Copper-Zirconium Tungstate Composites Exhibiting Low and Negative Thermal Expansion Influenced by Reinforcement Phase Transformations. *Metall. Mater. Trans. A* **2004**, *35A*, 1159-1165.

(36) Holzer, H.; Dunand, D. C. Phase transformation and thermal expansion of Cu/ZrW_2O_8 metal matrix composites. *J. Mater. Res.* **1999**, *14*, 780-789.

(37) Lind, C.; Coleman, M. R.; Kozy, L. C.; Sharma, G. R. Zirconium tungstate/polymer nanocomposites: Challenges and opportunities. *Phys. Status Solidi B* **2011**, *248*, 123-129.

(38) Romao, C. P.; Marinkovic, B. A.; Werner-Zwanziger, U.; White, M. A. Thermal Expansion Reduction in Alumina-Toughened Zirconia by Incorporation of Zirconium Tungstate and Aluminum Tungstate. *J. Am. Ceram. Soc.* **2015**, *98*, 2858-2865.

(39) Romao, C. P.; White, M. A. Negative stiffness in ZrW_2O_8 inclusions as a result of thermal stress. *Appl. Phys. Lett.* **2016**, *109*, 031902.

(40) Badrinarayanan, P.; Kessler, M. R. Zirconium tungstate/cyanate ester nanocomposites with tailored thermal expansivity. *Compos. Sci. Technol.* **2011**, *71*, 1385-1391.

(41) Chandra, A.; Meyer, W. H.; Best, A.; Hanewald, A.; Wegner, G. Modifying thermal expansion of polymer composites by blending with a negative thermal expansion material. *Macromolecular Materials and Engineering* **2007**, *292*, 295-301.

(42) Sigmund, O.; Torquato, S. Composites with extremal thermal expansion coefficients. *Appl. Phys. Lett.* **1996**, *69*, 3203-3205.

(43) Jin, S.; Mavoori, H. Low-thermal-expansion copper composites via negative CTE metallic elements. *JOM* **1998**, *50*, 70-72.

(44) Della Gaspera, E.; Tucker, R.; Star, K.; Lan, E. H.; Ju, Y. S.; Dunn, B. Copper-Based Conductive Composites with Tailored Thermal Expansion. *ACS Appl. Mater. Interfaces* **2013**, *5*, 10966-10974.

(45) Azuma, M.; Chen, W. T.; Seki, H.; Czapski, M.; Olga, S.; Oka, K.; Mizumaki, M.; Watanuki, T.; Ishimatsu, N.; Kawamura, N.; Ishiwata, S.; Tucker, M. G.; Shimakawa, Y.; Attfield, J. P. Colossal negative thermal expansion in $BiNiO_3$ induced by intermetallic charge transfer. *Nat. Commun.* **2011**, *2*, 347.

(46) Takenaka, K. Progress of Research in Negative Thermal Expansion Materials: Paradigm Shift in the Control of Thermal Expansion. *Front. Chem.* **2018**, *6*.

(47) Schlosser, W. F.; Graham, G. M.; Meincke, P. P. M. The Temperature and Magnetic Field Dependance of the Forced Magnetostriction and Thermal Expansion of INVAR. *J. Phys. Chem. Solids* **1971**, *32*, 927-938.

(48) Guo, X. G.; Lin, J. C.; Tong, P.; Wang, M.; Wu, Y.; Yang, C.; Song, B.; Lin, S.; Song, W. H.; Sun, Y. P. Magnetically driven negative thermal expansion in antiperovskite $Ga_{1-x}Mn_xN_{0.8}Mn_3$ ($0.1 \leq x \leq 0.3$). *Appl. Phys. Lett.* **2015**, *107*, 202406.

(49) Guo, X. G.; Tong, P.; Lin, J. C.; Yang, C.; Zhang, K.; Wang, M.; Wu, Y.; Lin, S.; Song, W. H.; Sun, Y. P. Large negative thermal expansion in $(Ga_{0.7}Cu_{0.3})_{1-x}Mn_xNMn_3$ ($x \leq 0.4$), compensating for the thermal expansion of cryogenic materials. *Scripta Mater.* **2017**, *128*, 74-77.

(50) Takenaka, K.; Takagi, H. Giant negative thermal expansion in Ge-doped anti-perovskite manganese nitrides. *Appl. Phys. Lett.* **2005**, *87*, 261902:(261903).

(51) Takenaka, K.; Takagi, H. Magnetovolume effect and negative thermal expansion in $Mn_3(Cu_{1-x}Ge_x)N$. *Mater. Trans.* **2006**, *47*, 471-474.

(52) Nakamura, H.; Wada, H.; Yoshimura, K.; Shiga, M.; Nakamura, Y.; Sakurai, J.; Komura, Y. Effect of chemical pressure on the magnetism of YMn_2 : magnetic properties of $Y_{1-x}Sc_xMn_2$and $Y_{1-x}La_xMn_2$. *J. Phys. F: Met. Phys.* **1988**, *18*, 981.

(53) Zhao, Y.-Y.; Hu, F.-X.; Bao, L.-F.; Wang, J.; Wu, H.; Huang, Q.-Z.; Wu, R.-R.; Liu, Y.; Shen, F.-R.; Kuang, H.; Zhang, M.; Zuo, W.-L.; Zheng, X.-Q.; Sun, J.-R.; Shen, B.-G. Giant Negative Thermal Expansion in Bonded MnCoGe-Based Compounds with Ni_2In-Type Hexagonal Structure. *J. Am. Chem. Soc.* **2015**, *137*, 1746-1749.

(54) Huang, R.; Liu, Y.; Fan, W.; Tan, J.; Xiao, F.; Qian, L.; Li, L. Giant negative thermal expansion in NaZn13-type La (Fe, Si, Co) 13 compounds. *J. Am. Chem. Soc.* **2013**.

(55) Chen, J.; Xing, X. R.; Liu, G. R.; Li, J. H.; Liu, Y. T. Structure and negative thermal expansion in the $PbTiO_3$–$BiFeO_3$ system. *Appl. Phys. Lett.* **2006**, *89*, 101914.

(56) Pan, Z.; Chen, J.; Jiang, X.; Hu, L.; Yu, R.; Yamamoto, H.; Ogata, T.; Hattori, Y.; Guo, F.; Fan, X. a.; Li, Y.; Li, G.; Gu, H.; Ren, Y.; Lin, Z.; Azuma, M.; Xing, X. Colossal Volume Contraction in Strong Polar Perovskites of $Pb(Ti,V)O_3$. *J. Am. Chem. Soc.* **2017**, *139*, 14865-14868.

(57) Alekseev, P. A.; Mignot, J. M.; Nefeodova, E. V.; Nemkovski, K. S.; Lazukov, V. N.; Tiden, N. N.; Menushenkov, A. P.; Chernikov, R. V.; Klementiev, K. V.; Ochiai, A.; Golubkov, A. V.; Bewley, R. I.; Rybina, A. V.; Sadikov, I. P. Magnetic spectral response and lattice properties in mixed-valence $Sm_{1-x}Y_xS$ solid solutions studied with x-ray diffraction, x-ray absorption spectroscopy, and inelastic neutron scattering. *Phys. Rev. B* **2006**, *74*, 035114.

(58) Salvador, J. R.; Guo, F.; Hogan, T.; Kanatzidis, M. G. Zero thermal expansion in YbGaGe due to an electronic valence transition. *Nature* **2003**, *425*, 702-705.

(59) Sleight, A. Zero-expansion plan. *Nature* **2003**, *425*, 674.

(60) Long, Y. W.; Hayashi, N.; Saito, T.; Azuma, M.; Muranaka, S.; Shimakawa, Y. Temperature-induced A-B intersite charge transfer in an A-site-ordered $LaCu_3Fe_4O_{12}$ perovskite. *Nature* **2009**, *458*, 60-U63.

(61) Yamada, I.; Tsuchida, K.; Ohgushi, K.; Hayashi, N.; Kim, J.; Tsuji, N.; Takahashi, R.; Matsushita, M.; Nishiyama, N.; Inoue, T.; Irifune, T.; Kato, K.; Takata, M.; Takano, M. Giant Negative Thermal Expansion in the Iron Perovskite $SrCu_3Fe_4O_{12}$. *Angew. Chem. Int. Ed.* **2011**, *50*, 6579-6582.

(62) Azuma, M.; Oka, K.; Nabetani, K. Negative thermal expansion induced by intermetallic charge transfer. *Sci. Technol. Adv. Mater.* **2015**, *16*, 034904.

(63) Dove, M. T.; Heine, V.; Hammonds, K. D. Rigid unit modes in framework silicates. *Miner. Mag.* **1995**, *59*, 629-639.

(64) Pryde, A. K. A.; Hammonds, K. D.; Dove, M. T.; Heine, V.; Gale, J. D.; Warren, M. C. Rigid Unit Modes and the Negative Thermal Expansion in ZrW_2O_8. *Phase Transitions* **1997**, *61*, 141-153.

(65) Tao, J. Z.; Sleight, A. W. The role of rigid unit modes in negative thermal expansion. *J. Solid State Chem.* **2003**, *173*, 442-448.

(66) Hummel, F. A. Thermal Expansion Properties of Some Synthetic Lithia Minerals. *J. Am. Ceram. Soc.* **1951**, *34*, 235-239.

(67) Milberg, M. E.; Blair, H. D. Thermal Expansion of Cordierite. *J. Am. Ceram. Soc.* **1977**, *60*, 372-373.

(68) Tschaufeser, P.; Parker, S. C. Thermal Expansion Behavior of Zeolites and $AlPO_4$s. *J. Phys. Chem.* **1995**, *99*, 10609-10615.

(69) Hammonds, K. D.; Dove, M. T.; Giddy, A. P.; Heine, V.; Winkler, B. Rigid-unit phonon modes and structural phase transitions in framework silicates. *Am. Mineral.* **1996**, *81*, 1057-1079.

(70) Attfield, M. P.; Sleight, A. W. Strong negative thermal expansion in siliceous faujasite. *Chem. Commun.* **1998**, 601-602.

(71) Lightfoot, P.; Woodcock, D. A.; Maple, M. J.; Villaescusa, L. A.; Wright, P. A. The widespread occurrence of negative thermal expansion in zeolites. *J. Mater. Chem.* **2001**, *11*, 212-216.

(72) Woodcock, D. A.; Lightfoot, P.; Villaescusa, L. A.; Díaz-Cabañas, M.-J.; Camblor, M. A.; Engberg, D. Negative Thermal Expansion in the Siliceous Zeolites Chabazite and ITQ-4: A Neutron Powder Diffraction Study. *Chem. Mater.* **1999**, *11*, 2508-2514.

(73) Carey, T.; Tang, C. C.; Hriljac, J. A.; Anderson, P. A. Chemical Control of Thermal Expansion in Cation-Exchanged Zeolite A. *Chem. Mater.* **2014**, *26*, 1561-1566.

(74) Hibble, S. J.; Chippindale, A. M.; Marelli, E.; Kroeker, S.; Michaelis, V. K.; Greer, B. J.; Aguiar, P. M.; Bilbe, E. J.; Barney, E. R.; Hannon, A. C. Local and average structure in zinc cyanide: towards an understanding of the atomistic origin of negative thermal expansion. *J. Am. Chem. Soc.* **2013**.

(75) Williams, D. J.; Partin, D. E.; Lincoln, F. J.; Kouvetakis, J.; O'Keefe, M. The Disordered Crystal Structures of $Zn(CN)_2$ and $Ga(CN)_3$. *J. Solid State Chem.* **1997**, *134*, 164-169.

(76) Fang, H.; Dove, M. T.; Rimmer, L. H.; Misquitta, A. J. Simulation study of pressure and temperature dependence of the negative thermal expansion in $Zn(CN)_2$. *Phys. Rev. B* **2013**, *88*, 104306.

(77) Phillips, A. E.; Goodwin, A. L.; Halder, G. J.; Southon, P. D.; Kepert, C. J. Nanoporosity and exceptional negative thermal expansion in single-network cadmium cyanide. *Angew. Chem. Int. Ed.* **2008**, *47*, 1396-1399.

(78) Margadonna, S.; Prassides, K.; Fitch, A. N. Zero Thermal Expansion in a Prussian Blue Analogue. *J. Am. Chem. Soc.* **2004**, *126*, 15390-15391.

(79) Goodwin, A. L.; Calleja, M.; Conterio, M. J.; Dove, M. T.; Evans, J. S. O.; Keen, D. A.; Peters, L.; Tucker, M. G. Colossal Positive and Negative Thermal Expansion in the Framework Material $Ag_3[Co(CN)_6]$. *Science* **2008**, *319*, 794-797.

(80) Chapman, K. W.; Chupas, P. J.; Kepert, C. J. Compositional dependence of negative thermal expansion in the Prussian blue analogues $(MPt^{IV})Pt^{II}(CN)_6$ (M = Mn, Fe, Co, Ni, Cu, Zn, Cd). *J. Am. Chem. Soc.* **2006**, *128*, 7009-7014.

(81) Goodwin, A. L.; Chapman, K. W.; Kepert, C. J. Guest-dependent negative thermal expansion in nanoporous Prussian Blue analogues $(MPt^{IV})Pt^{II}(CN)_6.x\{H_2O\}$ (0 <= x <= 2; M = Zn, Cd). *J. Am. Chem. Soc.* **2005**, *127*, 17980-17981.

(82) Adak, S.; Daemen, L. L.; Hartl, M.; Williams, D.; Summerhill, J.; Nakotte, H. Thermal expansion in 3d-metal Prussian Blue Analogs—A survey study. *J. Solid State Chem.* **2011**, *184*, 2854-2861.

(83) Pretsch, T.; Chapman, K. W.; Halder, G. J.; Kepert, C. J. Dehydration of the nanoporous coordination framework $Er^{iii}[Co^{iii}(CN)_6]\cdot 4(H_2O)$: single crystal to single crystal transformation and negative thermal expansion in $Er^{iii}[Co^{iii}(CN)_6]$. *Chem. Commun.* **2006**, 1857-1859.

(84) Duyker, S. G.; Peterson, V. K.; Kearley, G. J.; Ramirez-Cuesta, A. J.; Kepert, C. J. Negative Thermal Expansion in $LnCo(CN)_6$ (Ln=La, Pr, Sm, Ho, Lu, Y): Mechanisms and Compositional Trends. *Angew. Chem. Int. Ed.* **2013**, n/a-n/a.

(85) Rowsell, J. L. C.; Spencer, E. C.; Eckert, J.; Howard, J. A. K.; Yaghi, O. M. Gas Adsorption Sites in a Large-Pore Metal-Organic Framework. *Science* **2005**, *309*, 1350-1354.

(86) Dubbeldam, D.; Walton, K. S.; Ellis, D. E.; Snurr, R. Q. Exceptional negative thermal expansion in isoreticular metal-organic frameworks. *Angew. Chem. Int. Ed.* **2007**, *46*, 4496-4499.

(87) Han, S. S.; Goddard, W. A. Metal-organic frameworks provide large negative thermal expansion Behavior. *J. Phys. Chem. C* **2007**, *111*, 15185-15191.

(88) Wu, Y.; Kobayashi, A.; Halder, Gregory J.; Peterson, Vanessa K.; Chapman, Karena W.; Lock, N.; Southon, Peter D.; Kepert, Cameron J. Negative Thermal Expansion in the Metal-Organic Framework Material Cu_3(1,3,5-benzenetricarboxylate)$_2$. *Angew. Chem. Int. Ed.* **2008**, *47*, 8929-8932.

(89) Zhou, W.; Wu, H.; Yildirim, T.; Simpson, J. R.; Walker, A. R. H. Origin of the exceptional negative thermal expansion in metal-organic framework-5 Zn_4O(1,4-benzenedicarboxylate)$_3$. *Phys. Rev. B* **2008**, *78*, 054114.

(90) Martinek, C.; Hummel, F. A. Linear Thermal Expansion of Three Tungstates. *J. Am. Ceram. Soc.* **1968**, *51*, 227-228.

(91) Graham, J.; Wadsley, A. D.; Weymouth, J. H.; Williams, L. S. A New Ternary Oxide, ZrW_2O_8. *J. Am. Ceram. Soc.* **1959**, *42*, 570-570.

(92) Sleight, A. W. Thermal Contraction. *Endeavour* **1995**, *19*, 64-68.

(93) Pryde, A. K. A.; Hammonds, K. D.; Dove, M. T.; Heine, V.; Gale, J. D.; Warren, M. C. Origin of the Negative Thermal Expansion in ZrW_2O_8 and ZrV_2O_7. *J. Phys.: Condens. Matter* **1996**, *8*, 10973-10982.

(94) Ernst, G.; Broholm, C.; Kowach, G. R.; Ramirez, A. P. Phonon Density of States and Negative Thermal Expansion in ZrW_2O_8. *Nature* **1998**, *396*, 147-149.

(95) Mittal, R.; Chaplot, S. L.; Schober, H.; Mary, T. A. Origin of Negative Thermal Expansion in Cubic ZrW_2O_8 Revealed by High Pressure Inelastic Neutron Scattering. *Phys. Rev. Lett.* **2001**, *86*, 4692-4695.

(96) Yamamura, Y.; Nakajima, N.; Tsuji, T. Calorimetric and x-ray diffraction studies of α-to-β structural phase transitions in HfW_2O_8 and ZrW_2O_8. *Phys. Rev. B* **2001**, *64*, 184109.

(97) Lind, C.; Wilkinson, A. P.; Rawn, C. J.; Payzant, E. A. Preparation of the negative thermal expansion material cubic $ZrMo_2O_8$. *J. Mater. Chem.* **2001**, *11*, 3354-3359.

(98) Allen, S.; Evans, J. S. O. Negative thermal expansion and oxygen disorder in cubic $ZrMo_2O_8$. *Phys. Rev. B* **2003**, *68*, -.

(99) Evans, J. S. O.; Hanson, J. C.; Sleight, A. W. Room-Temperature Superstructure of ZrV_2O_7. *Acta Cryst.* **1998**, *B54*, 705-713.

(100) Khosrovani, N.; Sleight, A. W.; Vogt, T. Structure of ZrV_2O_7 from -263 to 470 ^oC. *J. Solid State Chem.* **1997**, *132*, 355-360.

(101) Withers, R. L.; Evans, J. S. O.; Hanson, J.; Sleight, A. W. An *In Situ* Temperature-Dependent Electron and X-ray Diffraction Study of Structural Phase transitions in ZrV_2O_7. *J. Solid State Chem.* **1998**, *137*, 161-167.

(102) Gover, R. K. B.; Withers, N. D.; Allen, S.; Withers, R. L.; Evans, J. S. O. Structure and Phase Transitions in SnP_2O_7. *J. Solid State Chem.* **2002**, *166*, 42-48.

(103) Stinton, G. W.; Hampson, M. R.; Evans, J. S. O. The 136-Atom Structure of ZrP_2O_7 and HfP_2O_7 from Powder Diffraction Data. *Inorg. Chem.* **2006**, *45*, 4352-4358.

(104) White, K. M.; Lee, P. L.; Chupas, P. J.; Chapman, K. W.; Payzant, E. A.; Jupe, A. C.; Bassett, W. A.; Zha, C. S.; Wilkinson, A. P. Synthesis, Symmetry, and Physical Properties of Cerium Pyrophosphate. *Chem. Mater.* **2008**, *20*, 3728-3734.

(105) Wallez, G.; Raison, P. E.; Dacheux, N.; Clavier, N.; Bykov, D.; Delevoye, L.; Popa, K.; Bregiroux, D.; Fitch, A. N.; Konings, R. J. M. Triclinic–Cubic Phase Transition and Negative Expansion in the Actinide IV (Th, U, Np, Pu) Diphosphates. *Inorg. Chem.* **2012**, *51*, 4314-4322.

(106) Gallington, L. C. The Role of Disorder in Determining the Physical Properties of Negative Thermal Expansion Materials. Georgia Institute of Technology, 2015.

(107) Taylor, D. Thermal Expansion Data. XII. Complex Oxides: AB_2O_6, AB_2O_7, $A_2B_2O_7$ plus complex aluminates, silicates, and analogous compounds. *British Ceramic Transactions and Journal* **1988**, *87(2)*, 39-45.

(108) Sleight, A. W. Compounds that Contract on Heating. *Inorg. Chem.* **1998**, *37*, 2854-2860.

(109) Onken, H. Uber Zirkonpyroarsenat. *Die Naturwissenschaften* **1965**, *52*, 344.

(110) Le Flem, G. L., J.; and Hagenmuller P. As_2O_5-ThO_2 system. *Bull. Soc. Chim. Fr.* **1966**, *6*, 1880-1883.

(111) Abrahams, S. C.; Bernstein, J. L. Crystal Structure of the Transition-Metal Molybdates and Tungstates. II. Diamagnetic $Sc_2(WO_4)_3$. *J. Chem. Phys.* **1966**, *45*, 2745-2752.

(112) Nassau, K.; Levinstein, H. J.; Loiacono, G. M. A comprehensive study of trivalent tungstates and molybdates of the type $L_2(MO_4)_3$. *J. Phys. Chem. Solids* **1965**, *26*, 1805-1816.

(113) Evans, J. S. O.; Mary, T. A.; Sleight, A. W. Negative Thermal Expansion in $Sc_2(WO_4)_3$. *J. Solid State Chem.* **1998**, *137*, 148-160.

(114) Sleight, A. W.; Brixner, L. H. A new ferroelastic transition in some $A_2(MO_4)_3$ molybdates and tungstates. *J. Solid State Chem.* **1973**, *7*, 172-174.

(115) Evans, J. S. O.; Mary, T. A. Structural Phase Transitions and negative thermal expansion in $Sc_2(MoO_4)_3$. *Int. J. Inorg. Mater.* **2000**, *2*, 143-151.

(116) Mary, T. A.; Sleight, A. W. Bulk thermal expansion for tungstate and molybdates of the type A2M3O12. *J. Mater. Res.* **2011**, *14*, 912-915.

(117) Forster, P. M.; Yokochi, A.; Sleight, A. W. Enhanced Negative Thermal Expansion in $Lu_2W_3O_{12}$. *J. Solid State Chem.* **1998**, *140*, 157-158.

(118) Forster, P. M.; Sleight, A. W. Negative thermal expansion in $Y_2W_3O_{12}$. *Int. J. Inorg. Mater.* **1999**, *1*, 123-127.

(119) Marinkovic, B. A.; Jardim, P. M.; de Avillez, R. R.; Rizzo, F. Negative thermal expansion in $Y_2Mo_3O_{12}$. *Solid State Sci.* **2005**, *7*, 1377-1383.

(120) De Meyer, C.; Bouree, F.; Evans, J. S. O.; De Buysser, K.; Bruneel, E.; Van Driessche, I.; Hoste, S. Structure and phase transition of Sn-substituted $Zr_{1-x}Sn_xW_2O_8$. *J. Mater. Chem.* **2004**, *14*, 2988-2994.

(121) De Buysser, K.; Van Driessche, I.; Vande Putte, B.; Vanhee, P.; Schaubroeck, J.; Hoste, S. Study of Negative Thermal Expansion and Shift in Phase Transition Temperature in Ti^{4+} and Sn^{4+} Substituted ZrW_2O_8 Materials. *Inorg. Chem.* **2008**, *47*, 736-741.

(122) Nakajima, N.; Yamamura, Y.; Tsuji, T. Synthesis and physical properties of negative thermal expansion materials $Zr_{1-x}M_xW_2O_{8-y}$ (M = Sc, In, Y) substituted for Zr(IV) sites by M(III) ions. *Solid State Commun.* **2003**, *128*, 193-196.

(123) Hashimoto, T.; Kuwahara, J.; Yoshida, T.; Nashimoto, M.; Takahashi, Y.; Takahashi, K.; Morito, Y. Thermal conductivity of negative-thermal-expansion oxide, $Zr_{1-x}Y_xW_2O_8$ (x=0.00, 0.01)—temperature dependence and effect of structural phase transition. *Solid State Commun.* **2004**, *131*, 217-221.

(124) Tsuji, T.; Yamamura, Y.; Nakajima, N. Thermodynamic properties of negative thermal expansion materials ZrW_2O_8 substituted for Zr site. *Thermochim. Acta* **2004**, *416*, 93-98.

(125) Yamamura, Y.; Nakajima, N.; Tsuji, T.; Kojima, A.; Kuroiwa, Y.; Sawada, A.; Aoyagi, S.; Kasatani, H. Drastic lowering of the order-disorder phase transition temperatures in $Zr_{1-x}M_xW_2O_{8-y}$ (M=Sc, Y, In) solid solutions. *Phys. Rev. B* **2004**, *70*, 104107 (104101-104106).

(126) Yamamura, Y.; Masago, K.; Kato, M.; Tsuji, T. Comprehensive Interpretation of a Substitution Effect on an Order−Disorder Phase Transition in $A_{1-x}M_xW_2O_{8-y}$ (A = Zr, Hf; M = Trivalent Cations) and Other ZrW_2O_8-Based Solid Solutions. *J. Phys. Chem. B* **2007**, *111*, 10118-10122.

(127) Oyetola, S.; Verbaere, A.; Guyomard, D.; Crosnier, M. P.; Piffard, Y.; Tournoux, M. New ZrP_2O_7-Like Diphosphates of Either Mixed $(M(III)_{1/2}M'(V)_{1/2})$ Cations (M: Sb, Bi, Nd, Eu; M′: Sb, Nb, Ta) or M′(V) Cations (M′: Ta, Nb): Synthesis and Structure. *ChemInform* **1991**, *22*.

(128) Varga, T.; Wilkinson, A. P.; Haluska, M.; Payzant, E. A. Preparation and thermal expansion of $(M^{III0.5}M'^{V0.5})P_2O_7$ with the ZrP_2O_7 structure. *J. Solid State Chem.* **2005**, *178*, 3541-3546.

(129) Yanase, I.; Kojima, T.; Kobayashi, H. Effects of Nb and Y substitution on negative thermal expansion of $ZrV_{2-x}P_xO_7$ (0 <= X <= 0.8). *Solid State Commun.* **2011**, *151*, 595-598.

(130) Sahoo, P. P.; Sumithra, S.; Madras, G.; Row, T. N. G. Synthesis, Structure, Negative Thermal Expansion, and Photocatalytic Property of Mo Doped ZrV_2O_7. *Inorg. Chem.* **2011**, *50*, 8774-8781.

(131) Baiz, T. I.; Gindhart, A. M.; Kraemer, S. K.; Lind, C. Synthesis of $MgHf(WO_4)_3$ and $MgZr(WO_4)_3$ using a non-hydrolytic sol-gel method. *J. Sol-Gel Sci. Technol.* **2008**, *47*, 128-130.

(132) Gindhart, A. M. Synthesis an Characterization of $AA'W_3O_{12}$ Compounds. University of Toledo, 2007.

(133) Gindhart, A. M.; Lind, C.; Green, M. Polymorphism in the negative thermal expansion material magnesium hafnium tungstate. *J. Mater. Res.* **2008**, *23*, 210-213.

(134) Baiz, T. I. Non-Hydrolytic Sol-Gel Synthesis and Characterization of Materials of the Type $AA'M_3O_{12}$. University of Toledo, 2010.

(135) Marinkovic, B. A.; Jardim, P. M.; Ari, M.; de Avillez, R. R.; Rizzo, F.; Ferreira, F. F. Low positive thermal expansion in $HfMgMo_3O_{12}$. *Physica Status Solidi B-Basic Solid State Physics* **2008**, *245*, 2514-2519.

(136) Martinek, C. A.; Hummel, F. A. Subsolidus Equilibria in the System ZrO_2-WO_3-P_2O_5. *J. Am. Ceram. Soc.* **1970**, *53*, 159-161.

(137) Evans, J. S. O.; Mary, T. A.; Sleight, A. W. Structure of $Zr_2(WO_4)(PO_4)_2$ from Powder X-ray Data: Cation Ordering with No Superstructure. *J. Solid State Chem.* **1995**, *120*, 101-104.

(138) Evans, J. S. O.; Mary, T. A.; Sleight, A. W. Negative Thermal Expansion in a Large Molybdate and Tungstate Family. *J. Solid State Chem.* **1997**, *133*, 580-583.

(139) Cetinkol, M.; Wilkinson, A. P. Pressure Dependence of Negative Thermal Expansion in $Zr_2(WO_4)(PO_4)_2$. *Solid State Commun.* **2009**, *149*, 421-424.

(140) Chatterji, T.; Hansen, T. C.; Brunelli, M.; Henry, P. F. Negative thermal expansion of ReO_3 in the extended temperature range. *Appl. Phys. Lett.* **2009**, *94*, 241902:(241903).

(141) Chang, T. S.; Trucano, P. Lattice-Parameter and Thermal-Expansion Of ReO_3 Between 291 And 464K. *J. Appl. Crystallogr.* **1978**, *11*, 286-288.

(142) Chatterji, T.; Freeman, P. G.; Jimenez-Ruiz, M.; Mittal, R.; Chaplot, S. L. Pressure- and temperature-induced M-3 phonon softening in ReO_3. *Phys. Rev. B* **2009**, *79*, 184302.

(143) Chatterji, T.; Henry, P. F.; Mittal, R.; Chaplot, S. L. Negative thermal expansion of ReO_3: Neutron diffraction experiments and dynamical lattice calculations. *Phys. Rev. B* **2008**, *78*, 134105.

(144) Rodriguez, E. E.; Llobet, A.; Proffen, T.; Melot, B. C.; Seshadri, R.; Littlewood, P. B.; Cheetham, A. K. The role of static disorder in negative thermal expansion in ReO_3. *J. Appl. Phys.* **2009**, *105*, 114901:(114906).

(145) Dapiaggi, M.; Fitch, A. N. Negative (and very low) thermal expansion in ReO_3 from 5 to 300 K. *J. Appl. Crystallogr.* **2009**, *42*, 253-258.

(146) Liu, Y.; Wang, Z.; Wu, M.; Sun, Q.; Chao, M.; Jia, Y. Negative thermal expansion in isostructural cubic ReO_3 and ScF_3: A comparative study. *Comput. Mater. Sci.* **2015**, *107*, 157-162.

(147) Mogusmilankovic, A.; Ravez, J.; Chaminade, J. P.; Hagenmuller, P. Ferroelastic Properties of TiF_3, VF_3, CrF_3, FeF_3, GaF_3, Compounds. *Mater. Res. Bull.* **1985**, *20*, 9-17.

(148) Daniel, P.; Bulou, A.; Rousseau, M.; Nouet, J.; Leblanc, M. Raman-Scattering Study of Crystallized MF_3 Compounds (M=Al,Cr,Ga,V,Fe,In) - an Approach to the Short-Range-Order Force-Constants. *Phys. Rev. B* **1990**, *42*, 10545-10552.

(149) Hepworth, M. A.; Jack, K. H.; Peacock, R. D.; Westland, G. J. The Crystal Structures of the Trifluorides Of Iron, Cobalt, Ruthenium, Rhodium, Palladium and Iridium. *Acta Crystallogr.* **1957**, *10*, 63-69.

(150) Kennedy, B. J.; Vogt, T. Powder X-ray diffraction study of the rhombohedral to cubic phase transition in TiF_3. *Mater. Res. Bull.* **2002**, *37*, 77-83.

(151) Chaudhuri, S.; Chupas, P. J.; Wilson, M.; Madden, P.; Grey, C. P. Study of the nature and mechanism of the rhombohedral-to-cubic phase transition in α-AlF_3 with molecular dynamics simulations. *J. Phys. Chem. B* **2004**, *108*, 3437-3445.

(152) Li, C. W.; Tang, X.; Muñoz, J. A.; Keith, J. B.; Tracy, S. J.; Abernathy, D. L.; Fultz, B. Structural Relationship between Negative Thermal Expansion and Quartic Anharmonicity of Cubic ScF_3. *Phys. Rev. Lett.* **2011**, *107*, 195504.

(153) Lazar, P.; Bučko, T.; Hafner, J. Negative thermal expansion of ScF_3: Insights from density-functional molecular dynamics in the isothermal-isobaric ensemble. *Phys. Rev. B* **2015**, *92*, 224302.

(154) Hu, L.; Chen, J.; Sanson, A.; Wu, H.; Guglieri Rodriguez, C.; Olivi, L.; Ren, Y.; Fan, L.; Deng, J.; Xing, X. New Insights into the Negative Thermal Expansion: Direct Experimental Evidence for the "Guitar-String" Effect in Cubic ScF_3. *J. Am. Chem. Soc.* **2016**, *138*, 8320-8323.

(155) Morelock, C. R.; Greve, B. K.; Gallington, L. C.; Chapman, K. W.; Wilkinson, A. P. Negative Thermal Expansion and Compressibility of $Sc_{1-x}Y_xF_3$ ($x < 0.25$). *J. Appl. Phys.* **2013**, *114*, 213501.

(156) Hu, L.; Chen, J.; Fan, L.; Ren, Y.; Rong, Y.; Pan, Z.; Deng, J.; Yu, R.; Xing, X. Zero Thermal Expansion and Ferromagnetism in Cubic $Sc_{1-x}M_xF_3$ (M = Ga, Fe) over a Wide Temperature Range. *J. Am. Chem. Soc.* **2014**, *136*, 13566-13569.

(157) Morelock, C. R.; Gallington, L. C.; Wilkinson, A. P. Evolution of negative thermal expansion and phase transitions in $Sc_{1-x}Ti_xF_3$. *Chem. Mater.* **2014**, *26*, 1936-1940.

(158) Morelock, C. R.; Hancock, J. C.; Wilkinson, A. P. Thermal expansion and phase transitions of α-AlF_3. *J. Solid State Chem.* **2014**, *219*, 143-147.

(159) Morelock, C. R.; Gallington, L. C.; Wilkinson, A. P. Solid solubility, phase transitions, thermal expansion, and compressibility in $Sc_{1-x}Al_xF_3$. *J. Solid State Chem.* **2015**, *222*, 96-102.

(160) Wang, T.; Xu, J.; Hu, L.; Wang, W.; Huang, R.; Han, F.; Pan, Z.; Deng, J.; Ren, Y.; Li, L.; Chen, J.; Xing, X. Tunable thermal expansion and magnetism in Zr-doped ScF_3. *Appl. Phys. Lett.* **2016**, *109*, 181901.

(161) Chen, J.; Gao, Q.; Sanson, A.; Jiang, X.; Huang, Q.; Carnera, A.; Rodriguez, C. G.; Olivi, L.; Wang, L.; Hu, L.; Lin, K.; Ren, Y.; Lin, Z.; Wang, C.; Gu, L.; Deng, J.; Attfield, J. P.; Xing, X. Tunable thermal expansion in framework materials through redox intercalation. *Nat. Commun.* **2017**, *8*, 14441.

(162) Hagenmuller, P.: *Inorganic Solid Fluorides*, 1985.

(163) Chassaing, J.; Monteil, C.; Bizot, D. Crystallochemical and Spectroscopic Study of Fluoroniobates $MNbF_6$ with M = Mg, Ca, Fe, Co, Ni, Zn and Cd. *J. Solid State Chem.* **1982**, *43*, 327-333.

(164) Goubard, F.; Llorente, S.; Bizot, D.; Chassaing, J.; Quarton, M. Antiferrodistortive Order in the New Solid Solution $CrZr_{0.75}Nb_{0.25}F_6$. *J. Solid State Chem.* **1997**, *131*, 231-235.

(165) Goubard, F.; Llorente, S.; Delobbe, V.; Bizot, D.; Chassaing, J. Synthesis and X-ray powder diffraction data for $MNbF_6$ (M=Fe, Co) compounds. *Powder Diffr.* **2013**, *13*, 134-135.

(166) Goubard, F.; Llorente, S.; Gaubicher, J.; Bizot, D.; Chassaing, J. Powder diffraction data for fluorocomplexes of niobium IV: $MNbF_6$ (M=Ca, Mg, Cd, Zn). *Powder Diffr.* **1998**, *13*, 163-165.

(167) Le Mercier, T.; Chassaing, J.; Bizot, D.; Quarton, M. Structural, spectroscopic and magnetic studies of $V^{II}M^{IV}F_6$ compounds with M^{IV} = Zr, Nb. *Mater. Res. Bull.* **1992**, *27*, 259-267.

(168) Poulain, M.; Lucas, J. The system MF_2-ZrF_4 (M=Mg,Mn,Fe,Co,Ni,Zn). The fluorozirconates of the cubic rare earths. *Rev. Chim. Miner.* **1975**, *12*, 9-16.

(169) Poulain, M. L. J. Nouveaux fluorozirconates de metaux de transition. *Comptes Rendus de Seances de l'Academie des Sciences, Serie C* **1970**, *271*, 822-824.

(170) Reinen, D.; Steffens, F. Structure and Bonding in Transition-Metal Fluorides $M^{II}Me^{IV}F_6$ .A. Phase-Transitions. *Z. Anorg. Allg. Chem.* **1978**, *441*, 63-82.

(171) Rodriguez, V.; Couzi, M.; Tressaud, A.; Grannec, J.; Chaminade, J. P.; Soubeyroux, J. L. Structural Phase-Transition in the Ordered Fluorides $M^{II}ZrF_6$ (M^{II} = Co, Zn).1. Structural Study. *Journal of Physics-Condensed Matter* **1990**, *2*, 7373-7386.

(172) Monteil, C.; Chassaing, J. Ternary Fluorides of Pentavalent Niobium and Alkaline Earth Elements. I. Fluorides $MNbF_7$ (M = Magnesium, Calcium). *Chemischer Informationsdienst* **1979**, *10*.

(173) Poulain, M.; Tofield, B. C. The structure of cubic YbZrF7. *J. Solid State Chem.* **1981**, *39*, 314-328.

(174) Bizot, D.; Chassaing, J.; Erb, A. Fluoniobates LnNbf7 de terres rares. *Journal of the Less Common Metals* **1981**, *79*, 39-45.

(175) Poulain, M.; Poulain, M.; Lucas, J. Les fluorozirconates de terres rares LnZrF7. *Mater. Res. Bull.* **1972**, *7*, 319-325.

(176) Poulain, M.; Poulain, M.; Lucas, J. Structure cristalline de SmZrF7. Relations structurales avec le type ReO3. *J. Solid State Chem.* **1973**, *8*, 132-141.

(177) Tofield, B. C.; Poulain, M.; Lucas, J. Non-stoichiometry in anion-excess ReO3 phases; the structure of Zr0.8Yb0.2F3.2O0.3(MX3.5) by powder neutron diffraction. *J. Solid State Chem.* **1979**, *27*, 163-178.

(178) Ticknor, J. O.; Hester, B. R.; Adkins, J. W.; Xu, W.; Yakovenko, A. A.; Wilkinson, A. P. Zero Thermal Expansion and Abrupt Amorphization on Compression in Anion Excess ReO_3-Type Cubic $YbZrF_7$. *Chem. Mater.* **2018**.

(179) Ticknor, J. O. Using Defects in Anion Excess Rhenium Trioxide Type Fluorides to Control Thermal Expansion; Ytterbium Zirconium Fluoride as a Case Study. Georgia Institute of Technology, 2017.

(180) Yang, C.; Zhang, Y.; Bai, J.; Qu, B.; Tong, P.; Wang, M.; Lin, J.; Zhang, R.; Tong, H.; Wu, Y.; Song, W.; Sun, Y. Crossover of thermal expansion from positive to negative by removing the excess fluorines in cubic ReO_3-type $TiZrF_{7-x}$. *J. Mater. Chem. C* **2018**, *6*, 5148-5152.

(181) Baxter, S. J. H., B. R.; Wright, B. R.; and Wilkinson, A. P. Controlling the Negative Thermal Expansion and Response to Pressure in ReO_3-type Fluorides by the Deliberate Introduction of Excess Fluoride: $Mg_{2-x}Zr_xF_{4+2x}$. *In Publication Process* **2019**.

(182) Yang, C.; Zhang, Y.; Bai, J.; Tong, P.; Lin, J.; Tong, H.; Zhang, L.; Wen, W.; Zhang, X.; Sun, Y. Isotropic Low Thermal Expansion over a Wide Temperature Range in Ti1–xZrxF3+x ($0.1 \leq x \leq 0.5$) Solid Solutions. *Inorg. Chem.* **2018**, *57*, 14396-14400.

(183) Miller, W.; Smith, C. W.; Dooling, P.; Burgess, A. N.; Evans, K. E. Reduced thermal stress in composites via negative thermal expansion particulate fillers. *Compos. Sci. Technol.* **2010**, *70*, 318-327.

(184) Yilmaz, S. Phase transformations in thermally cycled Cu/ZrW_2O_8 composites investigated by synchrotron x-ray diffraction. *J. Phys.: Condens. Matter* **2002**, *14*, 365-375.

(185) Yilmaz, S. Thermal mismatch stress development in Cu-ZrW_2O_8 composite investigated by synchrotron X-ray diffraction. *Compos. Sci. Technol.* **2002**, *62*, 1835-1839.

(186) Yilmaz, S.; Dunand, D. C. Finite-element analysis of thermal expansion and thermal mismatch stresses in a Cu 60vol% ZrW_2O_8 composite. *Compos. Sci. Technol.* **2004**, *64*, 1895-1898.

(187) Morelock, C. R.; Suchomel, M. R.; Wilkinson, A. P. A cautionary tale on the use of GE-7031 varnish: low-temperature thermal expansion studies of ScF_3. *J. Appl. Crystallogr.* **2013**, *46*.

(188) NIST Structural Ceramics Database (SCD). National Institute of Standards and Technology, Gaithersburg, MD, 20899: NIST Standard Reference Database Number 30, 2015.

(189) Birch, F. Equation of state and thermodynamic parameters of sodium chloride to 300 kbar in the high-temperature domain. *J. Geophys. Res. B* **1986**, *91*, 4949-4954.

(190) Fang, H.; Dove, M. T. Pressure-induced softening as a common feature of framework structures that have negative thermal expansion. *Phys. Rev. B* **2013**, *87*, 214109.

(191) Hong, F.; Martin, T. D. A phenomenological expression to describe the temperature dependence of pressure-induced softening in negative thermal expansion materials. *J. Phys.: Condens. Matter* **2014**, *26*, 115402.

(192) Fang, H.; Dove, M. T.; Phillips, A. E. Common origin of exotic properties in ceramic and hybrid negative thermal expansion materials. *Phys. Rev. B* **2014**, *89*.

(193) Wachtman, J. B.; Tefft, W. E.; Lam, D. G.; Apstein, C. S. Exponential Temperature Dependence of Young's Modulus for Several Oxides. *Phys. Rev.* **1961**, *122*, 1754-1759.

(194) Anderson, O. L. Derivation of Wachtman's Equation for the Temperature Dependence of Elastic Moduli of Oxide Compounds. *Phys. Rev.* **1966**, *144*, 553-557.

(195) Garai, J.; Laugier, A. The temperature dependence of the isothermal bulk modulus at 1bar pressure. *J. Appl. Phys.* **2007**, *101*, 023514.

(196) Sanson, A. On the Switching between Negative and Positive Thermal Exansion in Framework Structures. *ArXiv preprint arXiv:1809.04499v1* **2018**.

(197) Gatta, G. D.; Lee, Y. Zeolites at high pressure: A review. *Mineralogical Magazine* **2018**, *78*, 267-291.

(198) Demontis, P.; Gulín-González, J.; Ruiz-Puentes, A.; Sant, M.; Gabrieli, A.; Suffritti, G. B. Computational Studies on the Effects of Pressure and Temperature on Zeolite Framework Structures. *Adv. Sci. Lett.* **2017**, *23*, 5824-5827.

(199) Hriljac, J. A. High-pressure synchrotron X-ray powder diffraction studies of zeolites. *Crystallogr. Rev.* **2006**, *12*, 181-193.

(200) Hazen, R. M. Zeolite Molecular Sieve 4A: Anomalous Compressibility and Volume Discontinuities at High Pressure. *Science* **1983**, *219*, 1065.

(201) Lee, Y.; Vogt, T.; Hriljac, J. A.; Parise, J. B.; Artioli, G. Pressure-induced volume expansion of zeolites in the natrolite family. *J. Am. Chem. Soc.* **2002**, *124*, 5466-5475.

(202) Hazen, R. M.; Finger, L. W. Compressibility of zeolite 4A is dependent on the molecular size of the hydrostatic pressure medium. *J. Appl. Phys.* **1984**, *56*, 1838-1840.

(203) Ortiz, A. U.; Boutin, A.; Fuchs, A. H.; Coudert, F.-X. Investigating the Pressure-Induced Amorphization of Zeolitic Imidazolate Framework ZIF-8: Mechanical Instability Due to Shear Mode Softening. *J. Phys. Chem. Lett.* **2013**, *4*, 1861-1865.

(204) Rutter, M. D.; Uchida, T.; Secco, R. A.; Huang, Y.; Wang, Y. Investigation of pressure-induced amorphization in hydrated zeolite Li-A and Na-A using synchrotron X-ray diffraction. *J. Phys. Chem. Solids* **2001**, *62*, 599-606.

(205) Lee, Y.; Hriljac, J. A.; Vogt, T.; Parise, J. B.; Edmondson, M. J.; Anderson, P. A.; Corbin, D. R.; Nagai, T. Phase Transition of Zeolite RHO at High-Pressure. *J. Am. Chem. Soc.* **2001**, *123*, 8418-8419.

(206) Arletti, R.; Ferro, O.; Quartieri, S.; Sani, A.; Tabacchi, G.; Vezzalini, G. Structural deformation mechanisms of zeolites under pressure. *Am. Mineral.* **2003**, *88*, 1416-1422.

(207) Kaye, S. S.; Long, J. R. Hydrogen Storage in the Dehydrated Prussian Blue Analogues $M_3[Co(CN)_6]_2$ (M = Mn, Fe, Co, Ni, Cu, Zn). *J. Am. Chem. Soc.* **2005**, *127*, 6506-6507.

(208) Chapman, K. W.; Chupas, P. J. Pressure Enhancement of Negative Thermal Expansion Behavior and Induced Framework Softening in Zinc Cyanide. *J. Am. Chem. Soc.* **2007**, *129*, 10090-10091.

(209) Fang, H.; Phillips, A. E.; Dove, M. T.; Tucker, M. G.; Goodwin, A. L. Temperature-dependent pressure-induced softening in $Zn(CN)_2$. *Phys. Rev. B* **2013**, *88*, 144103.

(210) Goodwin, A. L.; Keen, D. A.; Tucker, M. G. Large negative linear compressibility of $Ag_3[Co(CN)_6]$. *Proc. Natl. Acad. Sci. U. S. A.* **2008**, *105*, 18708.

(211) Cairns, A. B.; Thompson, A. L.; Tucker, M. G.; Haines, J.; Goodwin, A. L. Rational Design of Materials with Extreme Negative Compressibility: Selective Soft-Mode Frustration in $KMn[Ag(CN)_2]_3$. *J. Am. Chem. Soc.* **2012**, *134*, 4454-4456.

(212) Cairns, A. B.; Catafesta, J.; Levelut, C.; Rouquette, J.; van der Lee, A.; Peters, L.; Thompson, A. L.; Dmitriev, V.; Haines, J.; Goodwin, A. L. Giant negative linear compressibility in zinc dicyanoaurate. *Nat. Mater.* **2013**, *12*, 212.

(213) Duyker, S. G.; Peterson, V. K.; Kearley, G. J.; Studer, A. J.; Kepert, C. J. Extreme compressibility in $LnFe(CN)_6$ coordination framework materials via molecular gears and torsion springs. *Nat. Chem.* **2016**, *8*, 270.

(214) Millward, A. R.; Yaghi, O. M. Metal−Organic Frameworks with Exceptionally High Capacity for Storage of Carbon Dioxide at Room Temperature. *J. Am. Chem. Soc.* **2005**, *127*, 17998-17999.

(215) Zhou, W.; Wu, H.; Hartman, M. R.; Yildirim, T. Hydrogen and Methane Adsorption in Metal−Organic Frameworks: A High-Pressure Volumetric Study. *J. Phys. Chem. C* **2007**, *111*, 16131-16137.

(216) Spencer, E. C.; Angel, R. J.; Ross, N. L.; Hanson, B. E.; Howard, J. A. K. Pressure-Induced Cooperative Bond Rearrangement in a Zinc Imidazolate Framework: A High-Pressure Single-Crystal X-Ray Diffraction Study. *J. Am. Chem. Soc.* **2009**, *131*, 4022-4026.

(217) Moggach, S. A.; Bennett, T. D.; Cheetham, A. K. The Effect of Pressure on ZIF-8: Increasing Pore Size with Pressure and the Formation of a High-Pressure Phase at 1.47 GPa. *Angew. Chem. Int. Ed.* **2009**, *48*, 7087-7089.

(218) Bennett, T. D.; Simoncic, P.; Moggach, S. A.; Gozzo, F.; Macchi, P.; Keen, D. A.; Tan, J.-C.; Cheetham, A. K. Reversible pressure-induced amorphization of a zeolitic imidazolate framework (ZIF-4). *Chem. Commun.* **2011**, *47*, 7983-7985.

(219) Hu, Y. H.; Zhang, L. Amorphization of metal-organic framework MOF-5 at unusually low applied pressure. *Phys. Rev. B* **2010**, *81*, 174103.

(220) Chapman, K. W.; Halder, G. J.; Chupas, P. J. Pressure-Induced Amorphization and Porosity Modification in a Metal−Organic Framework. *J. Am. Chem. Soc.* **2009**, *131*, 17546-17547.

(221) Bennett, T. D.; Cheetham, A. K. Amorphous Metal–Organic Frameworks. *Acc. Chem. Res.* **2014**, *47*, 1555-1562.

(222) Chapman, K. W.; Sava, D. F.; Halder, G. J.; Chupas, P. J.; Nenoff, T. M. Trapping Guests within a Nanoporous Metal–Organic Framework through Pressure-Induced Amorphization. *J. Am. Chem. Soc.* **2011**, *133*, 18583-18585.

(223) Chapman, K. W.; Halder, G. J.; Chupas, P. J. Guest-Dependent High Pressure Phenomena in a Nanoporous Metal−Organic Framework Material. *J. Am. Chem. Soc.* **2008**, *130*, 10524-10526.

(224) Evans, J. S. O.; Hu, Z.; Jorgensen, J. D.; Argyriou, D. N.; Short, S.; Sleight, A. W. Compressibility, Phase Transitions, and Oxygen Migration in Zirconium Tungstate, ZrW_2O_8. *Science* **1997**, *275*, 61-65.

(225) Perottoni, C. A.; de Jornada, J. A. H. Pressure-Induced Amorphization and Negative Thermal Expansion in ZrW_2O_8. *Science* **1998**, *280*, 886-889.

(226) Varga, T.; Wilkinson, A. P.; Jupe, A. C.; Lind, C.; Bassett, W. A.; Zha, C.-S. Pressure-induced amorphization of cubic ZrW_2O_8 studied in-situ and ex-situ by synchrotron x-ray absorption spectroscopy and diffraction. *Phys. Rev. B* **2005**, *72*, 024117.

(227) Jorgensen, J. D.; Hu, Z.; Short, S.; Sleight, A. W.; Evans, J. S. O. Pressure-induced cubic-to-orthorhombic phase transfromation in the negative thermal expansion material HfW_2O_8. *J. Appl. Phys.* **2001**, *89*, 3184-3188.

(228) Chen, B.; Muthu, D. V. S.; Liu, Z. X.; Sleight, A. W.; Kruger, M. B. High-pressure optical study of HfW_2O_8. *J. Phys.: Condens. Matter* **2002**, *14*, 13911-13916.

(229) Sakuntala, T.; Rao, R.; Garg, A. B.; Achary, S. N.; Tyagi, A. K. Amorphization-decomposition behavior of HfW_2O_8 at high pressure. *J. Appl. Phys.* **2008**, *104*, 6.

(230) Grzechnik, A.; Crichton, W. A.; Syassen, K.; Adler, P.; Mezouar, M. A New Polymorph of ZrW_2O_8 Synthesized at High Pressures and High Temperatures. *Chem. Mater.* **2001**, *13*, 4255-4259.

(231) Lind, C.; VanDerveer, D. G.; Wilkinson, A. P.; Chen, J.; Vaughan, M. T.; Weidner, D. J. New High-Pressure Form of the Negative Thermal Expansion Materials Zirconium Molybdate and Hafnium Molybdate. *Chem. Mater.* **2001**, *13*, 487-490.

(232) Varga, T.; Lind, C.; Wilkinson, A. P.; Xu, H.; Lesher, C. E.; Navrotsky, A. Heats of Formation for Several Crystalline Polymorphs and Pressure-Induced Amorphous Forms of AMo_2O_8 (A = Zr, Hf) and ZrW_2O_8). *Chem. Mater.* **2007**, *19*, 468-476.

(233) Carlson, S.; Krogh Andersen, A. M. High-pressure properties of TiP_2O_7, ZrP_2O_7 and ZrV_2O_7. *J. Appl. Crystallogr.* **2001**, *34*, 7-12.

(234) Hemamala, U. L. C.; El-Ghussein, F.; Goedken, A. M.; Chen, B.; Leroux, C.; Kruger, M. B. High-pressure x-ray diffraction and Raman spectroscopy of HfV_2O_7. *Phys. Rev. B* **2004**, *70*, 214114.

(235) Varga, T.; Wilkinson, A. P.; Jorgensen, J. D.; Short, S. Neutron powder diffraction study of the orthorhombic to monoclinic transition in $Sc_2W_3O_{12}$ on compression. *Solid State Sci.* **2006**, *8*, 289-295.

(236) Varga, T.; Wilkinson, A. P.; Lind, C.; Bassett, W. A.; Zha, C.-S. In-situ high pressure synchrotron x-ray diffraction study of $Sc_2W_3O_{12}$ at up to 10 GPa. *Phys. Rev. B* **2005**, *71*, 214106 (214101-214108).

(237) Tamas, V.; Angus, P. W.; Cora, L.; William, A. B.; Chang-Sheng, Z. High pressure synchrotron x-ray powder diffraction study of $Sc_2Mo_3O_{12}$ and $Al_2W_3O_{12}$. *J. Phys.: Condens. Matter* **2005**, *17*, 4271.

(238) Secco, R. A.; Liu, H.; Imanaka, N.; Adachi, G. Pressure-induced amorphization in negative thermal expansion $Sc_2(WO_4)_3$. *J. Mater. Sci. Lett.* **2001**, *20*, 1339-1340.

(239) Gates, S. D.; Colin, J. A.; Lind, C. Non-hydrolytic sol-gel synthesis, properties, and high-pressure behavior of gallium molybdate. *J. Mater. Chem.* **2006**, *16*, 4214-4219.

(240) Karmakar, S.; Deb, S. K.; Tyagi, A. K.; Sharma, S. M. Pressure-induced amorphization in $Y_2(WO_4)_3$: in situ X-ray diffraction and Raman studies. *J. Solid State Chem.* **2004**, *177*, 4087-4092.

(241) Liu, H.; Secco, R. A.; Imanaka, N.; Adachi, G. X-ray diffraction study of pressure induced amorphization in $Lu_2(WO_4)_3$. *Solid State Commun.* **2002**, *121*, 177-180.

(242) Jorgensen, J. D.; Hu, Z.; Teslic, S.; Argyriou, D. N.; Short, S.; Evans, J. S. O.; Sleight, A. W. Pressure-induced cubic-to-orthorhombic phase transition in ZrW_2O_8. *Phys. Rev. B* **1999**, *59*, 215-225.

(243) Pantea, C.; Migliori, A.; Littlewood, P. B.; Zhao, Y.; Ledbetter, H.; Lashley, J. C.; Kimura, T.; Van Duijn, J.; Kowach, G. R. Pressure-induced elastic softening of monocrystalline zirconium tungstate at 300 K. *Phys. Rev. B* **2006**, *73*, 214118.

(244) Aleksandrov, K. S.; Voronov, V. N.; Vtyurin, A. N.; Goryainov, S. V.; Zamkova, N. G.; Zinenko, V. I.; Krylov, A. S. Lattice dynamics and hydrostatic-pressure-induced phase transitions in ScF_3. *J. Exp. Theor. Phys.* **2002**, *94*, 977-984.

(245) Aleksandrov, K. S.; Voronov, V. N.; Vtyurin, A. N.; Krylov, A. S.; Molokeev, M. S.; Pavlovskii, M. S.; Goryainov, S. V.; Likhacheva, A. Y.; Ancharov, A. I. Pressure-induced phase transition in the cubic ScF_3 crystal. *Phys. Solid State* **2009**, *51*, 810-816.

(246) Aleksandrova, M. M.; Bendeliani, N. A.; Blank, V. D.; Dyuzheva, T. I. Phase-Transitions in ScF_3 Under Pressure at 300K. *Inorg. Mater.* **1990**, *26*, 1654-1657.

(247) Greve, B. K. Exploring the Thermal Expansion of Fluorides and Oxyfluorides with ReO_3-type Structures: from Negative to Positive Thermal Expansion. Georgia Institute of Technology, 2011.

(248) Jorgensen, J. E.; Marshall, W. G.; Smith, R. I. The compression mechanism of CrF_3. *Acta Crystallogr. Sect. B: Struct. Sci.* **2004**, *60*, 669-673.

(249) Jorgensen, J. E.; Smith, R. I. On the compression mechanism of FeF_3. *Acta Crystallogr. Sect. B: Struct. Sci.* **2006**, *62*, 987-992.

(250) Davis, M. E. Ordered porous materials for emerging applications. *Nature* **2002**, *417*, 813.

(251) Breck, D. W.: *Zeolite Molecular Sieves*; John Wiley and Sons: New York, 1974.

(252) Flanigan, E. M.: Molecular Sieve Zeolites Technology: The First Twenty-Five Years. In *Zeolites: Science and Technology*; Springer, 1984; Vol. 80.

(253) Li, B.; Wen, H.-M.; Zhou, W.; Xu, Jeff Q.; Chen, B. Porous Metal-Organic Frameworks: Promising Materials for Methane Storage. *Chem* **2016**, *1*, 557-580.

(254) Corma, A. From Microporous to Mesoporous Molecular Sieve Materials and Their Use in Catalysis. *Chem. Rev.* **1997**, *97*, 2373-2420.

(255) McBain, J. W.: The Sorption of Gases and Vapors by Solids. Rutledge and Sons: London, 1932.

(256) Milton, R. M. Molecular Sieves. *Society of Chemical Industry* **1968**, 199.

(257) Milton, R. M. Molecular Sieve Adsorbents. United States Patent 2,882,243.

(258) Flanigen, E. M.; Bennett, J. M.; Grose, R. W.; Cohen, J. P.; Patton, R. L.; Kirchner, R. M.; Smith, J. V. Silicalite, a new hydrophobic crystalline silica molecular sieve. *Nature* **1978**, *271*, 512.

(259) Yang, R. T.: *Gas Separatin by Adsorption Processes*; Butterworth: Boston, 1987.

(260) Breck, D. W.; Eversole, W. G.; Milton, R. M.; Reed, T. B.; Thomas, T. L. Crystalline Zeolites. I. The Properties of a New Synthetic Zeolite, Type A. *J. Am. Chem. Soc.* **1956**, *78*, 5963-5972.

(261) Vermesse, J.; Vidal, D.; Malbrunot, P. Gas Adsorption on Zeolites at High Pressure. *Langmuir* **1996**, *12*, 4190-4196.

(262) Walter J Sesny, L. H. S. Fluid Encapsulation Product. United States Patent.

(263) Fraenkel, D. Hydrogen Encapsulation. *Chem. Tech.* **1981**, *11*, 60-65.

(264) Davis, M. E.; Saldarriaga, C.; Montes, C.; Garces, J.; Crowdert, C. A molecular sieve with eighteen-membered rings. *Nature* **1988**, *331*, 698.

(265) Li, H.; Eddaoudi, M.; O'Keeffe, M.; Yaghi, O. M. Design and synthesis of an exceptionally stable and highly porous metal-organic framework. *Nature* **1999**, *402*, 276.

(266) Chen, B.; Eddaoudi, M.; Hyde, S. T.; O'Keeffe, M.; Yaghi, O. M. Interwoven Metal-Organic Framework on a Periodic Minimal Surface with Extra-Large Pores. *Science* **2001**, *291*, 1021-1023.

(267) Eddaoudi, M.; Kim, J.; Rosi, N.; Vodak, D.; Wachter, J.; O'Keeffe, M.; Yaghi, O. M. Systematic Design of Pore Size and Functionality in Isoreticular MOFs and Their Application in Methane Storage. *Science* **2002**, *295*, 469-472.

(268) Bunzen, H.; Kolbe, F.; Kalytta-Mewes, A.; Sastre, G.; Brunner, E.; Volkmer, D. Achieving Large Volumetric Gas Storage Capacity in Metal–Organic Frameworks by Kinetic Trapping: A Case Study of Xenon Loading in MFU-4. *J. Am. Chem. Soc.* **2018**, *140*, 10191-10197.

(269) Li, J.-R.; Kuppler, R. J.; Zhou, H.-C. Selective gas adsorption and separation in metal–organic frameworks. *Chem. Soc. Rev.* **2009**, *38*, 1477-1504.

(270) Grandjean, F. *Comptes Rendus de l'Academie des ciences* **1909**, *149*, 866.

(271) Barrer, R. M. Molecular-sieve action of solids. *Quarterly Reviews, Chemical Society* **1949**, *3*, 293-320.

(272) Barrer, R. M. *J. Soc. Chem. Ind.* **1945**, *64*, 130.

(273) Colella, C.: Natural zeolites in environmentally friendly processes and applications. In *Stud. Surf. Sci. Catal.*; Kiricsi, I., Pál-Borbély, G., Nagy, J. B., Karge, H. G., Eds.; Elsevier, 1999; Vol. 125; pp 641-655.

(274) Mumpton, F. A.: *Natural Zeolites, Occurrence, Properties, Use*; Pergamon: London, 1978.

(275) Pauling, L. The Formulas of Antimonic Acid and the Antimonates. *J. Am. Chem. Soc.* **1933**, *55*, 1895-1900.

(276) Bartlett, N. Xenon hexafluorolatinate(V), $Xe^{+}[PtF_6]^{-}$. *Proc. Chem. Soc.* **1962**, 218.

(277) Khriachtchev, L.; Pettersson, M.; Runeberg, N.; Lundell, J.; Räsänen, M. A stable argon compound. *Nature* **2000**, *406*, 874.

(278) Wang, Q.; Wang, X. Infrared Spectra of NgBeS (Ng = Ne, Ar, Kr, Xe) and BeS_2 in Noble-Gas Matrices. *J. Phys. Chem. A* **2013**, *117*, 1508-1513.

(279) Frenking, G.; Koch, W.; Gauss, J.; Cremer, D. Stabilities and nature of the attractive interactions in HeBeO, NeBeO, and ArBeO and a comparison with analogs NGLiF, NGBN, and NGLiH (NG = He, Ar). A theoretical investigation. *J. Am. Chem. Soc.* **1988**, *110*, 8007-8016.

(280) Wong, M. W. Prediction of a Metastable Helium Compound: HHeF. *J. Am. Chem. Soc.* **2000**, *122*, 6289-6290.

(281) Li, T.-H.; Mou, C.-H.; Chen, H.-R.; Hu, W.-P. Theoretical Prediction of Noble Gas Containing Anions FNgO- (Ng = He, Ar, and Kr). *J. Am. Chem. Soc.* **2005**, *127*, 9241-9245.

(282) Grochala, W. On Chemical Bonding between Helium and Oxygen. *Pol. J. Chem.* **2009**, *83*, 87-122.

(283) Tariq, N.; Taisan, N. A.; Singh, V.; Weinstein, J. D. Spectroscopic Detection of the LiHe Molecule. *Phys. Rev. Lett.* **2013**, *110*, 153201.

(284) Plisson, T.; Weck, G.; Loubeyre, P. $(N_2)_6Ne_7$ A High Pressure van der Waals Insertion Compound. *Phys. Rev. Lett.* **2014**, *113*, 025702.

(285) Kleppe, A. K.; Amboage, M.; Jephcoat, A. P. New high-pressure van der Waals compound $Kr(H_2)_4$ discovered in the krypton-hydrogen binary system. *Scientific Reports* **2014**, *4*, 4989.

(286) Dewaele, A.; Worth, N.; Pickard, C. J.; Needs, R. J.; Pascarelli, S.; Mathon, O.; Mezouar, M.; Irifune, T. Synthesis and stability of xenon oxides Xe_2O_5 and Xe_3O_2 under pressure. *Nat. Chem.* **2016**, *8*, 784.

(287) Zhu, Q.; Jung, D. Y.; Oganov, A. R.; Glass, C. W.; Gatti, C.; Lyakhov, A. O. Stability of xenon oxides at high pressures. *Nat. Chem.* **2012**, *5*, 61.

(288) Zhu, L.; Liu, H.; Pickard, C. J.; Zou, G.; Ma, Y. Reactions of xenon with iron and nickel are predicted in the Earth's inner core. *Nat. Chem.* **2014**, *6*, 644.

(289) Sun, J.; J. Pickard, C.; J. Needs, R. Formation of noble gas compounds with alkali oxides and sulfides under pressure. *arXiv preprint arXiv:1409.2227v1* **2014**.

(290) Liu, H.; Yao, Y.; Klug, D. D. Stable structures of He and H_2O at high pressure. *Phys. Rev. B* **2015**, *91*, 014102.

(291) Londono, D.; Kuhs, W. F.; Finney, J. L. Enclathration of helium in ice II: the first helium hydrate. *Nature* **1988**, *332*, 141.

(292) Loubeyre, P.; Jean-Louis, M.; LeToullec, R.; Charon-Gérard, L. High pressure measurements of the He-Ne binary phase diagram at 296 K: Evidence for the stability of a stoichiometric $Ne(He_2)$ solid. *Phys. Rev. Lett.* **1993**, *70*, 178-181.

(293) Dong, X.; Oganov, A. R.; Goncharov, A. F.; Stavrou, E.; Lobanov, S.; Saleh, G.; Qian, G.-R.; Zhu, Q.; Gatti, C.; Deringer, V. L.; Dronskowski, R.; Zhou, X.-F.; Prakapenka, V. B.; Konôpková, Z.; Popov, I. A.; Boldyrev, A. I.; Wang, H.-T. A stable compound of helium and sodium at high pressure. *Nat. Chem.* **2017**, *9*, 440.

(294) Miao, M. React with nobility. *Nat. Chem.* **2017**, *9*, 409.

(295) Liu, Z.; Botana, J.; Hermann, A.; Valdez, S.; Zurek, E.; Yan, D.; Lin, H.-q.; Miao, M.-s. Reactivity of He with ionic compounds under high pressure. *Nat. Commun.* **2018**, *9*, 951.

(296) Van Itterbeek, A.; Van Dingenen, W. Adsorption isotherms and heats of adsorption of helium gas on charcoal between 20°K and 6°K - new desorption experiments. *Physica* **1938**, *5*, 529-540.

(297) Hellemans, R.; Van Itterbeek, A.; Van Dael, W. The adsorption of helium, argon and nitrogen on graphite. *Physica* **1967**, *34*, 429-437.

(298) Schirber, J. E.; Kwei, G. H.; Jorgensen, J. D.; Hitterman, R. L.; Morosin, B. Room-Tempertaure Compressibility of C_{60} - Itercalcation Effects with He, Ne, and Ar. *Phys. Rev. B* **1995**, *51*, 12014-12017.

(299) Gunka, P. A.; Dziubek, K. F.; Gladysiak, A.; Dranka, M.; Piechota, J.; Hanfland, M.; Katrusiak, A.; Zachara, J. Compressed Arsenolite As_4O_6 and Its Helium Clathrate $As_4O_6 \cdot 2He$. *Cryst. Growth Des.* **2015**, *15*, 3740-3745.

(300) Sans, J. A.; Manjon, F. J.; Popescu, C.; Cuenca-Gotor, V. P.; Gomis, O.; Munoz, A.; Rodriguez-Hernandez, P.; Contreras-Garcia, J.; Pellicer-Porres, J.; Pereira, A. L. J.; Santamaria-Perez, D.; Segura, A. Ordered helium trapping and bonding in compressed arsenolite: Synthesis of $As_4O_6 \cdot 2He$. *Phys. Rev. B* **2016**, *93*, 5.

(301) Sato, T.; Takada, H.; Yagi, T.; Gotou, H.; Okada, T.; Wakabayashi, D.; Funamori, N. Anomalous behavior of cristobalite in helium under high pressure. *Phys. Chem. Miner.* **2013**, *40*, 3-10.

(302) Sato, T.; Funamori, N.; Yagi, T. Helium penetrates into silica glass and reduces its compressibility. *Nat. Commun.* **2011**, *2*, 5.

(303) Shen, G.; Mei, Q.; Prakapenka, V. B.; Lazor, P.; Sinogeikin, S.; Meng, Y.; Park, C. Effect of helium on structure and compression behavior of SiO_2 glass. *Proc. Natl. Acad. Sci. U. S. A.* **2011**, *108*, 6004-6007.

(304) Yagi, T.; Iida, E.; Hirai, H.; Miyajima, N.; Kikegawa, T.; Bunno, M. High-pressure behavior of a SiO_2 clathrate observed by using various pressure media. *Phys. Rev. B* **2007**, *75*, 6.

(305) Britvin, S. N.; Kashtanov, S. A.; Krzhizhanovskaya, M. G.; Gurinov, A. A.; Glumov, O. V.; Strekopytov, S.; Kretser, Y. L.; Zaitsev, A. N.; Chukanov, N. V.; Krivovichev, S. V. Perovskites with the Framework-Forming Xenon. *Angew. Chem. Int. Ed.* **2015**, *54*, 14340-14344.

(306) Mitchell, R. H.; Welch, M. D.; Chakhmouradian, A. R. Nomenclature of the perovskite supergroup: A hierarchical system of classification based on crystal structure and composition. *Mineralogical Magazine* **2018**, *81*, 411-461.

(307) Anderson, H. U. Review of p-type doped perovskite materials for SOFC and other applications. *Solid State Ionics* **1992**, *52*, 33-41.

(308) Bonanos, N.; Knight, K. S.; Ellis, B. Perovskite solid electrolytes: Structure, transport properties and fuel cell applications. *Solid State Ionics* **1995**, *79*, 161-170.

(309) Bhalla, A. S.; Guo, R.; Roy, R. The perovskite structure—a review of its role in ceramic science and technology. *Mater. Res. Innovations* **2000**, *4*, 3-26.

(310) Tilley, R. J. D.: *Perovskites: Structure-Property Relationships*; john Wiley and Sons, 2016.

(311) Zhu, J.; Li, H.; Zhong, L.; Xiao, P.; Xu, X.; Yang, X.; Zhao, Z.; Li, J. Perovskite Oxides: Preparation, Characterizations, and Applications in Heterogeneous Catalysis. *ACS Catalysis* **2014**, *4*, 2917-2940.

(312) Nitin, L.; Govindachetty, S.; Suresh Kumar, M.; Nilesh, M.; Rohini, K.; Pradeep, D.; Fabien, G. Perovskite-type catalytic materials for environmental applications. *Sci. Technol. Adv. Mater.* **2015**, *16*, 036002.

(313) Kenji, U. Glory of piezoelectric perovskites. *Sci. Technol. Adv. Mater.* **2015**, *16*, 046001.

(314) Raveau, B.; Maignan, A.; Martin, C.; Hervieu, M. Colossal Magnetoresistance Manganite Perovskites: Relations between Crystal Chemistry and Properties. *Chem. Mater.* **1998**, *10*, 2641-2652.

(315) Cava, R. J.; Batlogg, B.; van Dover, R. B.; Murphy, D. W.; Sunshine, S.; Siegrist, T.; Remeika, J. P.; Rietman, E. A.; Zahurak, S.; Espinosa, G. P. Bulk superconductivity at 91 K in single-phase oxygen-deficient perovskite $Ba_2YCu_3O_9$-δ. *Phys. Rev. Lett.* **1987**, *58*, 1676-1679.

(316) Murphy, D. W.; Sunshine, S.; van Dover, R. B.; Cava, R. J.; Batlogg, B.; Zahurak, S. M.; Schneemeyer, L. F. New superconducting cuprate perovskites. *Phys. Rev. Lett.* **1987**, *58*, 1888-1890.

(317) Cohen, R. E. Origin of ferroelectricity in perovskite oxides. *Nature* **1992**, *358*, 136.

(318) Wells, H. L. Über die Cäsium- und Kalium-Bleihalogenide. *Zeitschrift für anorganische Chemie* **1893**, *3*, 195-210.

(319) Goldschmidt, V. M.: *Titanium Pigment and Process of Producing the Same*, 1922.

(320) Weber, D. *Z. Naturforsch.* **1978**, 1443-1445.

(321) Mitzi, D. B.: Synthesis, Structure, and Properties of Organic-Inorganic Perovskites and Related Materials. In *Prog. Inorg. Chem.*, 2007; Vol. 48.

(322) Kojima, A.; Teshima, K.; Shirai, Y.; Miyasaka, T. Organometal Halide Perovskites as Visible-Light Sensitizers for Photovoltaic Cells. *J. Am. Chem. Soc.* **2009**, *131*, 6050-6051.

(323) Im, J.-H.; Lee, C.-R.; Lee, J.-W.; Park, S.-W.; Park, N.-G. 6.5% efficient perovskite quantum-dot-sensitized solar cell. *Nanoscale* **2011**, *3*, 4088-4093.

(324) Kim, H. S.; Lee, C. R.; Im, J. H.; Lee, K. B.; Moehl, T.; Marchioro, A.; Moon, S. J.; Humphry-Baker, R.; Yum, J. H.; Moser, J. E.; Grätzel, M.; Park, N. G. *Nat. Sci. Rep.* **2012**, *2*, 591.

(325) Lee, M. M.; Teuscher, J.; Miyasaka, T.; Murakami, T. N.; Snaith, H. J. Efficient Hybrid Solar Cells Based on Meso-Superstructured Organometal Halide Perovskites. *Science* **2012**, *338*, 643.

(326) Noh, J. H.; Im, S. H.; Heo, J. H.; Mandal, T. N.; Seok, S. I. Chemical Management for Colorful, Efficient, and Stable Inorganic–Organic Hybrid Nanostructured Solar Cells. *Nano Lett.* **2013**, *13*, 1764-1769.

(327) Manser, J. S.; Christians, J. A.; Kamat, P. V. Intriguing Optoelectronic Properties of Metal Halide Perovskites. *Chem. Rev.* **2016**, *116*, 12956-13008.

(328) Saparov, B.; Mitzi, D. B. Organic–Inorganic Perovskites: Structural Versatility for Functional Materials Design. *Chem. Rev.* **2016**, *116*, 4558-4596.

(329) Chen, Q.; De Marco, N.; Yang, Y.; Song, T.-B.; Chen, C.-C.; Zhao, H.; Hong, Z.; Zhou, H.; Yang, Y. Under the spotlight: The organic–inorganic hybrid halide perovskite for optoelectronic applications. *Nano Today* **2015**, *10*, 355-396.

(330) Correa-Baena, J.-P.; Abate, A.; Saliba, M.; Tress, W.; Jesper Jacobsson, T.; Grätzel, M.; Hagfeldt, A. The rapid evolution of highly efficient perovskite solar cells. *Energ. Environ. Sci.* **2017**, *10*, 710-727.

(331) Ansari, M. I. H.; Qurashi, A.; Nazeeruddin, M. K. Frontiers, opportunities, and challenges in perovskite solar cells: A critical review. *J. Photochem. Photobiol. C: Photochem. Rev.* **2018**, *35*, 1-24.

(332) Chen, J.; Hu, L.; Deng, J.; Xing, X. Negative thermal expansion in functional materials: controllable thermal expansion by chemical modifications. *Chem. Soc. Rev.* **2015**, *44*, 3522-3567.

(333) Lind, C.; Coleman, M. R.; Kozy, L. C.; Sharma, G. R. Zirconium Tungstate/Polymer Nanocomposites: Challenges and Opportunities. *Phys. Status Solidi B* **2011**, *248*, 123-129.

(334) Takenaka, K. Negative thermal expansion materials: technological key for control of thermal expansion. *Sci. Technol. Adv. Mater.* **2012**, *13*, 013001.

(335) Della Gaspera, E.; Tucker, R.; Star, K.; Lan, E. H.; Ju, Y. S.; Dunn, B. Copper-Based Conductive Composites with Tailored Thermal Expansion. *ACS Appl. Mater. Interfaces* **2013**, *5*, 10966-10974.

(336) Balch, D. K.; Dunand, D. C. Copper-Zirconium Tungstate Composites Exhibiting Low and Negative Thermal Expansion Influenced by Reinforcement Phase Transformations. *Metall. Mater. Trans. A* **2004**, *35A*, 1159-1165.

(337) Dove, M. T.; Fang, H. Negative thermal expansion and associated anomalous physical properties: review of the lattice dynamics theoretical foundation. *Rep. Prog. Phys.* **2016**, *79*, 066503.

(338) Maczka, M.; Souza Filho, A. G.; Paraguassu, W.; Freire, P. T. C.; Mendes Filho, J.; Hanuza, J. Pressure-induced structural phase transitions and amorphization in selected molybdates and tungstates. *Prog. Mater Sci.* **2012**, *57*, 1335-1381.

(339) Chen, J.; Nittala, K.; Forrester, J. S.; Jones, J. L.; Deng, J. X.; Yu, R. B.; Xing, X. R. The Role of Spontaneous Polarization in the Negative Thermal Expansion of Tetragonal $PbTiO_3$-Based Compounds. *J. Am. Chem. Soc.* **2011**, *133*, 11114-11117.

(340) Rong, Y. C.; Li, M. L.; Chen, J.; Zhou, M.; Lin, K.; Hu, L.; Yuan, W. X.; Duan, W. H.; Deng, J. X.; Xing, X. R. Large negative thermal expansion in non-perovskite lead-free ferroelectric $Sn_2P_2S_6$. *PCCP* **2016**, *18*, 6247-6251.

(341) Yoon, D.; Son, Y. W.; Cheong, H. Negative Thermal Expansion Coefficient of Graphene Measured by Raman Spectroscopy. *Nano Lett.* **2011**, *11*, 3227-3231.

(342) Hu, L.; Chen, J.; Fan, L.; Ren, Y.; Huang, Q.; Sanson, A.; Jiang, Z.; Zhou, M.; Rong, Y.; Wang, Y.; Deng, J.; Xing, X. High-Curie-Temperature Ferromagnetism in $(Sc,Fe)F_3$ Fluorides and its Dependence on Chemical Valence. *Adv. Mater.* **2015**, *27*, 4592-4596.

(343) Handunkanda, S. U.; Curry, E. B.; Voronov, V.; Said, A. H.; Guzmán-Verri, G. G.; Brierley, R. T.; Littlewood, P. B.; Hancock, J. N. Large isotropic negative thermal expansion above a structural quantum phase transition. *Phys. Rev. B* **2015**, *92*, 134101.

(344) Hu, L.; Chen, J.; Xu, J.; Wang, N.; Han, F.; Ren, Y.; Pan, Z.; Rong, Y.; Huang, R.; Deng, J.; Li, L.; Xing, X. Atomic Linkage Flexibility Tuned Isotropic Negative, Zero, and Positive Thermal Expansion in $MZrF_6$ (M = Ca, Mn, Fe, Co, Ni, and Zn). *J. Am. Chem. Soc.* **2016**, *138*, 14530-14533.

(345) Yang, C.; Tong, P.; Lin, J. C.; Guo, X. G.; Zhang, K.; Wang, M.; Wu, Y.; Lin, S.; Huang, P. C.; Xu, W.; Song, W. H.; Sun, Y. P. Size effects on negative thermal expansion in cubic ScF3. *Appl. Phys. Lett.* **2016**, *109*, 023110.

(346) Babel, D.; Tressaud, A.: Crystal Chemistry of Fluorides. In *Inorganic Solid Fluorides*; Hagenmuller, P., Ed.; Materials Science and Technology; Academic Press, Inc.: Orlando, 1985; pp 78-203.

(347) Chassaing, J.; Bizot, D. Synthesis, Spectroscopic and Magnetic Study of NbF_4. *J. Fluorine Chem.* **1980**, *16*, 451-459.

(348) Gortsema, F. P.; Didchenko, R. Preparation and Properties of Niobium Tetrafluoride and Oxyfluorides. *Inorg. Chem.* **1965**, *4*, 182-186.

(349) Goubard, F.; Llorente, S.; Gaubicher, J.; Bizot, D.; Chassaing, J. Powder diffraction data for fluorocomplexes of niobium IV: $MNbF_6$ (M=Ca, Mg, Cd, Zn). *Powder Diffr.* **1998**, *13*, 163-165.

(350) Wang, J.; Toby, B. H.; Lee, P. L.; Ribaud, L.; Antao, S. M.; Kurtz, C.; Ramanathan, M.; Von Dreele, R. B.; Beno, M. A. A dedicated powder diffraction beamline at the Advanced Photon Source: Commissioning and early operational results. *Rev. Sci. Instrum.* **2008**, *79*, 085105.

(351) Lee, P. L.; Shu, D.; Ramanathan, M.; Preissner, C.; Wang, J.; Beno, M. A.; Von Dreele, R. B.; Ribaud, L.; Kurtz, C.; Antao, S. M.; Jiao, X.; Toby, B. H. A twelve-analyzer detector system for high-resolution powder diffraction. *J. Synchrotron Rad.* **2008**, *15*, 427-432.

(352) Angel, R. J. The high-pressure, high tempertaure equation of state of calcium fluoride, CaF_2. *Journal of Physics-Condensed Matter* **1993**, *5*, L141-L144.

(353) Wilkinson, A. P.; Morelock, C. R.; Greve, B. K.; Jupe, A. C.; Chapman, K. W.; Chupas, P. J.; Kurtz, C. Reducing the background from pressure vessels using a BRIM. *J. Appl. Crystallogr.* **2011**, *44*, 1047-1053.

(354) Larson, A. C.; Von Dreele, R. B.: *GSAS - General Structure Analysis System*; Report LA-UR-86-748: Los Alamos Laboratory, 1987.

(355) Toby, B. H. EXPGUI, a graphical user interface for GSAS. *J. Appl. Crystallogr.* **2001**, *34*, 210-213.

(356) Niedervahrenholz, H. G.; Schafer, H. Oxidefluorides of niobium and tantalum. *Z. Anorg. Allg. Chem.* **1987**, *544*, 122-126.

(357) Boysen, H. Ferroelastic phase transitions and domain structures in powders. *Zeitschrift Fur Kristallographie* **2005**, *220*, 726-734.

(358) Gonzalez-Platas, J.; Alvaro, M.; Nestola, F.; Angel, R. EosFit7-GUI: a new graphical user interface for equation of state calculations, analyses and teaching. *J. Appl. Crystallogr.* **2016**, *49*, 1377-1382.

(359) Angel, R. J.; Gonzalez-Platas, J.; Alvaro, M. EosFit7c and a Fortran module (library) for equation of state calculations. *Zeitschrift Fur Kristallographie* **2014**, *229*, 405-419.

(360) Fang, H.; Dove, M. T.; Phillips, A. E. Common origin of negative thermal expansion and other exotic properties in ceramic and hybrid materials. *Phys. Rev. B* **2014**, *89*, 214103.

(361) Fang, H.; Dove, M. T. A phenomenological expression to describe the temperature dependence of pressure-induced softening in negative thermal expansion materials. *Journal of Physics-Condensed Matter* **2014**, *26*, 115402.

(362) Mavoori, H.; Jin, S. Low-Thermal-Expansion Copper Composites via Negative CTE Metallic Elements. *JOM - Journal of Metals* **1998**, 70-72.

(363) Ikuya, Y.; Kazuki, T.; Kenya, O.; Naoaki, H.; Jungeun, K.; Naruki, T.; Ryoji, T.; Masafumi, M.; Norimasa, N.; Toru, I.; Tetsuo, I.; Kenichi, K.; Masaki, T.; Mikio, T. Giant Negative Thermal Expansion in the Iron Perovskite SrCu3Fe4O12. *Angew. Chem. Int. Ed.* **2011**, *50*, 6579-6582.

(364) Goodwin, A. L.; Kepert, C. J. Negative thermal expansion and low-frequency modes in cyanide-bridged framework materials. *Phys. Rev. B* **2005**, *71*, 140301:(140304).

(365) Hester, B. R.; Hancock, J. C.; Lapidus, S. H.; Wilkinson, A. P. Composition, Response to Pressure, and Negative Thermal Expansion in $M^{II}B^{IV}F_6$ (M = Ca, Mg; B = Zr, Nb). *Chem. Mater.* **2017**, *29*, 823-831.

(366) Qin, F.; Chen, J.; Aydemir, U.; Sanson, A.; Wang, L.; Pan, Z.; Xu, J.; Sun, C.; Ren, Y.; Deng, J.; Yu, R.; Hu, L.; Snyder, G. J.; Xing, X. Isotropic Zero Thermal Expansion and Local Vibrational Dynamics in $(Sc,Fe)F_3$. *Inorg. Chem.* **2017**, *56*, 10840-10843.

(367) Han, F.; Hu, L.; Liu, Z.; Li, Q.; Wang, T.; Ren, Y.; Deng, J.; Chen, J.; Xing, X. Local Structure and Controllable Thermal Expansion in the Solid Solution $(Mn_{1-x}Ni_x)ZrF_6$. *Inorganic Chemistry Frontiers* **2017**.

(368) Ravez, J.; Vassilia.M; Muhll, R. V. D.; Hagenmuller, P. Les systems MF_2-TIF_4 (M=Ca, Sr, Ba)). *Rev. Chim. Miner.* **1970**, *7*, 967-973.

(369) Glazer, A. M. Classification of Tilted Octahedra in Perovskites. *Acta Crystallogr.* **1972**, *B28*, 3384-3392.

(370) Blank, H. R.; Frank, M.; Geiger, M.; Greneche, J. M.; Ismaier, M.; Kaltenhauser, M.; Kapp, R.; Kreische, W.; Leblanc, M.; Lossen, U.; Zapf, B. Systematic Investigations of MF_3 Crystalline Compounds (M = Al, Cr, Fe, Ga, In, Sc, Ti, and V) and $Fe_{1-X}M_XF_3$ Mixed Series (M = Ga, Cr, V). *Zeitschrift Fur Naturforschung Section a-a Journal of Physical Sciences* **1994**, *49*, 361-366.

(371) Daniel, P.; Bulou, A.; Rousseau, M.; Nouet, J. Structural Phase-Transitions and Lattice-Dynamics in the Trifluorides MF_3 (M = Al, Cr, Ga, V, Fe, In ...). *Phase Transitions* **1991**, *33*, 91-97.

(372) Herzig, P.; Zemann, J. AB_3 Nets Built from Corner-Connected Octahedra - Geometries, Electrosctatic Lattice Energies, and Stereochemical Discussion. *Zeitschrift Fur Kristallographie* **1993**, *205*, 85-97.

(373) Little, E. J.; Jones, M. M. A complete table of electronegativities. *J. Chem. Educ.* **1960**, *37*, 231.

(374) Shannon, R. Revised effective ionic radii and systematic studies of interatomic distances in halides and chalcogenides. *Acta Crystallographica Section A* **1976**, *32*, 751-767.

(375) Fang, H.; Dove, M. T. Pressure-Induced Softening as a Common Feature of Framework Structures with Negative Thermal Expansion. *Phys. Rev. B* **2013**, *87*, 214109.

(376) Mary, T. A.; Evans, J. S. O.; Vogt, T.; Sleight, A. W. Negative Thermal Expansion from 0.3 to 1050 Kelvin in ZrW_2O_8. *Science* **1996**, *272*, 90-92.

(377) Fisher, D. J.: *Negative Thermal Expansion Materials*; Materials Research Foundations, 2018; Vol. 22.

(378) Takenaka, K. Progress of Research in Negative Thermal Expansion Materials: Paradigm Shift in the Control of Thermal Expansion. *Frontiers in Chemistry* **2018**, *6*, 267.

(379) Hester, B. R.; Wilkinson, A. P. Negative Thermal Expansion, Response to Pressure and Phase Transitions in CaTiF6. *Inorg. Chem.* **2018**, *57*, 11275-11281.

(380) Bizot, D.; Chassaing, J.; Pannetier, J.; Leblanc, M.; Lebail, A.; Ferey, G. Fluorcomplexes of Niobium IV. 5. The Magnetgic-Structure of $MnNbF_6$. *Solid State Commun.* **1986**, *58*, 71-74.

(381) Daniel, P.; Bulou, A.; Rousseau, M.; Nouet, J.; Leblanc, M. Raman-Scattering Study of Crystallized MF_3 Compounds (M = Al, Cr, Ga, V, Fe, In) - An Approach to the Short-Range-Order Force-Constants. *Phys. Rev. B* **1990**, *42*, 10545-10552.

(382) Howard, C. J.; Kennedy, B. J.; Woodward, P. M. Ordered double perovskites - a group-theoretical analysis. *Acta Crystallographica Section B-Structural Science* **2003**, *59*, 463-471.

(383) Morelock, C. R. Thermal Expansion, Compressibility, and Local Structure of Fluorides and Oxyfluorides with the Rhenium Trioxide Structure. Georgia Institute of Technology, 2014.

(384) Shannon, R. D.; Prewitt, C. T. Effective Ionic Radii in Oxides and Fluorides. *Acta Crystallogr., Sect. B* **1969**, *25*, 925-946.

(385) Hester, B. R.; Wilkinson, A. P. Effects of Composition on Crystal Structure, Thermal Expansion, and Response to Pressure in ReO3-type MNbF6(M= Mn and Zn). *J. Solid State Chem.* **2018**.

(386) Qiu, X.; Thompson, J. W.; Billinge, S. J. L. PDFgetX2: a GUI-driven program to obtain the pair distribution function from X-ray powder diffraction data. *J. Appl. Crystallogr.* **2004**, *37*, 678.

(387) Howard, C. J.; Stokes, H. T. Group-theoretical analysis of octahedral tilting in perovskites. *Acta Crystallogr.* **1998**, *B54*, 782-789.

(388) Glazer, A. M. Simple Ways Of Determining Perovskite Structures. *Acta Crystallogr.* **1975**, *A31*, 756-762.

(389) Howard, C. J.; Stokes, H. T. Structures and phase transitions in perovskites - a group-theoretical approach. *Acta Crysatollgr.* **2005**, *A61*, 93-111.

(390) Lee, M. M.; Teuscher, J.; Miyasaka, T.; Murakami, T. N.; Snaith, H. J. Efficient Hybrid Solar Cells Based on Meso-Superstructured Organometal Halide Perovskites. *Science* **2012**, *338*, 643-647.

(391) Mi, Q. X.; Ping, Y.; Li, Y.; Cao, B. F.; Brunschwig, B. S.; Khalifah, P. G.; Galli, G. A.; Gray, H. B.; Lewis, N. S. Thermally Stable N_2-Intercalated WO_3 Photoanodes for Water Oxidation. *J. Am. Chem. Soc.* **2012**, *134*, 18318-18324.

(392) Tessier, F.; Le Gendre, L.; Chevire, F.; Marchand, R.; Navrotsky, A. Thermochemistry of a new class of materials containing dinitrogen pairs in an oxide matrix. *Chem. Mater.* **2005**, *17*, 3570-3574.

(393) Le Gendre, L.; Marchand, R.; Piriou, B. Raman scattering investigations of dinitrogen entities in oxidized $LaTiO_2N$ perovskite. *Eur. J. Solid State Inorg. Chem.* **1997**, *34*, 973-982.

(394) Ping, Y.; Li, Y.; Gygi, F.; Galli, G. Tungsten Oxide Clathrates for Water Oxidation: A First Principles Study. *Chem. Mater.* **2012**, *24*, 4252-4260.

(395) Collings, I. E.; Bykova, E.; Bykov, M.; Petitgirard, S.; Hanfland, M.; Paliwoda, D.; Dubrovinsky, L.; Dubrovinskaia, N. Neon-Bearing Ammonium Metal Formates: Formation and Behaviour under Pressure. *Chemphyschem* **2016**, *17*, 3369-3372.

(396) Haines, J.; Cambon, O.; Levelut, C.; Santoro, M.; Gorelli, F.; Garbarino, G. Deactivation of Pressure-Induced Amorphization in Silicalite SiO_2 by Insertion of Guest Species. *J. Am. Chem. Soc.* **2010**, *132*, 8860-8961.

(397) Efimchenko, V. S.; Fedotov, V. K.; Kuzovnikov, M. A.; Zhuravlev, A. S.; Bulychev, B. M. Hydrogen Solubility in Amorphous Silica at Pressures up to 75 kbar. *J. Phys. Chem. B* **2013**, *117*, 422-425.

(398) Efimchenko, V. S.; Fedotov, V. K.; Kuzovnikov, M. A.; Meletov, K. P.; Bulychev, B. M. Hydrogen Solubility in Cristobalite at High Pressure. *J. Phys. Chem. A* **2014**, *118*, 10268-10272.

(399) Li, G.; Shang, J.; Gu, Q.; Awati, R. V.; Jensen, N.; Grant, A.; Zhang, X.; Sholl, D. S.; Liu, J. Z.; Webley, P. A.; May, E. F. Temperature-regulated guest admission and release in microporous materials. *Nat. Commun.* **2017**, *8*, 15777.

(400) *Fuel Cell Technologies Office. Multi-Year Research, Development, and Demonstration Plan. Planned program activities for 2011-2020*2012.

(401) Hester, B. R.; dos Santos, A. M.; Molaison, J. J.; Hancock, J. C.; Wilkinson, A. P. Synthesis of Defect Perovskites (He2–x□x)(CaZr)F6 by Inserting Helium into the Negative Thermal Expansion Material CaZrF6. *J. Am. Chem. Soc.* **2017**, *139*, 13284-13287.

(402) Rivers, M.; Prakapenka, V. B.; Kubo, A.; Pullins, C.; Holl, C. M.; Jacobsen, S. D. The COMPRES/GSECARS gas-loading system for diamond anvil cells at the Advanced Photon Source. *High Pressure Research* **2008**, *28*, 273-292.

(403) Boehler, R.; Kennedy, G. C. Equation of State of Sodium Chloride up to 32 kbar and 500^{o}C. *J. Phys. Chem. Solids* **1980**, *41*, 517-523.

(404) Prescher, C.; Prakapenka, V. B. DIOPTAS: a program for reduction of two-dimensional X-ray diffraction data and data exploration. *High Pressure Research* **2015**, *35*, 223-230.

(405) Toby, B. H.; Von Dreele, R. B. GSAS-II: the genesis of a modern open-source all purpose crystallography software package. *J. Appl. Crystallogr.* **2013**, *46*, 544-549.

(406) Coates, C. S.; Goodwin, A. L. How to quantify isotropic negative thermal expansion: magnitude, range, or both? *Materials Horizons* **2019**.